

AD-A186 800

DTIC FILE COPY ②
Bulletin 51
(Part 3 of 3 Parts)

THE SHOCK AND VIBRATION BULLETIN

Part 3
Analytical Methods, Dynamic
Analysis, Vehicle Systems

MAY 1981

A Publication of
THE SHOCK AND VIBRATION
INFORMATION CENTER
Naval Research Laboratory, Washington, D.C.

DTIC
ELECTE
NOV 19 1987
S D
C&D



Office of
The Under Secretary of Defense
for Research and Engineering

Approved for public release; distribution unlimited.

87 10 28 006

**BLANK PAGES
IN THIS
DOCUMENT
WERE NOT
FILMED**

SYMPOSIUM MANAGEMENT

THE SHOCK AND VIBRATION INFORMATION CENTER

Henry C. Pusey, Director

Rudolph H. Volin

J. Gordan Showalter

Carol Healey

Elizabeth A. McLaughlin

Bulletin Production

**Publications Branch, Technical Information Division,
Naval Research Laboratory**

THE SHOCK AND VIBRATION BULLETIN

MAY 1981

A Publication of
**THE SHOCK AND VIBRATION
INFORMATION CENTER**
Naval Research Laboratory, Washington, D.C.

The 51st Symposium on Shock and Vibration was held at the Holiday Inn at the Embarcadero, San Diego, CA on October 21-23, 1980. The Naval Ocean Systems Center, San Diego CA was the Host.



**Office of
The Under Secretary of Defense
for Research and Engineering**

Accession For	
NTIS	CRA&I
DTIC	TAB
Unannounced	
Justification	
By	
Distribution /	
Availability Codes	
Dist	Avail and/or Special
A-1	

CONTENTS

PAPERS APPEARING IN PART 3

Analytical Methods

AN IMPROVEMENT TO SHAIKH'S METHOD FOR THE TORSIONAL VIBRATION ANALYSIS OF BRANCHED SYSTEMS 1
B. Dawson, Polytechnic of Central London, London, England and M. Davies, University of Surrey, Surrey, England

STUDY OF GUYAN REDUCTION OF TWO DEGREE OF FREEDOM SYSTEMS 11
F. H. Wolff, A. J. Molnar, Westinghouse R&D Center, Pittsburgh, PA and J. A. Gribik, Basic Technology, Inc., Pittsburgh, PA

A METHOD FOR ESTIMATING THE ERROR INDUCED BY THE GUYAN REDUCTION 19
G. L. Fox, NKF Engineering Associates, Inc., Vienna, VA

CRITICAL SPEEDS OF MULTI-THROW CRANKSHAFTS USING SPATIAL LINE ELEMENT METHOD 25
C. Bagci, Department of Mechanical Engineering, Tennessee Technological University, Cookeville, TN and D. R. Falconer, Durkron Valve Division, Cookeville, TN

Dynamic Analysis

A PARAMETRIC STUDY OF THE IBRAHIM TIME DOMAIN MODAL IDENTIFICATION ALGORITHM 43
R. S. Pappa, NASA Langley Research Center, Hampton, VA and S. R. Ibrahim, Old Dominion University, Norfolk, VA

EFFECTIVE DYNAMIC REANALYSIS OF LARGE STRUCTURES 73
B. P. Wang, University of Virginia, Charlottesville, VA and F. H. Chu, RCA/ASTRO, Princeton, NJ

EFFECT OF STIFFENER ARRANGEMENT ON THE RANDOM RESPONSE OF A FLAT PANEL 81
R. B. Bhat and T. S. Sankar, Department of Mechanical Engineering, Concordia University, Montreal, Quebec, Canada

ON NONLINEAR RESPONSE OF MULTIPLE BLADE SYSTEMS 89
A. Muszynska, University of Dayton Research Institute, Dayton, OH, D. I. G. Jones and T. Lagness, Air Force Wright Aeronautical Laboratories, Wright-Patterson AFB, OH and L. Whitford, Aeronautical Systems Division Computer Center, Wright-Patterson AFB, OH

VIBRATIONS OF A BEAM UNDER MOVING LOADS BY A FINITE ELEMENT FORMULATION CONSISTENT IN THE TIME AND SPATIAL COORDINATES 111
J. J. Wu, U.S. Army Armament Research and Development Command, Benet Weapons Laboratory, Watervliet, NY

THE BEND-BUCKLING OF A RING-STIFFENED CYLINDRICAL SHELL DUE TO WHIPPING EXCITATIONS 131
K. A. Bannister, Naval Surface Weapons Center, White Oak, Silver Spring, MD

RESPONSE OF HYDROFOIL STRUT-FOIL SYSTEMS AFTER IMPACT WITH DEAD-HEAD LOGS 143
H. S. Levine, Weidlinger Associates, Menlo Park, CA and A. P. Misovec, Weidlinger Associates, Chesapeake, VA

TRANSIENT RESPONSE ANALYSIS OF A LARGE RADAR ANTENNA 159
E. Maller, W. A. Loden, Lockheed Palo Alto Research Laboratory, Palo Alto, CA and W. Woltornist, Lockheed Electronics Company, Inc., Plainfield, NJ

FATIGUE LIFE PREDICTION FOR SIMULTANEOUS STRESS AND STRENGTH VARIANCES UNDER RANDOM VIBRATION 169
R. G. Lambert, General Electric Company, Aircraft Equipment Division, Utica, NY

DYNAMIC RESPONSE OF THE PROGRESSIVELY DAMAGING STRUCTURES 177
M. G. Srinivasan, Argonne National Laboratory, Argonne, IL and G. U. Fonseka and D. Krajcinovic, University of Illinois at Chicago Circle, Chicago, IL

Vehicle Systems

SECRET

LATERAL DYNAMICS OF C4 MISSILE F. H. Wolff, Westinghouse R&D Center, Pittsburgh, PA	189
ANALYSIS OF SUBCRITICAL RESPONSE MEASUREMENTS FROM AIRCRAFT FLUTTER TESTS J. C. Copley, Royal Aircraft Establishment, Farnborough, Hampshire, England	199
AIRCRAFT RESPONSE TO OPERATIONS ON RAPIDLY REPAIRED BATTLE DAMAGED RUNWAYS AND TAXIWAYS T. Gerardi, Air Force Wright Aeronautical Laboratories, Wright-Patterson AFB, OH and L. R. Caldwell, Lt Col, Air Force Engineering Services Center, Tyndall AFB, FL	205
A METHOD FOR DETERMINING THE EFFECT OF TRANSPORTATION VIBRATION ON UNITIZED CORRUGATED CONTAINERS T. J. Urbanik, U.S. Department of Agriculture, Madison, WI	213
ACOUSTIC ENVIRONMENT ON THE SURFACE OF A LARGE-SCALE POWERED MODEL OF A VECTORED-ENGINE-OVER-THE-WING STOOL CONFIGURATION L. L. Shaw, Air Force Wright Aeronautical Laboratories, Flight Dynamics Laboratory, Wright-Patterson AFB, OH and S. Y. Lee, Agency for Defense Development, Republic of Korea	225
ACTIVE STABILIZATION OF A SHIP BORNE CRANE S. Sankar and J. Svoboda, Department of Mechanical Engineering, Concordia University, Montreal, Quebec, Canada	237

PAPERS APPEARING IN PART 1

Keynote Address

KEYNOTE ADDRESS

Mr. James E. Colvard, Naval Material Command, Washington, DC

Invited Papers

AN APPROACH TO THE LIMITATION AND CONTROL OF SHIPBOARD VIBRATION
Edward F. Noonan, NKF Engineering Associates, Inc., Vienna, VA

STATE-OF-THE-ART ASSESSMENT OF MOBILITY MEASUREMENTS - A SUMMARY OF EUROPEAN RESULTS
David J. Ewins, Imperial College of London, London, England

DEPARTMENT OF DEFENSE POLICY ON RELIABILITY AND MAINTAINABILITY
Colonel Ben H. Swett, USAF Director of Engineering and Standardization, Defense Industrial Supply Center, Philadelphia, PA

NECESSARY AND SUFFICIENT QUALIFICATION FOR SHOCK
Robert Dyrdaahl, The Boeing Company, Seattle, WA

MYTHS AND SACRED COWS IN SHOCK AND VIBRATION
Henry Caruso, Westinghouse Electric Corporation, Baltimore, MD

Damping

ON MODELING VISCOELASTIC BEHAVIOR
L.C. Rogers, Flight Dynamics Laboratory, AFWAL/FIBA, Wright-Patterson AFB, OH

FINITE ELEMENT PREDICTION OF DAMPING IN BEAMS WITH CONSTRAINED VISCOELASTIC LAYERS
C. D. Johnson, D. A. Keinholtz, Anamet Laboratories, Inc., San Carlos, CA and
L. C. Rogers, Air Force Wright Aeronautical Laboratories, Flight Dynamics Laboratory, WPAFB, OH

DYNAMIC BEHAVIOR OF LATHE SPINDLES WITH ELASTIC SUPPORTS INCLUDING DAMPING BY FINITE ELEMENT ANALYSIS
A. M. Sharan, T. S. Sankar and S. Sankar, Department of Mechanical Engineering, Concordia University, Montreal, Canada

FINITE ELEMENT ANALYSIS OF VISCOELASTICALLY DAMPED SANDWICH STRUCTURES

M. L. Soti, University of Dayton Research Institute, Dayton, OH

PNEUMATIC VIBRATION CONTROL USING ACTIVE FORCE GENERATORS

S. Sanjar and R. R. Guntur, Department of Mechanical Engineering, Concordia University, Montreal, Canada

THE EXPERIMENTAL PERFORMANCE OF AN "ON-OFF" ACTIVE DAMPER

E. J. Krasnicki, Lord Kinematics, Erie, PA

Fluid-Structure Interaction

AN EVALUATION OF: DOUBLE ASYMPTOTIC APPROXIMATION; STAGGERED SOLUTION SCHEMES; USA-STAGS

R. S. Dunham, R. J. James, A. S. Kushner and D. E. Ranta, Pacifica Technology, San Diego, CA

MEDIA-STRUCTURE INTERACTION COMPUTATIONS EMPLOYING FREQUENCY DEPENDENT MESH SIZES WITH THE FINITE ELEMENT METHOD

A. J. Kalinowski and C. W. Nebelung, Naval Underwater Systems Center, New London, CT

SIMILITUDE ANALYSIS AND TESTING OF PROTOTYPE AND 1:13.8 SCALE MODEL OF AN OFFSHORE PLATFORM

C. S. Li, National Taiwan University, Taipei and C. S. Yang, N. G. Dagalakis, W. Messick, University of Maryland, College Park, MD

SOUND PROPAGATION THROUGH LIQUIDS IN VISCOELASTIC CIRCULAR CYLINDERS

R. A. Skop, Naval Research Laboratory, Washington, DC

PAPERS APPEARING IN PART 2

Environmental Testing

OPTIMIZING PRE AND POST PULSES FOR SHAKER SHOCK TESTING

R. T. Fandrich, Harris Corporation, Melbourne, FL

SHOCK, VIBRATION AND FATIGUE IN TRANSPORTATION INDUSTRIES

T. V. Sehadri, Fruehauf Corporation, Detroit, MI

RANDOM IMPACT VIBRATION TESTOR

W. D. Everett, Pacific Missile Test Center, Point Mugu, CA

PARAMETERS FOR DESIGN OF REVERBERANT ACOUSTIC CHAMBERS FOR TESTING AIR-CARRIED MISSILES

T. W. Elliott, Pacific Missile Test Center, Point Mugu, CA

SPACECRAFT MODAL TESTING USING SYSTEMATIC MULTI-SHAKERS SINE-DWELL TESTING TECHNIQUES

F. H. Chu, C. Voohees, W. W. Metzger and R. Wilding, RCA Astro-Electronics, Princeton, NJ

DEVELOPMENT OF A MULTIAXIAL FORCE-PULSE GENERATOR

R. D. Crowson, U.S. Army Waterways Experiment Station, Vicksburg, MS, F. B. Safford, Agabian Associates, El Segundo, CA, W. J. Schuman, Jr., U.S. Army Ballistic Research Laboratory, Aberdeen Proving Ground, MD and R. Frieberg, U.S. Army Electronic Research and Development Command, Fort Monmouth, NJ

VIBRATION QUALIFICATION OF EQUIPMENT MOUNTED IN TORBOPROP AIRCRAFT

L. G. Smith, Hughes Aircraft Company, Fullerton, CA

"QUICK LOOK" ASSESSMENT AND COMPARISON OF VIBRATION SPECIFICATIONS

J. H. Schmidt, The Marquardt Company, Van Nuys, CA

VIBRATION TEST LEVEL CRITERIA FOR AIRCRAFT EQUIPMENT

P. S. Hall, Flight Dynamics Laboratory, Air Force Wright Aeronautical Laboratories, Wright-Patterson AFB, OH

CONSERVATISM IN LEAST FAVORABLE RESPONSE ANALYSIS AND TESTING

T. L. Pass, The University of New Mexico, Albuquerque, NM

Shock Testing

CALCULATING RESPONSES IN HULL MOUNTED ITEMS OF EQUIPMENT IN SUBMARINES COMPARED WITH MEASUREMENTS CARRIED OUT DURING SHOCK TESTS

K. Hellqvist, Kockums AB, Malmo Sweden

A COMPUTER-CONTROLLED MEASURING SYSTEM HAVING 128 ANALOG MEASURING CHANNELS AND FACILITIES FOR SIGNAL ANALYSIS

K. Hellqvist, Kockums AB, Malmo, Sweden

A LARGE-SCALE SUBMARINE SHOCK TEST CARRIED OUT AS PART OF THE SWEDISH SHOCK DESIGN DEVELOPMENT PROGRAM

K. Hellqvist, Kockums AB, Malmo, Sweden

EDESS: AN ELECTROMAGNETICALLY-DRIVEN EXPLOSIVE-SHOCK SIMULATOR

F. J. Sazama and J. B. Whitt, Naval Surface Weapons Center, White Oak, Silver Spring, MD

ANALYSIS OF ENERGY-ABSORBING SHOCK MOUNTS

V. H. Neubert, The Pennsylvania State University, University Park, PA

ANALYSIS OF THE EFFECTS OF EXPLOSIVE FUEL IGNITION ON A AIRCRAFT NOISE SUPPRESSION SYSTEM

V. R. Miller, E. R. Hotz and D. L. Brown, Flight Dynamics Laboratory, Wright-Patterson AFB, OH

FEASIBILITY STUDY FOR THE SURFACE IMPULSE LOADING OF STRUCTURES USING MILD DETONATING FUZE

D. L. Shirey and F. H. Mathews, Sandia National Laboratories, Albuquerque, NM

A THEORY FOR THE CALCULATION OF EXPLOSIVE DEPOSITION PROFILES FROM THE SPRAY PAINTING OF LIGHT INITIATED EXPLOSIVE

F. H. Mathews, Sandia National Laboratories, Albuquerque, NM

Shock Analysis

THE RESPONSE SPECTRUM METHOD OF SOLUTION FOR DISPLACEMENT EXCITATION

F. C. Nelson, College of Engineering, Tufts University, Medford, MA

AN IMPROVED RECURSIVE FORMULA FOR CALCULATING SHOCK RESPONSE SPECTRA

D. O. Smallwood, Sandia National Laboratories, Albuquerque, NM

A FINITE ELEMENT MODEL FOR FAILURE INITIATION IN SHOCK LOADED STRUCTURAL MATERIALS

D. W. Nicholson, Naval Surface Weapons Center, White Oak, Silver Spring, MD

STUDY OF PENETRATION FORCES FOR SUPERSONIC WARHEAD DESIGNS

R. Hassett, J. C. S. Yang, J. Richardson and H. Walpert, Naval Surface Weapons Center, Silver Spring, MD

TITLES AND AUTHORS OF PAPERS PRESENTED IN THE SHORT DISCUSSION TOPICS SESSION

NOTE: These papers were only presented at the Symposium. They are not published in the Bulletin and are only listed here as a convenience.

ERROR EVALUATION OF INELASTIC RESPONSE SPECTRUM METHOD FOR EARTHQUAKE DESIGN

M. Paz, University of Louisville, Louisville, KY

EXPERIMENTAL EVALUATION OF APPROXIMATIONS OF RESPONSE TO RANDOM EXCITATION OF OSCILLATOR WITH NONLINEAR DAMPING

A. E. Galef, TRW, Redondo Beach, CA

NONLINEAR SHOCK ANALYSIS OF RESILIENTLY MOUNTED SHIPBOARD EQUIPMENT SYSTEMS

M. P. Pakstys, General Dynamics/Electric Boat Division, Groton, CT

THE APPLICATION OF VIBRATION THEORY TO THE DESIGN OF ACCELERATION RESISTANT MAN-MACHINE DEVICES

D. W. Repperger, Air Force Aerospace Medical Research Laboratory, Wright-Patterson AFB, OH

HUMAN VIBRATION TESTING USING FREQUENCY AND ACCELERATION SWEEPS
J.C. Guignard, Naval Biodynamics Laboratory, New Orleans, LA

BLADE FLUTTER INSTABILITY OF A HORIZONTAL AXIS WIND POWERED GENERATOR
A. Muszynska, University of Dayton Research Institute, Dayton, OH and G.T.S. Done, The City University, London, UK

SPIN PIT TESTS OF DAMPED TURBINE BLADES
R. Donicic, University of Dayton Research Institute, Dayton, OH

DYNAMIC AND THERMAL STRESS ANALYSIS OF AN 'MIC' MODULE
V. R. Beatty, Harris GISD, Melbourne, FL

DAMPING MATERIAL PROPERTIES FROM SANDWICH BEAM DATA USING SIXTH ORDER THEORY
L. Rogers and R. W. Gordon, Air Force Wright Aeronautical Laboratories, Wright-Patterson AFB, OH

REPORT OF THE I.E.S. SHOCK AND VIBRATION COMMITTEE'S BROADBAND VIBRATION WORKING GROUP ON SCREENING OF ELECTRONIC HARDWARE
W. Silver, Westinghouse Electric Corp., Baltimore, MD

RAILCAR VIBRATION TESTING IN THE RAIL DYNAMICS LABORATORY
W. D. Dorland, DOT-Transportation Test Center, Pueblo, CO

THE HOLOGRAPHIC ANALYSIS OF LARGE VEHICLE STRUCTURES
G. Gerhart and G. Arutunian, U.S. Army Tank-Automotive Research and Development Command, Warren, MI

SWEPT NARROW BAND RANDOM ON RANDOM IMPLEMENTED ON AN HP6451C FOURIER ANALYZER
F. T. Mercer, Sandia National Laboratories, Albuquerque, NM

ON COMPLEX-VALUED MODE SHAPES, MODELS FOR STRUCTURAL DAMPING, AND MINI-COMPUTER MODAL ANALYSIS TECHNIQUES
P. W. Whaley, University of Nebraska, Lincoln, NE

APPLICATION OF THE IEEE-488 INSTRUMENTATION BUS IN THE VIBRATION LABORATORY
L. G. Smith, Hughes Aircraft Company, Fullerton, CA

SHOCK RESPONSE AND SPECTRAL ANALYSIS DEMONSTRATION
C. T. Morrow, Consultant, Encinitas, CA

ANALYTICAL METHODS

AN IMPROVEMENT TO SHAIKH'S METHOD FOR THE TORSIONAL VIBRATION ANALYSIS OF BRANCHED SYSTEMS

B. Dawson
Polytechnic of Central London
London, England

and

M. Davies
University of Surrey
Surrey, England

A globally convergent iteration technique developed by the authors for application to residual function value vibration analysis methods is developed as an extension to the method proposed by Shaikh. This yields a fully automatic, efficient and foolproof method irrespective of the natural frequency distribution or frequency range of the problems.

The iteration formula in the extended method requires the first and second derivatives of the residual determinant as well as the determinant itself and the method of derivation of these derivatives via both a matrix transfer and Holzer procedure is presented.

Illustrative examples of the application of the extended method to the solution of the torsional natural frequencies of marine geared drive systems are presented which demonstrate the power and efficiency of the extended method, irrespective of the natural frequency distribution or the frequency range of the problem.

INTRODUCTION

The rapidly increasing adoption of branched drive arrangements for driven machinery coupled with increasing power requirements of geared systems has led to a requirement for efficient methods of torsional vibration analysis for large order multi-junction-point branched systems.

A number of methods are currently available and these may in general be divided into two types, namely (i) system matrix eigenvalue extraction methods, and (ii) trial and error search methods based on the matrix transfer/Holzer procedures.

System matrix methods have the advantage of ease of application to a wide variety of systems since all that is required is the formulation of the system matrix equation followed by eigenvalue extraction using a standard library program. The method, however, has limitations in respect of (i) size of computer required, and (ii) efficiency of solution if only a limited number of lower frequencies are required.

The Holzer method is well favoured by marine engineers on many years of system application. However, when applied to branched systems, computational problems arise since poles appear in the residual-function curve making the search procedure for zero residual function values far from a trivial task even using a digital computer.

Shaikh [1] has developed a matrix transfer procedure based on the formation of a residual-function determinant which assumes zero values at natural frequencies. This technique has the effect of removing the poles from the residual-function determinant curve. The method still, however, requires an efficient and automatic determinant search technique to make it an attractive alternative to system matrix methods. Standard techniques are far from automatic, efficient, foolproof procedures when faced with residual-function curves with very uneven zero distributions and with clusters of close zeros. In particular, at higher frequencies, where the residual curve becomes very sensitive to frequency, the search becomes a very time-consuming pin-pointing operation.

In this paper a globally convergent iteration technique developed by the authors [2] for application to residual-function methods of vibration analysis is applied to extend the method proposed by Shaikh. This yields a fully automatic, efficient and foolproof method over any frequency range, irrespective of the distribution of natural frequencies in that range.

The iteration formula in the extended method requires the first and second derivatives of the residual-function determinant as well as the determinant itself. The method of calculating these derivatives via both a matrix transfer and Holzer procedure is presented in this paper.

Illustrative examples of the application of the extended method to the solution of the torsional natural frequencies of marine geared drive systems are presented which demonstrate the power and efficiency of the extended method

HOLZER FORMULATION OF RESIDUAL-FUNCTION DETERMINANT

Considering first the straight torsional vibration system shown in Fig. 1, with rotor inertias I_r ($r = 1, \dots, n$) and shaft stiffnesses k_r ($r = 1, \dots, n-1$) as marked, the following equations may easily be derived:

$$\theta_s = \theta_{s-1} - \lambda \sum_{r=1}^{s-1} \frac{I_r \theta_r}{k_{s-1}} \quad (s = 2, \dots, n) \quad (1)$$

$$\text{and} \quad \lambda \sum_{r=1}^n I_r \theta_r = R \quad (2)$$

where $\lambda \equiv \omega^2$ denotes the square of a circular frequency ω , θ is the torsional vibration amplitude at rotor r , and R is the residual torque at rotor n which under free vibration conditions must be zero. The residual torque R is determined by assuming an arbitrary value for θ_1 and applying the set of equations (1) and (2) seriatim.

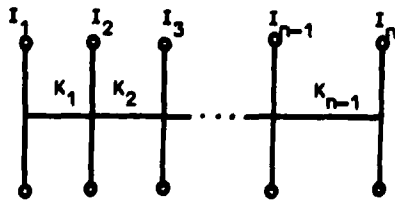


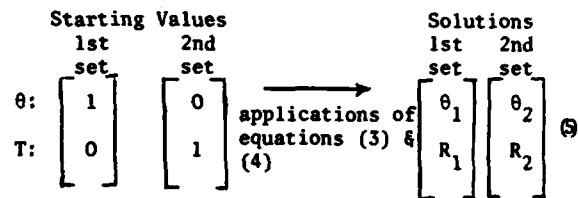
Fig. 1 - Straight torsional vibration system

If, however, the system shown in Fig. 1 is one of the branches of a multi-branched system there will be a torque T_1 present at rotor 1. The residual torque R may be derived assuming arbitrary values of both θ_1 and T_1 by using the modified equations:

$$\theta_s = \theta_{s-1} - \sum_{r=1}^{s-1} \frac{\lambda I_r \theta_r + T_1}{k_{s-1}} \quad (s = 2, \dots, n) \quad (3)$$

$$\text{and} \quad T_1 + \lambda \sum_{r=1}^n I_r \theta_r = R. \quad (4)$$

In this case the general solution is obtained as a linear combination of fundamental solutions obtained using two linearly independent sets of starting values θ_1 and T_1 . For this sub-system the procedure is indicated symbolically by the following representation:



The complete solution is a linear combination of the two linearly independent solutions namely:

$$\theta = \alpha_1 \theta_1 + \alpha_2 \theta_2 \quad (6)$$

$$R = \alpha_1 R_1 + \alpha_2 R_2, \quad (7)$$

corresponding to the starting values $\theta = \alpha_1$, $T = \alpha_2$. As before, the residual torque R is zero when λ is the square of a natural frequency of the system.

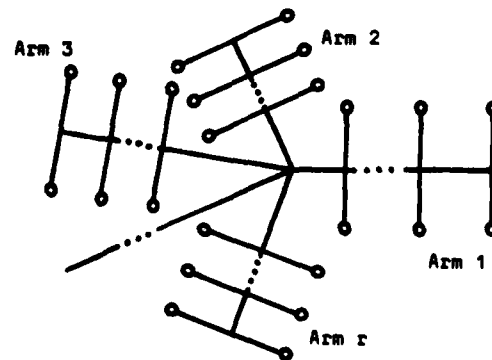


Fig. 2 - Single branch-point system

For the system illustrated in Fig. 2, which comprises r arms meeting in a single branch-point, the solution is obtained by applying the foregoing algorithm to each branch arm, in each case starting from the branch point with the starting values given in tabular form in the transformation (8) below. The significance of the notation in this and subsequent transformations is as follows: (i) for the starting values a single suffix or the first of a pair of suffices denotes the branch point and the second suffix the branch arm; (ii) for the solutions the first suffix is the number assigned to the solution set and the second suffix or a single suffix denotes the branch arm.

$$\Delta \equiv \begin{vmatrix} R_{11} & R_{21} & 0 & \dots & 0 \\ R_{12} & 0 & R_{32} & \dots & 0 \\ \vdots & \vdots & \vdots & \ddots & \vdots \\ R_{1r} & 0 & 0 & \dots & R_{r+1,r} \\ 0 & 1 & 1 & \dots & 1 \end{vmatrix} = 0. \quad (13)$$

Since the process of generating the residual torques via equations (3) and (4) give the variable elements of Δ as polynomials in λ ,

		Starting values					Solutions				
		1st set	2nd set	3rd set	..	(r+1)th set	1st set	2nd set	3rd set	..	(r+1)th set
Branch	θ_1	1	0	0	..	0	θ_{11}	θ_{21}	0	..	0
arm 1	T_{11}	0	1	0	..	0	R_{11}	R_{21}	0	..	0
Branch	θ_1	1	0	0	..	0	θ_{12}	0	θ_{32}	..	0
arm 2	T_{12}	0	0	1	..	0	R_{12}	0	R_{32}	..	0
	\vdots	\vdots	\vdots	\vdots	\vdots	\vdots	\vdots	\vdots	\vdots	\vdots	\vdots
Branch	θ_1	1	0	0	..	0	θ_{1r}	0	0	..	$\theta_{r+1,r}$
arm r	T_{1r}	0	0	0	..	1	R_{1r}	0	0	..	$R_{r+1,r}$

Application of equations (3) & (4) \longrightarrow

Having obtained the fundamental solutions shown in this table, the free-end conditions of the branch arms gives, in terms of the foregoing notation:

$$R_1 = \alpha_1 R_{11} + \alpha_2 R_{21} = 0 \quad (9)$$

$$R_2 = \alpha_1 R_{12} + \alpha_3 R_{32} = 0 \quad (10)$$

$$R_r = \alpha_1 R_{1r} + \alpha_{r+1} R_{r+1,r} = 0. \quad (11)$$

Equilibrium of the initial torques at the junction point requires

$$T_{11} + T_{12} + \dots + T_{1r} = 0,$$

i.e. $\alpha_2 + \alpha_3 + \dots + \alpha_{r+1} = 0. \quad (12)$

Equations (9) through (12) comprise a system of $r+1$ homogeneous linear algebraic equations in $\alpha_1, \alpha_2, \dots, \alpha_{r+1}$. Therefore at a natural frequency the $(r+1)$ th order residual-function determinant

it follows that the determinant Δ is itself a polynomial in λ and is therefore free from poles, as stated earlier.

AUTOMATIC ROOT SEARCHING METHOD

It has been shown by the authors [3] that for straight systems the Holzer method may be extended to calculate $dR/d\lambda$ and $d^2R/d\lambda^2$ using the recurrence relationships

$$\phi_s = \phi_{s-1} - \sum_{r=1}^{s-1} \frac{I_r (\lambda \phi_r + \theta_r)}{k_{s-1}} \quad (s = 2, \dots, n) \quad (14)$$

$$\psi_s = \psi_{s-1} - \sum_{r=1}^{s-1} \frac{I_r (\lambda \psi_r + 2\phi_r)}{k_{s-1}} \quad (s = 2, \dots, n) \quad (15)$$

contemporaneously with equations (3) and (4),

where $\phi_r = \frac{d\theta_r}{d\lambda}$ and $\psi_r = \frac{d^2\theta_r}{d\lambda^2}$.

The results expressed in equations (14) and (15) were obtained from equations (1) and (2) for straight torsional systems. However,

they continue to apply to equations (3) and (4) in respect of any branch of a branched system provided T_1 is held constant, and therefore to the fundamental solutions giving rise to the variable residual-elements of Δ in (13). Thus

$$\frac{dR}{d\lambda} = \sum_{r=1}^n I_r(\lambda\phi_r + \theta_r) \quad (16)$$

and
$$\frac{d^2R}{d\lambda^2} = \sum_{r=1}^n I_r(\lambda\psi_r + 2\phi_r). \quad (17)$$

The residual-function elements and their first and second derivatives are then used in the iteration formula

$$\lambda^{(k+1)} = \lambda^{(k)} + \left[\frac{|\Delta|}{\sqrt{\left(\frac{d\Delta}{d\lambda}\right)^2 - \Delta \frac{d^2\Delta}{d\lambda^2}}} \right]_{\lambda=\lambda^{(k)}} \quad (k=0,1,\dots) \quad (18)$$

which yields a fully automatic, globally convergent, root search procedure [2].

For the single branch point system shown in Fig. 2 the derivatives of the elements of the determinant in equation (13) are obtained contemporaneously with the fundamental solutions according to scheme (19), where primes denote differentiation with respect to λ . The first and second derivatives with respect to λ of the residual determinant Δ are then obtained by the determinant differentiation algorithm described by the authors [4]. Application of the square root iteration formula (18) then yields a fully automatic, efficient search procedure. This approach is readily extended to multi-branch point systems. Thus, for the two branch point system described by Shaikh [1] and illustrated in Fig. 3 the solution, ignoring higher derivatives, is obtained as shown in scheme (20).

	Starting Values					→	Solutions				
	1st set	2nd set	3rd set	..	(r+1)th set		1st soln	2nd soln	3rd soln	..	(r+1)th soln
Branch arm 1	θ_1	1	0	0	..	0	θ_{11}	θ_{21}	0	..	0
	T_{11}	0	1	0	..	0	R_{11}	R_{21}	0	..	0
	θ_1'	0	0	0	..	0	θ_{11}'	θ_{21}'	0	..	0
	T_{11}'	0	0	0	..	0	R_{11}'	R_{21}'	0	..	0
	θ_1''	0	0	0	..	0	θ_{11}''	θ_{21}''	0	..	0
	T_{11}''	0	0	0	..	0	R_{11}''	R_{21}''	0	..	0
Branch arm 2	θ_1	1	0	0	..	0	θ_{12}	0	θ_{32}	..	0
	T_{12}	0	0	1	..	0	R_{12}	0	R_{32}	..	0
	θ_1'	0	0	0	..	0	θ_{12}'	0	θ_{32}'	..	0
	T_{12}'	0	0	0	..	0	R_{12}'	0	R_{32}'	..	0
	θ_1''	0	0	0	..	0	θ_{12}''	0	θ_{32}''	..	0
	T_{12}''	0	0	0	..	0	R_{12}''	0	R_{32}''	..	0
Branch arm r	θ_1	1	0	0	..	0	θ_{1r}	0	0	..	$\theta_{r+1,r}$
	T_{1r}	0	0	0	..	1	R_{1r}	0	0	..	$R_{r+1,r}$
	θ_1'	0	0	0	..	0	θ_{1r}'	0	0	..	$\theta_{r+1,r}'$
	T_{1r}'	0	0	0	..	0	R_{1r}'	0	0	..	$R_{r+1,r}'$
	θ_1''	0	0	0	..	0	θ_{1r}''	0	0	..	$\theta_{r+1,r}''$
	T_{1r}''	0	0	0	..	0	R_{1r}''	0	0	..	$R_{r+1,r}''$

Equations (3), (4), (14)-(17) (19)

derivatives are computed for each arm in turn and the determinant then formed from the topology of the system.

MATRIX TRANSFER FORMULATION

It has been shown by the authors [5] that, for straight systems, extended point and field transfer matrices of order 6 may be used in a matrix multiplication process leading to the relationship $Z_n^R = [A]Z_1^L$ relating the state vectors at the two end-points, where $[A]$ is a 6×6 matrix whose elements a_{ij} ($i, j = 1, \dots, 6$) are functions of λ , and $\bar{Z} = \{\theta', T, \theta'', T'', \theta''', T'''\}$. The significance of the notation in this relationship is that a superfix denotes a point immediately to the left(L) or right(R) of the point indicated by the corresponding suffix when the system is viewed so that the numbering 1, 2, ..., n of consecutive inertias proceeds from left to right.

Since this relationship is unaffected by multiplication of both sides by an arbitrary scalar quantity, an arbitrary constant value may be assigned to θ_1^L , and using the boundary condition $T_1^L = 0$ (assuming a free end) the remaining elements of the vector Z_1^L become $\theta_1^L = T_1^L = \theta_1^{''L} = T_1^{''L} = 0$. The elements of the vectors Z_n^R are then functions of λ via the elements of $a_{ij}(\lambda)$, and inserting the boundary values we find that

$$T_n^R = a_{21}\theta_1^L; T_n'^R = a_{41}\theta_1^L; T_n''^R = a_{61}\theta_1^L$$

and

$$\theta_n^R = a_{11}\theta_1^L; \theta_n'^R = a_{31}\theta_1^L; \theta_n''^R = a_{51}\theta_1^L.$$

$$\text{Hence } a_{41} = a_{21}, a_{61} = a_{21}, a_{31} = a_{11}$$

$$\text{and } a_{51} = a_{11} \tag{29}$$

	Starting Values Z_1^L					$Z_n^R = [A]Z_1^L$	Solutions Z_n^R				
	1st set	2nd set	3rd set	..	(r+1)th set		1st set	2nd set	3rd set	..	(r+1)th set
arm 1	θ_1	1	0	0	..	0	$\theta_{11}^L = a_{111}$	$\theta_{21}^L = a_{121}$	0	..	0
	T_{11}	0	1	0	..	0	$R_{11}^L = a_{211}$	$R_{21}^L = a_{221}$	0	..	0
	θ_1'	0	0	0	..	0	$\theta_{11}'^L = a_{311}$	$\theta_{21}'^L = a_{321}$	0	..	0
	T_{11}'	0	0	0	..	0	$R_{11}'^L = a_{411}$	$R_{21}'^L = a_{421}$	0	..	0
	θ_1''	0	0	0	..	0	$\theta_{11}''^L = a_{511}$	$\theta_{21}''^L = a_{521}$	0	..	0
	T_{11}''	0	0	0	..	0	$R_{11}''^L = a_{611}$	$R_{21}''^L = a_{621}$	0	..	0
arm 2	θ_1	1	0	0	..	0	$\theta_{12}^L = a_{112}$	0	$\theta_{32}^L = a_{122}$..	0
	T_{12}	0	0	1	..	0	$R_{12}^L = a_{212}$	0	$R_{32}^L = a_{222}$..	0
	θ_1'	0	0	0	..	0	$\theta_{12}'^L = a_{312}$	0	$\theta_{32}'^L = a_{322}$..	0
	T_{12}'	0	0	0	..	0	$R_{12}'^L = a_{412}$	0	$R_{32}'^L = a_{422}$..	0
	θ_1''	0	0	0	..	0	$\theta_{12}''^L = a_{512}$	0	$\theta_{32}''^L = a_{522}$..	0
	T_{12}''	0	0	0	..	0	$R_{12}''^L = a_{612}$	0	$R_{32}''^L = a_{622}$..	0
arm r	θ_1	1	0	0	..	0	$\theta_{1r}^L = a_{11r}$	0	0	..	$\theta_{r+1,r}^L = a_{12r}$
	T_{1r}	0	0	0	..	1	$R_{1r}^L = a_{21r}$	0	0	..	$R_{r+1,r}^L = a_{22r}$
	θ_1'	0	0	0	..	0	$\theta_{1r}'^L = a_{31r}$	0	0	..	$\theta_{r+1,r}'^L = a_{32r}$
	T_{1r}'	0	0	0	..	0	$R_{1r}'^L = a_{41r}$	0	0	..	$R_{r+1,r}'^L = a_{42r}$
	θ_1''	0	0	0	..	0	$\theta_{1r}''^L = a_{51r}$	0	0	..	$\theta_{r+1,r}''^L = a_{52r}$
	T_{1r}''	0	0	0	..	0	$R_{1r}''^L = a_{61r}$	0	0	..	$R_{r+1,r}''^L = a_{62r}$

(30)

thus giving the λ -derivatives of the elements a_{21} and a_{11} in terms of other elements of the matrix [A].

Likewise an arbitrary constant value may be assigned to T_1^L , and θ_1^L set equal to zero, in which case it can similarly be shown that

$$a_{42} = a_{22}'; a_{62} = a_{22}''; a_{32} = a_{12}'$$

and $a_{52} = a_{12}''$. (31)

Thus, taking two sets of linearly independent boundary values in the same manner as for the Holzer method, on applying the extended transfer method to the several arms of a multi-branched system which meet at a particular junction point denoted by 1, we obtain scheme (30) above.

In scheme (30) the previous notation is extended by denoting the (i,j)th element of [A] for the rth branch arm by a_{ijr} .

Applying this table to the single junction shown in Fig. 2, the free-end boundary conditions give

$$\alpha_1 R_{11} + \alpha_2 R_{21} = 0,$$

i.e. $\alpha_1 a_{211} + \alpha_2 a_{221} = 0,$ (32)

$$\alpha_1 R_{12} + \alpha_3 R_{32} = 0,$$

i.e. $\alpha_1 a_{212} + \alpha_3 a_{222} = 0.$ (33)

.....

$$\alpha_1 R_{1r} + \alpha_{r+1} R_{r+1,r} = 0,$$

i.e. $\alpha_1 a_{21r} + \alpha_{r+1} a_{22r} = 0.$ (34)

The equilibrium of the initial torques at the junction 1 give

$$T_{11} + T_{12} + \dots + T_{1r} = 0,$$

i.e. $\alpha_2 + \alpha_3 + \dots + \alpha_{r+1} = 0.$ (35)

At a natural frequency the determinant of the coefficients of $\alpha_1, \alpha_2, \alpha_3, \dots, \alpha_{r+1}$ in equations (32) through (35) must vanish and hence

$$\Delta(\lambda) \equiv \begin{vmatrix} a_{211} & a_{221} & 0 & 0 & \dots & 0 \\ a_{212} & 0 & a_{222} & 0 & \dots & 0 \\ a_{213} & 0 & 0 & a_{223} & \dots & 0 \\ \vdots & \vdots & \vdots & \vdots & \vdots & \vdots \\ a_{21r} & 0 & 0 & 0 & \dots & a_{22r} \\ 0 & 1 & 1 & 1 & \dots & 1 \end{vmatrix} = 0. (36)$$

When applying the iterative formula (18) to find the zeros of this determinant, the first and

second λ -derivatives of the elements of Δ are given directly from the elements of [A] by applying formulae (29) and (31).

The extension to multi-junction branched systems is performed exactly in the way described under the Holzer formulation.

ILLUSTRATIVE EXAMPLES

The extension to Shaikh's method has been applied to solve the following systems:

Example (i): Shaikh's [1] single branch point main drive shaft system, shown schematically in Fig. 4.

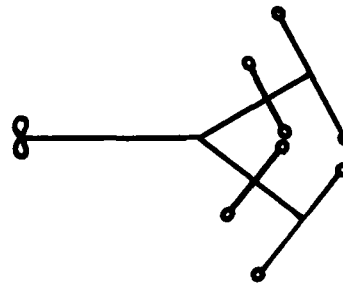
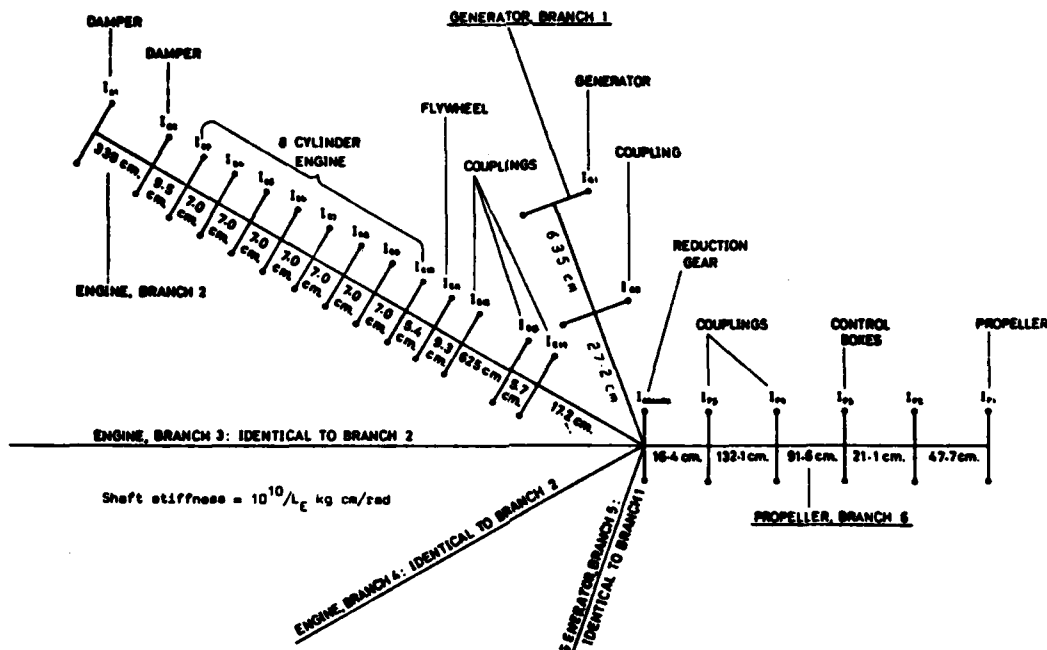


Fig. 4 - Shaikh's single branch point main drive ship system

Example (ii): A single branch point marine propulsion unit shown in Fig. 5. This unit comprises three identical engine branches, two identical generator branches, a reduction gear and a propeller drive shaft branch.

Example (iii): The same system as in Fig. 5, but augmented by a third generator, identical to those on branch arms 1 and 5, connected at the control box I_{p3} .

The results using the Holzer formulation of these problems are presented in Tables 1-3, which give the computed natural frequencies and the corresponding numbers of iterations. The program incorporates a control parameter set by the user for the frequency separation tolerance [2], i.e. the coarsest acceptable resolution for close frequencies. This was pre-set at 0.1 rad/s. However, the square root iterative algorithm (18) terminates at the limiting precision of the computer, and the number of iterations shown in the tables are those required to attain this limiting precision, which is many times finer than the prescribed tolerance.



BRANCH	I_{11}	I_{12}	I_{13} - I_{14}	I_{21}	I_{22}	I_{23}	I_{24}	I_{31}	I_{32}	I_{33}	I_{34}	I_{35}	I_{36}	I_{37}	I_{38}
INERTIA kg. cm. s^2	4880	248	2008	37080	2710	410	8820	36200	884	48000	4000	1478	672	374	40340

Fig. 5 - Equivalent branched system of marine propulsion unit

Table 1

Shaikh's Example
(Example (i). Fig.4)

Natural frequency (rad/s)	Number of iterations	Natural frequency Shaikh's values (rad/s)
13.264	3	13.25
43.950	3	43.95
179.937	3	-
847.487	7	-
852.778	6	-

RESULTS

Inspection of Table 1-3 demonstrates the excellent search characteristic of the method. It should, however, be pointed out that tuning-fork type frequencies (so-called anti-resonance frequencies) have been suppressed in examples having identical branch arms meeting in a common branch point. Thus in example (ii) the three identical engine branches and two identical generator branches were replaced in the computations by only one engine branch and only one generator branch. The in-phase torque contributions of all the engine arms and all the generator arms were allowed for by assuming respective torque contributions of $3T_{1,engine}$

Table 2

Marine Propulsion Unit
(Example (ii). Fig.5)

Nontuning-fork type natural frequencies

Natural frequency (c.p.m.)	Number of iterations
175.517	4
220.867	4
441.160	4
741.800	3
1823.189	5
2060.573	4
3340.436	5
4573.950	7
4717.807	4
6171.244	6
6268.212	4
7018.011	5
7343.151	4
9851.445	5
12028.960	5
13027.054	5
13789.528	6
15074.529	4
15850.686	5
20431.929	6
21425.442	4

and $2T_{1,generator}$ at the branch point. By means of this device the numerical difficulties associated with finding multiple zeros of the

Table 3
Marine Propulsion Unit
Example (iii). Two branch-point system
Nontuning-fork type natural frequencies.

Natural frequency values (c.p.m.)	Number of iterations
154.832	5
183.226	4
271.845	4
441.512	4
741.800	3
1823.188	5
1953.283	4
3340.312	5
4573.950	7
4623.500	6
5220.852	4
6171.491	6
6268.212	4
7343.151	4
9068.698	6
9851.445	5
12028.960	6
13027.127	7
13789.528	6
15074.529	5
15850.686	4
20431.929	5
21425.442	4

determinantal function is avoided, as well as reducing the order of the residual-function determinant - in this particular case from 7 to 4.

Of course, if the tuning-fork type frequencies of the system are required they may be found by a separate Holzer calculation for a straight system with the branch-point end fixed.

Application of the extension of Shaikh's method to complex multi-branched systems presents no further difficulties. The order of the residual-function determinant is equal to the total number of branch and link arms plus the number of branch points, and the structure of the determinant may easily be generated from the topology of the system.

CONCLUSIONS

An extension to Shaikh's method has been presented that enables the natural frequencies of branched systems to be efficiently and automatically determined over any frequency range.

The method has distinct advantages over system matrix methods insofar as (i) it has only a small random access memory requirement and (ii) a limited range of frequencies can be explored without the need to determine all the frequencies of the system.

REFERENCES

1. N. Shaikh, "A Direct Method for Analysis of branched torsional system", Trans. A.S.M.E. Section B. Jnl. of Engineering for Industry, 96, pp1001-1009, 1974
2. B. Dawson & M. Davies, "An Accelerated Automatic Root Search Algorithm for Iterative Methods in Vibration Analysis", Int. J. Num. Meth. Engng., 12, pp809-820, 1978
3. B. Dawson & M. Davies, "An Improved Holzer Procedure for torsional Vibration Analysis", Jnl. Mech. Engng. Sci., 17, pp26-30, 1975
4. M. Davies & B. Dawson, "The Iterative Solution of Two-point Linear Differential Eigenvalue Problems", Quart. J. Appl. Mech. and Math., 26, pp249-263, 1973
5. B. Dawson and M. Davies, "An Extended Matrix Transfer Method with an Automatic Root Search Capability", Int. J. Num. Meth. Engng., 10, pp67-76, 1976

DISCUSSION

Voice: Considering the Myklestad or Holzer methods applied to bending type beam problems. We finally gave up and started using an eigenvalue extraction method as being one that guarantees that you don't miss modes, one that is more automated and perhaps more appropriate for inexperienced engineers who may make a mistake. Are you going in this direction too?

Mr. Dawson: Oh yes, we are actually using this. In fact a lot of people still use Holzer method of course.

Voice: Not in this country I would think, I don't know.

Mr. Dawson: In the UK it is still used but I do confess the finite element method has taken over everything. In my opinion this is a very, very efficient procedure. The trouble with beams was that the Myklestad or the matrix transfer method tended to only work out the first few frequencies. This doesn't apply to torsional vibrations and so there is no problem on how many frequencies. But, when people used the Myklestad - transfer matrix methods for beams they found they could only get the first basic frequencies so it tended to have it's problems that way. It doesn't have the problems this way for torsional vibrations. It is basically a small iterative formula combined with a

searching technique. The cost store is remarkably small. You won't miss frequencies. I think the problem in the past was that there was not an efficient search method. We believe we've now developed an efficient search method and I will say that this is applicable to all problems where you have to search for zeros of a function and therefore it could be used to extract eigenvalues from the characteristic determinant.

Voice: Can you zero in any particular frequency, or do you have to go from the first?

Mr. Dawson: No, wherever you start it will then zero into the next frequency. So you can in fact consider a range of frequencies or you can start from any position you want. So if we give it a starting value it will immediately jump to the next eigenvalue or frequency to its increasing right. It always proceeds one way. We have published quite a number of papers on this technique and they are quoted in the paper. I will just say that in the paper I haven't mentioned the topology of the system so you won't actually get the ideas of the topology. All I did was to determine the determinant in the same way Shaikh did. And the point with Shaikh's work you couldn't see how the determinant is formed for different systems. Now in our technique you can immediately form that determinant.

STUDY OF GUYAN REDUCTION OF TWO
DEGREE OF FREEDOM SYSTEMS

F. H. Wolff and A. J. Molnar
Westinghouse R&D Center
Pittsburgh, Pennsylvania

J. A. Gribik
Basic Technology, Inc.
Pittsburgh, Pennsylvania

ABSTRACT

This paper evaluates errors in matching the 1st mode frequency and shape of a 2 mass model when a Guyan Reduction is applied to the model.

INTRODUCTION

Dynamic analyses of large complicated finite element models are efficiently managed by reducing the number of active degrees of freedom (d.o.f.). The Guyan Reduction Technique⁽¹⁾ which, in effect, eliminates d.o.f. by applying constraint forces to balance inertia forces at the eliminated nodes is frequently used. After a Guyan Reduction, the equations of motion consist of reduced mass and stiffness matrices and a reduced forcing function vector. In general, the reduced models will accurately represent the original model, at least for the lower modes of vibration, if the active d.o.f. are selected carefully:

- (1) select active d.o.f. that best describe the modes of interest,
- (2) avoid eliminating d.o.f. which have associated large mass,
- (3) retain d.o.f. which may have significant motion in modes whose frequencies are in the range of interest or lower.

Although there is evidence that accuracy can be maintained even after drastic reductions on d.o.f., little is known quantitatively about the errors incurred. This study was made to determine magnitudes of error involved in reducing a

simple 2 mass (2 d.o.f.) model. Two Guyan Reduced models were generated by first eliminating the interior node (Reduced Model No. 1), then by eliminating the exterior node (Reduced Model No. 2). Errors in matching the 2 mass model exact 1st mode frequency and shape with the approximate 1st mode frequency and shape of both reduced models were calculated for various mass and stiffness ratios. The errors can be formulated in terms of any 2 of several variables (mass ratio, stiffness ratio, frequency ratio, etc.). Since a scheme which automatically selects the active d.o.f. has been proposed^{(2), (3)}, the errors are presented as functions of stiffness ratio for various mass ratios. The definition of stiffness ratio is consistent with the criteria used in the automatic selection technique^{(2), (3)}, i.e., the stiffness at a node corresponds to the diagonal element of the stiffness matrix.

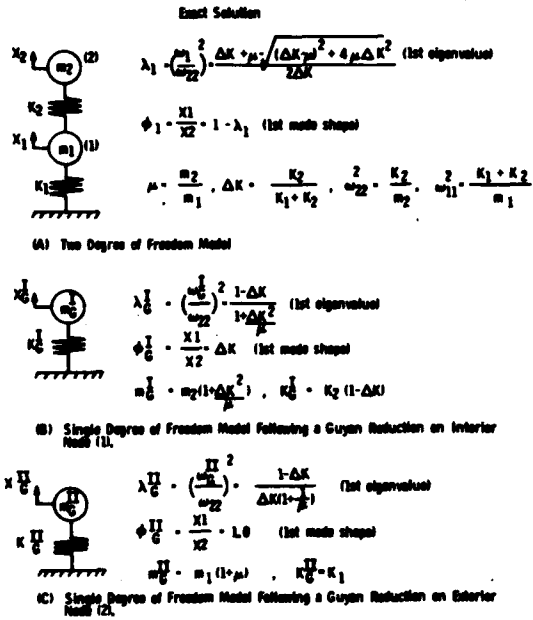


Fig. 1 - Original two degree of freedom model and reduced models

ERROR ANALYSIS

The exact solution (4) for the normalized 1st mode natural frequency of the 2 mass model (Fig. 1A) can be expressed in terms of a mass ratio and a stiffness ratio as

$$\lambda_1 = \left(\frac{\omega_1}{\omega_{22}}\right)^2 \quad (1)$$

$$= \frac{\Delta K + \mu - \sqrt{(\Delta K + \mu)^2 + 4\mu\Delta K^2}}{2\Delta K}$$

where

ω_1 is the 1st mode natural frequency

$$\Delta K = \mu\beta^2 = \frac{k_2}{k_1 + k_2} \quad \text{for } \beta = \omega_{22}/\omega_{11}$$

$$\mu = M_2/M_1$$

$$\omega_{22}^2 = k_2/M_2; \quad \omega_{11}^2 = \frac{k_1 + k_2}{M_1}$$

Also, the 1st mode shape is

$$\phi_1 = \frac{x_1}{x_2} = 1 - \lambda_1 \quad (2)$$

After a Guyan Reduction on the 2 mass model by eliminating the interior node (1), the 1st mode frequency and mode shape of the reduced model (Fig. 1B) are

$$\lambda_G^I = \left(\frac{\omega_G^I}{\omega_{22}^I}\right)^2 = \frac{1 - \Delta K}{1 + \frac{\Delta K^2}{\mu}} \quad (3)$$

and

$$\phi_G^I = x_1^I/x_2^I = \Delta K \quad (4)$$

where

superscript I means node (1) eliminated

The errors in 1st mode frequency (ϵ_f) and shape functions (ϵ_ϕ) are

$$\epsilon_f^I(\Delta K, \mu) = \frac{\omega_G^I - \omega_1}{\omega_1} = \sqrt{\frac{\lambda_G^I}{\lambda_1}} - 1 \quad (5)$$

and

$$\epsilon_\phi^I(\Delta K, \mu) = \frac{\phi_G^I - \phi_1}{\phi_1}$$

$$= \frac{\Delta K - (1 - \lambda_1)}{1 - \lambda_1} \quad \text{for } 1 - \lambda_1 \neq 0 \quad (6)$$

Similarly, eliminating the exterior node (2) gives for the 1st mode frequency and mode shape of the reduced model (Fig. 1C)

$$\lambda_G^{II} = \left(\frac{\omega_G^{II}}{\omega_{22}^{II}} \right)^2 = \frac{1 - \Delta K}{\Delta K \left(1 + \frac{1}{\mu} \right)} \quad (7)$$

and

$$\phi_G^{II} = 1.0 \quad (8)$$

where

superscript II means node (2) eliminated

Likewise, the corresponding error functions can be defined as

$$\epsilon_f^{II}(\Delta K, \mu) = \sqrt{\frac{\lambda_G^{II}}{\lambda_1}} - 1 \quad (9)$$

and

$$\epsilon_\phi^{II}(\Delta K, \mu) = \frac{\phi_G^{II} - \phi_1}{\phi_1} \quad (10)$$

$$= \frac{\lambda_1}{1 - \lambda_1} \quad \text{for } 1 - \lambda_1 \neq 0$$

The error functions (eq's (5), (6), (9) and (10)) were calculated for a range of parameters.

DISCUSSION OF RESULTS

When a degree of freedom is eliminated from the 2 mass model (Fig. 1A) the errors are functions of 2 variables, namely, mass ratio ($\mu = M_2/M_1$) and stiffness ratio

$$(\Delta K = \frac{K_2}{K_1 + K_2}).$$

Errors in both the 1st mode frequency and shape were studied for two Guyan reduced models:

- (1) Reduced Model No. 1 - interior node (1) eliminated
- (2) Reduced Model No. 2 - exterior node (2) eliminated

Maintaining accuracy in both frequency and mode shape is important in guaranteeing representative models since both are fundamental to any response calculations.

(1) Reduced Model No. 1

Fig. 2 shows the error in 1st mode frequency when the interior node (1) is eliminated as a function of all possible stiffness ratios ($0 < \Delta K < 1$) and a particular range of mass ratios ($.1 \leq \mu \leq 10.$). Because of the error function definitions, a positive error indicates the reduced model yields frequencies higher than the true frequencies. The frequency error curves are bounded over the stiffness ratio range; i.e., for any mass ratio the error in 1st mode frequency has a maximum at some intermediate value of stiffness ratio. The error in frequency increases as the ratio of mass at the active d.o.f. (M_2) to mass at the eliminated node (M_1) decreases; i.e., more mass located at the eliminated node means a larger error.

The error in the 1st mode shape is always negative; accordingly, the approximate mode shape amplitude is less than the true amplitude. With all other considerations equal, response calculations made with the reduced model would tend to be lower than those from the 2 mass model. Therefore, the reduced model may predict nonconservative results.

Fig.'s 2 and 3 show the frequency and mode shape error curves for a practical range of mass ratios ($\mu \geq 1$). Even when the mass ratio is unity, the maximum possible error in frequency is only 2.6%. Hence, eliminating the interior node whose mass is less than that at the active node guarantees an extremely accurate 1st mode frequency (Fig. 2) regardless of the ratio of stiffness between the 2 nodes. However, the error in mode shape can be as large as -0.2 (Fig. 3).

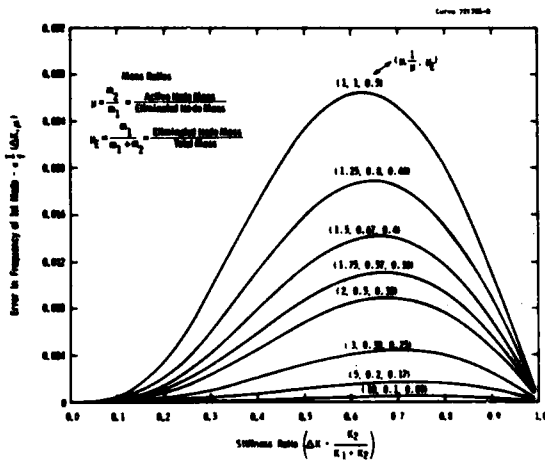


Fig. 2 - Error in frequency of 1st mode for reduced model No. 1 (interior node (1) eliminated as a D.O.F.)

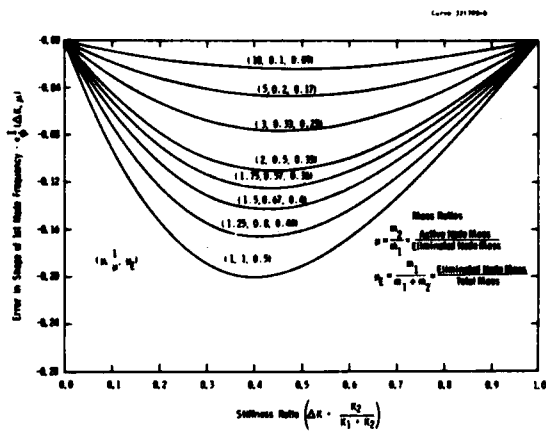


Fig. 3 - Error in shape of 1st mode for reduced model No. 1 (interior node (1) eliminated as a D.O.F.)

As an alternative way to present the error data, Fig.'s 4 and 5 show the error in frequency and shape of the 1st mode as a function of stiffness ratio for various frequency ratios (ratio of frequency at active node to eliminated node). Only cases where the frequency at the active node is less than or equal to the frequency at the eliminated node were considered ($\beta \leq 1$). The match in both the 1st mode frequency and shape improve with decreasing frequency ratio. For example, where the frequency at the active node is $\frac{1}{2}$ the frequency at the eliminated node ($\beta = .5$), the maximum errors are 0.0069 and -0.25 in frequency and shape, respectively. Although the error in shape is large at low stiffness ratios, it improves as the stiffness ratio increases.

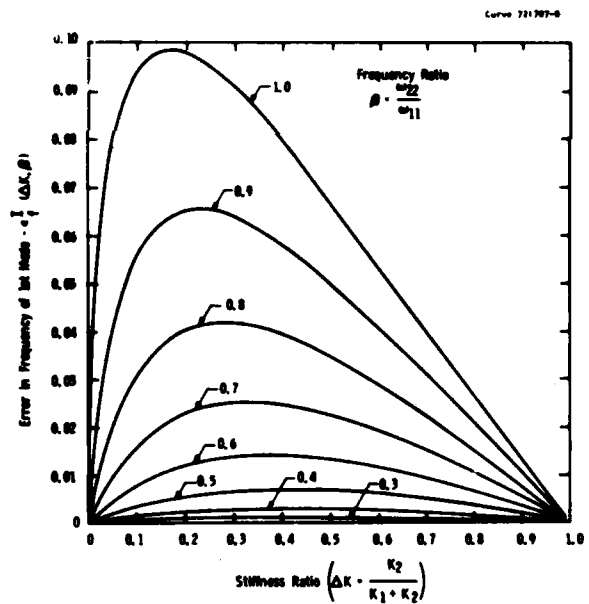


Fig. 4 - Error in frequency of 1st mode for reduced model No. 1 (interior node (1) eliminated as a D.O.F.)

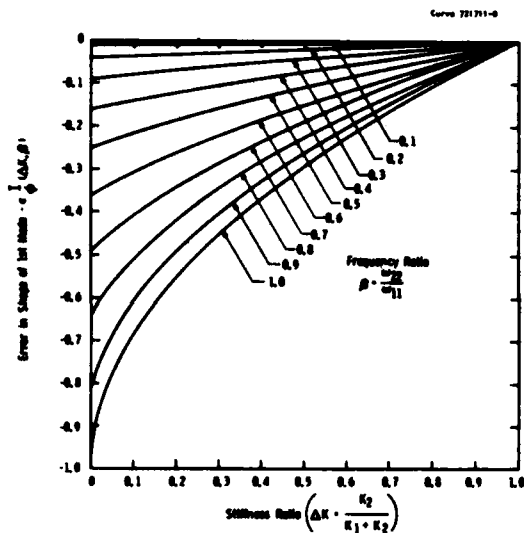


Fig. 5 - Error in shape of 1st mode for reduced model No. 1 (Interior node (1) eliminated as a D.O.F.)

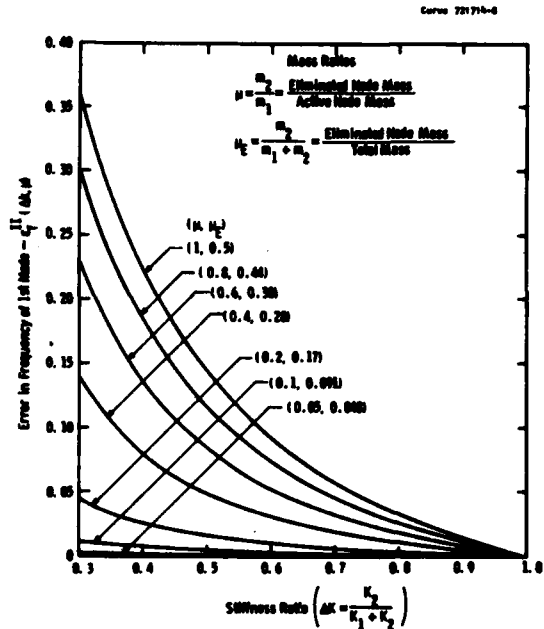


Fig. 6 - Error in frequency of 1st mode for reduced model No. 2 (exterior node (2) eliminated as a D.O.F.)

(2) Reduced Model No. 2

When the exterior node (2) is eliminated as a d.o.f., the error functions illustrate characteristics different from those observed in the foregoing model. Both the 1st mode frequency and shape errors are unbounded as the stiffness ratio (ratio of stiffness at active node to eliminated node) approaches 0, while both errors approach 0 as the stiffness ratio approaches unity. As before when the ratio of mass at the eliminated node (2) to the active node (1) increases the errors increase. Fig.'s 6 and 7 involve errors in 1st mode frequency and shape for cases where the mass at the eliminated node (2) is less than or equal to mass at the active node (1). For mass ratios near unity, the errors are acceptable only when the stiffness at the eliminated node (K_2) is nearly the stiffness at the active node ($K_1 + K_2$). However, for small mass ratios ($\mu \leq .2$) the errors are small over the entire range shown ($.3 < \Delta K < 1$); e.g., the error in frequency is less than 5% (Fig. 6). The error in mode shape for $\mu < .2$ becomes less than +20% once the stiffness ratio surpasses 0.5. Since the mode shape error is positive, the reduced model No. 2 response would tend to be conservative.

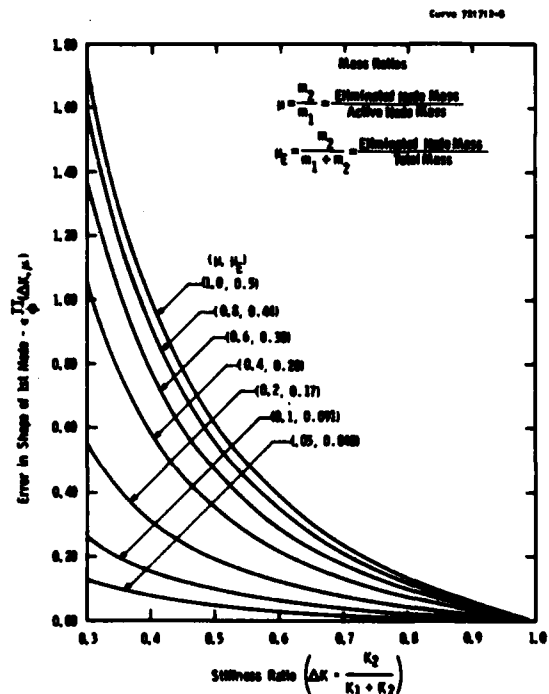


Fig. 7 - Error in shape of 1st mode for reduced model No. 2 (exterior node (2) eliminated as a D.O.F.)

Curves of the errors in 1st mode frequency and shape for various frequency ratios (ratio of frequency at eliminated node to active node = $\beta = \omega_{22}/\omega_{11}$) show as the frequency ratio increases, the errors decrease (Fig.'s 8 and 9). For example, when the frequency at the eliminated node is twice the frequency at the active node ($\beta = \frac{\omega_{22}}{\omega_{11}} = 2$) the maximum possible errors are +.7% and +33% in frequency and mode shape, respectively. Moreover, the error in mode shape decreases to +10% as the stiffness ratio becomes greater than 0.58.

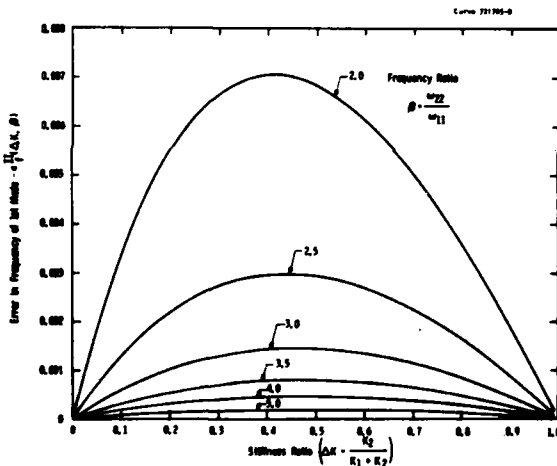


Fig. 8 - Error in frequency of 1st mode for reduced model No. 2 (exterior node (2) eliminated as a D.O.F.)

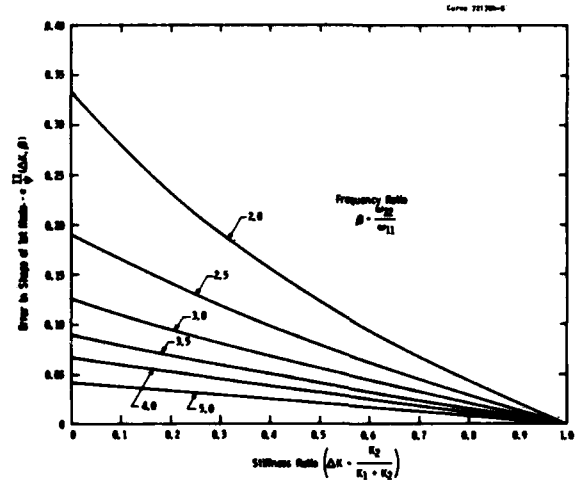


Fig. 9 - Error in shape of 1st mode for reduced model No. 2 (exterior node (2) eliminated as a D.O.F.)

CONCLUSIONS

A quantitative measure of errors in frequency and mode shape introduced by the Guyan Reduction Technique when applied to a 2 mass (2 d.o.f.) model has been determined. The errors are functions of 2 variables; therefore, any criteria prescribed for selecting active d.o.f. should be based on 2 parameters.

When the interior node was eliminated as a d.o.f., the errors corresponding to any finite mass ratio were bounded over the range of stiffness ratios (ratio of stiffness at active node to eliminated node). The errors were small for either very low ($\Delta K \rightarrow 0, \epsilon_f^I, \epsilon_\phi^I \rightarrow 0$) or very high stiffness ratios ($\Delta K \rightarrow 1, \epsilon_f^I, \epsilon_\phi^I \rightarrow 0$) even for small mass ratios (ratio of mass at active node to eliminated node). For mass ratios greater than unity, the errors were small for any stiffness ratio - less than 2% in frequency and 20% in mode shape. The approximate mode shape indicates less motion than the exact mode shape which could produce nonconservative response calculations.

When the exterior node was eliminated as a d.o.f., the errors were unbounded as the ratio of stiffness at eliminated node to active node approached 0 ($\Delta K \rightarrow 0$; $\epsilon_f^{II}, \epsilon_\phi^{II} \rightarrow \infty$). As the stiffness ratio approached unity, the errors approached 0 ($\Delta K \rightarrow 1$; $\epsilon_f^{II}, \epsilon_\phi^{II} \rightarrow 0$).

As in the foregoing model, the errors improved as the ratio of mass at eliminated node to active node decreased ($\mu \rightarrow 0$; $\epsilon_f^{II}, \epsilon_\phi^{II} \rightarrow 0$). Furthermore, the approximate mode shape indicates greater motion than the exact mode shape which could produce conservative response calculations.

APPENDIX

(I) Eliminate interior node (1)

The homogenous equation of motion for 2 mass model (Fig. 1A)

is

$$[M] \ddot{x} + [K] x = \{0\}$$

or

$$\begin{bmatrix} M_1 & 0 \\ 0 & M_2 \end{bmatrix} \begin{Bmatrix} \ddot{x}_1 \\ \ddot{x}_2 \end{Bmatrix} + \begin{bmatrix} K_1 + K_2 & -K_2 \\ -K_2 & K_2 \end{bmatrix} \begin{Bmatrix} x_1 \\ x_2 \end{Bmatrix} = \begin{Bmatrix} 0 \\ 0 \end{Bmatrix} \quad (A-1)$$

Applying the constraint equation

$$\begin{Bmatrix} x_1 \\ x_2 \end{Bmatrix} = \begin{bmatrix} \frac{K_2}{K_1 + K_2} \\ 1 \end{bmatrix} x_2 \quad (A-2)$$

$$= [T] \{x_G^I\}$$

to equations (A-1) gives

$$[T]^T [M] [T] \{x_G^I\} + [T]^T [K] [T] \{x_G^I\} = \{0\}$$

or

(A-3)

$$\begin{bmatrix} M_2 + M_1 \left(\frac{K_2}{K_1 + K_2} \right)^2 \\ \frac{K_1 K_2}{K_1 + K_2} \end{bmatrix} x_G^I = 0$$

Therefore,

$$\lambda_G^I = \left(\frac{\omega_G^I}{\omega_{22}^I} \right)^2 = \frac{1}{K_2/M_2} \frac{K_2 \left(\frac{K_1}{K_1 + K_2} \right)}{M_2 + M_1 \left(\frac{K_2}{K_1 + K_2} \right)^2}$$

$$= \frac{K_2/M_2}{K_2/M_2} \frac{\left(1 - \frac{K_2}{K_1 + K_2} \right)}{\left(1 + \frac{M_1}{M_2} \left(\frac{K_2}{K_1 + K_2} \right)^2 \right)}$$

$$= \frac{1 - \Delta K}{1 + \frac{\Delta K^2}{\mu}} \quad (A-4)$$

Also,

$$\phi_G^I = \frac{x_1}{x_2} = \frac{K_2}{K_1 + K_2} = \Delta K \quad (A-5)$$

(II) Eliminate exterior node (2)

Applying the constraint equation

$$\begin{Bmatrix} x_1 \\ x_2 \end{Bmatrix} = \begin{bmatrix} 1 \\ 1 \end{bmatrix} x_1 = [T] \{x_G^{II}\} \quad (A-6)$$

to eq. (A-1) gives

$$[M_1 + M_2] \ddot{x}_G^{II} + [K_1] x_G^{II} = 0 \quad (A-7)$$

where

$$\lambda_G^{II} = \left(\frac{\omega_G^{II}}{\omega_{22}^{II}} \right)^2 = \frac{1}{K_2/M_2} \frac{K_1}{M_1 + M_2}$$

$$= \frac{1}{K_2/M_2} \frac{K_2/M_2 \left(\frac{K_1}{K_2} \right)}{\left(1 + M_1/M_2 \right)}$$

$$= \frac{\frac{1}{\Delta K} - 1}{1 + 1/\mu} = \frac{1 - \Delta K}{\Delta K(1 + \frac{1}{\mu})} \quad (\text{A-8})$$

and

$$\phi_{\text{G}}^{\text{II}} = \frac{x_1}{x_2} = 1.0 \quad (\text{A-9})$$

REFERENCES

1. R. J. Guyan, "Reduction of Stiffness and Mass Matrices", AIAA Journal, Vol. 3, No. 2, February, 1965.
2. "Selection of Dynamic Degrees of Freedom", WECAN User's Manual, Westinghouse R & D Center.
3. B. Downs, "Accurate Reduction of Stiffness and Mass Matrices for Vibration Analysis and a Rationale for Selecting Master Degrees of Freedom", ASME Paper No. 79-DET-18, 1980.
4. W. T. Thompson, "Vibration Theory and Applications", 3rd Edition, Prentice-Hall, Inc., 1965, Chapter 6.

DISCUSSION

Mr. Scavuzzo (NKF Engineering): Did you investigate the effect of the error in the forces?

Mr. Wolff: The error in the forces was not addressed but it should be. I am not certain of this, but it means that you have to be careful because you could have non-conservative calculations. That should be investigated and if that is what that means, and I have always been under the impression that we are working with conservative calculations, then the real system is worse than what I have modeled.

Voice: You said in one case that you have a smaller mode shape and that means there would be more dynamic force from the upper mass, less than the smaller one. A good question is what is the dynamic force on the elements and for my purposes this remains to be done.

Mr. Wolff: That is right. This is only for the simple two mass system. I noticed in the program that there is a paper tomorrow afternoon that addresses the same general problem. It will be interesting to see what conclusions are drawn there.

A METHOD FOR ESTIMATING
THE ERROR INDUCED BY THE
GUYAN REDUCTION

Gary L. Fox
NKF Engineering Associates, Inc.
Vienna, Virginia

The Guyan Reduction refers to a method used to reduce the number of degrees of freedom in a structural model for dynamic analysis. Experience has shown that, if the method is properly employed, then this reduction method does in fact provide a "reasonably" accurate approximation of the dynamic characteristics of the unreduced model. To date, however, a cost (or computer time) effective method to estimate the actual error induced by the reduction process was not available. This paper presents an accurate and cost effective method to evaluate this error.

INTRODUCTION

Consider the well-known system of linear equations with constant coefficients

$$[M] \ddot{[X]} + [K] [X] = [P(t)] \quad (1)$$

where:

$[M]$ = mass matrix
 $[K]$ = stiffness matrix
 $[X], \ddot{[X]}$ = displacement, acceleration vector
 $[P(t)]$ = load vector

In current finite element models the degrees of freedom represented by equation (1) are often many thousand. This large number of equations is usually a result of the finite element technique itself rather than being necessary for a sufficiently accurate solution to a dynamic problem.

In a short, but significant paper [1] Guyan suggested that a transformation be applied to the mass matrix that was based on partitioning the stiffness matrix. This reduction of the number of

degrees of freedom for a dynamic analysis is cost effective, in terms of computer time, when the system of equations is reduced by a factor of four or more.

Computing efficiency is therefore a central issue to the consideration of any reduction process. A numerical procedure for estimating the error must not add significantly to the total computing time to solve the dynamic problem. The method presented here meets this basic requirement. This is particularly true when a modal analysis is required as part of the solution process.

It is the assumption that the analyst wishes to calculate a significant number, say ten percent, of the lowest modes represented by the homogeneous form of equation (1),

$$[M] \ddot{[X]} + [K] [X] = 0 \quad (2)$$

Modal analysis provides an insight into the dynamic behavior of a complex system, provides a means by which a finite element model may be checked for errors, or provides a basis for estimating the response of the system to a specific, simple excitation. Modal analysis plays a central role in the U.S.

Navy's Dynamic Design Analysis Method (DDAM) as well as many other well known techniques of enforced motion boundary problems that use shock response spectra as a statistical technique for dynamic analysis. In addition, the system response to transient or harmonic excitation may be calculated by an eigenvector expansion. Eigenvector expansion techniques are also cost effective when a number of different load conditions are analyzed for a given set of equations.

DERIVATION OF THE ERROR TERM

Presume that the eigenvalue Equation (2), is partitioned into two sets; the "0" set of DOF to be omitted and the "a" set of DOF to be retained in the Guyan Reduction, i.e.,

$$\begin{bmatrix} \bar{K}_{aa} & K_{ao} \\ K_{oa} & K_{oo} \end{bmatrix} \begin{bmatrix} \bar{\phi}_a^i \\ \bar{\phi}_o^i \end{bmatrix} = \bar{\lambda}^i \begin{bmatrix} \bar{M}_{aa} & M_{ao} \\ M_{oa} & M_{oo} \end{bmatrix} \begin{bmatrix} \bar{\phi}_a^i \\ \bar{\phi}_o^i \end{bmatrix} \quad (3)$$

Where $\bar{\lambda}^i$ is the true eigenvalue and $\begin{bmatrix} \bar{\phi}_a^i \\ \bar{\phi}_o^i \end{bmatrix}$ is the true eigenvector for the i^{th} mode.

The reader is reminded that the solution of the reduced equations using the Guyan reduction is

$$[K_{aa}] [\phi_a^i] = \lambda^i [M_{aa}] [\phi_a^i] \quad (4)$$

where

$$\begin{aligned} [K_{aa}] &\equiv [\bar{K}_{aa}] + [K_{ao} G_{oa}] \\ [M_{aa}] &\equiv [\bar{M}_{aa}] + [G_{oa} M_{oa}] \\ &\quad + [M_{ao} G_{oa}] + [G_{oa} M_{oo} G_{oa}] \\ [G_{oa}] &\equiv [K_{oo}^{-1} K_{oa}] \end{aligned}$$

Consider the exact solution of equation (3) in partitioned form by solving the second set of equations for $\bar{\phi}_o^i$ in terms of $\bar{\phi}_a^i$

$$[\bar{\phi}_o^i] = -[K_{oo} - \bar{\lambda}^i M_{oo}]^{-1} [K_{oa} - \bar{\lambda}^i M_{oa}] [\bar{\phi}_a^i] \quad (5)$$

The first term of the matrix product indicated above can be expanded in a

power series

$$\begin{aligned} & [K_{oo} (I_{oo} - \bar{\lambda}^i K_{oo}^{-1} M_{oo})]^{-1} = \\ & [I_{oo} + \bar{\lambda}^i K_{oo}^{-1} M_{oo} + \dots] K_{oo}^{-1} \end{aligned} \quad (6)$$

Substituting (6) into the first of equations (3) for the i^{th} eigenvalue and eigenvector

$$[\bar{\phi}_o^i] = [G_{oa}] [\bar{\phi}_a^i] + \bar{\lambda}^i [E_{oa}] [\bar{\phi}_a^i] + \text{higher order terms} \quad (7)$$

where

$$[E_{oa}] = -K_{oo}^{-1} [M_{oo} K_{oo}^{-1} K_{oa} - M_{oa}]$$

The first term on the right in Equation (7) provides the theoretical justification for the Guyan Transformation, being correct to first order in λ^i . The second term is the second order correction to the Guyan Transformation,

$$[\phi^i] = \begin{bmatrix} \phi_a^i \\ G_{oa} \phi_a^i \end{bmatrix} \quad (8)$$

The condition that the term containing $[E_{oa}]$ in equation (7) be small can be expressed as

$$[I_{oo}] \gg \lambda^i [K_{oo}^{-1} M_{oo}] \quad (9)$$

and

$$[G_{oa}] \gg \lambda^i [E_{oa}] \quad (10)$$

Assuming that the second term, M_{oa} in the error matrix, E_{oa} is negligible, Equation (10) reduces to Equation (9). Equation (9) is thus the condition that a particular eigenvalue be accurate for a specific set of omitted DOF. The lower the λ^i and larger the product $[K_{oo}^{-1} M_{oo}]$, the more accurate the eigenvalue and therefore the eigenvector.

Equation (9) points out the well-known dependency of the Guyan reduced error on frequency; the lower the mode, the lower the error. Another well-known rule, to keep all large masses in the a-set, is also confirmed by this equation. The influence of the stiffness term, however, has evidently not been generally recognized.

EVALUATION OF THE ERROR TERM

Numerical studies indicate that errors in frequency and errors in amplitude have the same magnitude[2]. A

relationship between the error in frequency and the first order correction term in equation is required. Consider the i^{th} eigenvalue given by Rayleigh's quotient.

$$\lambda^i = \frac{[\phi^i]^T [K] [\phi^i]}{[\phi^i]^T [M] [\phi^i]} \quad (11)$$

Taking the natural log of (11) yields

$$\ln \lambda^i = \ln K_g^i - \ln M_g^i \quad (12)$$

where

$$K_g^i = i^{\text{th}} \text{ generalized stiffness}$$

$$M_g^i = i^{\text{th}} \text{ generalized mass}$$

Taking differentials of (12) provides the relationship in error between the eigenvalue, λ^i , and stiffness and mass weighed eigenvector,

$$\frac{d\lambda^i}{\lambda^i} = \frac{1}{K_g^i} dK_g^i - \frac{1}{M_g^i} dM_g^i \quad (13)$$

Writing the differential of the first term of (13)

$$dK_g^i = \sum_{l,m} d(\phi_l^i) K_{lm} \phi_m^i + \sum_{l,m} \phi_l^i K_{lm} d(\phi_m^i) \quad (14)$$

Since the two terms in Equation (14) are identical,

$$dK_g^i = 2[\phi^i]^T [K] [d\phi^i] \quad (15)$$

Similarly

$$dM_g^i = 2[\phi^i]^T [M] [d\phi^i]$$

It is now required to evaluate

$$[d\phi^i] = \begin{bmatrix} d\phi_a^i \\ d\phi_o^i \end{bmatrix}$$

to first order in λ^i . Using the Guyan transformation, $[\phi_o^i] = [G_{oa}^i] [\phi_a^i]$ in the second of Equation (3).

$$[0] = [M_{oa}^i] [\phi_a^i] + \lambda [M_{oo}^i] [G_{oa}^i] [\phi_a^i] \quad (16)$$

Pre-multiplying Equation (16) by $[G_{oa}^i]^T$

and adding it to the first of Equation (3) one finds that to first order in λ ,

$$[K_{aa}^i] [\phi_a^i] = \lambda [M_{aa}^i] [\phi_a^i] \quad (17)$$

It is therefore seen that

$$[d\phi_a^i] = [0] \quad (18)$$

From Equation (7)

$$\{d\phi_o^i\} = \lambda^i [E_{oa}^i] \{d\phi_a^i\} \quad (19)$$

Therefore, from Equation (18) and (19)

$$\{d\phi^i\} = \begin{bmatrix} [0] \\ \lambda^i [E_{oa}^i] \{d\phi_a^i\} \end{bmatrix} \quad (20)$$

and

$$[\phi^i] = \begin{bmatrix} \{\phi_a^i\} \\ [G_{oa}^i] \{\phi_a^i\} \end{bmatrix} \quad (21)$$

Evaluation of the first term of Equation (13) using Equations (20) and (21) yield

$$dK_g^i = \lambda^i \{d\phi_a^i\}^T [K_{ao} E_{oa} + G_{oa}^T K_{oo} E_{oa}] \{d\phi_a^i\} \quad (22)$$

The term in brackets is identically zero,

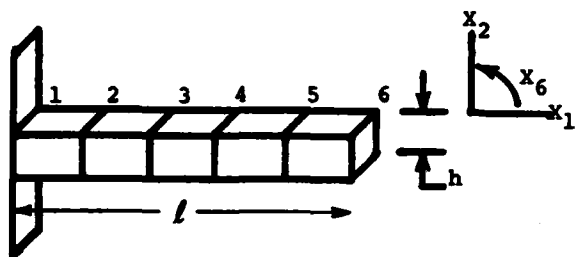
$$dK_g^i = 0 \quad (23)$$

to first order in λ . The error in λ , to first order of λ , is due to the second term in Equation (13), i.e.,

$$\frac{d\lambda^i}{\lambda} = \frac{1}{M_g^i} [\phi^i]^T [M] [d\phi^i] \quad (24)$$

NUMERICAL EXAMPLE

In order to test the results presented in the previous sections, the bending modes of a 5-cell cantilever beam is considered. The physical parameters of the beam are shown in Figure 1.



$h = 0.86$ Depth and width of beam
 $l = 8.66025$ Length of beam
 $\phi = 7.28E-4$ Mass density of beam
 $I = h^4/12 = 0.0456$ Second moment of area
 $A = h^2 = 0.7396$ Cross-sectional area
 $E = 3.0E+7$ Modulus of elasticity
 $\lambda_i = c_i^4 EI/A$ i^{th} theoretical eigenvalue
 $c = 1.875, 4.694, 7.855, 10.996$ First theoretical four eigenvalue coefficients

Figure 1. Five cell beam

The NASTRAN computer code was used for the numerical calculations because of the powerful DMAP compiler available and the generality of the results. The Guyan transformation is available through the use of Alter statements which allows the evaluation of the error simply by performing some inexpensive matrix multiplications. A complete description of the NASTRAN DMAP alters will appear in the proceedings of the next NASTRAN users colloquium.

Many elements in NASTRAN offer two options for the form of the mass matrix; lumped parameter or coupled mass. The bulk data parameter COUPMASS identifies the elements for which coupled mass matrices are to be used. The first four eigenvalues of the finite element model are compared to the coupled mass results in Table 1.

Table 1. Comparison of Theoretical and FEM Coupled Mass Eigenvalues.

MODE NO.	THEORETICAL	FEM (COUPLED MASS)	ERROR (%)
1	5.50829E6	5.50839E6	1.81E-3
2	2.16363E8	2.16547E8	8.50E-2
3	1.69667E9	1.70827E9	6.84E-1
4	6.51554E9	6.66659E9	2.32

Let the ten DOF system, five translational, and five rotational, be Guyan reduced to four degrees-of-freedom and evaluate the estimated and "actual" error. The "actual" error is defined as the difference in frequency between the 10-DOF system and the Guyan reduced system. Table 2 shows the four eigenvalues and the predicted and actual error. The analysis set is defined as 6-2, 5-2, 4-2, and 3-2; the first number being the grid point, and the second number the direction.

Table 2. Comparison Between Predicted & Actual Guyan Reduction Error.

MODE NO.	EIGENVALUE	"ACTUAL" ERROR (%)	PREDICTED ERROR (%)
1	5.50856E6	3.09E-3	3.22E-3
2	2.17408E8	3.98E-1	3.89E-1
3	1.86197E9	8.62	7.55
4	1.01909E10	52.9	27.3

The accuracy with which the error is predicted decreases with increasing predicted error. Also, as expected, the error increases as the mode number increases. Small studies of the actual error have led to the "rule of thumb" that in a Guyan reduced model, the lower 50% of the modes in the reduced model are reasonably accurate; similar to the above result.

As an additional example of the accuracy of the error analysis let concentrated masses of $1.0 E-1$ and $1.0 E-2$ be located at grid points 2 and 4. These masses are large compared with the mass of a cell, $4.7 E-4$. A Guyan reduction to the 3-DOF of 2-2, 4-2, and 6-2 yields the results shown in Table 3.

Notice that all three modes are acceptable for normal engineering practices. This accuracy is surprising when compared to the "rule of thumb" mentioned above. The analysis set included the two large mass points as well as the extreme point of the model.

Table 3. Predicted & Actual Error for the 5-Cell Beam with Two Concentrated Masses.

MODE NO.	EIGENVALUE	"ACTUAL" ERROR (%)	PREDICTED ERROR (%)
1	1.6754E6	1.06E-2	1.06E-2
2	1.9465E7	9.50E-2	9.40E-2
3	1.5367E8	2.11	2.05

Consider, as a final example, the 15-DOF system that is identical to that above but includes the axial, X_1 , directions of the grid points. The analysis set is defined as 2-2, 3-1, 4-2, 5-2, and 6-2. The comparison of "actual" vs. Guyan reduced eigenvalues and the actual vs. predicted errors are compared in Table 4.

The interesting effect shown in this model is that the third mode of the Guyan reduced model is predicted to have less than 0.2% error, but when compared to the third mode of the com-

plete model, the eigenvalue is more than 50% different! A comparison of mode shapes reveal that the third mode of the reduced model is the first axial mode, the fourth mode of the complete model. This example points out the pitfall of comparing the first few eigenvalues of two models without making sure that the eigenvalues represent the same mode. This kind of comparison is commonly used to ascertain the accuracy of two Guyan reduced modes or of a reduced model to the first few modes of the complete model.

Table 4. Guyan Error Analysis for 15-DOF System with Two Concentrated Masses. A= Axial Mode, B= Bending Mode.

MODE NO.	EIGENVALUE		ERROR (%)	
	ACTUAL	REDUCED	ACTUAL	PREDICTED
1	1.675228E7 (B-1)	1.675243E6 (B-1)	8.95E-4	9.00E-4
2	1.944648E7 (B-2)	1.944747E7 (B-2)	5.67E-3	5.10E-3
3	1.663417E8 (A-1)	1.504932E8 (B-3)	1.86E-1	1.84E-1
4	1.507730E8 (B-3)	1.087748E8 (A-1)	34.6	48.2
5	5.896351E8 (A-2)	3.532273E9 (B-4)	53.6	18.5
6	5.098570E9 (B-4)			

CONCLUSION

In summary it has been shown that a method exists that provides a useful, cost effective method for estimating the error induced by the Guyan Reduction. The method presented produces a single number for the error in each mode, making it easy for the analyst to evaluate the accuracy of the reduced model that will produce reliable results.

REFERENCES

1. Guyan, Robert J., "Reduction of Stiffness and Mass Matrices," AIAA Journal, Vol. 3, No. 2
2. NASTRAN THEORETICAL MANUAL, Section 11.3 (Available from COSMIC, Suite 112, Barrow Hall, Athens, Ga 30602)

DISCUSSION

Voice: Would the inclusion of the second order theoretical improve your results?

Mr. Fox: That's a good question. I tried to do that and I didn't get the results that I was looking for. It seemed to me like one should be able to get a second order correction to the eigen vector but I haven't been able to prove that. Also that term should be able to tell us how to optimize for Guyan reduction and that is a challenge to the audience if you can figure out how to do it. I haven't been able to do it yet. I've been working a year on that.

CRITICAL SPEEDS OF MULTI-THROW CRANKSHAFTS
USING SPATIAL LINE ELEMENT METHOD

Cemil Bagci, Professor
Department of Mechanical Engineering
Tennessee Technological University
Cookeville, Tennessee

and

Donald R. Falconer, Project Engineer
Duriron Valve Division
Cookeville, Tennessee

A finite element method for the determination of the critical speeds of multi-throw crankshafts is presented. A crankshaft is considered as a three-dimensional dynamic system and throws in their actual geometries spaced at some angles relative to each other and subjected to flexural, axial, and torsional deformations. The method uses spatial actual finite line element whose each end may experience six degrees of freedom of spatial motion—three rotations and three linear displacements. Both regular and irregular elements are used. Masses and rotary inertias are lumped to the joint freedoms chosen as generalized coordinates, using either discrete element mass matrix or the consistent element mass matrix plus the discrete external load mass matrix, depending on the model used. Equations of free motion are solved for natural frequencies and the corresponding mode vectors as an eigenvalue problem by matrix iteration, using the reduced dynamics matrix for higher modes. An experimental unbalanced crankshaft having three throws of different sizes, supported by four bearings, connected to a variable speed drive by a flexible coupling, and carrying three external load disks is designed, tested, and results are compared with those of analytical finite element solutions for different models, including those considering rotary inertias, flexible bearings, and equivalent pure torsional straight shaft models, showing the method of the article to be a very efficient tool for the dynamic design of industrial crankshafts.

INTRODUCTION

Critical speeds of a crankshaft are its most important dynamic characteristics since the operational speeds of machines where the crankshaft is operating are bound by these critical speeds. Available literature show that critical speeds of a crankshaft is in general estimated by reducing the crankshaft to a pure torsional system using rules of thumb to approximate throws as shaft portions and disks, then using Holzer's assume-and-iterate method [1-3], or using planar finite line element technique presented in [4]. Investigations of crankshafts considering the actual three dimensional geometry of throws has been limited due to the complex geometry involved. Available literature on the three dimensional study of crankshafts again use simplified models applying Myklestad Method and iteration [5,6].

This article presents a three-dimensional finite element method for the determination of

critical speeds of crankshafts considering their three-dimensional actual geometries and as systems experiencing axial, flexural and torsional deformations, and using lumped mass systems. Equations of free motion of a crankshaft are written making use of the matrix-displacement method, which makes use of the stiffness influence coefficient matrix of the crankshaft. The finite element technique is used in the formulation of the global external stiffness matrix $[K]$ of the crankshaft and in the formulation of the global mass matrix $[M]$. The generalized coordinate influence coefficient matrix is determined by partitioning $[K]$ or its inverse according to the number of the generalized coordinates used, to which masses and rotary mass moments of inertias are lumped [4, 7-14]. Equations of free motion are then transformed into the eigenvalue form and solved for the natural frequencies and the corresponding mode vectors by matrix iteration. Natural frequencies determine the critical speeds of the crankshaft. The

method permits the inclusion of the rotary inertias of elements as well as of the externally mounted objects and investigation of their effects on the predicted value of the critical speed with ease. It also eliminates the rules-of-thumb techniques of the conventional modeling.

EQUATIONS OF MOTION

Equations of motion for the forced and damped vibration of a dynamic system written using the method of influence coefficients in the form of uncoupled displacements, and in matrix form, are [8, 13]:

$$\{x_g\} = [\delta_g] \{-[M]\{\ddot{x}_g\} - [C]\{\dot{x}_g\} + \{F(t)\}\} \quad (1)$$

where $\{x_g\}$, $\{\dot{x}_g\}$, and $\{\ddot{x}_g\}$ are the $N_g \times 1$ vectors of generalized coordinate displacements, velocities, and accelerations, respectively. g stands for "generalized". N_g designates the number of the generalized coordinates used. $[M]$ is the $N_g \times N_g$ global mass matrix in which masses are lumped to linear generalized coordinates and rotary inertias are lumped to rotary generalized coordinates. $[C]$ is the $N_g \times N_g$ global damping coefficient matrix. $\{F(t)\}$ is the $N_g \times 1$ time dependent forcing vector. $[\delta_g]$ is the $N_g \times N_g$ generalized coordinate flexibility influence coefficient matrix whose determination for the crankshaft becomes the major aim of the finite element formulation. Thus, to determine $[\delta_g]$, the global stiffness matrix $[K]$ is formed by the finite element technique. Then, it is inverted or partitioned. The global stiffness matrix $[K]$ relates all the active joint freedoms $\{x\}$ to the external joint forces $\{P\}$ by

$$\{P\} = [K]\{x\} \quad (2)$$

where $\{x\}$ and $\{P\}$ are of sizes $N_p \times 1$, $[K]$ is of size $N_p \times N_p$, and N_p is the number of active joint freedoms. An active freedom is a neutral freedom, if no mass is lumped to it. It is generalized coordinate freedom otherwise. Let the number of neutral freedoms be N_0 . Then, $N_p = N_0 + N_g$. The number of the external joint freedoms are assigned such that the early numbers 1, ..., N_0 are for the neutral freedoms and the remaining numbers N_0+1 , ..., N_p are for the generalized coordinate freedoms, so that the inverse of $[K]$ is easily partitioned to obtain $[\delta_g]$. Thus, from eq. (2),

$$\begin{Bmatrix} \{x_0\} \\ \{x_g\} \end{Bmatrix} = [K]^{-1} \begin{Bmatrix} \{p_0\} \\ \{p_g\} \end{Bmatrix} = \frac{1}{N_0} \begin{bmatrix} \delta_1 & \delta_2 \\ \delta_2 & \delta_4 \end{bmatrix} \begin{Bmatrix} \{p_0\} \\ \{p_g\} \end{Bmatrix} \quad (3)$$

in which $\{x_0\}$ is the $N_0 \times 1$ neutral coordinate displacement vector, $\{p_0\}$ is the $N_0 \times 1$ neutral coordinate forcing vector and is zero. $\{p_g\}$ is the $N_g \times 1$ generalized coordinate forcing vector which is the post multiplier of $[\delta_g]$ in eq. (1). Hence, from eq. (3), $[\delta_g] = [\delta_4]$. Then, to find $[\delta_g]$, one only needs to form $[K]$ and partition its inverse to extract $[\delta_4]$ of size $N_g \times N_g$.

Determining $[\delta_g]$ by partitioning $[K]$ saves computer time. Thus, rewriting eq. (2), one has

$$\begin{Bmatrix} [K_1] & [K_2] \\ [K_3] & [K_4] \end{Bmatrix} \begin{Bmatrix} \{x_0\} \\ \{x_g\} \end{Bmatrix} = \begin{Bmatrix} \{P_0\} \\ \{P_g\} \end{Bmatrix} \quad (3a)$$

from which

$$\{x_0\} = -[K_1]^{-1} [K_2] \{x_g\} \quad (3b)$$

$$[K_3] \{x_0\} + [K_4] \{x_g\} = \{P_g\} \quad (3c)$$

$$[K_4] - [K_3][K_1]^{-1}[K_2] \{x_g\} = \{P_g\} \quad (3d)$$

Then, $[\delta_g] = [K_g]^{-1}$, where $[K_g] = [K_4] - [K_3][K_1]^{-1}[K_2]$. Inverted matrices are $[K_1]$ of size $N_0 \times N_0$ and $[K_g]$ of size $N_g \times N_g$.

For the free motion $\{P\} = -[M]\{\ddot{x}_g\}$ which upon substituting into eq. (1), along with the form of the harmonic motion $\{x_g\} = \cos(\omega t + \gamma)\{R\}$, give the eigenvalue form of the equations of free motion:

$$[\lambda[I] - [D_m]] \{R\} = 0 \quad (4)$$

where $\lambda = 1/\omega^2$ is the eigenvalue of the dynamic matrix $[D_m] = [\delta_g][M]$. ω is a modal natural frequency of the crankshaft, $\{R\}$ is the corresponding modal amplitude vector and γ the phase angle. N_g values of λ determines the N_g values of ω and the corresponding values of $\{R\}$. Equation (4) is solved for the values of λ_k and $\{R\}_k$ easily by matrix iteration. The solution of eq. (4) by matrix iteration using the original value of $[D_m]$ gives the fundamental mode frequency ω_1 and the corresponding mode amplitude vector $\{R\}_1$ [14]. For higher mode frequencies $[D_m]$ must be reduced. Thus, for the $(k+1)^{th}$ mode it is given by [14]:

$$[D_m]_{k+1} = [D]_k - \frac{\{R\}_k [M] \{R\}_k^T}{\omega_k^2 \{R\}_k^T [M] \{R\}_k} \quad (5)$$

The fundamental frequency ω_1 of a crankshaft determines its critical operational speed, so does ω_k for the k^{th} mode. $\{R\}_k$ defines the modal amplitudes of the generalized coordinates with respect to the undeformed geometry of the crankshaft. The corresponding neutral coordinate modal amplitudes are given by eq. (3b) as $\{R_0\}_k = -[K_1]^{-1} [K_2] \{R\}_k$.

THE EXTERNAL JOINT FREEDOM (P - x) DIAGRAM

Figure 1 shows an external joint displacement diagram for a crankshaft having two throws. This figure illustrates several rules and considerations in modeling a crankshaft. A joint is introduced where the cross-sectional properties of the crankshaft varies, where a mass or mass moment of inertia is to be lumped, and where there is a support. Between two joints an

element is formed. Since the finite element technique is a numerical method, the more elements means better accuracy in the results obtained. Single-headed solid arrows designate active linear joint freedoms. Double-headed solid arrows designate active rotary joint freedoms. The restrained joint freedoms are designated by dashed arrows, and they will assume the freedom number N_p+1 . Joint freedoms are restrained to satisfy the existing boundary conditions such as at the fixed end at A in Fig. 1 and at rigid support location, such as the linear joint freedoms at support C and N. If a support (bearing) is designed to permit axial play of the journal (which is done to permit axial expansion of the shaft in high temperature environments) the axial freedom at the support location is not restrained, such as the freedom 105 at support Y. The transverse linear freedoms at a support become active freedoms when a bearing is considered flexible in the transverse directions (which may be the case when the bearing housing is mounted on vibration isolator or when the effect of the bearing housing deformations is to be considered). Freedoms are sometimes restrained to obtain the type of model desired. For example, in Fig. 1, all the joint freedoms except the torsional freedom 1 at the flexible coupling joint are restrained to permit the flexible coupling experience torsional deformation only and replace it by an element, element 1, which experiences torsional deformation only. Axial freedoms at joints L, M, N, O, and P are restrained so that elements 12, 13, 14, and 15 do not

experience axial deformations. For example, $(x_7, -x_{72})$ defines the axial deformation experienced by element 5. However, axial freedoms along the IL side of throw 1 are all numbered 84 so that elements 9, 10, and 11 do not experience axial deformations, even though the joints I, J, K, and L experience axial joint displacement 84. Similarly, elements 21, 22, and 23; elements 19 and 20; and elements 24 and 25 do not experience axial deformations, although their joints experience the linear freedoms 99, 95, and 105, respectively. The O end of element 15 experiences torsional freedom 51 only, fixing this joint for flexural and axial displacements. The P end, however, experiences the torsional freedom 52 and the flexural freedom 53, while the freedom 53 is experienced as a torsional freedom by element 16. The freedom numbering on the PS side of the second throw eliminates the displacements of joints P, Q, R, and S in the axial Y' direction. So, elements 16, 17, and 18 do not experience axial deformations; and no flexural rotation in the X'Y' plane, but linear freedoms 91, 93, and 95 with zero slope of the deflection curve at P, Q, R, and S on this plane. In this manner desired elastic model experiencing the desired freedoms can be formed.

IRREGULAR AND REGULAR ELEMENTS

One of the throws, preferably the first one, throw 1 in Fig. 1, is used as a reference throw when forming the P-x diagram. The reference throw lies in the XY plane of the XYZ

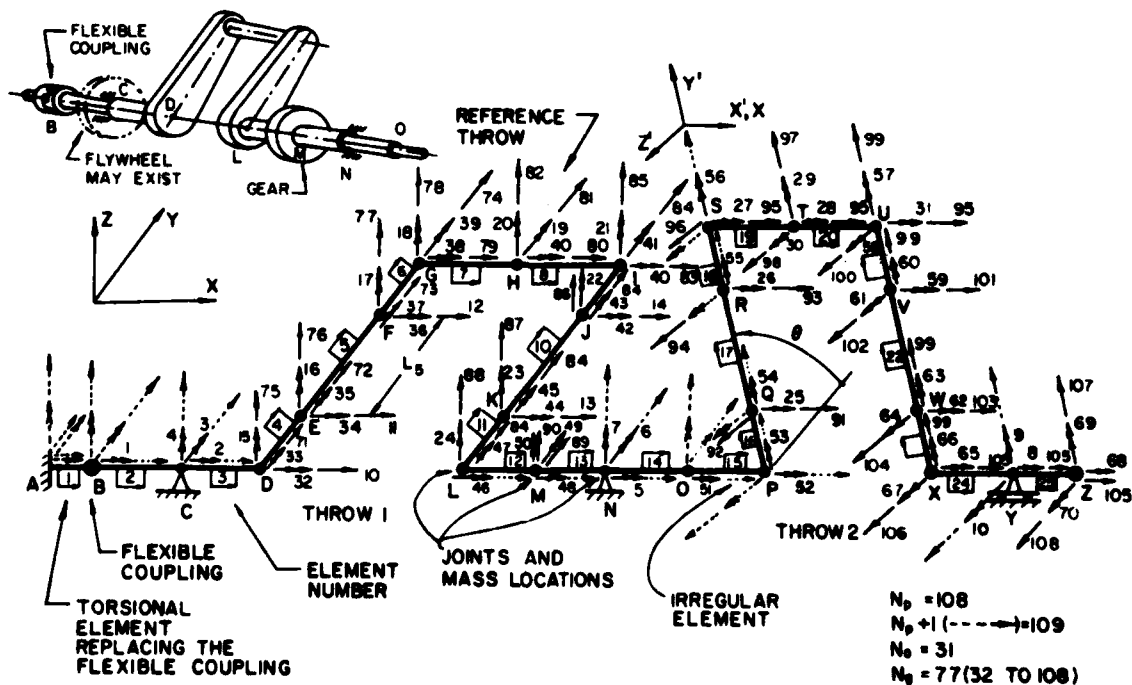


Fig. 1 - A sample external joint P-x diagram for a lumped mass model of a crankshaft having two throws

reference system. Successive throws are positioned with respect to the previous one by the angle, θ . Since the freedoms of the joints on the throw sides are assigned such that some are parallel to the axis of rotation of the crankshaft and some lie along the element line (the Y' axis), the elements connecting a throw to the previous one, such as the element 15 in Fig. 1, consist of two external joint freedom end-coordinate systems which are displaced relative to each other through rotation θ about the X axis. Since this requires the transformation of the end forces and moments in the element equations of equilibrium, elements such as the element 15 are called irregular elements. Other elements which require no transformation are called regular elements.

Assigning freedoms along the element lines of the throws have several purposes: to permit the use of element mass matrices of simplified geometries, to permit mass displacements to occur in the directions orthogonal to the element lines and to the principal axes of the element cross-sections, and to provide simple means to eliminate certain freedoms and neglect the effect of certain mass properties.

DYNAMIC MODEL

The dynamic model of a crankshaft is characterized and formed when one decides which of the active external joint freedoms are to be used as the generalized coordinates. In Fig. 1 freedoms 1 to 31 are considered neutral coordinate freedoms. Then $N_g=78$. If there was a flywheel at C, the freedom 2 would be considered within the generalized coordinates. Freedoms 3 and 4 could have been included in the generalized coordinates also if the effect of flexural rotary inertias of the flywheel about the Y and Z axes was to be included, but their numbers would be in those defining the generalized coordinate freedoms. At M the effect of mass (due to freedoms 89 and 90), effect of torsional rotary inertia (due to freedom 48), and effect of flexural rotary inertias (due to freedoms 49 and 50) are included. Effect of torsional rotary inertias about the Y axis of the elements 4-6, 9-11, 16-18, 21-23, and about the X axis of the elements 21-25 are considered. The effect of the flexural rotary inertias of masses at H, Q, R, and T is neglected, so is of the torsional rotary inertias at S, T, and U ends of elements 19 and 20. The effect of masses corresponding to linear freedoms, except in the directions of joint freedoms 10-14, is considered. In case of the discrete mass matrix, the sum of the masses at S, T, and U is lumped to freedom 95, the sum of those at U, V, W, and X is lumped to freedom 99, that of at I, J, K, and L to freedom 84, and that of at X, Y, and Z to freedom 105. These masses contribute also to off-diagonal elements in case of the consistent mass matrix. The global mass matrix [M] is formed considering all these effects by using element mass matrices--discrete element mass matrix or the consistent element mass matrix, depending on the method

used--as described in the following section.

THE ELEMENT P-x DIAGRAM AND THE ELEMENT EXTERNAL STIFFNESS MATRIX

The general geometry of the spatial finite line element used is shown in Fig. 2. Figure 2(a) shows the element P-x diagram and the order of the local external joint displacements $x(N_1)$ to $x(N_{12})$. Each end of an element experiences three rotary displacements and three linear displacements. X, Y, and Z position the terminal end with respect to the initial end of the element. $x(N_1)$, $x(N_2)$, and $x(N_3)$ are joint rotations at the initial end; $x(N_4)$, $x(N_5)$, and $x(N_6)$ are joint rotations at the terminal end; $x(N_7)$, $x(N_8)$, $x(N_9)$, and $x(N_{10})$, $x(N_{11})$, $x(N_{12})$ are the linear joint freedoms at the initial and terminal ends, respectively. N_1 to N_{12} designate the global numbers of the joint displacements. For example, for element 6 in Fig. 1, $N_1=36$, $N_2=37$, $N_3=17$, $N_4=38$, $N_5=39$, $N_6=18$, $N_7=12$, $N_8=73$, $N_9=77$, $N_{10}=79$, $N_{11}=74$, $N_{12}=78$, and $X=Z=0$, $Y=L$, where the XYZ system is the element reference system. For element 18, these numbers are (26, 55, 109; 27, 56, 109; 93, 109, 94; 95, 109, 96), where the X'Y'Z' system is the element reference system, and $X=Z=0$, $Y=L$. α , β , and γ are the direction angles and $\cos \alpha=X/L$, $\cos \beta=Y/L$, $\cos \gamma=Z/L$, $L^2=X^2+Y^2+Z^2$.

Element external stiffness matrix relates the element external joint displacements $x(N_1)$ to $x(N_{12})$ to the corresponding element external joint forces $P(N_1)$ to $P(N_{12})$ as they contribute. Thus,

$$\{P\}_e = [K_e]\{x\}_e \quad (6)$$

where $\{P\}_e^T = [P(N_1), P(N_2), \dots, P(N_{12})]$, $\{x\}_e^T = [x(N_1), x(N_2), \dots, x(N_{12})]$, $[K_e]$ is the 12x12 element external stiffness matrix and is given by

$$[K_e] = [A]_e [S]_e [A]_e^T \quad (7)$$

in which $[A]_e$ is 12x6 element statics matrix as described below for both regular and irregular elements, $[A]_e^T$ is its transpose and is the deformation matrix, $[S]_e$ is the element internal stiffness matrix and relates the internal end moments and end forces to the end deformations of the element [15, 16]. Refer to Figs. 2(b) and (c), where shown are the element internal forces; axial force F_1 and axial deformation e_1 ; torsional moment F_2 and the torsional deformation e_2 of the terminal end with respect to the initial end; flexural moments F_3 and F_4 about the axes normal the X'Z plane, but parallel to the 1-1 principal axis of the element cross-section, and the corresponding flexural deformations e_3 and e_4 about their axes; flexural moments F_5 and F_6 about the axes normal to the element axes but lying in the X'Z plane being parallel to the 2-2 principal axis of the element cross-section and the corresponding flexural deformations e_5 and e_6 about their axes; and the shearing forces V_1 and V_2 being normal to the axes of corresponding end moments and the element axis.

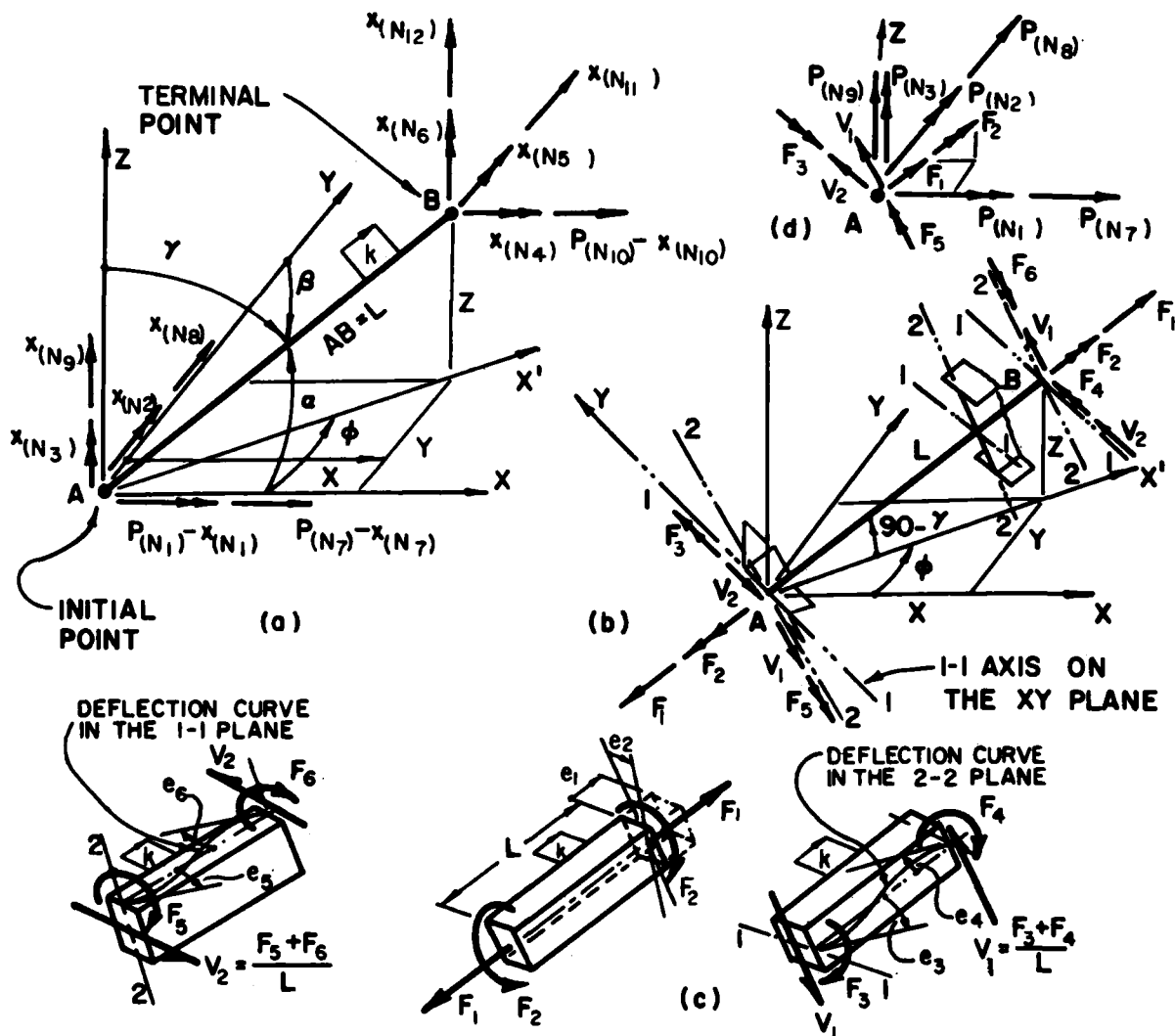


Fig. 2 - Element properties, (a) element external joint P-x diagram and the order of element freedoms, (b) element end internal forces and moments, (c) internal end deformations, (d) free-body diagram for the initial end joint

It should be noted that the 1-1 principal axis of an element always remains in the XY plane of the reference throw and in the X'Y' plane of the other throws. Hence, $[S]_e$ is defined by

$F \backslash e$	1	2	3	4	5	6
1	S_1					
2		S_2				
3			$4S_3$	$2S_3$		
4			$2S_3$	$4S_3$		
5					$4S_4$	$2S_4$
6					$2S_4$	$4S_4$

(8)

where $S_1=EA/L$, $S_2=GJ/L$, $S_3=EI_1/L$, $S_4=EI_2/L$, E is the modulus of elasticity, G is the modulus of torsional rigidity, A is the cross-sectional area of the element, I_1 and I_2 are the area moments of inertia of the element cross-section about the principal axes 1-1 and 2-2, respectively, and J is the torsional constant of the cross-section.

Statics Matrix for Regular Element.

Regular element is that element whose external joint freedoms at initial and terminal ends are defined in parallel coordinate systems as in Fig. 2(a). All the elements, except element 15, in Fig. 1 are regular elements. Element statics matrix $[A]_e$ relates the element internal forces F_1, F_2, \dots, F_6 to the element external joint forces, $P_{(N_1)}, P_{(N_2)}, \dots, P_{(N_{12})}$. It is obtained by simply writing the equations

of force and moment equilibrium at the joints in the directions of the external joint forces $P(N_1)$. Thus, observing the joint free-body diagram for the initial end shown in Fig. 2(d), one writes

$$P(N_7)\bar{i} + P(N_8)\bar{j} + P(N_9)\bar{k} + F_1\bar{U}_1 + V_1\bar{U}_2 + V_2\bar{U}_3 = 0 \quad (9)$$

as the force equation of equilibrium, and

$$P(N_1)\bar{i} + P(N_2)\bar{j} + P(N_3)\bar{k} + F_2\bar{U}_1 + F_3\bar{U}_2 - F_3\bar{U}_3 = 0 \quad (10)$$

as the equation of moment equilibrium. Similarly, the equations of force and moment equilibrium for the joint at the terminal end are written to be

$$P(N_{10})\bar{i} + P(N_{11})\bar{j} + P(N_{12})\bar{k} - F_1\bar{U}_1 - V_1\bar{U}_2 - V_2\bar{U}_3 = 0 \quad (11)$$

and

$$P(N_4)\bar{i} + P(N_5)\bar{j} + P(N_6)\bar{k} - F_2\bar{U}_1 - F_3\bar{U}_3 + F_3\bar{U}_2 = 0 \quad (12)$$

where \bar{i} , \bar{j} , and \bar{k} are the unit vectors of the XYZ reference system; \bar{U}_1 , \bar{U}_2 , and \bar{U}_3 are the unit vectors that position end forces in the joint coordinate system as shown in Fig. 2(d) and are defined as

$$\bar{U}_1 = a\bar{i} + b\bar{j} + c\bar{k}, \quad \bar{U}_2 = -c\bar{i} - d\bar{j} + h\bar{k}, \quad \bar{U}_3 = -d\bar{i} + g\bar{j}$$

where $a = \cos\alpha$, $b = \cos\beta$, $c = \cos\gamma$, $d = \sin\phi = b/(a^2 + b^2)^{1/2}$, $h = \sin\gamma$, also $a = hg$ and $b = hd$. Separating \bar{i} , \bar{j} , and \bar{k} components of eqs. (9)-(12), the element statics matrix for the regular element is obtained to be that given in eq. (13). $[A]_e =$

P	1	2	3	4	5	6
N_1		-a	-d		cg	
N_2		-b	g		cd	
N_3		-c			-h	
N_4		a		-d		cg
N_5		b		g		cd
N_6		c				-h
N_7	-a		cg/L	cg/L	d/L	d/L
N_8	-b		cd/L	cd/L	-g/L	-g/L
N_9	-c		-h/L	-h/L		
N_{10}	a		-cg/L	-cg/L	-d/L	-d/L
N_{11}	b		-cd/L	-cd/L	g/L	g/L
N_{12}	c		h/L	h/L		

Although this element statics matrix may be simplified for the crankshaft elements lying along an X axis, for which $a=g=h=1$, $b=c=d=0$, and for the throw side elements for which $a=g=c=0$, $b=d=h=1$, it is preferable to maintain it in its general form within the program to account for the throws whose sides may not be parallel to the Y or Y' axis.

Statics Matrix for Irregular Elements.

Observing Fig. 1, the irregular elements in a crankshaft will be formed on one side of a nonreference throw, such as the element 15 in Fig. 1, and again on one side of an inner flexible support as it is seen in Fig. 4. Figure 3 shows the general geometry of an irregular element where the external joint freedoms at the terminal end are defined in the XY'Z" system which is displaced through rotation θ about the X axis. The end forces and end moments on the element remain as defined in Fig. 2 (b) and (c). Equations (9) and (10) are the same for the irregular element. Then, the rows 1, 2, 3, 7, 8, and 9 of $[A]_e$ in eq. (13) are also the corresponding rows of the irregular element. The remaining rows of the statics matrix are determined by re-writing the equations of equilibrium given in eqs. (11) and (12) involving the necessary transformation through rotation θ . Thus, the force and moment equations of equilibrium for the terminal end joint of the irregular element are

$$\begin{Bmatrix} P(N_{10}) \\ P(N_{11}) \\ P(N_{12}) \end{Bmatrix} - [T_\theta] (F_1\bar{U}_1 + V_1\bar{U}_2 + V_2\bar{U}_3) = 0 \quad (14)$$

and

$$\begin{Bmatrix} P(N_4) \\ P(N_5) \\ P(N_6) \end{Bmatrix} - [T_\theta] (F_2\bar{U}_1 + F_3\bar{U}_3 - F_3\bar{U}_2) = 0 \quad (15)$$

where

$$[T_\theta] = \begin{bmatrix} 1 & 0 & 0 \\ 0 & \cos\theta & \sin\theta \\ 0 & -\sin\theta & \cos\theta \end{bmatrix} \quad (16)$$

is the matrix that transforms the internal forces at the terminal end joint from the XYZ coordinate system into the XY'Z" coordinate system. Thus, the statics matrix for the crankshaft irregular elements becomes that given in eq. (17). The numerical value of θ is a positive number when the rotation has taken in the right hand screw direction, negative otherwise. Note that rows 4 and 10 of matrices in eqs. (13) and (17) are the same since the rotation has taken place about the X axis, the axis of $P(N_4)$ and $P(N_{10})$.

Element internal stiffness matrix for an irregular element remains as given by eq. (8).

Since $[A]_e$ and $[S]_e$ matrices are determined by element properties such as E, G, A, X, Y, Z, L, I₁, I₂, J; the numbers of the global external joint freedoms at ends of an element; and if the element is an irregular one; reading these data for each element within a program, the element external stiffness matrix $[K_e]$ for each element is formed according to eq. (7), and its elements are stored to the corresponding locations of the global external stiffness matrix $[K]$. Thus, $[K_e]$ has the form of eq. (18). For example, for element 24 in Fig. 1, $N_1=65$, $N_2=66$, $N_3=67$,

$[A]_{e_{IR}} =$

P \ F	1	2	3	4	5	6
N ₁		-a	-d			
N ₂		-b	g		cg	
N ₃		-c			cd	
N ₄		a		-d	-h	cg
N ₅		b.cosθ +c.cosθ		g cosθ		cd.cosθ -h.sinθ
N ₆		c.cosθ -b.cosθ		-g sinθ		-cd.sinθ -h.cosθ
N ₇	-a		cg/L	cg/L	d/L	d/L
N ₈	-b		cd/L	cd/L	-g/L	-g/L
N ₉	-c		-h/L	-h/L		
N ₁₀	a		-cg/L	-cg/L	-d/L	-d/L
N ₁₁	b.cosθ +c.sinθ		(h.sinθ -cd.cosθ)/L	(h.sinθ -cd.cosθ)/L	$\frac{g}{L}\cos\theta$	$\frac{g}{L}\cos\theta$
N ₁₂	c.cosθ -b.sinθ		(cd.sinθ +h.cosθ)/L	(cd.sinθ +h.cosθ)/L	$-\frac{g}{L}\sin\theta$	$-\frac{g}{L}\sin\theta$

(17)

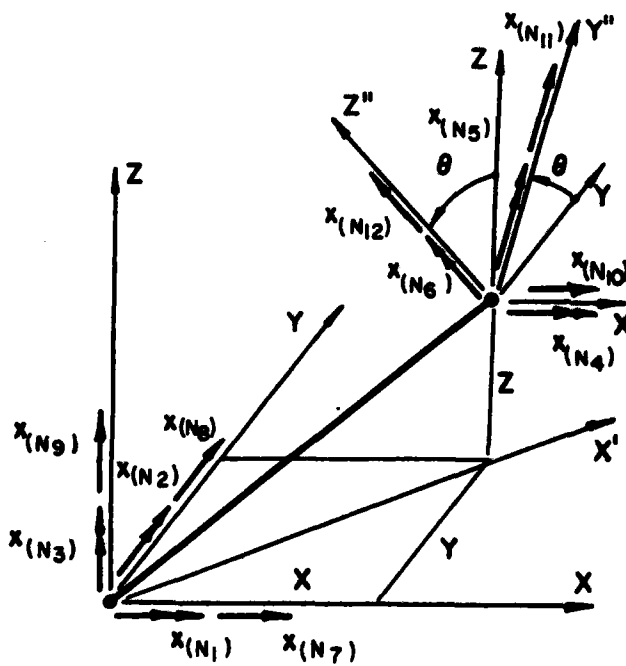


Fig. 3 - Element P-x diagram for irregular element with terminal point irregularity

$N_4=8, N_5=9, N_6=10, N_7=105, N_8=99, N_9=106, N_{10}=105, N_{11}=N_{12}=109, N_p+1$; and the (3, 10) element of its [K] matrix will be its contribution to the (67, 105) element of the global [K] matrix. In order that the element P-x diagrams defined in Figs. 2(a) and 3 can be applied to all the elements, the restrained freedoms are given the number N_p+1 . Although, this forms (N_p+1)th row and (N_p+1)th column during the formulation of [K] when superposing all the element [K_e] matrices, these column and row of [K] are discarded. For example, both (3,11) and (3,12) elements of [K_e] for element 24 in Fig. 1 will contribute to the (67, 109) element of [K].

$[K_e] =$

P \ X	N ₁	N ₂		N ₁₀	N ₁₁	N ₁₂
N ₁	x	x	f	x	x	x
N ₂	x	x	f	x	x	x
N ₃	x	x	f	x	x	x
N ₁₁	x	x	f	x	x	x
N ₁₂	x	x	f	x	x	x

(18)

THE MASS MATRIX

The global mass matrix [M] for the crankshaft is formed as a discrete mass matrix or as a consistent mass matrix. In both cases the global mass matrix is the sum of two global mass matrices:

$$[M] = [M_1] + [M_2] \quad (19)$$

where [M₁] is the contribution of the element masses and mass moments of inertia to the global mass matrix, [M₂] is the mass matrix consisting of the masses and mass moments of inertia of the externally mounted and concentrated objects on the crankshaft such as the gears, flywheels, and pulleys. Since in general objects are mounted on a crankshaft having their principal axes parallel to the external joint freedom axes, the products of mass inertia will vanish and [M₂] matrix will be a diagonal matrix. Depending on the number of externally mounted objects and the number of generalized coordinates used, some of the diagonal elements of [M₂] may be zero. No diagonal element of [M] can be zero, however. For example, in the system shown in Fig. 1, the mass of the gear at Z would form the (74, 74), (76, 76) and (77, 77) elements of [M₂] being lumped to the similarly numbered generalized coordinate freedoms which correspond to the external joint freedoms x₁₀₅, x₁₀₇, and x₁₀₈. mk²_x, mk²_y, and mk²_z will form the (37, 37), (38, 38), and (39, 39) elements of [M₂], respectively, corresponding to the external joint freedoms x₆₈, x₆₉, and x₇₀, respectively. m is the mass of the gear; k_x, k_y, and k_z are the radii of gyration about the axes designated by the subscripts.

The mass matrix [M₁] may be formed in two manners; either as a discrete mass matrix or as a consistent mass matrix. As a discrete mass matrix, [M₁] is a diagonal mass matrix for crankshafts such as the one shown in Fig. 1. Diagonal elements of [M₁] can be formed without the need for a discrete element mass matrix, although an element mass matrix simplifies the process by the aid of a computer. As an example, consider the generalized coordinates at point F in Fig. 1. Lumped to the generalized coordinates x₈₅(x₃₆), x₈₆(x₃₇), x₈₇(x₃₈), and x₈₈(x₃₉) are (m₅k₅²+m₆k₅²)/2, (m₅k_{5y}²+m₆k_{5y}²)/2, (m₅+m₆)/2, and (m₅+m₆)/2, respectively, where m₅, m₆ are the masses of elements 5 and 6. k₅ and k₆ are the radii of gyration of one half of elements 5 and 6 on the sides of F, about F. k_{5y} and k_{6y} are the radii of gyrations of these element masses about the Y axis. No rotary inertia about Z axis is considered since x₁₇ is not a generalized coordinate freedom. When a sufficient number of masses are used in a discrete mass model almost exact solution results are achieved [14].

Discrete Element Mass Matrix.

The global discrete mass matrix [M] can be formed as the superposition of discrete element mass matrices. Thus, the discrete element mass matrix [M_e]_D for a regular element whose princi-

pal axes lie along the axes of the joint freedom coordinate systems is given by eq. (20) in which q_i=N_i-N₀ designates the generalized coordinate corresponding to the external joint freedom x(N_i). ρ is the mass density (kg/m³) or lbf-sec²/in³). The radii of gyration are k_n=(L/4)²+k_{cn}² about any axis normal to the element axis, where n=1, 2, 3 designates axes X,Y,Z; k_{cn} is the centroidal radius of gyration of one-half of the element about the axis designated by n. When element data are read into a computer program, the nonzero elements of [M_e]_D are formed and stored to the locations of the global mass matrix designated by the global joint freedom numbers q₁=(N₁-N₀), q₂=(N₂-N₀), ..., q₁₂=(N₁₂-N₀). When q_i<0 and q_i>N_g, the mass matrix element is discarded since q_i<0 defines a neutral coordinate freedom and q_i>N_g defines a restrained freedom. Tapered elements are approximated by straight elements using the centroidal properties. The effect of element rotary inertias on the natural frequency of a system is very small and negligible in many instances. To neglect the effect of a rotary inertia, the corresponding joint freedom is considered a neutral coordinate freedom or restrained depending on the model used. If a torsional freedom is used as a neutral coordinate freedom, the torsional rotary inertia at the location is neglected, but the shear deformation still occurs, and the global stiffness of the system has the effect of shear deformations.

Consistent Element Mass Matrix.

The consistent mass matrix is a discrete mass matrix consisting of the effects of products of inertia, and it is the best approximation for the continuous mass model [9, 10, 12]. For the spatial finite line element used in this article, when the X or X' axis lies along the element line, the consistent element mass matrix [M_e]_{CX} is given by eq. (21), where r₁=J_t/ (3A), J_t being the torsional constant of the element cross-section, r₂=L²/105+2k_x²/15, r₃=-13L/420+k_x²/10L, r₄=-L²/140-k_x²/30, r₅=L²/105+2k_x²/15, r₆=11L/210+k_x²/10L, r₇=13L/420-k_x²/10L, r₈=13/35+6k_x²/5L, r₉=9/70-6k_x²/5L², r₁₀=13/35+6k_x²/5L², r₁₁=-11L/210-k_x²/10L, r₁₂=9/70-6k_x²/5L², r₁₃=13L/420-k_x²/10L, r₁₄=-L²/140-k_x²/10. k_y and k_z are the centroidal radii of gyration of the element cross-section about Y(or Y') and Z(or Z') axes, respectively.

For the elements that lie along a Y or Y' axis, the consistent mass matrix given in eq. (21) takes a different form since the principal axes of the element cross-section lie in a different joint freedom reference system. Thus, [M_e]_{CY} is given by eq. (22) where r₁₅=L²/105+2k_y²/15, r₁₆=-L²/140-k_y²/10, r₁₇=13/35+6k_y²/5L², r₁₈=9/70-6k_y²/5L², r₁₉=13L/420-k_y²/10L, r₂₀=11L/210+k_y²/10L, r₂₁=13L/420-k_y²/10L, and k_x is the centroidal radius of gyration of the element cross-section about the X axis.

When the effect of rotary inertias is to be neglected, k_x, k_y, k_z, and J_t are set to be zero in the element data.

$$[M_e]_D = \frac{\rho AL}{2}$$

q	q1	q2	q3	q4	q5	q6	q7	q8	q9	q10	q11	q12
q1	k_1^2											
q2		k_2^2										
q3			k_3^2									
q4				k_1^2								
q5					k_2^2							
q6						k_3^2						
q7							1					
q8								1				
q9									1			
q10										1		
q11											1	
q12												1

(20)

$$[M_e]_{C_x} = \rho AL$$

q	q1	q2	q3	q4	q5	q6	q7	q8	q9	q10	q11	q12
q1	r_1			$r_1/2$								
q2		r_2			r_4				r_{11}			r_3
q3			r_5			r_{14}		r_6			r_{13}	
q4	$r_1/2$			r_1								
q5		r_4			r_2				r_7			$-r_{11}$
q6			r_{14}			r_5		$-r_{13}$			$-r_6$	
q7							$1/3$		$1/6$			
q8			r_6			$-r_{13}$		r_8			r_9	
q9		r_{11}			r_7				r_{10}			r_{12}
q10							$1/6$		$1/3$			
q11			r_{13}			$-r_6$		r_9			r_8	
q12		r_3			$-r_{11}$				r_{12}			r_{10}

(21)

Element mass matrix for an irregular crankshaft element is the same as given by eqs. (20)-(22) depending on the type of model used, since the irregular element is of circular cross-section.

MODELING FLEXIBLE SUPPORTS

Flexible supports tend to reduce the critical speed level of a crankshaft. When a bearing housing is mounted on flexible mounts for the purpose of absorbing vibration, the rigidity of the support is lost and an appreciable amount of reduction in the critical speed is observed. Hence, it becomes important to know the reducing effect of flexible bearings on the operating speeds of

crankshafts, straight shafts, and the machine in which they operate. Incorporating a flexible bearing in the dynamic model of a crankshaft merely introduces restrained linear regular elements, and it may cause some regular shaft elements to become irregular elements. Shown in Fig. 4(a) is a portion of a crankshaft mounted on flexible bearings at A and D, where it is assumed that the bearings are linear springs experiencing axial deformations only in Y and Z directions under the radial loading. K_1 and K_2 , for example, represent linear spring rates of the support at A for loading in Z and Y directions, respectively. In the finite element model they are bars experiencing axial deformations only. Thus, bar AB and AC experience

$$[M_e]_{C_y} = \rho AL$$

q	q1	q2	q3	q4	q5	q6	q7	q8	q9	q10	q11	q12
q1	r15			r16					r20			r21
q2		r1			r1/2							
q3			r5			r14	-r6			-r13		
q4	r16			r15					-r21			-r20
q5		r1/2			r1							
q6			r14			r5	r19			r20		
q7			-r6			r19	r8			r19		
q8								1/3			1/6	
q9	r20			-r21						r17		r18
q10			-r13			r20	r18			r8		
q11								1/6			1/3	
q12	r21			-r20						r18		r17

(22)

joint freedoms x_{53} and x_{56} , respectively. All the other freedoms on these elements are restrained. The shaft experiences all three rotary freedoms at the support; x_{50} , x_{51} , x_{52} . At support D the only difference is in that the shaft is permitted to experience axial play in the bearing housing due to the linear freedom x_9 , that the joint of the shaft experiences. Ends of the bars representing the springs do not experience linear freedoms in the X direction. When preparing the element data for these spring bars, E_1 , A_1 , and L_1 values must be assigned to render $K_1 = E_1 A_1 / L_1$.

If the bearing housing experiences a considerable amount of rotational deformations about X, Y, and Z axes, rotary freedoms such as those designated by (*), (**), and (***) for the spring element AC are considered active freedoms, respectively, within the neutral coordinate freedoms. In that case the spring element is a cantilevered beam element experiencing flexural and torsional deformations, and the element data must furnish G, I_1 , I_2 , and J values also to render the flexural and torsional spring rates of the bearing housing in the respective directions. In Fig. 4(b) elements 11 and 12 are regular elements. However, elements 15, 23, and 24 are irregular elements, and in their statics matrices given by eq. (17) one must use $\theta = \beta_1$, $\theta = -\beta_1$, and $\theta = \beta_2$, respectively.

COMPUTER PROGRAM

A digital computer program in FORTRAN IV language is prepared to perform the frequency analysis of crankshafts having any nonuniformity along the shaft and along the throw sides, any number of throws and externally mounted objects,

any number of rigid or elastic supports? The program forms the global external stiffness matrix [K] and the global generalized coordinate element mass matrix $[M_1]$ as it reads the element data one element at a time where the type of element mass matrix to be used must be defined for each element. The nonzero elements of the external load mass matrix $[M_2]$ are read separately in an array in the order of the corresponding generalized coordinates. The program inverts [K] and partitions it according to N_0 and N_g to determine $[\delta g]$, then forms [Dm] and solves eq. (4) for λ_1 and $\{R_1\}_1$ for the fundamental critical speed of the crankshaft. It reduces [Dm] by eq. (5) and solves eq. (4) for the higher mode frequencies and the corresponding mode vectors as many as desired.

Element data requires E, G, I_1 , I_2 , J, X, Y, Z, ρ global joint freedom numbers N_1 , N_2 , ..., N_{12} , identification number designating if the element is regular or irregular, θ if there is any, identification number designating if discrete or consistent element mass matrix is to be used, k_x , k_y , k_z , k_{G_1} , k_{G_2} , k_{G_3} , if required.

NUMERICAL EXAMPLE AND EXPERIMENTAL RESULTS

A very flexible unbalanced crankshaft, supported by four ball bearing supports, having three equally spaced throws of different crank radii and carrying three externally mounted disks, shown in Fig. 5, was designed for experiments to verify computer solutions for different finite element-dynamic models at low speeds. The crankshaft was driven by a variable speed drive motor

* The copy of the program is available for the interested reader.

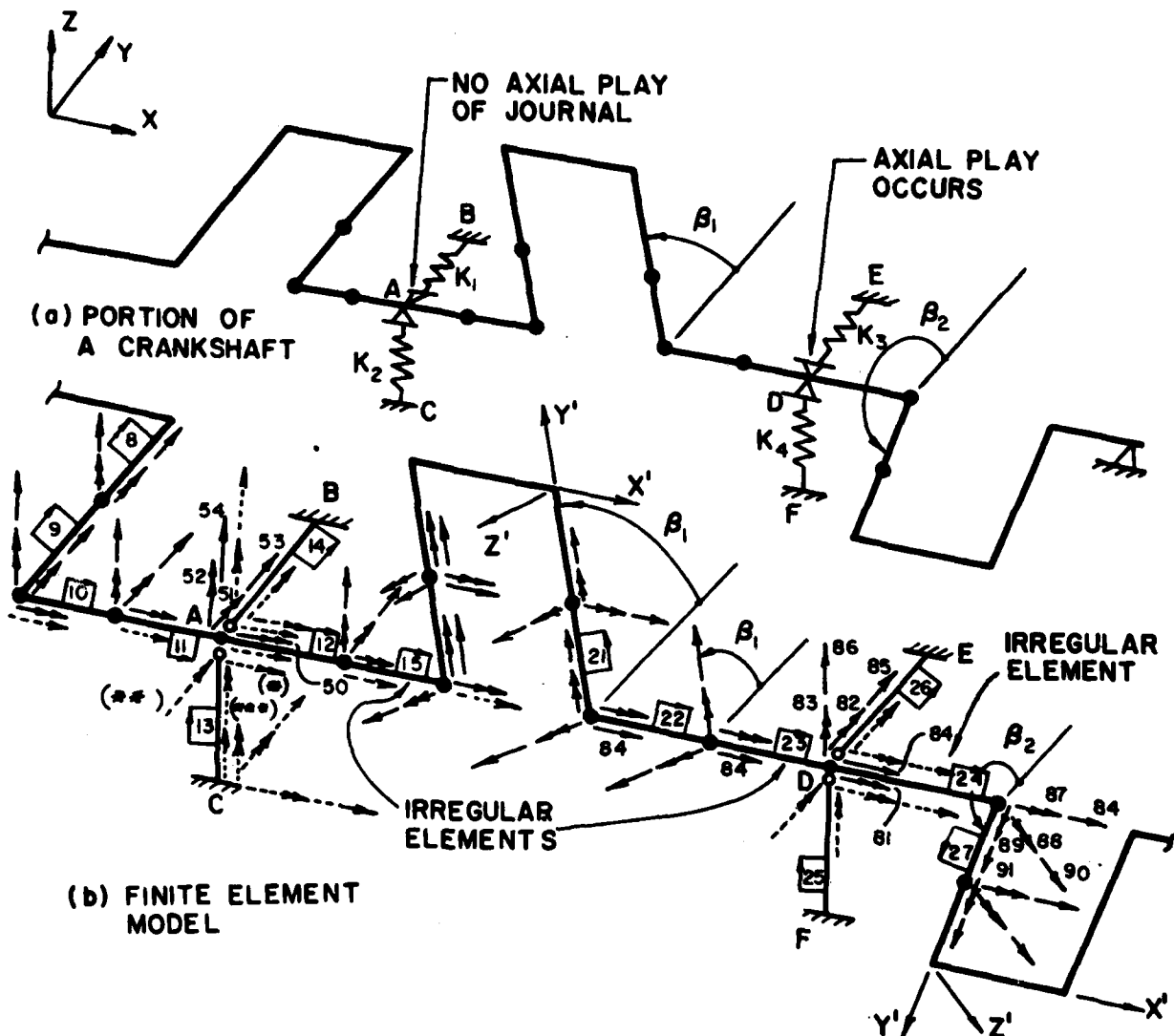


Fig. 4 - Modeling of Flexible Supports

to which it was connected by a flexible coupling, LOVEJOY No: L-100, of torsional stiffness 5156 in.-lbf/rad. The whole crankshaft assembly was mounted on a steel frame. See the experimental setup in Fig. 6. Material is steel of density 0.28 lbf/in³, $E=30 \times 10^6$ psi, $G=11 \times 10^6$ psi. Shaft portions and crank pins are connected to the throw sides by silver soldering. Using 45 elements and the aforementioned digital computer program, the frequency analysis of this crankshaft was performed for several dynamic models to investigate the effect of different system properties. Figure 7 shows locations of joints. These models are considered in eleven cases described in the following. The frequen-

cies and the critical speeds for the first four modes are given in Table 1 for each case.

Case 1. Pure torsion of shaft elements about the X axis considering linear freedoms on the throw joints in the Z and Z' directions as generalized coordinates since throw and crank pin masses contribute to torsional moment. Rotary inertia of the externally mounted disks about the X axis are considered along with the throw masses contributing to torsion. Shaft elements experience no flexural and axial deformations; throw and crankpin elements experience no axial deformation, no linear freedom and flexural rotation in the XY and X'Y' planes. $N_p=93$, $N_0=42$,

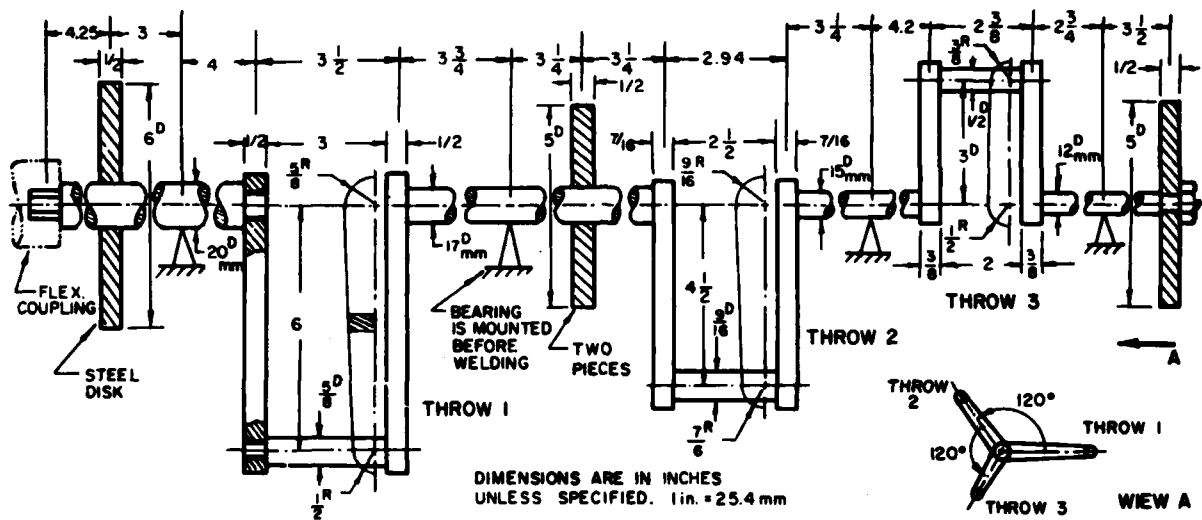


Fig. 5 - Geometry and the Dimensions of the Experimental Crankshaft

$N_g=51$. Discrete mass matrix is used. The sample P-x diagram for the reference throw is shown in Fig. 8(a), where the element AB is the flexible coupling element experiencing torsional deformation only in all cases.

Case 2. This is the same as in Case 1 but included are the torsional rotary inertias of the shaft elements. The corresponding freedoms such as x_2 to x_6 in Case 1 are included in the generalized coordinates. $N_p=93$, $N_g=66$. Discrete mass matrix is used.

Case 3. In this case every element experiences torsional and flexural deformations except the

axial deformations. No flexural and torsional rotary inertia of elements and externally mounted disks are considered. Only masses of the elements and disks are considered. This, certainly considers inertial torque effect of throw sides and crankpins. $N_p=214$, $N_g=79$. Figure 8 (b) shows the sample P-x diagram for this case. Discrete mass matrix is used.

Case 4. In addition to masses considered in Case 3, this case includes torsional rotary inertias of the shaft and crankpin elements and of the disks. No flexural rotary inertia is considered except those of the elements on the throw sides about the X and X' axes contributing



Fig. 6 - Experimental setup: Textronix Type 562 oscilloscope, Perkin M377 power supply, Berkley 7160 electronic counter, ELECTRO 3060 AN magnetic pick-up, vibration pick-up General Radio 1560-P52, vibration pick-up on the second bearing, vibration meter General Radio 1553-A

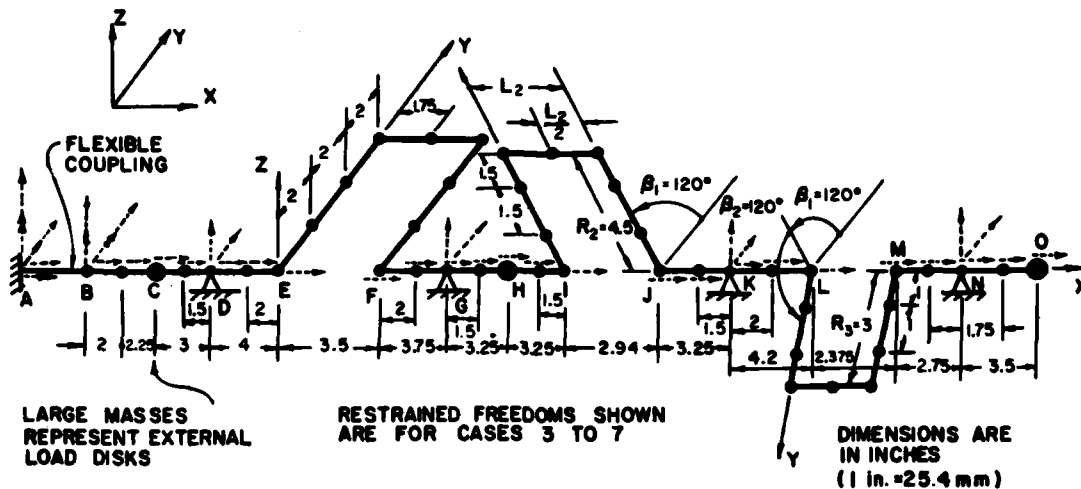


Fig. 7 - Joint locations and the restrained joint freedoms in Cases 3 to 10

to the torsional rotary inertia of the shaft. Torsional rotary inertias of the throw side elements are not considered. $N_p=214$, $N_g=124$. Figure 8(c) shows the sample P-x diagram for this case. Discrete mass matrix is used.

Case 5. In this case the masses and flexural rotary inertias of the shaft elements, crankpins, throw side elements and external load disks are considered. No torsional rotary inertia is considered except those of the throw side elements since they contribute to flexural deformations of shaft and crankpin elements. $N_p=214$ and $N_g=169$. Figure 8(d) shows the sample P-x diagram for this case. Discrete mass matrix is used.

Case 6. In this case masses, torsional, and flexural rotary inertias of every element in the model and of the external load disks are considered. $N_p=N_g=214$. Discrete mass matrix is used.

Case 7. This is as in Case 6, but consistent element mass matrix is used along with the discrete external load mass matrix $[M_2]$. The masses and rotary inertias due to extensions at throw-shaft and throw-crankpin joints are considered as discrete masses in their proper directions in $[M_2]$. $N_p=214$ and $N_g=214$.

Case 8. In this case the crankshaft is reduced to an equivalent straight shaft experiencing torsional deformations only, where a throw is replaced by its crankpin introducing one additional joint at the midpoint of the crankpin for each throw. The rotary inertia of the crankpin about the axis of the shaft, that is, its centroidal moment of inertia about the X axis plus the product of its mass with the square of the crank radius, is lumped as the torsional rotary inertia to the newly introduced torsional joint

freedom. The rotary inertia of a throw side about the axis of the shaft is lumped to rotary freedom at the joint connecting the throw to the shaft. $N_p=27$ and $N_g=27$. The P-x diagram for this case for the same portion of the shaft is given in Fig. 8(e). There are ways of forming equivalent straight shafts to replace the crankshafts, which are somewhat of rule-of-thumb type arbitrary procedures and considered in Case 9 [1, 17]. The modeling of the crankshaft in this Case offers a rational way of reducing a crankshaft into an equivalent straight shaft whose torsional frequency may also be determined by using finite element techniques incorporating simpler line elements. One such technique is given in [4]. Discrete mass matrix is used in this case.

Case 9. In this case the straight shaft equivalent torsional model of the crankshaft is similar to that of Case 6, but the throw is replaced by an equivalent shaft portion using the rules given in [1] and [17] which are formulated to reduce the torsional frequency of the equivalent shaft considerably to achieve conservative results and overdesigns, and are suited for crankshafts having small crank radii and thick throw sides, where the crankpin and throw sides are reduced to shaft portions of diameter on the side of the throw or of the crankpin (as used in this case). The sum of the rotary inertias of the crankpin and of the throw sides is lumped to the joint at the center of the equivalent portion. In this case the freedoms at the throw sides are not generalized coordinates, although they may exist due to diameter change along the equivalent shaft. Thus, $N_p=21$ and $N_g=21$. The rule of [1] recommends the length of the equivalent shaft portion replacing the throw to be about the length of the throw. The frequencies for the models obtained using the rules of [1] and [17] are given in Table 1.

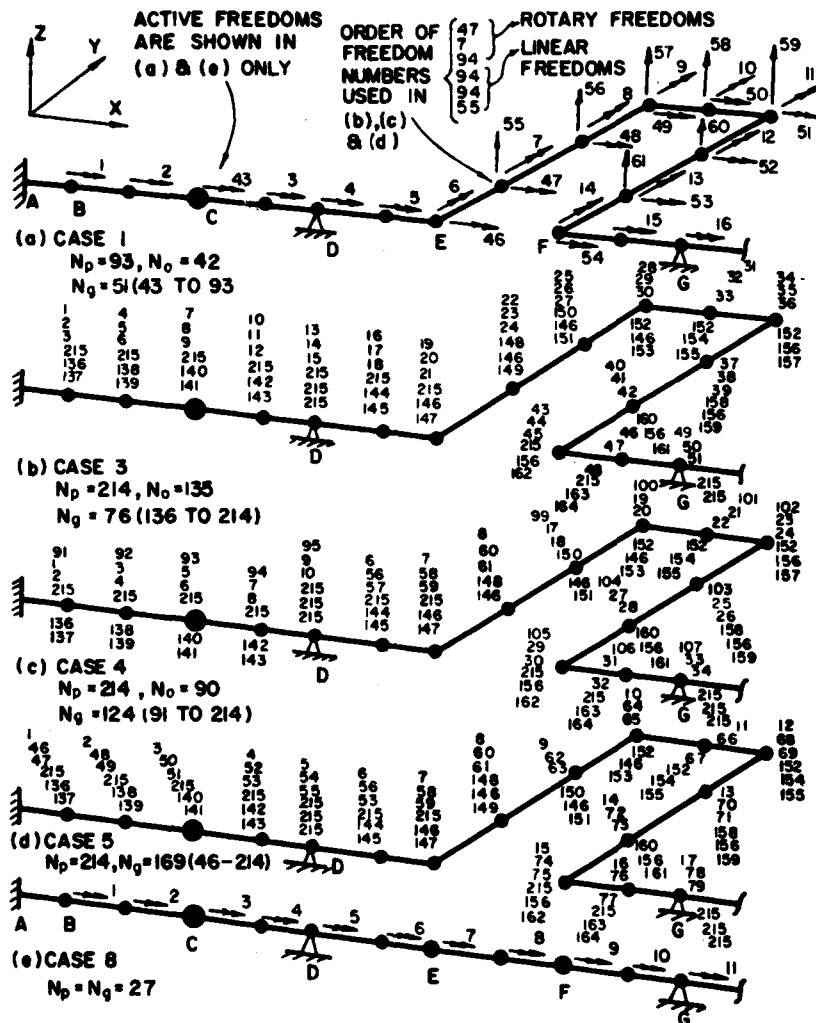


Fig. 8 - Sample P-x diagrams for the first throw portion of the crankshaft:
 (a) for Case 1, (b) for Case 3, (c) for Case 4
 (d) for Case 5, and (e) for Case 8

Case 10. This is the same as Case 6 but the torsional stiffness of the flexible coupling is reduced to 3000 in.-lbf/rad. Reduction in the operable critical speed of the shaft is noticeable.

Case 11. This is the same as Case 6, but all the supports are considered flexible and are replaced by two linear springs each as shown at support A in Fig. 4, where the spring rates of both springs at each support at D, G, K, and N in Fig. 7, respectively, are 1000, 800, 600, 400 lbf/in. The effect of flexible supports on the operable critical speed of a crankshaft is noticeable.

Experimental Results.

The experimental crankshaft of Fig. 5, mounted on a steel frame was run at different speeds and the amplitude of the vertical acceleration of the top of the second bearing from the left was measured by vibration meter (see the experimental setup in Fig. 6) and plotted with respect to the crank speed rps (Hz.) in Fig. 9. The peak of the acceleration plot shows the actual critical speed of the shaft to be 1350 rpm, or 141.37 rad/s. The first peak at 13 rps was due to the noticeable vibration of the plate at the top of the supporting frame.

Discussion of the Results.

Studying the results for different dynamic models given in Table 1 following conclusions can be drawn. Any of Cases 6 and 7 is a complete and most reliable model. Comparison of Cases 1, 2, and 6 shows that the system is primarily torsional. However, comparison of Cases 3 and 5 with Case 4 shows that maintaining the flexural flexibility of throws is most desirable. The model of Case 8 appears to be a reliable equivalent straight shaft model of a crankshaft for the determination of the fundamental critical speed of the crankshaft. A healthier and rational one in comparison to those of conventional rules, since the model of Case 8 is entirely dependent on the crankshaft geometry. It leads to error on the unsafe side for the higher mode critical speeds.

Comparison of Cases 6 and 7 with Case 8 also shows the considerable effect of the flexural properties of the crankshaft on the higher mode critical speeds.

Flexible coupling and slugs in belts, chains, and clearances in geared connections tend to make the crankshaft behave as a free-free system in the direction of the torsional freedoms along the shaft axis, and drastically reduce the operable critical speeds of the crankshafts. Case 10 illustrates the phenomena. The fundamental critical speeds for Cases 4 and 5 with the reduced torsional stiffness of the flexible coupling were 2159.10 and 1400.84 rpm, respectively. Conventional methods of forming equivalent pure torsional models for crankshafts appears to be arbitrary and may lead to over-designs, as seen in Cases 8 and 9, or they may lead to unsafe designs. The effect of flexible supports on the critical speed level is reduction as seen in Case 11.

CONCLUSIONS

The method of determining critical speeds of crankshafts using finite line element method considering the throws in their actual geometries presented in the foregoing with experimental verification is a very efficient, reliable, and powerful tool for the dynamic design of industrial crankshafts. Farewell to costly test-and-modify type conventional designs based on experiments on prototype models. Modelings in Cases 6 and 7 are the most recommended ones. When only the fundamental critical speed is of the prime interest, the modeling of Case 8 offers a very simple tool which can also be handled with finite element techniques using simpler elements [4].

It is hoped that the contents of the article and the computer program made available will be of value for the practicing engineers and the teachers of mechanical design.

REFERENCES

1. J. P. Den Hartog, *Mechanical Vibrations*, pp. 184-200, McGraw-Hill, New York 1956.
2. R. K. Vierck, *Vibration Analysis*, Second Edition, pp. 333-357, Harper and Row, publishers, New York, 1979.
3. N. Shaikh, "A Direct Method for Analysis of Branched Torsional Systems," ASME Paper No. 73-DET-134, four pages.
4. C. Bagci, "A Computer Method for Computing Torsional Natural Frequencies on Nonuniform Shafts, Geared Systems, and Curved Assemblies," Proceedings of the 3rd OSU Applied Mechanisms Conference, Stillwater, Oklahoma, 1973, pp. 40.1-40.15.
5. V. F. Groza, and V. F. Yanushevskaya, "Natural Frequency Analysis of Crankshafts Using Three-Dimensional Beam Elements by the Method of Orthogonal Dynamic Joint Equilibrium Vector," *Izvestiya Vysshikh Uchebnykh Zavedenii Mashinostroyeniya*, No. 8, 1971, pp. 34-39.
6. J. L. Kempner and S. V. Nesterova, "Critical Speed Study of Crankshafts in Their Spatial Forms Using Myklestad Iteration Technique," *Izvestiya Vysshikh Uchebnykh Zavedenii Mashinostroyeniya*, No. 9, 1974, pp. 22-25.
7. C. Bagci, "A Computer Method for Computing Critical Speeds of Nonuniform Shafts on Many Rigid or Elastic Supports," Proceedings of the 3rd OSU Applied Mechanisms Conference, Stillwater, Oklahoma, 1973, pp. 39.1-39.13.
8. S. Kalaycioglu and C. Bagci, "Determination of the Critical Operating Speeds of Planar Mechanisms by the Finite Element Method Using Planar Actual Line Elements and Lumped Mass Systems," *Trans. ASME, Journal of Mechanical Design*, Vol. 101, No. 2, 1979, pp. 210-223.
9. J. S. Przemieniecki, *Theory of Matrix Structural Analysis*, pp. 287-309, McGraw-Hill, New York, 1968.
10. J. S. Archer, "Consistent Mass Matrix for Distributed Mass Systems," *Proceedings of ASCE, Journal of the Structural Division*, Vol. 89, No. ST4, 1963, pp. 161-178.
11. R. E. Sholl, "Dynamic Analysis of Three-Dimensional Frames," *Proceedings of ASCE, Journal of the Structural Division*, Vol. 98, ST1, 1972, pp. 401-406.
12. F. Venancio-Filho, "3-D Frame Vibrations by Consistent Mass Matrix," *Proceedings of ASCE, Journal of the Structural Division*, Vol. 99, ST9, 1973, pp. 1965-1969.
13. C. Bagci and S. Kalaycioglu, "Elastodynamics of Planar Mechanisms Using Planar Actual Finite Line Elements, Lumped Mass Systems,

Matrix-Exponential Method, and the Method of 'Critical-Geometry-Kineto-Elasto-Statics' (CGKES)," *Trans. ASME, Journal of Mechanical Design*, Vol. 101, No. 3, 1979, pp. 417-427.

14. C. K. Wang, *Computer Methods in Advanced Structural Analysis*, InText Press, Inc., pp. 14-23, New York, 1973.
15. C. K. Wang, *Matrix Methods of Structural Analysis*, Second Edition, pp. 268-282, International Textbook Company, Scranton, Pennsylvania, 1979.

16. C. Bagci, "Elastic Stability and Buckling Loads of Three-Dimensional Nonuniform Framed Systems by Finite Element Method Using Spatial Line Elements," *Computers and Structures*, Vol. 10, No. 5, 1979, pp. 731-743.

17. J. M. Siegel, V. L. Maleev and J. B. Hartman. *Mechanical Design of Machines*, pp. 394-400, International Textbook Company, Scranton, Pennsylvania, 1965.

TABLE 1

Frequencies and the Corresponding Critical Speeds of the Experimental Crankshaft for the First Four Modes for the Eleven Cases Studied as Computed by the Analytical Finite Element Method

CASE	NUMBER OF ELEMENTS N _p N _g	FREQUENCY ω (rad./s) AND CRITICAL SPEED (rpm)	η MODE NUMBERS			
			1	2	3	4
1	45	ω	159.18	513.73	816.11	1586.04
	93	rpm	1520.06			
2	45	ω	143.01	469.71	867.25	1423.68
	93	rpm	1365.64			
3	45	ω	185.29	441.64	474.17	709.78
	214	rpm				
4	45	ω	249.66	287.50	474.56	617.63
	214	rpm	2384.08			
5	45	ω	185.28	407.95	437.38	704.55
	214	rpm	1769.29			
6 DISCRETE MASS	45	ω	140.48	390.26	431.46	440.26
	214	rpm	1341.49			
7 CONSISTENT MASS	45	ω	141.03	392.47	435.23	446.61
	214	rpm	1346.74			
8 EQUIVALENT PURE TORSIONAL REDUCTION	27	ω	140.29	418.85	767.94	1248.84
	27	rpm	1339.67			
9 CONVENTIONAL PURE TORSIONAL	21	ω [1]	123.60	339.78	608.16	988.34
	21	ω [17]	112.36	308.89	552.88	810.11
10 AS IN CASE 6 WITH FLEXIBLE COUPLING STIFFNESS OF 3000 in.-lbf/rad.	45	ω	111.09	387.99	428.54	439.22
	214	rpm	1060.83			
11 AS IN CASE 6 WITH FLEXIBLE SUPPORTS	45	ω	96.22	272.91	308.19	323.72
	214	rpm	918.83			

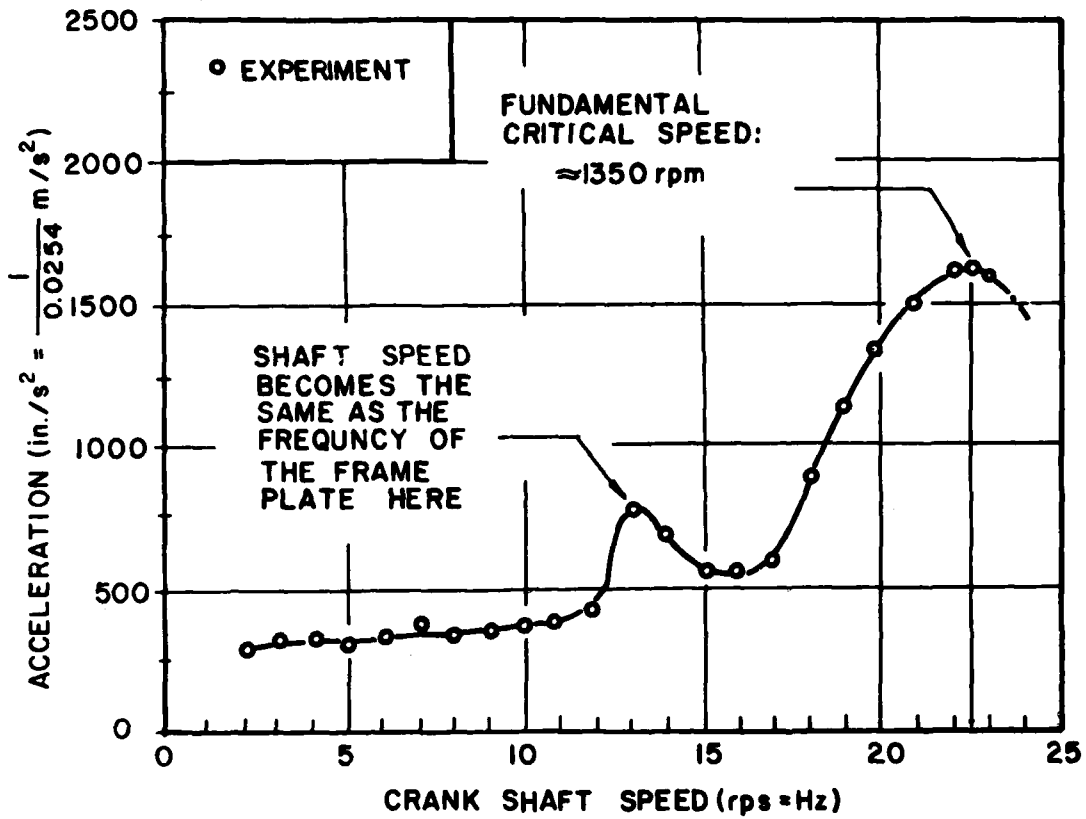


Fig. 9 - Acceleration amplitude measured at the top of the second bearing at different speeds of the experimental crankshaft shown in Figs. 5 and 6, depicting its critical speed to be about 1350 rpm

DYNAMIC ANALYSIS

A PARAMETRIC STUDY OF THE IBRAHIM TIME DOMAIN MODAL IDENTIFICATION ALGORITHM

Richard S. Pappa
Structural Dynamics Branch
NASA Langley Research Center
Hampton, Virginia

and

Samir R. Ibrahim
Department of Mechanical Engineering and Mechanics
Old Dominion University
Norfolk, Virginia

The accuracy of the Ibrahim Time Domain (ITD) identification algorithm in extracting structural modal parameters from free-response functions has been studied using computer-simulated data for 65 positions on an isotropic, uniform-thickness plate, with mode shapes obtained by NASTRAN analysis. Natural frequencies, damping factors, and response levels of the first 15 plate modes were arbitrarily assigned in forming the response functions, to study identification results over ranges of modal parameter values and user-selectable algorithm constants. Effects of superimposing various levels of noise onto the functions were investigated in detail. A particularly interesting result is that no detrimental effects were observed when the number of computational degrees-of-freedom allowed in the algorithm was made many times larger than the minimum necessary for adequate identification. This result suggests the use of a high number of degrees-of-freedom when analyzing experimental data, for the simultaneous identification of many modes in one computer run. Details of the procedure used for these identifications are included.

INTRODUCTION

A fundamental problem in experimental structural dynamics is the accurate determination of parameters characterizing the important vibration modes of a test structure. These parameters--natural frequencies, damping factors, and mode shapes--are used for a variety of purposes, including:

1. trouble-shooting excessive vibration or noise from mechanical equipment;
2. dynamic analysis of portions of a structure that are too difficult to model analytically;
3. refinement or verification of an analytical model; and
4. direct calculation of dynamic loads or response levels that a structure may experience during operation.

An additional future use of experimentally determined modal parameters, of current research interest to NASA, is in the active attitude control of large space structures.

Obviously, the applications and corresponding accuracies which are required of these data vary considerably. Results adequate for one use may be unacceptable for another. In addition, accuracy requirements for particular applications may be difficult to quantify and may be subject to error. Establishing the adequacy of experimental modal data still often includes a judgement of whether the most accurate set of data, within an allocated period of time, has been obtained.

Before the widespread use of mini-computers in the laboratory, modal testing and analysis were conducted almost exclusively with analog instrumentation. As the advantages of digital computation

because apparent, many data analysis techniques that had been developed on the analog systems were simply converted to their digital counterparts. These techniques are, in fact, still used today in successfully measuring the dominant modal patterns of "well-behaved" structures. Accompanying the conversion to digital-based laboratory equipment was an increased use of random force, as opposed to sinusoidal force, for exciting test structures. This trend was closely related to the revolutionary switch in the late 1960's to fast Fourier transform (FFT) methods for rapidly computing frequency-domain characteristics of random response signals. Although many structures are still tested with the classical multiple-shaker, sine-dwell approach, the majority of experimental dynamists now select the faster random-force methods for modal testing.

A standard step in the data-reduction phase of most modal test programs is the computation of frequency-domain characteristics of the measured structural responses. In controlled ground vibration tests where the input force(s) as well as the responses can be accurately measured, acceleration/force frequency response functions are usually formed; in cases where the input forces cannot be measured, the response information alone is used. Many single- and multi-degree-of-freedom algorithms have been developed to identify the structural modal parameters by curvefitting analytical expressions to these data [1]. Single-degree-of-freedom methods use a few data points near each resonant frequency for quickly estimating the modal parameters of one mode at a time. Because in these techniques it is assumed that the overall response near each resonance is dominated by the characteristics of a single mode, however, the degree of modal coupling in any frequency interval significantly affects identification results. On the other hand, multi-degree-of-freedom algorithms, developed to identify the parameters of several modes simultaneously, nearly always work well on data that can be reasonably analyzed with single-degree-of-freedom methods, but may differ appreciably in more difficult cases.

Various aspects of using time-domain response data rather than frequency-domain functions in the experimental modal identification of structures excited by random forces(s) have been discussed previously by Ibrahim [2-6]. An early multi-degree-of-freedom time-domain identification procedure [2] required numerical integration (assuming the measurement of acceleration responses) to obtain displacement and velocity time

histories at each response measurement point, in addition to the measured acceleration time histories. This approach was later abandoned in favor of a more straightforward method [3] in which any one of displacement, velocity, or acceleration free-response functions are used in an eigenvalue solution scheme to obtain the desired modal parameters. This newer procedure is referred to in this paper as the ITD ("Ibrahim Time Domain") algorithm. The term "free-response" function is used throughout this paper to denote any of three time response forms which may be used in the identification algorithm: actual free-decays measured following random excitation of a structure; unit-impulse-response functions formed by inverse Fourier transformation of frequency response functions; or "random-decrement" functions [4] computed from random operating time histories.

The ITD algorithm has been used to analyze test data from several structures [7, eg]. As now implemented, the identification process is a "blind" technique, requiring a minimal amount of operator input to compute parameters for many modes from a set of free-response functions. A large number of structural modes, often 20 or more, are identified in a single computer run. In general, the parameters computed for the dominant modes of these structures agreed well with those obtained by other methods. Parameters for modes identified by the ITD analyses, but not determined with other analysis methods, however, lacked verification and their accuracy was rightfully questioned.

The work reported in this paper was initiated to help interpret these experimental results. For this study, computer-simulated free-response data, for linear, multi-mode models with known modal parameters, were processed with the ITD algorithm. The identified parameters were used to quantify the ability and accuracy of the identification process, to look for anomalous numerical behavior under severe identification conditions, and to compare results for ranges of the few user-selectable algorithm constants. The modeling approach consisted of constructing free-response functions for 65 positions on an isotropic, uniform-thickness rectangular plate by the linear summation of the free-responses of the first 15 analytical modes. The mode shapes were obtained from a finite-element analysis, and modal frequencies, damping factors, and response levels were arbitrarily assigned for each desired modal model. Various levels of noise, calculated on an rms-

percentage basis, were superimposed onto the free-response functions.

Techniques for obtaining distortion-free sets of free-response functions from experimental measurements, an important phase in the modal identification process when the ITD algorithm is used, are not addressed in this paper.

Somewhat new terminology is used in describing the algorithm. To avoid confusion in correlating the identification results with the usage of the free-response data in the procedure, complete details of the technique are included. The methods used in constructing the free-response functions and in quantifying the accuracy of identified mode shapes are described in the following report sections. The remainder of the report contains a summary of the identification results. These data illustrate typical identification accuracies over a wide range of simulated modal models and user-selectable algorithm constants.

LIST OF SYMBOLS

$a_k + ib_k$	k'th complex eigenvalue of [A]
[A]	the "system" matrix
[A] ^T	Transpose of [A]
C	a damping coefficient
(C/C _c) _k	damping factor (fraction of critical damping) of k'th mode
f_k	frequency corresponding to k'th eigenvalue of [A]
f_x	multiples of the frequency $1/(2(\Delta t)_3)$
f_π	"folding frequency" based on $(\Delta t)_1$
i	measurement station index
j	time index
k	mode index
K	a spring constant
m	number of assumed modes (= NDOF)
M	a mass
N_1, N_2, N_3	number of time samples corresponding to $(\Delta t)_1$, $(\Delta t)_2$, and $(\Delta t)_3$
P_0	number of response measurements available
s	number of time samples in each free-response function (= NCOL)
t_j	time instant j
T	total time length of response functions
x_{ij}	free-response of station i at time instant j
$(\Delta t)_1$	time increment between the two response matrices, [ϕ] and [$\hat{\phi}$]
$(\Delta t)_2$	time increment in forming "transformed stations"

$(\Delta t)_3$	time increment between data in upper and lower halves of the response matrices
Δt	an arbitrary time increment
ϵ	a small uncertainty in an eigenvalue determination
θ_k	angular position of k'th eigenvalue in the a-b plane
λ_k	characteristic value of mode k
[Λ]	a matrix of complex exponentials
σ_k	damping value of k'th mode (= real part of characteristic value)
σ_{k2}	damping value of k'th mode using alternate method
[ϕ]	response matrix whose rows contain the free-response functions
[$\hat{\phi}$]	The [ϕ] matrix delayed $(\Delta t)_1$
[ψ] _k	complex eigenvector of mode k
[Ψ]	matrix whose columns are the system's eigenvectors
[$\hat{\Psi}$]	the [Ψ] matrix with responses delayed $(\Delta t)_1$
$(\omega_d)_k$	damped natural frequency of k'th mode (= imaginary part of characteristic value)
$(\omega_n)_k$	undamped natural frequency of k'th mode

Abbreviations

ITD	Ibrahim Time Domain (technique)
MAR	Modal Amplitude Ratio
MCF	Modal Confidence Factor
MSCC	Mode Shape Correlation Constant
NCOL	Number of Columns in [ϕ] and [$\hat{\phi}$]
NST	Number of (measurement) Stations used in calculation of OAMCF
OAMCF	Overall Modal Confidence Factor
RMS	Root-Mean-Square (value)
SF	data Sampling Frequency (= reciprocal of time interval between data samples)

THEORY OF THE IDENTIFICATION TECHNIQUE

The Eigenvalue Solution Approach

The characteristic equation for a classical single-degree-of-freedom structural system, governed during its free response by

$$M \ddot{x} + C \dot{x} + K x = 0 \quad (1)$$

is $\lambda^2 M + \lambda C + K = 0$, and the general solution form is $x(t) = \psi e^{\lambda t}$. For an overdamped system, ψ and λ are both real-valued; for an underdamped system, they are complex, occurring in conjugate pairs.

In the more common underdamped case, the roots of the characteristic equation

are $\lambda = \sigma \pm i \omega_d$, where ω_d is the damped natural frequency in radians/sec-ond, $\omega_n = \sqrt{\sigma^2 + \omega_d^2}$ the undamped natural frequency, and $\zeta = \sigma/\omega_n$ the damping factor or fraction of critical damping, C/C_c .

For a linear multi-degree-of-freedom system with m excited modes, the free response of the structure at any (measurement) station i and instant of time t_j can be expressed by the summation of the individual response of each mode as:

$$x_i(t_j) = x_{ij} = \sum_{k=1}^{2m} \psi_{ik} e^{\lambda_k t_j} \quad (2)$$

where ψ_{ik} and λ_k are both complex numbers, in general. Note that the summation extends to $2m$ since there are $2m$ roots of the characteristic equation.

Free-response values for $2m$ stations and s instants of time, calculated using Eq. (2), can be arranged into matrix form as:

$$\begin{bmatrix} x_{11} & x_{12} & \dots & x_{1s} \\ x_{21} & x_{22} & \dots & x_{2s} \\ \cdot & & & \cdot \\ \cdot & & & \cdot \\ \cdot & & & \cdot \\ x_{2m,1} & \dots & x_{2m,s} \end{bmatrix}$$

$$= \begin{bmatrix} \psi_{11} & \psi_{12} & \dots & \psi_{1,2m} \\ \psi_{21} & \psi_{22} & \dots & \psi_{2,2m} \\ \cdot & & & \cdot \\ \cdot & & & \cdot \\ \cdot & & & \cdot \\ \psi_{2m,1} & \dots & \psi_{2m,2m} \end{bmatrix} \chi$$

$$\begin{bmatrix} e^{\lambda_1 t_1} & e^{\lambda_1 t_2} & \dots & e^{\lambda_1 t_s} \\ e^{\lambda_2 t_1} & e^{\lambda_2 t_2} & \dots & e^{\lambda_2 t_s} \\ \cdot & & & \cdot \\ \cdot & & & \cdot \\ \cdot & & & \cdot \\ e^{\lambda_{2m} t_1} & \dots & e^{\lambda_{2m} t_s} \end{bmatrix} \quad (3)$$

or simply

$$[\Phi] = [\Psi] [\Lambda] \quad (4)$$

$$(2m \times s) = (2m \times 2m)(2m \times s)$$

Similarly, free-response values $(\Delta t)_1$ later in time than those in Eq. (2), measured at the same stations, can be expressed as:

$$\begin{aligned} x_i[t_j + (\Delta t)_1] &= \sum_{k=1}^{2m} \psi_{ik} e^{\lambda_k [t_j + (\Delta t)_1]} \\ &= \sum_{k=1}^{2m} \left[\psi_{ik} e^{\lambda_k (\Delta t)_1} \right] e^{\lambda_k t_j} \\ &= \sum_{k=1}^{2m} \hat{\psi}_{ik} e^{\lambda_k t_j} \end{aligned} \quad (5)$$

or, in matrix form, for $2m$ stations and s instants of time:

$$[\hat{\Phi}] = [\hat{\Psi}] [\Lambda] \quad (6)$$

$$(2m \times s) = (2m \times 2m)(2m \times s)$$

For $s \geq 2m$, $[\Psi]$ and $[\hat{\Psi}]$ are related through Eqs. (4) and (6), eliminating $[\Lambda]$, by:

$$[A] [\Psi] = [\hat{\Psi}] \quad (7)$$

$$(2m \times 2m)(2m \times 2m) = (2m \times 2m)$$

where

$$[\Phi]^T [A]^T = [\hat{\Phi}]^T \quad (8)$$

$$(s \times 2m)(2m \times 2m) = (s \times 2m)$$

Since the columns of $[\Psi]$ and $[\hat{\Psi}]$ are related from Eq. (5) by $\{\hat{\psi}\}_k = e^{\lambda_k (\Delta t)_1} \{\psi\}_k$, the complete system can now be placed in the form of a single eigenvalue problem as:

$$[A]\{\psi\}_k = e^{\lambda_k (\Delta t)_1} \{\psi\}_k \quad (9)$$

The matrix $[A]$ is referred to in this paper as the "system matrix," and contains information characterizing the complete set of modal parameters of the system.

The desired structural (damped) natural frequencies and damping factors are determined from the eigenvalues of

$[A]$, $e^{\lambda_k(\Delta t)_1} = a_k + ib_k$, by:

$$(\omega_d)_k = 2\pi f_k = \frac{1}{(\Delta t)_1} \tan^{-1}(b_k/a_k)$$

$$\sigma_k = \frac{1}{2(\Delta t)_1} \ln(a_k^2 + b_k^2) \quad (10)$$

$$(C/C_c)_k = \frac{\sigma_k}{\sqrt{\sigma_k^2 + (\omega_d)_k^2}}$$

The eigenvectors of $[A]$ are the desired (complex) structural mode shapes, $\{\psi\}_k$.

Equations (8) and (9) form the basics of the solution approach: free-response functions are placed into the rows of $\hat{\phi}$ and $\hat{\psi}$; $[A]^T$ is obtained by a least-squares solution of Eq. (8); and the complex eigenvalues and eigenvectors of $[A]$ are then found, to which the system's modal parameters are directly related.

The dimension 'm' is referred to throughout this paper as the "number of allowed (computational) degrees-of-freedom," NDOF. This term should not be confused with the more widely used meaning of "degrees-of-freedom" as the number of independent spatial coordinates necessary to define the motion of a system. The "number of assumed modes" or the "order of the math model" are other descriptors that have been used to denote this fundamental analysis constant. The matrix dimension 's', the number of columns in $[\hat{\phi}]$ and $[\hat{\psi}]$ (i.e., the number of time samples used from each free-response function), is referred to throughout as NCOL. The matrices $[\hat{\phi}]$ and $[\hat{\psi}]$ are referred to as the two "response matrices."

Three distinct, user-selectable, time shifts are used in positioning overlapping segments of the measured free-response functions into the rows of the response matrices. The fundamental time increment between all data placed into $[\hat{\phi}]$ and $[\hat{\psi}]$ is $(\Delta t)_1$. Two other time shifts, denoted by $(\Delta t)_2$ and $(\Delta t)_3$, will be discussed in the report section entitled "Transformed Stations and Modal Confidence Factors." The number of consecutive time samples

corresponding to each of the shifts will be denoted hereafter by simply N_1 , N_2 , and N_3 , respectively.

Figure 1 provides an example of the placement of free-response data into the two response matrices, assuming that three response functions are available. In this example, NDOF and NCOL are selected equal to 7 and 30, and the three data shifts, N_1 , N_2 , and N_3 , are 3, 8, and 4. This figure should be used as a reference in clarifying the definition of each of these five primary user-selectable analysis constants.

Solution Considerations

Equations (8) and (9) are forms whose computer solution have been studied in depth by numerical analysts. Eq. (8) is an over-determined system of simultaneous linear equations, and Eq. (9) is an algebraic eigenvalue problem, where the (2m) eigenvalues of $[A]$ are $\lambda_k(\Delta t)_1$ and the corresponding eigenvectors are $\{\psi\}_k$.

The "conventional transpose approach" of solving Eq. (8) consists of pre-multiplying both sides by $[\hat{\phi}]$ and then solving for $[A]^T$ by any of several methods for the solution of 2m simultaneous linear equations in 2m unknowns. This is the approach used for the results shown in this paper. In particular, pre-multiplying Eq. (8) by $[\hat{\phi}]$ results in:

$$([\hat{\phi}] [\hat{\phi}]^T) [A]^T = ([\hat{\phi}] [\hat{\psi}]^T) \quad (11)$$

Equation (11) was then solved by a standard Gaussian elimination subroutine using an LU decomposition of the $([\hat{\phi}] [\hat{\phi}]^T)$ matrix of coefficients.

Other methods are available for solving Eq. (8) which do not require the pre-multiplication of each side by $[\hat{\phi}]$, [8,9]. These methods have been developed for the express purpose of increasing the solution accuracy when the matrix of coefficients, in this case $[\hat{\phi}]^T$, is ill-conditioned; the pre-multiplication will increase any ill-conditioning of the coefficient matrix. A limited number of comparison identifications have been run using two other computer subroutines available for the solution of Eq. (8), namely:

1. by singular value decomposition of the coefficient matrix using Householder transformations, obtaining the isometric matrix $[U]$ and orthogonal matrix $[V]$,

such that $[\phi]^T = [U][Q][V]^T$, where the singular values comprise the diagonal matrix $[Q]$. The least-squares solution is then formed by $[A]^T = [V][Q^+][U]^T[\phi]^T$, where $[Q^+]$ contains the reciprocals of the non-zero values of $[Q]$.

2. by using Householder transformations to perform the QR decomposition of the coefficient matrix, where $[Q]$ is an orthogonal matrix and $[R]$ is an upper triangular matrix. The least-squares solution is then formed as $[A]^T = [R]^{-1}[Q_1]^T[\phi]^T$, where $[Q]$ is partitioned in the form $[Q] = (Q_1, Q_2)$ with $[\phi]^T = [Q_1][R]$.

In all cases run using these other methods, no changes in the computed modal parameters were observed to the precision used in printing the results shown in this paper. On the other hand, each of the two methods described above required considerably more computer memory to implement using available FORTRAN subroutines than the conventional transpose approach. In both cases, the $[\phi]^T$ and $[\phi]$ matrices--each of size $(s \times 2m)$ --needed to reside in core, whereas the transpose method was implemented with two matrices of order $2m$ each. For a typical $s/2m$ ratio of 3 used in many of the identifications, selection of either optional solution method required a factor of 6 times more core storage.

The details of available techniques for the solution of Eq. (8) are compiled in several numerical analysis textbooks [8,9]. A subroutine pack containing a standardized set of computer code for implementing these methods is available [10].

The numerical techniques for solving Eq. (9) are not as plentiful; the QR method advocated by Wilkinson [8,11], is the accepted approach for determining the complete set of real and complex eigenvalues and eigenvectors of $[A]$, a fully-populated general matrix with real elements. This is the method used to obtain all results presented in this paper. A subroutine pack [12] containing standardized code for the computer solution of eigenvalue problems is also available.

"Transformed Stations" and

"Modal Confidence Factors"

Two aspects of the practical implementation of the method described thus far, which have been discussed in previous papers [2,3,5], are: (1) processing data when the number of available free-response measurements is less than the number of rows in $[\phi]$ (equal to twice the number of degrees-of-freedom desired in the identification process), and (2) distinguishing those eigenvalues of $[A]$ corresponding to the desired structural modes from those eigenvalues corresponding to "noise modes," computed whenever NDOF is larger than the number of structural modes contributing to the responses.

When the number of response measurements that are available, say p_0 , is less than the number of computational degrees-of-freedom which are desired, fewer than half the rows of $[\phi]$ are filled by the original, unshifted, response functions. Under these circumstances, "assumed" or "transformed" stations [2] are created for the additional rows of both response matrices by simply shifting the original functions placed in the first p_0 rows by multiples of a second user-selectable time shift, $(\Delta t)_2$: $(\Delta t)_2$, $2(\Delta t)_2$, $3(\Delta t)_2$, etc., until the upper halves of both matrices are filled. This process of adding transformed stations does not mathematically affect the eigenvalues of the system matrix, $[A]$, assuming perfect identification. (If NDOF is selected smaller than p_0 , only NDOF of the available response functions are used in the analysis.)

The bottom halves of the two response matrices are formed by duplicating the upper rows, but delaying an additional user-selectable time shift, $(\Delta t)_3$. The rationale for filling only the upper halves of the matrices with the available response functions (and transformed stations) and filling the bottom halves with a time-shifted form of the upper halves is based on the calculation of "Modal Confidence Factors," to be discussed next.

If two segments of a free-response function obtained from the same measurement station, but separated by an arbitrary time interval $\Delta\tau$, are placed into different rows of the response matrices, the elements in each computed eigenvector of $[A]$ corresponding to these two rows, ψ_{ik} and ψ_{ik}^+ , will be related (again assuming perfect identification) by:

$$\psi_{ik}^{\dagger} = \psi_{ik} e^{\lambda_k \Delta \tau} \quad (12)$$

for each linear structural mode k .

This fundamental property, Eq. (12), and the time-shift relationship between the data in the upper and lower halves of the response matrices, $(\Delta t)_3$, are used in the calculation of "Modal Confidence Factors," MCF [5], devised to distinguish "noise modes" from the desired structural modes. The (complex-valued) MCF's for accurately identified linear structural modes--one MCF calculated for each of the first p_0 elements in each computed (complex) eigenvector of $[A]$ --will cluster near unity in amplitude and near 0° in phase; those calculated for "noise modes" will be randomly distributed in value. To form the MCF's, the first p_0 elements in the lower halves of the computed eigenvectors are compared with "expected" values for these elements, calculated using Eq. (12) by the product of the corresponding p_0 upper-half eigenvector elements and the complex exponentials, $e^{\lambda_k (\Delta t)_3}$, where λ_k are the computed characteristic values. The MCF is defined as the amplitude ratio and phase difference between each of these "expected" values and the corresponding values computed by the eigenvalue analysis. If the amplitude ratio is greater than 1.0, the reciprocal is taken. The phase angle is normalized to range between -180° and 180° . Obtaining MCF values near 100% in amplitude and 0° in phase is certainly a necessary (but not sufficient) condition to indicate that an accurate identification of a linear structural mode of the system has been made.

This process can be thought of as the comparison of two sets of eigenvectors, corresponding to the same set of eigenvalues, computed simultaneously for the system using two different segments of the available free-response functions. An important user advantage in obtaining both sets of eigenvectors in one eigensolution is that no effort is needed to "pair up" corresponding eigenvectors if somewhat different eigenvalues are computed for each set of segments. A single eigenvalue set is obtained using information derived from both sets of data, and the two eigenvector sets are correctly compared in the computer analysis with no user decisions required.

An MCF is calculated in this manner for each of the p_0 stations, for each

identified complex eigenvalue. To compact this information to a more manageable level, an "Overall MCF," OAMCF, is calculated for each "mode" (that is, for each computed complex eigenvalue) as the percentage of p_0 stations whose MCF values are at least 95% in amplitude and within 10° of 0.0 in phase. The OAMCF parameter, introduced for this study, has been found very effective in distinguishing the desired structural modes from the "noise modes," and is a fundamental part of the identification results presented in this paper. Its value has been found to provide a good characterization of the p_0 MCF's calculated for each mode and, in general, a closer examination of the individual station-by-station MCF data was unnecessary.

The time shift $(\Delta t)_3$ should not be selected equal to either $(\Delta t)_1$ or $(\Delta t)_2$. If equal to $(\Delta t)_1$, all MCF's will be computed as 100% in amplitude and 0° in phase, and be of no use. If equal to $(\Delta t)_2$, and at least one transformed station has been used, $[\phi]$ and $[\hat{\phi}]$ will each have two identical rows and Eq. (8) cannot be solved. Setting $(\Delta t)_3$ equal to one-half the value of $(\Delta t)_2$ has been found satisfactory in most cases. To clarify the relationship between these time shifts, refer again to Fig. 1, which shows a typical placement of data into the response matrices when three free-response functions are used.

CONSTRUCTION OF THE SIMULATED FREE-RESPONSE FUNCTIONS

Mode shapes used in constructing the simulated free-response functions were obtained from a NASTRAN finite-element analysis of an isotropic, uniform-thickness plate with 8×24 square elements. Data for 65 stations were obtained by using the analytical mode shape data (for motion normal to the plate only) from every other grid point in both directions, including the outside border. The first 15 modes of this analysis were used in forming the responses. For each desired modal model, a damped natural frequency, damping factor, and response amplitude were arbitrarily selected for each mode. The effects of randomizing the initial phase angle for all stations of each mode and of selecting other than 0° or 180° between the stations in a mode (i.e., complex modes) were studied for several cases, and no changes in the identification accuracy were noted. Thus, unless otherwise stated, the contribution of each mode in the responses was represented as a damped cosine function multiplied by an appropriate (positive or negative) mode shape amplitude constant.

That is, each free-response function was formed as

$$x_i(t_j) = \sum_{k=1}^{15} \psi_{ik} e^{-\sigma_k t_j} \cos[(\omega_d)_k t_j] \quad (13)$$

For this study, each simulated free-response function consisted of 1000 data points calculated using Eq. (13), at a sampling rate of 400 samples per second. Uniformly distributed noise was added to these functions on a function-by-function, rms-percentage basis, with the rms value of each noise-free function calculated using all 1000 available data points. The mode shapes used in forming each modal model were assigned to the 15 mode indices in the order determined by the finite-element analysis.

For ease in interpreting identification results, the modal frequencies were arbitrarily selected for all models in this study (i.e., the natural frequencies of the plate obtained from the NASTRAN normal-mode analysis were not used). Many of the simulated models were formed by spacing the 15 modal frequencies every 2 Hz from 10.0 to 38.0 Hz, and setting the modal damping factors and response amplitudes equal for each of the modes. Each of these basic modal models are characterized by a single modal damping factor and noise percentage, and are referred to throughout this paper for simplicity as "baseline models."

EVALUATION OF IDENTIFICATION ACCURACY

The accuracy of all mode shape identifications for this study has been quantified by computing a "Mode Shape Correlation Constant," MSCC, between the identified mode shapes and each of the 15 input mode shapes. The constant is calculated in a manner analogous to that of coherence, often computed in time-series analysis work. The functional form is that of the square of the correlation coefficient defined in basic statistics, computed between two sequences of complex numbers.

Mathematically, if $\{\psi_1\}$ is a known input (complex) mode shape, and $\{\psi_2\}$ is an identified (complex) mode shape:

$$MSCC = \frac{|\{\psi_1\}^T \{\psi_2\}^*|^2}{[\{\psi_1\}^T \{\psi_1\}^*][\{\psi_2\}^T \{\psi_2\}^*]} \times 100 \quad (14)$$

where T denotes the transpose and $*$ the complex conjugate.

The MSCC between two mode shapes will always range from zero--for no resemblance of the two shapes--to 100%--for perfect resemblance. Values intermediate between 0.0 and 100.0 can be interpreted as the amount of coherent information in the two compared mode shapes.

The accuracy of identified frequency and damping parameters was assessed by direct observation only.

RESULTS AND DISCUSSION

In processing a set of free-response functions with the identification algorithm, five primary user-selectable constants must be chosen. They are NDOF, NCOL, $(\Delta t)_1$, $(\Delta t)_2$, and $(\Delta t)_3$. Secondary considerations include the selections of data sampling rate and analog or digital filtering ranges, the particular stations to be analyzed in one computer run, and the absolute starting times of the free-response data (i.e., whether any data points are skipped at the beginning of the functions). An optimum selection of the analysis options is a function of the characteristics of the data being analyzed, and "cookbook" instructions are difficult to develop. The results to be shown in this section, however, provide guidelines for their selection and for judging the sensitivity of the choices, and illustrate identification accuracies which may be expected.

All results shown in this paper were obtained using a vectorized version of the code on Langley's CDC Cyber 203 (formerly Star-100) computer. Typical CPU times for identification were 15 seconds for NDOF = 65 and NCOL = 390, and 340 seconds for NDOF = 200 and NCOL = 968. The required computer time varied approximately as the number of columns used in $[\phi]$ and $[\delta]$, NCOL, and as the square of the number of allowed computational degrees-of-freedom, NDOF.

Some Baseline Model Results

Figure 2 shows the time- and frequency-domain responses at measurement Station No. 1 (a corner of the plate) for three of the baseline models analyzed in the study. In Figs. 2(a) and 2(b), the damping factor, C/C_c , of all 15 modes was set to 2%. The rms noise levels in these two cases were 2% and 20%, respectively. Similarly, Fig. 2(c) shows the response of Station No. 1 with

all 15 modes assigned 5% damping and 10% noise. The dashed lines on the time history plots designate the range of points used from each function in ITD analyses whose results will be presented in Table I and Figs. 3 through 5. The center and right-hand plots in Fig. 2 show the quadrature (imaginary) component and modulus, respectively, of the Fourier transform of the corresponding free-response function.

Table I contains MSCC values for these three identifications calculated between each of the 15 input mode shapes and each identified mode (whose OAMCF was 2% or larger), rounded to the nearest whole number. Also included are the identified frequencies in Hertz, the identified damping factors in percent, and the OAMCF for each mode. The column to the right of the OAMCF data contains the number of stations of 65, NST, that were used in calculating the corresponding OAMCF value; only those stations with non-negligible modal response (at least 3% of the maximum value of the mode) are included in the calculation. This 3% criterion was imposed on the calculation of OAMCF because many of the selected 65 measurement stations were located exactly on mode shape node lines; the variance in the calculated MCF data for these stations was generally high, as to be expected, because very small modal amplitudes identified for these stations were used in the calculations. Each of these identifications were run using NDOF of 65 and NCOL of 390. The other 50 "modes" obtained in each identification were "noise modes," differentiated by low (<2%) OAMCF values.

For these identifications, the user-selectable time-shift constants, $(\Delta t)_1$, $(\Delta t)_2$, and $(\Delta t)_3$, were set to $3/SF$, $8/SF$, and $4/SF$, respectively, where SF is the data sampling rate. The values $N_1 = 3$, $N_2 = 8$, $N_3 = 4$ were used in obtaining all identification results shown in this paper, unless otherwise noted. (These are the values selected for Fig. 1 in illustrating a typical placement of free-response data into the two response matrices.)

Figure 3 shows the 15 identified (complex) mode shapes for the 2%-damping, 2%-noise baseline model, corresponding to the data contained in Table I. These identified mode shapes are indistinguishable from those used in constructing the model. Note that the ITD algorithm identifies complex mode shapes, consisting of a magnitude and phase at each selected measurement station; the identified mode-shape phase angles are included adjacent to each mode shape, assigned by

consecutive station number from the center of the circle to the outer ring, as depicted in the lower-right corner of Fig. 3; the data for the accompanying mode shape plots were obtained by the product of the identified mode-shape amplitudes and the cosine of the corresponding phase angle.

Figures 4 and 5 show the mode shapes identified for the two other baseline models whose results were presented in Table I, also using NDOF of 65 and NCOL of 390 in the analyses. As before, only those "modes" with an OAMCF of at least 2% are shown. In Fig. 4, for the 2%-damping, 20%-noise model, the identified shapes are also indistinguishable from the exact, input mode shapes, and the phase-angle scatter averages only a few degrees. Identification results for the 5%-damping, 10%-noise model, provided in Fig. 5, show mode shapes that are slightly distorted for modes 11 through 14, with significant phase angle scatter in several of the modes. In interpreting these results, however, the reader is cautioned that more accurate identifications are obtainable for these models; as shown later, allowing higher degrees-of-freedom in the identification will increase the accuracy to some degree. These identifications all used NDOF of 65 and NCOL of 390, and the results typify the effects of changing modal damping and noise level while holding all of the algorithm constants fixed.

Note in Table I that an MSCC of 100% was calculated for each of the accurately identified mode shapes of the 2%-damping, 2%-noise baseline model, shown in Fig. 3. Also of interest in these MSCC results is the slight "blending" of the higher-numbered mode shapes for the 5%-damping, 10%-noise model, corresponding to the small distortions seen in the plots in Fig. 5.

The Number of Allowed Degrees-of-Freedom

The number of computational degrees-of-freedom allowed in the identification, NDOF, should be selected equal to the number of modes excited in the responses if the free-response functions are noise-free. For any deviation of the response data from the exact analytical form--that is, some level of superimposed noise--more degrees-of-freedom than this must be allowed for accurate identification. It is somewhat intuitive that better identification of the underlying deterministic modal data may result when one allows for the calculation of extra "noise modes," in addition to the number of actual structural modes contributing to the responses, to provide

an outlet in the assumed model for the noise contribution.

To illustrate the effect of increasing the allowed degrees-of-freedom, identified modal frequencies for the 2%-damping baseline model, using values of NDOF from 1 to 75, are plotted in Figs. 6 and 7 for each of eight increasing levels of superimposed noise. At each value of NDOF, the identified frequencies are denoted by vertical line segments at the corresponding frequencies, whose heights are proportional to the OAMCF value computed for each mode. As before, only those identified "modes" with negligible OAMCF (less than 2%) are not shown. When the individual segments align to form a solid, vertical line, the OAMCF's are all 100% and the identified modal frequency is invariant with increasing NDOF. On examining these eight plots, a consistent trend in the requirement for increased degrees-of-freedom to accurately identify all 15 frequencies, with increased noise level, is noted. Another interesting trend is that after an NDOF level is attained for each noise level where all 15 frequencies are accurate, increasing NDOF above this value did not degrade the frequency identification accuracy. These plots will be referred to as "NDOF-frequency maps," and have been found very useful in interpreting experimental identification results. The identifications at each NDOF level in Figs. 6 and 7 were run using NCOL of 300.

The lowest value of NDOF for accurate identification has been found in this study to be related to the signal-to-noise ratios of the modal responses. The considerable shifting of the frequency "lines" in these NDOF-frequency maps at low values of NDOF results largely from setting all 15 modal response levels equal. When experimental data are processed, the lowest NDOF values for identification of each mode vary considerably more between modes than the data shown in Figs. 6 and 7, due to different response levels, and almost no line shifting occurs.

Typical accuracy at much higher allowed degrees-of-freedom are included in Table II for the 2%-damping, 20%-noise baseline model with analyses at NDOF of 65, 200, 250, and 300. These identifications used all 1000 data points in each of the 65 response functions; that is, NCOL was made as large as possible in each case. Although the parameters for all 15 modes are of acceptable accuracy for most applications at NDOF

of 200, it is interesting that the accuracy (of the damping factors) continued to increase as NDOF was raised beyond this point. Only those "modes" with an OAMCF of less than 2% are excluded from these results; at NDOF of 300, for example, 285 additional "noise modes" were computed, all of which are differentiated by the OAMCF parameter. Also very important is that no anomalous identification problems or numerical instabilities were observed in this or any other identification conducted in this study using such high values of NDOF. These results suggest that the ITD algorithm, used with a high number of degrees-of-freedom, may accurately identify all of the excited structural modes, for large modal surveys, in one computer run.

Note that the results shown in Table II for NDOF of 65 were not as accurate as those shown earlier in Table I for analysis of the same 2%-damping, 20%-noise baseline model; the results in Table I were obtained using NCOL of 390 and those in Table II with NCOL of 993. The effects of the selection of NCOL on identification accuracy will be addressed in a later report section.

The Selection of $(\Delta t)_1$

To help understand the effects of the user-selectable algorithm constant $(\Delta t)_1$ (the time increment between corresponding data in the two response matrices), note from Eq. (9) that the computed eigenvalues of $[A]$, $a_k + ib_k$, are exponential functions of the product of the system's characteristic values, λ_k , and $(\Delta t)_1$. The desired structural modal frequencies and damping factors are then calculated directly from these eigenvalues by Eqs. (10). Using these relationships, loci of constant damping factor are plotted in Fig. 8 in the complex a-b plane, for $f_d = \omega_d / (2\pi)$ ranging from 0 to $1 / (2(\Delta t)_1)$. A typical eigenvalue of $[A]$ is denoted by point 'k,' whose corresponding natural frequency in radians/sec is simply the angle θ_k divided by $(\Delta t)_1$. Since equal damping values, σ_k , lie on equal radii in the a-b plane, by Eq. (10), the contours of constant damping factor (equal to the damping value divided by the undamped natural frequency) will converge to the point (1,0) for $f_d = 0$ and separate from one another as f_d increases. As C/C_c increases, the contours lie inside one another, until, at 100%, the locus is simply the positive x-axis.

The frequency in Hertz corresponding to $\theta_k = \pi$, denoted as f_π , is the

point at which the identified frequencies will "fold" because of the circular nature of the exponential function--analogous to the well-known "Nyquist folding-frequency" which results from the circular nature of the discrete Fourier Transform. That is, all identified frequencies will fall in the range 0 to f_{π} , regardless of their actual value; only those modal frequencies no larger than f_{π} will be correctly calculated. The value of f_{π} is simply $1/(2(\Delta t)_1)$. Of course, this "eigenvalue aliasing" will lead to erroneous frequency and damping factor results for modes with frequencies greater than f_{π} , contributing to the response functions used in the identification; as with the well-understood Nyquist-frequency aliasing, however, the phenomenon can also be used beneficially, with the results accordingly adjusted, if the data are pre-filtered to contain information only in a certain, known frequency interval.

Obviously, for two eigenvalues of [A] separated by ϵ , any inaccuracy in their calculation may translate to a considerable inaccuracy in their corresponding modal frequencies and damping factors, depending on the location in the a-b plane. To quantify this characteristic, Fig. 9 provides contours of minimum and maximum percent deviation in the identified modal frequencies and damping factors for three magnitudes of uncertainty in the eigenvalue determination. Note, in Fig. 9(a), that percent frequency deviations are nearly independent of damping level, and are large only for values less than $0.1 f_{\pi}$ (because the data are shown on a percent-deviation basis, and f is small in this range). For all three uncertainty levels, the percent frequency deviations are no greater than 2% at all frequencies at least $0.2 f_{\pi}$, for $C/C_c < 10\%$. The envelopes of maximum percent deviation in the damping factor identification, on the other hand, are considerably larger, as shown in Fig. 9(b). These data suggest that damping factors derived from eigenvalues of [A] subtending small angles in the a-b plane may be subject to appreciable error.

As $(\Delta t)_1$ increases, the frequency interval corresponding to eigenvalues located at $\theta_k = 0$ and $\theta_k = \pi$ decreases, and the eigenvalues for any two modal frequencies separate in the a-b plane. When this occurs, a more accurate analysis generally can be made of a smaller total frequency interval. Figure 10 shows typical results of this effect in the identification of the 2%-damping, 20%-noise baseline model for

two selections of N_1 (the number of data samples corresponding to the time-shift interval $(\Delta t)_1$). The results in Fig. 10(a) were obtained with $N_1 = 1$ and those in Fig. 10(b) with $N_1 = 3$, holding all other algorithm constants unchanged. In the polar plots of Fig. 10, the symbols denote the locations of all identified eigenvalues of [A] in the a-b plane; the eigenvalues corresponding to the 15 structural modes, distinguishable from the "noise modes" whose OAMCF's were all less than 2%, lie approximately equally spaced along the 2%-damping (dashed) line in each figure. As shown in the tabulated results, the identification accuracies of both damping factors and mode shapes were improved when N_1 was increased from 1 to 3.

An Alternate Method for Calculating Modal Damping

In addition to the straightforward calculation method for the desired modal damping factors using the eigenvalues of [A], shown in Eq. (10), limited study has been done of an alternate method using the first p_0 elements in the upper and lower halves of the computed eigenvectors--data used previously in computing the MCF values. Based on experience, the identified damping factors often show the greatest variance of all the computed modal parameters. By assuming that the eigenvector data are more accurate than the identified damping data, a method similar to the reverse process used in computing the MCF data can be used to obtain a second estimate of the modal damping factors.

Mathematically, a form analogous to that for obtaining the amplitude of a frequency response function using the Fourier components of input and response signals can be used to compute an average modal amplitude ratio between the 'upper' and 'lower,' p_0 -element, mode shape vectors. In particular, if $\{\psi_U\}$ is an upper identified (complex) mode shape, and $\{\psi_L\}$ is a lower identified (complex) mode shape, a Modal Amplitude Ratio (MAR) can be calculated as:

$$\text{MAR} = \frac{|\{\psi_U\}^T \{\psi_L\}^*|}{\{\psi_U\}^T \{\psi_U\}^*} \quad (15)$$

from which an alternate modal damping factor can be calculated, using the corresponding damped natural frequency, ω_d , obtained directly from the eigenvalue of [A], by:

$$(C/C_c)_k = \frac{\sigma_{k2}}{\sqrt{\sigma_{k2}^2 + (\omega_d)_k^2}} \quad (16)$$

where $\sigma_{k2} = \ln(\text{MAR})/(\Delta t)_3$.

This estimate of modal damping was found more accurate in many cases--but not all--particularly for modes with poor signal-to-noise ratios. Figure 11 shows modal damping factors identified by each of the two methods for the 2%-damping, 5%-noise baseline model for NDOF in steps of 20 from 60 to 200. Only data for the first 10 modes are included. Although the data for modes 1 and 2 (circle and square symbols) are significantly over-estimated by either method, overall, the data in Fig. 11(b), obtained indirectly using the eigenvector and identified frequency data, cluster appreciably closer to the true value of 2% than the data in Fig. 11(a), calculated directly from the eigenvalues of [A].

When the modal damping is calculated using this alternate method, an MSCC between the upper and lower p_0 -element vectors used in the calculation should also be formed to be used as an indication of the consistency of the eigenvector data, which may itself be inaccurate. A conservative approach would certainly be to calculate the damping factors by both methods, and use any discrepancy in their values as a indicator of inaccurate identification. Unless otherwise noted, the damping identification results shown in this paper were obtained using the direct calculation method from the eigenvalues of [A].

Modal Response Level

In all identification results presented thus far, the response levels of all 15 modes in the simulated models were set equal; for actual experimental data this would not be the case. To examine identification accuracy of modes with significantly different response level, Figs. 12(a) and 12(b) show NDOF-frequency maps for the 2%-damping, 2%-noise baseline model when the response level of mode 8 (at 24 Hz) was reduced to 1% and 5%, respectively, of the level selected for each of the other 14 modes. The 1%-response case represents the approximate lower limit at which this mode was identifiable for NDOF up to 75. Compared with a similar plot shown earlier in Fig. 6(c) for all modes of equal response level, note that these plots have several randomly scattered dots,

corresponding to "modes" with OAMCF less than 2%, the cutoff used for plotting the data shown in Figs. 6 and 7. This cutoff criterion was removed for these plots to allow the 24-Hz mode data in Fig. 12(a) to be discernible.

Although Figs. 12(a) and 12(b) show that the 24-Hz modal frequency was identified in both cases, these data do not indicate the accuracy of either the identified mode shapes or modal damping factors; this information is included in Figs. 12(c) and 12(d), respectively. In Fig. 12(c), MSCC's calculated between the identified mode shapes and the known input shape are plotted for each case as a function of NDOF. For the 5%-response case, denoted by the square symbols, the MSCC is essentially 100% for all NDOF above 46; for the 1%-response case, on the other hand, the MSCC value does not rise above the 83% level. In fact, when the 1%-response model was analyzed using NDOF of 250, the MSCC of the 24-Hz mode remained at approximately 83%.

Identified modal damping factors for these cases, calculated both using Eq. (10) and by the alternate method discussed in the previous report section, are shown in Fig. 12(d). In all cases, the data appear to be approaching the correct value of 2% with increasing NDOF; the results for the 5%-response case being closer to the true value than those for the 1%-response case. Additionally, the damping factors calculated by the alternate method using the computed eigenvector data are more accurate at each value of NDOF than the damping factors calculated directly from the identified eigenvalues of [A].

The Selection of NCOL

In establishing the two response matrices, both the number of rows (equal to twice NDOF) and the number of columns, NCOL, must be selected for each identification. As shown in NDOF-frequency maps in Figs. 6, 7, 12(a), and 12(b), the minimum required NDOF is related to the signal-to-noise ratio of the modes. The value for NCOL, denoted by 's' in the THEORY section of this report, is restricted to be at least twice NDOF, so that Eq. (8) contains no fewer equations than unknowns. An intuitive upper limit in selecting NCOL corresponds to the time at which the free-response signal for the mode to be identified becomes smaller than the noise level; beyond this point each additional data point used from the response functions would provide more noise than additional information to the identification algorithm.

The effects of the selection of NCOL on identification results for the 2%-damping, 20%-noise baseline model are shown in Fig. 13. To estimate the time at which the superimposed noise exceeds the signal information in the free-responses, a 20-point, running mean-square value, averaged over all 65 functions used for the model, is plotted in Fig. 13(a). These data have been normalized so that the asymptotically approached noise level corresponds to 0 dB. Since all 15 modes have the same response level in this model, the mean-square value of the free-response signal for each mode equals the mean-square noise level when the function of Fig. 13(a) equals $10 \log(16)$ or 12 dB. This corresponds to NCOL of approximately 225.

Using NDOF of 65, all 15 modal frequencies for this model were accurately identified for NCOL ranging from 200 to 950, and their values are not shown. Of interest, though, are the corresponding MSCC values and identified modal damping factors for these cases. These results are shown in Figs. 13(b) and 13(c), respectively. To maintain clarity, data for only the first five modes (which typify the results obtained for all 15 identified structural modes) are included. Of particular interest in these figures is the rapid deterioration of the identification results when NCOL is less than 200. Above NCOL of 200, the MSCC data are affected only slightly as NCOL increases to 950, although a slight downward trend is noted for NCOL greater than 300. Optimum mode shape identification was obtained for NCOL ranging from 200 to 300. The identified modal damping factors, on the other hand, diverge from the selected value of 2% considerably faster than the MSCC data from 100%, as shown in Fig. 13(c). Selecting NCOL near 200 would also provide the best damping identification over the range of NCOL from 170 to 950. It is of interest to note that the identified damping factors in Fig. 13(c) all tend to approach the correct value of 2% as NCOL decreases. This effect is similar to that shown in Fig. 11(a) for an increase in NDOF with NCOL held constant.

Close Natural Frequencies

A classic problem using any modal identification technique is the accurate determination of the modal parameters for two or more structural modes of approximately the same natural frequency. Assuming no attempt was made to apportion the force used in exciting the structure, the response levels of two

modes close in frequency may well be approximately equal in a set of response measurements obtained during wide-band force excitation. If T seconds of data are available for analysis, the corresponding frequency-domain functions will be determined to a resolution of $1/T$ Hz by Fourier methods. For the models constructed in this study, $T = 2.5$ seconds, which corresponds to a frequency resolution of 0.4 Hz. To obtain accurate modal parameters with methods that rely on visual determination of response peaks in frequency spectra or frequency response functions is unreasonable when the modal frequency separation approaches the frequency resolution value.

To study the frequency resolution ability of the ITD algorithm, several modal models were constructed by moving the frequency of mode 8, originally at 24.0 Hz in the baseline model, to a lower value, close to mode 7 at 22.0 Hz. All 14 other modes were maintained at their original spacing of 2 Hz from 10.0 to 38.0 Hz. Table III shows the identification results using the 2%-damping, 2%-noise baseline model, for 0.10, 0.05, and 0.01 Hz frequency separation between modes 7 and 8. Sixty-five degrees-of-freedom, with NCOL of 390, were used in the identifications. At each frequency separation value, the damping in mode 8 was successively changed from 2% (the same value assigned to mode 7), to 3%, to 10%. For all three frequency separations, near-perfect identification of the parameters for all 15 modes was obtained for the cases when the mode 8 damping was either 3% or 10%. Identification accuracy of modes 7 and 8 in the cases where both modes were assigned 2% damping successively deteriorated as the frequency separation was decreased. These trends are consistent with the fact that two modes, although of equal natural frequency, will correspond to different eigenvalues of $[A]$ if their damping factors are different—the larger the difference in damping, the larger the corresponding eigenvalue separation.

To extend the study of eigenvalue resolution one step further, modal models were constructed with five of the 15 modal frequencies set to 22.0 Hz. Figure 14 provides identification results for two of these models: Fig. 14(a) with the five modes assigned damping factors of 1, 2, 3, 4 and 5%; and Fig. 14(b) with damping factor assignments of 2, 4, 6, 8 and 10%. Of course, as shown in the frequency spectrum plots, only one response peak is discernible at 22 Hz in both cases. The parameters of all 15 modes were accurately identified in each model, as shown, when the

percentage of added noise was held to a very low level: 0.01% in the $\Delta C/C_C = 1\%$ case and 0.1% in the $\Delta C/C_C = 2\%$ case. Although these noise levels are extremely low--often unattainable with experimental data--these results do illustrate the potential accuracy of the method and the relationship between noise level and the attainable eigenvalue resolution. These two identifications were run with NDOF of 65; the same models could be identified with somewhat higher noise levels at the (computational) expense of allowing more degrees-of-freedom.

A Condition on the Selection of $(\Delta t)_3$

The selection of the time shift between the upper and lower halves of the two response matrices, $(\Delta t)_3$, can significantly affect the identification accuracy of modes at or near certain frequencies; in particular, if all of the data in the lower halves are obtained by delaying the data in the upper halves by $(\Delta t)_3$, frequencies $f_x = n/(2(\Delta t)_3)$, for integer values of n , will not be identified. Using a different time shift on one or more of the stations will help alleviate this problem, which may occur whenever $f_x < f_\pi$. Of course, selecting $(\Delta t)_3 < (\Delta t)_1$ will always eliminate the condition by forcing the lowest value of f_x to be larger than f_π , the upper limit of the analysis range.

CONCLUDING REMARKS

Using simulated free-response functions, the Ibrahim Time Domain (ITD) algorithm has been found capable of accurately identifying known, structural modal parameters over a wide range of frequency separations, damping factors, mode response levels, signal-to-noise ratios, and user-selectable algorithm constants. It has been found that the modal parameters can often be identified in cases of poor signal-to-noise ratio if sufficient computational degrees-of-freedom are allowed in the identification process. A significant finding is that no detrimental effects were observed when many times more degrees-of-freedom were allowed than the minimum necessary for reasonable identification; this result suggests the use of a high number of degrees-of-freedom for the "blind" use of the algorithm in analyzing experimental data.

For many of the models analyzed, the identified modal frequencies and

mode shapes were more accurate than the corresponding modal damping factors. When the identified damping factors were plotted as a function of either the number of allowed degrees-of-freedom, NDOF, or the number of time samples used from each response function, NCOL, however, the correct values were often asymptotically approached. An alternate method for calculating modal damping, using the identified eigenvectors and modal frequencies, was found more accurate in some instances than using the identified eigenvalues directly.

For each set of user-selectable algorithm constants, direct correlation was found between the variance in the identification results and the signal-to-noise level of the responses. In analyzing noisy data, when sufficient degrees-of-freedom were allowed in the analyses, all natural frequencies and mode shapes were identified with good accuracy in nearly every instance. Low values of Overall Modal Confidence Factor, OAMCF, for modes with reasonably identified mode shapes, were usually indicative of inaccuracy in the estimated damping factors. For noise-free input data, the identification accuracy of all parameters approached the computational accuracy of the computer.

The required computer time varied approximately as the number of columns in the response matrices, NCOL, and as the square of the number of allowed degrees-of-freedom, NDOF. Typical CPU times for identification on the CDC Cyber 203 computer were 15 seconds using NDOF of 65 and NCOL of 390, and 340 seconds using NDOF of 200 and NCOL of 968.

Related areas of work which need further attention include the study of:

1. techniques to minimize noise and distortion on free-response functions from experimental measurements;
2. effects of structural nonlinearities on ITD identification results; and
3. resolution and roundoff errors which may occur in using the technique on smaller-wordlength computers.

REFERENCES

- [1] Brown, D. L., Allemang, R. J., Zimmerman, R., and Mergeay, M.: Parameter Estimation Techniques for Modal Analysis. SAE Paper 790221. Feb. 1979.
- [2] Ibrahim, S. R., and Mikulcik, E. C.: The Experimental Determination of Vibration Parameters from Time Responses. Shock and Vibration Bulletin. No. 46, Part 5, Aug. 1976, pp. 187-196.
- [3] Ibrahim, S. R., and Mikulcik, E. C.: A Method for the Direct Identification of Vibration Parameters from the Free Response. Shock and Vibration Bulletin. No. 47, Part 4, Sept. 1977, pp. 183-198.
- [4] Ibrahim, S. R.: Random Decrement Technique for Modal Identification of Structures. J. Spacecraft and Rockets. Vol. 14, No. 11, Nov. 1977, pp. 696-700.
- [5] Ibrahim, S. R.: Modal Confidence Factor in Vibration Testing. J. Spacecraft and Rockets. Vol. 15, No. 5, Sept. 1978, pp. 313-316.
- [6] Ibrahim, S. R.: Application of Random Time Domain Analysis to Dynamic Flight Measurements. Shock and Vibration Bulletin. No. 49, Part 2, Sept. 1979, pp. 165-170.
- [7] Hanks, B. R., Miserentino, R., Ibrahim, S. R., Lee, S. H., and Wada, B. K.: Comparison of Modal Test Methods on the Voyager Payload. SAE Paper 781044. Nov. 1978.
- [8] Wilkinson, J. H., and Reinsch, C.: Handbook for Automatic Computation, Vol. II, Linear Algebra. Springer-Verlag, Heidelberg. 1971.
- [9] Forsythe, G. E., and Moler, C. B.: Computer Solution of Linear Algebraic Systems. Prentice-Hall, Englewood Cliffs, N.J. 1967.
- [10] Dongarra, J. J., Bunch, J. R., Moler, C. B., and Stewart, G. W.: LINPACK User's Guide. SIAM Press. 1979.
- [11] Wilkinson, J. H.: The Algebraic Eigenvalue Problem. Oxford University Press, London. 1965.
- [12] Garbow, B. S., and Dongarra, J. J.: Path Chart and Documentation for the EISPACK Package of Matrix Eigensystem Routines. Argonne National Laboratory, Applied Mathematics Division, TM-250, 1975.

TABLE I.- IDENTIFICATION RESULTS FOR THREE BASELINE MODELS.

NDOF = 65; NCOL = 390 in each identification.

(All "Noise Modes" had OAMCF < 2%)

C/C_c = 2% in all modes. 2% noise.

(See Figure 3 for mode shapes)

MODE NO.	FREQUENCY, HZ	C/C _c , %	OAMCF	NST	MSCC WITH INPUT MODE NO. -														
					1	2	3	4	5	6	7	8	9	10	11	12	13	14	15
1	10.000	2.042	100	65	100	0	0	0	6	0	0	0	0	0	8	0	11	0	0
2	11.999	2.047	100	48	0	100	0	0	0	3	0	0	0	0	0	4	0	0	0
3	14.002	2.020	100	60	0	0	100	0	0	0	4	0	0	1	0	0	0	9	0
4	15.998	1.990	100	48	0	0	0	100	0	0	0	0	4	0	0	0	0	0	4
5	17.998	2.004	100	65	6	0	0	0	100	0	0	0	0	0	0	0	0	5	0
6	20.001	1.999	100	48	0	3	0	0	0	100	0	0	0	0	0	6	0	0	0
7	21.998	1.993	100	60	0	0	4	0	0	0	100	0	0	2	0	0	0	2	0
8	24.000	2.005	100	63	0	0	0	0	0	0	0	100	0	0	1	0	1	0	0
9	26.001	2.012	100	52	0	0	0	4	0	0	0	0	100	0	0	0	0	0	6
10	28.001	2.016	100	60	0	0	1	0	0	0	2	0	0	100	0	0	0	2	0
11	30.002	2.016	100	57	8	0	0	0	0	0	0	1	0	0	100	0	1	0	0
12	31.996	2.009	100	44	0	3	0	0	0	6	0	0	0	0	0	100	0	0	0
13	33.998	2.005	100	65	11	0	0	0	5	0	0	1	0	0	1	0	100	0	0
14	36.004	1.997	100	54	0	0	9	0	0	0	2	0	0	2	0	0	0	100	0
15	37.998	2.007	100	52	0	0	0	4	0	0	0	0	6	0	0	0	0	0	100

C/C_c = 2% in all modes. 20% noise.

(See Figure 4 for mode shapes)

MODE NO.	FREQUENCY, HZ	C/C _c , %	OAMCF	NST	MSCC WITH INPUT MODE NO. -														
					1	2	3	4	5	6	7	8	9	10	11	12	13	14	15
1	9.983	4.373	95	65	100	0	0	0	6	0	0	0	0	0	8	0	11	0	0
2	11.973	4.475	88	53	0	99	0	0	0	3	0	0	0	0	0	4	0	0	0
3	14.008	2.927	98	61	0	0	100	0	0	0	4	0	0	1	0	0	0	9	0
4	15.982	3.159	91	50	0	0	0	100	0	0	0	0	5	0	0	0	0	0	4
5	17.987	2.396	93	65	6	0	0	0	100	0	0	0	0	0	0	0	5	0	0
6	20.002	2.752	89	50	0	3	0	0	0	100	0	0	0	0	0	5	0	0	0
7	21.983	2.432	86	61	0	0	4	0	0	0	100	0	0	1	0	0	0	2	0
8	24.004	2.334	89	64	0	0	0	0	0	0	0	100	0	0	1	0	1	0	0
9	26.016	2.598	94	55	0	0	0	5	0	0	0	0	99	0	0	0	0	0	6
10	28.026	2.785	93	61	0	0	1	0	0	0	1	0	0	99	0	0	0	2	0
11	30.031	2.492	81	58	8	0	0	0	0	0	0	1	0	0	100	0	1	0	0
12	31.973	2.608	72	55	0	3	0	0	0	6	0	0	0	0	1	99	0	0	0
13	34.014	2.393	89	64	10	0	0	0	5	0	0	1	0	0	1	0	99	1	0
14	36.053	2.541	75	58	0	0	9	0	0	0	2	0	0	2	0	0	0	99	0
15	37.954	2.429	86	53	0	0	0	4	0	0	0	0	6	0	0	0	0	0	100

C/C_c = 5% in all modes. 10% noise.

(See Figure 5 for mode shapes)

MODE NO.	FREQUENCY, HZ	C/C _c , %	OAMCF	NST	MSCC WITH INPUT MODE NO. -														
					1	2	3	4	5	6	7	8	9	10	11	12	13	14	15
1	10.016	5.740	100	65	100	0	0	0	6	0	0	0	0	0	8	0	11	0	0
2	12.030	6.031	92	52	0	100	0	0	0	3	0	0	0	0	0	3	0	0	0
3	14.000	5.654	96	61	0	0	100	0	0	0	4	0	0	1	0	0	0	9	0
4	16.006	6.419	83	55	0	0	0	99	0	0	0	0	4	0	0	0	0	0	4
5	18.026	5.497	89	65	6	0	0	0	99	1	0	0	0	0	0	0	5	0	0
6	19.932	6.447	75	56	0	3	0	0	0	98	1	0	0	0	0	5	0	0	0
7	22.071	6.092	68	60	0	0	3	0	0	1	96	2	0	1	0	0	0	2	0
8	24.065	5.874	64	64	0	0	0	0	0	1	97	2	1	1	0	1	0	0	0
9	26.121	6.620	46	62	0	0	0	0	0	0	2	88	9	0	0	0	0	0	5
10	28.231	8.047	32	65	1	0	0	0	0	1	1	2	86	7	2	0	2	0	0
11	30.184	6.578	37	61	8	0	0	0	1	0	0	0	5	84	10	1	0	0	0
12	32.432	8.862	15	64	2	0	0	0	0	6	0	0	1	1	7	74	10	4	0
13	34.061	7.484	30	62	5	1	0	0	3	2	0	1	1	0	0	14	63	19	0
14	35.688	8.131	17	64	1	0	7	0	1	1	2	0	1	2	0	3	12	81	1
15	37.860	5.351	70	61	0	0	0	4	0	0	0	0	6	0	0	0	0	4	95

TABLE II.- IDENTIFICATION RESULTS FOR THE 2%-DAMPING, 20%-NOISE
BASELINE MODEL AT HIGH ALLOWED DEGREES-OF-FREEDOM.

MODE NO.	NDOF = 65 (NCOL = 993)				NDOF = 200 (NCOL = 969)				NDOF = 250 (NCOL = 969)				NDOF = 300 (NCOL = 961)			
	F	C/C _c	OAMCF	MSCC	F	C/C _c	OAMCF	MSCC	F	C/C _c	OAMCF	MSCC	F	C/C _c	OAMCF	MSCC
1	9.99	8.11	90	99	10.01	2.70	96	100	10.01	2.44	98	100	10.01	2.31	98	100
2	11.99	7.69	80	99	11.99	2.72	94	100	11.99	2.48	92	100	11.99	2.42	94	100
3	13.99	4.28	95	99	14.00	2.44	100	100	14.01	2.27	98	100	14.01	2.18	96	100
4	15.99	5.39	76	99	16.00	2.53	98	100	16.01	2.38	96	100	16.01	2.34	93	100
5	17.99	3.44	87	98	18.01	2.29	95	100	18.01	2.21	96	100	18.00	2.11	96	100
6	20.05	4.36	76	98	19.99	2.49	89	100	19.99	2.32	90	100	20.00	2.24	95	100
7	22.02	3.59	77	98	22.01	2.28	89	100	22.01	2.15	93	100	22.00	2.08	93	100
8	24.04	2.84	85	99	24.01	2.16	95	100	24.00	2.13	92	100	24.01	2.07	93	100
9	26.09	3.87	59	96	26.02	2.34	96	99	26.02	2.22	94	100	26.01	2.13	92	100
10	28.00	4.64	35	95	28.00	2.57	89	99	27.99	2.48	88	100	27.99	2.27	93	100
11	30.04	3.51	70	95	30.00	2.31	94	100	30.00	2.25	91	100	30.02	2.14	87	100
12	32.05	4.41	39	91	32.03	2.39	85	99	32.03	2.21	81	100	32.03	2.09	87	100
13	34.25	4.22	33	86	34.00	2.18	89	99	33.99	2.15	89	100	34.00	2.07	90	100
14	36.30	5.24	17	51	36.02	2.29	85	100	36.02	2.21	83	100	35.99	2.08	85	100
15	37.43	6.12	19	87	37.98	2.22	94	100	37.98	2.14	96	100	37.97	2.06	88	100

(All "Noise Modes" had OAMCF < 2%)

TABLE III.- IDENTIFICATION RESULTS WITH FREQUENCIES OF MODES 7 AND 8
SET NEARLY EQUAL IN 2%-DAMPING, 2%-NOISE BASELINE MODEL.

(NDOF = 65; NCOL = 390 in each identification.)

$\Delta f = 0.10$ Hz				$\Delta f = 0.05$ Hz				$\Delta f = 0.01$ Hz					
INPUT PARAMETERS													
CASE	f_7 (Hz)	f_8 (Hz)	$(C/C_c)_7$	$(C/C_c)_8$	f_7 (Hz)	f_8 (Hz)	$(C/C_c)_7$	$(C/C_c)_8$	f_7 (Hz)	f_8 (Hz)	$(C/C_c)_7$	$(C/C_c)_8$	
1	22.000	22.100	2.00	2.00	22.000	22.050	2.00	2.00	22.000	22.010	2.00	2.00	
2				3.00				3.00				3.00	
3				10.00				10.00				10.00	
IDENTIFIED PARAMETERS													
CASE	MODE NO.	f	C/C _c	OAMCF	MSCC	f	C/C _c	OAMCF	MSCC	f	C/C _c	OAMCF	MSCC
1	7	21.998	2.51	87	78	21.941	4.28	57	66	21.184	36.69	1	33
	8	22.074	2.07	100	77	22.034	2.01	100	66	22.007	2.01	100	66
2	7	22.000	2.11	96	99	22.001	2.12	96	99	22.001	2.12	98	99
	8	22.101	3.08	98	99	22.053	3.09	100	99	22.015	3.09	100	99
3	7	22.001	2.01	100	100	22.001	2.01	100	100	22.001	2.01	100	100
	8	22.101	10.02	100	100	22.051	10.02	100	100	22.011	10.02	100	100

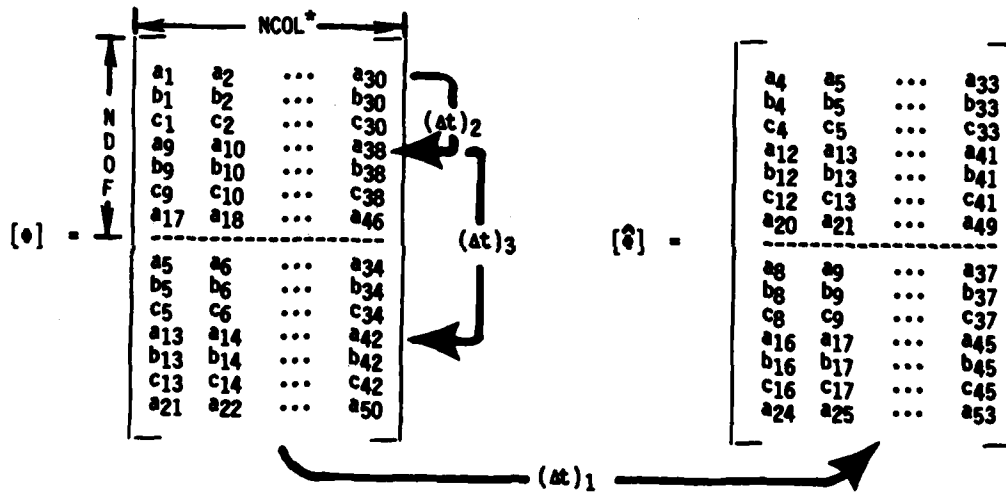
(Identification accuracy of other 13 modes comparable to values shown in Table I for 2%-damping, 2%-noise model.)

3 free-response functions : $a_1 a_2 a_3 \dots a_{100}$
 (100 samples each) $b_1 b_2 b_3 \dots b_{100}$
 $c_1 c_2 c_3 \dots c_{100}$
 $t \rightarrow$

$P_0 = 3$ $N_1 = 3$
 $NDOF = 7$ $N_2 = 8$
 $NCOL = 30$ $N_3 = 4$

$(\Delta t)_1 = N_1/SF$
 $(\Delta t)_2 = N_2/SF$
 $(\Delta t)_3 = N_3/SF$

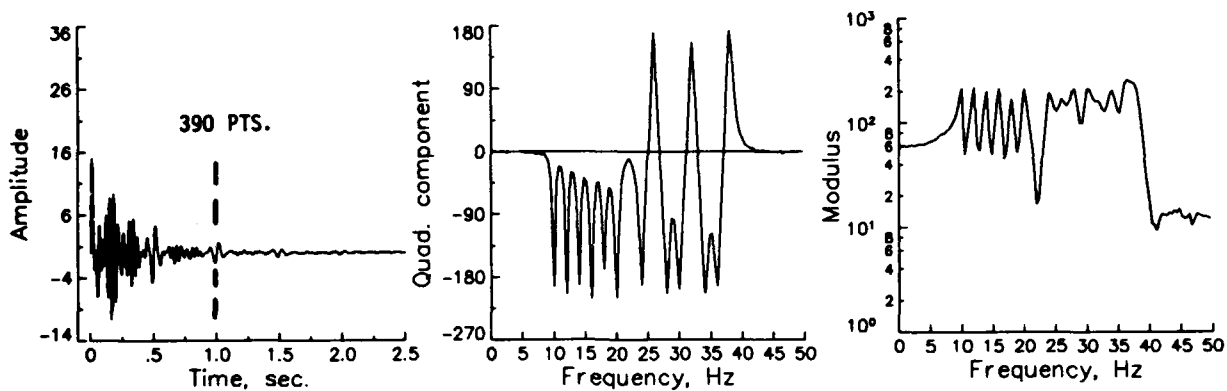
(SF = data sampling frequency)



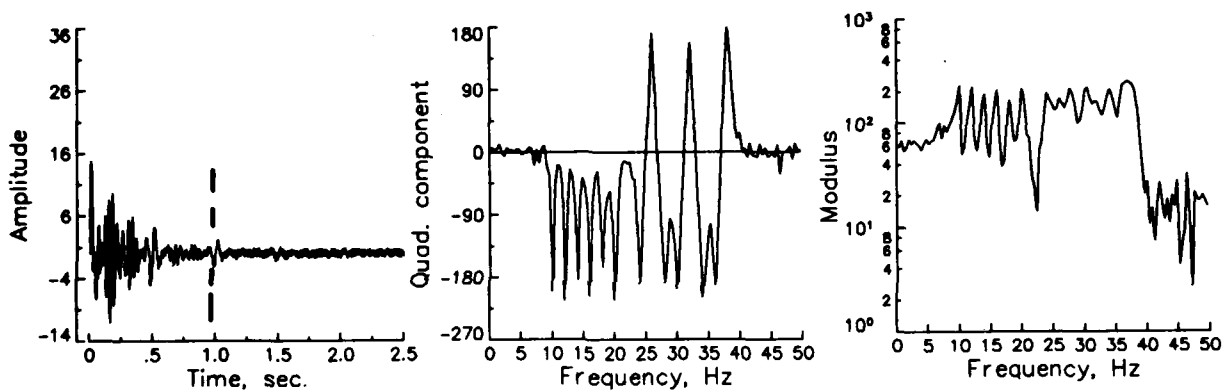
* $NCOL \geq 2 \cdot NDOF$

Figure 1.- Example Placement of Free-Response Data into the Two Response Matrices.

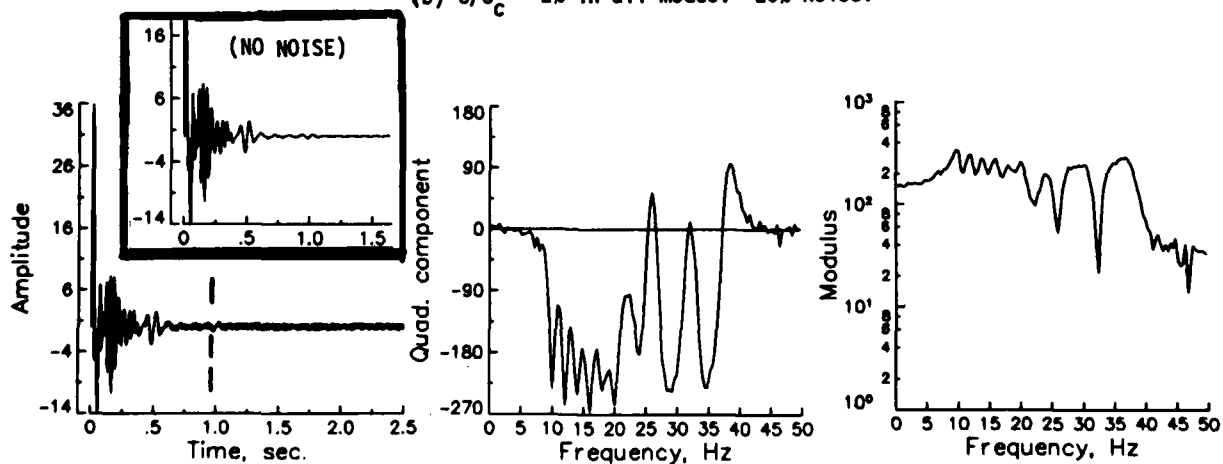
SAMPLING FREQUENCY = 400 HZ (1000 PTS. IN EACH FREE-RESPONSE FCT.)



(a) $C/C_c = 2\%$ in all modes. 2% noise.



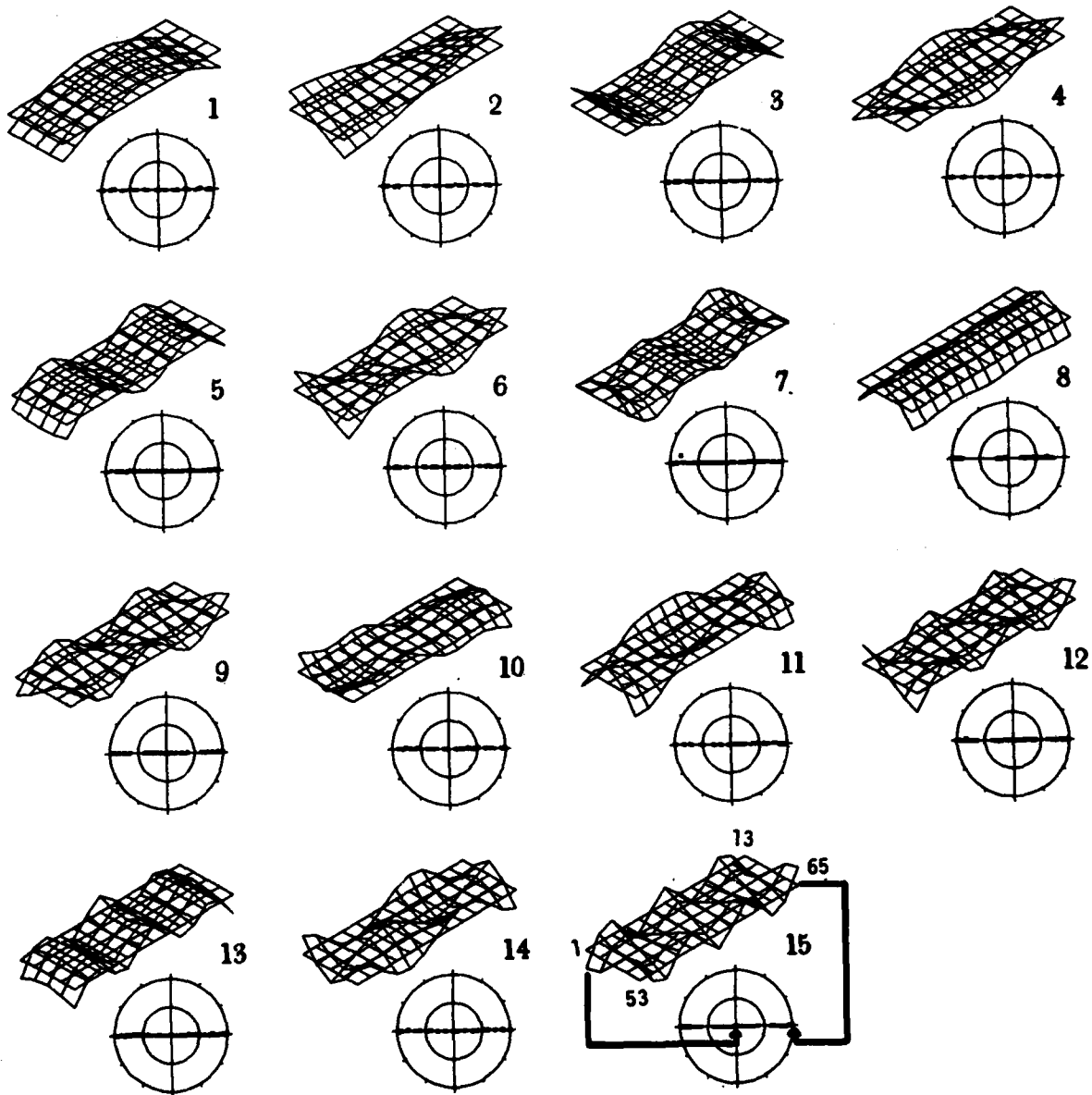
(b) $C/C_c = 2\%$ in all modes. 20% noise.



(c) $C/C_c = 5\%$ in all modes. 10% noise.

Figure 2.- Typical free-responses and frequency spectra for three baseline models, with modal frequencies spaced every 2 Hz from 10 to 38 Hz.

NDOF = 65; NCOL = 390.



(Mode shape phase angles indicated in polar plots)

Figure 3.- Identified (complex) mode shapes for baseline model with 2% damping in all modes and 2% noise.

NDOF = 65; NCOL = 390.

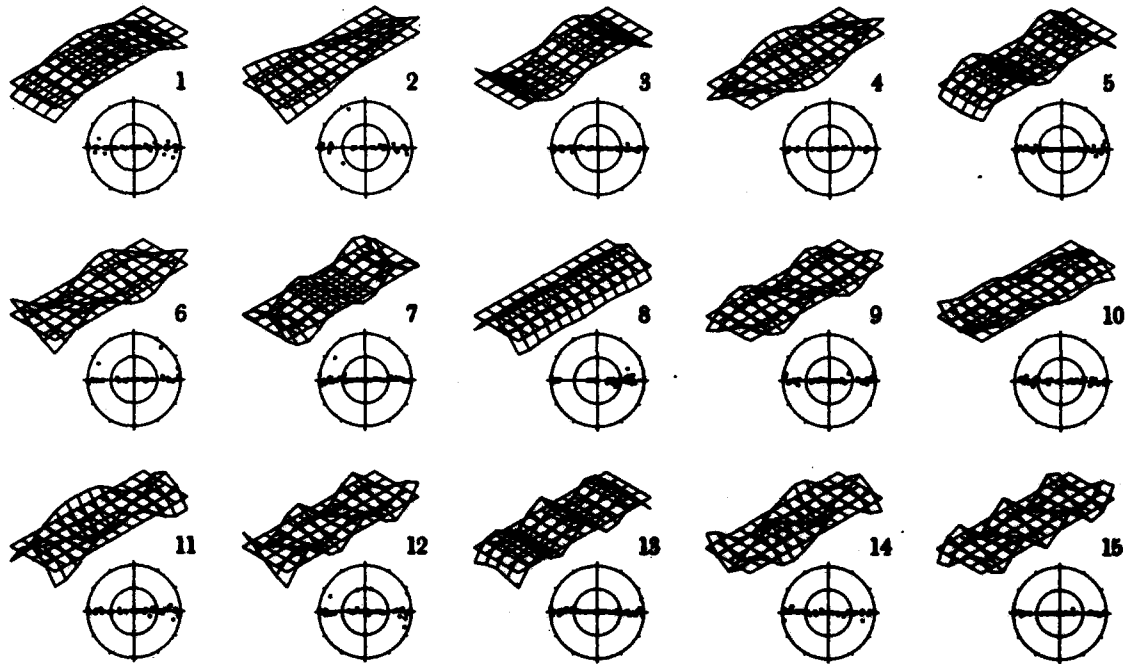


Figure 4.- Identified (complex) mode shapes for baseline model with 2% damping in all modes and 20% noise.

NDOF = 65; NCOL = 390.

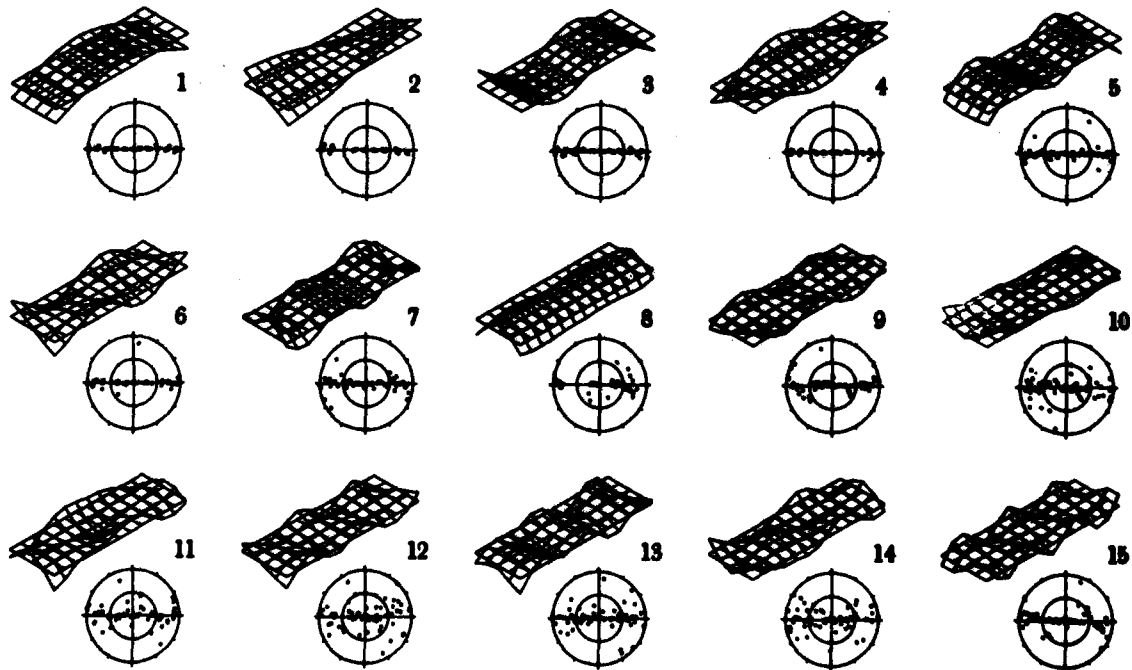
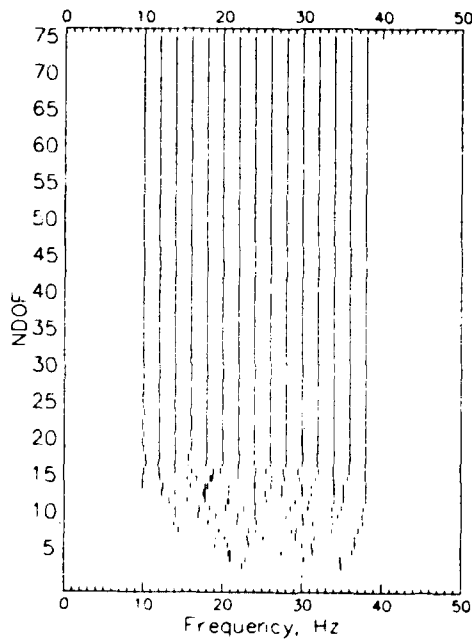


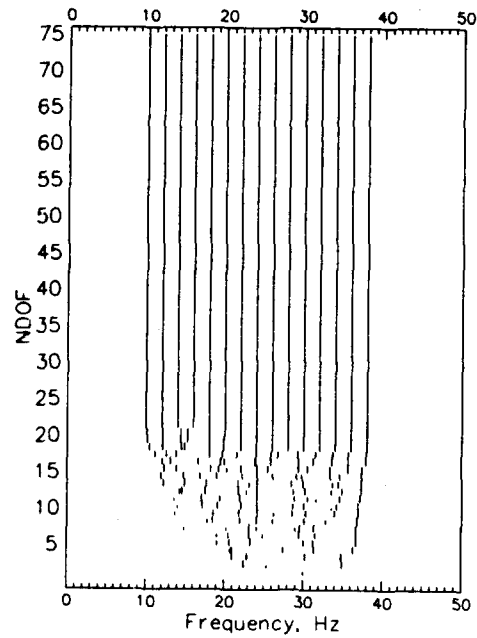
Figure 5.- Identified (complex) mode shapes for baseline model with 5% damping in all modes and 10% noise.

NCOL = 300 in each identification.

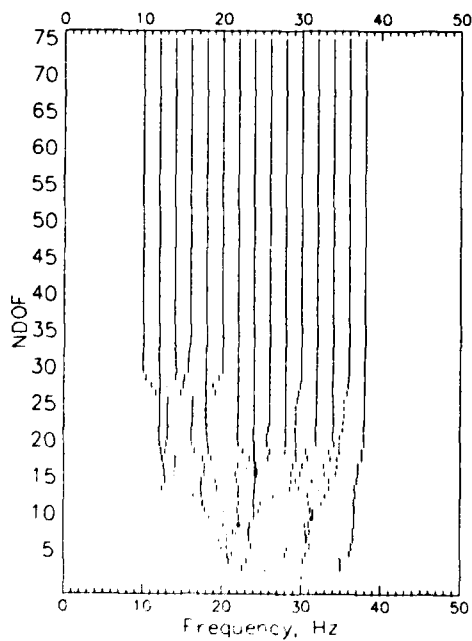
(Heights of vertical line segments proportional to OAMCF values)



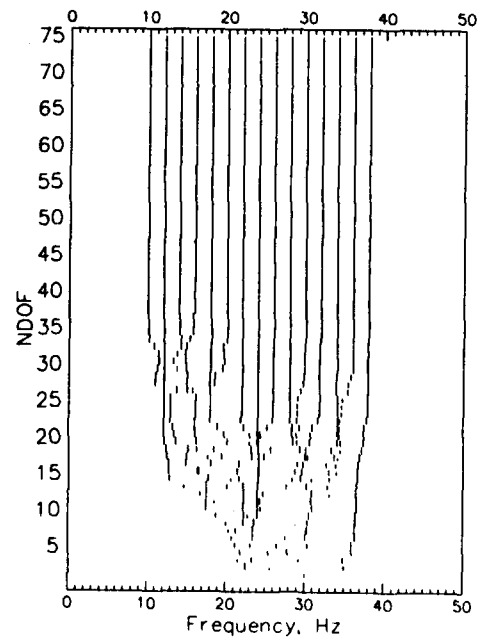
(a) 0.001% Noise



(b) 0.1% Noise



(c) 2% Noise

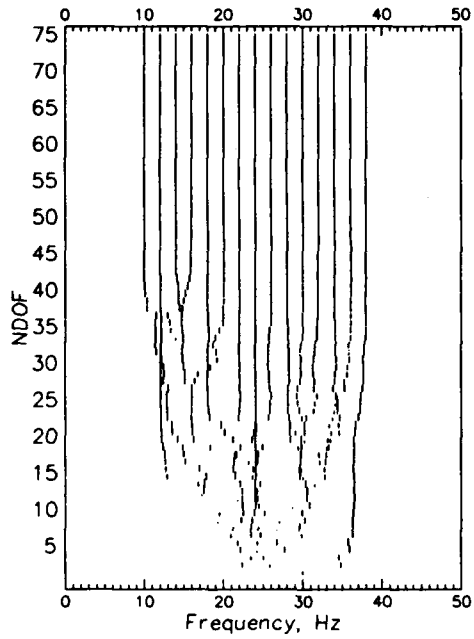


(d) 5% Noise

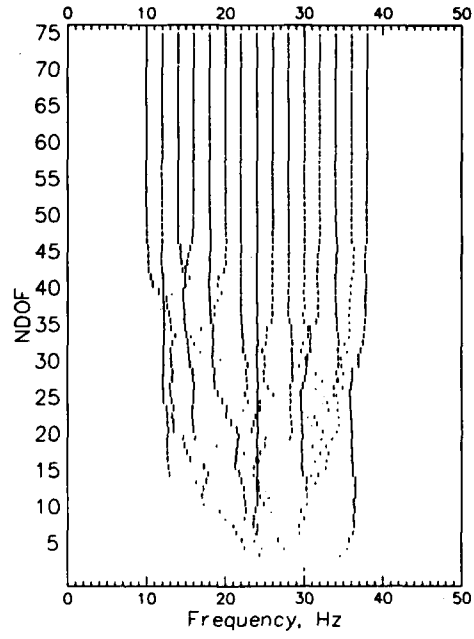
Figure 6.- "NDOF-Frequency Maps" for 2%-damping baseline model at several low noise/signal ratios.

NCOL = 300 in each identification.

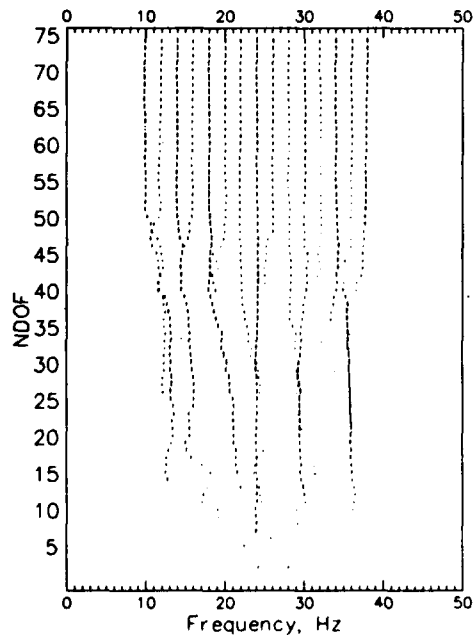
(Heights of vertical line segments proportional to OAMCF values)



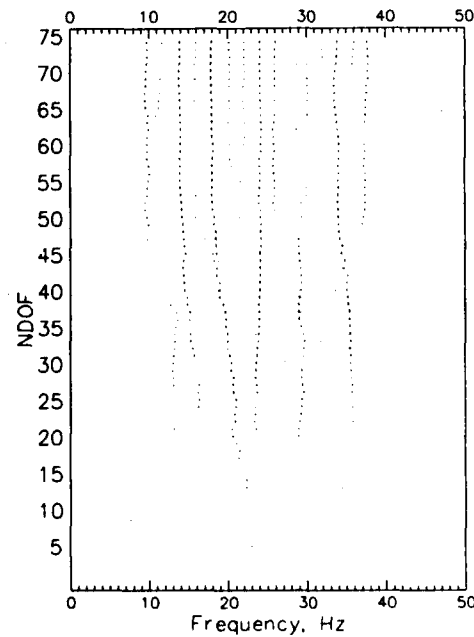
(a) 10% Noise



(b) 20% Noise



(c) 50% Noise



(d) 100% Noise

Figure 7.- "NDOF-Frequency Maps" for 2%-damping baseline model at several high noise/signal ratios.

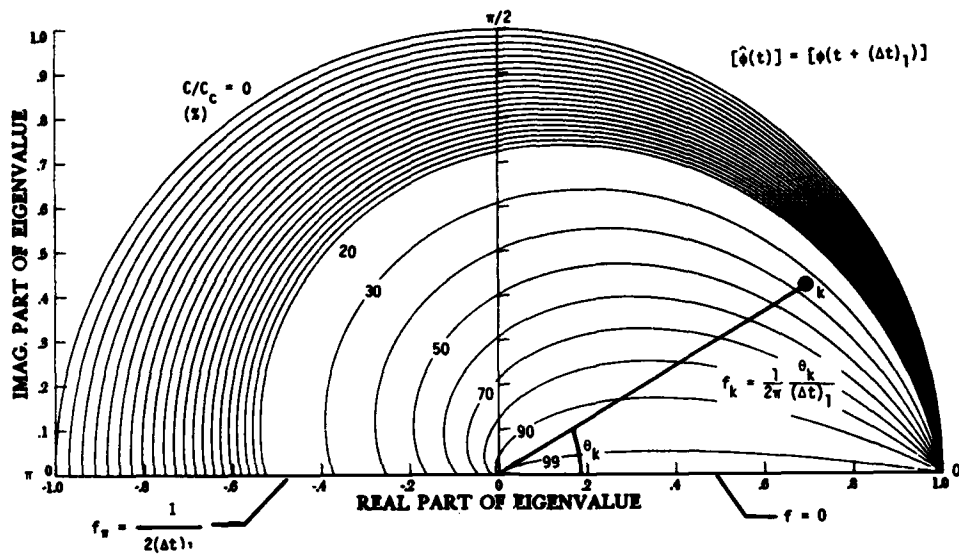
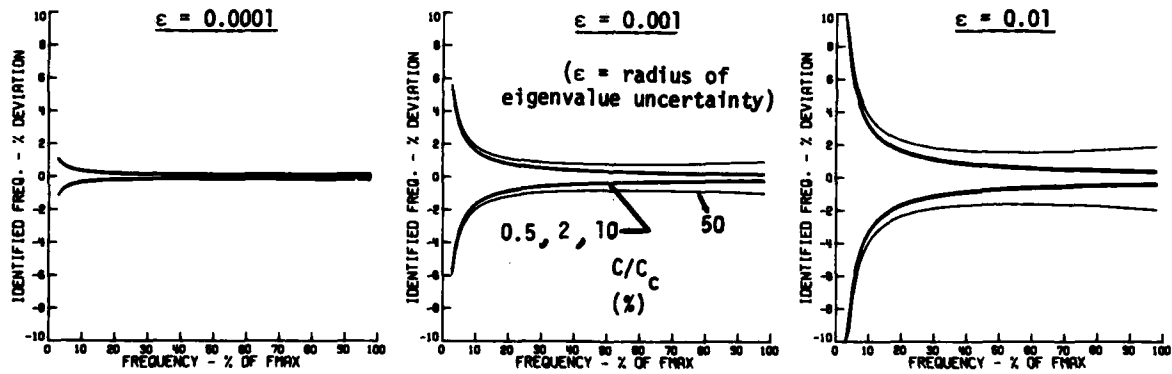
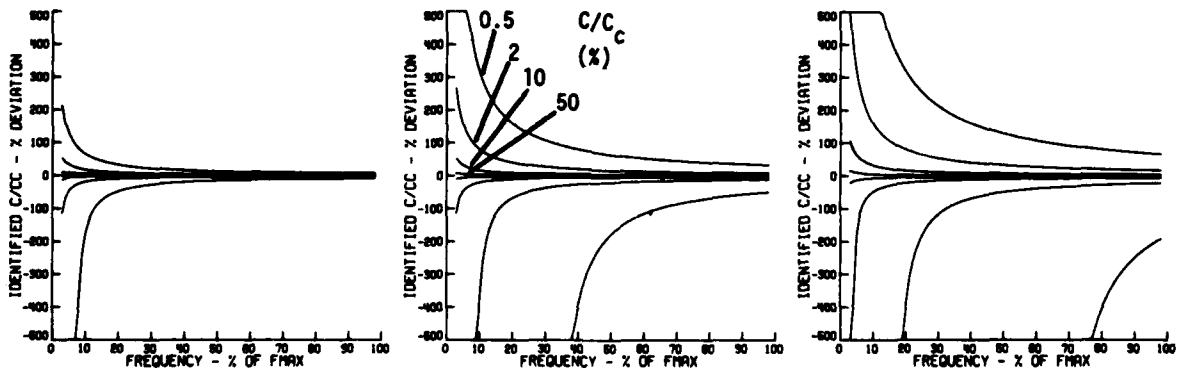


Figure 8.- Contours of equal damping factor in the plane of the eigenvalues of [A].



(a) Envelopes of % freq. deviation



(b) Envelopes of % C/C_c deviation

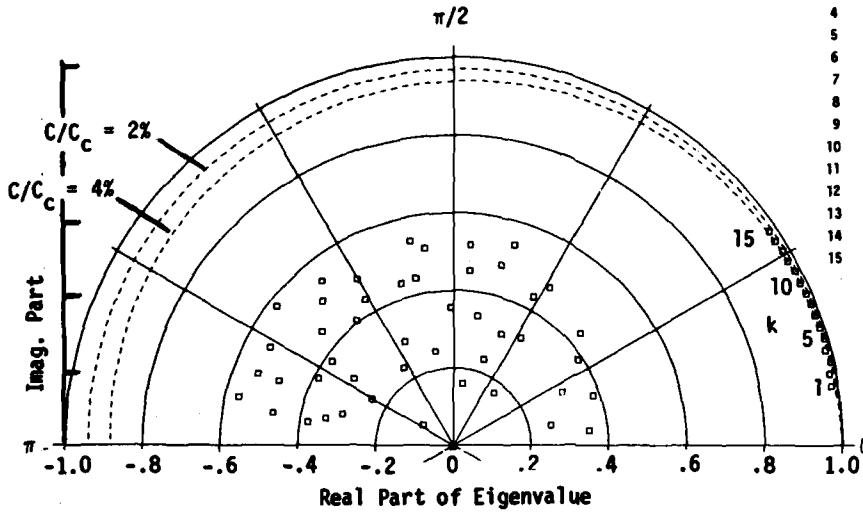
Figure 9.- Sensitivity of identified frequency and damping factors at three uncertainty levels in computation of the eigenvalues of [A].

2%-damping, 20%-noise baseline model.

NDOF = 65; NCOL = 390.

Identification Results

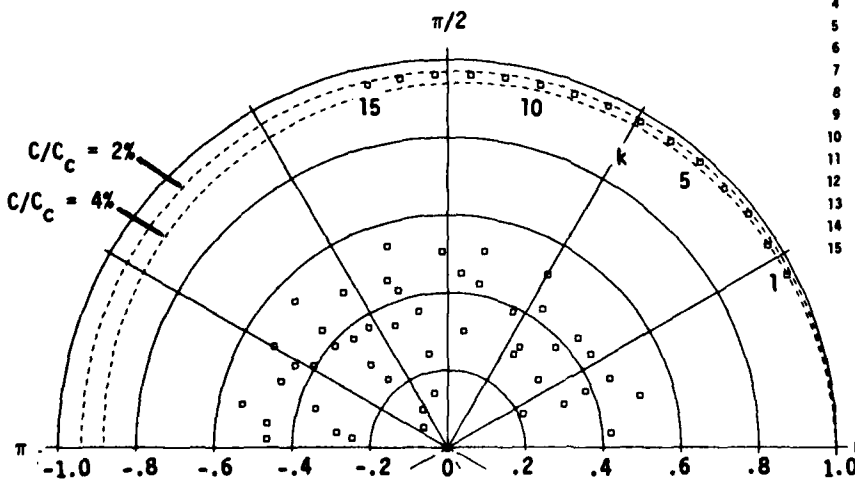
Mode k	F, Hz	C/C _c , %	DMCF	MSCC
1	9.97	10.26	95	99
2	12.02	8.98	80	98
3	14.00	4.22	93	98
4	16.03	6.20	84	99
5	17.98	3.24	89	99
6	19.94	4.10	85	98
7	22.02	3.51	84	98
8	24.02	3.06	85	99
9	25.98	3.72	68	96
10	27.99	4.10	51	96
11	30.07	3.12	78	97
12	32.07	3.99	37	96
13	34.02	3.28	68	93
14	36.03	3.70	59	94
15	37.92	3.30	79	98



(a) $N_1 = 1$ [$(\Delta t)_1 = 1/SF$; $F_\pi = 200$ Hz]

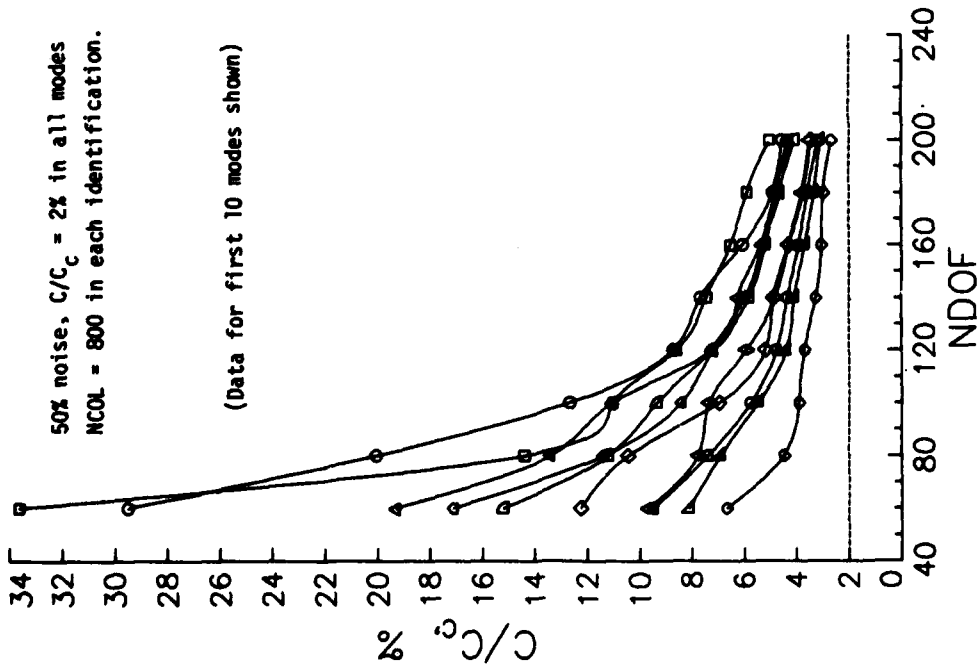
Identification Results

Mode k	F, Hz	C/C _c , %	DMCF	MSCC
1	9.98	4.37	95	100
2	11.97	4.48	88	99
3	14.01	2.93	98	100
4	15.98	3.16	97	100
5	17.99	2.40	93	100
6	20.00	2.75	89	100
7	21.98	2.43	86	100
8	24.00	2.33	89	100
9	26.02	2.60	94	99
10	28.03	2.79	93	99
11	30.03	2.50	81	100
12	31.97	2.61	72	99
13	34.01	2.40	87	99
14	36.05	2.54	75	99
15	37.95	2.43	86	100

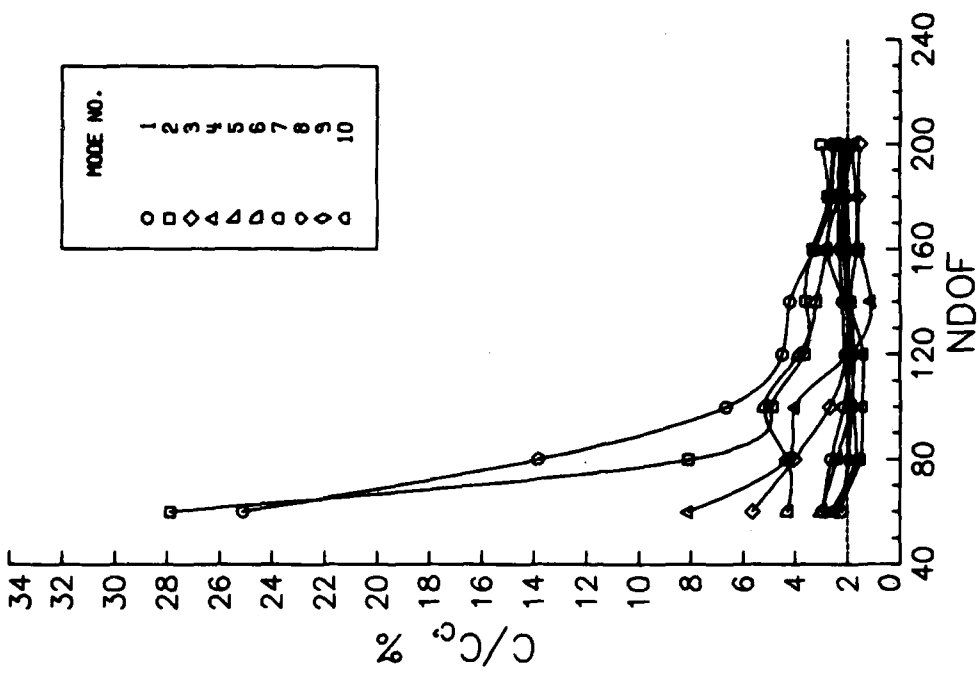


(b) $N_1 = 3$ [$(\Delta t)_1 = 3/SF$; $F_\pi = 66.67$ Hz]

Figure 10.- Typical effect of changing $(\Delta t)_1$ on identification accuracy. Polar plots show eigenvalues of [A].

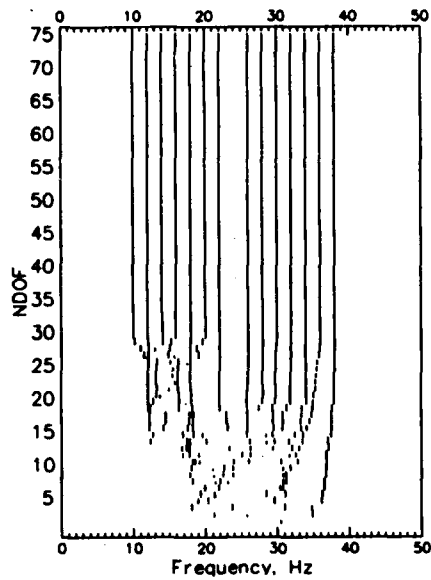


(a) Damping factors from eigenvalues of [A] (Std. method)

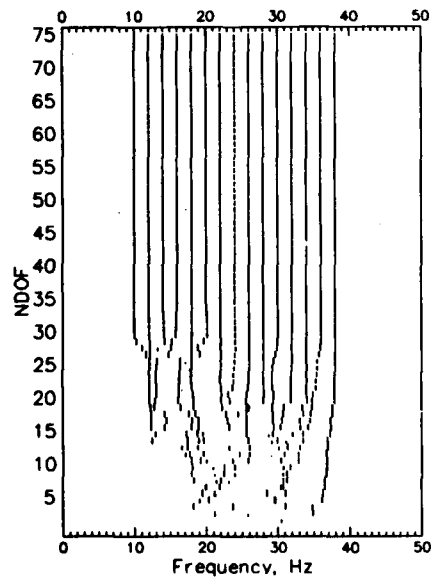


(b) Damping factors from eigenvector data using frequencies from eigenvalues of [A] (Alternate method)

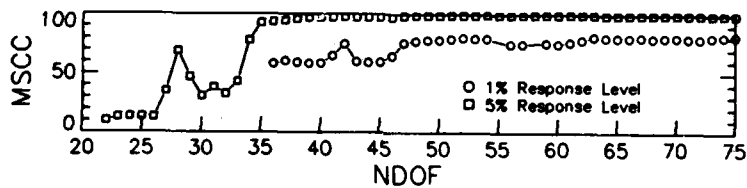
Figure 11.- Comparison of modal damping computed by standard and alternate methods, for 2%-damping, 50%-noise baseline model.



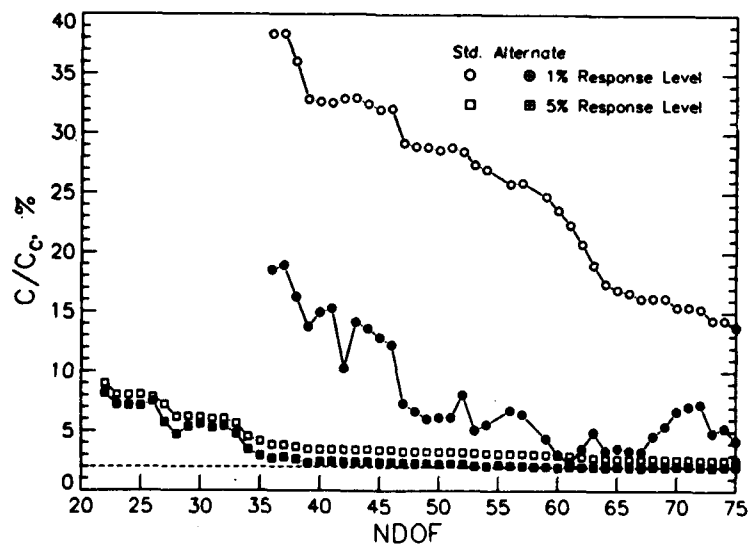
(a) NDOF-frequency map with mode 8 response level 1% that of other modes.



(b) NDOF-frequency map with mode 8 response level 5% that of other modes.

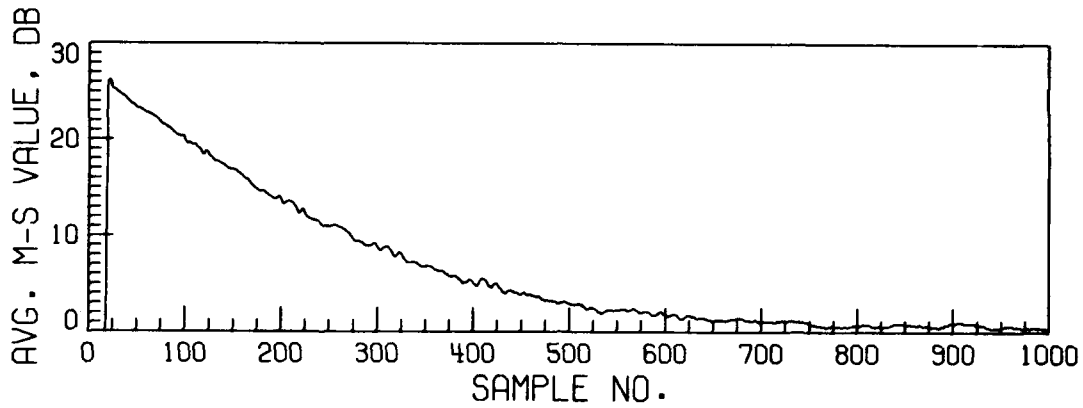


(c) Mode 8 MSCC values.

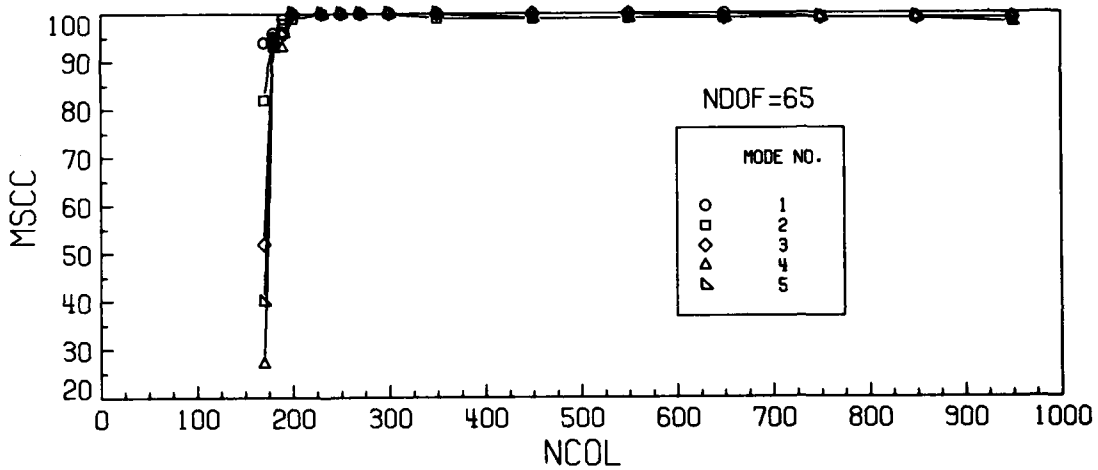


(d) Mode 8 damping factors calculated by standard and alternate methods.

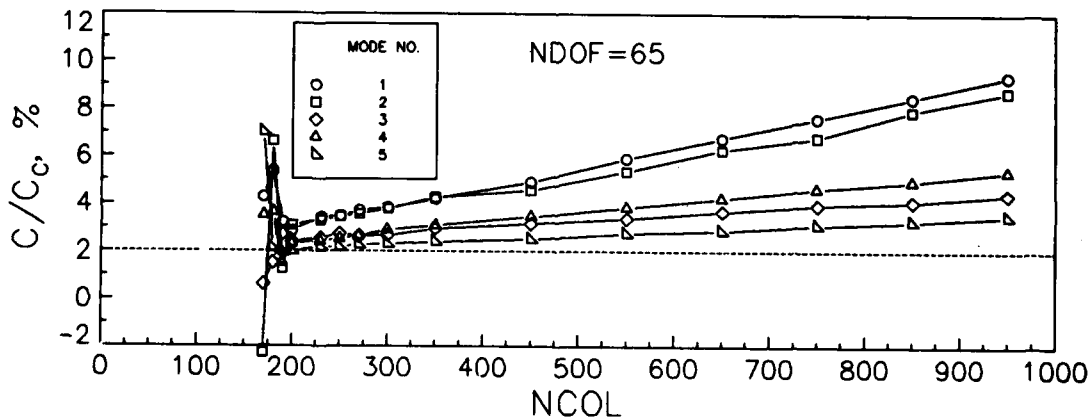
Figure 12.- Identification results for 2%-damping, 2%-noise baseline model with response level of mode 8 equal to 1% and 5% that of other modes.



(a) Running average mean-square value of all 65 free-response functions for 2%-damping, 20%-noise baseline model.



(b) Calculated MSCC values as a function of NCOL.



(c) Identified modal damping factors as a function of NCOL.

Figure 13.- Effect of NCOL on identification results for 2%-damping, 20%-noise baseline model.

NDOF = 65; NCOL = 390 in each identification.
 $C/C_c = 2\%$ in modes 1-5 & 11-15.

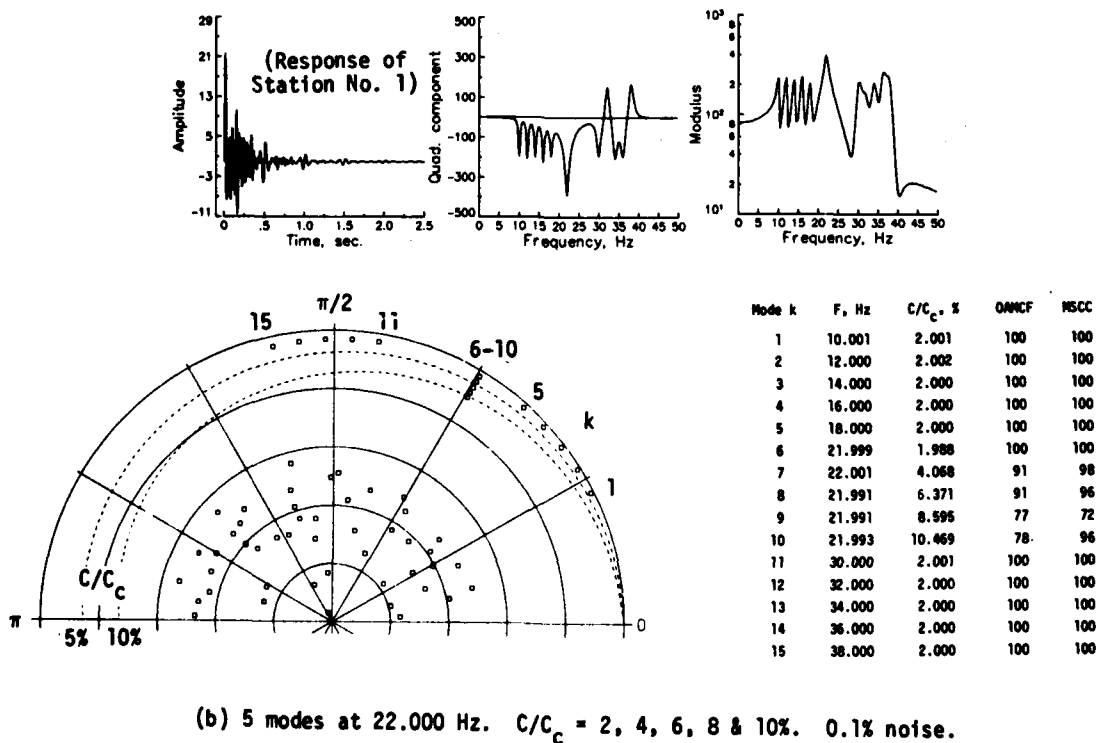
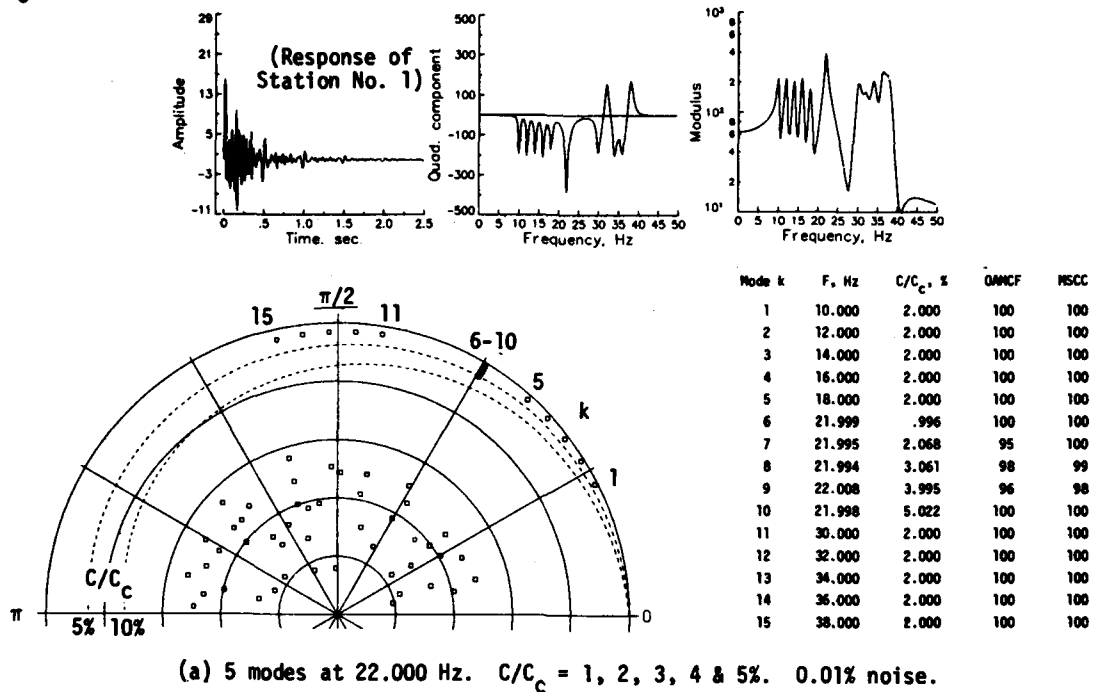


Figure 14.- Identification results for 15-mode model with FIVE modes at 22,000 Hz, for C/C_c separations of 1% and 2%. Polar plots show eigenvalues of [A].

DISCUSSION

Mr. Ewins (Imperial College, London):

Are you convinced that the theoretical data you have used which was polluted with noise, realistically represents the kind of data you get from experiments on real structures?

Mr. Ibrahim: From my previous experience, I would rather work with experimental data than simulated data.

Mr. Ewins: I asked because we've been through a similar kind of process and we find that experimental data contains a quite different type of error to that which you put in with random errors superimposed on the theoretical ideal. The structures have systematic errors. You have non-linearities and I wonder whether the method is equally effective on real data as you have shown on the synthesized.

Mr. Ibrahim: Yes, we have lots of previous applications and we will put the paper in the AIAASDM Conference in April and we are dealing with large modal surveys of real experimental full scale structures. And to answer your question, I personally feel as comfortable with experimental noise as with simulated noise because the experimental noise is nice and random. What you generate in the computer usually has some distribution. The other question is non-linearity. We did not include a non-linearity here, but non-linearity of the structures is another completely different ball game and it has to be dealt with separately. But we get as good results with experimental data, yes.

EFFECTIVE DYNAMIC REANALYSIS OF LARGE STRUCTURES

B. P. Wang
University of Virginia
Charlottesville, Virginia 22901

and

F. H. Chu
RCA Astro
Princeton, New Jersey 08540

This paper describes an effective dynamic reanalysis method which can be used to estimate the new natural frequencies of the structure after modification using the modal information of the original structure (i.e., natural frequencies, mode shapes at the location of the changes, and the generalized mass for each of the modes). A nonlinear algebraic equation is derived and by solving this equation using either the Newton Raphson's iteration method or simply the bisection method will give the new natural frequencies of the structure after modification. This method can be applied to the change of a linear spring, a concentrated mass, an extension member, a beam, and a plate element. A group change of the above mentioned elements can be achieved by solving a set of coupled nonlinear algebraic equations. Since this method makes no assumption on the changes of the mode shapes after modification, it is not restricted to small local modifications as in most of the dynamic reanalysis methods. The accuracy of the method can be improved by including the static deflections of the original structure at the modification locations due to a unit force at these locations to simulate the effect of higher modes of the original structure. A finite element model of a 196 degree of freedom solar array panel system is used to demonstrate the effectiveness and accuracy of the method.

INTRODUCTION

In the dynamic analysis of large structures, an analytical finite element model is usually constructed to calculate the resonant frequencies of the structure. This model may contain hundreds of degree of freedom and if the model is changed locally, either due to a design change or a modeling change reanalysis of such a model by solving a new eigenvalue problem is expensive.

This paper describes an application of the general formulation of the efficient structural reanalysis techniques of References 1 and 2. In particular, a method of estimation for the new resonant frequencies of the modified structure using the modal information of the original system will be presented. The modal information needed is the natural frequencies, the mode shape coefficients at the location of modifications, and the generalized mass for each mode. For structure modification involving one parameter at a local location (such as add a spring

to ground), it can be shown that the frequency equation is a nonlinear algebraic equation in terms of the modal parameters of the original system. When all the modes of the original system are used, this equation will yield the exact solution of the modified system. When only partial modes are available, the accuracy of the method can be improved by including the static deflections of the original structure at the modification locations due to a unit force at these locations to approximate the effect of higher modes of the original structure.

To find the natural frequencies of the modified system, the above frequency equations are to be solved numerically using Newton-Raphson iteration or the bisection method.

The above method can be applied to the change of a linear spring, a concentrated mass, an extension member a beam, or a plate element, etc. A group change of the above mentioned elements can be achieved by solving a set of coupled nonlinear algebraic equations. Since

this method makes no assumption on the changes of the mode shapes after modification, it is not restricted to small local modifications as in most of the perturbation type dynamic reanalysis methods.

A 196 degree of freedom finite element model of a solar array panel system is used to demonstrate the effectiveness and accuracy of the method.

GENERAL FORMULATION

Consider the free vibration of an undamped nonrotating N-dof structure model described by the well known equation of motion

$$[M]\{\ddot{u}\} + [K]\{u\} = \{0\} \quad (1)$$

Equation (1) describes the behavior of the "original system". When the structure is modified, the mass and stiffness matrices will be changed and the equation of free vibration of the modified system becomes

$$[M']\{\ddot{u}'\} + [K']\{u'\} = \{0\} \quad (2)$$

where

$$[M'] = [M] + [\Delta M] \quad (3a)$$

$$[K'] = [K] + [\Delta K] \quad (3b)$$

By substituting (3) into (2), the modified system equation of motion can be written as

$$[M]\{\ddot{u}'\} + [K]\{u'\} = -[\Delta M]\{\ddot{u}'\} - [\Delta K]\{u'\} \quad (4)$$

Assume harmonic motion

$$\{u'\} = \{\bar{U}'\}e^{i\omega t} \quad (5)$$

(4) becomes

$$(-\omega^2[M] + [K])\{\bar{U}'\} = (\omega^2[\Delta M] - [\Delta K])\{\bar{U}'\} \quad (6)$$

Now if the structural modification is localized, then the modification matrices $[\Delta M]$ and $[\Delta K]$ will be highly sparse, i.e., they will have only a few nonzero entries. Under these conditions, we can rewrite (6) as

$$(-\omega^2[M] + [K])\{\bar{U}'\} = \{L(\bar{U}')\} \quad (7)$$

where $\{\bar{U}'\}$ contains only the dof's affected by the modification. When the modification is localized, the dimension of $\{\bar{U}'\}$ is much smaller than the dimension of $\{U'\}$. Each element $L_i(\bar{U}')$ of the vector $\{L(\bar{U}')\}$ is a linear function of $\{\bar{U}'\}$. Equation (7) can be solved now as

$$\{U'\} = [R]\{L(\bar{U}')\} \quad (8)$$

where

$$[R] = (-\omega^2[M] + [K])^{-1} \quad (9)$$

= receptance matrix of the original system

When the modal superposition approach is used, the element R_{ij} of the receptance matrix can be expressed as

$$R_{ij} = \sum_{\ell=1}^n \frac{\phi_{i\ell} \phi_{j\ell}}{G_{\ell}(\omega_{\ell}^2 - \omega^2)} \quad (10)$$

where

ω_{ℓ} = natural frequency of the ℓ^{th} mode

$\phi_{i\ell}$ = mode shape coefficient of dof i of ℓ^{th} mode

G_{ℓ} = generalized mass of the ℓ^{th} mode
 $= \{\phi_{\ell}\}^T [M] \{\phi_{\ell}\}$

Note that ω_{ℓ} , $\{\phi_{\ell}\}$ and G_{ℓ} are assumed known in the solution of the original system. Now from equation (8), one can extract a subset of equations such that

$$\{\bar{U}'\} = [W]\{\bar{U}'\} \quad (11)$$

where the elements W_{ij} of the matrix $[W]$ is a function of elements of the known matrices $[R]$, $[\Delta M]$ and $[\Delta K]$ as well as the unknown frequency ω . From (11), the condition of the nontrivial solution leads to the frequency equation for the modified system, which is

$$\det([I] - [W]) = 0 \quad (12)$$

The dimension of matrix $[W]$ of $c \times c$ where c is the number of dof's affected by the modification.

For specific modifications, equation (12) can be simplified to explicit equations in terms of unknown frequencies and known parameters. Once the natural frequency of the modified system are solved for the corresponding mode shape can be computed by first computing $\{\bar{U}'\}$ using equation (11) and then computing $\{U'\}$ using equation (8). The above general formulation will be applied to special cases in the next section.

APPLICATION OF GENERAL FORMULATION

In the following, we will apply the general formulation derived in the previous section to a few special cases of local modification.

Case 1: Add Spring K_a between dof i and dof j

Assume the added spring is massless, then

$$[\Delta M] = [0]$$

$$[\Delta K] = \begin{bmatrix} & i & j \\ 0 & \dots & 0 & \dots & 0 & \dots & 0 \\ \vdots & & & & & & \\ 0 & K_a & \dots & -K_a & \dots & 0 & 0 \\ \vdots & & & & & & \\ 0 & \dots & -K_a & \dots & K_a & \dots & 0 \\ \vdots & & & & & & \\ 0 & 0 & 0 & 0 & 0 & 0 & 0 \end{bmatrix} \begin{matrix} \\ \\ i \\ \\ j \\ \\ \\ \end{matrix}$$

and

$$\{\bar{U}'\} = \begin{Bmatrix} U'_i \\ U'_j \end{Bmatrix}$$

for this case,

$$\{L_i(\bar{U}')\} = -[\Delta K]\{U\} = \begin{Bmatrix} 0 \\ \vdots \\ 0 \\ -K_a U'_i + K_a U'_j \\ 0 \\ \vdots \\ 0 \\ K_a U'_i - K_a U'_j \\ 0 \\ \vdots \\ 0 \end{Bmatrix} \quad (13)$$

Substituting (13) into (8), we can write the equations for U'_i and U'_j :

$$\begin{aligned} U'_i &= R_{ii}(-K_a U'_i + K_a U'_j) + R_{ij}(K_a U'_i - K_a U'_j) \\ U'_j &= R_{ji}(-K_a U'_i + K_a U'_j) + R_{jj}(K_a U'_i - K_a U'_j) \end{aligned} \quad (14)$$

Comparing equations (14) with (11), we can identify

$$[W] = K_a \begin{bmatrix} R_{ii} + R_{ij} & R_{ii} - R_{ij} \\ -R_{ji} + R_{jj} & R_{ji} - R_{jj} \end{bmatrix} \quad (15)$$

and the frequency equation becomes

$$\det([I] - [W]) = \begin{vmatrix} 1 - K_a(-R_{ii} + R_{ij}) & K_a(-R_{ii} + R_{ij}) \\ K_a(R_{ji} - R_{jj}) & 1 - K_a(R_{ji} - R_{jj}) \end{vmatrix} = 0$$

which can be simplified to (note that $R_{ji} = R_{ij}$)

$$1 + K_a(R_{ii} + R_{jj} - 2R_{ij}) = 0 \quad (16)$$

Express R_{ii} and R_{ij} in terms of modal data of the original system

$$R_{ii} = \sum_{l=1}^N \frac{\phi_{il}^2}{G_l(\omega_l^2 - \omega^2)}$$

$$R_{ij} = \sum_{l=1}^N \frac{\phi_{il} \phi_{jl}}{G_l(\omega_l^2 - \omega^2)}$$

Thus, equation (16) becomes

$$\frac{1}{K_a} + \sum_{l=1}^L \frac{(\phi_{il} - \phi_{jl})^2}{G_l(\omega_l^2 - \omega^2)} = 0 \quad (17)$$

Equation (17) is the frequency equation of the system with spring K_a added between dof i and dof j . If all the n modes of the original system are available, then the equation is exact. Otherwise, the equation will give an approximate solution to the natural frequencies of the modified system.

As a special case of adding spring K_a between dof i and ground at which $\phi_{jl} = 0$, equation (17) becomes

$$\frac{1}{K_a} + \sum_{l=1}^L \frac{\phi_{il}^2}{G_l(\omega_l^2 - \omega^2)} = 0 \quad (18)$$

Case II: Add Mass M_a at node P with 3 dof i, j, k

Assume that the mass is a point matrix and does not change the affect of the stiffness property of the system. Then

$$[\Delta M] = \begin{bmatrix} & i & j & k \\ 0 & & & \\ & M_a & & \\ & & M_a & \\ & & & M_a \\ & & & & 0 \\ & & & & & \ddots \\ & & & & & & 0 \end{bmatrix} \begin{matrix} \\ i \\ j \\ k \\ \\ \\ \end{matrix}$$

$$[\Delta K] = [0]$$

$$\{\bar{U}'\} = \begin{Bmatrix} U'_i \\ U'_j \\ U'_k \end{Bmatrix}$$

$$\{L(\bar{U}')\} = \omega^2 [\Delta M]\{\bar{U}'\} = \begin{Bmatrix} 0 \\ \vdots \\ \omega^2 M_a U'_i \\ \omega^2 M_a U'_j \\ \omega^2 M_a U'_k \\ 0 \\ \vdots \\ 0 \end{Bmatrix}$$

and the frequency equation becomes

$$[\bar{R}] = \begin{bmatrix} R_{aa} & R_{ab} & R_{ac} & R_{ad} \\ R_{ba} & R_{bb} & R_{bc} & R_{bd} \\ R_{ca} & R_{cb} & R_{cc} & R_{cd} \\ R_{da} & R_{db} & R_{dc} & R_{dd} \end{bmatrix}$$

The frequency equation becomes

$$\det ([I] + [\bar{R}] [\Delta K]) = 0$$

which can be expanded and simplified to

$$\left(\frac{\Delta EI}{L^3}\right)^2 (A_P B_Q - A_Q B_P) - \left(\frac{\Delta EI}{L^3}\right) (A_P + B_Q) + 1 = 0 \quad (21)$$

where

$$\begin{aligned} A_P &= \sum_{l=1}^L P_l A_l, & B_P &= \sum_{l=1}^L P_l B_l, & A_Q &= \sum_{l=1}^L Q_l A_l, & B_Q &= \sum_{l=1}^L Q_l B_l \\ P_l &= 12\phi_{a,l} + 6L\phi_{b,l} - 12\phi_{c,l} - 6L\phi_{d,l} \\ Q_l &= 6L\phi_{a,l} + 4L^2\phi_{b,l} - 6L\phi_{c,l} + 2L^2\phi_{d,l} \\ A_l &= \frac{-\phi_{a,l} + \phi_{c,l} - L\phi_{d,l}}{G_l(\omega_l^2 - \phi_l^2)}, & B_l &= \frac{-\phi_{b,l} + \phi_{d,l}}{G_l(\omega_l^2 - \omega_l^2)} \end{aligned} \quad (22)$$

ACCURACY IMPROVEMENT OF RECEPTANCE MATRIX

The receptance matrix can be expressed using modal data as

$$[R] = \sum_{l=1}^L \frac{\{\phi\}_l \{\phi\}_l^T}{G_l(\omega_l^2 - \omega_l^2)} \quad (23)$$

when $L < n$, the above representation is not complete. Hirai et al [3] and Leung [4], have suggested ways of improving (23) using the static solution plus L lower modes. Their developments are based on the following two identities:

$$\frac{1}{\omega_l^2 - \omega^2} = \frac{1}{\omega_l^2} + \frac{\omega^2}{\omega_l^4} + \dots + \frac{(\omega^2)^{r-1}}{\omega_l^{2r}} + \frac{(\omega^2/\omega_l^2)^r}{(\omega_l^2 - \omega^2)} \quad (24)$$

$$([K]^{-1} \omega^2 [M])^{r-1} [K]^{-1} = \{\phi\} \left[\begin{array}{c} (\omega^2)^{r-1} \\ G_l(\omega_l^2) \end{array} \right] \{\phi\}^T$$

Using the above identities, the exact spectral representation of $[R]$ becomes:

$$\begin{aligned} [R] &= \sum_{l=1}^N \sum_{\zeta=1}^r \frac{\{\phi\}_l \{\phi\}_l^T (\omega^2)^{\zeta-1}}{G_l \omega_l^{2\zeta}} + \frac{\{\phi\}_l \{\phi\}_l^T \omega^2}{(\omega_l^2 - \omega^2) (\omega_l^2)^r} \\ &= \sum_{S=1}^r \sum_{l=1}^N \frac{\{\phi\}_l \{\phi\}_l^T (\omega^2)^{S-1}}{G_l \omega_l^{2S}} + \sum_{l=1}^N \frac{\{\phi\}_l \{\phi\}_l^T \omega^{2r}}{\omega_l^2 - \omega^2} \end{aligned} \quad (25)$$

when only p lower modes are available, the above equation becomes:

$$[R] = \sum_{S=1}^{r-1} ([K]^{-1} \omega^2 [M])^{S-1} [K]^{-1} + \sum_{l=1}^L \frac{\{\phi\}_l \{\phi\}_l^T \omega^{2r}}{G_l \omega_l^{2r} (\omega_l^2 - \omega^2)} \quad (26)$$

For $r = 1$, we have

$$[R] = [K]^{-1} + \sum_{l=1}^L \frac{\{\phi\}_l \{\phi\}_l^T \omega^2}{G_l \omega_l^2 (\omega_l^2 - \omega^2)} \quad (27)$$

In practice, when applying Eq. (27), one does not have to compute $[K]^{-1}$, instead, only the required columns of $[K]^{-1}$ are computed. For example, if the i th column of $[K]^{-1}$ is required, we solve $\{x\}$ from

$$[K] \{x\} = \{F\}$$

where

$$\{F\}^T = [0, \dots, 0, 1, 0, \dots, 0]$$

Then $\{x\} = i$ th column of $[K]^{-1}$.

As an example of applying the improvement in receptance matrix, we apply the case of $r = 1$ to the case of adding spring K_a between dof i and dof j . The resulting frequency equation is

$$K_a + \sum_{l=1}^L \frac{(\phi_{il} - \phi_{jl})^2}{G_l(\omega_l^2 - \omega^2)} - \sum_{l=1}^L \frac{(\phi_{il} - \phi_{jl})^2}{G_l \omega_l^2} - (\hat{u}_i - \hat{u}_j) = 0 \quad (28)$$

where

$$\hat{u}_i \text{ \& } \hat{u}_j = \text{STATIC DEFLECTION DUE TO}$$

$$\{F\}^T = \{0 \dots 0 \ 1 \ 0 \dots 0 \ -1 \ 0 \dots 0\}$$

NUMERICAL EXAMPLES

A deployed solar array system shown in Fig. 2 is used to demonstrate the accuracy of the present method. The system is composed of a short and a long boom and two solar panels on each side of the supporting casing. The panels are modeled as beam elements using the stiffness on the back of the panels and general springs

are used to represent the hinge joints and the supporting casing. This finite element model is shown in Fig. 3.

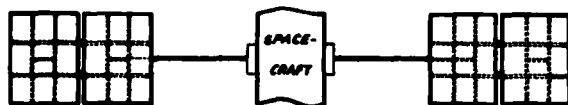


Fig. 2 A deployed solar array system



Original System $K_{\theta} = 10^5$ in-lb/rad.
Modified System $K_{\theta} = 10^4$ in-lb/rad.

Fig. 3 Finite element model of solar array system with 196 dynamic degree-of-freedom

The first case considered is the effect of rotating spring K_{θ} at the support. The original system is designed using $K_{\theta} = 10^5$ in-lb/rad. It is desired to investigate the case when this stiffness is reduced by a factor of 10. Thus, a change in spring rate 9×10^4 in-lb/rad is required to correct the model. Since the modification is localized affect only one dof, the frequency equation (18) is applied here. For this case,

$$K_a = -9 \times 10^4 \text{ in-lb/sec}$$

The modified system frequencies are solved for using Eq. (18) with the first 8 of the original system modes. The solutions are not satisfactory when compared with the exact solution of the modified system. (See Table 1) The improved receptance formula with $r = 1$ is then applied to this problem. The results are put under the title "8 modes plus static deflection" in Table 1. It can be seen that the first mode frequency is improved drastically over using 8 mode without static deflection.

As a second example, consider adding a 1.5 lb mass at node A as shown in Fig. 3. This mass could represent the additional balance weight added to the system after the structural analysis has been performed. This mass had 3 dof's. The modified system natural frequencies are computed using Eq. (19). The elements of the receptance matrix are computed by using 8 modes of the original system. The results are summarized in Table 2, along with the exact solution. It can be seen that all the 8 frequencies computed using Eq. (19) are in very good agreement with the exact solution. The computation cost ratio of the exact solution to the reanalysis

solution is 25. Thus, a considerable saving is achieved

TABLE 1 Comparison of Natural Frequencies of the Modified System

Mode No	Natural Frequencies of Modified Systems		
	Exact Solution	Local Modification Theory	
		8 Mode	8 Mode Plus Static Deflection
1	0.234Hz	0.394Hz	0.243Hz
2	0.737	0.738	0.737
3	0.890	0.890	0.890
4	1.090	1.090	1.090
5	1.735	1.735	1.735
6	2.450	2.573	2.454
7	3.162	3.472	3.162
8	3.467	3.474	3.470

TABLE 2 Comparison of Natural Frequencies of the Modified System (Mass Modification)

Mode No.	Exact Solution of Modified System	Local Modification Theory, Use 8 Modes
1	0.526 Hz	0.526 Hz
2	0.729	0.729
3	0.857	0.857
4	1.089	1.089
5	1.709	1.709
6	2.674	2.675
7	3.114	3.115
8	3.457	3.458

CONCLUSIONS

A systematic method of deriving the frequency equation of modified structures is presented in this paper. It has been shown that the frequency equation can be expressed as a determinant of the order equal to the number of degrees of freedom affected by the modification and is independent of the number of dof of the original system. Frequency equations for special cases of local modification are derived. It is clear that those equations can be used to perform parametric studies of large structures effectively. The accuracy of the method depends on the number of modes, methods of improving accuracy are indicated. The numerical example shows that even with $r = 1$, i.e., static correction, the results are improved drastically.

REFERENCES

1. B.P. Wang, A.B. Palazzolo, and W.D. Pilkey, "Reanalysis, Modal Synthesis and Dynamic Design," Chapter 8 of State of the Art Review of Finite Element Methods edited by A. Noor and W. Pilkey.
2. B.P. Wang and W.D. Pilkey, "Efficient Re-analysis of Locally Modified Structures," was presented at the First Chautauqua on Finite Element Modeling, Sept. 15-17, 1980, Cape Cod, Massachusetts.
3. I. Hirai, T. Yoshimura, and K. Takamura, "On a Direct Eigenvalue Analysis for Locally Modified Structures," Inter. Journal for Numerical Methods in Engineering, Vol. 6, p. 441-442, 1973.
4. Y.T. Leung, "Accelerated Convergence of Dynamic Flexibility in Series Form," Engineering Structures, Vol. 1, p. 203-206, 1979.

EFFECT OF STIFFENER ARRANGEMENT ON THE RANDOM
RESPONSE OF A FLAT PANEL

R.B. Bhat and T.S. Sankar
Department of Mechanical Engineering
Concordia University
Montreal, Quebec, Canada

The effect of stiffener arrangement on the random response of a flat panel is investigated. The panel is stiffened in two orthogonal directions and simply supported on all edges. A stationary random load whose power spectral density is a band limited white noise, acts at the geometric center of the panel. The mean square values of displacement, velocity and acceleration responses at the center of the panel as well as the space averaged values of these responses over the entire area of the panel are obtained. Equivalent viscous damping of the structure is included to account for the structural damping in the material of the panel. Response analysis is carried out by the normal mode approach using finite element techniques and generalized harmonic analysis with damping assumed proportional to the mass and stiffness. It is concluded that it is possible to reduce the response of a stiffened structure by a nonuniform arrangement of the stiffeners. The results are discussed for design applications.

INTRODUCTION

Stiffened structures are extensively used in aerospace applications to minimize structural weight while satisfying the required strength criteria in operation. They are also used in design situations where weight may not be the primary concern such as in ship construction, buildings etc. The current practice is to space the stiffeners uniformly on the structure and the advantages of such an arrangement are mainly the convenience in fabrication and simplicity in design analysis. The random response of panels stiffened uniformly may be obtained using any one of the following methods, namely: i) smearing the effect of stiffeners over the panel area [1] and analyzing the response of the resulting orthotropic panel using the techniques in [2], ii) the finite element methods [3,4], iii) the transfer matrix methods [5] and iv) the wave propagation approach [6].

The aim of the present investigation is to critically study the effect of nonuniform stiffener arrangement on the random response of the panel. When the stiffeners are arranged nonuniformly, only the finite element methods and transfer matrix methods are suitable for carrying out the response analysis. In this paper, the finite element technique by the normal mode approach is employed for analysis. The structure under consideration is a square

panel stiffened in two orthogonal directions and simply supported on all edges. A stationary random load whose power spectral density is a band limited white noise acts at the geometric center of the panel. Equivalent viscous damping of the structure is included to account for the hysteretic structural damping in the material of the panel. The mean square values of displacement, velocity and acceleration responses at the center of the panel as well as the space averaged values of these responses over the panel area are obtained for design recommendations.

RANDOM RESPONSE ANALYSIS

Normal mode analysis is used along with finite element techniques and a generalized harmonic analysis to obtain the random response of the stiffened panel. The equation of motion of the structure can be written as:

$$[M]\{\ddot{w}\} + [C]\{\dot{w}\} + [K]\{w\} = \{F\} \quad (1)$$

where $[M]$ is the mass matrix, $[C]$ is the damping matrix, $[K]$ is the stiffness matrix, $\{w\}$ is the displacement vector and $\{F\}$ is the vector of forces acting on the structure. The admittance matrix is then given by:

$$[H(i\omega)] = [-\omega^2[M] + i\omega[C] + [K]]^{-1} \quad (2)$$

When the forces acting on the panel are

stationary and ergodic, the relation between the response cross power spectral density (PSD) and the cross PSD of forces is given by [7]

$$[S_w(i\omega)] = [H^*(i\omega)][S_F(i\omega)][H(i\omega)]^T \quad (3)$$

The asterisk denotes the complex conjugate and $(i\omega)$ denotes the complex functional dependence on ω . The cross PSD matrices are hermitian and can be expressed as

$$[S(i\omega)] = [P(\omega)] + i[Q(\omega)] \quad (4)$$

where $[P(\omega)]$ is a real symmetric matrix (co-power spectral density) and $[Q(\omega)]$ is a real skew-symmetric matrix (quad-power spectral density). The equation of motion is solved for undamped free vibration, by discarding the damping and the forcing terms in Equation (1), which provides the natural frequencies ω_j and the normal modes ϕ_j of the structure. The damping is assumed to be proportional to mass and stiffness in the form

$$[C] = \mu[M] + \lambda[K] \quad (5)$$

where μ and λ are proportionality factors. Hence the normal modes ϕ_j can be used to diagonalize the mass, stiffness and the damping matrices. The generalized mass of the i -th mode is given by

$$M_j = \{\phi_j\}^T [M] \{\phi_j\} \quad (6)$$

and the generalized admittance of j -th mode is

$$H_j(i\omega) = \{\phi_j\}^T [H(i\omega)] \{\phi_j\} \quad (7)$$

which can be written as

$$H_j(i\omega) = 1/M_j [-\omega^2 + i\omega(\mu + \lambda\omega_j^2) + \omega_j^2] \quad (8)$$

The modal damping factor ζ_j for the j -th mode is related to the damping proportionality factors μ and λ as

$$\zeta_j = \mu/2\omega_j + \lambda\omega_j/2 \quad (9)$$

Using Equation (7) in (3) the total cross PSD of the response is obtained as the double summation of the cross PSD of the response of pairs of modes as

$$[S_w(i\omega)] = \sum_{j=1}^m \sum_{k=1}^m H_j^*(i\omega) H_k(i\omega) [S_F^{jk}(i\omega)] \quad (10)$$

where $[S_F^{jk}(i\omega)]$ is the cross PSD of generalized forces of pairs of modes and is given by

$$[S_F^{jk}(i\omega)] = \{\phi_j\} \{\phi_k\}^T [S_F(i\omega)] \{\phi_k\} \{\phi_j\}^T \quad (11)$$

When the damping in the structure is small, an approximate solution for the response is obtained by neglecting the cross product terms in Equation (10) which leads to a single summation over the modes and is given by

$$[P_w(\omega)] = \sum_{j=1}^m |H_j(i\omega)|^2 [P_F^{jj}(\omega)] \quad (12)$$

The joint deflection moment for a structure can be obtained by integrating the corresponding cross PSD terms in Equation (12) over the entire frequency range. Denoting such an operation by a matrix integration, the joint deflection moments for the pairs of structural node points are given by

$$[\langle w_q w_r \rangle] = \int_0^\infty [P_w(\omega)] d\omega \quad (13)$$

where angular brackets denote time averages and the subscripts q and r denote the q th and r th structural node pairs. The diagonal elements of $[\langle w_q w_r \rangle]$ are the mean square deflections.

In the present study, the PSD of excitation is assumed to be a band limited white noise, which covers all the major structural modes. Hence the joint deflection moments can be written after integration of Equation (13) as

$$[\langle w_q w_r \rangle] = \sum_{j=1}^m [P_F^{jj}(\omega_j)] \pi/4M_j^2 \omega_j^2 \zeta_j \quad (14)$$

Frequency response expressions for the velocity and acceleration response for the j -th mode can be written, respectively, as

$$H_j(i\omega)_{vel.} = i\omega/M_j [-\omega^2 + i\omega(\mu + \lambda\omega_j^2) + \omega_j^2] \quad (15)$$

and

$$H_j(i\omega)_{acc.} = -\omega^2/M_j [-\omega^2 + i\omega(\mu + \lambda\omega_j^2) + \omega_j^2] \quad (16)$$

Using Equation (15) in (12) and performing the necessary integrations, the joint moments of velocities are obtained as

$$[\langle \dot{w}_q \dot{w}_r \rangle] = \sum_{j=1}^m [P_F^{jj}(\omega_j)] \pi/4M_j^2 \omega_j \zeta_j \quad (17)$$

Assuming that the band limited white noise excitation covers a frequency range of 0 to ω_0 , and using Equation (16) in (12), the joint moments of accelerations are given by

$$[\langle \ddot{w}_q \ddot{w}_r \rangle] = \sum_{j=1}^m [P_F^{jj}(\omega_j)] (\omega_j/M_j^2) \left[\left(\frac{\omega_0}{\omega_j} \right) + \frac{1-4\zeta_j^2}{4\zeta_j} \tan^{-1} \frac{2\zeta_j(\omega_0/\omega_j)}{1-(\omega_0/\omega_j)^2} + \frac{(4\zeta_j^2-3)}{8(1-\zeta_j^2)^{1/2}} \right] \ln \left\{ \frac{(\omega_0/\omega_j)^2 + 2(\omega_0/\omega_j)(1-\zeta_j^2)^{1/2} + 1}{(\omega_0/\omega_j)^2 - 2(\omega_0/\omega_j)(1-\zeta_j^2)^{1/2} + 1} \right\} \quad (18)$$

STIFFENER SPACING PARAMETER

Although there are several possible ways of arranging the stiffeners with nonuniform

spacing, in this study it is accomplished in accordance with a single parameter. This parameter, m , is established such that

$$\sum_{i=1}^n s_i = l/2 \quad (19)$$

and

$$s_{i+1} = s_i + m \quad i = 1, 2, \dots, n-1 \quad (20)$$

where s_1, s_2, \dots, s_n are stiffener spacings, starting at the center and proceeding towards the boundaries as shown in Figure 1, and l is the length of the side of the square panel. In this arrangement, $m > 0$ indicates an arrangement where the stiffeners are densely packed near the panel center whereas $m < 0$ shows that stiffeners are denser near the panel edges. This particular configuration of stiffener spacing is chosen because it provides a single spacing parameter against which the responses can be plotted for comparison.

RESULTS AND DISCUSSIONS

The panel studied is shown in Figure 1 with a dimension 1.2×1.2 m and 2 mm thick. There are seven channel stiffener sections, which were 10 cm deep with 5 cm flange and 4 mm thick, placed along each of the two orthogonal directions. The damping proportionality factors μ and λ are taken as 0.1 rad/sec and 0.1×10^{-5} sec, respectively. The response analysis of the structure was carried out using SPAR structural analysis program [8].

The natural frequencies and normal modes of the stiffened panel are obtained by solving the problem of free vibration for the undamped structure. The mean square values of displacement, velocity and acceleration responses are given at all points on the panel surface using Equations (14), (17) and (18). The space averages of the mean square responses are evaluated by summing the mean square responses at all points on the panel and dividing it by the total panel area.

The variation of first eight natural frequencies with the stringer spacing parameter, m , is shown in Figure 2. The fundamental frequency decreases as m is increased but it increases for negative values of m (indicating closer spacing near the edges) until around $m = -8$, beyond which the frequency starts decreasing again. The increase in fundamental frequency when the spacing of stringers is changed from a uniform configuration, ($m = 0$) to a nonuniform configuration with $m = -8$ is approximately 21.4%. An explanation of this behavior is that a closer spacing of stringers near the panel edges reduces the inertia of the panel in the fundamental mode, and increases its stiffness resulting in a higher fundamental frequency. The natural frequencies corresponding to the higher modes increase with increasing m .

The variations of the central mean square

displacement with the spacing parameter, m , are shown in Figure 3. The response at the panel center reduces with an increase in m until m is around 8 (when the response becomes 89% of the value at $m = 0$) and then starts increasing again. However, the space averaged mean square displacement response increases monotonically with m . Since the panel is loaded at the center, the response is predominant in the fundamental panel mode, and hence the above behavior can be explained by looking at the fundamental mode shapes of the panel for different values of m , shown in Figure 4. When $m > 0$, the fundamental mode is shallower compared to that when $m = 0$ (uniform stringer spacing). Hence, when $m > 0$, the mean square displacement response at the center is less, but because the response is more evenly distributed on the panel surface compared to the case of $m = 0$, the space averaged displacement response is more than that corresponding to $m = 0$.

The mean square velocity at the panel center and the space average mean square velocities are plotted against the stringer spacing parameter, m , in Figure 5. The response at the panel center decreases monotonically with increasing m , for the range of m values studied. The space averaged mean square velocity also decreases as m is increased until m is around 6 and then starts increasing. The same trend is observed in the case of mean square acceleration responses as shown in Figure 6.

The above results indicate that by rearranging the stiffeners in a nonuniform fashion, it is possible to change the natural frequencies of the structure and to reduce the panel response. A reduction in vibration response of the structure will result in a reduction of the noise produced by the structure and hence these results have greater significance in providing optimum aerospace structural design, for reducing interior noise in aircraft fuselages etc. In the case of floor mounted machinery, the response of the floor can be reduced by the suggested rearrangement of the floor beams. For any particular application, an optimum value of m can be found from the results shown here.

CONCLUSIONS

The effect of nonuniform stiffener arrangement on the random response of a flat panel stiffened in two orthogonal directions is studied for design applications. The mean square responses of the panel, both at its center and its space averaged value, when excited by a stationary random load at the panel center, were calculated when the stiffeners were arranged uniformly and nonuniformly. The results indicated that it is possible to reduce the displacement, velocity and acceleration responses of the panel by arranging the stiffeners nonuniformly over the panel surface by a proper choice of m for a specified limiting response of the structure. These results are quite

useful in the design of aerospace structures, in the design of floor beams in buildings with machinery mounted on floors, etc. where stiffened structures are used for minimizing the response at a given location.

ACKNOWLEDGEMENTS

The investigation presented was supported by the grant A7104 from the Natural Sciences and Engineering Research Council of Canada.

REFERENCES

1. M.M. Mikulus, Jr. and J.A. McElman, "On Free Vibration of Eccentrically Stiffened Cylindrical Shells and Flat Plates", NASA-TND-3010, 1965.
2. A.C. Eringen, "Response of Beams and Plates to Random Loads", Journal of Applied Mechanics, Vol. 24, p. 46, 1957.
3. C.D. Newsom, J.R. Fuller and R.E. Sherrer, "A Finite Element Approach for the Analysis of Randomly Excited Complex Elastic Structures", presented at the AIAA/ASME 8th Structures, Structural Dynamics and Materials Conference, Palm Springs, Calif., March 29, 1967.

4. L.D. Jacobs, D.R. Lagerquist and F.L. Gloyna, "Response of Complex Structures to Turbulent Boundary Layers", Journal of Aircraft, Vol. 7, p. 210, 1970.
5. Y.K. Lin and B.K. Donaldson, "A Brief Survey of Transfer Matrix Techniques with Special Reference to the Analysis of Aircraft Panels", Journal of Sound and Vibration, Vol. 10, p. 103, 1969.
6. D.J. Mead, "Vibration Response and Wave Propagation in Periodic Structures", ASME Paper 70-WA/DE-3, January 1971.
7. Y.K. Lin, Probabilistic Theory of Structural Dynamics, McGraw-Hill Book Company, New York, 1967.
8. W.D. Whetstone, "SPAR Structural Analysis Reference Manual System Level II, Volume I", NASA CR-145098-1, February 1977.

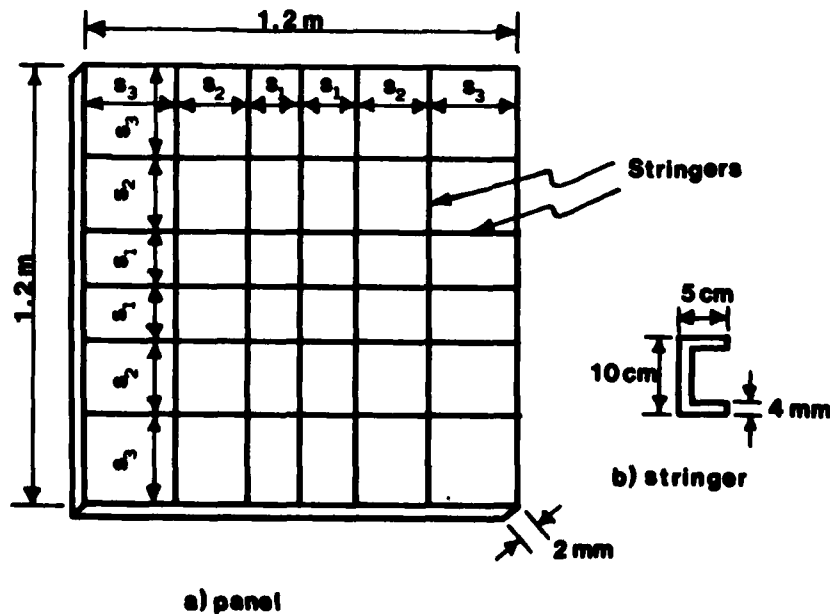


Fig. 1 - Schematic sketch of the stringered plate

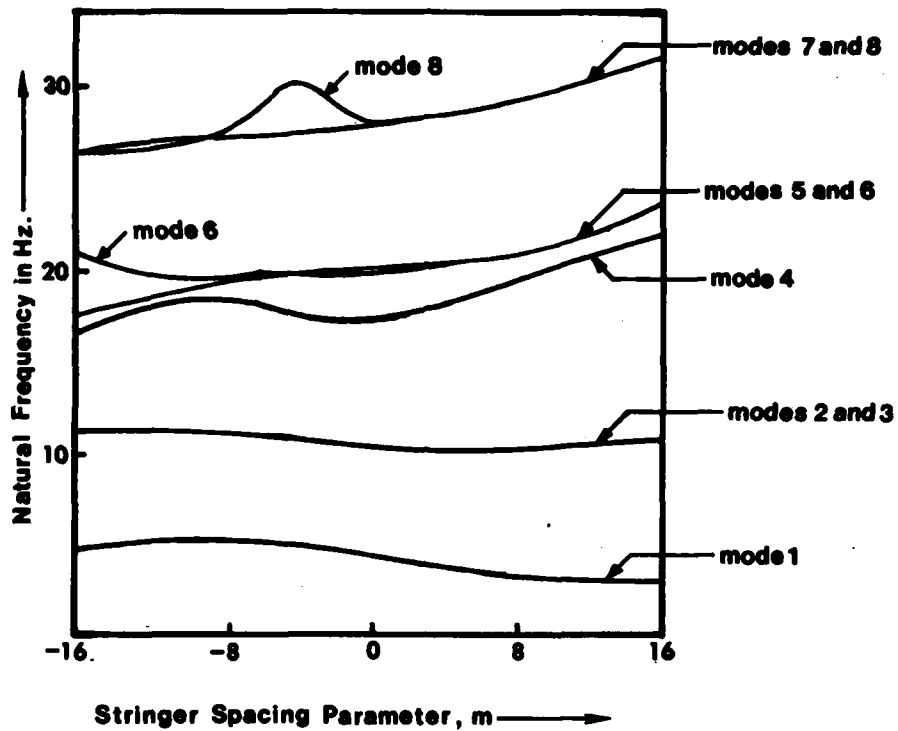


Fig. 2 - Variation of natural frequencies with stringer spacing

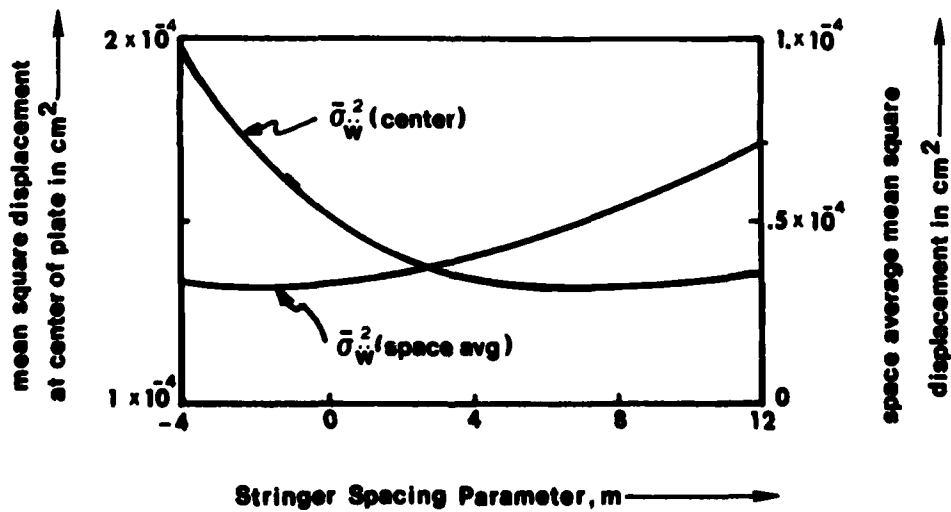


Fig. 3 - Variation of mean square displacement with stringer spacing

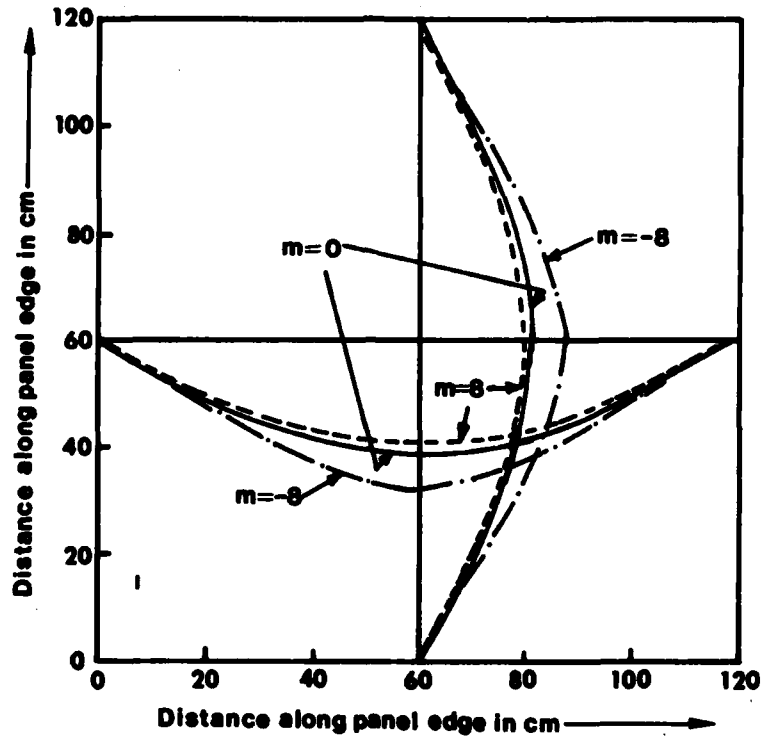


Fig. 4 - Variation of fundamental mode shape of panel with stringer spacing

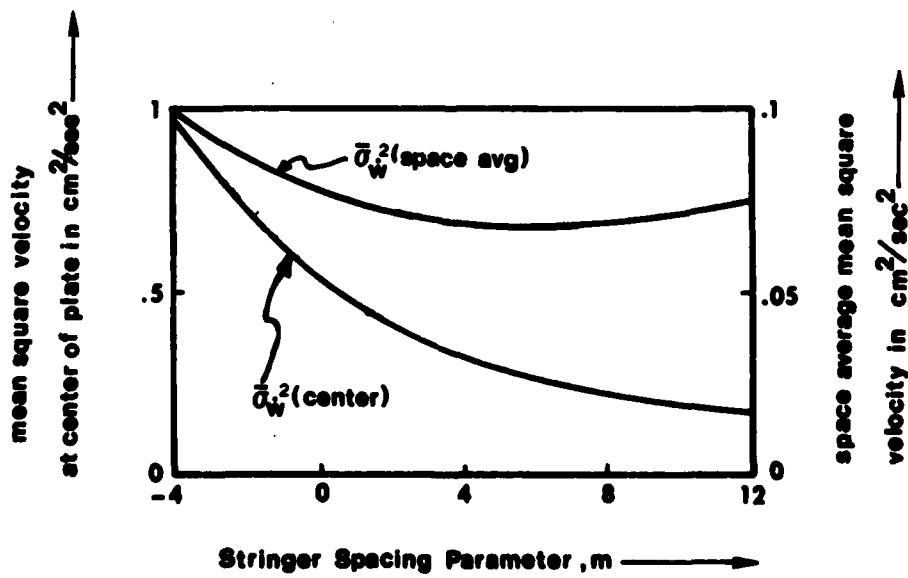


Fig. 5 - Variation of mean square velocity with stringer spacing

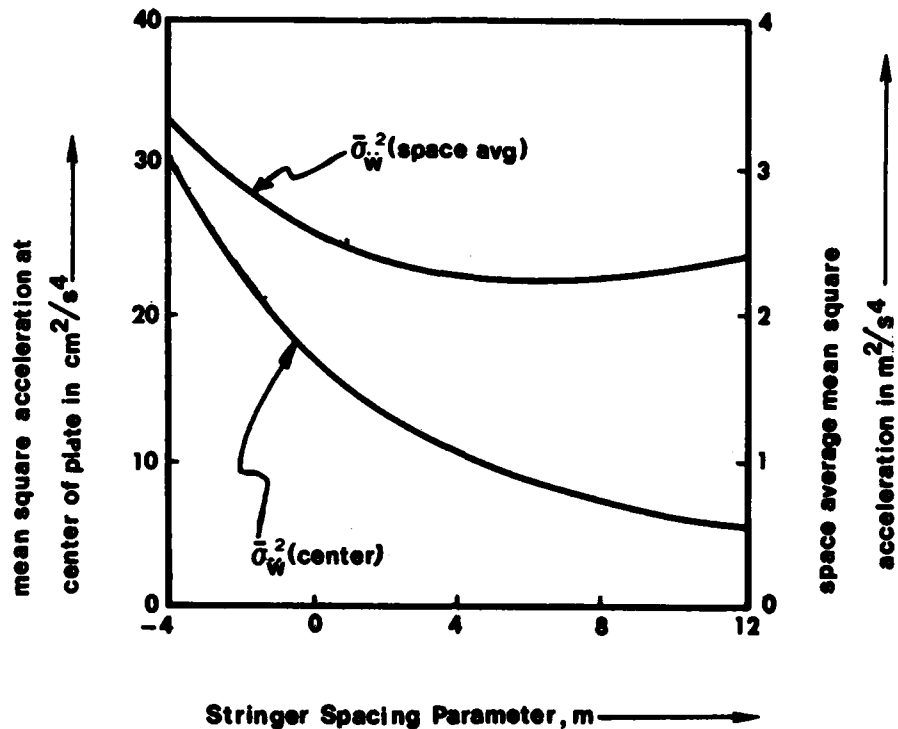


Fig. 6 - Variation of mean square acceleration with stringer spacing

DISCUSSION

Mr. Yang (University of Maryland): In your study you varied the spacing of stiffeners when you used the finite element technique. Did you actually do any optimization studies or did you just plug in different values and vary the parameters during each run?

Mr. Bhat: We haven't done any optimization study to date. It is possible we may do some in the future. Right now we are seeing how the parameter M varies. Parameter M affects the vibration response and that is what we are studying. However, it is possible to use an optimization technique to find out the optimum value of M.

Mr. Yang: But with an optimization technique you need mathematical equations. You really cannot operate on the finite element. What I just wanted to mention is that there has been a lot of work in this area starting off with Dr. Klosterman of University of Cincinnati back 5 to 6 years ago with his PhD thesis. With that technique you use the

measured data to get the modal parameters then you do a parametric study to get a mathematical model. Two years ago a student of mine, Dr. Rhee, did work in this area. He actually obtained a mathematical model from measured modal parameters. The advantage of this is that once you have the mathematical equations then you do the optimization study without changing all the parameters and plugging into the finite element technique. I think now they are also coming out with hardware with which one can do this type of study.

ON NONLINEAR RESPONSE OF MULTIPLE BLADE SYSTEMS

A. Muszyńska
University of Dayton Research Institute
Dayton, Ohio

D. I. G. Jones and T. Lagnese
Air Force Wright Aeronautical Laboratories
Wright-Patterson Air Force Base, Ohio

and

L. Whitford
Aeronautical Systems Division Computer Center
Wright-Patterson Air Force Base, Ohio

In the first part of this paper, modal and discrete models are examined from the point of view of predicting the dynamic response of a single jet engine turbine or compressor blade to harmonic excitation by an external force and with restraint provided by a dry friction link to ground. Experimental identification of parameters in the modal and discrete models is discussed. The discrete model is then used as a basis to characterize the nonlinear response of a set of several blades connected at their roots to a rigid disk, and having dry friction coupling from blade-to-blade and from blade-to-ground. The nonlinear differential equations of motion of the system are transformed into a set of nonlinear algebraic equations, which are solved numerically using an iterative method. The results, which are given in terms of amplitudes and phase angles of the response, illustrate several effects including blade mistuning, magnitude and distribution of excitation forces, and phase differences between exciting forces on adjacent blades. Two general types of conclusions may be drawn so far, concerning the influence of dry friction between blades. One concerns the effect of dry friction in reducing response amplitudes (damping effect) and the other concerns effects of blade mistuning (effects of blade-to-blade coupling). These conclusions will be discussed in the paper.

1. INTRODUCTION

Vibration induced fatigue failures in turbomachinery blading occur very often in modern systems, partly because ever-increasing performance requirements inhibit traditional modifications such as changes in blade geometry, which have often been found effective in the past, usually on an empirical basis. The high stresses which lead to such failures are due to flutter and/or aerodynamic or mechanical excitation of blades at frequencies equal to some multiple of the rotation speed, coupled with coincidence of mechanical resonances of the bladed disk system, under conditions where aerodynamic sources of damping are ineffective. For this reason, other sources of damping, such as material or structural have been of considerable interest for the past several years. However, the very nonlinear nature of the phenomena involved has made rational analysis difficult, so that much of the industrial

application work has usually been done on an empirical basis.

The problem of predicting the response of a bladed disk system with allowance for interblade coupling, mistuning, and frictional forces is very difficult to solve exactly. Several approaches to the problem are possible, including finite element modeling, syntheses of harmonic receptances and discrete element modeling. Finite element techniques are becoming ever more widely applied, and have been applied to some extent to this problem [1-3]. However, these will not be discussed further in this paper, except to note that running times can be quite high, making it expensive to study the effect of all possible relevant parameters. Receptance methods are potentially applicable, and have been used to solve many different linear

problems [4]. For systems having nonlinear elements and for very complex structures, it is more difficult to apply and iterative solutions will probably have to be sought for multiple blade systems. Up to the present, however, only a single-blade analysis has been completed for the nonlinear damping from dry friction forces, and this will be discussed and the results compared with the discrete analysis, which is the main subject of the paper.

Two main problems will be addressed, namely single blade response and multiple blade response, in each case with allowance for frictional damping. The single blade analysis is of interest in its own right, and to establish the limits of the discrete model in comparison with receptance methods, including identifying single blade parameters in a discrete model, which in turn forms the basis for a discrete analysis of a multiple blade system. The results of the multiple blade analysis are of considerable interest and throw light on several effects, including (a) mistuning of blades, (b) amplitude and phase relationships between excitation forces on each blade, and (c) influence of blade-to-blade friction forces.

2. IDENTIFICATION OF SINGLE BLADE PARAMETERS

2.1 Modal Analysis

In order to provide a basis for the analytical modeling of a single blade clamped at the root, one may resort to finite element analysis [1-7], other analytical methods [8-9], or experimentally measured receptances at two or more points, along with measured mode shapes for the important modes of vibration [10-19]. In this paper, the latter approach will be adopted and applied to a typical jet engine compressor blade, as described in more detail in Appendix 1.

The first set of test results were obtained for the test blade clamped in a rigid fixture, which was set in turn on rubber isolator pads, with excitation and response pickup at the tip leading edge, as illustrated in Figure 1. Several measurements were made of the driving point receptance $\alpha_{11}(\omega)$, being a function of the frequency ω , for various driving force levels in the linear, low amplitude range, and the results are shown in Figure 2 [20]. Following Ewins and others [18,19,21,22], the receptances $\alpha_{ij}(\omega)$ were represented by the form:

$$\alpha_{ij} = \sum_{n=1}^N \frac{\phi_n(x_i, y_i) \phi_n(x_j, y_j)}{M_n [\omega_n^2 (1 + i\eta_n) - \omega^2]} \quad (1)$$

where M_n is the n -th modal mass, $\phi_n(x, y)$ is the n -th modal function, normalized here at the tip leading edge, η_n is the modal loss factor in the n -th mode, $\omega_n = 2\pi f_n$ is the n -th natural frequency, and i and j are the two points where the receptance was measured.

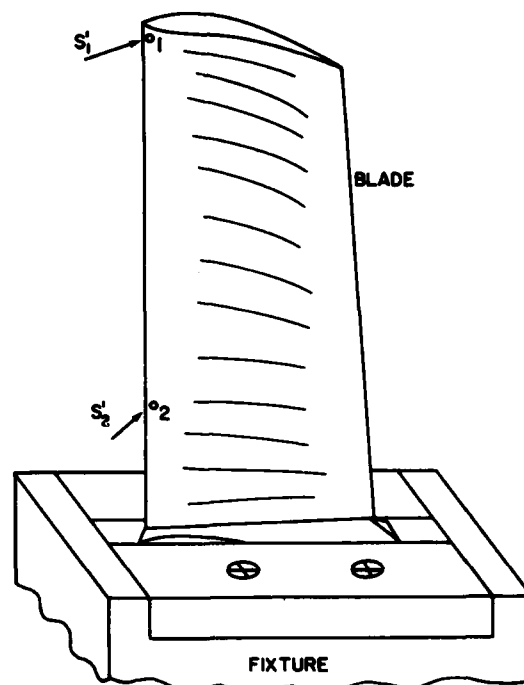


Fig. 1. Compressor blade with excitation and pickup points.

$\alpha_{11}(\omega)$ is the driving point receptance at point 1, the tip leading edge, $\alpha_{22}(\omega)$ that at another point 2, and $\alpha_{12} = \alpha_{21}$ are the cross receptances.

The modal functions ϕ_n were measured from receptance tests and from laser holographic interferometry [20,23], and are illustrated for the first three modes in Figure 3. The η_n 's and f_n 's were determined for each mode from the receptance plots, and M_n were estimated from the peak value of α_{11} at point 1. If the modes are well spaced:

$$\begin{aligned} |\alpha_{11}|_{\max} &= 1/M_n \eta_n \omega_n^2 \\ M_n &= 1/\eta_n \omega_n^2 |\alpha_{11}|_{\max} \end{aligned} \quad (2)$$

for each mode n . This procedure is most effective, of course, for widely separated natural frequencies and would have to be modified if they were close. Figure 2 shows the fit between such a series representation and the experimental data, for specific values of ω_p (or $2\pi f_n$) and M_n , the series being terminated at the third mode. The agreement is quite good, and it does not seem that in this case neglect of higher order modes leads to any significant high frequency residuals in the estimation of α_{11} [19].

The data in Figure 2 was fitted using the following parameter values;

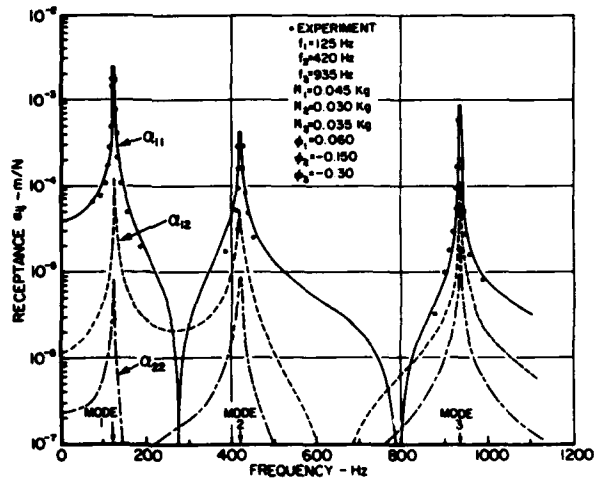


Fig. 2. Measured receptances and modal representation.

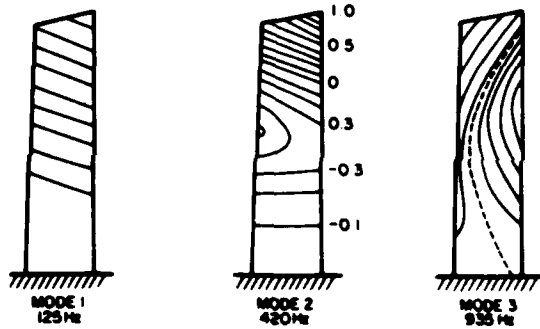


Fig. 3. Modal functions for compressor blade.

$$\begin{aligned}
 M_1 &= 0.045 \text{ kg} \\
 M_2 &= 0.030 \text{ kg} \\
 M_3 &= 0.035 \text{ kg} \\
 f_1 = \omega_1/2\pi &= 125 \text{ Hz} \\
 f_2 = \omega_2/2\pi &= 420 \text{ Hz} \\
 f_3 = \omega_3/2\pi &= 935 \text{ Hz} \\
 \phi_1(x_2, y_2) &= 0.06 \\
 \phi_2(x_2, y_2) &= -0.15 \\
 \phi_3(x_2, y_2) &= -0.30 \\
 \phi_1(x_1, y_1) &= 1.00 \quad (1 = 1, 2, 3)
 \end{aligned}$$

This identification of receptances for the blade serves three purposes. First, to obtain analytical expressions for α_{ij} to be used in further analysis of nonlinear problems, such as that of a blade with dry friction damping at point 2; secondly, to model several blades in a rigid disk through vector addition of receptances (not done in this paper) and, thirdly, to fill gaps in the sparse measured

data set for use in establishing the best discrete model of the blade, as will be discussed in section 2.2.

2.2 Discrete Model

The advantage of a discrete model is that the differential equations of motion of a system encompassing several structural elements may be described quite simply in terms of ordinary second order differential equations, and therefore reasonably accurate solutions may be obtained at low cost. Customarily, one identifies the parameters in a discrete model in such a way that the lowest order natural frequencies of the more complex system are properly replicated, but for analyses involving nonlinear forces, such as friction damping, one needs a model in which the receptances α_{ij} are accurately reproduced also, and this is much more difficult to do.

Consider, for example, the two degree of freedom system shown in Figure 4. The two masses m_1 and m_2 , and the springs K_1 and K_2 , allow one to replicate the first two natural frequencies of the blade, both of which represent bending type modes in this case, as well as α_{11} in the vicinity of the fundamental resonant frequency. The modeling of α_{12} and α_{22} is much poorer, but the parameter R_2 which controls the apparent amplitude of the force S_2 does allow one some scope for improvement of the model. Hence R_2 represents a correction coefficient for the continuous nature of the real blade. Consider the equations of motion of the system in Figure 4:

$$m_1 \ddot{x}_1 + K_1(x_1 - x_2) = S_1 e^{i\omega t} \quad (4)$$

$$m_2 \ddot{x}_2 + K_1(x_2 - x_1) + K_2 x_2 = S_2 R_2 e^{i\omega t} \quad (5)$$

These equations are solved, with S_1 and S_2 having harmonic time dependence (steady-state solution), and the corresponding receptances obtained in the form:

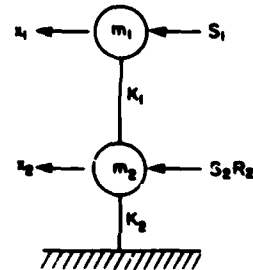


Fig. 4. Discrete model of compressor blade.

$$\alpha_{11} = \frac{\partial x_1}{\partial S_1} = \frac{K_1 + K_2 - m_2 \omega^2}{\Delta} \quad (6)$$

$$\alpha_{12} = \frac{\partial X_1}{\partial S_2} = \alpha_{21} = \frac{\partial X_2}{\partial S_1} = \frac{K_1 R_2}{\Delta} \quad (7)$$

$$\alpha_{22} = \frac{\partial X_2}{\partial S_2} = \frac{(K_1 - m_1 \omega^2) R_2}{\Delta} \quad (8)$$

$$\Delta = (K_1 - m_1 \omega^2)(K_1 + K_2 - m_2 \omega^2) - K_1^2 \quad (9)$$

Figure 5 shows the variation of the receptances $\alpha_{ij}(i,j=1,2)$ with frequency for the set of parameters:

m_1	=	0.040 kg
m_2	=	0.022 kg
K_1	=	35,530 N/m
K_2	=	111,034 N/m
R_2	=	0.1

It is seen that α_{11} and α_{12} are reproduced quite well in the vicinity of the fundamental mode, but α_{22} not quite so well, although α_{22} does approach zero as the frequency approaches about 150 Hz, as it should. This is evident from Equation (8). For the fundamental mode, therefore, the discrete model is reasonably accurate, although by no means perfect, and will form the basis for investigations of multiple blade systems. The second mode is not well modeled, except that the resonant frequency is properly reproduced. Clearly, much improvement is needed, and is possible if one looks at models having more than two degrees of freedom, but this does defeat the purpose of a simple model. The problem of identifying continuous systems in terms of discrete models has attracted much attention [11-17], but it seems clear that more attention must yet be paid to perfecting such models to properly duplicate the receptances of the continuous systems in the lower order modes, in addition to matching the resonant frequencies.

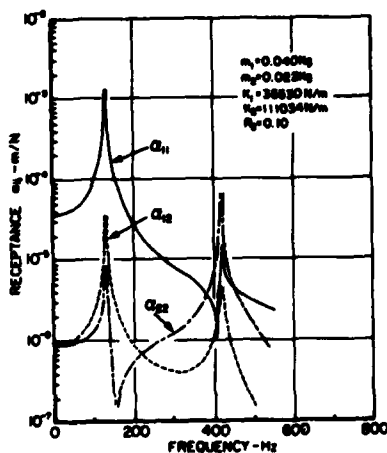


Fig. 5. Receptance of discrete model.

2.3 Receptance Analysis of Single Blade with Slip at Point 2

If now the blade is excited by a force $S_1(t) = S_1 \cos(\omega t)$ at point 1, and is linked to ground at point 2 through a dry friction joint, as illustrated in Figure 6, then the equations of motion can be written in terms of a summation of receptances as follows:

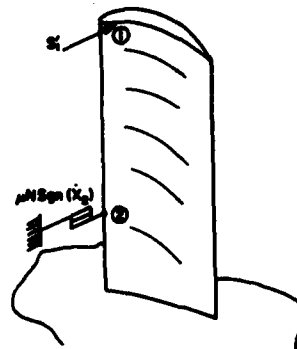


Fig. 6. Blade with friction damper at point 2.

$$X_1 = S_1 \alpha_{11} + \mu N \operatorname{sgn}(\dot{X}_2) \alpha_{12} \quad (10)$$

$$X_2 = S_1 \alpha_{21} + \mu N \operatorname{sgn}(\dot{X}_2) \alpha_{22} \quad (11)$$

where $\mu N \operatorname{sgn}(\dot{X}_2)$ represents the Coulomb model of the friction forces, μ is the coefficient of friction (dynamic) and N is the normal force. Even though the term $\mu N \operatorname{sgn}(\dot{X}_2)$ is nonlinear, the linear summing of receptances is permitted because the nonlinearity is external to the blade itself. The Equations (10) and (11) are, of course, nonlinear. They can be solved for steady-state vibrations by the method of Harmonic Balance, as shown in Appendix 2, to give the magnitudes of the responses D and A of the points 1 and 2 respectively:

$$D = \sqrt{\alpha_{11}^2 S_1^2 - (4\mu N/\pi)^2 (2\alpha_{11}\alpha_{22} - \alpha_{12}^2)} \quad (12)$$

$$A = \alpha_{21} \sqrt{S_1^2 - (4\mu N/\pi)^2 (\alpha_{22}/\alpha_{21})^2} \quad (13)$$

where $X_1 = D \cos(\omega t + \gamma)$ and $X_2 = A \cos(\omega t + \alpha)$. It is evident from Equation (13) that A can exist only when:

$$|S_1| > (4\mu N/\pi) |\alpha_{22}/\alpha_{21}| \quad (14)$$

and if this condition is not satisfied, A must be assumed to be zero, and the solution for which $X_2 = 0$ must be sought. This can be found by introducing any constant amplitude force F in place of $\mu N \operatorname{sgn}(\dot{X}_2)$ in Equations (10) and (11), letting $X_2 \rightarrow 0$ and eliminating F between the equations, so that:

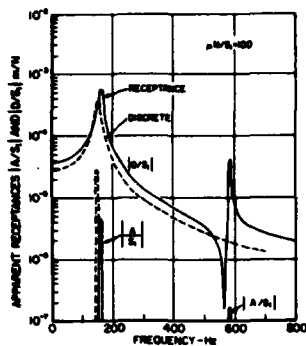


Fig. 7. Apparent receptance of continuum and discrete models with friction.

$$\alpha_{11} = \begin{bmatrix} X_1 \\ S_1 \end{bmatrix}_{X_2=0} = \frac{\alpha_{11} \alpha_{22} - \alpha_{21} \alpha_{12}}{\alpha_{22}} \quad (15)$$

Using the expressions for the receptances α_{ij} from earlier, and/or the experimental results directly, one can therefore predict the nonlinear response of the single blade. Figure 7 illustrates the predicted variation of $|D/S_1|$ and $|A/S_1|$ with frequency for the compressor blade, using the same values of $M_1, M_2, M_3, f_1, f_2, f_3, \phi_1, \phi_2,$ and ϕ_3 as were tabulated earlier, and for the case $\mu N/S_1 = 100$. It is seen that, for this particular case, $|A/S_1|$ exists over only a very narrow frequency range, defined by inequality (14), for modes 1 and 2. The three mode expansion does not allow one to predict more modes, because the combination of $\alpha_{11}, \alpha_{12},$ and α_{22} always leads to the loss of one mode when α_{11} is determined; hence more terms in the expansion would be needed to model more modes.

2.4 Discrete Analysis of Single Blade with Slip at Point 2

If the blade is represented by a two degree of freedom model, as in Figure 8, the equations of motion can be written in the form:

$$m_1 \ddot{X}_1 + K_1(X_1 - X_2) = S_1(t) \quad (16)$$

$$m_2 \ddot{X}_2 + K_1(X_2 - X_1) + K_2 X_2 + \mu R_2 N \operatorname{sgn}(\dot{X}_2) = 0 \quad (17)$$

where μ is the dry friction coefficient, N is the normal load, and R_2 is a correction coefficient. Again, using the method of Harmonic Balance, we get the solution:

$$\left| \frac{A}{S_1} \right| = \frac{1}{K_1} \sqrt{\frac{\left[1 - \frac{K_2}{K_1} - \frac{m_2}{m_1} \frac{m_1 \omega^2}{K_1} \right]^2 \left[1 - \left(\frac{4\mu NR_2}{\pi S_1} \right)^2 \left(1 - \frac{m_1 \omega^2}{K_1} \right)^2 \right]}{\left[\left(1 - \frac{m_1 \omega^2}{K_1} \right) \left(1 + \frac{K_2}{K_1} - \frac{m_2}{m_1} \frac{m_1 \omega^2}{K_1} \right) - 1 \right]^2}} \quad (18)$$

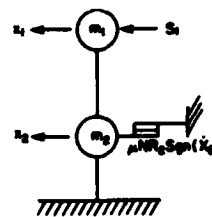


Fig. 8. Discrete model of blade with friction damper.

$$\left| \frac{A}{S_1} \right| = \frac{1}{K_1} \sqrt{\frac{\left[1 - \left(\frac{4\mu NR_2}{\pi S_1} \right)^2 \left(1 - \frac{m_1 \omega^2}{K_1} \right)^2 \right]}{\left[\left(1 - \frac{m_1 \omega^2}{K_1} \right) \left(1 + \frac{K_2}{K_1} - \frac{m_2}{m_1} \frac{m_1 \omega^2}{K_1} \right) - 1 \right]^2}} \quad (19)$$

Note that A does not exist unless:

$$|S_1| > (4\mu NR_2/\pi) \left| 1 - m_1 \omega^2 / K_1 \right| \quad (20)$$

so that only one mode can be modeled for this case. Discrete models with more than two inertial elements would be needed to account for slip in more than one mode. Using the values of the parameters $m_1, m_2, K_1,$ and K_2 determined earlier, the response of the damped blade is plotted in Figure 7 for $\mu N/S_1 = 100$. The specific values of the parameters used are:

m_1	=	0.040 kg
m_2	=	0.049 kg
K_1	=	35,530 N/m
K_2	=	111,034 N/m
R_2	=	0.1
$\mu N/S_1$	=	100

The value of m_2 is found to be not very critical, and this value was used instead of 0.022 kg because it reduces the second resonant frequency, to correspond to some degree with the mass loading effect of a platform of a real blade. It is seen that the discrete and receptance model agree quite well in the vicinity of the fundamental mode. This section completes and extends some of the previous work in the area of single-blade response [20, 25-29].

3. ANALYSIS OF RESPONSE OF MULTIPLE BLADE SYSTEM

3.1 Equations of Motion

It is for systems involving many blade elements, in a disk, that the discrete model of the blade becomes most useful, since it allows one to reduce the analytical problems to manageable proportions while retaining some measure of the real behavior of the original

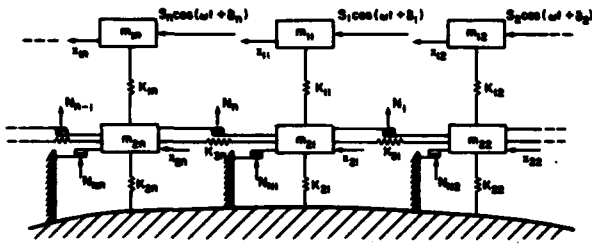


Fig. 9. Discrete model of Multiple Blade System.

system. For example, for a rigid disk having n blades, one might create a discrete model as illustrated in Figure 9. In this figure, the masses m_v represent the platform (or perhaps a shroud) on the v th blade, so one can allow for frictional coupling between blades and between blade and disk. Since m_v and K_{1v} can be varied, one can allow for mistuning of the blades. The interblade stiffness elements K_{3v} allow one to model interblade coupling. They can represent the disk flexibility to some limited extent. The equations of motion of the system, and the method of solution, are described in Appendix 4. At this point it is sufficient to say that the method of Harmonic Balance is used to obtain the steady-state harmonic solution, but an iterative procedure is now necessary, in contrast to the closed form solutions obtained for a single-blade. The numerical solution obtained from the computer program consists of printed values of amplitudes D_v and A_v , and phases γ_v and α_v of the response of each blade (see Appendix 4), as a function of the system parameters m_{1v} , m_{2v} , K_{1v} , K_{2v} , K_{3v} , μ , N_v , N_{Hv} , S_v , δ_v , etc.

3.2 Solutions for Zero Friction (Linear Cases)

Since many prior analyses [7, 21, 22, 31] have addressed the problem of predicting the damped response of a bladed disk, or multiple blade, system to various types of excitation, the first task to be addressed before proceeding to a study of the effects of friction was to establish that the present approach and the related computer program predicted the same behavior.

The first case considered was that of 12 blades, both tuned and mistuned. The basic blades were modeled by the discrete parameters listed in Table 1, representing the compressor blade discussed earlier. Figures 10 and 11 show the predicted response of the tuned and mistuned systems as a function of frequency. Figure 10 shows the effect of a stationary "Cosine excitation" on the response of a typical blade (blade 1). This type of excitation is described analytically by the expres-

$$S'_v = S_v \cos(\omega t) = S \cos[2j\pi(v-1)/n]_{j=1} \cos(\omega t) \quad (21)$$

where n is the number of blades (12) and S is the maximum driving force (0.1 N), and j is an integer. If $j = 0$, S_v is constant for all blades; if $j = 1$, then $S_v = 0$ for blade number $v = 3$ and $v = 9$, and so on. Figure 11 shows the effect of a stationary "Sine excitation," described by:

$$S'_v = S_v \cos(\omega t) = S \sin[2j\pi(v-1)/n]_{j=1} \cos(\omega t) \quad (22)$$

TABLE 1
PARAMETERS FOR BLADES (ZERO FRICTION)

Parameters	COMPRESSOR BLADE		SHORT BLADE [31]	
	Tuned (30)	Mistuned (31.02/31.03)	Tuned (50)	Mistuned (51)
n	12	12	12	12
m_{2v}	0.049	0.049	0.0064	0.0064
m_{1v}	0.040	$0.0364f_1(v)$	0.0052	$0.0043f_1(v)$
K_{1v}	35,530	35,530	40,530	40,530
K_{2v}	111,034	111,034	126,850	126,850
K_{3v}	20,000	20,000	40,000	40,000
n, n_1	$0.001+0.01$	$0.001+0.01$	$0.001+0.01$	$0.001+0.01$
K_v, N_{Hv}	0	0	0	0
μ	0.15	0.15	0.15	0.15
S_v	$0.1 f_2(v)$	$0.1 f_2(v)$	$0.1 f_2(v)$	$0.1 f_2(v)$
δ_v	0	0	0	0

$$f_1 = 1 + 0.1 \sin[\pi(v-1)/n]$$

$$f_2 = \frac{\cos}{\sin}[2\pi j(v-1)/n]$$

For the tuned case, no difference is seen, of course, but for the mistuned case, some clear differences in response are seen, including different frequencies of maximum amplitude. It is also seen that mistuning allows several response peaks to appear, in contrast to the tuned case [31]. The second case considered was to predict the effects of mistuning on the response of a simplified blade comprising a beam about 80 mm long (as compared with 203 mm for the compressor blade), and discussed by Ewins [31]. The estimated discrete parameters corresponding to Ewins' geometry are also listed in Table 1. Figure 12 shows the

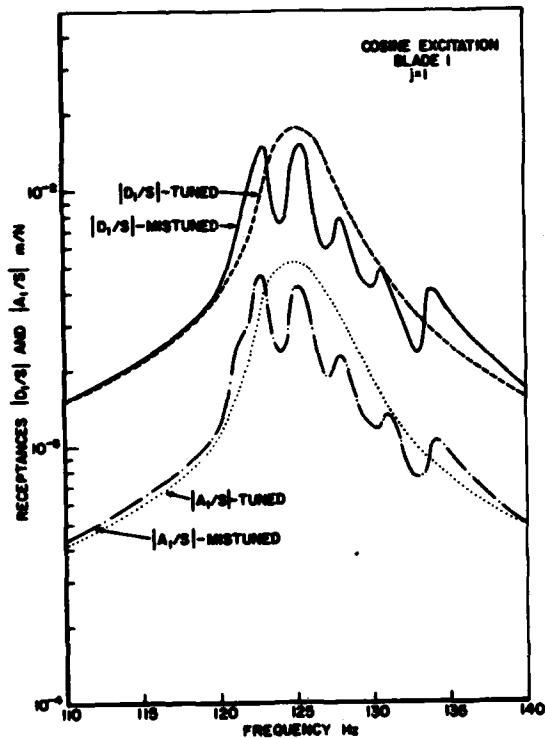


Fig. 10. Response of Tuned and Mistuned Systems to Stationary "Cosine Excitation" (Blade 1; Cases 30,31, author's not.).

predicted response to a stationary "Cosine excitation" ($j = 6$), for the tuned and mistuned cases, as was considered by Ewins. In this case, the "cosine excitation" corresponds to a 180° phase shift in excitation on adjacent blades, and S_v is of constant amplitude for each blade. Figure 12 also shows a histogram of the relative amplitudes, D_v/D_{vmax} , and phases γ_v of each blade, at frequencies corresponding to each resonant peak in the tuned and mistuned cases.

3.3 Frictionally Damped Systems

Having established that the dynamic response behavior without friction is in keeping with previous work, one is now faced with the task of varying a large number of parameters in order to gain insight into the non-linear effects, since each parameter configuration is now unique, and generalizations cannot be made as readily as in the linear case.

For the present, we have confined attention to a limited number of cases, including: (a) a tuned system, (b) a mistuned system with smooth variation of masses m_{jv} , and (c) a mistuned system with random variation of m_{jv} . Parameters varied for each case include (i) the excitation force amplitude S_v on each blade, (ii) phase angle δ_v of excitation force on each blade, for traveling wave excitation of the form:

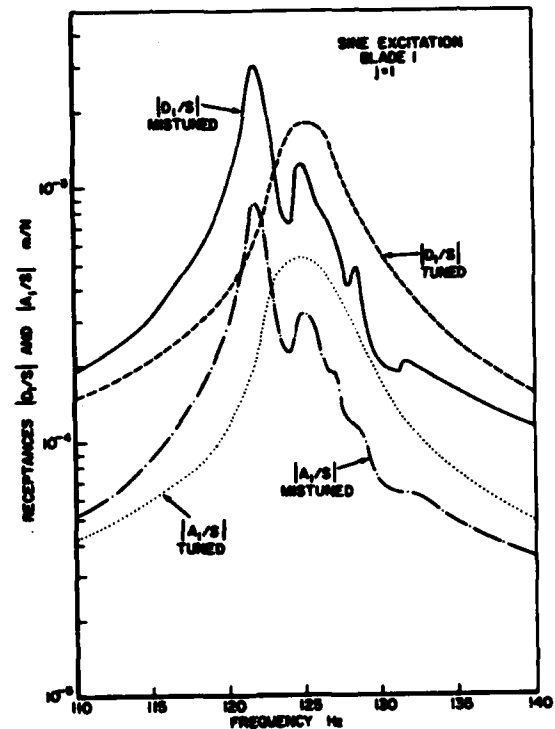


Fig. 11. Response of Tuned and Mistuned Systems to Stationary "Sine Excitation" (Blade 1; Cases 30,31, author's not.).

$$S'_v = S_v \cos(\omega t - \delta_v) \quad (23)$$

where $\delta_v = 2\pi j(\nu-1)/n$; $j = 0, 1, 2, \dots$; (iii) stationary excitation of the form:

$$S'_v = S_v \cos(\omega t) = S \cos \left\{ \left[\frac{2\pi j(\nu-1)}{n} \right] \cos(\omega t) \right\} \quad (24)$$

(iv) effects of irregularities in the phase of exciting forces, such as:

$$\delta_v = \frac{2\pi j(\nu-1)}{n + \Delta n} \quad (25)$$

where $\Delta n \neq 0$, and an irregularity in phase occurs between blade n and blade 1; and, finally; (v) the effect of the number of blades.

The first case considered in this section was a tuned system (author's working notation, Case 16) of n blades, each having identical mass and stiffness characteristics, as given in Table 2. Each blade ν was excited by a force S_v of constant amplitude, with constant increment of phase angle between blade ν and blade $\nu + 1$, again as given in Table 2, such that the phase angle δ_v is equal to $2\pi(\nu-1)/n$. Figure 13 shows the predicted values of D_v/S , for all blades and for one value of $\mu N/S$, and for several values of n . It is seen that this

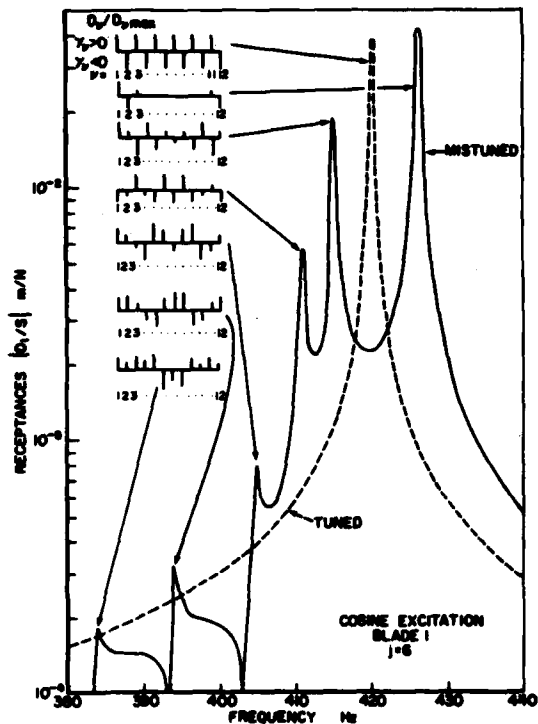


Fig. 12. Response of tuned and mistuned multiple blade systems to "Cosine excitation" (Blade 1; Cases 50, 51). Histograms of relative amplitude $D_v/D_{v,max}$ and phases γ_v of each blade at frequencies corresponding to resonant peaks.

behavior is qualitatively similar to that for a single blade. The peak amplitude steadily varies from a large peak near 125 Hz at $\delta_v = 0$ ($n \rightarrow \infty$), to a large peak near 150 Hz for δ_v growing, with lowest amplitudes occurring for certain values of n . Figure 14 shows the effect of varying N/S ratio between normal force and amplitude of driving force for $n = 11$, $\mu = 0.15$, on the values of response amplitudes $|A_v/S|$ and $|D_v/S|$. It is seen that the effect of varying n is similar to that of varying $\mu N/S$. A later case will examine the same behavior for a mistuned system.

When the blades are mistuned in a regular manner (author's Case 20, Table 2), the mass m_{1v} vary smoothly from 0.04 kg to 0.044 kg, as illustrated in Figure 15. This figure also shows the random distribution to be discussed presently. Figures 16 and 17 show typical graphs of amplitudes of response, $|D_v/S|$ and $|A_v/S|$, for several values of N/S . Figures 18 to 20 show three-dimensional, computer generated plots of $|D_v/S|$ and $|A_v/S|$ versus frequency and blade number for particular values of $\mu N/S$ ($\mu = 0.15$, $N = 10$, S variable, see Table 3). Note the systematic variation of the peak

TABLE 2
PARAMETERS FOR BLADE (FINITE FRICTION)

Parameter	Tuned System		Mistuned System		Random Mistuned System
	Traveling Wave (16)	Stationary (30)	Traveling Wave (21)	Stationary (31)	
n	11	12	11	12	11
m_{1v}	0.040	0.040	$0.040f_1(v)$	$0.040f_2(v)$	Random
m_{2v}	0.049	0.049	0.049	0.049	0.049
K_{1v}	35,530	35,530	35,530	35,530	35,530
K_{2v}	111,034	111,034	111,034	111,034	111,034
K_{3v}	0	0 to 120,000	0	0 to 120,000	0
n, η_1	0.01	0.01	0.01	0.01	0.01
m_{3v}	0	0	0	0	0
N/S	10	10	10	10	10
μ	0.15	0.15	0.15	0.15	0.15
S_v	0.1	0.1	0.001 to 10	$0.1f_2(v)$	0.001 to 10
δ_v	$2\pi(v-1)/n$	0	$2\pi(v-1)/n$	0	$2\pi(v-1)/n$

$$f_1 = 1 + 0.1 \sin [2\pi(v-1)/n]$$

$$f_2 = \cos [2\pi j(v-1)/n]$$

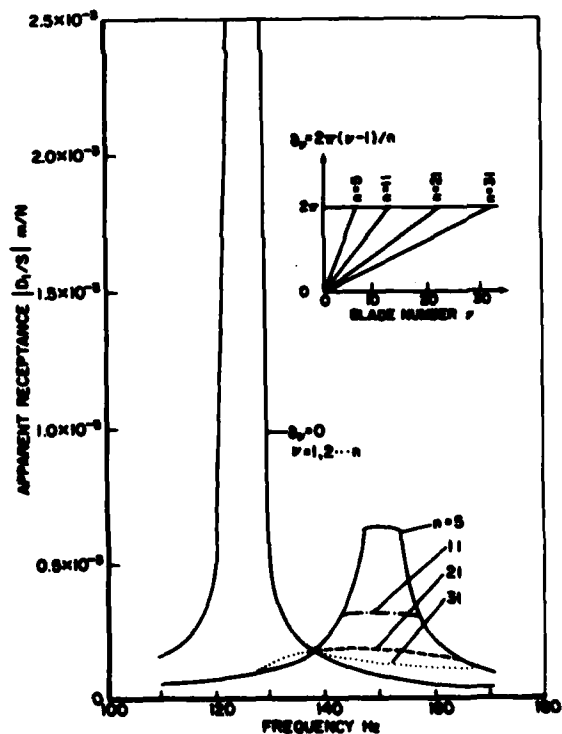


Fig. 13. Response of n -blade systems to traveling wave excitation (Case 16, effect of number of blades n and phase angle of excitation δ_v , $\mu N/S = 15$).

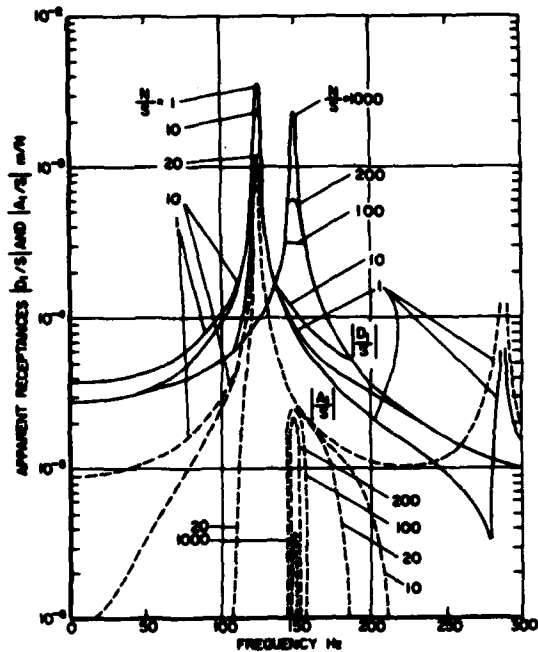


Fig. 14. Response of tuned 11-blade system to traveling wave excitation (effects of N/S, Case 16, symmetric case, all blades behave identically).

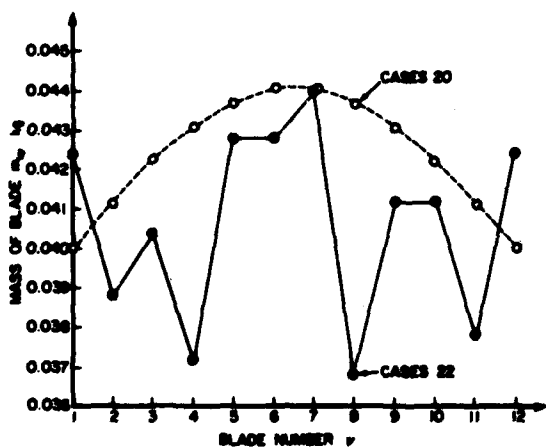


Fig. 15. Mass distribution of mistuned compressor blade systems ($n = 11$; Cases 20, regular mistuning and Cases 22, random mistuning).

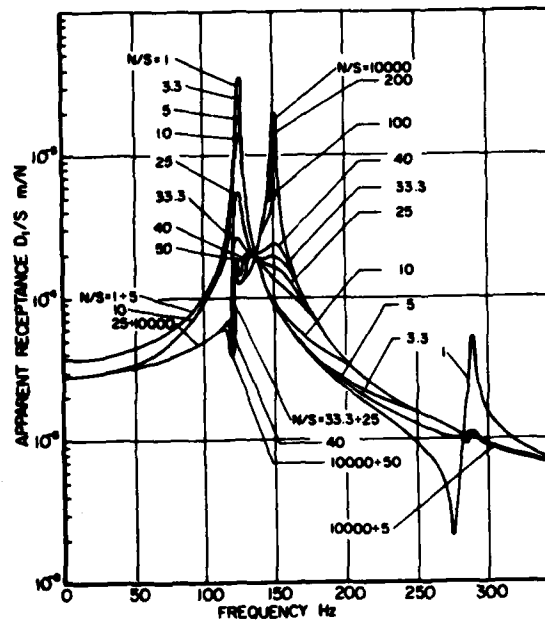


Fig. 16. Response of mistuned system to traveling wave excitation (blade 1, D_1/S , Case 20—Table 3, effects of ratio of normal force to exciting force amplitude).

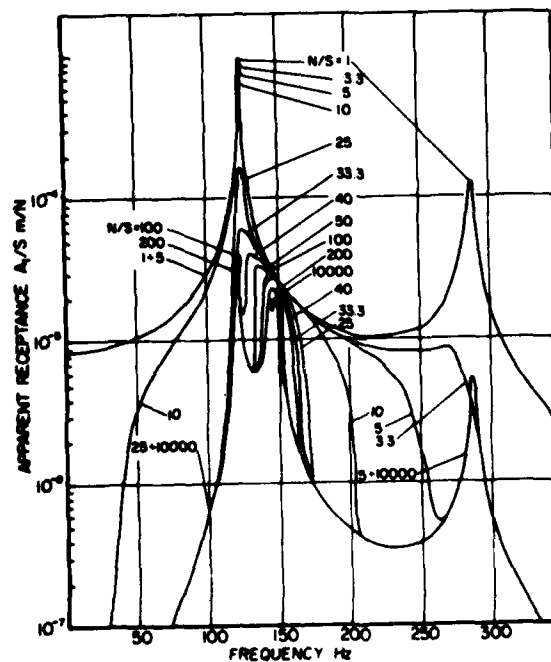


Fig. 17. Response of mistuned system to traveling wave excitation (blade 1, A_1/S , Cases 20—Table 3, effects of ratio of normal force to exciting force amplitude).

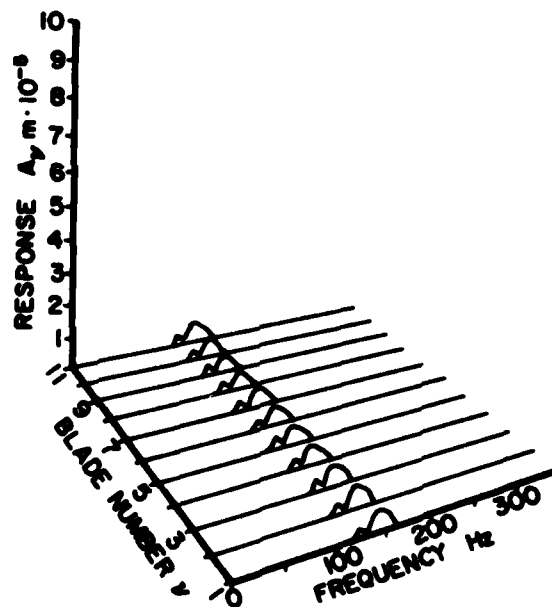
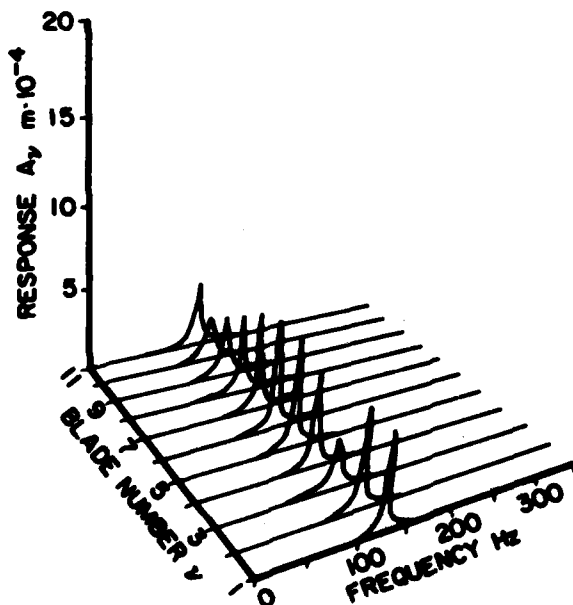
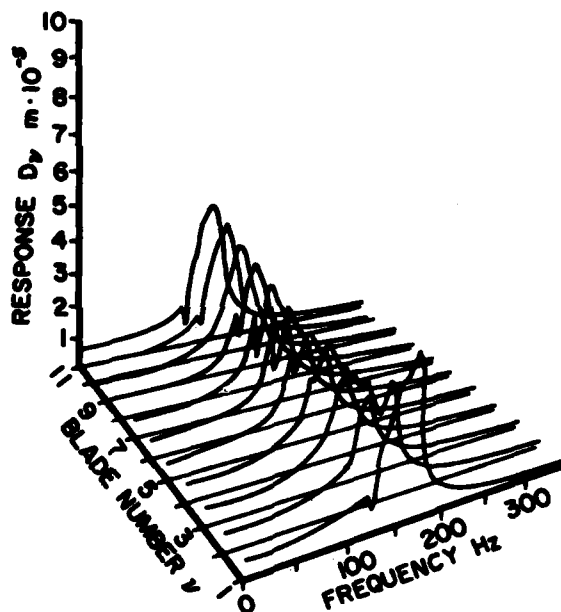
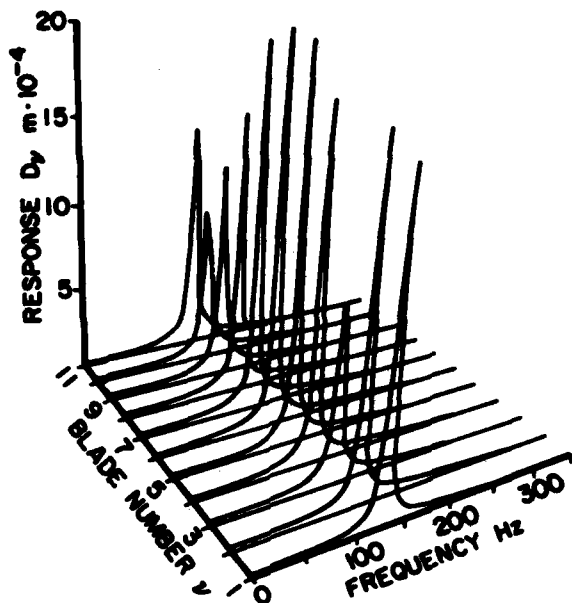


Fig. 18. Computer generated plot of response (D and A) versus frequency and blade number (for case 20.05—Table 3, $S_v = 1.0N$, $N_v = 10N$).

Fig. 19. Computer generated plot of response (D and A) versus frequency and blade number (for Case 20.18—Table 3, $S_v = 0.2N$, $N_v = 10N$).

response $|D_v/S|$ from a peak at 125 Hz to one at 150 Hz, as $\mu N/S$ varies from 0 to ∞ (Fig. 16). The limiting case $N/S = \infty$ corresponds to all masses m_{2v} locked together. Note also that $|A_v/S|$ varies somewhat differently than in the tuned case, and exists over a wider frequency range. Figures 21 and 22 show similar variations of $|D_v/S|$ and $|A_v/S|$ for a blade with

randomly mistuned masses m_{1v} , as illustrated in Figure 15. Despite the different types of mistuning, the response plots appear remarkably similar to the previous case (author's Case 20), and on the basis of this very limited sample, one might conclude tentatively that, while the exact type of mistuning will affect precisely which blade sees the maximum response, it does

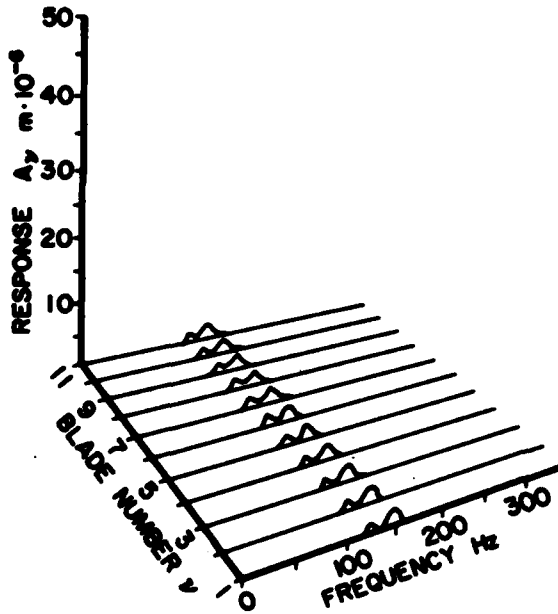
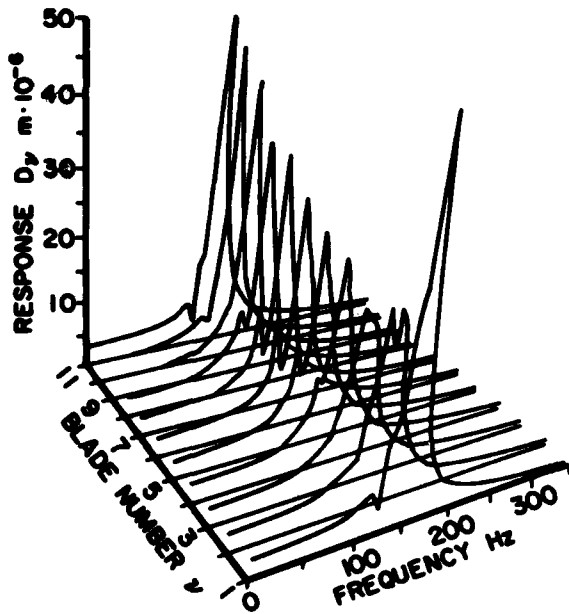


Fig. 20. Computer generated plot of response (D and A) versus frequency and blade number (for Case 20.09—Table 3, $S_v = 0.1N$, $N_v = 100N$).

not affect the value of the maximum response. Obviously, this is not a final conclusion, and further investigation seems warranted, especially for large values of $\mu N/S$. Figure 23 shows the values of $|D_v/S|_{max}$ versus $\mu N/S$ for these two cases, and for the tuned case, and does seem to bear out this tentative conclusion.

TABLE 3
PARAMETERS FOR VARIOUS CASES

Parameter	Case 20.05	Case 20.18	Case 20.09
n	11	11	11
m_{1v}	$0.04f_1(\nu)$	$0.04f_1(\nu)$	$0.04f_1(\nu)$
m_{2v}	0.049	0.049	0.049
K_{1v}	35,530	35,530	35,530
K_{2v}	111,034	111,034	111,034
K_{3v}	0	0	0
η	0.01	0.01	0.01
η_1	0.01	0.01	0.01
N_{Nv}	0	0	0
N_v	10	10	100
μ	0.15	0.15	0.15
S_v	1.0	0.2	0.1
δ_v	$2\pi(\nu-1)/n$	$2\pi(\nu-1)/n$	$2\pi(\nu-1)/n$

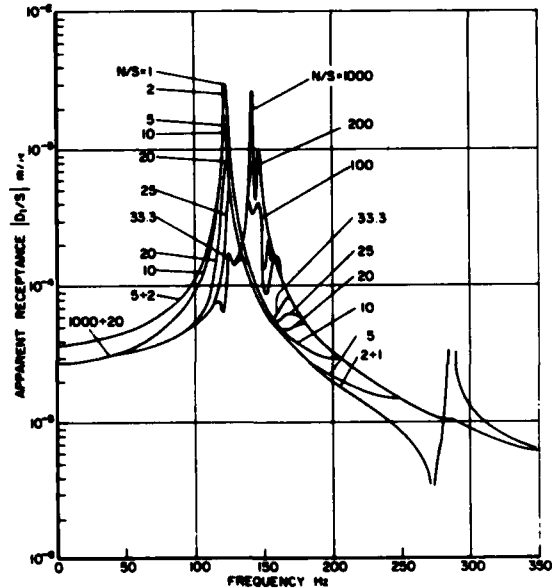


Fig. 21. Response of mistuned system to traveling wave excitation (blade 1, D_1/S , Cases 22—Table 3, $\mu = 0.15$, effect of ratio of normal force to exciting force amplitude).

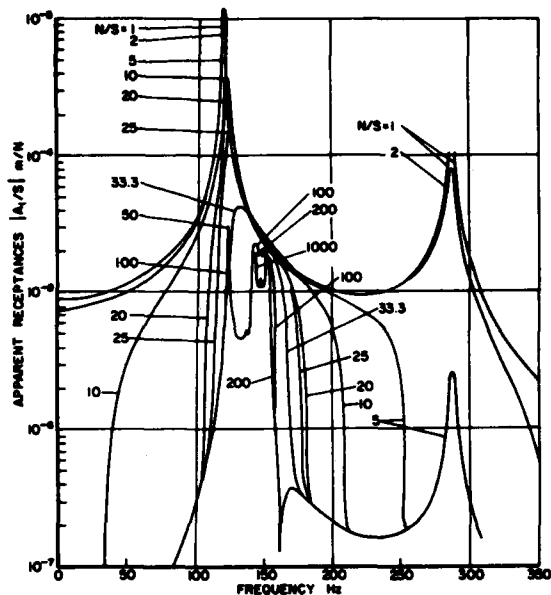


Fig. 22. Response of mistuned system to traveling wave excitation (blade 1, A_j/S , Cases 22-Table 3, $\mu = 0.15$, effects of ratio of normal force to exciting force amplitudes).

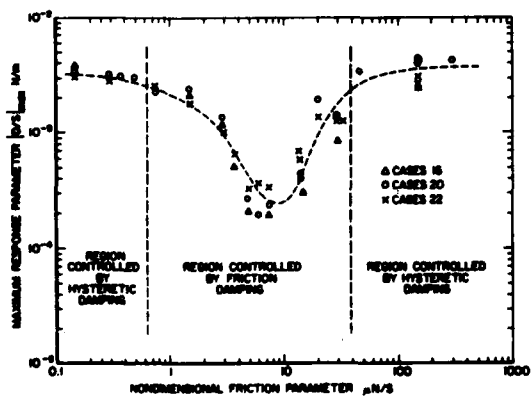


Fig. 23. Variation of $(D/S)_{max}$ with $\mu N/S$ for traveling wave excitation.

Another set of calculations determined the effect of an irregularity in the phase between exciting forces on blade 5 and blade 1, for $n = 5$, for traveling wave excitation ($j=1$) of the tuned system (author's Case 16). This was accomplished in the computer program simply by letting $\delta_v = 2\pi(\nu-1)/(n+\Delta n)$, where Δn is a positive or negative number. Figures 24 to 26 show the response $|D_v/S|$ for all blades of the five-blade system and several values of Δn with

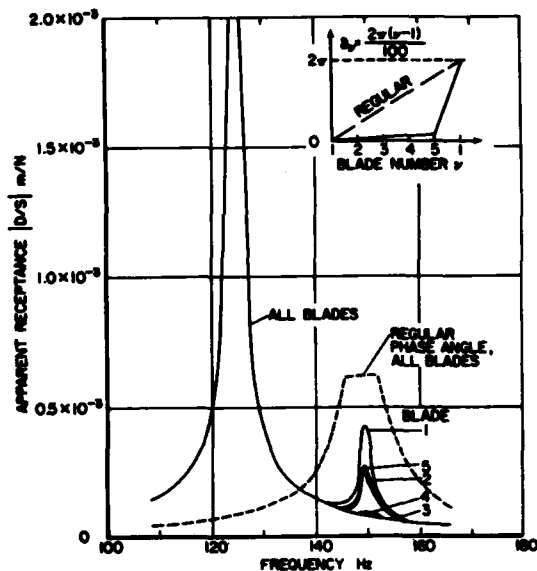


Fig. 24. Response of tuned system to traveling wave excitation (effect of phase irregularity of the exciting force, $\mu N/S = 15$, Case 16).

$S_v = 0.1$. It is seen that the phase irregularity occurs between blades 1 and 5. It is also seen that blades 1 and 5 typically see the highest response amplitudes, and that the behavior changes from dominant response near 125 Hz, for large phase irregularity, to dominant response near 150 Hz when the phase shift is less severe. Further evidence of the effects of phase irregularities in a mistuned system is shown in Figures 27 and 28, where an 11-blade system (author's Case 20) is examined. The properties are given in Table 2, column 3, except that Figure 27 corresponds to $\delta_v = 2\pi(\nu-1)/(n+2)$ and Figure 28 to $\delta_v = 2\pi(\nu-1)/(n-2)$. These results should be compared with Figure 16, which corresponds to a uniform distribution of phase $\delta_v = 2\pi(\nu-1)/n$. Again, large amplitudes are seen for blades 1 and 11. Further investigation of the effect of other parameters, especially in regard to minimizing the large increases in amplitude, seem indicated, and can be accommodated by this model.

Finally, further consideration is given to the effect of variation in the number of blades, other parameters being equal, on the response of tuned and mistuned systems under traveling wave excitation. The system parameters are given in Table 2, column 1 (tuned system) and column 3 (mistuned system). In these cases, $\delta_v = 2\pi(\nu-1)/n$, so no phase

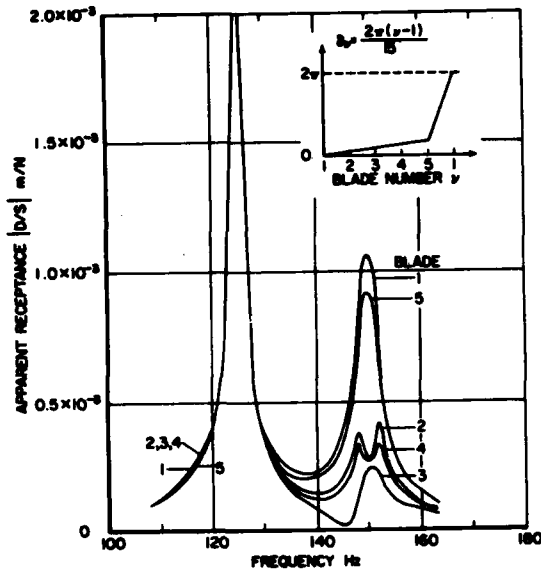


Fig. 25. Response of tuned system to traveling wave excitation (effect of phase irregularity of the exciting force, $\mu N/S = 15$, Case 16).

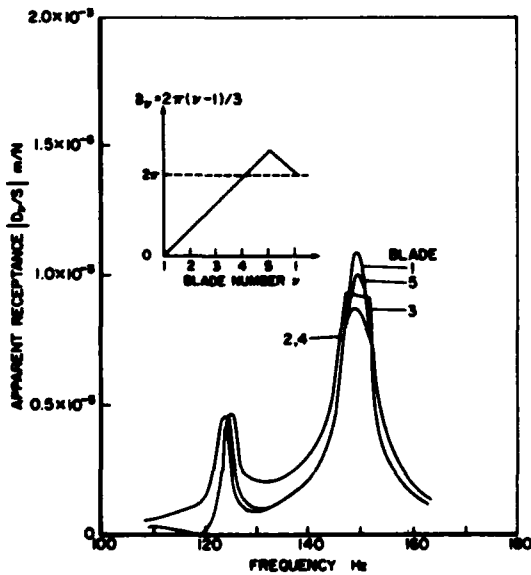


Fig. 26. Response of tuned system to traveling wave excitation (effect of phase irregularity of the exciting force, $\mu N/S = 15$, Case 16).

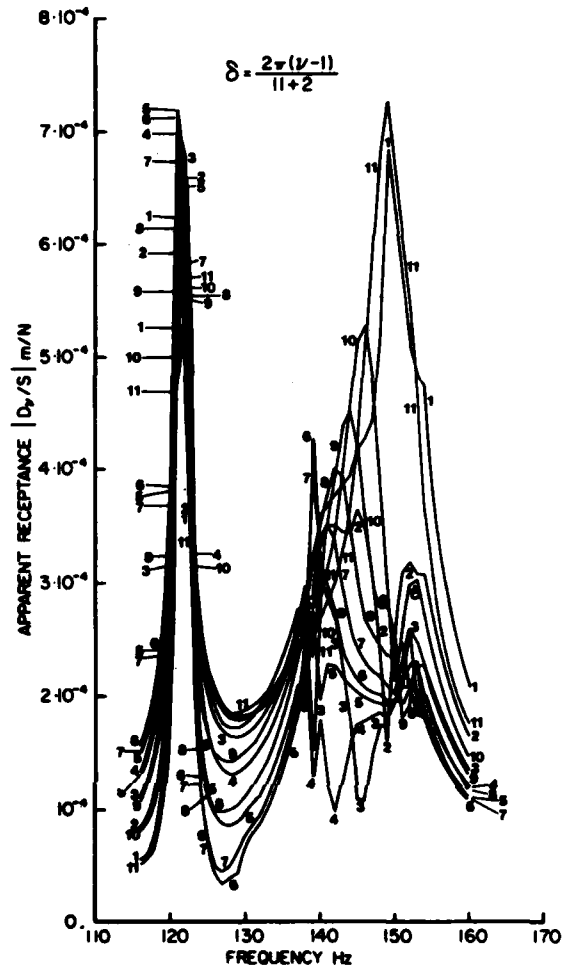


Fig. 27. Response of mistuned system to traveling wave excitation (effect of phase irregularity of the exciting force, $\mu N/S = 15$, Case 20).

irregularity occurred, but the interblade exciting force phase angles do change, becoming smaller as n increases. This is reflected in the response behavior, as Figure 29 (tuned) and Figure 30 (mistuned) show. Comparing Figure 14 and 29 and Figures 16 and 17 with Figure 30, we see that increasing the value of n has an effect similar to that of decreasing N/S . In fact, it can be shown [32] that a single parameter

$2 \frac{\mu N}{S} \left| \sin \frac{\pi}{n} \right|$ combines the effect of $\mu N/S$ and n .

Obviously, many more cases need to be considered, but it is not possible to consider more in this paper. What is clear is that non-linear response behavior is much more difficult to classify and generalize than linear behavior, so that special rather than general conclusions must be drawn, both from these results and

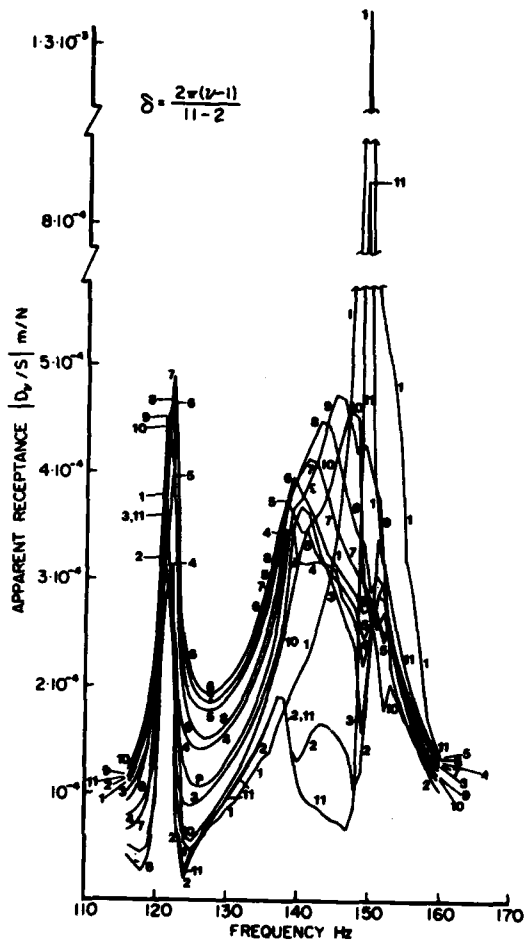


Fig. 28. Response of mistuned system to traveling wave excitation (effect of phase irregularity of the exciting force, $\mu N/S = 15$, Case 20).

from any results obtained by other methods of analysis.

4. CONCLUSIONS

In this paper, the authors have developed a simple multiple degree of freedom model of a multiple blade array capable of accounting for effects of mistuning, blade-to-blade and blade-to-ground frictional damping, blade-to-blade compliant coupling and different magnitudes and phases of exciting forces on each blade. The applicability and limitations of the two degree of freedom model of each blade have been discussed and compared with receptance models and experimental data for a nominally undamped blade in a rigid fixture. It is shown that modes of the system which correspond to the fundamental mode of the blades can be quite accurately modeled. The second mode of the blade cannot be so well modeled by a two degree of freedom system. It has also been shown that receptance techniques of response synthesis can be further developed to solve such nonlinear multiple blade problems in a more exact manner. In this

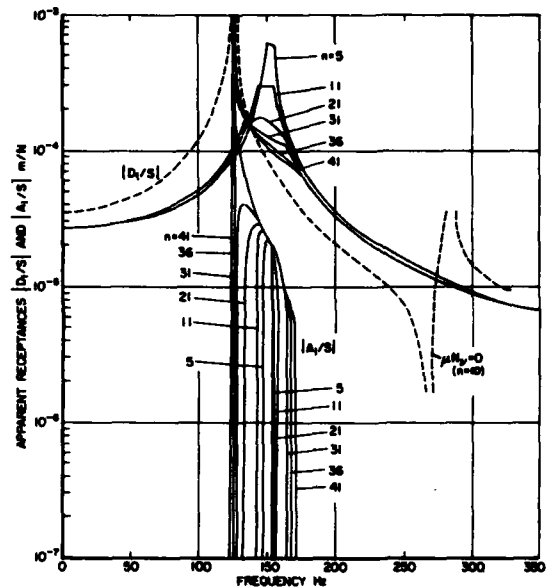


Fig. 29. Effect of number of blades on response of tuned system (Case 16, $\mu N/S = 15$).

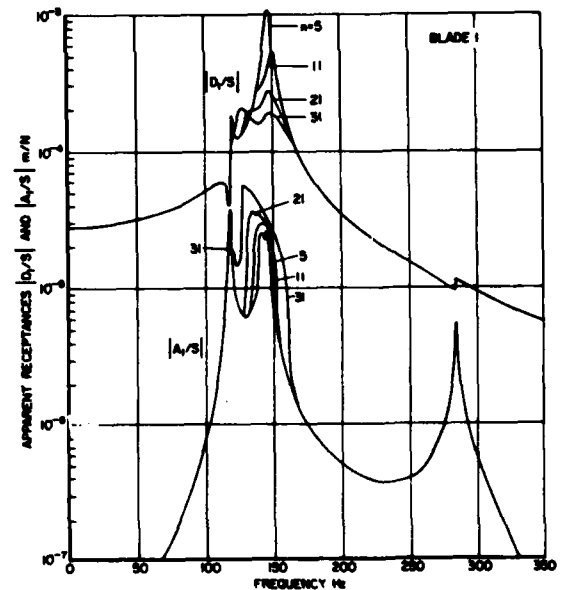


Fig. 30. Effect of number of blades on response of mistuned system (Case 20, $\mu N/S = 15$).

paper, however, a single blade receptance analysis only is completed.

Specific conclusions emerging from the numerical results of the computer program

generated to solve the equations of motion are as follows:

1. The effects of mistuning are to introduce blade-to-blade coupling through the stiffness elements K_{3v} , and this leads to typical mistuned behavior in which several response peaks are observed, scattered on both sides of the tuned-system resonant frequency.
2. When friction is introduced between blades, it usually becomes the most important blade-to-blade factor and the effects of K_{3v} are less evident. See Figures 27 and 28, for example.
3. The type of harmonic excitation variation of amplitudes and phases has a very great effect on the qualitative as well as the quantitative form of the response, and different types of excitation lead to different types of response behavior, including on occasion very high response levels. Lowest response amplitudes seem generally to correspond with the "smoothest" δ_v (least radical excitation distributions) and it is deviations from uniformity which seem to lead to high amplitudes.
4. For a given number of blades, an optimum value of the friction parameter $\mu N/S$ (ratio of friction force to driving force amplitude) seem to exist, for which response amplitudes are a minimum in all blades, provided that uniformity of the phase angle δ_v occurs. This optimum does not seem to be very strongly dependent on the type or amount of mistuning (smooth or random variation from blade-to-blade), except that at high values of $\mu N/S$ (typical of real engine conditions), the randomly mistuned cases seem to have somewhat lower amplitudes under the same (smooth) excitation conditions. This, however, remains to be verified when more cases are examined.
5. The mathematical model and corresponding computer program which has been developed for numerical calculations have quite general character within limits and may be used for prediction of amplitudes of blade or disk vibration (and corresponding stresses) for various bladed disk systems. The particular interest of this program lies in the possibility of investigation of structural friction damping, which exists in joints or is deliberately introduced to the system through platforms or special friction dampers.

Several other parametric investigation, reflecting various blade configurations and dynamic conditions are still being conducted, and will be the subject of future publications.

A computer program has been developed and individuals interested in defining specific problems for calculation are invited to communicate with the authors.

REFERENCES

1. D. A. Rimkunas and H. M. Frye, "Investigation of Fan Blade Shroud Mechanical Damping," AFAPL-TR-79-2054, June 1979.
2. B. Sadighi, "An Analysis of Root Flexibility Effects on Turbine Blade Vibration Characteristics," Report No. 78004, Imperial College, London (M.S. Thesis), 1977.
3. E. O. Dickerson, "Turbine Blade Structural Dynamic Analysis," AIAA Paper, 80-0782, 21st Structures, Seattle, Washington, 1980.
4. R. L. Bielawa, "An Analytic Study of the Energy Dissipation of Turbomachinery Bladed Disk Assemblies Due to Inter-Shroud Segment Rubbing," ASME Paper, 77-DET-73, 1977.
5. A. L. Salama and M. Petyt, "Dynamic Response of Packets of Blades by the Finite Element Method," ASME Paper, 77-DET-70, 1977.
6. S. Umemura, M. Mase, and Y. Kadoya, "Vibration Analysis of Grouped Blades of Turbines by the Finite Element Method," Technical Review, Mitsubishi Heavy Industries, Ltd., Tokyo, 16 (2), Series 45, 1979.
7. A. V. Srinivasan (Ed), Structural Dynamic Aspects of Bladed Disk Assemblies, ASME Publication, Proc. ASME Winter Annual Meeting, New York, 1976.
8. K. W. Lang and S. Nemat-Nasser, "An Approach for Estimating Vibration Characteristics of Nonuniform Rotor Blades," AIAA Journal, 17(9), pp. 995-1002, 1979 (Paper No. AIAA 79-4111).
9. Huang Wen-hu, "Free and Forced Vibration of Closely Coupled Turbomachinery Blades," AIAA Paper 80-0700, 21st Structures, Structural Dynamic and Materials Conference, Seattle, Washington, 1980.
10. A. V. Srinivasan, S. R. Lionberger, and K. W. Brown, "Dynamic Analysis of an Assembly of Shrouded Blades Using Component Modes," J. Mechanical Design (ASME Paper, 77-DET-72) v.100, pp. 520-527, 1978.
11. N. Miramand, J. F. Billand, F. Leleux, and J. P. Kernevez, "Identification of Structural Modal Parameters by Dynamic Tests at a Single Point," Shock and Vibration Bulletin 46 (5), pp. 197-212, 1976.
12. J. P. Raney, "Identification of Complex Structures Using Near-Resonance Testing," Shock and Vibration Bulletin 38 (2), pp. 23-32, 1968.
13. M. T. Soifer and A. W. Bell, "Reducing the Number of Mass Points in a Lumped Parameter System," Shock and Vibration Bulletin 38 (2), pp. 57-66, 1968.
14. M. T. Soifer and A. W. Bell, "Simplifying a Lumped Parameter Model," Shock and Vibration Bulletin 39 (3), pp. 153-160, 1969.

15. F. H. Wolff and A. J. Molnar, "Reduced System Models Using Modal Oscillators for Subsystems (Rationally Normalized Modes)," Shock and Vibration Bulletin 48 (4), pp. 111-118, 1978.
16. G. J. O'Hara and G. M. Remmers, "Measurement of a Structure's Modal Effective Mass," Shock and Vibration Bulletin 39 (3), pp. 143-151, 1969.
17. H. G. D. Goyder, "Methods and Application of Structural Modeling from Measured Structural Frequency Response Data," J. Sound and Vibration 68 (2) pp. 209-230, 1980.
18. S. Mahalingam, "The Synthesis of Vibrating Systems by Use of Internal Harmonic Receptances," J. Sound and Vibration 40 (3), pp. 337-350, 1975.
19. D. J. Ewins, "Whys and Wherefores of Modal Testing," SEE Journal, September 1979.
20. D. I. G. Jones, "Vibration of a Compressor Blade with Slip at the Root," AFVAL-TR-80-4003, Air Force Wright Aeronautical Laboratories, 1980.
21. D. J. Ewins, "Studies to Gain Insight Into the Complexities of Blade Vibration Phenomena," Paper C 184/76, Reference 7.
22. D. J. Ewins, "Vibration Characteristics of Bladed Disk Assemblies," J. Mechanical Engr. Science, 15(3), pp. 165-186, 1973.
23. R. Koop, Air Force Wright Aeronautical Laboratories (AFVAL/POTP), private communication.
24. L. E. Goodman and J. H. Klumpp, "Analysis of Slip Damping with Reference to Turbine-Blade Vibration," J. Applied Mechanics, pp. 421-629, 1956.
25. D. I. G. Jones and A. Muszyńska, "Effect of Slip Damping on Response of a Vibrating Compressor Blade," ASME Paper 77-WA/GT-3, 1977.
26. D. I. G. Jones and A. Muszyńska, "Vibration of a Compressor Blade with Slip at the Root," Shock and Vibration Bulletin 48, 1978.
27. D. I. G. Jones and A. Muszyńska, "Non-linear Modelization of Nonconservative Blade Vibration Response," Proc. ICNO Conference on Nonlinear Oscillations, Prague, Czechoslovakia, 1978.
28. D. I. G. Jones and A. Muszyńska, "Design of Turbine Blades for Effective Slip Damping at High Rotational Speeds," Shock and Vibration Bulletin 49(2), pp. 87-96, 1979.
29. A. Muszyńska and D. I. G. Jones, "On Discrete Modelization of Response of Blades with Slip and Hysteretic Damping," Proc. 5th World Congress on Theory of Machines and Mechanisms, Montreal, Canada, 1978.
30. E. J. Williams and S. W. E. Earles, "Optimization of the Response of Frictionally Damped Beam Type Structures with Reference to Gas Turbine Compressor Blading," ASME Paper 73-DET-108, 1973.
31. D. J. Ewins and Y. V. K. Sadasiva Rao, "A Theoretical Study of the Damped Forced Vibration Response of Bladed Disks," pp. 29-43, Reference 7.
32. A. Muszyńska and D. I. G. Jones, "Tuned Bladed Disk Dynamics," to appear.
33. R. Plunkett, "Friction Damping," Published in Proc. of ASME Symposium, Damping Application for Vibration Control (Ed. P. J. Torvik), Chicago, Illinois, November 1980.
34. J. R. Bunch and B. V. Parlett, "Direct Methods for Solving Symmetric Indefinite Systems of Linear Equations," SIAM, J. Numer. Anal., 8, 639-655, (1971).
35. J. R. Bunch, "Analysis of the Diagonal Pivoting Method," SIAM J. Numer. Anal., 8, 656-680, 1971.

NOMENCLATURE

A	amplitude of $X_2(t)$
A_v	amplitude of $X_{2v}(t)$
C_1, C_2	constants
D	amplitude of $X_1(t)$
D_v	amplitude of $X_{1v}(t)$
f_{1v}, f_{2v}	functions (see Tables 1-3)
f_n	n-th natural frequency (Hz)
i, j	points on blade surface (i, j = 1, 2)
j	integer
K_1, K_2	stiffnesses
K_{1v}, K_{2v}	stiffnesses
K_{3v}	coupling stiffness
M_n	modal mass
m_1, m_2	masses
m_{1v}, m_{2v}	masses of v-th elements
N	number of modes, also normal force
N_v, N_{Nv}	normal forces for v-th blade
n	number of blades, also integer
P, Q, Z	matrices
R_2	correction coefficient
S, S_1	driving force amplitudes

S_i	driving force
S_v	driving force
t	time
x_i, y_i	coordinates
X_i, Y_i	response displacements at point i
\dot{x}_i, \dot{y}_i	velocities
X_{1v}	response of mass m_1
X_2	response of mass m_2
a_{ij}, a_{ij}^i	cross receptances
α, γ, δ	phase angles
$\alpha_v, \gamma_v, \delta_v$	phase angles
β_1, β_2	constants
Δ	see Equation 9
Δn	irregularity in n
ϵ_1, ϵ_2	precision indicators
η, η_1	loss factors
η_n	loss factor of n -th mode
ϕ_n	n -th modal function
μ	coefficient of friction
v	integer
σ	iteration index ($\sigma = 0, 1, \dots$)
ω	circular frequency
ω_n	natural frequency of n -th mode

APPENDIX 1: EXPERIMENTAL INVESTIGATIONS

The specific blade chosen for base-line tests was a typical slightly twisted, cambered, steel compressor blade with a simple dovetail geometry. The blade was held in a heavy fixture, Figure 31, having mating surfaces that matched the contours of the blade root. For the receptance tests, the root conditions were such that the clamping pressure prevented slip from occurring. However, the centrifugal loads which exist in the operational environment were not simulated, because of the difficulty of duplicating this effect without masking other blade characteristics, such as low damping. The test fixture for the blade was a 102 mm square broach block, made of steel. In the first set of tests, this block was placed directly on a rubber pad to isolate the fixture from the surroundings. Later tests were conducted with the broach block fixture attached

to a 51-mm-thick by 460-mm-square aluminum plate, which in turn was mounted on rubber isolators, to even more completely isolate the blade from the surroundings.

The test system is illustrated by block diagrams in Figure 32. The Bruel and Kjaer Model 1014 Beat Frequency Oscillator could generate a harmonically varying voltage of magnitude 0 to 120 volts, at any selected frequency from 20 Hz to 20 kHz. The output impedance, measured in Ohms, was variable within limits to accommodate various impedance exciters. As the frequency was varied, the current through the output terminals to the exciter, or driver, could be controlled by means of a "compressor." This was simply a feedback loop which measured the voltage across a fixed resistor in the output circuit, and used it to control the output current. A meter gave a reading of nominal voltage across the terminals.

The output current from the oscillator was fed directly to a magnetic transducer (Electro Model 3030-HTB), with the output impedance set at 600 Ohms to best match the transducer. The transducer consisted, essentially, of a magnetized iron rod with many coils of fine wire surrounding it, through which the oscillating current flows. This current produces an oscillating magnetic field which modulates the steady magnetic field of the rod, and hence produces an oscillating harmonic force on any iron object placed nearby. The magnitude of this force depends on the amplitude of the current and on the gap between the end of the magnetized rod and the structure being excited.

The waveforms of the input and response signals were monitored on a dual beam oscilloscope (Ballantine Model 1066S). The frequency of the input signal was measured by a digital frequency meter (HP Model 5216A). The pickup system used a miniature high impedance quartz accelerometer (Endevco Model 22), of mass about 0.2 grams and having a very thin and flexible cable to minimize interference. An MB Zero Drive (MB M400) amplifier was used to amplify and condition the accelerometer signals, so that they could be read off a voltmeter (HP Model 3400A). A "line driver" was used in conjunction with the high impedance amplifier to minimize losses of signal strength in the cables. This system was used to measure the driving point receptances at point 1, namely a_{11} , illustrated in Figure 2.

This system has been further updated for further analog tests at the Materials Laboratory. The sweep oscillator was replaced by an SD Model 104A-5 system to give more flexibility in testing procedures and display of results, and was connected with a 250-watt power amplifier so that the controllable input force amplitudes could have a greater range. This was particularly important because of the

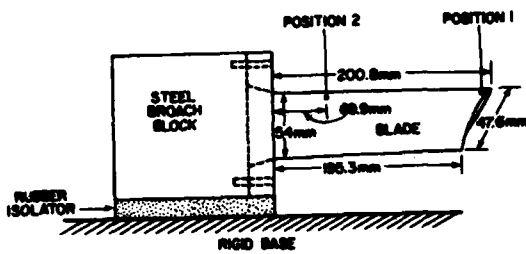


Fig. 31. Blade in test fixture.

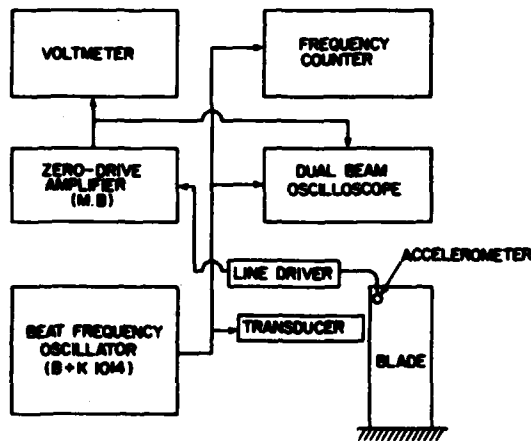


Fig. 32. Analog test system.

inductive drop-off of the magnetic transducer output force at high frequencies. To correctly match the output impedance of the amplifier (4 Ohms) to that of the transducer (1,600 Ohms), an audio transformer was used. This minimized distortion of the input signal. To ensure constant output force from the transducer, the current was monitored by observing the voltage across a fixed (1 Ohm) resistor. Voltage to the transducer was monitored so as to control the input power, thereby minimizing the danger of fusing the wire coils together in the transducer, which could lead to loss of signal strength and increased distortion, as well as disturb the calibration of the system.

A digital signal analyzer (HP Model 3582) has also been used to conduct tests. The capability of this digital system to conduct spectrum analysis in conjunction with impulsive excitation of the blade (calibrated hammer) allowed for very effecting testing procedures. The impact hammer (PCB 068A60) and accelerometer (PCB 3031) were both low impedance devices so that electronic noise was minimized. Even so, great care had to be taken in calibrating

the system and in ensuring that each individual test was well conditioned. A block diagram of the test system is given in Figure 33.

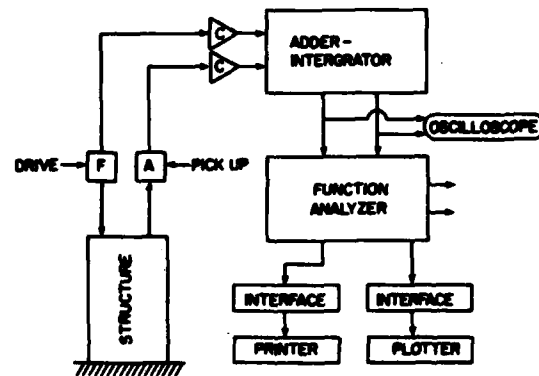


Fig. 33. Digital test system.

APPENDIX 2: RECEPTANCE ANALYSIS OF BLADE WITH SLIP

Equations (10) and (11) are solved by assuming, for steady state response (the existence of the steady state response of the form Equation (26) was analyzed by Plunkett [33] from the viewpoint of a solution in the time domain) that

$$X_2 = A \cos \omega t,$$

$$S_1 = S_{11} \cos \omega t + S_{12} \sin \omega t \quad (26)$$

$$X_1 = D_1 \cos \omega t + D_2 \sin \omega t = D \cos(\omega t + \gamma)$$

Then: $\text{sgn}(X_2) \approx -4/\pi \text{sgn}(A) \sin \omega t$ if we take the first term and the Fourier expansion of $\text{sgn}(\sin \omega t)$. Putting these into Equations (10) and (11) gives:

$$\begin{aligned} D_1 \cos \omega t + D_2 \sin \omega t &= a_{11}(S_{11} \cos \omega t + S_{12} \sin \omega t) \\ &\quad - \frac{4}{\pi} \mu N \text{sgn}(A) \sin \omega t a_{12} \quad (27) \\ A \cos \omega t &= (S_{11} \cos \omega t + S_{12} \sin \omega t) a_{21} \\ &\quad - \frac{4}{\pi} \mu N \text{sgn}(A) \sin \omega t a_{22} \end{aligned}$$

Equating terms in $\cos \omega t$ and $\sin \omega t$ gives the four equations:

$$\begin{aligned} D_1 &= a_{11} S_{11} \\ D_2 &= a_{11} S_{12} - \frac{4\mu N}{\pi} \text{sgn}(A) a_{12} \quad (28) \\ A &= S_{11} a_{21} \end{aligned}$$

$$0 = S_{12}a_{21} - \frac{4\mu N}{\pi} \operatorname{sgn}(A)a_{22}$$

which are readily solved for D_1 , D_2 , S_{11} , and S_{12} .

$$S_{12} = \frac{4\mu N}{\pi} \operatorname{sgn}(A) \frac{a_{22}}{a_{21}}$$

$$\therefore S_1 = S_{11} \cos \omega t + \frac{4\mu N}{\pi} \operatorname{sgn}(A) \frac{a_{22}}{a_{21}} \sin \omega t \quad (29)$$

$$\therefore S_1^2 = S_{11}^2 + \left(\frac{4\mu N}{\pi}\right)^2 \left(\frac{a_{22}}{a_{21}}\right)^2$$

$$\therefore S_{11} = \sqrt{S_1^2 - \left(\frac{4\mu N}{\pi}\right)^2 \left(\frac{a_{22}}{a_{21}}\right)^2}$$

Hence:

$$x_1 = a_{11} S_{11} \cos \omega t + \frac{4\mu N}{\pi} \operatorname{sgn}(x_2) \left(\frac{a_{11}a_{22}}{a_{21}} - a_{12} \right) \sin \omega t$$

$$\therefore D^2 = a_{11}^2 S_{11}^2 + \left(\frac{4\mu N}{\pi}\right)^2 \left(\frac{a_{11}a_{22} - a_{12}a_{21}}{a_{21}} \right)^2 \quad (30)$$

$$D^2 = a_{11}^2 \left[S_1^2 - \left(\frac{4\mu N}{\pi}\right)^2 \left(\frac{a_{22}}{a_{21}}\right)^2 \right] + \left(\frac{4\mu N}{\pi}\right)^2 \left(\frac{a_{11}a_{22} - a_{12}a_{21}}{a_{21}} \right)^2$$

Hence, Equation (12). Since $A = S_{11} a_{21}$, Equation (13) follows also.

APPENDIX 3: DISCRETE ANALYSIS OF BLADE WITH SLIP

Equations (16) and (17) are solved, for steady state response, by assuming that

$$x_2 = A \cos \omega t$$

$$x_1 = D_1 \cos \omega t + D_2 \sin \omega t = D \cos(\omega t + \gamma) \quad (31)$$

$$S_1 = S_{11} \cos \omega t + S_{12} \sin \omega t \quad (32)$$

$$\text{and } \mu NR_2 \operatorname{sgn}(\dot{x}_2) = \frac{-4}{\pi} \mu NR_2 \operatorname{sgn}(A) \cdot \sin \omega t$$

Hence, Equations (16) and (17) become:

$$\begin{aligned} (K_1 - m_1 \omega^2) (D_1 \cos \omega t + D_2 \sin \omega t) - K_1 A \cos \omega t \\ = (S_{11} \cos \omega t + S_{12} \sin \omega t) \end{aligned} \quad (33)$$

$$(K_1 + K_2 - m_2 \omega^2) A \cos \omega t - K_1 (D_1 \cos \omega t + D_2 \sin \omega t)$$

$$- \frac{4\mu NR_2}{\pi} \operatorname{sgn}(A) \sin \omega t = 0$$

equating terms in $\cos \omega t$ and $\sin \omega t$ gives the four equations:

$$(K_1 - m_1 \omega^2) D_1 - K_1 A = S_{11}$$

$$(K_1 - m_1 \omega^2) D_2 = S_{12} \quad (34)$$

$$(K_1 + K_2 - m_2 \omega^2) A - K_1 D_1 = 0$$

$$-K_1 D_2 = \frac{4\mu NR_2}{\pi} \operatorname{sgn}(A).$$

Hence:

$$\therefore S_1 = S_{11} \cos \omega t + (K_1 - m_1 \omega^2) \left(\frac{-4\mu NR_2}{\pi K_1} \right) \operatorname{sgn}(A) \times \sin \omega t$$

$$\therefore S_1 = S_{11}^2 + \left(\frac{4\mu NR_2}{\pi K_1} \right)^2 (K_1 - m_1 \omega^2)^2 \quad (35)$$

$$\therefore S_{11} = \sqrt{S_1^2 - \left(\frac{4\mu NR_2}{\pi} \right)^2 \left(1 - \frac{m_1 \omega^2}{K_1} \right)^2}$$

From the first and third of Equations (34), by eliminating D_1 , we get the expression (19) for $|A|$. Further, we get the expressions for D_1 and D_2 :

$$D_1 = \frac{\left(1 + \frac{K_2}{K_1} - \frac{m_2}{m_1} \frac{m_1 \omega^2}{K_1} \right) \sqrt{1 - \left(\frac{4\mu NR_2}{\pi S_1} \right)^2 \left(1 - \frac{m_1 \omega^2}{K_1} \right)^2}}{K_1 \left[\left(1 - \frac{m_1 \omega^2}{K_1} \right) \left(1 + \frac{K_2}{K_1} - \frac{m_2}{m_1} \frac{m_1 \omega^2}{K_1} \right) - 1 \right]} S_1 \quad (36)$$

$$D_2 = \frac{4\mu NR_2}{\pi K_1} \operatorname{sgn}(A) \quad (37)$$

Hence, since $|D|^2 = D_1^2 + D_2^2$, we get the expression (18) for $|D|$.

APPENDIX 4: ANALYSIS OF MULTIPLE BLADE SYSTEM WITH SLIP

The equations of motion for the v -th blade, in Figure 9 are:

$$m_{1v} \ddot{x}_{1v} + K_{1v} (x_{1v} - x_{2v}) + \frac{K_{1v} n}{\omega} (\dot{x}_{1v} - \dot{x}_{2v}) =$$

$$= S_v \cos(\omega t + \delta_v) \quad (38)$$

$$\begin{aligned} m_{2v} \ddot{x}_{2v} - k_{1v} x_{1v} + \frac{k_{1v} \eta}{\omega} (\dot{x}_{2v} - \dot{x}_{1v}) \\ + \frac{k_{2v} \eta}{\omega} \dot{x}_{2v} + \frac{k_{3v} \eta_1}{\omega} (\dot{x}_{2v} - \dot{x}_{2,v+1}) \\ + \frac{k_{3,v-1} \eta_1}{\omega} (\dot{x}_{2v} - \dot{x}_{2,v-1}) - k_{3v} x_{2,v+1} \\ - k_{3,v-1} x_{2,v-1} \\ + \mu N_{v,R_2} \operatorname{sgn}(\dot{x}_{2v} - \dot{x}_{2,v+1}) + \mu N_{v,R_1} \operatorname{sgn}(\dot{x}_{2v}) \\ + \mu N_{v-1,R_2} \operatorname{sgn}(\dot{x}_{2v} - \dot{x}_{2,v-1}) + (k_{1v} + k_{2v} \\ + k_{3v} + k_{3,v-1}) x_{2v} = 0 \quad (39) \end{aligned}$$

for $v = 1, 2, \dots, n$, where n is the number of blades in the system. These are a set of nonlinear differential equations of the second order, with the only nonlinear term representing a Coulomb model of the frictional forces.

In Equation (38) and (39) η and η_1 are loss factors in elastic members (hysteretic damping model), R_1 and R_2 are correcting coefficients, N_v , and $N_{v,v}$ are normal forces, and μ is the dry friction coefficient.

Applying again the method of harmonic balance, we let

$$x_{1v} = D_v \cos(\omega t + \gamma_v) \quad (40)$$

$$x_{2v} = A_v \cos(\omega t + \alpha_v) \quad (41)$$

If we introduce these into the equation of motion, and introduce the simplifications:

$$\begin{aligned} \operatorname{sgn}[C_1 \sin(\omega t + \beta_1) - C_2 \sin(\omega t + \beta_2)] \\ \approx \frac{4}{\pi} \frac{C_1 \sin(\omega t + \beta_1) - C_2 \sin(\omega t + \beta_2)}{\sqrt{C_1^2 + C_2^2 - 2C_1 C_2 \cos(\beta_1 - \beta_2)}} \quad (42) \end{aligned}$$

(first term of the Fourier expansion; $C_1, C_2, \beta_1, \beta_2$ are constants) then the equations for the unknowns:

$$Z_{2v-1} = A_v \cos \alpha_v$$

and

$$Z_{2v} = -A_v \sin \alpha_v \quad v = 1, \dots, n$$

can be written in the form of a nonlinear algebraic matrix equation:

$$P(Z)Z = Q, \quad (43)$$

where Z is the column matrix ($m \times 1$) of variables Z_{2v-1} and Z_{2v} where $v = 1, \dots, n$ and \bar{i} $m = 2n$, Q is the column matrix ($m \times 1$) of the excitation vectors, and P is a nonlinear square matrix of dimension $m \times m$.

The matrices P , Z , and Q are given by expressions (44) through (51).

$$Z = \begin{bmatrix} Z_1 \\ Z_2 \\ \vdots \\ \vdots \\ Z_{m-1} \\ Z \end{bmatrix} = \begin{bmatrix} A_1 \cos \alpha_1 \\ -A_1 \sin \alpha_1 \\ A_2 \cos \alpha_2 \\ -A_2 \sin \alpha_2 \\ \vdots \\ A_n \cos \alpha_n \\ -A_n \sin \alpha_n \end{bmatrix} \quad (44)$$

$$Q = \begin{bmatrix} Q_1 \\ Q_2 \\ \vdots \\ Q_{m-1} \\ Q_m \end{bmatrix} = \begin{bmatrix} S_1(R_{11} \cos \delta_1 + R_{21} \sin \delta_1) \\ S_2(R_{11} \sin \delta_1 - R_{21} \cos \delta_1) \\ \vdots \\ S_n(R_{1n} \cos \delta_n + R_{2n} \sin \delta_n) \\ S_n(R_{1n} \sin \delta_n + R_{2n} \cos \delta_n) \end{bmatrix} \quad (45)$$

In the matrices we further have:

$$\begin{aligned} P_{v1} = k_{2v} + k_{3v} + k_{3,v-1} - m_2 \omega^2 \\ - \frac{k_{1v} m_{1v} \omega^2 [(1+\eta)^2 k_{1v} - m_{1v} \omega^2]}{(k_{1v} - m_{1v} \omega^2)^2 + (k_{1v} \eta)^2} \quad (46) \end{aligned}$$

$$\begin{aligned} P_{v2} = \eta k_{2v} + \eta_1 (k_{3v} + k_{3,v-1}) \\ + \frac{\eta k_{1v} m_{1v}^2 \omega^4}{(k_{1v} - m_{1v} \omega^2)^2 + (k_{1v} \eta)^2} \end{aligned}$$

$$A_v = \sqrt{(Z_{2v-1})^2 + (Z_{2v})^2} \quad (54)$$

$$D_v = \{S_v^2 + A_v^2 K_{1v}^2 (1+n^2) + 2A_v S_v K_{1v} [\cos(\delta_v - \alpha_v) + n \sin(\delta_v - \alpha_v)]\}^{1/2} [(K_{1v} - m_{1v} \omega^2)^2 + (K_{1v} n)^2]^{-1/2} \quad (55)$$

$$\alpha_v = \arctan \left(\frac{-Z_{2v}}{Z_{2v-1}} \right) \quad (56)$$

$$Y_v = \arctan \left[\frac{(S_v (K_{1v} - m_{1v} \omega^2) \sin \delta_v - K_{1v} n \cos \delta_v) + A_v K_{1v} \sin \alpha_v [K_{1v} (1+n^2) - m_{1v} \omega^2] - A_v \cos \alpha_v m_{1v} K_{1v} n \omega^2}{(S_v (K_{1v} - m_{1v} \omega^2) \cos \delta_v + K_{1v} n \sin \delta_v) + A_v K_{1v} \cos \alpha_v [K_{1v} (1+n^2) - m_{1v} \omega^2] + A_v \sin \alpha_v m_{1v} K_{1v} n \omega^2} \right] \quad (57)$$

$$v = 1, \dots, n$$

ACKNOWLEDGMENT

The authors wish to thank Louise Farren, University of Dayton Research Institute, for typing the manuscript; Reed Mihalow, Aeronautical Systems Division Computer Center, for the graphics; In Sook Oh, University of Dayton Research Institute, for the drafting; M. Lake and R. Darrah of Universal Energy Systems Inc., Dayton, Ohio, for administrative coordination; and AFWAL/MLLN, Wright-Patterson Air Force Base, Ohio, for financial support. Finally, thanks are due to Dale H. Whitford, University of Dayton Research Institute, for his encouragement.

VIBRATIONS OF A BEAM UNDER MOVING LOADS BY A FINITE ELEMENT
FORMULATION CONSISTENT IN TIME AND SPATIAL COORDINATES

Julian J. Wu
U.S. Army Armament Research and Development Command
Large Caliber Weapon Systems Laboratory
Benet Weapons Laboratory
Watervliet, NY 12189

A finite element formulation, which discretizes the time dimension in the same manner as it does to the spatial dimension, is presented and applied to the vibration analysis of elastic beams under moving load and to the lateral motions of a gun tube affected by a moving projectile. The procedure is based on an unconstrained variational approach. Bi-cubic polynomials are used as element shape functions. "Stiffness" matrices and "force" vectors integrated both in time and spatial coordinates are described. The versatility of this formulation is demonstrated by numerical results obtained for moving loads with constant and variable velocity beams with sundry support conditions and with differential equations which can be nonself-adjoint and with variable coefficients. Numerical convergence of several simple cases have been verified with a series solution. Results of motions of a typical cannon tube are included.

INTRODUCTION

A general and versatile procedure is introduced and applied to vibration analysis of beams subjected to moving loads. Depending on the range of speed and acceleration of the load, this problem is often associated with the design and analysis of rails and bridges affected by moving vehicles, tracks for rocket-firing and the gun barrel dynamics as affected by a moving projectile. Most of the work in the existing literature are concerned with railroad structures (see, for example reference [1] and many papers cited therein from the year 1911 to 1971). Recently, application of this mathematical model has been extended to gun dynamics analysis [2,3].

Only linear problems will be considered in this paper. The basic differential equation is that of a Euler-Bernoulli beam including inertia effect. This equation can be modified to include structural damping, elastic foundation and axial force. There can be a wide range of support conditions. Frequently, the reality of multiple spans of a beam must be dealt with. Finally, there are the moving loads. These loads may be concentrated or varying in spatial as well as in time coordinates. They may be moving with constant or varying speeds. If the moving load is associated with a mass, the inertia effect must be included. Classical analyses on the dynamic behavior of beams with moving loads were usually carried out either by eigenfunction expansions (with appropriate

boundary conditions), or, by transform methods. These approaches are ad hoc and have many restrictions. On the other hand, the finite element method has not yet been exploited to its full potential in solving transient dynamic problems which are of our concern here.

In Section 2, the partial differential equation of an Euler-Bernoulli beam subjected to a moving force and on elastic foundation and that of a gun tube motions are stated. These equations are nondimensionalized; and the normalized parameters are introduced for the convenience of parametric studies and for generality. The moving mass problem can be considered as a special case of the gun motion equation. In Section 3, the variational problems equivalent to the stated differential equations and a general set of end conditions are presented. One special feature of the present formulation is that all the end conditions - i.e., boundary as well as initial condition are made to be natural "boundary" conditions through the use of some large "spring" constants, or the so called penalty functions method in optimization theories. Based on these variational problems, a finite element discretization is implemented. This is outlined in Section 4. The shape function is chosen to be a product of two third order (hermitian) polynomials, one in spatial coordinates and the other in time. This element shape function has been used previously with success in conjunction with a heat conduction problem [4]. Some numerical results obtained by the present formulation are presented in Section 5. The moving force

problem with constant velocity is studied with various velocities. The results are compared with a series solution. Then the effect of acceleration is examined. The solutions to a beam on elastic foundation, a two-span beam and that of a moving mass, are presented. Finally some calculations for the motion of a typical cannon tube are presented.

2. DIFFERENTIAL EQUATIONS AND NONDIMENSIONALIZATION

2.1. Moving Force on a Beam on Elastic Foundation

Let us begin with the differential equation of a uniform Euler-Bernoulli beam on elastic foundation subjected to a moving, concentrated force.

$$EIy'''' + ky + \rho Ay = P\delta(x_p - x) \quad \begin{matrix} 0 < x < l \\ 0 < t < T \end{matrix} \quad (1)$$

where

- E, ρ = Young's modulus, density of the beam material
- I, A = second moment, area of the beams cross-section
- l = length of the beam
- $y = y(x, t)$ = beam deflection
- x, t = coordinates in beams' axial direction and in time
- P = magnitude of the concentrated force
- $\delta(x)$ = Dirac delta function
- $x_p = x_p(t)$ = location of P
- T = some finite time of interest
- k = spring constant of the foundation

As usual, a prime (') denotes differentiation with respect to x ; and a dot (·), differentiation with respect to time t .

It is convenient to employ nondimensional parameters and equations. These will be introduced by way of eq. (1). The nondimensional parameters will first be identified by an asterisk (*). When everything appears with an asterisk at the end of nondimensionalization, we then drop all the asterisks to save some writing, but with the realization that they are now nondimensional quantities. Thus, let

$$y^* = y/l, \quad x^* = x/l, \quad t^* = t/T \quad (2)$$

Use (2) in (1), one has

$$y^{*''''} + k^*y^* + \gamma^2y^* = Q\delta(x_p^* - x^*) \quad \begin{matrix} 0 < x^* < 1 \\ 0 < t^* < 1 \end{matrix} \quad (3)$$

where

$$k^* = \frac{k l^4}{EI}, \quad \gamma = \frac{c}{T} \quad (4)$$

$$c^2 = \frac{\rho A l^4}{EI}, \quad Q = P^* = \frac{P l^2}{EI}$$

Also note in eq. (3) that the differentiations are now with respect to the nondimensionalized variables x^* and t^* . From now on, we shall use eq. (3) with the asterisks dropped altogether.

$$y'''' + ky + \gamma^2y = Q\delta(x_p - x) \quad \begin{matrix} 0 < x < 1 \\ 0 < t < 1 \end{matrix} \quad (5)$$

2.2. Gun Tube Dynamics and Moving Mass Problems

The second differential equation considered here is that of gun tube vibration. We shall simply introduce the equation and state the meaning of each term. The detailed derivations of this equation are given in reference [2].

$$(EIy'')'' - [P(x, t)y']' + \rho Ay = -\bar{P}(x, t)H(x_p - x) - m_p[\ddot{x}_p^2 y'' + 2\dot{x}_p \dot{y}' + \ddot{y}] \delta(x_p - x) - (m_p g \cos \alpha) \delta(x_p - x) - \rho A g \cos \alpha \quad (6)$$

Referring to Figure 1, $y(x, t)$ denotes the lateral motion of a gun tube approximated by a Euler-Bernoulli beam. Symbols in addition to those already defined in Section 2.1 are the following:

$$P(x, t) = \pi R^2(x) \rho(t)$$

$$R(x) = \text{inner tube radius}$$

$$p(t) = \text{bore pressure}$$

$$\bar{P}(x, t) = (-P(0, t) + g \sin \alpha \int_0^l \rho A dx) \frac{\int_x^l \rho A dx}{\int_1^l \rho A dx}$$

$$m_p, x_p = \text{projectile mass and velocity, respectively}$$

$$g = \text{gravitational acceleration}$$

$$\alpha = \text{elevation angle (see Figure 1)}$$

$$H(x) = \text{Heaviside step function}$$

$$x = x_p$$

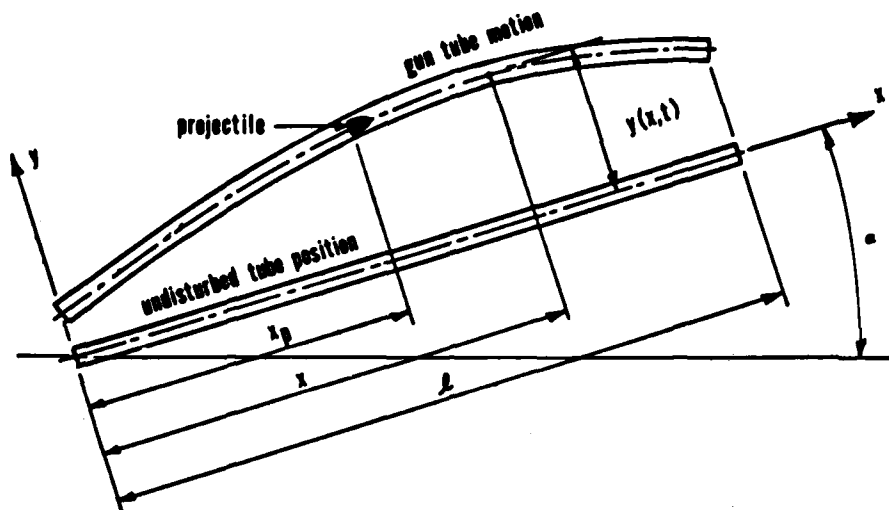


Fig. 1 - A schematic drawing of the gun tube motion problem

Assuming uniform cross-section for simplicity at the present time, the nondimensionalized equation of (6) can be written as

$$\begin{aligned} \underline{y''''} + (\underline{-P} + g \sin \alpha)[(1-x)y']' + \underline{\gamma^2 y''} \\ = \underline{-Py''}H(x-x) - \underline{\gamma^2 m[x^2 y'' + 2xy' + y]\delta(x-x)} \\ - (gm \cos \alpha)\delta(x-x) - g \cos \alpha \end{aligned} \quad (7)$$

where m is the projectile mass (normalized).

It is noted that, with only the terms underlined retaining, eq. (7) become one for a moving mass problem.

3. VARIATIONAL PROBLEMS AND END CONDITIONS

It is well known that many procedures for the obtaining of approximate solutions to initial and boundary value problems can be based either on some variational problems (principles) or on the concept of weighed residuals [5]. In case of self-adjoint problems, the two can be made equivalent to each other and the convergence proofs of such procedures are well established including finite element discretizations (see, for example [6]). The general proof of convergence of such procedures applied to non-self adjoint problems is not known to this writer except in some very special cases [7,8]. Since the problems considered in this paper are non-self adjoint in general, the solution procedure can be viewed as numerical experimentations. For many problems experimented,

including non-self adjoint boundary value problems and initial value problems, the results have been encouraging [4].

3.1. Moving Force Problems

To establish a desired variational problem, one begins with the given differential equation and perform integrations-by-parts upon the inner products formed by the equation and the variation of some properly chosen functions. In our procedure, the adjoint variable has been taken for this purpose. Thus, for the equation considered in Subsection 2.1, we have obtained the following variational problem.

$$\delta I(y, y^*) = 0 \quad (8a)$$

where

$$\begin{aligned} I = \int_0^1 \int_0^1 [y'' y^* - \gamma^2 y y^* + k y y^* - Q \delta(x_p - x) y^*] dx dt \\ + \int_0^1 [k_1 y(0, t) y^*(0, t) + k_2 y'(0, t) y^{*'}(0, t) \\ + k_3 y(1, t) y^*(1, t) + k_4 y'(1, t) y^{*'}(1, t) \\ + \int_0^1 [k_7] y(x, 0) - y_0(x) y^*(x, 1) \\ - y_1(x) y^*(x, 0)] dx \end{aligned} \quad (8b)$$

where $y^*(x, t)$ is a function "adjoint" to $y(x, t)$ [9]. By carrying out the first variations of eqs. (8) and at the same time restraining the original function $y(x, t)$ from varying at all, one arrives at:

$$\delta I = 0$$

$$\begin{aligned} &= \int_0^1 \int_0^1 [y'''' + y + \gamma^2 y - Q\delta(x_p - x)] \delta y^* dx dt \\ &+ \int_0^1 \{ [y'''(0,t) + k_1 y(0,t)] \delta y^*(0,t) \\ &\quad - [y''(0,t) - k_2 y'(0,t)] \delta y^*(0,t) \\ &\quad - [y''(1,t) - k_3 y(1,t)] \delta y^*(1,t) \\ &\quad + [y''(1,t) + k_4 y'(1,t)] \delta y^*(1,t) \\ &\quad + k_5 y(x_s, t) \delta y^*(x_s, t) \} dt \\ &+ \int_0^1 \{ [-\dot{y}(x, 1) + k_7 (y(x, 0) - y_0(x))] \delta y^*(x, 1) \\ &\quad + [\dot{y}(x, 0) - y_1(x)] \delta y^*(x, 0) \} dx \quad (9) \end{aligned}$$

By virtue of the fundamental lemma of the calculus of variation [10] and the fact that $\delta y^*(x, t)$ is not restricted in any way whatever, eq. (9) leads to the recovery of the original differential equation plus the initial conditions:

$$\begin{aligned} y(x, 0) &= y_0(x) \\ \dot{y}(x, 0) &= y_1(x) \end{aligned} \quad (10)$$

a set of very general boundary conditions

$$y'''(0, t) + k_1 y(0, t) = 0, \quad y''(0, t) - k_2 y'(0, t) = 0 \quad (11)$$

$$y''(1, t) - k_3 y(1, t) = 0, \quad y''(1, t) + k_4 y'(1, t) = 0$$

and an intermediate support condition:

$$y(x_s, t) = 0 \quad (12)$$

It should be noted that the first eq. (10) and eq. (12) are valid only when k_7 and k_5 goes to infinity, respectively. This use of k_5 was employed previously with success in obtaining numerical solution to a simple heat conduction problem. It is also known as the penalty functions method in optimization theories for example, [11]). However, from our point of view, k_7 is an extension of k_1 , k_2 , etc. are simply the spring constants known to structural engineers long before the so called "penalty function method" came into being.

Thus, one has established the equivalence between a variational problem and an initial boundary problem for a particular set of parameters to be selected. For example, if one chooses $k_1 = k_2 = \infty$, $k_3 = k_4 = k_5 = 0$, the problem becomes a cantilevered beam without intermediate support.

3.2. Gun Motions and Moving Mass Problems. The variational associated with eq. (7) for gun tube motions can be written as follows:

$$\delta I = (\delta I)_y = \sum_{i=1}^{12} (\delta I_i)_y - \sum_{j=1}^3 (\delta J_j) = 0 \quad (13a)$$

with

$$I_1 = \int_0^1 \int_0^1 y'' y^* dx dt$$

$$I_2 = (\bar{P} - g \sin \alpha) \int_0^1 \int_0^1 (1-x) y' y^* dx dt$$

$$I_3 = -\gamma^2 \int_0^1 \int_0^1 y y^* dx dt$$

$$I_4 = -P \int_0^1 \int_0^1 y' y^* H(\bar{x}-x) dx dt$$

$$I_5 = -P \int_0^1 \int_0^1 y' y^* \delta(\bar{x}-x) dx dt$$

$$I_6 = -m\beta^2 \gamma^2 \int_0^1 \int_0^1 t y' y^* \delta(\bar{x}-x) dx dt$$

$$I_7 = -m\beta^2 \gamma^2 \int_0^1 \int_0^1 t y' y^* \delta'(\bar{x}-x) dx dt$$

$$I_8 = 2m\beta \gamma^2 \int_0^1 \int_0^1 t y' y^* \delta(\bar{x}-x) dx dt$$

$$I_9 = -m\gamma^2 \int_0^1 \int_0^1 y y^* \delta(\bar{x}-x) dx dt$$

$$I_{10} = -m\gamma^2 \int_0^1 \int_0^1 y y^* \delta'(\bar{x}-x) dx dt$$

$$\begin{aligned} I_{11} &= \int_0^1 \{ k_1 y(0, t) y^*(0, t) + k_2 y'(0, t) y^*(0, t) \\ &\quad + k_3 y(1, t) y^*(1, t) + k_4 y'(1, t) y^*(1, t) \} dt \end{aligned}$$

$$I_{12} = k_7 \int_0^1 y(x, 0) y^*(x, 1) dx \quad (13b)$$

and

$$J_1 = -g(\cos \alpha) \int_0^1 \int_0^1 y^* dx dt$$

$$J_2 = -gm(\cos \alpha) \int_0^1 \int_0^1 y^* \delta(\bar{x}-x) dx dt$$

$$J_3 = k_7 \int_0^1 Y(x) y^*(x, 1) dx \quad (13c)$$

Similar to eqs. (11) and (12), the boundary and initial conditions turn out to be respectively:

$$y''(0,t) - k_2 y'(0,t) = 0$$

$$y''(1,t) + k_4 y'(1,t) = 0$$

$$y''(0,t) + k_1 y(0,t) + (-\bar{P} + g \cos \alpha) y'(0,t)$$

$$+ \bar{P} y'(0,t) H(\bar{x}(t)) + m \delta^2 y'(0,t) \delta(\bar{x}(t)) = 0$$

$$y''(1,t) - k_3 y(1,t) + \bar{P} y'(1,t) H(\bar{x}(t)-1)$$

$$+ m \delta^2 y'(1,t) \delta(\bar{x}(t)-1) = 0 \quad (14a)$$

and

$$\dot{y}(x,0) = 0$$

$$\dot{y}(x,1)[1 + m \delta(\bar{x}(1)-x)] + k_7 [y(x,0) - Y(x)] = 0 \quad (14b)$$

It is noted that with I_2 , I_5 , and I_6 dropped in eqs. (13), the problem becomes that of a moving mass including the inertia of the beam.

Equations (19) and (13) are then the bases from which the numerical procedures are established.

4. FEATURES IN FINITE ELEMENT DISCRETIZATION

4.1. Local Coordinates and Shape Functions

As the normalized parameters are used, the domain of interest of a problem is always a unit square. The elements then consist of the sub rectangles resulting from a division into K equal segments in x -direction and one into L equal segments in t -direction. A typical element scheme is shown in Figure 2. The relation

between global coordinates (x,t) and local (ξ,n) of the $(i,j)^{th}$ element can be written as

$$\xi = \xi(i) = Kx - i+1 \quad (15)$$

$$n = n(j) = Lt - j+1$$

In terms of local coordinates, eq. (9) becomes

$$\begin{aligned} & \sum_{i=1}^K \sum_{j=1}^L \int_0^1 \int_0^1 \left[\frac{K^3}{L} y''(i,j) \delta y^{*''}(i,j) \right. \\ & \quad \left. - \frac{\gamma^2 L}{K} y(i,j) \delta y^{*}(i,j) \right] d\xi dn \\ & + \sum_{j=1}^L \int_0^1 dn \left[\frac{k_1}{L} y(i,j)(0,n) \delta y^{*}(i,j)(0,n) \right. \\ & \quad \left. + k_2 \frac{K^2}{L} y'(i,j)(0,n) \delta y^{*'}(i,j)(0,n) \right. \\ & + \sum_{i=1}^K \int_0^1 \frac{d\xi}{K} [\gamma^2 k_5 y(i,j)(\xi,0) \delta y^{*}(i,j)(\xi,1)] \\ & = \sum_{i=1}^K \sum_{j=1}^L \frac{Q}{L} \int_0^1 \int_0^1 \bar{\delta}(x-\bar{x}) \delta y^{*}(i,j)(\xi,n) d\xi dn \\ & + \sum_{i=1}^K \frac{\gamma^2 k_5}{K} \int_0^1 d\xi [Y(i)(\xi) \delta y^{*}(iL)(\xi,1)] \quad (16) \end{aligned}$$

The shape function vector is now introduced. Let

$$y(i,j)(\xi,n) = \underline{a}^T(\xi,n) \underline{Y}(i,j) \quad (17)$$

$$y^{*}(i,j)(\xi,n) = \underline{a}^T(\xi,n) \underline{Y}^{*}(i,j) = \underline{Y}^{*T}(i,j) \underline{a}(\xi,n)$$

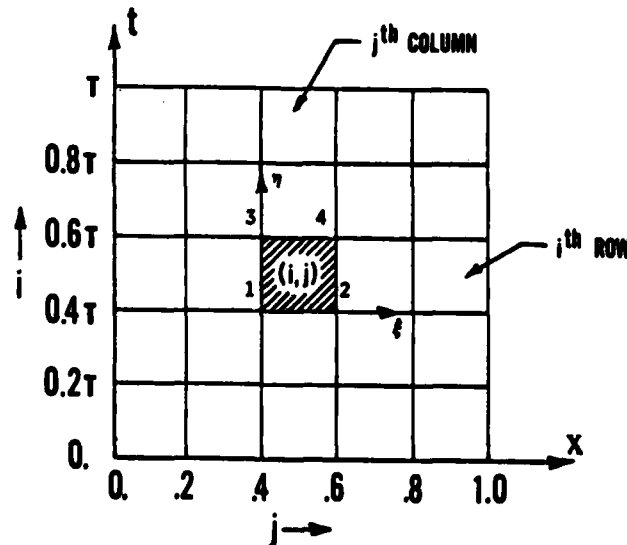


Fig. 2 - A typical finite element grid scheme showing and the global, local coordinates

In this present work, we have chosen $a(\xi, \eta)$ to be in the following form:

$$a_m(\xi, \eta) = b_p(\xi)b_q(\eta) \quad \begin{matrix} m = 1, 2, \dots, 16 \\ p, q = 1, 2, 3, 4 \end{matrix} \quad (18a)$$

with

$$\begin{aligned} b_1(\xi) &= 1 - 3\xi^2 + 2\xi^3 \\ b_2(\xi) &= \xi - \xi^2 + \xi^3 \\ b_3(\xi) &= 3\xi^2 - 2\xi^3 \\ b_4(\xi) &= -\xi^2 + \xi^3 \end{aligned} \quad (18b)$$

As a result of this choice of shape functions, the generalized coordinates $Y_{(1j)}$ for the $(1, j)^{th}$ element can be written as

$$\begin{aligned} \underline{Y}^T_{(1j)} &= \{Y_1 \ Y_2 \ \dots \ Y_{16}\}_{(1j)} \quad (19) \\ &= \{(y \ y, \xi \ y, \eta \ y, \xi \eta)_1 \ (y \ y, \xi \ y, \eta \ y, \xi \eta)_2 \\ &\quad (y \ y, \xi \ y, \eta \ y, \xi \eta)_3 \ (y \ y, \xi \ y, \eta \ y, \xi \eta)_4\} \end{aligned}$$

where the superscript T denotes the transpose of a matrix (in this case, a vector) and the subscripts 1, 2, 3, and 4 indicate the local nodes also shown in Figure 2. The correspondence between the index m and the pair (p, q) in eq. (18a) is given in Table I below.

Table I. Correspondence Between (p, q) and m in Displacement Functions $a_m(\xi, \eta) = b_p(\xi)b_q(\eta)$

m	(p, q)	m	(p, q)
1	(1, 1)	9	(1, 3)
2	(2, 1)	10	(2, 3)
3	(1, 2)	11	(1, 4)
4	(2, 2)	12	(2, 4)
5	(3, 1)	13	(3, 3)
6	(4, 1)	14	(4, 3)
7	(3, 2)	15	(3, 4)
8	(4, 2)	16	(4, 4)

With shape functions introduced above, we shall describe the obtaining of element "stiffness", "mass" matrices and element "force" vector which involves integrations in time as well as in spatial coordinates in the next subsection.

4.2. Stiffness Matrices and Force Vectors Integrated in Time and Space Coordinates

Substituting eq. (17) into (16), one has

$$\begin{aligned} &\sum_{i=1}^K \sum_{j=1}^L \delta \underline{Y}^{*T}_{(1j)} \left\{ \frac{K^3}{L} \underline{A} - \frac{\gamma^2 L}{K} \underline{B} \right\} \underline{Y}_{(1j)} \\ &+ \sum_{i=1}^L \delta \underline{Y}^{*T}_{(1j)} \left\{ \frac{k_1}{L} \underline{B}_1 + \frac{k_2 K^2}{L} \underline{B}_2 \right\} \underline{Y}_{(1j)} \end{aligned}$$

$$\begin{aligned} &+ \sum_{i=1}^L \delta \underline{Y}^{*T}_{(Kj)} \left\{ \frac{k_3}{L} \underline{B}_3 + \frac{k_4 K^2}{L} \underline{B}_4 \right\} \underline{Y}_{(1j)} \\ &+ \sum_{i=1}^K \delta \underline{Y}^{*T}_{(1L)} \left\{ \frac{\gamma^2 k_5}{K} \underline{B}_5 \right\} \underline{Y}_{(1L)} \\ &= \sum_{i=1}^K \sum_{j=1}^L \delta \underline{Y}^{*T}_{(1j)} \frac{Q}{L} \underline{F}_{(1j)} \\ &+ \sum_{i=1}^K \delta \underline{Y}^{*T}_{(1L)} \frac{\gamma^2 k_5}{K} \underline{G}_{(1)} \quad (20) \end{aligned}$$

where, as it can be seen easily, that

$$\begin{aligned} \underline{A} &= \int_0^1 \int_0^1 a_{, \xi \xi} a_{, \xi \xi}^T d\xi d\eta \\ \underline{B} &= \int_0^1 \int_0^1 a_{, \eta} a_{, \eta}^T d\xi d\eta \\ \underline{B}_1 &= \int_0^1 a(0, \eta) a^T(0, \eta) d\eta \\ \underline{B}_2 &= \int_0^1 a_{, \xi}(0, \eta) a_{, \xi}^T(0, \eta) d\eta \\ \underline{B}_3 &= \int_0^1 a(1, \eta) a^T(1, \eta) d\eta \\ \underline{B}_4 &= \int_0^1 a_{, \xi}(1, \eta) a_{, \xi}^T(1, \eta) d\eta \\ \underline{B}_5 &= \int_0^1 a(\xi, 1) a^T(\xi, 0) d\xi \quad (21) \end{aligned}$$

and

$$\begin{aligned} \underline{F}_{(1j)} &= \int_0^1 \int_0^1 a(\xi, \eta) \delta_{(1j)}(\xi - \bar{\xi}) d\xi d\eta \\ \underline{G}_{(1)} &= \int_0^1 a(\xi, 1) Y_{(1)}(\xi) d\xi \quad (22) \end{aligned}$$

It is noted that the matrix \underline{A} , in eq. (21) is analogous to the usual stiffness matrix except now, it also includes the integration in the time dimension. The matrix \underline{B} is the corresponding "mass" matrix, etc. These matrices are easily obtained. However, we shall describe the procedure of obtaining the "force" vector $\underline{F}_{(1j)}$ in eq. (22) in some detail:

$$\underline{F}_{(1j)} = \int_0^1 \int_0^1 a(\xi, \eta) \delta_{(1j)}(\xi - \bar{\xi}) d\xi d\eta \quad (23)$$

where the components of a is given in eq. (18a). Note that equation (18b) can be written as

$$b_p(\xi) = \sum_{p'=1}^4 b_{pp'} \xi^{p'-1} \quad (24)$$

and the value of $b_{pp'}$ can be tabulated as in Table II.

Table II. Values of $b_{pp'}$ in Equation (24)

$p \backslash p'$	1	2	3	4
1	1	0	-3	1
2	0	1	-2	1
3	0	0	3	-2
4	0	0	-1	1

Now, let us consider $\bar{\delta}_{(ij)}(\xi-\bar{\xi})$. This "function" represents the effect of the Dirac delta function $\delta(x-\bar{x})$ in the (ij)th element. If the curve of travel $x = x(t)$ does not go through the element (i,j), $\bar{\delta}_{(ij)}(\xi-\bar{\xi}) = 0$. If it passes through that element, one has

$$\bar{\delta}_{(ij)}(\xi-\bar{\xi}) = \delta(x-\bar{x}) = K\delta(\xi-\bar{\xi}) \quad (25a)$$

with

$$\bar{\xi} = \bar{\xi}(\eta) \quad (25b)$$

The function $\bar{\xi}(\eta)$ is derived from $\bar{x} = \bar{x}(t)$. For example, if the force moves with a constant velocity, one has

$$\bar{x} = \bar{x}(t) = vt \quad (26a)$$

it follows from Eqs. (15) that

$$\bar{\xi} = \bar{\xi}(\eta) = -i+1 + \frac{vK}{L} (\eta+j-1) \quad (26b)$$

With Eqs. (18), (24), (25), and (26), one writes (23) as

$$F_{(ij)k} = K \int_0^1 \int_0^1 a_k(\xi, \eta) \bar{\delta}(\xi-\bar{\xi}) d\xi d\eta \quad (27a)$$

$$F_{(ij)k} = \sum_{p=1}^4 \sum_{q=1}^4 K \int_0^1 \int_0^1 b_{ip} b_{jq} \xi^{p-1} \eta^{q-1} \bar{\delta}(\xi-\bar{\xi}) d\xi d\eta \quad (27b)$$

Equation (27) can then be evaluated easily once the exact form of $\bar{\xi}$ is written. For example, if $\bar{\xi} = \eta$, Eq. (27) reduces to

$$\begin{aligned} F_{(ij)k} &= \sum_{p=1}^4 \sum_{q=1}^4 K b_{ip} b_{jq} \int_0^1 \xi^{p+q-2} d\xi \\ &= \sum_{p=1}^4 \sum_{q=1}^4 \frac{K b_{ip} b_{jq}}{p+q-1} \end{aligned} \quad (28)$$

With all element matrices and force vectors in eqs. (20), (21), and (22) evaluated one can routinely assemble the global scalar equation

$$\delta Y^* T K Y = \delta Y^* F \quad (29)$$

By virtue of the fact that δY^* is not subjected to any constrained conditions, one has

$$K Y = F \quad (30)$$

which can then be solved routinely.

The assembling of equations for a gun dynamics problem is more involved. The basic procedures, however, are the same. We shall omit such details here.

5. NUMERICAL RESULTS

The solution formulation presented in the previous section clearly can be applied to a wide range of problems. Here in this Section, a number of demonstrative examples will now be given.

5.1. Moving Force With Constant Velocity

First, let us consider a simply supported beam subjected to a moving force with a constant velocity

$$v = \frac{l}{T}$$

As T varies from ∞ to 0, the velocity varies from 0 to ∞ .

It will be helpful to compare v with some reference velocity which is a characteristic of the given beam. It is known that for a simply-supported beam, the first mode of vibration has a frequency (see, for example, [1])

$$f_1 = \frac{\omega}{2\pi} = \frac{1}{2\pi} \left(\frac{\pi^2}{c} \right) = \frac{\pi}{2c} \quad (\text{cycles per seconds})$$

and the corresponding period,

$$T_1 = \frac{2c}{\pi} = \frac{2l^2}{\pi} \sqrt{\frac{\rho A}{EI}}$$

The letter symbols l , T , and C all have been defined in Section 2.

The velocity of the flexural waves corresponding to the first mode is

$$v_1 = 2lf_1 = \frac{\pi l}{c}$$

Hence the relative velocity of the moving load is defined by

$$\frac{v}{v_1} = \frac{v}{\frac{\pi l}{c}} = \frac{c}{\pi T} = \frac{T_1}{2T}$$

In several examples to follow, the value of c is taken to be unity (1.0 sec.).

Thus

$$f_1 = \frac{\pi}{2} = 1.578 \text{ Hz} ; T_1 = 0.6367 \text{ sec.}$$

and

$$\frac{v}{v_1} = \frac{1}{\pi T}$$

For $T = 100$ sec. or more, the relative velocity \bar{v} ($= 0.0032$ or less), the solution of beam's deflection are almost purely static. The results for $T = 10^{10}$ and for $T = 100$ are shown in Tables III and IV and also in Figure 3. For $T = 0.1$ sec. and 0.05 sec. ($\bar{v} = 3.2$ and $\bar{v} = 6.4$ respectively), the dynamic effect becomes evident as shown in Figures 4 and 5 and also in Tables V and VI with various values of T . These solutions agree quite well with a Fourier series solution [1] given in parentheses in these Tables mentioned. It should also be pointed out that the grid scheme used is 4×4 , a rather coarse one. The spring constants used for a simply supported beam are that

$$k_1 = k_3 = 10^{10}$$

$$k_2 = k_4 = 0$$

and for the initial condition to converge to zero displacement, the value $k_7 = 10^{10}$ was used.

Table IV. Deflection of a Simply Supported Beam Under a Moving Load
 $T = 100$ sec., Constant Velocity

$y(x,t)/l$ [$x 10^{-1}$]

x/l t/T	0.	0.25	0.50	0.75	1.00
0.	0. (0.)	0. (0.)	0. (0.)	0. (0.)	0. (0.)
0.25	0. (0.)	.1172 (.1167)	.1432 (.1426)	.0911 (.0907)	0. (0.)
0.50	0. (0.)	.1431 (.1433)	.2082 (.2085)	.1431 (.1434)	0. (0.)
0.75	0. (0.)	.0908 (.0916)	.1427 (.1438)	.1168 (.1176)	0. (0.)
1.00	0. (0.)	-.0047 (-.0002)	-.0066 (-.0003)	-.0046 (-.0002)	0. (0.)

Table V. Deflection of a Simply Supported Beam Under a Moving Force
 $T = 1.0$ sec., Constant Velocity

$y(x,t)/l$ [$x 10^{-1}$]

x/l t/T	0.	0.25	0.50	0.75	1.00
0.	0. (0.)	0. (0.)	0. (0.)	0. (0.)	0. (0.)
0.25	0. (0.)	.0949 (.0980)	.1135 (.1141)	.0711 (.0694)	0. (0.)
0.50	0. (0.)	.2056 (.2080)	.3040 (.3026)	.2149 (.2113)	0. (0.)
0.75	0. (0.)	.0387 (.0583)	.0952 (.0940)	.0964 (.0809)	0. (0.)
1.00	0. (0.)	-.1020 (.0200)	.0519 (.0315)	.1157 (.0241)	0. (0.)

Table III. Deflection of a Simply Supported Beam Under a Moving Force*
 $T = 10^{10}$ sec., Constant Velocity

$y(x,t)/l$ [$x 10^{-1}$]

x/l t/T	0.	0.25	0.50	0.75	1.00
0.	0.	0.	0.	0.	0.
0.25	0.	0.11719	0.1432	0.09115	0.
0.50	0.	0.14323	0.2083	0.14323	0.
0.75	0.	0.09115	0.1432	0.11719	0.
1.00	0.	0.	0.	0.	0.

*Results identical to static deflection for at least the number of digits shown.

Table VI. Deflection of a Simply Supported Beam Under a Moving Force
 $T = 0.1$ sec., Constant Velocity

$y(x,t)/L [\times 10^{-2}]$

$x/L \backslash t/T$	0.	0.25	0.50	0.75	1.00
0.	.0 (.0)	.0 (.0)	.0 (.0)	.0 (.0)	.0 (.0)
0.25	.0 (.0)	.0619 (.0645)	-.0148 (-.0149)	.0043 (.0033)	.0 (.0)
0.50	.0 (.0)	.2002 (.1952)	.1228 (.1262)	-.0494 (-.0479)	.0 (.0)
0.75	.0 (.0)	.3007 (.2929)	.3837 (.3849)	.0770 (.0801)	.0 (.0)
1.00	.0 (.0)	.4601 (.4018)	.4912 (.4880)	.5767 (.5959)	.0 (.0)

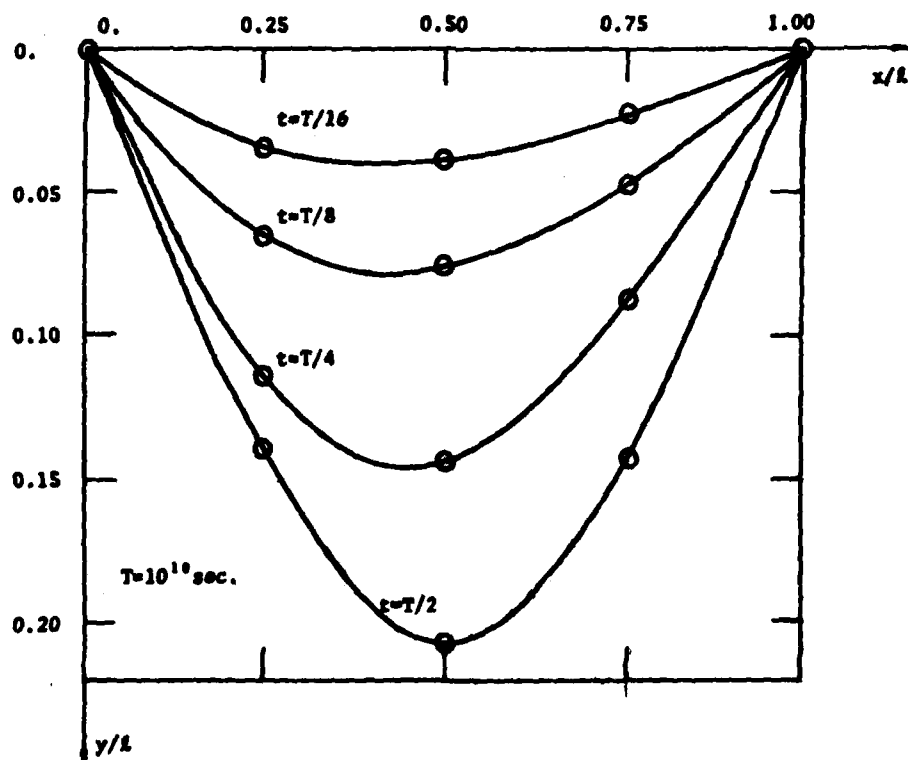


Fig. 3 - Deflection of a simply supported beam under a moving force:
 constant velocity, $T = 10^{10}$ sec. (cf. $T_1 = 0.637$ sec.)

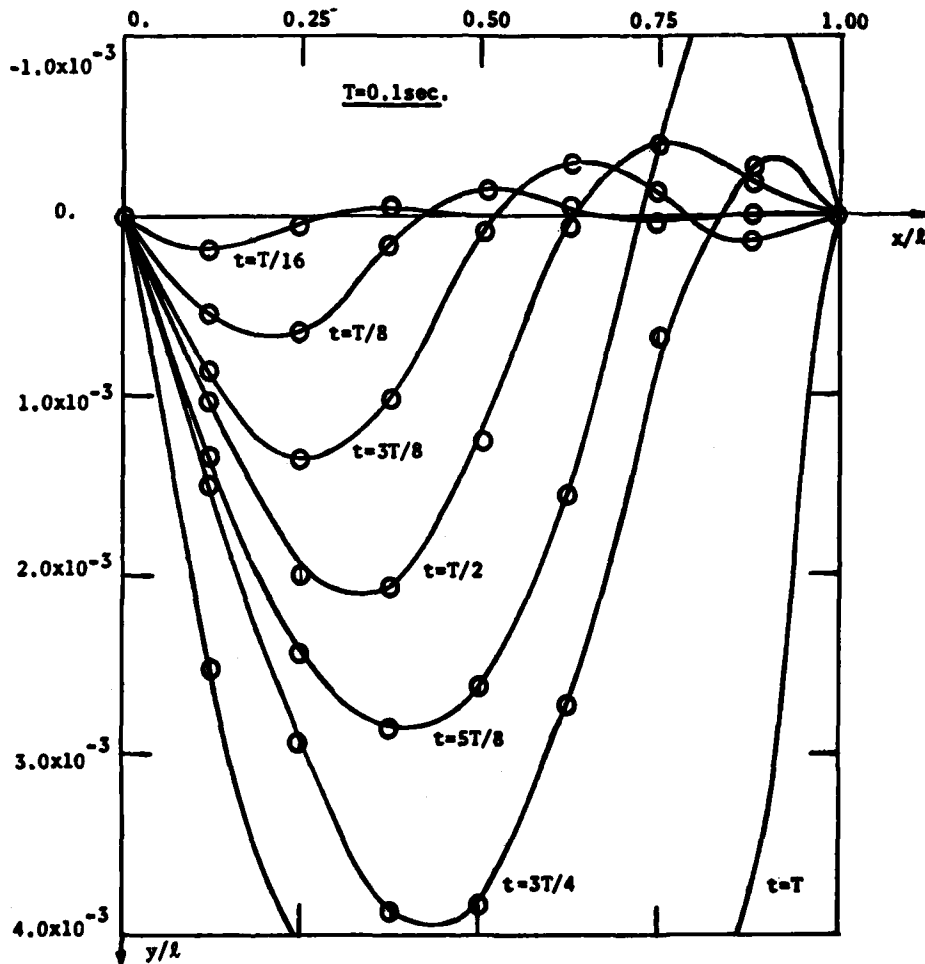


Fig. 4 - Deflection of a simply supported beam under a moving force: constant velocity, $T = 0.1$ sec. (cf. $T_1 = 0.637$ sec.)

For a cantilevered beam, one only needs to replace k_1 , $1 = 1, 2, 3,$ and $4,$ with the following set

$$k_1 = k_2 = 10^{10}$$

$$k_3 = k_4 = 0$$

Solutions similar to the simply supported beam are shown in Tables VII, VIII, and IX (Figures 6, 7, and 8) for $T = 10^{10}$, $T = 1.0$, $T = 0.1$ and $T = 0.05$ sec. As before, the case for $T = 100$ sec. or more the results are almost purely static. But in the case for $T = 0.1$ and 0.05 , the dynamic effect becomes evident.

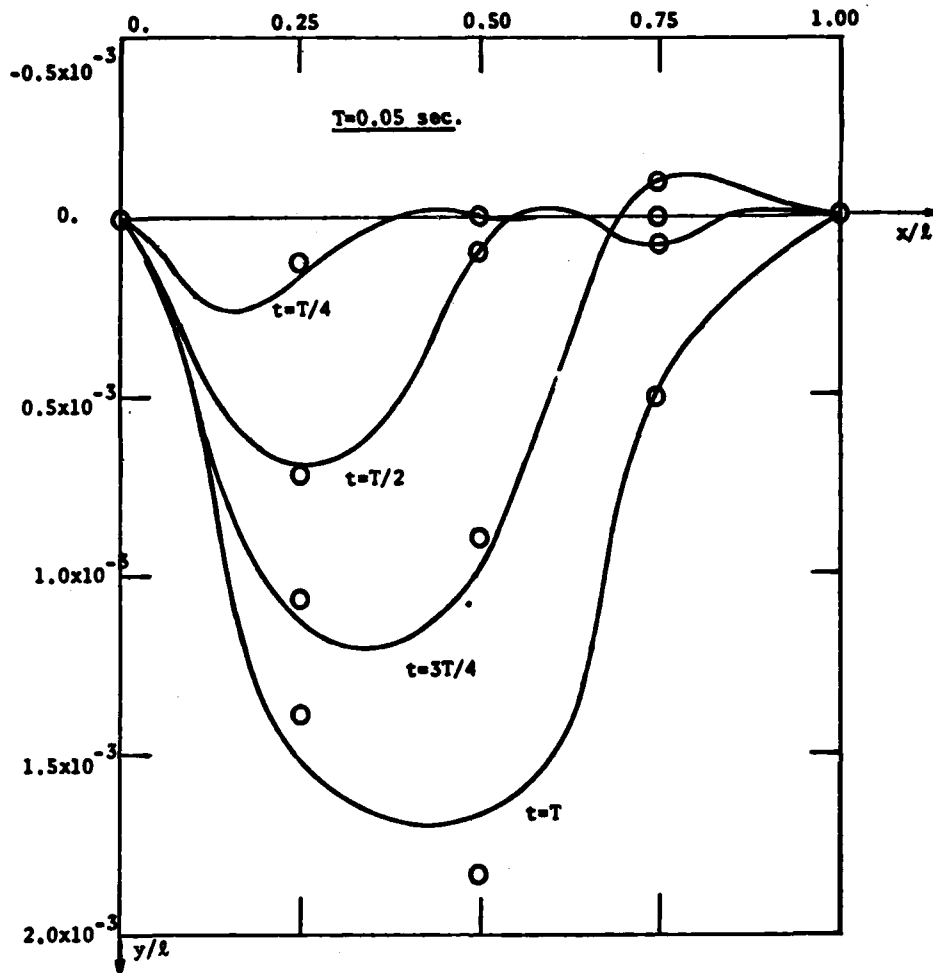


Fig. 5 - Deflection of a simply supported beam under a moving force: constant velocity, $T = 0.5 \text{ sec.}$ (cf. $T_1 = 0.637 \text{ sec.}$)

Table VII. Deflection of a Cantilevered Beam Under a Moving Force*
 $T = 10^{10} \text{ sec.}$, Constant Velocity

$y(x,t)/l \text{ [} \times 10^{-1} \text{]}$

$x/l \backslash t/T$	0.	0.25	0.50	0.75	1.00
0.	0.	0.	0.	0.	0.
0.25	0.	0.05208	0.13021	0.20833	0.28646
0.50	0.	0.13021	0.41667	0.72917	1.04167
0.75	0.	0.20833	0.72917	1.40625	2.10938
1.00	0.	0.28646	1.04167	2.10938	3.33333

*Results identical to static deflection for at least the number of digits shown.

Table VIII. Deflection of a Cantilevered Beam Under a Moving Force
 $T = 1.0$ sec., Constant Velocity

$$y(x,t)/l \text{ [} \times 10^{-1} \text{]}$$

$x/l \backslash t/T$	0.	0.25	0.50	0.75	1.00
0.	0.	0.	0.	0.	0.
0.25	0.	0.02522	0.03512	0.01532	-0.01155
0.50	0.	0.05213	0.14333	0.12242	1.22543
0.75	0.	0.11526	0.39630	1.76307	1.13685
1.00	0.	0.28681	1.84846	1.77227	2.85636

Table IX. Deflection of a Cantilevered Beam Under a Moving Force
 $T = 0.1$ sec., Constant Velocity

$$y(x,t)/l \text{ [} \times 10^{-2} \text{]}$$

$x/l \backslash t/T$	0.	0.25	0.50	0.75	1.00
0.	0.	0.	0.	0.	0.
0.25	0.	0.0402	-0.0082	0.0021	-0.0006
0.50	0.	0.1161	0.1162	-0.0454	0.0544
0.75	0.	0.1561	0.2849	1.1623	-0.2216
1.00	0.	0.1079	1.4904	0.4668	-0.2138

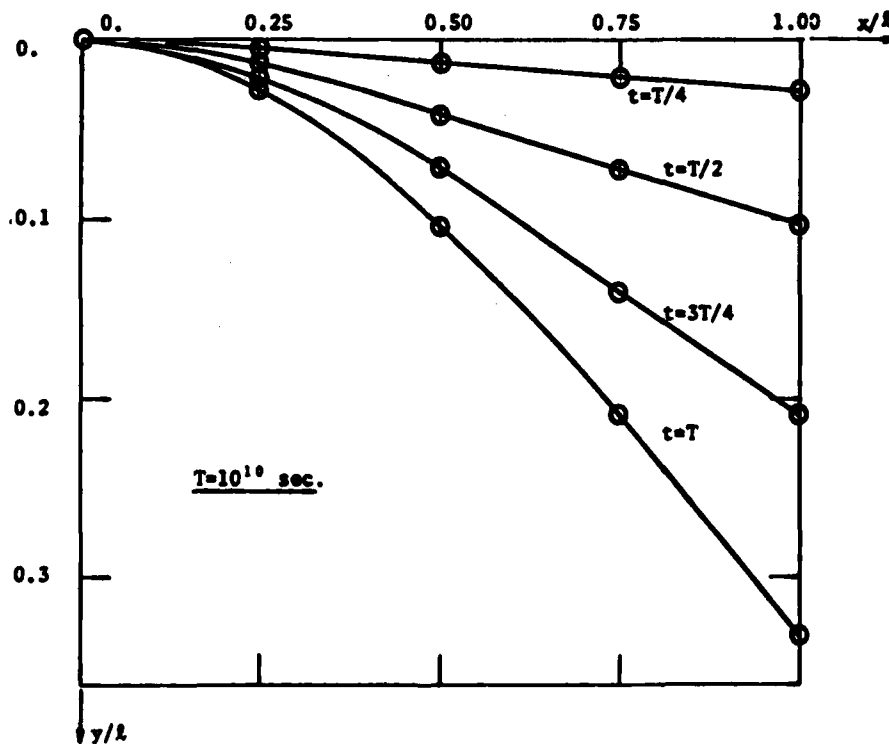


Fig. 6 - Deflection of a cantilevered beam under a moving force:
 constant velocity, $T = 10^{10}$ sec. (cf. $T_1 = 1.787$ sec.)

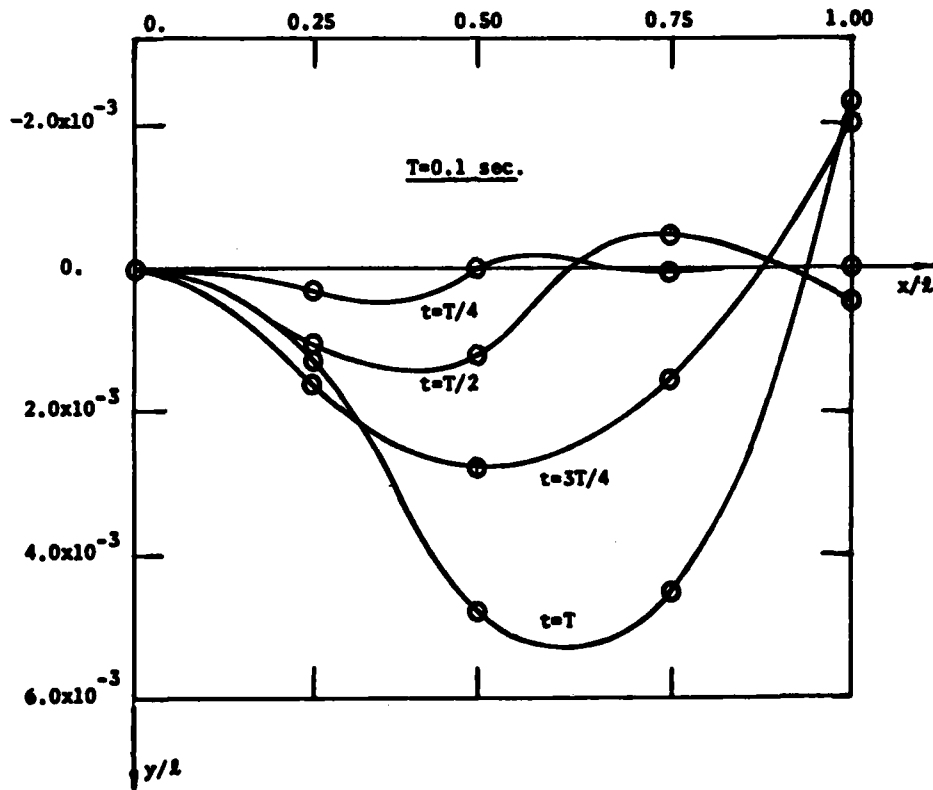


Fig. 7 - Deflection of a cantilevered beam under a moving force: constant velocity, $T = 0.1 \text{ sec.}$ (cf. $T_1 = 1.787 \text{ sec.}$)

Table X. Deflection of a Cantilevered Beam Under a Moving Force $T = 0.1 \text{ sec.}$, Constant Acceleration

$y(x,t)/l \text{ [} \times 10^{-2} \text{]}$

$x/l \backslash t/T$	0.	0.25	0.50	0.75	1.00
0.	0.	0.	0.	0.	0.
0.25	0.	0.0611	-0.0111	0.0181	0.
0.50	0.	0.1036	0.0704	-0.0327	0.
0.75	0.	0.2306	0.1746	-0.0656	0.
1.00	0.	0.3153	1.3872	0.1522	0.

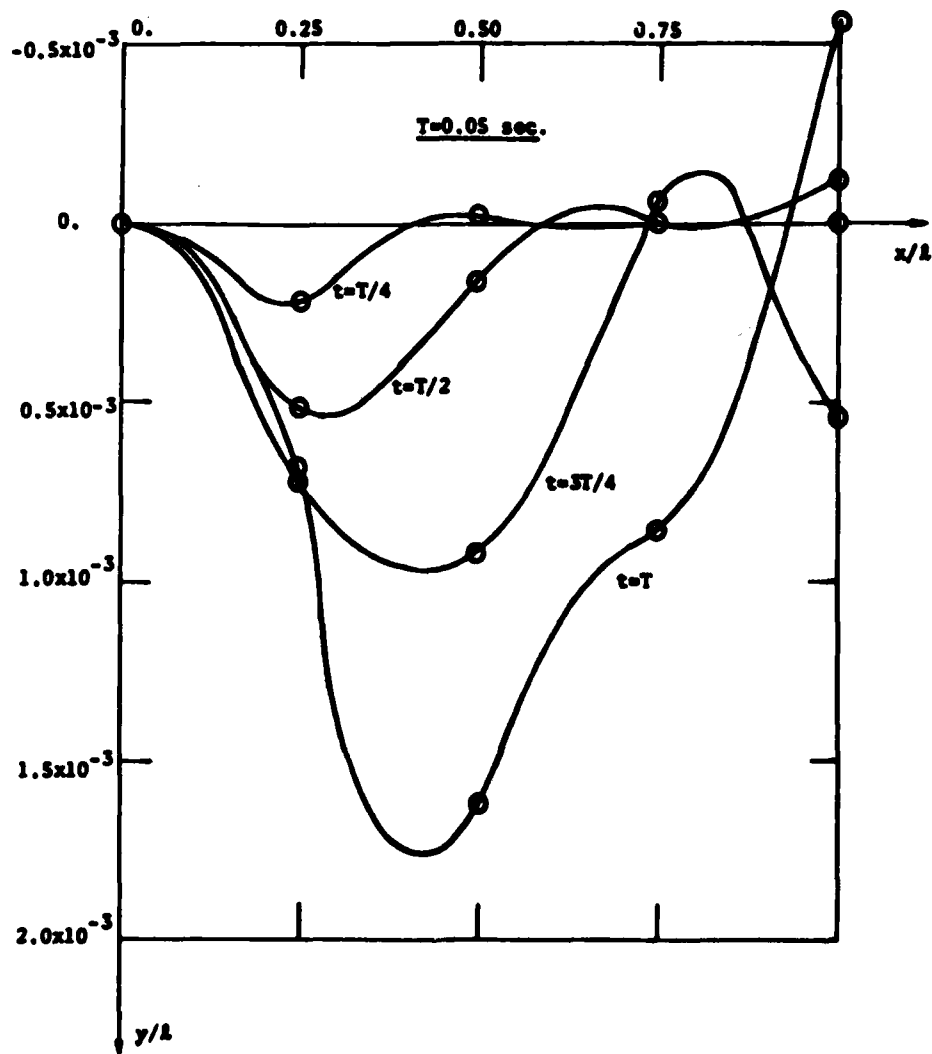


Fig. 8 - Deflection of a cantilevered beam under a moving force: constant velocity, $T = 0.05$ sec. (cf. $T_1 = 1.787$ sec.)

5.2. Moving Force With Constant Acceleration

When the force is moving with constant acceleration rather than constant velocity, the only change necessary in this solution formulation is to replace Eq. (26a) by

$$\bar{x} = \frac{1}{2} \beta t^2$$

where β is the nondimensional acceleration. Hence the path of integration of the force vector is changed and this can be done with very little effort. The solution for a cantilevered beam with $T = 0.1$ is shown in Table X and Figures 9 and 10.

The average velocity for this case is the same as for the case of $T = 0.1$ with constant velocity, the effect of acceleration is observed by comparing Figure 10 with Figure 7 (or Table X with Table IX).

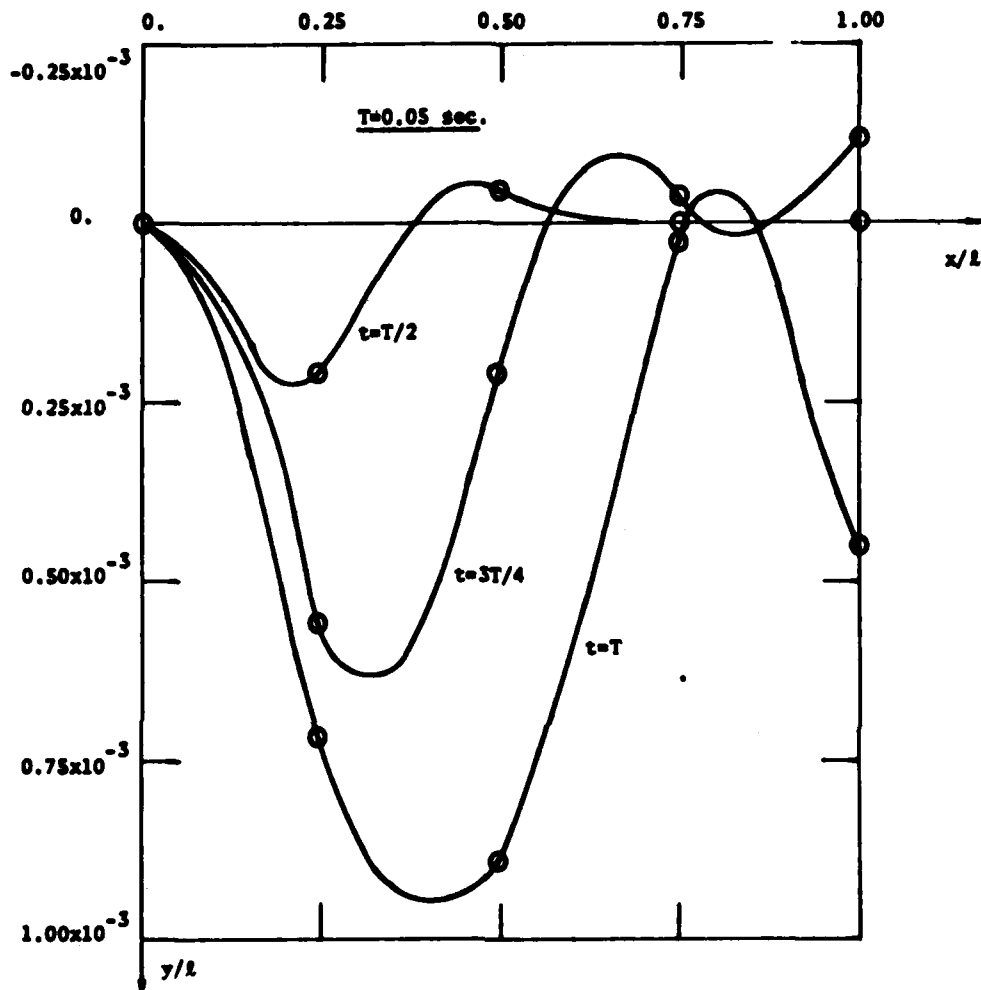


Fig. 9 - Deflection of a cantilevered beam under a moving force: constant acceleration, $T = 0.05$ sec. (cf. $T_1 = 1.787$ sec.)

5.3. Beam on Elastic Foundation With Two Spans

The versatility of this solution formulation is demonstrated by another example of a beam resting on an elastic foundation and with three rigid supports. In this case we have taken again the simply supported beam with a force moving with constant speed. The deflection curves shown in Figure 11 are for $T = 0.1$ and with an intermediate rigid support at the midspan and without an elastic foundation. Figure 11 is for the same with a uniform elastic support with a spring constant of $k = 10,000$ per unit length.

5.4. Gun Tube Motions Affected by a Moving Projectile

The differential equation of this problem is not only non-self adjoint, but also has variable coefficients and with several discontinuous loads. However, the solution formulation presented here also can be routinely applied. The parameters used are from a model M68 - 105 mm cannon tube. The relevant ones are listed below:

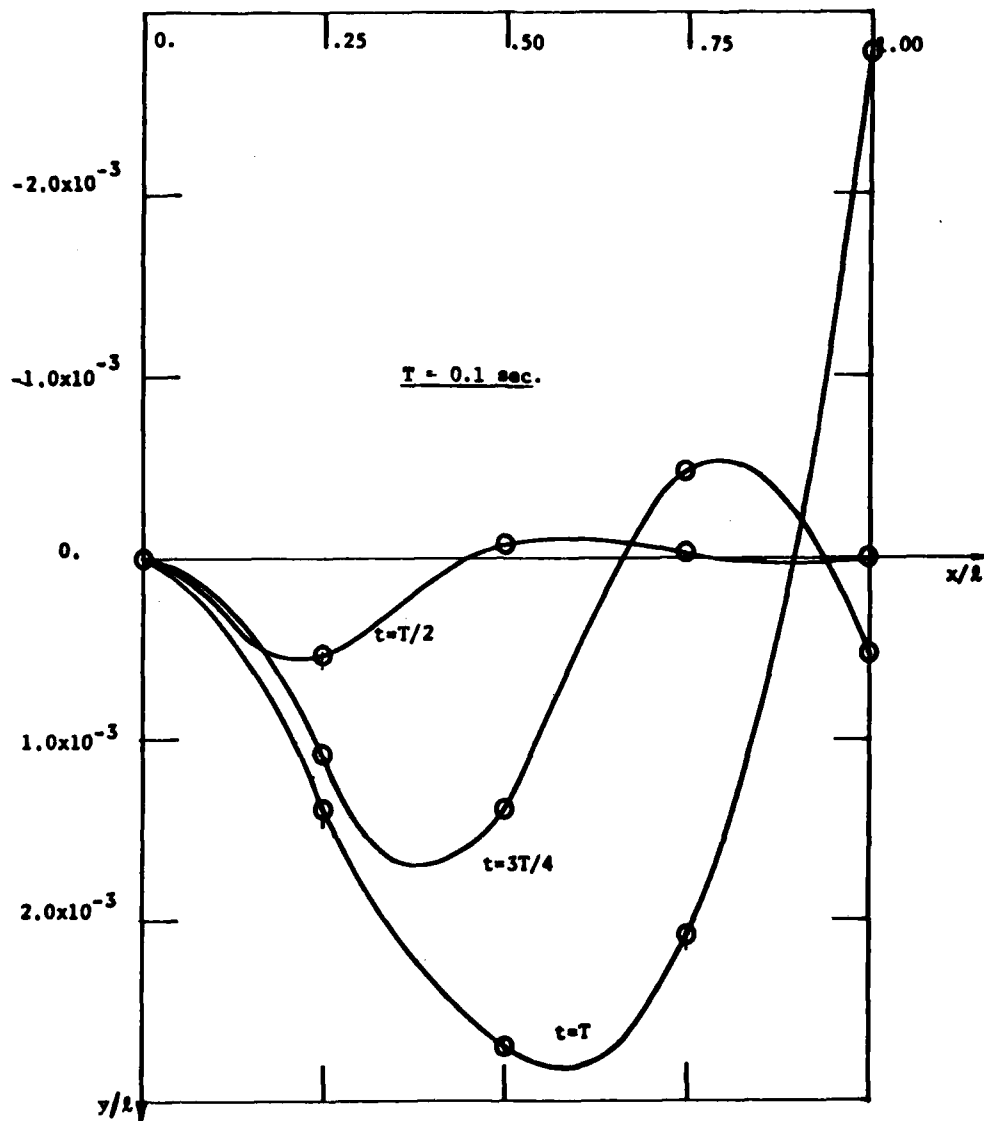


Fig. 10 - Deflection of a cantilevered beam under a moving force: constant acceleration, $T = 0.1 \text{ sec.}$ (cf. $T_1 = 1.787 \text{ sec.}$)

For the tube:

$E = 2.068 \times 10^{12} \text{ dyne/cm}^2$	$(30 \times 10^6 \text{ psi})$
$\rho = 7.8 \text{ g/cm}^3$	(0.2818 lb/in^3)
$l = 5.334 \text{ m}$	(17.5 ft)
$(\text{O.D.})_{\text{ave}} = 18.50 \text{ cm}$	(7.284 in.)
$\text{I.D.} = 10.5 \text{ cm}$	(4.130 in.)
$A = 182.13 \text{ cm}^2$	(28.23 in^2)
$I = 5.145 \times 10^3 \text{ cm}^4$	(123.60 in^4)

and

$$c = \left(\frac{\rho A l^4}{EI} \right)^{1/2} = 0.10396 \text{ sec.}$$

For the projectile, we have

$m_p = 9.07 \text{ kg}$	(20 lb (m))
$P = 27.58 \times 10^8 \text{ dynes/cm}^2$	$(40,000 \text{ psi})$
$\beta = 2.36 \times 10^6 \text{ cm/sec}^2$	$(6 \times 10^6 \text{ in/sec}^2)$
$T = 0.008 \text{ sec} \approx 0.01 \text{ sec.}$	

Consequently, the nondimensionalized parameters are

$$\beta^* = 2.0, \quad c = 0.104, \quad P^* = 6.40$$

$$m_p^* = 0.012, \quad g^* = 0.020$$

And, with $T = 0.01 \text{ sec.}$, the deflection curve is shown in Figures 13 and 14.

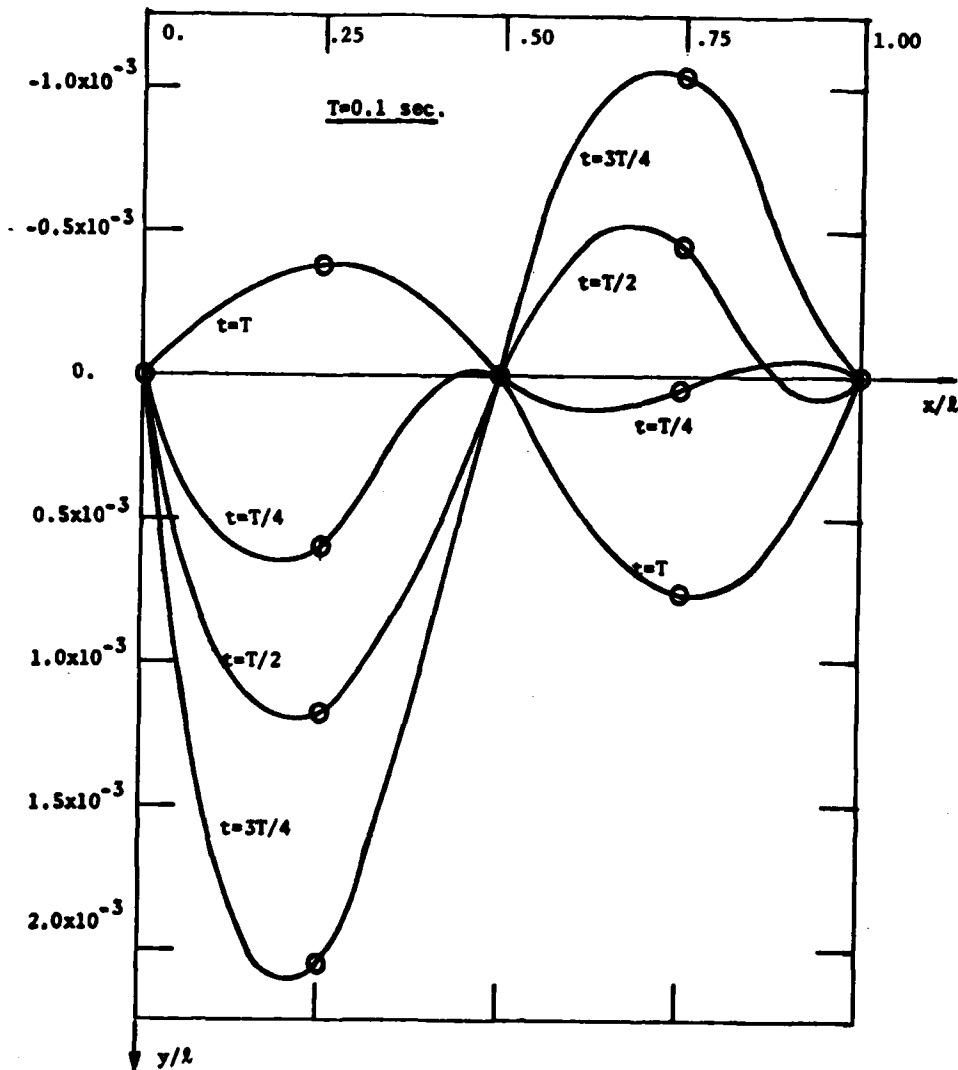


Fig. 11 - Deflection of a beam with three supports and under a moving force constant velocity, $T = 0.1 \text{ sec.}$

6. CONCLUDING REMARKS

A finite element formulation based on variational concepts has been established for gun motions analysis. A special feature of this formulation is that it discretizes the time dimension of a dynamic problem in the same way that the spatial dimension is discretized. Comparisons of numerical results with series solutions of a moving force problem indicate that the present method generates correct results. For gun tube motions analysis in this paper, the effects due to a moving projectile, the recoil force and the curvature induced force have been included. The support condition of a cantilevered used in the analysis is obviously unrealistic. Numerical data obtained here appear to be small by as much as two orders of magnitude compared with experimental data and

some analysis reported earlier [13,14]. Thus, future analysis, which includes such parameters as support flexibilities support locations, projectile eccentricity (which contributes to a moving "couple" to the gun tube) is planned.

REFERENCES

1. L. Fryba, *Vibrations of Solids and Structures Under Moving Loads*, Noordhoff International Publishing Company, Groningen, 1971.
2. T. E. Simkins, "Radial and Transverse response of Gun Tubes by Finite Element methods," 1977 Proceedings of First Conference on Dynamics of Precision Gun Weapons, pp. 373-469.

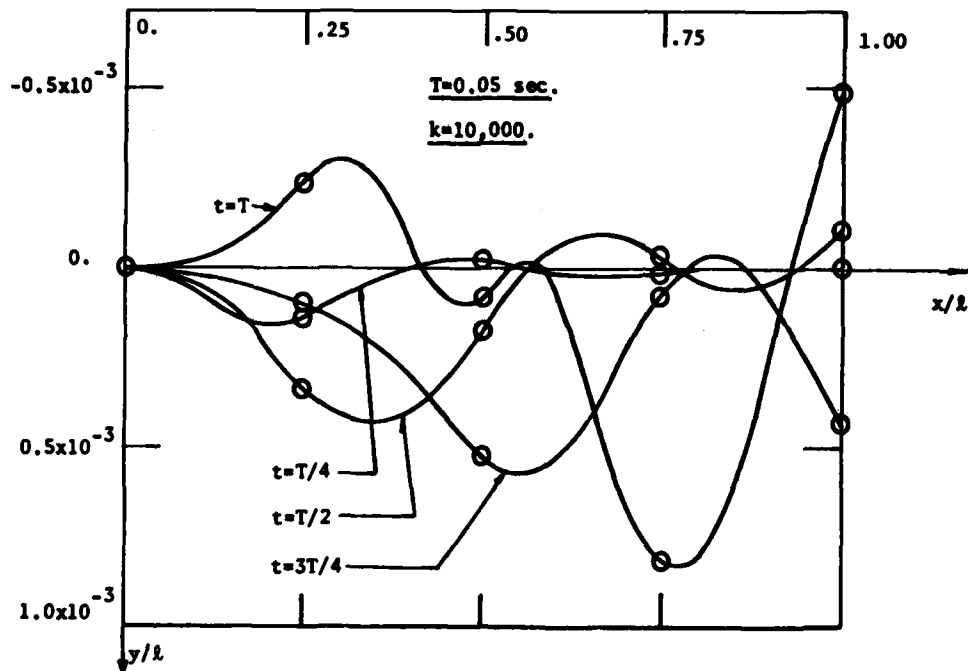


Fig. 12 - Deflection of a cantilevered beam on elastic foundation and under a moving force; constant velocity, $T = 0.05 \text{ sec.}$, $k = 10,000$

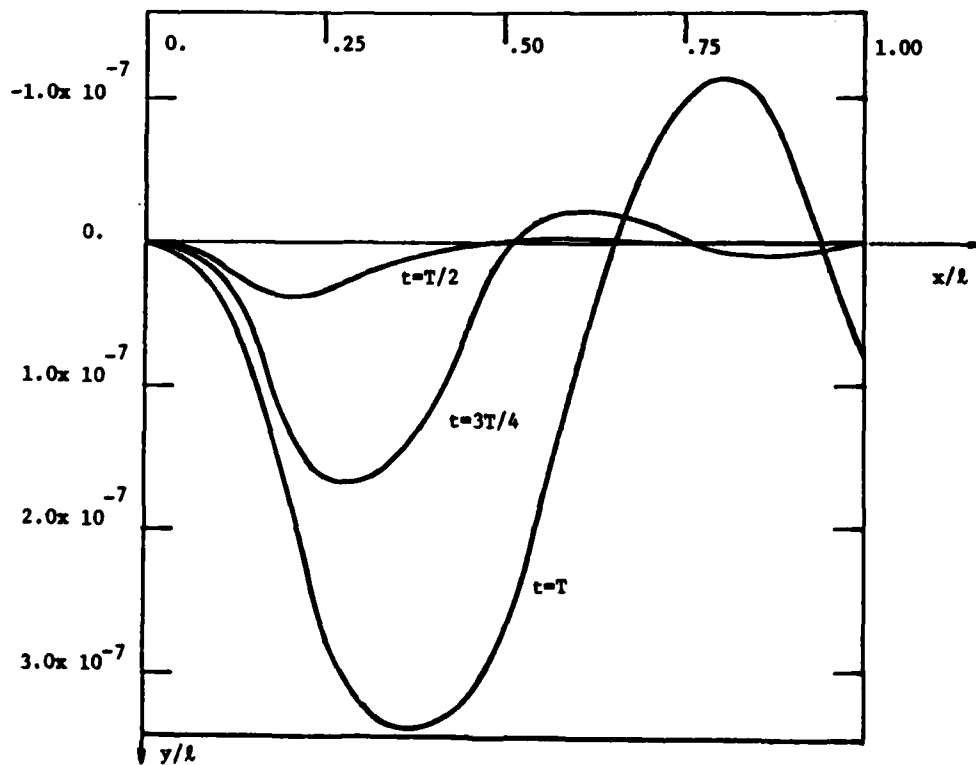


Fig. 13 - Gun tube motions during firing: data from a simplified M68 - 105 mm cannon (see page 16), $T = 0.01 \text{ sec.}$

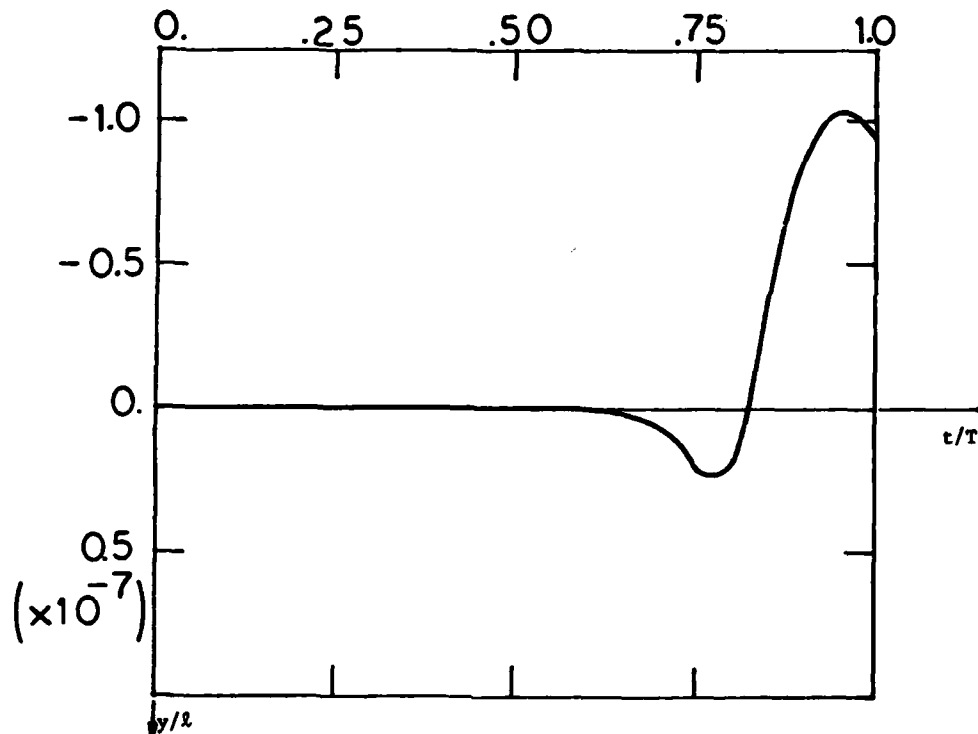


Fig. 14 - Muzzle motion during firing: tube and projectile data from a simplified M68 - 105 mm cannon (see page 16), $T = 0.01$ sec

3. J. J. Wu, "The Initial Boundary Value of Gun Dynamics Solved by Finite Element Unconstrained Variational Formulations," *Innovative Numerical Analysis For the Applied Engineering Science*, R. P. Shaw, et al., Editors, University Press of Virginia, Charlottesville, pp. 733-741, 1980.
4. J. J. Wu, "Solutions to Initial Value Problems by Use of Finite-Elements-Unconstrained Variational Formulations," *1977 Journal of Sound and Vibration*, 53, pp. 341-356.
5. B. A. Finlayson, *The Method of Weighted Residuals and Variational Principles*, p. 229, Academic Press, New York and London, 1972.
6. E. R. A. Oliveira, "Theoretical Foundations of the Finite Element Method," *International Journal of Solids and Structures*, Vol. 4, pp. 929-952, 1968.
7. H. Leipholz, "The Convergence of the Galerkin Procedure for Quasi-Linear Boundary Value Problems," *Acta Mechanica*, Vol. 1, pp. 339-353, 1965.
8. H. Leipholz, "On the Choice of the Trial Functions in the Application of the Method of Galerkin," *Acta Mechanica*, Vol. 3, pp. 295-317, 1967.
9. J. J. Wu, "On Adjoint Operators Associated With Boundary Value Problems," *Journal of Sound and Vibration*, 39, pp. 195-206, 1975.
10. R. Courant and D. Hilbert, *Methods and Mathematical Physics*, p. 211, McGraw-Hill, New York, 1953.
11. D. G. Luenberger, *Optimization by Vector Space Methods*, p. 302, John Wiley, New York, 1969.
12. K. N. Tong, *Theory of Mechanical Vibration*, p. 257, p. 308, John Wiley, New York, 1960.
13. H. Gay and A. Elder, "The Lateral Motion of a Tank Gun and Its Effect on the Accuracy of Fire," *Ballistic Research Laboratory Report No. 1070 AD217657*, 1959.
14. T. E. Simkins, "Transverse Response of Gun Tubes to Curvature-Induced Load Functions," *Proceedings of the Second US Army Symposium on Gun Dynamics*, Watervliet Arsenal Tech. Report, ARLCB-SP-78013 p. 1-67, 1978.

DISCUSSION

Mr. Yang (University of Maryland): That is a very interesting paper. On a couple of slides you had a capital T that was equal to a 10 to the 10th power times something?

Mr. Wu: We are using an arbitrary large number to approximate infinity. As a matter of fact if we use anything more than say 100 or a couple of 100 the nominal number would be one, would be unity. So if we take say 100 or 200 essentially it is the same.

Mr. Yang: I understand now. You also indicated that in some of your runs the time was 1.2 micro seconds. If that were the case, then this curve looks awfully smooth. I mean did you consider the wave propagation and the size of the front element meshes or steps?

Mr. Wu: OK, I understand. You see the number of elements that were taken is very very small. We take something like four elements. The most that we have is a four segments in space and eight in time. In other words this kind of wiggle is the most we can pick up - any higher frequency we would not be able to pick it up. To pick up any higher frequency, you would have to use much finer mesh.

THE BEND-BUCKLING OF A RING-STIFFENED CYLINDRICAL SHELL
DUE TO WHIPPING EXCITATIONS

Kenneth A. Bannister
Naval Surface Weapons Center
White Oak, Silver Spring, Maryland 20910

The problem of interest is the bend-buckling of a ring-stiffened cylindrical shell executing a low frequency beam-like "whipping" motion in one plane. This topic is related to the design of practical ring-stiffened shell structures subjected to in-service bending loads, for example, submarine pressure hulls. The larger objective is a systematic investigation into the dependence of the critical bend-buckling load of the structure on discrete stiffener parameters such as spacing, eccentricity (whether the ring is inside or outside), shape, and area. As a simple initial study, we will focus on just one ring placed on a very long uniform shell. Three different models for the problem will then be briefly reviewed: (1) A Dirac- δ formulation which explicitly treats discrete effects; (2) A linear "smeared" stiffener model in which the ring is smoothed over the shell, thus effectively replacing the original ring/shell by a uniform shell with orthotropic material properties; and (3) A numerical model using the "STAGS" finite difference computer program. Finally, calculations for typical large shells will be presented in order to compare these models.

INTRODUCTION

We discuss here work in progress on the relationship of overall and local buckling modes of a metal structure. In particular, we seek a method for predicting the critical load of a ring-stiffened cylindrical shell subjected to a state of pure bending. We term this critical load value the "bend-buckling" load to distinguish it from the other well-known loading patterns that can lead to cylinder buckling—axial compression, hydrostatic compression, and torsion. The motivation for this research is that ring-stiffened cylinders are widely used in submarine pressure hull design, aircraft and missile structures, and in many industrial applications such as tanks for storage or transport of chemicals. These structures can experience static or quasistatic bending loads of differing severities depending on their external environments. Pressure hulls, for example, may be subjected to low frequency bending vibrations (i.e., "whipping") due to a nearby noncontact underwater explosion. This motion is of such low

frequency compared to much higher local structural frequencies that it can be considered a quasistatic or static response even though the vibrations sometimes appear transient and irregular in character. In this study, then, since we wish to determine the local buckling response to what are essentially quasistatically applied loads, the analysis will proceed with the assumption that "whipping"-generated loads are static loads.

Although the buckling behavior of stiffened shells has been intensively investigated for many types of shell geometries, stiffener arrangements, and load conditions, the problem at hand has not received much attention. This paper therefore describes a "new start" on the problem, discusses previous work, and presents reasonable approaches to obtaining bend-buckling loads. The larger goal of the study is a systematic investigation into the dependence of bend-buckling loads of general stiffened shells to discrete stiffener parameters like spacing, shape, area, and eccentricity. Determining the relationship ("sensitivity") of the

bend-buckling load to local stiffener discreteness parameters would provide very useful design data for purposes of preventing bend-buckling collapse of stiffened shell structures.

Real pressure hulls are quite complicated structures to analyze; rife with imperfections, residual stresses, material inhomogeneities, diameter changes, and so forth. To reduce the problem to manageable size, we represent the hull as a constant diameter thin circular shell stiffened by equi-spaced rings of identical properties. We ignore the effects of hydrostatic loading here but at some phase of the study such effects should be considered. The entire stiffened shell is placed in a state of static pure bending--representing, for example, the situation at a given instant in a submarine undergoing whipping response. Local dynamic effects are assumed small so that inertial terms can be neglected. Lastly, the local fluid pressures due to the hull moving through water will be ignored. (This latter assumption generally applies except perhaps at regions of the hull opposite the explosion where high speed flow impinges on the hull surface.)

It is instructive to describe the bend-buckling behavior of unstiffened and stiffened cylinders observed in experiments. Figure 1 shows an unstiffened cylinder subjected to end moments. The shell is made of a linearly elastic isotropic metal (Young's Modulus E), is assumed to be very long ($L/R > 20$), and has a circular cross section with moment of inertia I . The shell bends like a beam with curvature $1/\rho$ in response to the applied moment. Axial stress resultants thereby appear in the shell wall and, as shown in Figure 1, have inwardly pointing components which pull outer fibers of the cross section inward. Thus, as M increases, the shell flattens (ovalizes) and reduces its moment of inertia I ; in turn the bending stiffness EI is reduced. This process yields a nonlinear moment-curvature plot (Figure 2) with a horizontal slope at the critical moment. Attempts to increase the applied moment beyond this critical value will cause a precipitous collapse of the shell--this sort of collapse can be easily demonstrated with an ordinary plastic soda straw.

For short shells, with ends held circular by rigid end supports, the bend-buckling resembles axial compression buckling. With increased applied moment, small amplitude axial

waves, "wrinkles," form on the compressed side of the shell. Unlike the axially compressed shell, these wrinkles decay in amplitude with circumferential distance away from the most compressed fibers. In general, the exact source of the wrinkles is not known but is believed to be the low amplitude wavy imperfections always present in real shells. The amplitudes of the wrinkles grow with increasing load until the shell suddenly "snaps" into the classical diamond-faceted pattern characteristic of axially compressed shells.

For shells of intermediate length, the ovalization modes occur simultaneously and one or the other will dominate the final precipitous collapse. These mechanisms are not unique to the elastic regime leading up to instability; careful observations of the buckling behavior of relatively thick walled (low R/t ratio) shells show that ovalization and wrinkling modes occur when the shell wall is fully plastic.

The trends in bend-buckling modes of ring-stiffened cylinders are much less well understood due to the greater experimental difficulties and the vast number of possible combinations of boundary conditions and stiffener arrangements. It is reasonable to expect, however, that the buckling modes will resemble those of axially compressed shells. First, two kinds of "panel instability" or local buckling between rings may occur: the shell takes on a lobar pattern with an integer number of circumferential half-waves, or it buckles into an "accordion pleat" pattern. Secondly, an overall "general instability" mode can occur in which a substantial length of the shell, along with several adjacent rings, buckles. This latter mode is somewhat akin to the ovalization mode in an unstiffened cylinder, except that rings are present which tend to control the extent of shell affected. Generally, we can expect that the two panel instability modes are local and will be strongly affected by the discreteness parameters of the rings, while general instability will be dependent on gross structural properties (e.g., compartmentation of a pressure hull) of the entire shell rather than on local details.

PREVIOUS INVESTIGATIONS

A brief review of the source of underwater loading and dynamic response we are concerned with here is given in [1]. It is shown there that the low

frequency flexural motion of a submerged structure requires a blend of methods from the fields of hydrodynamics, structural dynamics, and fluid-structure interaction approximation for its analysis. It is shown that due to the low frequency modal content of the motions, a relatively simple lumped mass finite element beam model suffices for calculations of overall response. It turns out also that fairly simple fluid loading and fluid-structure coupling models, of about the same order of complexity and accuracy as the finite element model, are available. In recent years, more sophisticated fluid-structure analyzers, such as the USA-STAGS computer code, are being applied to a variety of problems involving explosive loads on submerged structures. More will be said about this later.

Numerous investigators have conducted analytical and experimental studies of the bend-buckling of unstiffened cylinders beginning with the classic 1927 paper by Brazier [2] and continuing until the present [3] - [15]. A vast literature exists on the buckling of general stiffened shells owing to their many practical applications within structures requiring low weight and high strength. General surveys of this topic can be found in [17] - [19]. The literature on the narrower topic of ring-stiffened cylinder buckling is also large since these structures traditionally have been used in industrial pressure vessel and submarine pressure hull design. Kendrick [20] has summarized the state-of-the-art of this field (at least up until 1970). On the problem of interest here, that is, sensitivity of the critical bending load to local discrete ring parameters, very little if anything has been published. Bushnell [21] has carefully studied the interactions of ring stiffeners with cylindrical shells in buckling with the aid of a version of the BOSOR computer program. Although the primary goal of his investigation was to demonstrate how different analytical models of rings (and their attachment to a shell) can affect buckling and frequency calculations, he also found that local shell deformations (which vary with choice of ring model) can have unexpectedly large effects on overall buckling behavior.

ANALYSIS

We review here three approaches to predicting the sensitivity of the

bend-buckling load of a ring-stiffened cylinder to local discrete ring properties. First, a Dirac- δ method developed by Baruch [22] - [23] and applied to the special case of a ring-stiffened cylinder by Singer and Haftka [24] will be discussed. This technique, at least for symmetric loadings, yields results applicable to smeared rings ("first order approximation") and to discrete rings ("infinite order approximation"). Secondly, the well-known "smearing" technique will be briefly described. This method is widely used for design of layered (filament wound) shells and in situations involving closely spaced integral or attached stiffeners. It is also used in standard design manuals such as [25] and [26]. Shaker [27] has conducted detailed non-linear analyses with this approach applied to ring- and stringer-stiffened oval cylinders. Lastly, a few comments will be made about approximate shell analysis techniques such as the STAGS computer program which is based on a finite difference energy formulation.

A DIRAC- δ METHOD

The theory of this method has been developed by Baruch [22] - [23] and applied to buckling of ring-stiffened cylinders under symmetric loadings by Singer and Haftka [24]. Geometry of the shell and nomenclature is shown in Figure 3. The following assumptions are made in this theory:

1. The shell obeys linear Donnell shell [4] theory and is thin; thus $R/t \gg 1$ and higher powers of R/t can be neglected;
2. The number of circumferential waves in buckling is large, i.e., $n^2 \gg 1$;
3. The rings have the usual properties of a beam cross section but are of zero thickness; the Dirac- δ function is used to locate a given ring at a particular x ;
4. Normal strains vary linearly in the shell wall and ring and are continuous across the ring/shell juncture;
5. The shear resultant $N_{x\theta}$ is carried by the shell entirely; the rings do not carry shear loads;
6. The rings have torsional stiffness.

A system of homogeneous stability equations is derived by equating the first variation of the total system potential energy to zero:

$$\delta U = 0 \quad (1)$$

In terms of the force resultants, this can be written:

$$\begin{aligned} & \int_0^{L/R} \int_0^{2\pi} \left\{ \left[-N_{x,x} - N_{x\theta,\theta} \right] R \delta u \right. \\ & + \left[-N_{\theta,\theta} - N_{x\theta,x} \right] R \delta v + \\ & \left[-M_{x,xx} - RN_{\theta} - M_{\theta,\theta\theta} + M_{x\theta,x\theta} \right. \\ & - M_{\theta x,x\theta} - R(N_{x0} w',x),x \\ & - R(N_{\theta0} w',\theta),\theta - R(N_{x\theta0} w',\theta),x \\ & \left. \left. - R(N_{x\theta0} w',x),\theta \right] \right\} R dx d\theta \\ & + \int_0^{2\pi} \left[N_x R \delta u + N_{x\theta} R \delta v - M_x \delta(w,x) \right. \\ & + (M_{x,x} - M_{x\theta,\theta} + M_{\theta x,\theta} + RN_{x0} w',x \\ & \left. + RN_{x\theta0} w',\theta) \delta w \right]_{x=0}^{x=L/R} R d\theta = 0 \end{aligned} \quad (2)$$

where, for a single ring located at $x = L/2R$, the force resultants can be specialized to the following in terms of non-dimensional displacements and Dirac- δ functions (these locate the ring):

$$N_x = \frac{Et}{(1-\nu^2)} (u',x + \nu (u',\theta - w))$$

$$N_{\theta} = \frac{Et}{(1-\nu^2)} \left[v',\theta - w + \nu u',x \right.$$

$$\left. + \delta \left(x - \frac{L}{2R} \right) (u(v',\theta - w) \right.$$

$$\left. - x w',\theta\theta \right) \text{RING} \Big]$$

$$N_{x\theta} = N_{\theta x} = \frac{Et}{2(1+\nu)} (u',\theta + v',x)$$

$$M_x = -\frac{D}{R} (w',xx + \nu w',\theta\theta) \quad (3)$$

$$M_{\theta} = -\frac{D}{R} \left[w',\theta\theta + \nu w',xx + \delta \left(x - \frac{L}{2R} \right) \cdot \right. \\ \left. (n w',\theta\theta - \zeta (v',\theta - w)) \text{RING} \right]$$

$$M_{x\theta} = \frac{D}{R} (1-\nu) w',x\theta$$

$$M_{\theta x} = -\frac{D}{R} \left[(1-\nu) w',\theta x + \delta \left(x - \frac{L}{2R} \right) \cdot \right. \\ \left. (n_t w',x\theta) \text{RING} \right]$$

where () RING indicates that the quantities within parentheses must be evaluated at the ring itself. Substitution of Eqs. (3) into Eq. (2) eliminates the force resultant terms but not the prebuckling membrane force resultants N_{x0} , $N_{\theta0}$, and $N_{x\theta0}$. These latter terms must be specified a priori by the analyst to represent the particular loading state of interest. Usually these terms are just set to constants (or zero) in problems of symmetric loading. For bending they may be written:

$$N_{\theta0} = N_{x\theta0} = 0 \quad (4)$$

$$N_{x0} = -N \cos \theta$$

Singer and Haftka considered only symmetry-type loadings and assumed the following displacement function forms:

$$u = \sin n\theta \sum_{m=1}^{\infty} A_m \cos m\beta x$$

$$v = \cos n\theta \sum_{m=1}^{\infty} B_m \sin m\beta x \quad (5)$$

$$w = \sin n\theta \sum_{m=1}^{\infty} C_m \sin m\beta x$$

which satisfy the simple support boundary conditions,

$$\left. \begin{aligned} v = w = 0 \\ N_x = M_x = 0 \end{aligned} \right\} x = 0, L/R$$

Substitution of Eqs. (5) into the displacement component form of Eq. (2) produces a set of order $2m$ of homogeneous algebraic equations in the unknown coefficients A_m , B_m , and C_m .

Buckling loads are calculated from the vanishing of the determinant of the coefficients of A_m , B_m , and C_m .

At present, it is uncertain that the assumed displacement functions (Eqs. (5)) are applicable to the bending problem. Flügge [28] has conducted a similar analysis of an unstiffened cylinder subjected to combined axial compression and bending. He shows that the resultant $N_{x0} = -N \cos \theta$ leads to a

fundamentally different kind of stability equation in the displacement components than that derived by Singer and Haftka; i.e., the differential equations have variable, rather than constant, coefficients. To handle these variable coefficients (in θ), Flügge uses infinite series expressions in θ for the displacements. Flügge also examined anti-symmetric as well as symmetric circumferential modes (by interchanging $\sin n\theta$ and $\cos n\theta$ terms in his series) in order to be sure the minimum critical bending load was found. A study of this technique is now underway with regard to the present analysis method.

LINEAR SMEARED STIFFENER THEORY

A traditional method in the analysis of buckling of stiffened shells is to ignore the local features and perturbing effects of the stiffeners by smoothing or averaging them in some manner over the shell surface. This yields a continuous but orthotropic shell. Smearing is satisfactory for very closely stiffened shells that will likely buckle by general instability. A standard methodology, adopted by NASA for shell design guidelines, has been developed by Jones [29]. This method, originally derived only for axial compression of layered composite shells with eccentric stiffeners, can be modified for bend-buckling according to recommended procedures given in [26].

Accounting for differences that may exist between bending and axial compression buckling loads, [26] recommends that for bend-buckling, the shell should be designed so that the maximum axial force resultant in the outer fibers N_x should not exceed a certain fraction of N_x calculated for axial compression. That is,

$$(N_x)_{\text{bending}} \leq \frac{3}{4} (N_x)_{\text{axial compression}} \quad (6)$$

where the factor $\frac{3}{4}$ is based on a "lower bound" estimate derived from rather limited test data. Jones's expression for the axial compression buckling load is:

$$\begin{aligned} (N_x)_{\text{axial compression}} \\ = \left(\frac{L}{m\pi}\right)^2 \frac{|A_{ij}|}{|A_{kl}|} \text{ for } n \geq 4 \end{aligned} \quad (7)$$

where $(i, j = 1, 2, 3)$, $(k, l = 1, 2)$ and $||$ signifies the determinant. The terms in the determinants are given by:

$$\begin{aligned} A_{11} &= E_x \left(\frac{m\pi}{L}\right)^2 + G_{xy} \left(\frac{n}{R}\right)^2 \\ A_{22} &= E_y \left(\frac{n}{R}\right)^2 + G_{xy} \left(\frac{m\pi}{L}\right)^2 \\ A_{33} &= D_x \left(\frac{m\pi}{L}\right)^4 + D_{xy} \left(\frac{m\pi}{L}\right)^2 \left(\frac{n}{R}\right)^2 \\ &\quad + D_y \left(\frac{n}{R}\right)^4 + \frac{E_y}{R^2} + \frac{2C_y}{R} \left(\frac{n}{R}\right)^2 \\ &\quad + \frac{2C_{xy}}{R} \left(\frac{m\pi}{L}\right)^2 \\ A_{12} &= A_{21} = (E_{xy} + G_{xy}) \frac{m\pi}{L} \frac{n}{R} \\ A_{23} &= A_{32} = (C_{xy} + 2K_{xy}) \left(\frac{m\pi}{L}\right)^2 \frac{n}{R} \\ &\quad + \frac{E_y}{R} \frac{n}{R} + C_y \left(\frac{n}{R}\right)^3 \end{aligned} \quad (8)$$

$$A_{31} = A_{13} = \frac{E_{xy}}{R} \frac{m\pi}{L} + C_x \left(\frac{m\pi}{L}\right)^3 + (C_{xy} + 2K_{xy}) \frac{m\pi}{L} \left(\frac{n}{R}\right)^2$$

where E = shell elastic modulus
 ν = shell Poisson ratio
 R, L = shell radius and length
 m, n = number of axial half-waves and number of circumferential waves.

For rings, the elastic coefficients become:

$$E_x = \frac{Et}{1-\nu^2}$$

$$E_y = \frac{Et}{1-\nu^2} + \frac{E_r A_r}{d}$$

$$E_{xy} = \frac{\nu}{1-\nu^2} Et$$

$$G_{xy} = \frac{Et}{2(1+\nu)}$$

$$D_x = \frac{Et^3}{12(1-\nu^2)} \quad (9)$$

$$D_y = \frac{Et^3}{12(1-\nu^2)} + \frac{E_r I_r}{d} + z_r^2 \frac{E_r A_r}{d}$$

$$D_{xy} = \frac{Et^3}{6(1+\nu)} + \frac{G_r J_r}{d}$$

$$C_x = C_{xy} = K_{xy} = 0$$

$$C_y = z_r \frac{E_r A_r}{d}$$

where d = ring spacing

E_r = ring elastic modulus

G_r = ring shear modulus

A_r = ring cross sectional area

I_r = ring moment of inertia about its centroid

J_r = ring torsional constant

z_r = ring centroid offset distance from shell middle surface (positive for external rings)

Eqs. (9) clearly show the various groupings of ring cross section properties which enter the basic buckling equation (eq. (7)) but the ring spacing d in their denominators shows that these "discrete" quantities are actually smeared over the panels between rings.

The integers m and n can be independently chosen so that a methodical search of all (m, n) combinations over reasonable ranges of m and n must be conducted to ensure a minimum buckling load is found. This task can easily be programmed for a computer. The term " $\frac{3}{4}$ " in Eq. (6) is a "knockdown" factor typically applied in shell design work and is derived based on experimental work. It serves to ensure that a conservative design results.

NUMERICAL ANALYSIS METHODS

Since the mid-1950's when computers had been developed far enough to carry out routine numerical solution algorithms, approximate numerical methods have come to dominate the shell buckling analysis field. In the last 15 years or so, computer programs have been written with sufficient generality to be applied to three dimensional smeared or discretely stiffened shell problems. Current examples are STAGS [30] and BOSOR 5 [21] which are both primarily designed for shell work, although STAGS, by design, is more general in scope in being able to handle three dimensional branched shells. BOSOR 5, the most recent code in the BOSOR series, is specialized to axisymmetric shells and can be used for very detailed studies of local shell non-linear response and shell-stiffener

interactions. An investigation of this kind has been conducted by the code author [21]. A recent STAGS version, named USA-STAGS [31], is equipped to handle fluid-structure interaction problems for submerged shells subjected to high and low frequency loads. An example of the use of this code for explosion bubble-induced whipping analysis is discussed in [1].

Given the obvious usefulness of a code such as STAGS in determining the bend-buckling behavior of ring-stiffened cylinders, apparently no such studies have yet been done. In the case of unstiffened cylinders, however, a very thorough investigation has been published by Stephens, et al [11]. There, STAGS was used to compute buckling loads for long uniform cylinders subjected to pure bending and combined bending and pressure loads. The "Brazier" flattening (or ovalization) and wrinkling modes of failure were considered for $R/t = 100$ and over the length/radius range $6 < L/R < 20$. Since STAGS requires some means to permit bifurcation from the non-linear prebuckling state, a small-amplitude wavy imperfection in both x and θ -directions had to be introduced at the outset. This is a reasonable approximation since real shells invariably have such imperfections in a more-or-less random pattern. In general, the results confirmed the work of earlier investigators [2], [6], [9] and new results for combined bending and internal or external were presented. It was found also that lower L/R cases ($L/R = 10, 6$) had large deviations (due to wrinkling behavior) from recommended design values. These findings are relevant to a ring-stiffened cylinder which can be roughly modeled as a series of short cylinders.

SAMPLE RESULT

An interesting application of the Dirac- δ method described in Section 2.1 shows dramatically, at least for axial compression, that ring discreteness properties can lead to local buckling at loads much lower than those predicted by smearing techniques. It should be noted that at the local shell level, compression loading will yield a stress state that resembles the compression side of a shell in pure bending. Reddy [13] - [15] has exploited this fact in his analyses of bend-buckling. Table 1 shows comparisons of "smeared" and discrete buckling loads calculated by Singer and Haftka for $R/t = 100$ and for just a single ring placed at the shell center.

Specific ring properties are indicated there also and represent a fairly strong ring, somewhat like a "deep frame" often used in pressure hull design. The sharp differences in smeared and discrete buckling loads indicate that serious consideration should be given to local buckling effects and the sensitivity of the applied load to them.

SUMMARY AND CONCLUSIONS

The problem of predicting the sensitivity of bend-buckling loads of ring-stiffened cylinders to discreteness properties at the local ring level has been reviewed. It turns out that this specialized problem in stiffened shell buckling apparently has received little attention. It appears reasonable to say that this problem therefore needs attention and that a careful study of it will yield practical design data as well as insights into the modeling of buckling. Three approaches to the analysis of bend-buckling have been briefly summarized. Of the three, the Dirac- δ (analytical) and the numerical analysis (STAGS, BOSOR codes) show the most promise for yielding useful results. Work is now in progress on the use of these methods for the present problem.

REFERENCES

1. Bannister, K. A., "Whipping Analysis Techniques for Ships and Submarines," in Proceedings of the 50th Shock and Vibration Symposium, 16-18 October 1979, Colorado Springs Springs, Colorado
2. Brazier, L. G., "On the Flexure of Thin Cylindrical Shells and Other 'Thin' Sections," Proceedings of the Royal Society of London, Series A, Vol. 116, 1927, pp 104-114
3. Flügge, W., "Die Stabilität der Kreiszyllinderschale," Ingenieurarchiv, Vol. 3, 1932, pp 463-506
4. Donnell, L. H., "A New Theory for the Buckling of Thin Cylinders Under Axial Compression and Bending," Journal of Applied Mechanics, Vol. 56, Trans. ASME, 1934, pp 795-806
5. Wood, J. D., "The Flexure of a Uniformly Pressurized, Circular Cylindrical Shell," Journal of Applied Mechanics, Vol. 25, Trans. ASME, Vol. 80, 1958, pp 453-458

6. Seide, P., and Weingarten, V. I., "On the Buckling of Circular Cylindrical Shells Under Bending," *Journal of Applied Mechanics*, Vol. 28, Trans. ASME, 1961, pp 112-116
7. Weingarten, V. I., "Effects of Internal Pressure on the Buckling of Circular-Cylindrical Shells Under Bending," *Journal of the Aerospace Sciences*, Vol. 29, 1962, pp 804-807
8. Reissner, E., and Weinitzschke, H.J., "Finite Pure Bending of Circular Cylindrical Tubes," *Quarterly of Applied Mathematics*, Vol. 20, No. 4, 1963, pp 305-319
9. Aksel'rad, E. L., "Refinement of the Upper Critical Loading of Pipe Bending Taking Account of the Geometrical Nonlinearity," *AN, SSSR, OTN, Mekhanika i Mashinostroenie*, No. 4, 1965, pp 123-139
10. Almroth, B. O., and Starnes, J. H., Jr., "The Computer in Shell Stability Analysis," *Journal of the Engineering Mechanics Div.*, Vol. 101, Trans. ASCE, 1975, pp 873-888
11. Stephens, W. B., Starnes, J. H., Jr., and Almroth, B. O., "Collapse of a Long Cylindrical Shell Under Combined Bending and Pressure Loads," *AIAA Journal*, Vol. 13, 1975, pp 20-25
12. Storaker, B., "On Buckling of Axisymmetric Thin Elastic-Plastic Shells," *International Journal of Solids and Structures*, Vol. 11, 1975, pp 1329-1346
13. Reddy, B. D., and Calladine, C. R., "Classical Buckling of a Thin-Walled Tube Subjected to Bending Moment and Internal Pressure," *International Journal of Mechanical Science*, Vol. 20, 1978, pp 641-650
14. Reddy, B. D., "An Experimental Study of the Plastic Buckling of Circular Cylinders in Pure Bending," *International Journal of Solids and Structures*, Vol. 15, 1979, pp 669-683
15. Reddy, B. D., "Plastic Buckling of a Cylindrical Shell in Pure Bending," *International Journal of Mechanical Science*, Vol. 21, 1979, pp 671-679
16. Fabian, O., "Collapse of Cylindrical Elastic Tubes Under Combined Bending, Pressure and Axial Loads," *International Journal of Solids and Structures*, Vol. 13, 1977, pp 1257-1270
17. Singer, J., "Buckling of Integrally Stiffened Cylindrical Shells - A Review of Experiment and Theory," *Contribution to the Theory of Aircraft Structures*, (Rotterdam: Delft University Press, 1972)
18. Singer, J., "Buckling, Vibrations, and Postbuckling of Stiffened Metal Cylindrical Shells," *Proceedings of the Conference on Behavior of Offshore Structures*, The Norwegian Institute of Technology, 1976
19. Singer, J., "Recent Studies on the Correlation Between Vibration and Buckling of Stiffened Cylindrical Shells," *Proceedings of the Colloquium "Schalenbeultagang"*, Darmstadt, June, 1979
20. Kendrick, S., "Externally Pressurized Vessels," *The Stress Analysis of Pressure Vessels and Pressure Vessel Components*, Edited by S. S. Gill (New York: Pergamon Press, 1970)
21. Bushnell, D., "Evaluation of Various Analytical Models for Buckling and Vibration of Stiffened Shells," *AIAA Journal*, Vol. 11, 1973, pp 1283-1291
22. Baruch, M., "Equilibrium and Stability Equations for Stiffened Shells," *Israel Journal of Technology*, Vol. 2, No. 1, 1964, pp 117-124
23. Baruch, M., "Equilibrium and Stability Equations for Discretely Stiffened Shells," *Israel Journal of Technology*, Vol. 3, No. 2, 1965, pp 138-146
24. Singer, J., and Haftka, R., "Buckling of Discretely Ring Stiffened Cylindrical Shells," *Israel Journal of Technology*, Vol. 6, No. 1-2, 1968, pp 125-137
25. Baker, E. H., et al, "Shell Analysis Manual," NASA CR-912, April 1968
26. NASA SP-8007, "Buckling of Thin Walled Circular Cylinders," NASA, August 1968

27. Shaker, F. J., "Buckling of Eccentrically Stiffened Oval Cylinder Under Combined Bending and Compression," Ph.D. Thesis, Case Western Reserve University, 1973
28. Flügge, W., Stresses in Shells, 2nd ed. (New York: Springer Verlag), 1973
29. Jones, R. M., "Buckling of Cylindrical Shells with Multiple Orthotropic Layers and Eccentric Stiffness," AIAA Journal, Vol. 6, No. 12, December 1968, pp 2301-2305
30. Bushnell, D., Almroth, B. O., and Brogan, F., "Finite-Defference Energy Method for Nonlinear Shell Analysis," Computers and Structures, Vol. 1, 1971, pp 361-387
31. DeRuntz, J. A., et al, "The Underwater Shock Analysis (USA) of Non-linear Structures, A Reference Manual for the USA-STAGS Code," LMSC-D624355, February 1978

Table 1

Comparison of "Smearred" and Discrete Axial Compression Buckling Loads (after [24])

<u>R/t</u>	<u>L/R</u>	<u>P*(Smearred)</u>	<u>P*(Discrete)</u>
100	0.5	1303	533.8
100	1.0	1288	229.9
100	2.0	1281	107.4

NOTES:

(1) For single ring at shell center

(2) Discreteness properties:

$$\frac{A_2}{at} = 0.5, \quad \frac{I_{22}}{at^3} = 5.0, \quad \frac{e_2}{t} = 5.0$$

(3) P* (Smearred) = nondimensional critical "smearred" load (see [24])

(4) P* (Discrete) = nondimensional critical "discrete" load (see [24])

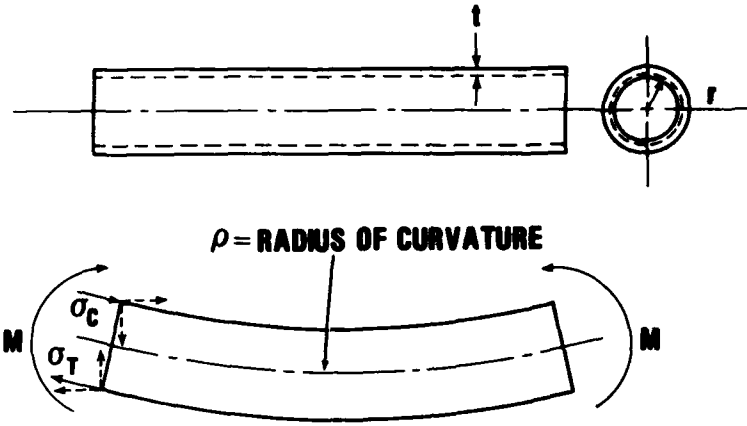
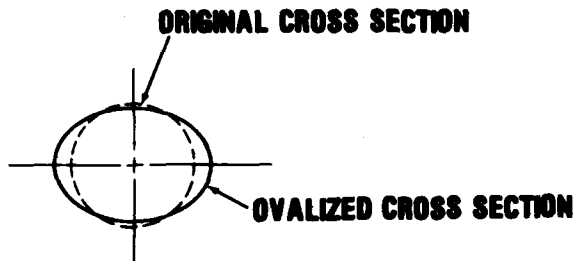


FIGURE 1 TUBE BENDING



MECHANISM 1: COLLAPSE DUE TO FLATTENING OF CROSS SECTION

AXIAL WRINKLING IN COMPRESSED REGION



MECHANISM 2: FORMATION OF AXIAL WRINKLES

FIGURE 2a BEND-BUCKLING MECHANISMS

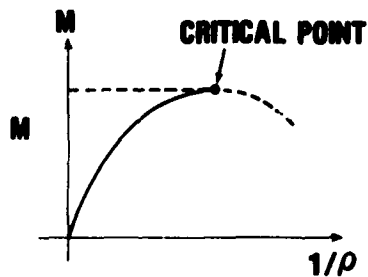
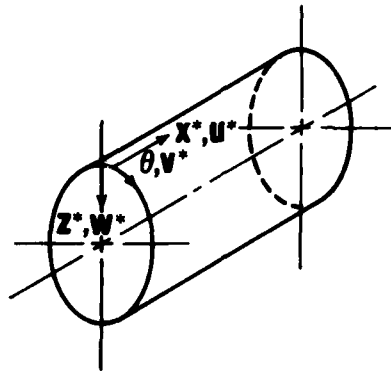
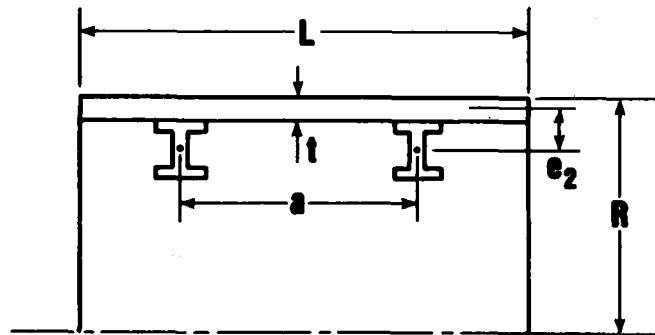


FIGURE 2b NON-LINEAR MOMENT-CURVATURE RELATIONSHIP



DEFINITION OF COORDINATE SYSTEM



- | | |
|--|---|
| A_2 = RING AREA | $u, v, w = u^*/R, v^*/R, w^*/R$ |
| $D = Et^3/(12(1-\nu^2))$ | NONDIMENSIONAL DISPLACEMENTS |
| E = YOUNG'S MODULUS | $x, z = x^*/R, z^*/R$ NONDIMENSIONAL LENGTH COORDINATES |
| e_2 = RING CENTROID OFFSET FROM SHELL MIDDLE SURFACE, POSITIVE AS SHOWN ABOVE | $\zeta = EA_2e_2/D$ |
| G = SHEAR MODULUS | $\eta = El_{02}/(RD)$ |
| I_{22}, I_{02} = RING MOMENTS OF INERTIA ABOUT ITS CENTROID AND THE SHELL MIDDLE SURFACE | $\eta_t = GJ/(RD)$ |
| J = RING TORSIONAL CONSTANT | $X = (1-\nu^2)EA_2e_2/(EtR^2)$ |
| | ν = POISSON'S RATIO |
| | $N_{x0}, N_{\theta 0}, N_{x\theta 0}$ = PREBUCKLING MEMBRANE RESULTANTS |

FIGURE 3 NOMENCLATURE FOR DIRAC- δ METHOD

DISCUSSION

Voice: When you do your "Hondo" calculation, since your target is double layer stiffened, how do you come up with an equivalent plate thickness to use?

Mr. Bannister: We based our previous study with a deform. We used an equivalent thickness also and as a matter of fact with this kind of velocity, 2500 feet per second, the worst case is not really when you hit the stringer and the web. The worst case is when you hit in between the stringer and the web, or the ribs, or when you don't have any reinforcing in the back. The reasoning for that is that it gives a little bit. If you have a break where it hits the middle it gives a little bit, where as the other way it just runs right through because the thickness of the material and the ribs really don't slow this particular projectile down that much under 2500 feet per second. So for that study we initially looked at the ship hull itself. This is contrary to our usual studies, where the worst case is when you hit against a stringment.

Mr. Rubin (The Aerospace Corp.): Many years ago I was involved with some work for the Navy involving water entry loads on torpedoes slamming into the sea. I

was involved with making the kinds of loads calculations you talked about. After acquiring some field data and seeing some field failures we concluded that the kinds of calculations that we were making then, which relate to what you are making now, bear very little relationship to the real world in terms of the kinds of accelerations that one will experience on a penetrating body. We concluded that it was useless to make those calculations and we went to an empirical approach of actually measuring the acceleration responses of the penetrating bodies and then going from there. What is the correlations between actual experimental results and the kinds of calculations you are making?

Mr. Bannister: Your point is very well taken and I am sure many of the people that did this study found the same thing. For this particular type of study I refer you to the PhD thesis done by John Baldwin from the University of Maryland, in which he correlated some experimental work with the analysis and arrived with some empirical equations. There were some tests that were run by a group from NSWC, Ed Rzepka's group, that actually obtained some experimental data and John Baldwin tried to correlate that too.

RESPONSE OF HYDROFOIL STRUT-FOIL SYSTEMS
AFTER IMPACT WITH "DEAD-HEAD" LOGS*

Howard S. Levine
Weidlinger Associates
Menlo Park, California

and

Andrew P. Misovec
Weidlinger Associates
Chesapeake, Virginia

Hydrofoils have recently experienced debris strikes from "dead-head" or vertical floating logs. The present study represents an initial step in the prediction of the response of strut-foil systems after such impact, with the eventual application being the design of composite strut-foil systems. In the early stages of the investigation reported upon here, the response of steel foils and struts was studied. A simplified technique to determine the log-foil interaction force is first developed. This is then applied to a beam model of a generic strut-foil system to predict its response. A more sophisticated finite element model is then used to study the early-time strut-foil-log interaction. Basic phenomenology is studied and recommendations for improving the analytical techniques are made.

INTRODUCTION

Hydrofoils such as the ACEH-1 Plainview and the PCH-1 Mod 1 have recently experienced debris strikes from "dead-head" or vertical floating logs [1]. These strikes on the forward foils induced torsional oscillations and serious damage to the strut and steering mechanisms. In addition, the strut also experienced large bending loads as a result of rapid rotation following actuator failure.

The present study represents an initial step in the prediction of the response of strut-foil systems after such impacts with the eventual application being the design of composite strut-foil systems. In the early stages of the investigation reported upon here, the response of steel foils and struts was studied with several objectives in mind. These included:

(1) Development of a simple model to predict the interaction forces on the foil during impact with the log.

(2) Using the results of (1) with currently available finite element codes to predict the long-term response of a generic strut-foil system.

(3) Predict the initial interaction forces on the foil during impact using a sophisticated 3D finite element code and verify the model developed in (1), if possible.

(4) Identify the prevalent structural response mechanisms and failure modes.

(5) Recommend an experimental program to verify the analytical results and confirm any unusual findings.

The first four of these topics are addressed in the following sections. In all cases, the assumptions made are outlined and areas where the analytical techniques can be improved are recommended.

DEVELOPMENT OF SIMPLIFIED MODEL TO PREDICT
IMPACT FORCES

Fig. 1 shows the configuration at the instant of impact. After impact, it is assumed that the hull velocity is unchanged at v_0 and the foil depth is unchanged at z . What happens next depends on the relative strength properties of the log and the foil. There are four possibilities:

(1) The foil is weaker than the log so that the foil sustains damage while the log moves as either a rigid or elastic body;

(2) The log is weaker than the foil, in which case the log receives damage while the foil remains elastic in the neighborhood of impact;

*This work was supported by David W. Taylor Naval Ship R&D Center, Carderock, MD and performed under subcontract to McDonnell Douglas Astronautics Co., Huntington Beach, CA.

(3) The impact velocity is of low enough speed so that both the log and the foil respond elastically; or

(4) The log and the foil are of roughly equal strength so that both sustain damage during impact.

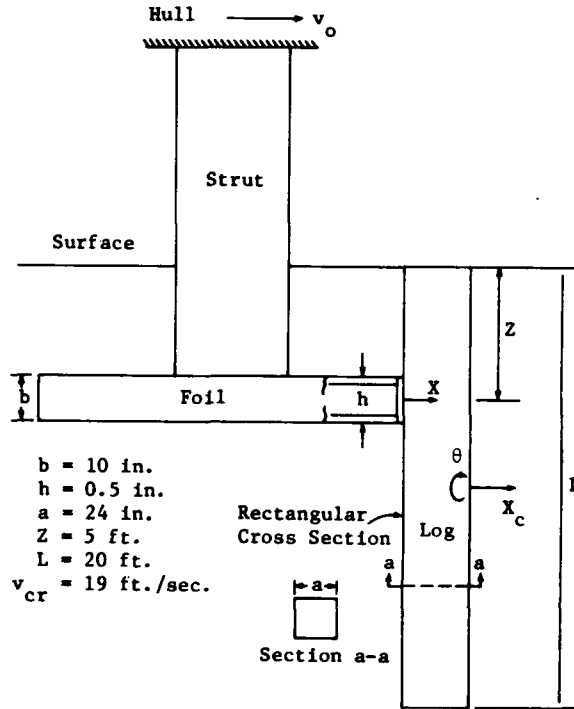


Fig. 1 - Initial impact conditions and assumed structural configuration

The response analysis for each of these cases is quite different. Thus, it is important to establish which of the four cases listed above takes place. To proceed then, we must first decide whether the log and/or the foil will receive damage in the impact area. We then must see if the impact velocity is sufficient to cause damage. Then we can get on with the analysis.

The relative strengths of the log and the foil structure may be assessed by first determining an initial interaction stress σ_1 and then applying that stress over the contact area to get the equivalent interaction force. For purposes of simplification, the log is assumed to be uniform and of square cross section. The foil is assumed to impact the log perpendicular to a rectangular side, as shown in Fig. 1. The foil structure is assumed to consist of a flat leading edge plate with an upper and a lower plate extending back, as shown in the figure.

The initial interaction stress may be estimated from acoustic assumptions as:

$$\sigma_1 = \rho_L C_L \dot{x}_o \quad (1)$$

$$\sigma_1 = \rho_f C_f (v_o - \dot{x}_o) \quad (2)$$

$$\dot{x}_o = v_o / (1 + \rho_L C_L / \rho_f C_f) \quad (3)$$

$$\sigma_1 = \frac{(\rho_f C_f)(\rho_L C_L)}{\rho_f C_f + \rho_L C_L} v_o \quad (4)$$

ρ_L is the density of the log, C_L is the transverse speed of sound in the log, ρ_f is the foil density and C_f is the speed of sound in the foil.

Table 1 lists the strengths (compressive yield stresses) and acoustic impedances (ρC) of aluminum, boron-epoxy and graphite-epoxy. A typical hardwood was selected for the log and it appears that the log yields well in advance of the foil. Although the yield strengths of aluminum, boron-epoxy and graphite-epoxy may vary substantially with composition, and therefore significantly alter the values shown in Table 1, these materials are still substantially stronger than wood. Thus, it is reasonable to expect the wood to yield first when a single foil plate impacts a log, as shown in Fig. 1.

The most substantial log listed in [2] is Hickory Shagbark. The log is actually anisotropic, with much greater strength in the longitudinal direction. A quick calculation reveals that the maximum impact load is not large enough to cause yielding in the longitudinal log fiber. Thus, we may treat the log as a flexible elastic beam until the foil causes enough damage to substantially reduce the log section modulus.

In order to determine an interaction force, one would consider an interaction problem between the log and the foil. The simplest forcing function that can be assumed is consistent with assuming a rigid log and a one-dimensional elastic-plastic response in the neighborhood of the impact. To illustrate, we will consider the problem in Fig. 2. The assumptions may be listed as follows:

- (1) The log is rigid and prismatic.
- (2) The log has a rectangular cross section.
- (3) The foil velocity is constant at v_o .
- (4) The impact duration is small compared to the highest structural period.
- (5) The foil is loaded uniformly along the surface in contact with the log.
- (6) The interaction load along a surface parallel to the velocity is equal to zero.
- (7) The log rotation (θ in Fig. 2) is small ($\tan \theta \approx \theta$).
- (8) The foil is assumed to be elastic for $v_o - \dot{x} < v_{cr}$ so that the interaction force is given by

$$F = \frac{F_o}{v_{cr}} (v_o - \dot{x}) \text{ for } v_o - v_{cr} \leq \dot{x} \leq v_o. \quad (5)$$

TABLE 1
Initial Impact Characteristics

Foil Material	Yield Stress (ksi)	Acoustic* Impedance (lb sec ² /ft ³)	$\dot{x}_o/v_o = \sigma_i/\rho_L C_L v_o$ $\rho_L C_L = 17000 \text{ lb sec}^2/\text{ft}^3$	v_o To Cause Wood Yield ($\sigma_{\text{wood}} = 2000 \text{ psi}$) (fps)
Aluminum	35	109355	.866	18.7
Boron-Epoxy	112.7	131146	.886	19.1
Graphite-Epoxy	60	115800	.872	18.8

*For wood $\rho C \approx 17000 \text{ lb sec}^2/\text{ft}^3$, $C \approx 13000 \text{ fps}$
 $\sigma_w = 2000 \text{ psi}$ Transverse
 $= 10000 \text{ psi}$ Along Grain

(9) The impact zone is assumed to be plastic when $v_o - \dot{x} \geq v_{cr}$ so that the interaction force F is given by

$$F = F_o \text{ when } 0 \leq \dot{x} \leq v_o - v_{cr} \quad (6)$$

$$(10) \quad v_o > v_{cr}.$$

(11) The centroid of the log is assumed to move with a virtual water mass M_v in addition to the log mass $\rho_L LA$ (A is the log cross sectional area, L is the log length and ρ_L is the log density).

If the "yield stress" σ_o can be estimated, F_o can be approximated from

$$F_o = \sigma_o A_i \quad (7)$$

where A_i is the impact area.

The interaction stress σ may be approximated from the acoustic equations as

$$\sigma = \rho_L C_L \dot{x} \quad (8)$$

$$\sigma = \rho_c C_c (v_o - \dot{x}) \quad (9)$$

where ρ_c and C_c are composite density and sound speed and ρ_L and C_L are respective log density and sound speed. Thus, the first assumption is relaxed in order to approximate the velocity $\dot{x}_{cr} = v_{cr}$ at which the composite or log behavior changes from elastic to plastic or vice versa. This occurs when $\sigma = \sigma_o$. Hence,

$$v_{cr} = \frac{\sigma_o (\rho_c C_c + \rho_L C_L)}{(\rho_c C_c) (\rho_L C_L)} \quad (10)$$

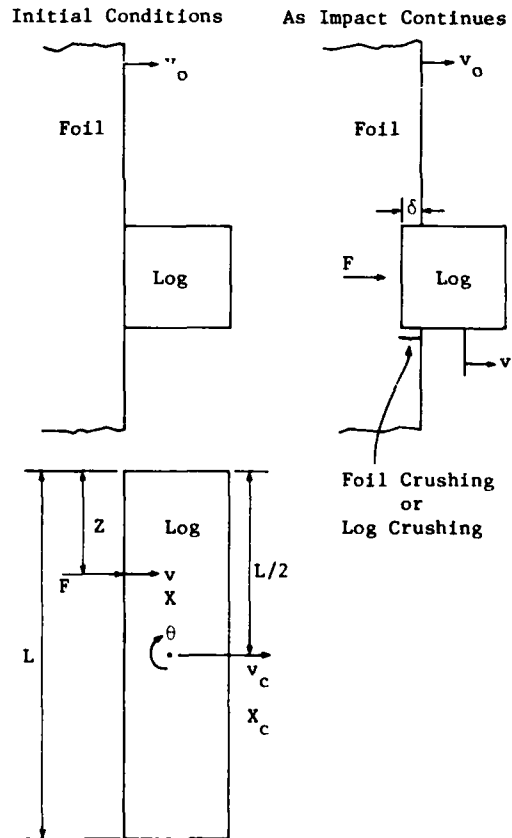


Fig. 2 - Assumed impact configuration

The equations of motion of the log are taken as

$$M \ddot{x}_c = F, \quad M = \rho_L LA + M_v = 2\rho_L LA \quad (11)$$

$$I \ddot{\theta} = (L/2 - Z)F, \quad I = 2\rho_L L^3 A / 12 \quad (12)$$

with the constraint condition

$$x = x_c + (L/2 - Z)\theta \quad (13)$$

x , x_c , Z and θ are defined in Fig. 2 and F is defined by equations (5) and (6).

The solutions may be written in non-dimensional form as follows:

In the plastic response region

$$0 \leq V \leq V_1 \quad V = T \quad \text{and} \quad f = 1; \quad (14)$$

in the elastic region

$$V_1 \leq V \leq V_2 \quad V = V_2 - \text{EXP}(-(T-T_1)) = V_1 + 1 - \text{EXP}(-(T-T_1)) \quad (15)$$

$$f = \text{EXP}(-(T-T_1));$$

where

$$V = \frac{\dot{x}}{v_{cr}}, \quad f = F/F_0 \quad \text{and} \quad T = \frac{C_0 t}{v_{cr}}$$

$$\left[1 + \frac{(L/2 - Z)^2 M}{I} \right] \left(\frac{F_0 t}{M v_{cr}} \right) \quad (16)$$

$$V_2 = v_0/v_{cr}, \quad V_1 = V_2 - 1 =$$

$$\frac{v_0 - v_{cr}}{v_{cr}}, \quad t_1 = \frac{v_0 - v_{cr}}{C_0}$$

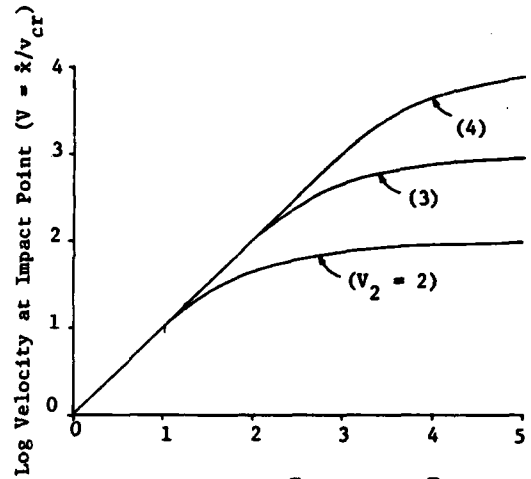
and t_1 is the time at which

$$\dot{x}_1 - v_1 = v_0 - v_{cr}.$$

These solutions are displayed in Fig. 3 for impact velocities v_0 which are multiples of v_{cr} . The interaction force $f(T)$ which is consistent with assumptions (1) through (11) is also shown in Fig. 3.

The damage incurred to the log may be estimated by integrating the relative velocity, thus

$$\delta = \int_0^{t_1} (v_0 - \dot{x}) dt \quad (17)$$



$$\text{Time } T = \frac{F_0}{M v_{cr}} \left[1 + \frac{(L/2 - Z)^2 M}{I} \right] t$$

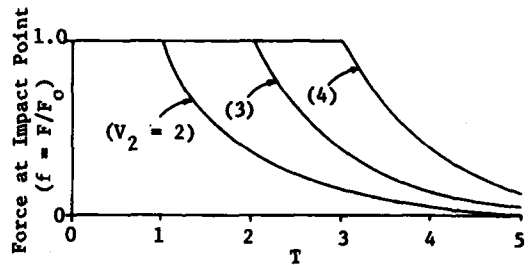


Fig. 3 - Interaction force and log velocity as functions of time

Substituting from equation (14) and integrating, results in

$$\delta = \frac{1}{2} \frac{M v_0^2}{F_0} \left[\frac{1 - (v_{cr}/v_0)^2}{1 + \frac{(L/2 - Z)^2 M}{I}} \right] \quad (18)$$

The preceding formulation is sorely lacking in experimental verification. Equations (8) and (9) give very good predictions to the elastic data reported in [3] in which a stricken plate of aluminum impacted both aluminum and graphite-epoxy plates edge on. These experiments were conducted at low impact velocities so that the responses were entirely elastic and essentially one-dimensional.

Solving the problem for the geometry shown in Fig. 1 results in $\delta = 22.36$ in. for $v_0 = 101$ fps. Premature log damage of this sort would likely result in reduced foil damage. Hence, lower impact speeds could increase foil damage. It is therefore reasonable to expect to find a range of impact speed for which foil damage is maximized.

Equations (17) and (14) may be combined to give the log damage as a function of time

$$\delta = v_o t - \frac{1}{2} C_o t^2 \quad (19)$$

and equation (18) may be rewritten as

$$v_o^2 = 2C_o \delta + v_{cr}^2 \quad (20)$$

If we select a damage level δ_c beyond which the log ruptures and no longer loads the foil (a rather presumptuous fracture criterion), equation (20) gives the foil impact velocity correlating with that damage level

$$v_{oc} = \sqrt{2C_o \delta_c + v_{cr}^2} \quad (21)$$

Equation (14) gives the time at which the log breaks as

$$t_c = \frac{v_{oc} - v_{cr}}{C_o} \quad (22)$$

or from equation (19)

$$t_c = \frac{v_o}{C_o} \left\{ 1 - \sqrt{1 - 2\delta_c C_o / v_o^2} \right\} \quad (23)$$

for $v_o > v_{oc}$

$$\text{or } t_c \approx \frac{\delta_c}{v_o}$$

The impulse \bar{J} and energy \bar{E} can be obtained with integrations of equations (15) and (16) as

$$\bar{J} = \frac{F_o v_o}{C_o} \quad \text{for } v_o < v_{oc} \quad (24)$$

$$\bar{E} = \frac{F_o v_o^2}{C_o}$$

and

$$\bar{J} = \frac{F_o v_o}{C_o} \left\{ 1 - \sqrt{1 - \frac{2\delta_c C_o}{v_o^2}} \right\}$$

$$\bar{J} \approx \frac{F_o \delta_c}{v_o} \quad \text{for } v_o > v_{oc} \quad (25)$$

$$\bar{E} = \frac{F_o v_o^2}{C_o} \left\{ 1 - \sqrt{1 - \frac{2\delta_c C_o}{v_o^2}} \right\}$$

$$\bar{E} \approx F_o \delta_c$$

The energy \bar{E} is simply $v_o \bar{J}$ for our illustrative case of constant foil velocity v_o .

Impulse and energy imparted to the foil are plotted as functions of v_o in Figs. 4a and 4b for an assumed critical damage parameter of $\delta_c = .5$ ft. It can be seen that both of these integrals achieve a maximum at $v_{oc} = 54.8$ fps and then decrease sharply with increasing impact energy. Fig. 5 gives the force for 3 selected impact velocities. The simple explanation is that the rupturing log is much less efficient than the intact log. Since it is reasonable to expect the foil response to follow either the energy or impulse curves (usually the energy), one may expect to find a range of impact velocity for which the foil response is maximized.

This type of response velocity relationship is not uncommon in impact phenomena and is frequently observed in penetrations into plates by artillery rounds. Beyond a critical velocity, the round ruptures prematurely and loses its penetrating capability. This trend in foil-log collisions could be sought experimentally with a series of small scale experiments.

In these calculations, no provision has been made to identify a critical angle of rotation beyond which the log slides off the foil and further reduces the loading into the log.

The selection of a critical angle may depend upon δ_c in that the log may become "impaled" on the foil and refuse to slide off. Also, if the log is struck at its centroid, no rotation is predicted by these linear equations. The reasons listed above, coupled with the fact that omitting the consideration of a critical "slide-off angle", θ_c , is generally conservative in that the foil load tends to be overestimated, lead us to simply omit θ_c in this initial analysis.

There are some general remarks that should be made at this juncture. We must recognize that although some of the general trends we have identified in this preliminary study should persist, we cannot afford to attach too much significance to the included numerical results. A more detailed analysis would consider the log to be elastic plastic and would incorporate more sophisticated yield and fracture criteria. These calculations indicate that in moderate impact velocity regions the impact duration is on the order of the highest structural period. Thus, F becomes an "interaction" function and is somewhat more complicated. Log fracture and yield criteria also grow in complication due to the log response. High frequency water responses may affect the log motion.

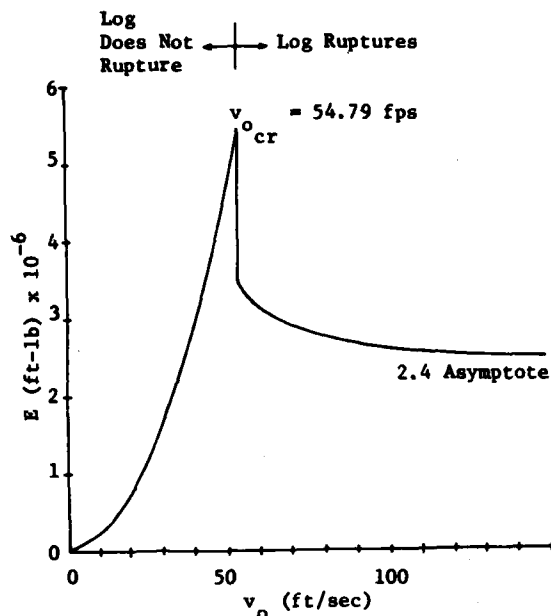


Fig. 4a - Energy absorbed by foil as a function of impact velocity

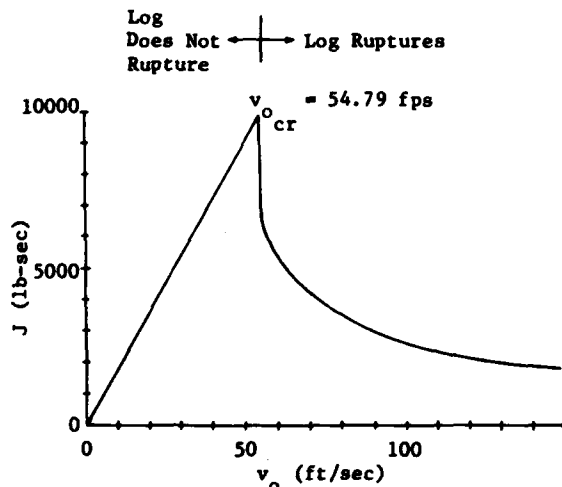


Fig. 4b - Impulse imparted to foil as a function of impact velocity (rotation constraint is omitted)

PREDICTION OF STRUCTURAL RESPONSE OF GENERIC STRUT-FOIL SYSTEM WITH FORCING FUNCTION BASED UPON SIMPLIFIED THEORY

The forcing function developed in the previous section was applied to a beam model of the hydrofoil strut system to determine if a simple beam theory could adequately predict the structural response characteristics of the system as observed in operational collisions [1].

The strut and foil were modeled with a total of 46 beam elements using the DYCAST code [4]. This is a dynamic, large deflection, elastoplastic structural code. The beam elements were assumed to have hollow cross sections with the dimensions shown in Fig. 6. The beam elements are based upon Bernoulli-Euler beam theory (i.e. normals perpendicular to the cross section remain straight and normal) and torsional effects include only those due to St. Venant torsion (cross sectional warping is not allowed). Lateral displacements are represented by cubic functions, while axial displacements and the angle of twist are represented by linear interpolation polynomials. A constant EI and GJ were chosen for strut and foil. The values chosen are typical of those used in hydrofoil design [5,6]. Again, the material chosen was steel with a yield strength of 80 ksi. The forcing function shown in Fig. 7 was used to load the foil over a 24-inch span centered 60 inches from the foil centerline. No attempt was made to model the virtual mass of the water by modifying the density of the submerged portion of the strut-foil system. The top of the strut was assumed to be fully restrained.

For this problem, an impact velocity of 54.8 fps was used, a critical velocity of $v_{cr} = 19$ fps and a peak force of 75,000 lbs was assumed. The latter value was obtained from [1] and was experimentally obtained from actual impact data. The duration of the load at peak value, t_1 , becomes 56 milliseconds for a 20-ft long, 2-ft square cross section log. A picture of the angle of twist/unit length-time histories is given in Fig. 8. These were essentially identical at all points on the strut because of the uniform GJ assumed. The initial peak occurs at 40 milliseconds and the torsional response has a period of 80 milliseconds. This is a factor of three smaller than the 250

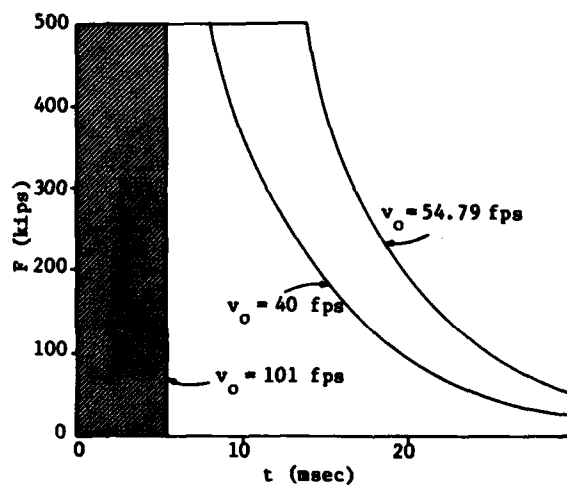


Fig. 5 - Force on foil for 3 different impact velocities (shaded area denotes case for which log ruptures)

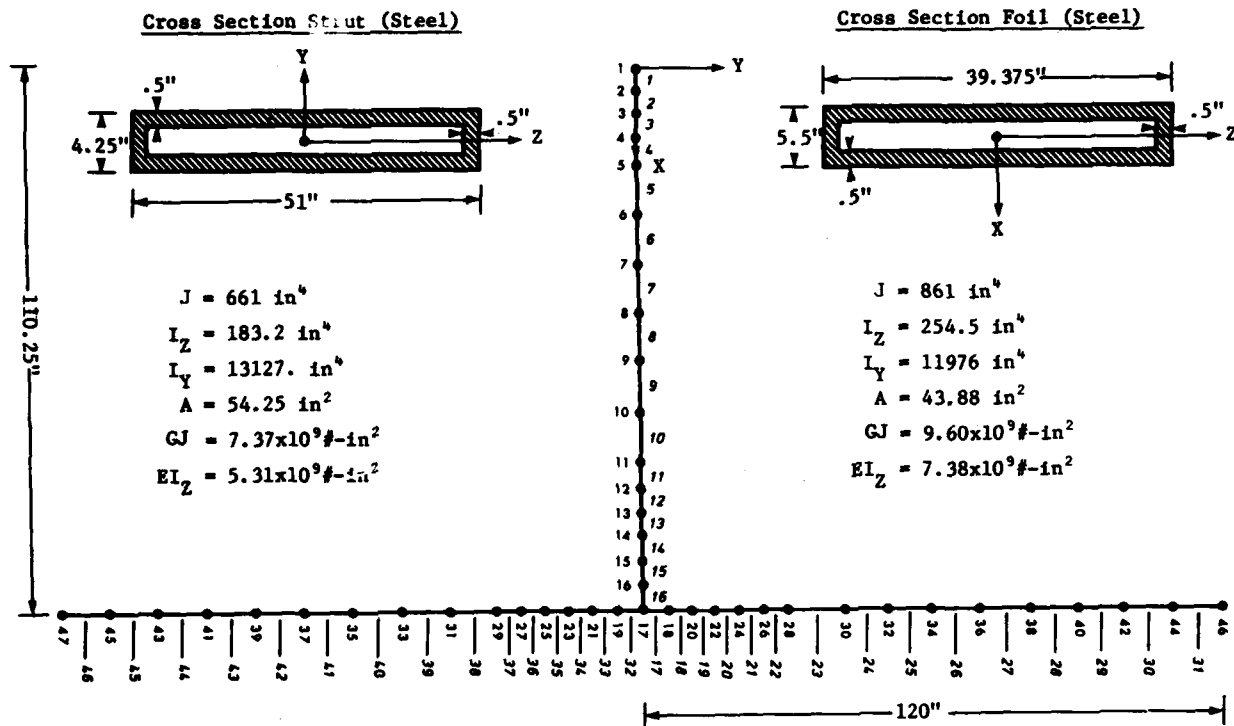


Fig. 6 - Discretization and cross-sectional properties used in beam model of strut-foil impact using approximate interaction load

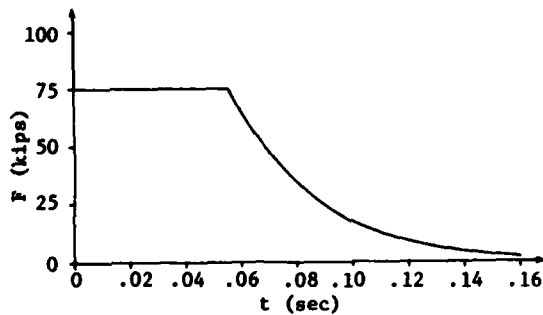


Fig. 7 - Interaction load based upon simplified analysis used in strut-foil structural response calculation using DYCAST

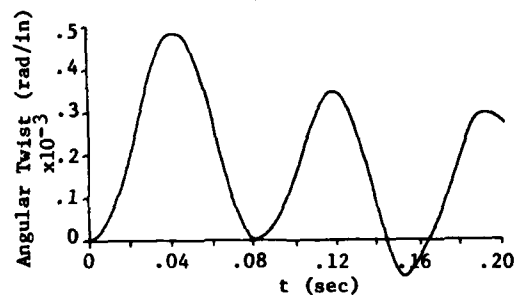


Fig. 8 - Angle of twist/unit length in strut obtained from DYCAST calculation

millisecond period indicated in the experimental data [1]. The inclusion of the virtual mass of the water would tend to increase the period but the effect of hydrodynamic side forces on the response is difficult to assess. The strains obtained from the calculation may be derived by multiplying the torsional curvatures by the distances to various points on the cross section (Fig. 8). This gives a peak strain due to torsion alone of .0125. This is well into the

plastic range and three times the yield strain in shear. Again, it must be emphasized that cross sectional warping is neglected in the theory. The maximum bending stresses that occur at the strut root near peak torsional response between 30 and 40 milliseconds are ± 18.5 ksi. These have been limited by the plasticity yield criteria and are due to log impact alone. At no time does any point on the foil experience inelastic response. This could only occur locally

and be predicted by an interaction analysis. The results of the previous section indicate local inelastic behavior will not occur. The implications of this result are that, even though the impact load does not cause local foil damage, or even inelastic behavior, the "longer term" strut torsional response is critical enough to cause inelastic strut response and eventual actuator failure when combined with lateral hydrodynamic fluid loads caused by large strut rotations. This is qualitatively what is shown in experimental data, although a quantitative comparison should not be made. These comparisons should not be made: a) because of uncertainty of the meaning of some measurements in the experimental data; b) the simplicity of the structural model which was developed to illustrate phenomenology and not detailed quantitative response; c) the neglect of certain effects such as the water mass and side forces; and finally d) lack of knowledge of the structure and size of the impacted log, the depth of impact, and other such pertinent data required for a quantitative prediction.

PREDICTION OF INITIAL IMPACT FORCES IN THE FOIL USING A SOPHISTICATED FINITE ELEMENT CODE, TRANAL

The prediction of the response of a strut-foil system to impact loads is a complicated problem involving the disciplines of impact dynamics, elastic-plastic and geometric nonlinear behavior, possible fracture, fluid-structure interaction and structural mechanics. In addition, the possibility of fluid cavitation and hydroelastic instability exists. The latter two phenomena were not considered in the current study.

For purposes of studying the initial interaction forces on a foil subject to impact with a dead-head log, certain theoretical and geometrical assumptions were made. In some cases, these were necessitated by current limitations of the computer code, TRANAL [7], that was used for this part of the analysis.

TRANAL is a finite element code for the nonlinear transient analysis of three-dimensional problems. It employs a central difference time integration technique with subcycling capability. This allows different time steps to be used in different zones based upon the Courant stability criterion for each zone. It includes material nonlinearities and a version also has large deformation capability. The small strain version was used for the present work. For the purposes of the initial study, the following problem was formulated.

A solid rectangular strut and foil were chosen for the analysis. The dimensions were chosen to be within the range of EI and GJ for an actual strut-foil system [5,6]. Table 2 defines the actual values used in the calculation. The geometry was deliberately kept simple to reduce modeling time and because modeling the typical hollow sections and thicknesses employed

in real structures would have imposed severe restrictions on the time-step size (and hence cost) required in the analysis. A 20-foot long square log of 2-foot width was impacted five feet below the water surface and 60 inches from the foil centerline (see Figs. 9, 10). All points on the strut and foil were given an initial velocity of 60 knots (30.9 m/sec). All points at the top of the strut were maintained at a horizontal velocity of 60 knots to simulate the ship speed.

A picture of the grid used is given in Figs. 9 and 10. The model consists of 24, 22 and 22 elements in the X, Y and Z directions, respectively. This is a total of 11,616 elements, minus some void elements, and represents over 30,000 degrees of freedom. All elements used were eight-node isoparametric hexahedra elements using one-point integration. The steel was modeled as an elastic, ideally plastic material with a yield stress of 80 ksi. The wood properties were those of Hickory Shagbark [2]. The yield stress of 2000 psi employed in the Von Mises yield surface was that perpendicular to the fibers [2]. The log density was assumed to be equal to that of the water. The water was modeled as an elastic material with a negligible shear modulus and a tension cutoff of 0.0 psi based upon the mean normal pressure. Table 2 contains a complete description of the properties used in the analysis. Because of the vast differences in wave speeds and element sizes in different portions of the grid, the subcycling capability of TRANAL was used. A major time step of .23 milliseconds required subcycling ratios of up to 40 for stability purposes in the steel elements versus the larger water elements. The calculation was run for 154 major time steps out to 35.4 milliseconds.

To simulate the impact of the steel with the log, a gap element was used for the four log elements adjacent to the foil at their contact region (see Figs. 9,10). This gap element allows compression stresses normal to the surface to develop in the contact region but no tensile stresses are allowed. An initial gap of .58 inches was assumed. This closed within .92 msec (see Fig. 11) at the 60-knot initial speed.

One problem in the analysis is that the forces of the fluid on the strut-foil system are included in the analysis, and it is difficult to isolate these from the stresses due to impact of the foil with the log. This would require incorporation of equilibrium "in-flight" forces and velocities in the free-field region which is beyond current capabilities. Transmitting boundaries (Lysmer-type [8]) were used on all sub-surface boundaries to minimize reflections and simulate a fluid halfspace.

In the discussion and related figures that follow, all compressive normal stresses and strains are positive and tensile stresses and strains are negative. Shearing stresses and strains are the negative of those in the standard elasticity conventions. Shearing strains

TABLE 2
Geometry and Material Properties Used in TRANAL Strut-Foil Impact Problem

Material	STRUT*	FOIL*	LOG [5]	WATER**
	Steel	Steel	Hickory Shagbark	Water
K(ksi) ⁺	24170.	24170.	747.	300.
G(ksi) ⁺	11150.	11150.	1007.	.3
σ_0 (ksi) ⁺	80.	80.	2.0	N.A.
ρ (kip-msec ² /in ⁴)	.7322	.7322	.0935	.0935
I_{min} (in ⁴)	164. (I_Y)	219. (I_Y)	--	--
I_{max} (in ⁴)	37400. (I_Z)	20700. (I_X)	--	--
J(torsional rigidity)-in ⁴	658.	876.	--	--

*Steel values correspond to $E = 29 \times 10^6$ psi and Poisson's Ratio = 0.3.
 **Tension cutoff value of $J_1 = 0.0$ used, although a value $J_1 = 3p = 3(P_0 + \rho gh)$ would be more realistic, with $P_0 =$ atmospheric pressure. Probable effect on calculation is negligible.
⁺K \equiv Bulk modulus
 G \equiv Shear modulus
 $\sigma_0 \equiv$ Uniaxial yield stress

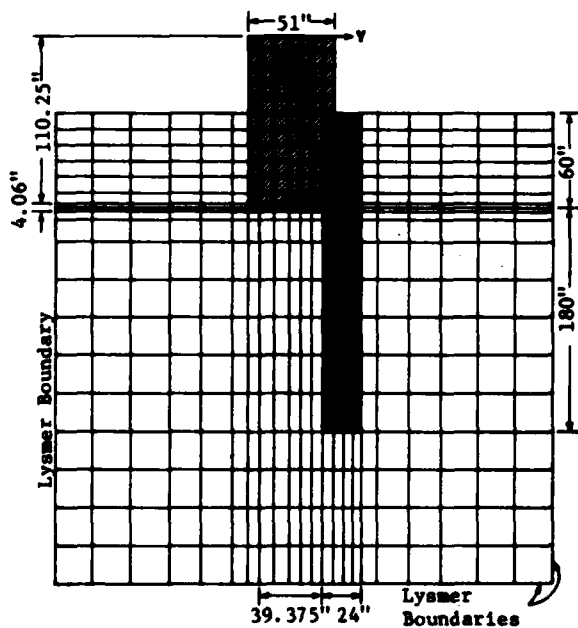


Fig. 9 - Discretization of strut-foil system for log impact (elevation view)

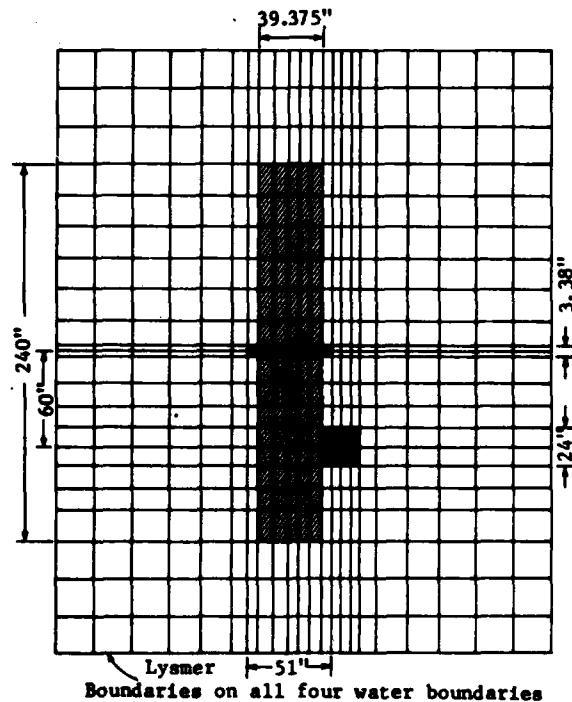


Fig. 10 - Discretization of strut-foil system for log impact (plan view)

are tensor components. To obtain engineering shearing strains, they must be multiplied by two. Velocities are nodal quantities, while stresses and strains are element-centered.

Fig. 11 shows the stresses in the log after impact in the GAP elements immediately adjacent to the foil. We see they are constant after an initial spike and equal to 4.4 ksi at both the top and bottom elements adjacent to the foil. This is higher than the 2 ksi yield stress of the wood because σ_x and σ_z stresses present have allowed the stress point to move on the failure surface. This also has significance because the actual yield strength of the material in longitudinal fibers is 10 ksi. Hence, it is possible even larger interface stresses could develop if an anisotropic yield criterion, such as Hill's or Tsai-Wu's [9], were used. This also has relevance for the work in the first section where a simplified interaction force representation was developed.

The next figure (Fig. 12) shows the strains through the width of the log in the top elements at the foil level. The strains in elements adjacent to the foil reach almost 200 percent and are really meaningless because the theory is not valid for such large strains. They do say, however, that the log will crush at least twelve

inches in the front and 4 inches at the rear during the time span of the calculation. There is a region between twelve and eighteen inches that has "relatively small" strain of almost three percent. Although the calculation was terminated after 35.4 msec, it appears that the log velocities have peaked below the 1215 inches per second velocity of the hydrofoil. Fig. 13 shows horizontal velocities of the log at points through the depth. A comparison of the velocities at the top and bottom shows some rigid body rotation has begun. However, the velocities in between indicate "rupture and crushing" and possible log failure is likely at this impact speed. If the log ruptures, the load will be cut off reducing further strut/foil damage.

Let us now consider the response of the foil over the initial 35 msec time span. The interaction stress (σ_{yy}) in the strut are only about 7500 psi (see Fig. 14). (Remember all stresses are cell-centered.) The corresponding radial strains are small too and only reach 0.4 millistrain, which is well below the elastic limit. The largest stresses in the foil are the σ_{zz} stresses, which are the bending stresses (see Fig. 15). These are shown at the impact location. These stresses oscillate with a period of about 11.5 msec (90 Hz) and reach 30 ksi, well below the steel yield stress. The only

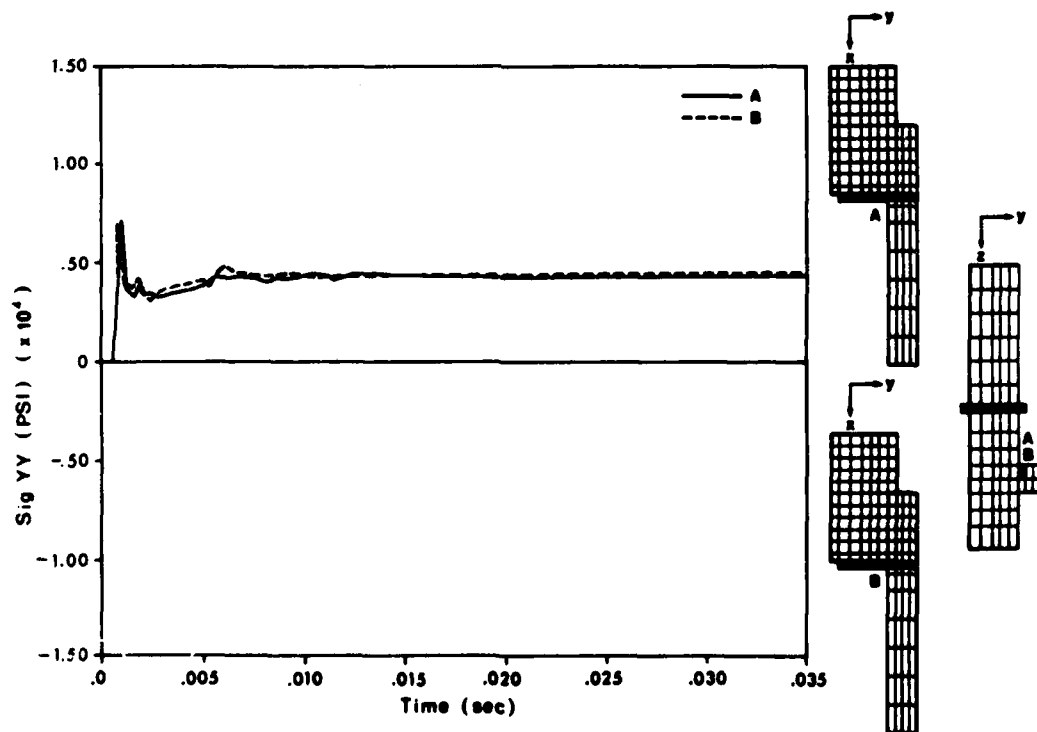


Fig. 11 - Interaction normal stresses in log (σ_{yy})

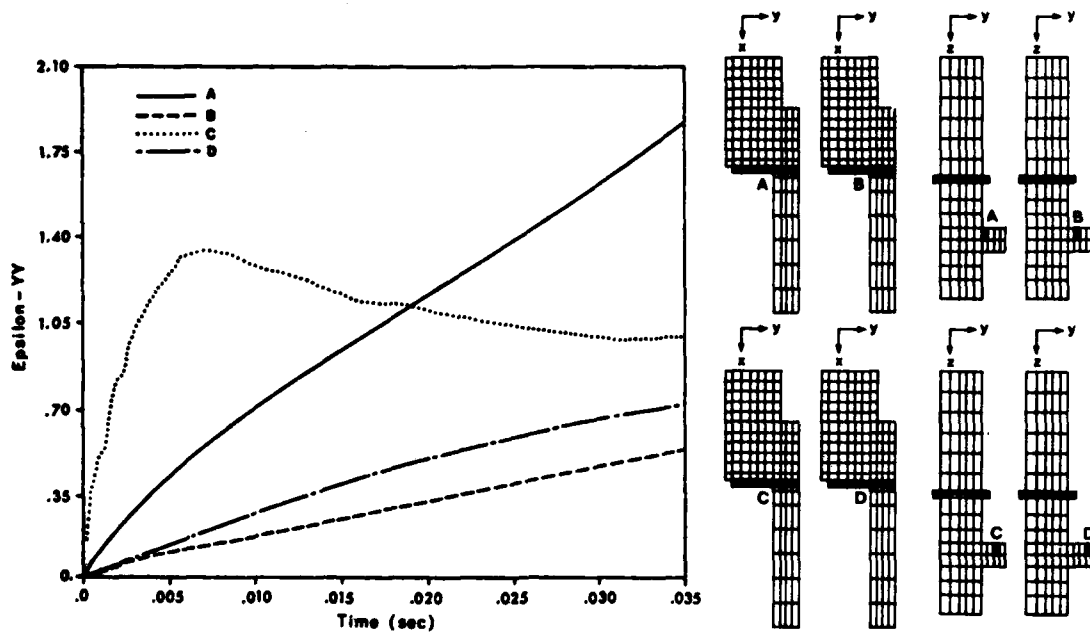


Fig. 12 - Normal strain in log (ϵ_{YY})

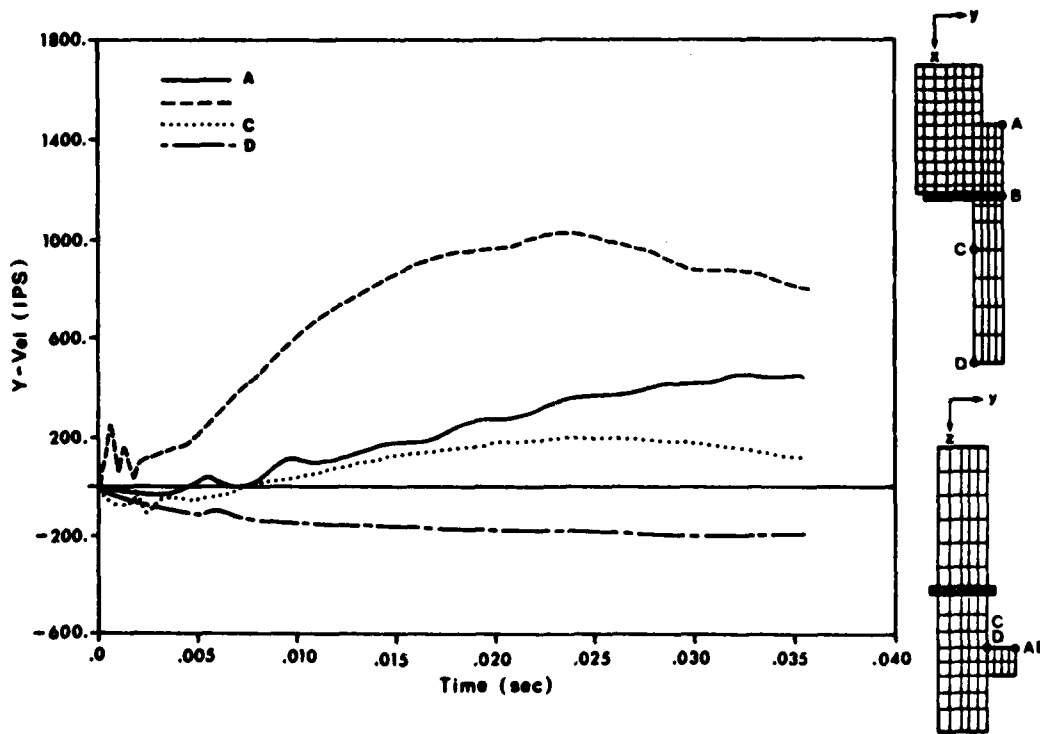


Fig. 13 - Horizontal velocity of log (V_Y)

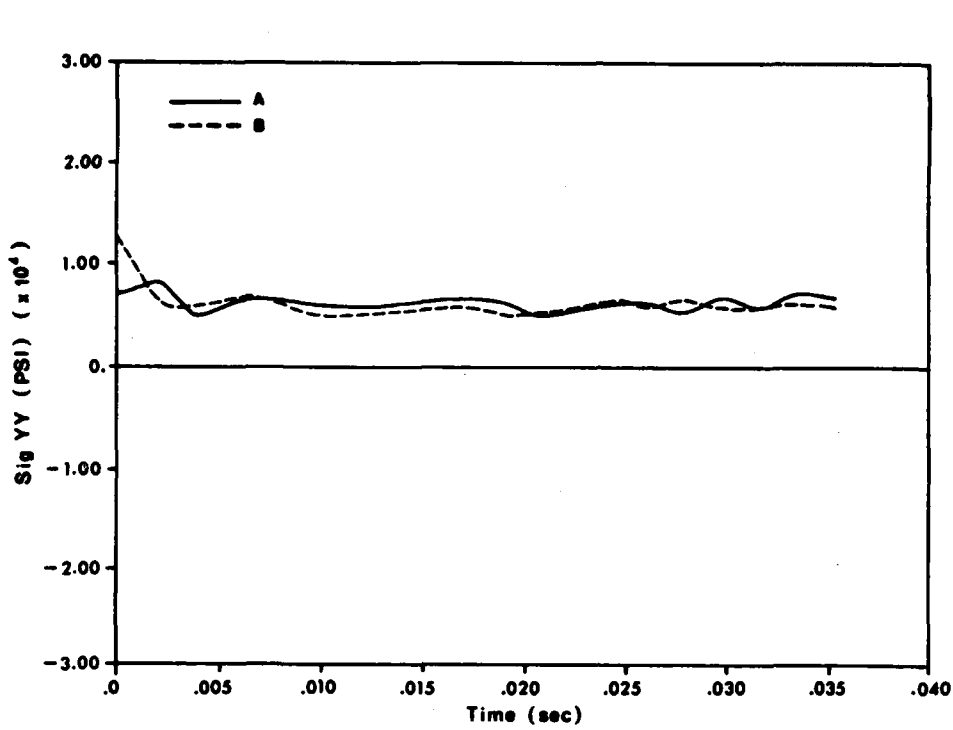


Fig. 14 - Interaction stress in foil (σ_y)

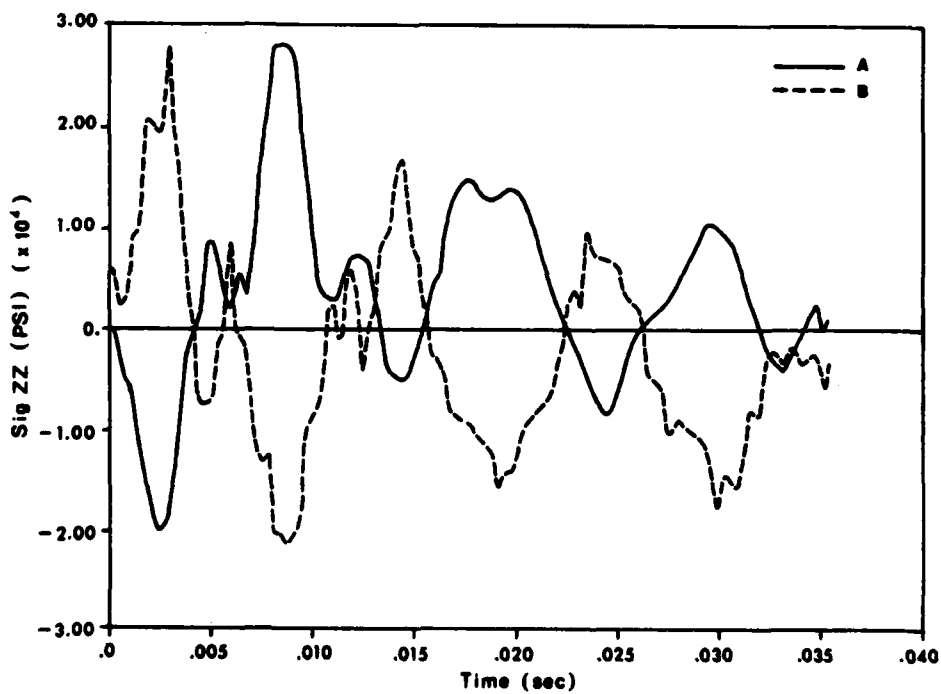


Fig. 15 - Normal stress in foil (σ_{zz})

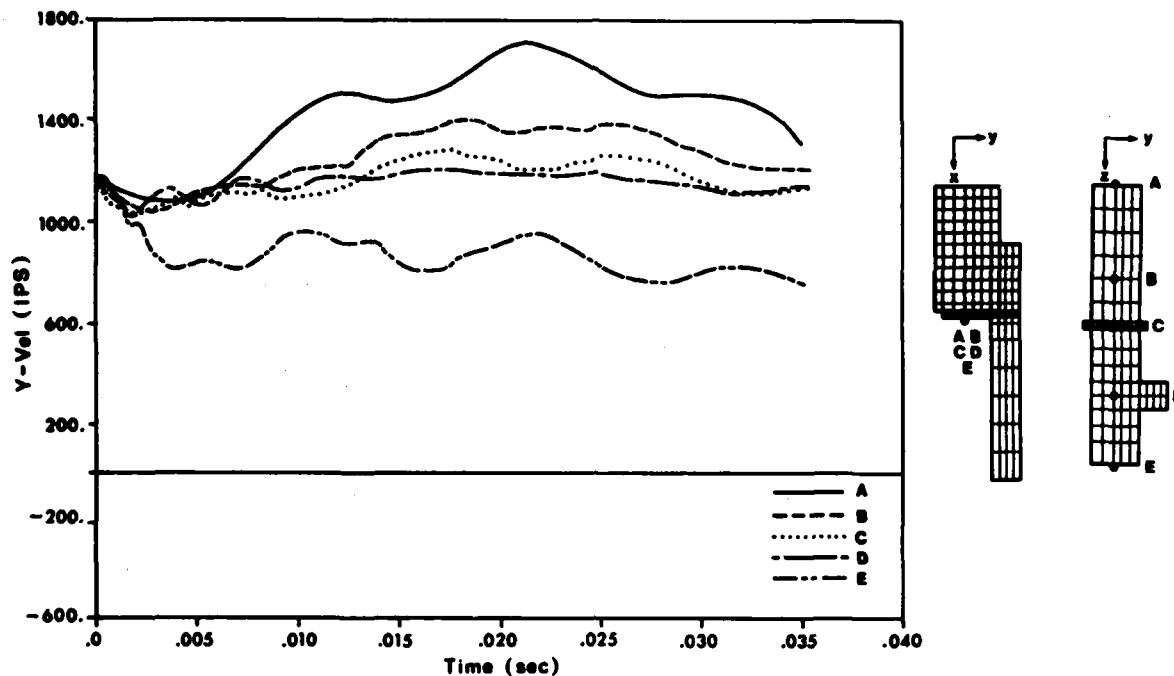


Fig. 16 - Horizontal velocity at points along foil (V_y)

other relatively large stresses in the foil are torsional stresses which reach approximately 10 ksi and are starting to build up at about 23 msec. These are a result of the strut bending, inducing torsional oscillations in the foil. Their period is estimated at 50 msec, based upon a quarter of a cycle between initiation and end of the oscillation. The magnitudes of all these stresses up to this point indicate no inelastic response in the foil.

Evidence of the rotation of the foil about a vertical axis (X-axis) is indicated in Fig. 16. These represent Y velocities at the bottom of the foil at various locations along the length of the foil. The increase in velocity above 1215 inches/second due to rotation on the side opposite impact and the decrease in velocity on the impact side are obvious.

Vertical stresses at the top of the strut are shown in Fig. 17. Inelastic response occurs here because of the bending due to the water forces and impact with the log. The aft stress point shows bending stresses reaching 90 ksi compression, while the stress point forward of the centerline illustrates the bending with over 80 ksi in tension. The torsional shearing stresses at these locations show no definitive evidence yet of the buildup of the torsional mode of oscillation, although they do reach almost 20 ksi at 35 msec.

Vertical bending strains in the strut in the aftmost position at the top reach over 1.5

percent, well into the plastic range. The other strains ϵ_{yy} and ϵ_{zz} are smaller and reach 0.6 to 0.9 percent and are still increasing. Torsional strains reach 0.4 percent at this location (Fig. 18) and .14 percent at mid-depth near top and bottom of the strut.

In summary, then, the following findings can be reported for the first 35 msec of impact of a generic steel strut-foil system with a dead-head log at 60 knots.

- The interaction stress of 4.4 ksi is higher than the 2 ksi yield stress because of the actual triaxial stress state in the log. If a different failure criterion is used, this could be expected to change.
- For a 60-knot impact, the log will probably rupture, based upon strain data in Fig. 12.
- The foil remains elastic during the time of impact, despite bending stresses of 30 ksi and impact stresses of 7 ksi (σ_{yy}).
- Torsional stresses are generated in the foil as a result of beam-like bending of the strut initiated by impact.
- Some inelastic response at the top of the strut occurs as a result of

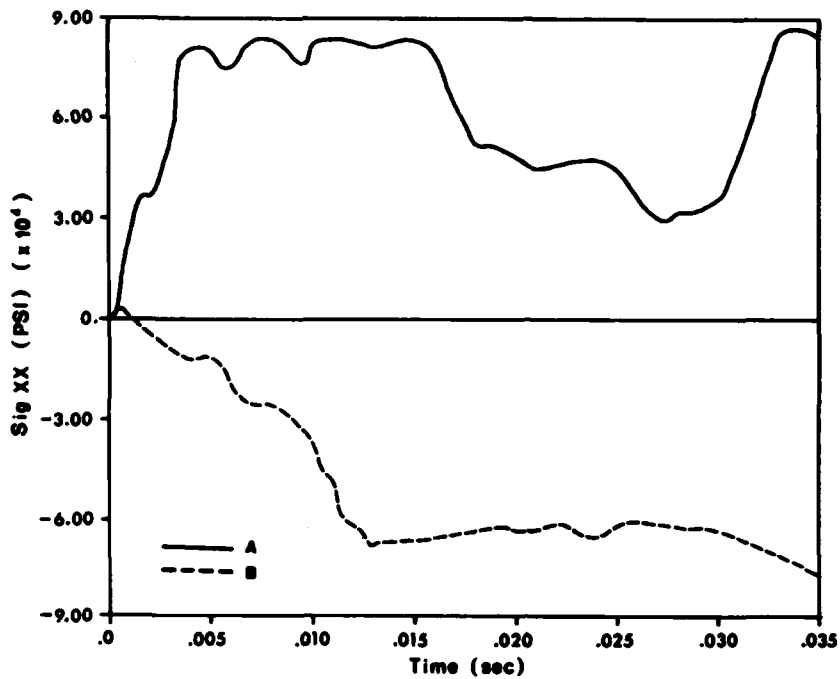


Fig. 17 - Vertical stress at root of strut (σ_{XX})

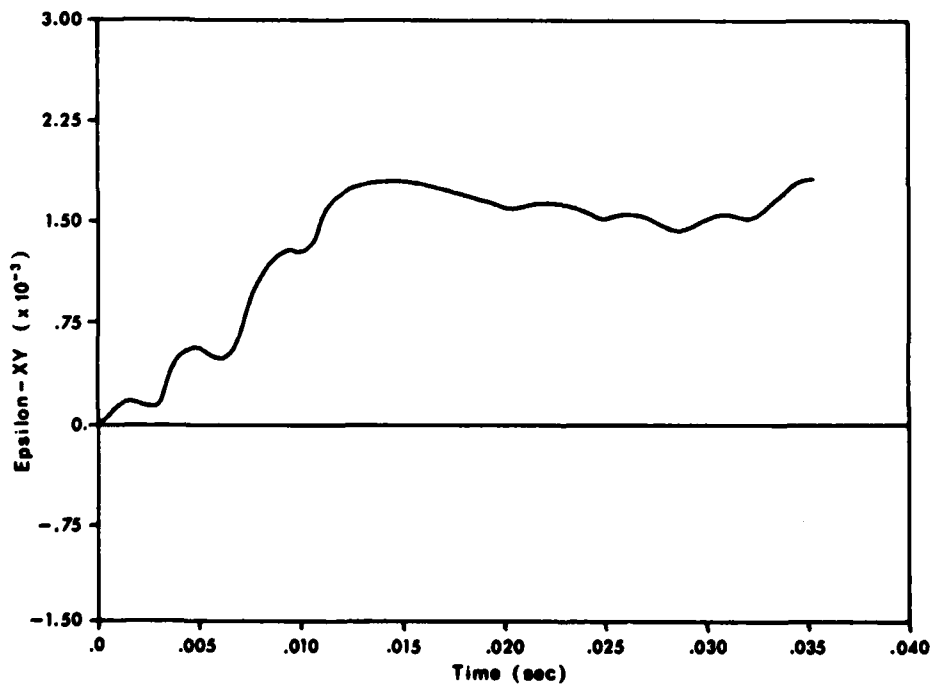


Fig. 18 - Torsional strain at root of strut (ϵ_{XY})

bending stresses due to log impact and forces of the water on the foil.

•Torsional stresses up to 20 ksi are generated in the strut during the initial 35 msec, but the slow torsional oscillation of the strut is not fully developed.

POSSIBLE ANALYTIC IMPROVEMENTS

Based upon results discussed in the previous sections, the following suggestions for improved capability in impact prediction techniques of strut-foil systems with "dead-head" logs are presented:

(1) Beam elements can be developed to better represent elasto-plastic torsion of non-circular sections through the inclusion of a warping function. In addition, the beam element should be capable of simulating arbitrary composite layups and anisotropic failure criteria. This capability may be sufficient in many cases to predict the dynamic response of strut-foil systems to impact loads. Only comparison with test data would verify this.

(2) It is more likely an anisotropic composite plate (shell) element with bending, stretching and transverse shear effects will need to be developed because of the platelike characteristics and dimensions of struts and foils. A simplified element based upon an "effective modulus" theory should prove adequate to predict the structural response (as opposed to wave propagation effects) of the strut and foil.

(3) The simplified interaction force function developed in the first section can be improved and extended to composite foil impacts with "dead-head" logs.

(4) The full 3D interaction force prediction capability can be improved by incorporating large deformation effects and anisotropic material properties and failure criteria in the work. The expense of the calculation can be reduced by using approximations similar to the DAA [10], i.e. pcv dampers and virtual mass representation of the water, perhaps directly attached to the structure and log or the log only. The adequacy of this would have to be verified against experimental data generated in an experimental program.

REFERENCES

- [1] D. Wilson, W. Buckley, T. Nomura and J. Snyder, "Patrol Hydrofoil, Guided Missile (PHN-1), Structural Redesign Recommendations," NAVSEC Report 6166-75-3, Mar. 10, 1975.
- [2] T. Bannister and L.S. Marks, Structural Handbook for Mechanical Engineers, 7th ed., pp. 6-150 to 6-153. McGraw Hill, New York, 1978.
- [3] R.W. Mortimer, P.C. Chou and J. Carleone, "Behavior of Laminated Composite Plates Subjected to Impact," Foreign Object Impact Damage to Composites, ASTM, STP 568, ASTM, pp. 173-182, 1975.
- [4] H. Armen, H. Levine, A. Pifko and A. Levy, "Nonlinear Analysis of Structures," NASA CR-2351, Mar. 1974.
- [5] L.B. Greszczuk and A.V. Hawley, "Application of Advanced Composites to Patrol Craft Hydrofoils," Final Report, Naval Ship Systems Command, Contract N00024-72-C-5536, McDonnell Douglas Astronautics Co., Huntington Beach, CA, Apr. 1973.
- [6] L.B. Greszczuk and A.V. Hawley, "Application of Advanced Composites to Hydrofoil Strut," Final Report, Naval Ship Systems Command, Contract N00024-72-C-5536, McDonnell Douglas Astronautics Co., Huntington Beach, CA, Dec. 1973.
- [7] J.L. Baylor, J.P. Wright and C.F. Chung, "TRANAL User's Guide, Part I (Small Strain, Small Displacement Version), Weidlinger Associates, Final Report, Contract DNAS001-76-C-0125, DNA 4960F, Mar. 1979.
- [8] J. Lysmer and R.L. Kuhlemeyer, "Finite Dynamic Model for Infinite Media," J. Eng. Mech. Div., Proc. ASCE, 95, No. EM4, Aug. 1969.
- [9] S.W. Tsai and E.M. Wu, "A General Theory of Strength for Anisotropic Materials," J. Comp. Mtls., 5, pp. 58-80, 1971.
- [10] T.L. Geers, "Residual Potential and Approximate Methods for Three-Dimensional Fluid-Structure Interaction Problems," J. Acoust. Soc. Am., 49(5), Part 2, p. 1505, 1971.

LIST OF SYMBOLS

C	speed of sound in material
C ₀	constant defined in Eq. 16
E	Young's modulus of material
\bar{E}	energy imparted to foil
F ₀	initial impact force
G	shear modulus of material = $\frac{E}{2(1+\nu)}$
I _{Y,Z}	moments of inertia about Y or Z axis
J	torsional rigidity
\bar{J}	impulse imparted to foil
K	bulk modulus of material = $\frac{E}{3(1-2\nu)}$
L	length of log
M	mass of log
v _{cr}	velocity of foil at which plastic deformation is initiated in log

v_0 initial velocity of foil
 \dot{x}_0 initial velocity of log
 $\epsilon_{xx}, \epsilon_{yy}, \epsilon_{zz}$ normal strains
 $\epsilon_{xy}, \epsilon_{yz}, \epsilon_{zx}$ tensor components of shear strains
 ($\epsilon_{ij} = \frac{1}{2}\gamma_{ij}, i \neq j$)
 σ_0 uniaxial yield stress
 $\sigma_{xx}, \sigma_{yy}, \sigma_{zz}$ normal stresses
 $\sigma_{xy}, \sigma_{yz}, \sigma_{zx}$ shear stresses
 ν Poisson's ratio
 ρ mass density

DISCUSSION

Mr. Skop (Naval Research Laboratory):
 In one of your initial slides, when you simplified your analysis, the first assumption was that the log was acting as a rigid body and then you said it went plastic.

Mr. Misovec: That's right. The strength of the beam, with respect to the longitudinal fibers is 10,000 psi so it has a much larger bending rigidity than the strength perpendicular to the fibers which is only 2,000 psi. So in order to get an interaction function for this particular case we used a simplified acoustic approximation, a one dimensional wave approximation, and we found what the interaction force might be for a simplified one dimensional approximation. Then to get the rotation of the beam itself we assumed that it acted as a rigid body once we knew the force. That was one of the approximations.

TRANSIENT RESPONSE ANALYSIS OF A LARGE RADAR ANTENNA

E. Meller, W. A. Loden
Lockheed Palo Alto Research Laboratory
Palo Alto, California

and

W. Woltornist
Lockheed Electronics Company, Inc.
Plainfield, New Jersey

The approach used in determining the transient response of a large shipboard-mounted radar antenna to shock loading resulting from an underwater explosion is described. The dynamic behavior of the antenna configuration, represented by a finite element model of moderate complexity, was determined through direct time integration, using as the "forcing" function the anticipated motion of the ship platform on which the antenna was mounted. The location in the antenna where the peak stresses occurred was determined by inspection of the stress results from this transient response analysis, and a refined finite element model of this region was used to compute more accurate stresses.

INTRODUCTION

A primary concern of structural engineers is to ascertain that, for various loading conditions, stress levels throughout the structure being considered do not exceed the strength capabilities of the materials being used. This task, which can be difficult under any circumstances, usually becomes more formidable when the loading conditions are dynamic rather than static. In the static case, any given loading condition is independent of time, and only one solution is required. In the dynamic case, however, one must solve the differential equations of motion by some appropriate method or methods. This is generally much more difficult and more expensive to do.

For complex structural configurations, the finite element method has proved to be a convenient and powerful tool for performing these static and dynamic analyses; and there are a number of commercially-available and independently-developed programs and program systems for treating such problems, especially for those that can be dealt with in the linear elastic domain. For transient response analyses, there is a choice to be made between modal superposition methods and direct time-integration methods, with different consequences and complications, depending on which path is chosen. In either case, the solution process involves efforts to obtain a finite number of solutions. With the modal superposition approach, the number of modes that must be used to characterize the structure's dynamic behavior properly can be difficult to determine, especially for shock loadings. For complex structures, the computational expense for obtaining all of the modes that might be required could also be

quite significant. The direct time integration approach is attractive because it is potentially more accurate, does not require the analyst to extract and select candidates from the set of modal solutions, and because it can be significantly less expensive to use. With the direct time integration approach, one of the basic choices that must be made is between the set of explicit versus the set of implicit integration methods. Explicit methods, requiring the solution of a set of uncoupled algebraic equations, are attractive because of their simplicity and lower cost for obtaining the solution for any single time step. These methods, however, usually do require the use of very small timestep sizes (due to stability considerations). The primary attraction of the most widely used implicit methods, requiring the solution of a set of coupled algebraic equations, is the fact that significantly larger timestep sizes are possible, with far fewer solutions being required in order to integrate over a given time span.

The primary purpose of the radar antenna analysis described herein was to determine the transient response of the configuration to a given underwater shock environment, focusing special attention on one of the highest-stressed regions, in order to obtain more accurate stress results there. The basic approach used in this analysis was to create a finite element model with which the transient response behavior of the antenna could be determined with reasonable accuracy. Those results were then used, in connection with a more refined finite element model representing the region where the highest stresses were obtained, to determine the stresses there with more accuracy than was possible with the original model.

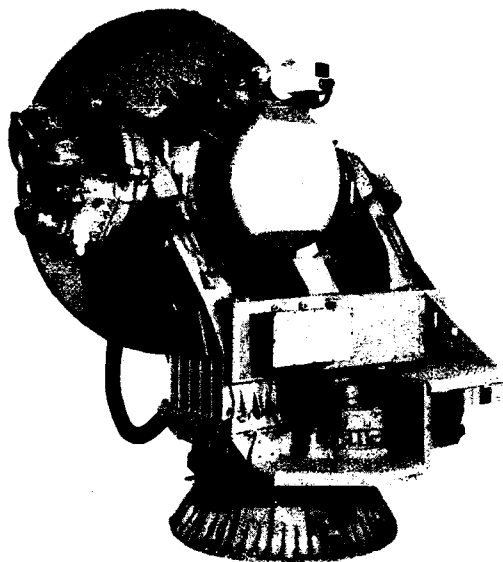


Figure 1. Radar Antenna

A BRIEF DESCRIPTION OF THE RADAR ANTENNA CONFIGURATION

The radar antenna shown in Figures 1 and 2 consists of several major structural components: a base, a turntable, two arms, an antenna support, and an antenna reflector. The lower surface of the base structure is rigidly tied to the deck of the ship (or, for shock survival integrity tests, to the floating shock platform). The turntable is connected to the base through a cross-roller bearing that permits rotation about a vertical (z) "azimuthal" axis. The outer race of this bearing is connected to the base, while the inner race is connected to the turntable. An azimuth motor and gear-drive component is used to rotate the turntable on command in a prescribed motion to attain a desired azimuthal orientation, and it also serves to maintain a fixed position while the ship maneuvers.

The two arms are rigidly connected to the turntable, as is the antenna reflector to the antenna support structure. The support structure is connected to the arms via bearings that permit rotation about an "elevation" axis, and the elevation motor and gear-drive there serve functions that are similar to those of the azimuthal counterparts. Various other pieces of equipment, including wiring cables and counterweights, are also connected to the radar antenna.

APPROACH TO THE PROBLEM

For performing detailed stress analyses from which accurate and useful engineering information can be obtained, finite element models that include all significant structural elements and features, with

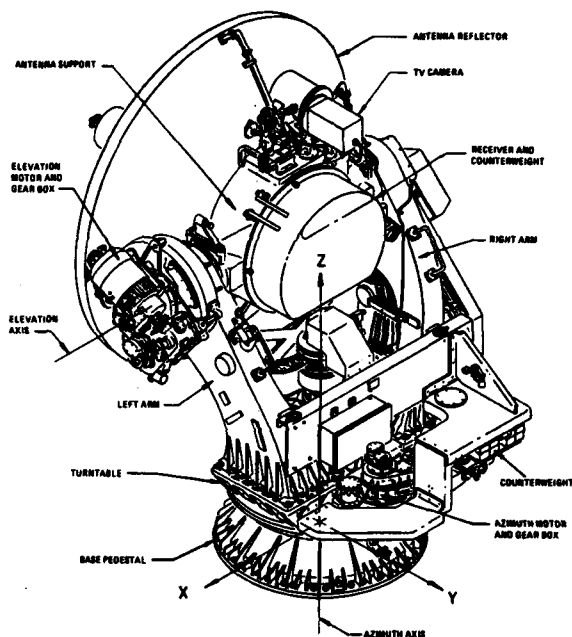


Figure 2, Schematic Drawing of a Radar Antenna with Nomenclature and Coordinate Axes

cutouts, stress-concentration effects and other niceties, are generally necessary. Dynamic analyses, on the other hand, are usually less sensitive to the degree of structural detail, and much useful information can usually be obtained from "dynamic" models that are less complex than their static-analysis counterparts. The construction of a detailed model that is suitable for both static and dynamic analyses can be quite expensive, but not necessarily prohibitively so. The execution of transient response analyses with that kind of model, however, might very well be prohibitively expensive.

In order to perform the required stress analysis for this large and complex antenna structure, which is subjected to shock loads, the following approach was selected:

First, the finite element model for the dynamic analysis, herein called the "dynamic" model, was constructed. This model is sufficiently detailed to represent the dynamic characteristics of the configuration accurately, but the level of detail is not sufficient for the performance of refined stress analyses.

A transient response analysis was then performed using this "dynamic" model, subjected to the appropriate initial conditions and loading history. Structural damping effects were not considered in this analysis, primarily because of the lack of available information about how it should be characterized. The results obtained from this analysis indicate the regions (spatial locations) and times (temporal locations) where the stresses are highest.

Next, the finite element model for the highest-stressed region (the turntable, in this case), was refined to include the greater detail that is appropriate for the accurate stress analysis that was desired.

This "static" model was then subjected to displacement boundary constraints and to interior forces (static equivalents to the inertia forces) that were obtained from the results of the dynamic analysis at the selected time, t . Displacements along the boundary at "old" node points (which are common to the original and to the refined model) can be extracted directly from the results obtained in the analysis with the original "dynamic" model. For "new" boundary nodes, (which did not exist in the original model), displacements can be obtained through interpolations of order compatible with those used in the element shape function definitions. The interior forces can be obtained via linear interpolations of the accelerations from the "dynamic" model nodes to the "static" model nodes, followed by multiplication by the "static" model nodal masses.

Stress analyses with this "static" model yield refined stress distributions (for the selected instant of time) that are compatible with the degree of refinement of the model. It should be mentioned here that the application of displacement boundary constraints yields boundaries that are somewhat stiffer than would be the case when only forces are applied there. This results in underestimation of the stress levels near these boundaries. The stress levels in the interior of the "static" model, however, should be much more accurate than those obtained from the "dynamic" model.

Refined "static" models of other regions (which might be portions of the major components, complete components, or combinations thereof) may be constructed and analyzed for several different times, as required or judged necessary by the responsible engineer.

DESCRIPTION OF THE COMPUTER CODES USED

The bulk of the analyses described herein was performed with the two computer programs REXBAT [1,2] and STINT [3,4], and the graphic results were generated with REXBAT and with the DEFORM program [5]. The REXBAT program, a linear elastic in-house code the current version of which is called REXBAT-7, is actually an ensemble of processors (called program "stages") that are intimately related through local and global data bases. These stages, each of which is a stand-alone processor the internal construction of which has been optimized for efficiency in performing the task(s) at hand, work together to define the finite element model; to compute and assemble the element and other contributions to the mass and stiffness supermatrices $[M]$ and $[K]$ that characterize the configuration to be analyzed; to impose boundary conditions and define loading cases; to perform static and eigensolution analyses; and to determine element forces and stresses corresponding to the displacement results that are obtained by the REXBAT program and/or by

other programs (principally STINT, in these efforts). Related analysis tasks, including "debugging" and plotting of the finite element models and substructuring operations, are performed by appropriate members (stages) in the REXBAT ensemble.

One of the many diagnostic and model-verification tools employed in constructing the individual and combined finite element models for the antenna configuration with REXBAT-7 was its "rigid body" checkout process, a sort of global "patch" test [6] in which the model is subjected to six independent rigid body motions $\{r\}$ and where the forces $\{f\} = [K] \{r\}$ corresponding to these motions are computed using the assembled stiffness supermatrix $[K]$. For a correctly constructed model, these forces must be zero; so the presence of any sizeable values in $\{f\}$ uncovers many (but not all) kinds of modeling errors. The existence in the model of non-rectangular or non-planar elements that (by virtue of their stiffness matrix generation routines) should be rectangular or planar, or the existence of elements that are connected to node points that do not have the correct number or types of degrees of freedom, is easily discerned by examination of the various rigid-body $\{f\}$ vectors. On the other hand, it is not possible to detect slightly incorrect material properties and/or element thicknesses by this process; and a variety of other model-verification checks must also be made.

The preliminary static and modal solutions obtained with the REXBAT program also served to "verify" the individual and combined finite element models by ensuring that (at least for appropriate sets of uncomplicated static loading conditions) the applied loads were being transmitted through the models, without losses (which are sometimes caused by otherwise-undetected groundings and other modeling errors), via reasonable load paths, and that the lowest-frequency vibratory responses (the fundamental modes) were accurate.

The initial displacement field for the transient response analysis, corresponding to one g gravity loading conditions, was also obtained via a static analysis with the REXBAT program.

The transient response analysis was performed with the out-of-core version of the STINT program, which employs the REXBAT generated mass and stiffness supermatrices for the "dynamic" model (as discussed above) in its direct integration of the equations of motion

$$[M] \{a(t)\} + [K] \{x(t)\} = \{f(t)\} \quad (1)$$

(where $\{a(t)\}$ is the vector of nodal accelerations) to produce the desired displacement and velocity histories, $\{x(t)\}$ and $\{v(t)\}$, respectively. The STINT program that was employed in these efforts is an implicit time-integration program, designed to treat large problems, for which the supermatrices describing the finite element model and required by the integrator are too large and complex to fit within the available core space on the computer system being used. This version of STINT, which is especially suitable for treating "stiff" systems of

equations that are often encountered with structural dynamics problems, can use the trapezoidal rule or the 3-step Park linear multistep method [3], employing pseudo-force techniques to shift the nonlinear contributions from $[M]$ and $[K]$ (and from other sources) into the modified right-hand-side vector $\{f\}$, and using matrix-scaling techniques [3] to avoid refactorizations with variable timestep computations. For this analysis, the trapezoidal rule was used with a constant timestep size in order to minimize the computational expenses and to simplify the stress and graphic post-processing operations.

The DEFORM program was used to generate "snapshot" plots of the "dynamic" model of the antenna configuration at various times during its transient response (showing the deflections of the complete antenna and showing the deformations, which were obtained by removing the ship motions from the entire displacement field) and to produce motion pictures of the entire transient response history.

CONSTRUCTION OF THE "DYNAMIC" MODEL

The "dynamic" model of the complete radar antenna was assembled from the set of finite element models constructed to represent the individual major structural components: the base, the turntable, the arms, the antenna support, and the antenna reflector. In the construction of these individual models, attempts were made to describe the actual structural components that they represent as faithfully as possible; but in order to keep the sizes and complexities of these models within reasonable bounds, and in order to keep the computational expenses for solving the transient response problem for the assembled antenna as low as possible, it was necessary to omit some structural details judged to be of minor importance in determining the overall dynamic behavior of the configuration. Small cutouts, bosses, stress concentration effects, and various other details, therefore, were not included in these "dynamic" models.

These finite element models were constructed in the usual way by definition of node points (which are characterized by their initial spatial locations and the sets of admissible displacements, called "degrees of freedom", associated with them), and by specification of the sets of finite elements which have specified geometric and material property attributes, that are connected to each other via these node points. In constructing these models, eccentric stiffeners were represented by beams with "rigid links". For these elements, the beam end-point centroids are attached to "slave" nodes, which in turn are connected to the "primary" structural node points via rigid links. The "slave" nodes, here, have no degrees of freedom associated with them; the primary nodes do. Closely-spaced ribs were modeled with orthotropic quadrilateral plates utilizing a "smearing" technique.

Before assembling the complete "dynamic" model of the antenna configuration, the individual major structural component models (see Fig. 3) were checked, as described above, to ensure that no

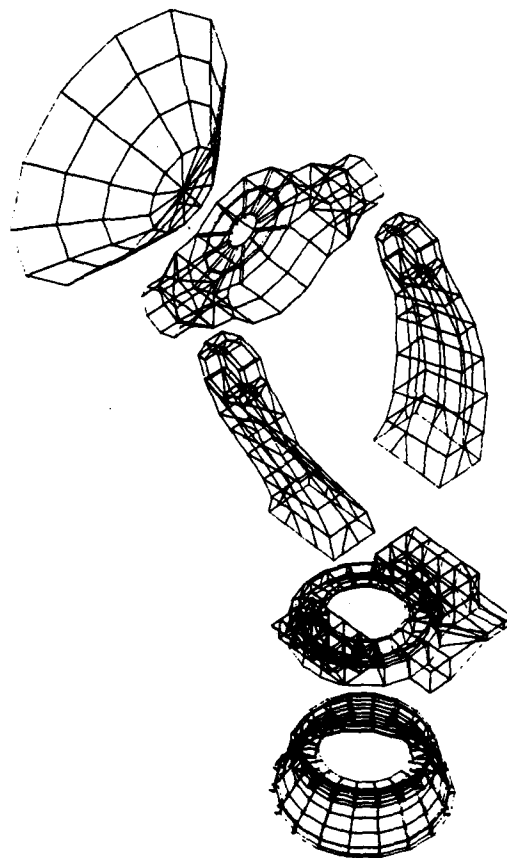


Figure 3. Finite Element Models of Major Structural Components

extraneous forces are introduced by rigid-body motions and to validate their load-transfer capabilities.

In the actual radar antenna, as noted above, the turntable and its attached structural components can rotate about the azimuthal axis, and the antenna-support structure can rotate about the elevation axis. In assembling the complete "dynamic" model for this analysis, however, it was necessary to choose a single fixed position with specific azimuthal and elevation orientations. These orientations could, of course, be varied, if necessary, in future analyses.

All of the bearings in the assembled "dynamic" model were modeled in the following manner. Each pair of nodes, one located on the outer race of the bearing and the other on the inner race, is linked with radial and normal springs representing the bearing stiffnesses (spring constants) in these directions. Additionally, one pair of nodes is linked with a tangential spring representing the motor and gear-drive inertia restraint against rotation. This modeling technique is valid as long as the torques produced by the dynamic forces do not exceed the locked rotor torque of the motor and gear-drive combination. It should be noted that the radial springs only approximate the true bearing behavior. The actual behavior can only be accurately

TABLE 1

VITAL STATISTICS FOR FINITE ELEMENT "DYNAMIC" MODELS
OF THE MAJOR STRUCTURAL RADAR ANTENNA COMPONENTS

MAJOR COMPONENTS	NODE POINTS	BEAM ELEMENTS	TRIANGLE ELEMENTS	QUAD ELEMENTS	SOLID ELEMENTS
REFLECTOR	37	0	12	36	0
SUPPORT	164	68	32	72	0
ARMS	195	32	20	200	16
TURNTABLE	255	66	96	213	18
BASE	402	126	36	234	18

represented by contact elements, which are not available in the REXBAT program.

Non-structural equipment such as motors, gear drives, cables, counterweights, etc., were represented in the assembled "dynamic" model by inclusion of concentrated mass points. These points were located at the centers of gravity of the equipment and were connected to adjacent structure by a network of "rigid" bars that are only capable of transmitting axial forces.

The complete assembled "dynamic" model has 1061 node points with 4152 degrees of freedom, and includes 62 bars, 292 beams, 196 triangles, 755 quadrilaterals, 52 solid elements, 8 concentrated mass points, and 26 stiffnesses representing bearing springs. Table 1 displays some pertinent information regarding the finite element "dynamic" models of the individual major structural components. The assembled "dynamic" model is shown in Figure 4, in which some lines have been removed for clarity.

As with the individual component models, the assembled "dynamic" model of the antenna configuration was checked to ensure that no extraneous forces are introduced by rigid-body motions, for load-transfer capabilities, and for several of its fundamental vibration modes.

TRANSIENT RESPONSE ANALYSIS

During an underwater shock test, the shock wave travels through the fluid medium and the ship (or floating shock platform) to the antenna configuration. The response of the ship (or the floating shock platform) at the lower surface of the base of the radar antenna was used as the forcing function for the transient response analysis performed here. The initial conditions for this analysis were the displacement field that corresponds to a one g gravitational force field (the displacements of the antenna structure under its own weight) and a nulled velocity vector.

The transient response analysis described here was performed with an implicit time integration scheme using the trapezoidal rule and a fixed time step. The use of an implicit, rather than explicit, integration method made it possible to employ a relatively large time step, with the particular step

size being chosen here to give a sufficiently large number of steps in the lowest fundamental response modes. This step size choice was, of course, strongly influenced by the conflicting requirements to represent the higher-frequency responses as accurately as possible, and to keep the computational expenses reasonable.

The forces and stresses for each element in the assembled "dynamic" model were computed using the displacement fields for each time step during the transient response analysis, with the appropriate stages of the REXBAT program. The highest stressed region was earmarked for further detailed study, as described below. The radar antenna, in various

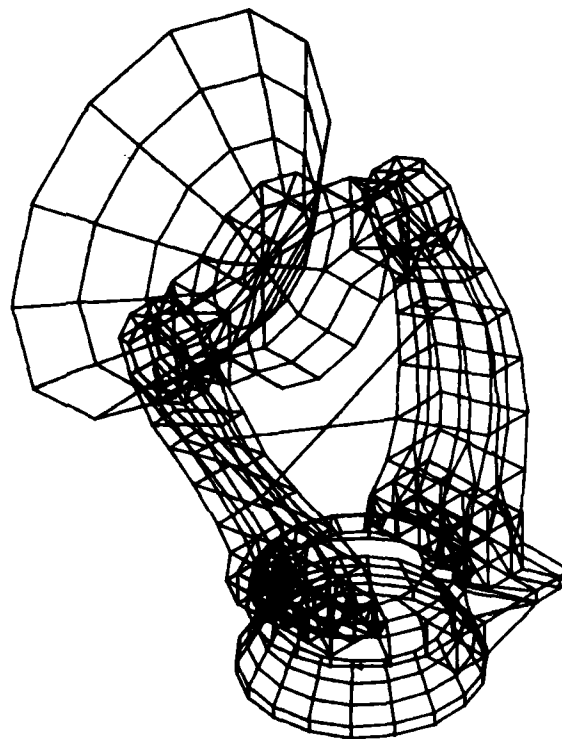


Figure 4. Finite Element Model of Complete Antenna

undeformed and deformed states, is shown in Figures 4 through 8. Figure 4 shows the undeformed configuration at time $t = 0$; Figures 5 and 6 show the undeformed configuration (dashed lines) and the deformed configuration (solid lines) at two representative instants of time. Figures 7 and 8 show similar results, but here the "rigid-body" motions (i.e., the displacements at the lower surface of the base structure) have been removed in order to make the deformations of the structure more apparent. In all of these figures, the actual displacements, and deformations, have been exaggerated in order to illustrate the response results more clearly.

The displacement results for each time step of the transient response analysis were employed, with a slightly simplified version of the "dynamic" finite element model, to make motion pictures of the responding radar antenna configuration. These movies, produced with the DEFORM program, proved most valuable in providing physical insight into and confidence in the computed structural responses. Qualitative data about the largest deformations and the most rapid changes of deformations, difficult to extract from the large stacks of printed output obtained, were easily observed in the movies. It is interesting to note, too, that for this analysis the region of highest stress was not one in which these motions were greatest.



Figure 6. Undeformed and Deformed Configuration at $t=t_2$



Figure 5. Undeformed and Deformed Configuration at $t=t_1$

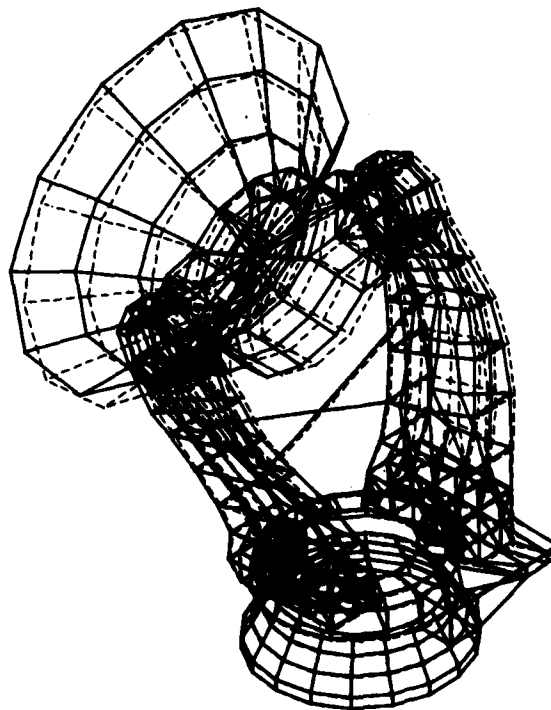


Figure 7. Undeformed and Deformed Configuration at $t=t_1$, with Floating Barge Platform Motion Removed

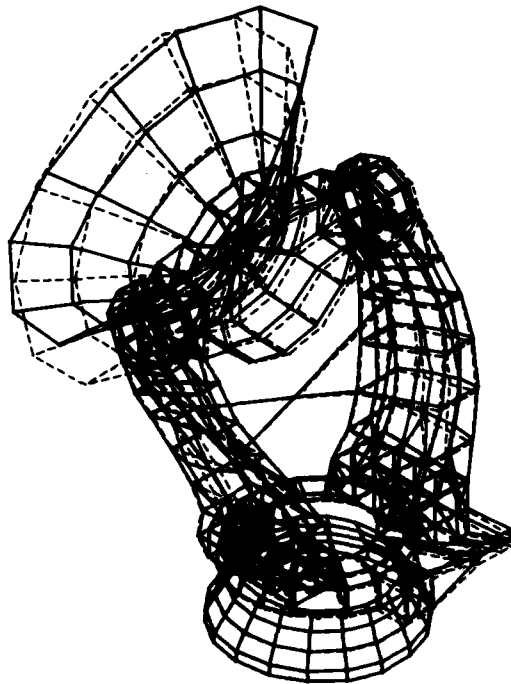


Figure 8. Undeformed and Deformed Configuration at $t=t_2$, with Floating Barge Platform Motion Removed

STRESS ANALYSIS OF A SELECTED REGION

Examination of the stress results obtained from the transient response analysis of the complete "dynamic" model indicated the spatial locations where, and the times when, the stresses in the complete model were highest. With accurate, useful stress results as the ultimate goal of this analysis, a refined finite element model containing the highest-stressed region (which turned out to be within the turntable structure, in this case) was constructed. This model included many structural details that had to be omitted in the "dynamic" model of that component. In doing this, one naturally wishes to ensure that the boundaries of this refined model are far enough away from the peak stress region that is of interest, since the stress levels at, and very near, these boundaries are not free to vary significantly from the levels obtained in the transient response analysis for the original, "dynamic" model.

The boundaries for the turntable component are located at the interfaces between it and the arms and between it and the base structure. It is important to be sure that the boundaries for the refined "static" model contain at least all of the corresponding node points in the counterpart "dynamic" model. It is most

convenient if the spatial locations of the boundary nodes that are common to the two models coincide exactly, so that the displacements from the transient response analysis at those nodes can be imposed directly on the boundary of the refined model as displacement boundary constraints, without the need to use a suitable (and possibly quite complex) interpolation scheme to determine the desired conditions from the information that is available.

The refined model constructed in this effort for the turntable structure, shown in Figure 9, has 729 node points with 4104 degrees of freedom. It includes 32 bar elements, 40 beams, 145 triangles and 720 quadrilateral plate elements. As usual, this refined model was subjected to the above-described "rigid-body" check and was examined for load transmission capabilities by independent analyses with the REXBAT program.

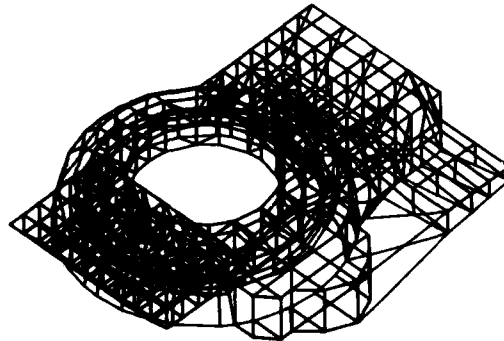


Figure 9. Refined Finite Element Model of Antenna Turntable

Displacements obtained from the transient response analysis for a selected time "t" were applied as boundary constraint conditions, and interior forces, computed as described above, were applied as "external" loadings. The linear elastic stress analysis then performed, with REXBAT, produced the desired refined stress distribution. The peak stress obtained with the refined model was 67% higher than that obtained in the turntable from the transient response analysis.

CONCLUDING REMARKS

Details pertaining to the time history for base excitation and the time increment used for the integration scheme, and concerning the structural responses (in particular the stress levels) obtained, are given in [7]. Analytical results obtained with both the "dynamic" and "static" models will be compared with test results when they become available.

REFERENCES

1. W. A. Loden and L. E. Stearns, "What Is This Thing Called 'REXBAT'?", Lockheed Missiles and Space Company (LMSC) Report, May 1975
2. W. A. Loden and L. E. Stearns, "User's Manual for the REXBAT Program", LMSC Report D460625, January 1976
3. P. G. Underwood and K. C. Park, "Implementation of a Variable-Step Integration Technique for Nonlinear Structural Dynamic Analysis", Proceedings, 4th International Conference on Structural Mechanics in Reactor Technology, 1977
4. W. A. Loden, "The 'MARK 1' Out-of-Core Version of the Implicit Implementation of the STINT Program", LMSC Report D682045, May 1979
5. W. A. Loden and F. G. Morton, "DEFORM: A Program for Making Plots of Deformed Structures Analyzed with the REXBAT Program", LMSC Report 6-C1-71-1, August 1972
6. G. Strang and G. J. Fix, An Analysis of the Finite Element Method, Prentice-Hall, Inc., Englewood Cliffs, N.J., 1973
7. Final Report CGN-41 Shock Test Evaluation Mk 86 FCS Design Agent Engineering Services. Prepared for Naval Ship Weapon Systems Engineering Station, Port Hueneme, California, under task order 04 contract N00123-80-C-0179, September 1980

DISCUSSION

Mr. Dyr Dahl (Boeing Co): Did this analysis result in changing the hardware at all? Was it a worthwhile thing to do for that kind of equipment?

Mr. Meller: Yes, it resulted in some improvement.

Mr. Dyr Dahl: A better understanding or better hardware?

Mr. Meller: It resulted in a better understanding of the structure to determine the stress levels, but not particularly that chart that I showed, a similar analysis resulted in stress levels which caused some modification to the structure.

Mr. Dyr Dahl: How much time did you have to spend on this analysis?

Mr. Meller: I have done so many together that I really can't tell you exactly how much one single one would take because we analyze a particular loading condition.

Voice: Could it be done in a month?

Mr. Meller: It would take about between a month and two months just to create the dynamic model. But once you have the finite element model then the analysis itself shouldn't last longer than a couple of weeks.

Mr. Urbanik (Forest Products Laboratory): Could you comment on the number of slides it took to prepare or the number of computer drawn graphs that you had to prepare for the animated mode shape movie?

Mr. Meller: The second and fifth parts of the movie contain somewhere around 650 slides and each slide corresponds to one time indication point. The last part, that was slowed down by a factor of three, contains three times as many slides but the additional points were

obtained by linear interpolations other than by direct timing conditions. The time step is of the order of 62 microseconds.

Mr. Repperger (Wright-Patterson AFB): How do you know whether that finite element model really replicates the empirical data. What is your goodness of fit, what are your criteria?

Mr. Meller: In this particular case we knew the frequency of the complete antenna so when we subjected the model to the frequency search we could determine whether or not it was a suitable representation of the actual structure, and it was.

Mr. Repperger: Do you have any empirical data to validate the model response and the empirical data response to show that they were equivalent or similar in some sense?

Mr. Meller: In some previous analysis I predicted some responses that were later verified by tests.

Mr. Repperger: Did you just look at the response modes and resonances?

Mr. Meller: Just the actual response. The only reason I was looking for modes is just to be sure that the model had the correct fundamental or at least the lowest fundamental resonant frequency. But once that is done, there is no more modal analysis.

Mr. Walchak (NSWC White Oak): I am interested in your forcing function, did you use the one from the at sea tests or were they from the FSP inputs?

Mr. Meller: This particular one was from the FSP tests.

Mr. Walchak: Did you find this to be more severe?

Mr. Meller: No.

FATIGUE LIFE PREDICTION FOR SIMULTANEOUS STRESS
AND STRENGTH VARIANCES UNDER RANDOM VIBRATION

R.G. Lambert
General Electric Company
Aircraft Equipment Division, Utica, NY 13503

Simple closed form expressions have been found to accurately predict the fatigue life of structures subjected to random stresses where the applied stress and the material's strength are simultaneous random variables. These equations are in familiar engineering terms. Comparisons between analytical predictions and empirical results have been shown to be good whenever such comparisons were made.

INTRODUCTION

Many closed form analytical expressions have previously been derived to predict structural fatigue life and mechanical reliability for randomly applied stresses [1-5]. These expressions have been shown to be simple, practical and accurate. They apply to single and multi-degree-of-freedom systems as well as to single level or step-stress load situations. Fracture Mechanics effects are included. In all of these cases, the stress/strength parameters were treated as random variables independently, not simultaneously.

In most practical cases, the stress/strength parameters are simultaneous random variables. Stresses vary from part to part and subassembly to subassembly due to dimensional and geometrical differences between parts, fabrication and assembly variances, and structural damping and stiffness variances of adjacent structures. Strengths vary because materials' fatigue curves are a scatterband of failure points, not single lines.

APPROACH SUMMARY

An attempt to rigorously derive a fatigue life expression with the stress/strength parameters treated as simultaneous random variables was unsuccessful in that the final expression was exceedingly complex. Therefore, a different approach was evaluated. This approach modified the variable strength fatigue life expression (1) by adding the stress (δ) and strength (Δ) standard deviations in the mean-square sense and substitut-

ing the resulting standard deviation

$$(\psi = \sqrt{\Delta^2 + \delta^2})$$

in place of the strength standard deviation term (Δ). The reasoning behind this approach was as follows: Fatigue failure occurs when stress exceeds strength regardless of whether the stress is "too high" or the strength is "too low". Both deviations from nominal cause a reduction in fatigue life. Since the standard deviations of stress and strength are independent of each other, they should be added in the mean-square sense. This approach, as judged by Monte Carlo simulation techniques, gives somewhat accurate results but not as accurate as hoped for.

Accuracy was improved by multiplying the stress standard deviation (δ) by the term $(2N_m)^{1/\beta}$. N_m is the median stress cycles to failure. It is the fatigue life if the analysis is done deterministically (i.e., if Δ and δ are zero). β is the slope parameter of the material's "S-N" fatigue curve. This term made the entire expression almost identical to the rigorously derived equation for the case of $\Delta = 0$.

Accuracy was further improved in the region of early fatigue failures by subtracting the term

$$\frac{(2N_m)^{1/\beta} \Delta \delta}{\sqrt{2\beta - \pi/\beta}}$$

The portion $\sqrt{2\beta - \pi/\beta}$ was required to provide accuracy for brittle and ductile

materials. This worsened the accuracy in the region of the late failures. The above term needed to be added instead of subtracted in that region (i.e., a sign change for $N > N_m$). This worsened the accuracy in the middle failure region. The multiplying term

$$\xi = 2 \operatorname{erf} \left[20 \left(\frac{N}{N_m} - 1 \right) \right]$$

restored accuracy to all failure regions.

The resultant standard deviation term is:

$$\psi = \sqrt{\Delta^2 + (2N_m)^{2/\beta} \delta^2 + \xi \frac{(2N_m)^{1/\beta} \Delta \delta}{\sqrt{2\beta - \pi/\beta}}}$$

Accuracy of the above expressions was judged by comparison to Monte Carlo simulation results. The Monte Carlo simulation technique had its accuracy and practicality checked by comparing its results with those known to be theoretically correct and with available empirical results.

Fatigue life is expressed in terms of probability of failure as a function of applied stress cycles and both average and minimum cycles to first failure. For the most part data is presented in the form of histograms of cycles to failure because of the histogram's sensitivity to differences between theoretical and tallied results.

FATIGUE CURVE REPRESENTATION

Figure 1 shows the typical sinusoidal and random fatigue curves for a given structural material. These curves are of the following form:

$$S = \frac{\Delta S}{2} = \bar{A} N_s^{-1/\beta} \text{ stress units} \quad (1)$$

$$\sigma = \bar{C} N_m^{-1/\beta} \text{ stress units} \quad (2)$$

where \bar{A} and \bar{C} are fatigue curve constants and β is a slope parameter [1]. ΔS is the cyclic sinusoidal stress range. σ is the random rms stress. N_s is the sinusoidal cycles to failure. N_m is the median number of random stress cycles to failure. These fatigue curves are zero-width (i.e., nonscatterband) lines of failure points.

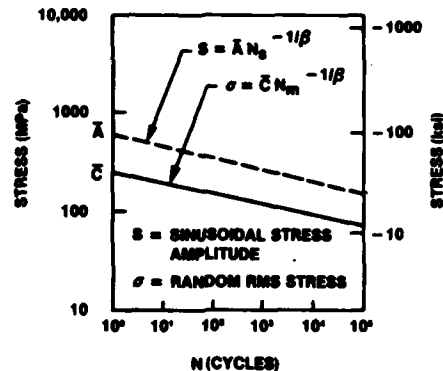


Fig. 1 - Typical sinusoidal and random fatigue curves

Table 1 shows typical parameter values for several materials. Refer to the Symbols section for Metric-Conventional Units conversion.

$$\bar{C} = \left[\frac{\bar{A}}{\sqrt{2}} \right] \left[\frac{1}{\Gamma \left(\frac{2 + \beta}{2} \right)} \right]^{1/\beta} \text{ stress units} \quad (3)$$

$$\bar{A} = 2^{-1/\beta} \sigma_f' \text{ stress units} \quad (4)$$

where σ_f' = fatigue strength coefficient [6,7]. σ_f' may be thought of as being the material's cyclic "true" ultimate strength. It should be noted that $\beta = 9$ for ductile materials and $\beta = 20$ for brittle materials.

Equation (2) represents a fatigue strength-life curve where both the ma-

TABLE 1. TYPICAL FATIGUE CURVE CONSTANTS

	\bar{A}		β	\bar{C}	
	(ksi)	(MPa)		(ksi)	(MPa)
Copper Wire	81.9	565	9.28	36.9	254
7075-T6 Aluminum Alloy	180	1240	9.65	80	552
AZ31B Magnesium Alloy	43.3	299	22.37	13.6	94

terial strength \bar{C} and applied rms stress are deterministic. The fatigue strength can be treated as a Gaussian random variable of mean value \bar{C} and standard deviation Δ . The applied stress can also be treated as a Gaussian random variable of mean value $\bar{\sigma}$ and standard deviation δ .

Equation (2) then becomes

$$N_m = \left(\frac{\bar{C}}{\bar{\sigma}} \right)^\beta \text{ cycles} \quad (5)$$

where

N_m = median cycles to failure

\bar{C} = mean value of strength

$\bar{\sigma}$ = mean value of applied stress

ANALYTICAL DERIVATION

The derivation of the fatigue life expressions begins with the derivations of equations for the probability density function of cycles to failure $p(N_f)$ and the probability of failure at N applied stress cycles $F(N)$. It can be shown

$$p(N_f) = \frac{2^{1/\beta} N_f^{(1/\beta)-1}}{\beta \Delta \delta \pi} \left[\frac{1}{2\sqrt{r}} e^{-\frac{(h^2 - rv)}{r}} \cdot \left\{ 2\bar{\sigma} \operatorname{erf}(\alpha_1) + \frac{1}{\pi} e^{-h^2/r} - \frac{2h}{\sqrt{r}} \operatorname{erf}(\alpha_2) \right\} \right] \quad (6)$$

where the variables α_1 , α_2 , h , r and v are complicated functions of N_f .

$F(N)$ = Probability that $N_f > N$

$$F(N) = \int_0^N P(N_f) dN_f \quad (7)$$

It can be seen by examining equations (6) and (7) that finding a simple closed form expression for $F(N)$ does not appear likely.

SIMULATION TECHNIQUE

A Monte Carlo technique was used as the simulation method for judging the accuracy of the proposed fatigue life expressions. From equation (5),

$$N_f = \left(\frac{C}{\sigma} \right)^\beta \text{ cycles} \quad (8)$$

where C and σ are Gaussian random variables of mean values \bar{C} and $\bar{\sigma}$ and stand-

ard deviations Δ and δ stress units respectively. N_f is a dependent random variable that depends upon the parameter values in equation (8). N_m is the median value of the random variable N_f . Both N_m and N_f represent cycles to failure.

A sample of the random variable N_f is generated by generating a sample of each C and σ , then performing the operation indicated by equation (8). Each sample of C is drawn from a Gaussian distribution of mean value \bar{C} and standard deviation Δ . Each sample of σ is similarly drawn from a Gaussian distribution of mean $\bar{\sigma}$ and standard deviation δ . Negative values of C and σ are discarded. The samples of N_f are sorted and stored in array bins according to the sample's value. The quantity of N_f samples that fall into each bin is summed and stored. A printout of the quantity of samples in each bin of the array represents a histogram of N_f for specific values of \bar{C} , Δ , $\bar{\sigma}$, δ and β .

COMPARISON OF SIMULATION AND THEORETICAL RESULTS

Theoretical results for the case where the applied stress is not a random variable (i.e., $\delta = 0$) are as follows [1]:

$$F(N) = 0.5 + \operatorname{erf} \left[\frac{\bar{C}}{\Delta} \left\{ \left(\frac{N}{N_m} \right)^{1/\beta} - 1 \right\} \right] \quad (9)$$

A histogram array bin quantity q for a bin that extends from N_a to N_b is

$$q = \{F(N_b) - F(N_a)\} Q \quad (10)$$

where

Q = total N_f sample size

q = bin quantity

Q = 10,000 for all cases.

Figure 2 shows the expected excellent agreement between theoretical and tallied results for Case 1 of Table 2.

Similarly theoretical results for the case where the fatigue curve is treated as a single line (i.e., $\Delta = 0$) are as follows [1]:

$$F(N) = 0.5 - \operatorname{erf} \left[\frac{\bar{\sigma}}{\delta} \left\{ \left(\frac{N_m}{N} \right)^{1/\beta} - 1 \right\} \right] \quad (11)$$

Figure 3 shows the expected excellent agreement between theoretical and tallied

results for Case 2 of Table 2. Thus, the simulation technique is considered to be qualified for further use.

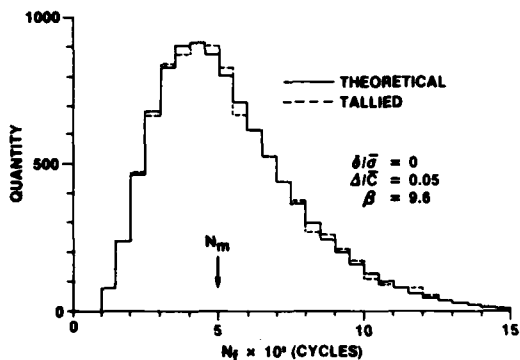


Fig. 2 - Histogram of N_f : Case 1

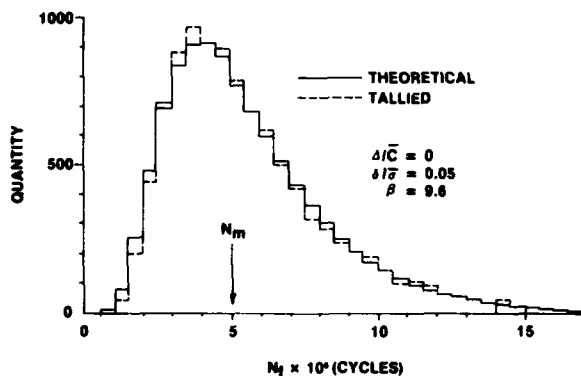


Fig. 3 - Histogram of N_f : Case 2

INITIAL EVALUATION

The first proposed method of analyzing cases where both the applied rms stress and strength are simultaneous was to add both variances in the mean square

sense and substitute this result into equation (9) as follows:

$$F(N) = 0.5 + \operatorname{erf} \left[\frac{\bar{C}}{\psi'} \left\{ \left(\frac{N}{N_m} \right)^{1/\beta} - 1 \right\} \right] \quad (12)$$

where

$$\psi' = \sqrt{\Delta^2 + \delta^2} \quad (13)$$

Figure 4 shows the theoretical and tallied results for Case 3 of Table 2 and equation (12). Comparison of the above results indicates that ψ' gives reasonable accuracy but not as good as hoped for. This is especially true in the region of first failures where ψ' gives results that are not conservative.

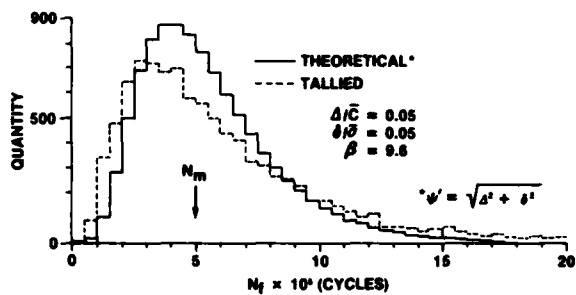


Fig. 4 - Histogram of N_f : Case 3

It should be noted that δ is usually less than Δ in absolute value by a factor of approximately four. This is because σ is usually less than \bar{C} by the same factor for N_m in the high cycle fatigue region (e.g., from equation (5),

$$\bar{C}/\bar{\sigma} = N_m^{1/\beta}$$

For $N_m = 6.5 \times 10^5$ and $\beta = 9.6$, $\bar{C}/\bar{\sigma} = 4$. Therefore, ψ' is relatively insensitive to values of δ and will no longer be considered as a candidate expression.

TABLE 2. CASE PARAMETER VALUES

Case	\bar{C}		Δ		$\bar{\sigma}$		δ		β	N_m (cycles)
	(MPa)	(ksi)	(MPa)	(ksi)	(MPa)	(ksi)	(MPa)	(ksi)		
1	1187	172.11	63.8	9.25	302	43.87	0	0	9.6	5×10^5
2	1187	172.11	0	0	238	34.52	11.9	1.73	9.6	5×10^6
3	1187	172.11	63.8	9.25	302	43.87	15.2	2.2	9.6	5×10^5
4	1187	172.11	63.8	9.25	302	43.87	15.2	2.2	9.6	5×10^5
5	93.8	13.6	4.8	0.70	52	7.56	26.1	3.78	22.37	5×10^5

NOTE: Except for zero values, $\Delta/\bar{C} = \delta/\bar{\sigma} = 0.05$

PROPOSED FATIGUE LIFE EXPRESSIONS

The following expressions are proposed for computing fatigue life parameters:

$F(N)$ = probability of failing at N applied stress cycles

$$F(N) = 0.5 + \operatorname{erf} \left[\frac{\bar{C}}{\psi} \left\{ \left(\frac{N}{N_m} \right)^{1/\beta} - 1 \right\} \right] \quad (14)$$

$$\operatorname{erf}(\alpha) = \frac{1}{\sqrt{2\pi}} \int_0^\alpha e^{-y^2/2} dy \quad (15)$$

N_m = median cycles to failure

$$N_m = \left(\frac{\bar{C}}{\bar{\sigma}} \right)^\beta \text{ cycles} \quad (16)$$

$\bar{\sigma}$ = mean value of applied rms stress

\bar{C}, β are random fatigue curve constants

$$\psi = \sqrt{\Delta^2 + (2N_m)^{2/\beta} \delta^2 + \xi \frac{(2N_m)^{1/\beta} \Delta \delta}{\sqrt{2\beta - \pi/\beta}}} \quad (17)$$

$$\xi = 2 \operatorname{erf} \left[20 \left(\frac{N}{N_m} - 1 \right) \right] \quad (18)$$

Figure 5 is a plot of ξ versus N/N_m .

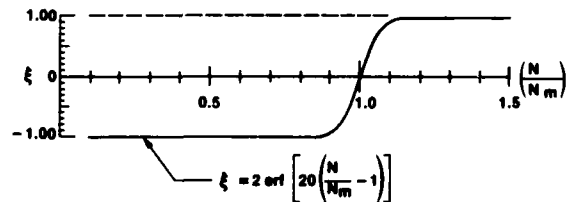


Fig. 5 - Correction factor versus N/N_m

\bar{N}_1 = average number of cycles to first failure

$$\bar{N}_1 = N_m \left[1 - \frac{3.7195451}{(2^{1/\beta} \bar{C} \psi)} \right]^\beta \text{ cycles} \quad (19)$$

$N_{1\text{Min}}$ = minimum cycles to first failure

$$N_{1\text{Min}} = \left[\frac{\bar{C} - 4.2\Delta}{\bar{\sigma} + 4.2\delta} \right]^\beta \text{ cycles} \quad (20)$$

PROPOSED EXPRESSION RESULTS

Many cases of parameter values using equations (14) through (20) were evalu-

ated. Only two typical ones will be reported here. Refer to Cases 4 and 5 of Table 2. Case 4 is identical to Case 3 except ψ from equation (17) is used instead of ψ' from equation (13).

Histograms of N_f are shown in Figs. 6 and 7. Agreement between theoretical and tallied results are considered excellent. The following observations can be made:

- 1) The material's ductility (i.e., β value) has a large effect on the spread of the histogram.
- 2) The shape of the histogram is nonsymmetrical. The general shape is to rise more sharply than to decay.
- 3) Agreement between theoretical and tallied results is still excellent even when the histogram is so spread that it appears to be truncated at the left (i.e., greatly distorted).
- 4) Large enough values were assigned to Δ and δ to cause the first failure to occur at cycles well below N_m . From a practical viewpoint such unreliable structural elements would most likely be redesigned.

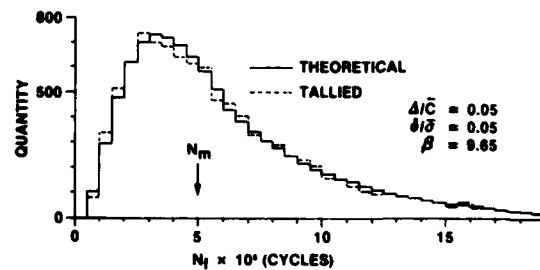


Fig. 6 - Histogram of N_f : Case 4

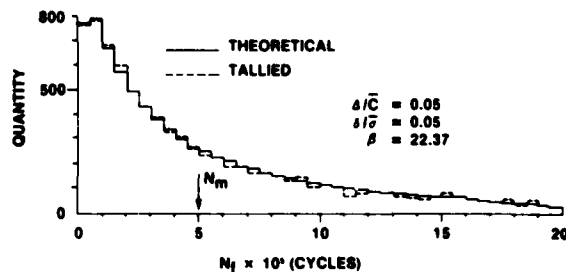


Fig. 7 - Histogram of N_f : Case 5

Table 3 shows a comparison between theoretical and tallied results of the average and minimum cycles to first failure, \bar{N}_1 and $N_{1\text{Min}}$, respectively. Agree-

TABLE 3. COMPARISON OF CYCLES TO FIRST FAILURE RESULTS

Case	N_m (cycles)	\bar{N}_1 (cycles)		N_{1Min} (cycles)	
		Tallied	Calculated	Tallied	Calculated
1	500,000	61,916	69,356	39,116	42,749
2	5,000,000	947,484	693,326	800,307	706,843
4	500,000	35,177	32,507	12,374	6,014
5	500,000	981	734	442	17

ment is considered excellent. Equations (19) and (20) are considered accurate.

COMPARISON WITH EMPIRICAL DATA

The proposed fatigue life expressions have previously been shown to agree with the Monte Carlo simulation tallied results. Now the theoretical and tallied results will be compared with the empirical results reported in Refs. 2, 8 and 9. In Ref. 8, J.T. Broch describes fatigue life test results of fiberglass single-degree-of-freedom end mass cantilever beams subjected to random stresses. A sample size of 100 beams was used for the tests. The test parameters are as follows:

- $\bar{\sigma} = 84 \text{ MPa (12.2 ksi)}$
- $\delta = 2.4 \text{ MPa (0.348 ksi)}$
- $\bar{C} = 228 \text{ MPa (33 ksi)}$
- $\Delta = 12.1 \text{ MPa (1.75 ksi)}$
- $E = 1.86 \times 10^4 \text{ MPa (2700 ksi)}$
- $\beta = 12.1$

Figure 8 shows a comparison of the theoretical and tallied histograms for the above parameters. Large variances in the tallied are noted. However, the overall histogram shapes are in general agreement. Figure 9 compares theoretical and empirical data. Again large variances are noted in the empirical data. The overall histogram shapes are in general agreement. Figure 10 compares the empirical and tallied histograms. They too generally are in agreement with each other. Figure 11 shows that the variance of the tallied data is smoothed out considerably as expected by increasing the sample size from 100 to 10,000. This indicates that the previous relatively large variances for the tallied and empirical data are an expected result of the small sample size of 100.

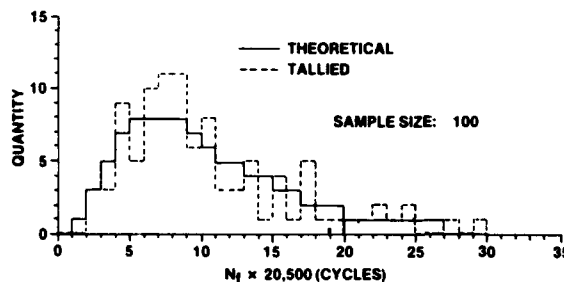


Fig. 8 - Histogram of N_f : J.T. Broch example

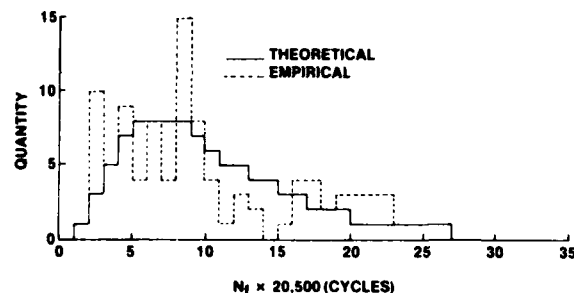


Fig. 9 - Histogram of N_f : J.T. Broch data

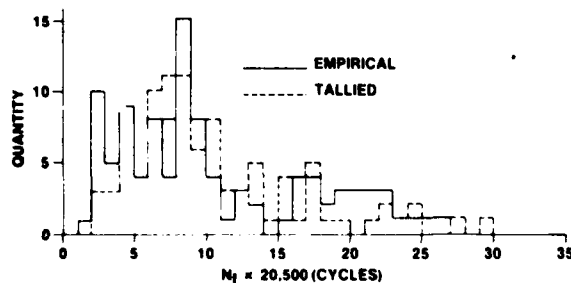


Fig. 10 - Empirical-Tallied Histograms: J.T. Broch example

Figure 12 is a histogram of cycles to first failure N_1 . Also shown are calculated and tallied values of \bar{N}_1 and N_1 empirical. Quantitatively,

$$\bar{N}_1^{\text{calc'd}} = 33,983 \text{ cycles}$$

$$\bar{N}_1^{\text{tallied}} = 37,914 \text{ cycles}$$

$$\bar{N}_1^{\text{empirical}} = 42,950 \text{ cycles}$$

All of the data indicates good agreement among theoretical, Monte Carlo and empirical results.

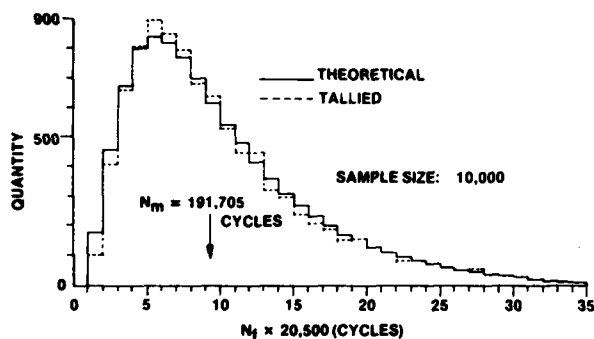


Fig. 11 - Histogram of N_f : Large sample size

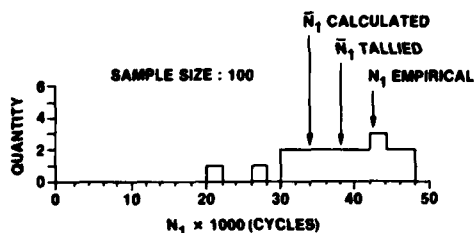


Fig. 12 - Histogram of N_1 : J.T. Broch example

Figure 13 shows additional empirical fatigue data [9]. Again the theoretical results are in good agreement with empirical results for 7075-T6 Aluminum alloy (sample size: 100) regarding histogram shape. The following parameter values were used for the theoretical curve:

$$N_m = 1.8 \times 10^5 \text{ cycles}$$

$$\psi/\bar{C} = 0.052$$

$$\beta = 9.65$$

SUMMARY OF RESULTS

The single expression for ψ provides accurate fatigue life results for ductile and brittle materials. All of the fatigue life and mechanical reliability equations in Refs. 1 through 5 that originally applied to cases where strength

alone was the random variable can be used for simultaneous stress/strength variances by substituting ψ for Δ .

The Monte Carlo simulation technique was judged to be both accurate and practical due to good comparisons with results known to be theoretically correct and with available empirical results.

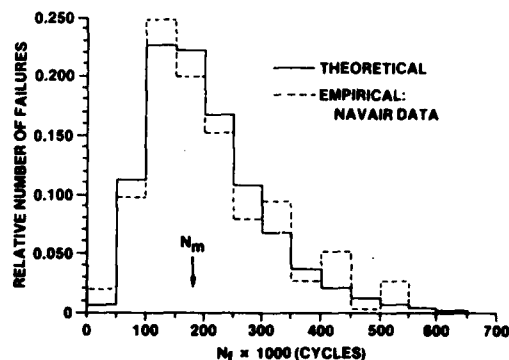


Fig. 13 - Histogram of N_f : NAVAIR data

SYMBOLS

\bar{A}	material constant; true ultimate stress
\bar{C}	constant of random fatigue curve
E	modulus of elasticity
$\text{erf}(\alpha)$	error function of argument α
$F(N)$	probability of failure at N cycles
ksi	thousands of pounds per square inch
N	applied stress cycles
N_a, N_b	histogram bin width
N_f	number of stress cycles to failure
N_m	median stress cycles to failure; cycles to 50% failures
N_1	stress cycles to first failure
\bar{N}_1	average value of N_1
$N_{1\text{Min}}$	minimum value of N_1
$p(\alpha)$	probability density function of α
q	histogram quantity
Q	total sample size
rms	root mean square

S applied sinusoidal stress amplitude

ΔS applied sinusoidal stress range

x,y,z general variables
r,h,v

α general variable

β fatigue curve slope parameter

$\Gamma(\alpha)$ gamma function of argument α

Δ standard deviation of material's random fatigue curve

δ standard deviation of applied rms stress

ξ correction factor

σ'_f fatigue strength coefficient

$\bar{\sigma}$ average value of random rms stress

ψ resultant stress standard deviation

ψ' modified form of ψ

MPa mega-Pascals

6.895 MPa/ksi

REFERENCES

1. R.G. Lambert, "Analysis of Fatigue under Random Vibration," The Shock and Vibration Bulletin 46, Naval Research Laboratory, Washington, DC, August 1976.
2. R.G. Lambert, "Fatigue Analysis of Multi-Degree-of-Freedom Systems under Random Vibration," The Shock and Vibration Bulletin 47, Naval Research Laboratory, Washington, DC, September 1977.
3. R.G. Lambert, "Fracture Mechanics Applied to Step-Stress Fatigue under Sine/Random Vibration," The Shock and Vibration Bulletin 48, Naval Research Laboratory, Washington, DC, October 1978.
4. R.G. Lambert, "Probability of Failure Prediction for Step-Stress Fatigue under Sine or Random Stress," Presented at 49th Shock and Vibration Symposium, Washington, DC, October 1978.
5. R.G. Lambert, "Fatigue Life Prediction for Multi-Level Step-Stress Application," Presented at 50th Shock and Vibration Symposium, Washington, DC, October 1979.
6. R.W. Landgraf, "Cumulative Fatigue Damage under Complex Strain Histories," Cyclic Stress-Strain Behavior - Analysis, Experimentation, and Failure Prediction, STP 519, ASTM, p. 213, December 1971.
7. Technical Report on Fatigue Properties - SAE J1099, Society of Automotive Engineers, Inc., February 1971.
8. J.T. Broch, "Peak Distribution Effects in Random Load Fatigue," Brüel and Kjaer Technical Review 1-1968.
9. "Fatigue of Aircraft Structures," NAVAIR 01-1A-13, Naval Air Systems Command, Department of the Navy, p. 306, 1960.

This work was performed on Navy contract N00019-78G-0407.

DYNAMIC RESPONSE OF THE PROGRESSIVELY DAMAGING STRUCTURES*

M. G. Srinivasan
Argonne National Laboratory
Argonne, Illinois

and

G. U. Fonseka and D. Krajcinovic
University of Illinois at Chicago Circle
Chicago, Illinois

The continuous damage theory, originally suggested by Kachanov, is extended to a dynamical problem. The theory is characterized by a kinematic state variable defining the evolution of voids and microcracks in a smoothed or statistical sense. Concentrating on brittle cracking, a simple fracture surface is proposed. The derived equations are subsequently used to solve a one-dimensional wave propagation problem using the method of characteristics. Numerical results for several pressure pulses are presented, thus illustrating a method for obtaining estimates of the damage level in a solid as a function of time and space.

INTRODUCTION

In many instances of practical interest the ultimate failure of a solid body is preceded by a gradual evolution of countless number of microcracks, voids and defects. Failure occurs when this process reaches a critical level at some point or region of the solid. Away from this region of total failure the density of microcracks, voids etc., gradually decreases with distance. In this context it is appropriate to introduce the concept of a "continuous or distributed damage" for the quantitative description of the phenomenon. The conventional fracture mechanics approach of studying the initiation and propagation of one or more well defined macrocracks is not suitable for treating the phenomenon described above.

The distinguishing characteristic of the continuous damage theory is an internal (or hidden) kinematic state variable that defines the growth and

spread of the population of defects in a smoothed or statistical sense. The introduction of this state variable makes the relation between the theory and actual phenomenon similar to the relationship between the classical plasticity theory and the rearrangement of dislocation distribution in a plastic solid. This phenomenological theory provides useful results for practical applications although it does not account for the detailed stress distribution in the neighborhood of actual microcracks.

This subject of study has attracted many investigators in the last few decades (Refs. [1]-[25]). Some of these works have been summarized briefly in [26]. According to the presented evidence it appears unlikely that a simple universal damage model applicable to both ductile and brittle types of failures could be constructed. Experimental observations suggest, for example, that the voids generated by plastic flow are more or less spherical while the microcracks generated at the interface of crystals are planar.

Kachanov [17] has proposed a model defining damage as the loss in effective area of each cross section in solving problems of brittle (low strain) creep

*Work reported in this paper was conducted under the support of the Argonne National Laboratory and the National Science Foundation through grants to the University of Illinois at Chicago Circle.

rupture. Many other investigators have employed the same model seeking solutions for other problems. In most of these cases the investigations are characterized by monotonically increasing loads. In the present paper Kachanov's original model is extended to dynamical loading of a brittle rod. A simple fracture surface is proposed in order to study the phenomenon of spalling. Numerical results for different loading cases are obtained by using the method of characteristics.

ANALYTICAL MODEL

Consider a one-dimensional rod made of a brittle material. Let $\sigma(x,t)$ and $\epsilon(x,t)$ be the stress and strain respectively at section "x" at time "t." When this rod is subjected to some dynamic loading causing spalling to occur at some section, the only irreversible mechanical process taking place is cracking. In order to record the history of the process an internal variable characterizing spatial and temporal evolution of damage needs to be introduced. Let $\omega(x,t)$ be the damage parameter related to the density of defects such as voids, microcracks, etc.

Based on thermodynamic and statistical grounds Krajcinovic et al [26] showed that the fracture surface (analogous to the yield surface of plasticity) and the differential damage law may be written as:

$$F(\epsilon, \omega) = \epsilon - \frac{S}{E} \hat{\omega} \quad (1)$$

and

$$\left. \begin{aligned} d\omega &= \frac{E}{S} d\epsilon \text{ for } F=0 \text{ and } \epsilon>0, d\epsilon>0 \\ d\omega &= 0 \text{ otherwise} \end{aligned} \right\} \quad (2)$$

where E is the Young's modulus, S the damage constant and $\hat{\omega}$ the largest value of ω actually recorded at a point up to the current time. The stress-strain law, derived from energy considerations (see [26]) is given by

$$\sigma = E(1-\omega)\epsilon \quad (3)$$

The ultimate failure criterion - which also corresponds to infinite energy dissipation density rate - is obtained from the condition that rupture occurs in a static, monotonic test when

$$\frac{d\sigma}{d\epsilon} = 0 \quad (4)$$

By manipulating equations (2)-(4), one can verify that at fracture the value

of ω is given by

$$\omega_F = 0.5 \quad (5)$$

and

$$S = 4\sigma_F \quad (6)$$

where σ_F is the tensile strength of the material. It may be noted that in the above formulation no material constants unrelated to tensile strength are introduced. Damage, ω , varies spatially and temporally from 0 (undamaged) to 0.5 (fractured) in a continuous manner.

FREE-FREE ROD

As an illustration of the general theory consider the problem of the dynamic behavior of a finite, brittle rod with free boundaries subjected to a compressive stress-pulse at one of its free boundaries. The constitutive equations (2 and 3) for the rod in the incremental form are

$$d\sigma = E(1-\omega)d\epsilon - E\epsilon d\omega \quad (7)$$

and

$$d\omega = \begin{cases} \frac{E}{S} d\epsilon & \text{if } \sigma > 0 \text{ and } d\sigma > 0 \\ 0 & \text{otherwise} \end{cases} \quad (8)$$

since it can be shown that $\sigma > 0$ and $d\sigma > 0$ is equivalent to $\epsilon > 0$ and $d\epsilon > 0$.

The equation of motion for the rod is

$$\rho v_{,t} - \sigma_{,x} = 0 \quad (9)$$

where ρ is the mass density of the rod material (assumed constant) and v the particle velocity. The subscripts t and x stand for the time and space variables respectively and the comma denotes partial differentiation. Making use of the continuity relation

$$\epsilon_{,t} = v_{,x} \quad (10)$$

and the damage law (8), Eq. (7) may be shown to take the form

$$\sigma_{,t} - E \left\{ (1-\omega) - \left\langle \frac{\sigma}{S(1-\omega)} \right\rangle \right\} v_{,x} = 0 \quad (11)$$

where the notation $\langle \rangle$ is used to denote the term that will vanish unless σ and $d\sigma$ are both positive.

Equations (9) and (11) form a system of quasi-linear partial differential equations which is particularly well suited for the application of the method of characteristics.

The governing system of equations can be rewritten in matrix form as

$$\underline{A} \underline{w}_{,t} + \underline{B} \underline{w}_{,x} = 0 \quad (12)$$

where

$$\underline{w} = \begin{bmatrix} v \\ \sigma \end{bmatrix}, \quad \underline{A} = \begin{bmatrix} \rho & 0 \\ 0 & \phi \end{bmatrix}, \quad \underline{B} = \begin{bmatrix} 0 & -1 \\ -1 & 0 \end{bmatrix} \quad (13)$$

with

$$\phi = \frac{1}{E \left\{ (1-\omega) - \frac{\sigma}{S(1-\omega)} \right\}} \quad (14)$$

Omitting the intermediate details, it can be shown [27], that the wave speeds $\pm c$ are given by

$$c = c_0 \sqrt{(1-\omega) - \frac{\sigma}{S(1-\omega)}} \quad (15)$$

where c is the speed at which stress waves propagate and $c_0 = \sqrt{E/\rho}$, the uniaxial wave speed in an undamaged elastic rod. Note that the wave speed, c , during compression or unloading from tension is constant, and equal to $c_0 \sqrt{1-\omega}$. This follows from Eq. (8), and implies nondissipative, purely elastic behavior with a reduced elastic modulus, $E(1-\omega)$ if $\sigma < 0$ or $d\sigma < 0$. Further, the characteristic conditions are

$$\frac{d\sigma}{dt} - \rho c \frac{dv}{dt} = 0 \quad \text{on} \quad \frac{dx}{dt} = c \quad (16)$$

$$\frac{d\sigma}{dt} + \rho c \frac{dv}{dt} = 0 \quad \text{on} \quad \frac{dx}{dt} = -c \quad (17)$$

Since c is not constant in general, it is not always possible to integrate the characteristic equations (16) and (17) in closed form. However, it is relatively simple to solve them by means of a finite difference approximation.

The rod is replaced by a series of nodes at equal intervals Δx . A typical step in the integration procedure is to express the solution at the n -th node for time $t + \Delta t$, given the solution at nodes $n-1$, n and $n+1$ for time t . For a given Δx , the time increment Δt must satisfy the stability requirement,

$$\Delta t \leq \frac{\Delta x}{c} \quad (18)$$

It is convenient to select a value for Δt that is constant and satisfies the above inequality everywhere in the x - t plane. Since $c \leq c_0$, the time step can be selected as $\Delta t = \frac{\Delta x}{c_0}$.

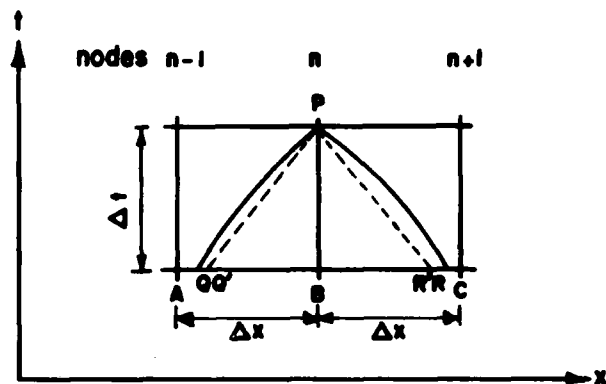


Fig. 1. Scheme for Numerical Integration

Referring to Fig. 1 and denoting by P the n -th node at time $t + \Delta t$, let Q and R be the points at which the two characteristic curves drawn from P intersect the time line t , at which the solution is known. Since the exact curves PQ and PR are not known *a priori*, it is possible to approximate them by straight line segments drawn from P with slopes $\frac{dx}{dt} = c_Q$, and $\frac{dx}{dt} = -c_R$, where Q' and R' are points at which the two approximate characteristic lines PQ' and PR' intersect the time line at t . The values $c_{Q'}$ and $c_{R'}$ are obtained by linear interpolation as

$$c_{Q'} = \frac{c_B}{1 + \left(\frac{c_B - c_A}{c_0} \right)}; \quad c_{R'} = \frac{c_B}{1 - \left(\frac{c_C - c_B}{c_0} \right)} \quad (19)$$

The solutions for σ and v at Q' and R' are also obtained by linear interpolation as:

$$\begin{aligned} \sigma_{Q'} &= \sigma_B - (\sigma_B - \sigma_A) \left(\frac{c_{Q'}}{c_0} \right) \\ \sigma_{R'} &= \sigma_B + (\sigma_C - \sigma_B) \left(\frac{c_{R'}}{c_0} \right) \\ v_{Q'} &= v_B - (v_B - v_A) \left(\frac{c_{Q'}}{c_0} \right) \\ v_{R'} &= v_B + (v_C - v_B) \left(\frac{c_{R'}}{c_0} \right) \end{aligned} \quad (20)$$

The characteristic equation (16) on PQ' takes the difference form

$$(\sigma_P - \sigma_{Q'}) - \rho c_{Q'}(v_P - v_{Q'}) = 0 \quad (21)$$

Similarly the characteristic equation (17) on PR' takes the form

$$(\sigma_P - \sigma_{R'}) + \rho c_{R'}(v_P - v_{R'}) = 0 \quad (22)$$

Simultaneous solution of equations (21) and (22) yields the solution at the n-th node for time $t + \Delta t$ as:

$$\sigma_P = \frac{c_Q \sigma_{R'} + c_{R'} \sigma_{Q'} + \rho c_{Q'} c_{R'} (v_{R'} - v_{Q'})}{(c_{Q'} + c_{R'})} \quad (23)$$

$$v_P = \frac{(c_{Q'} v_{R'} + c_{R'} v_{Q'}) - (\sigma_{Q'} - \sigma_{R'})}{\rho (c_{Q'} + c_{R'})}$$

It remains to determine the damage factor ω and wavespeed c at P. If σ_P and $(\sigma_P - \sigma_B)$ are both positive, using equations (7) and 8 it is possible to write

$$\omega_P - \frac{\sigma_P}{S(1-\omega_P)} = \omega_B - \frac{\sigma_B}{S(1-\omega_B)} \quad (24)$$

Solving this quadratic equation for ω_P and choosing the negative sign for the radical, it follows that

$$\omega_P = \frac{1}{2} \left[\left\{ 1 + \omega_B - \frac{\omega_B}{S(1-\omega_B)} \right\} - \sqrt{\left\{ 1 - \omega_B + \frac{\sigma_B}{S(1-\omega_B)} \right\}^2 - \frac{4\sigma_P}{S}} \right] \quad (25)$$

Subsequently c_P is obtained by Eq. (15) as

$$c_P = c_Q \sqrt{1 - \omega_P - \frac{\sigma_P}{S(1-\omega_P)}} \quad (26)$$

On the other hand, if both σ_P and $(\sigma_P - \sigma_B)$ are not positive

$$\begin{aligned} \omega_P &= \omega_B \\ c_P &= c_B \end{aligned} \quad (27)$$

At the boundary nodes the above procedure needs some modification. If P is a node on the left boundary only Eq. (22) is available. If P is a node on the right boundary only Eq. (21) is available. In either case the additional equation required for determination of σ_P and v_P comes from the prescribed boundary condition at the boundary. For instance in the case of free boundary σ_P is known while for a fixed boundary v_P vanishes.

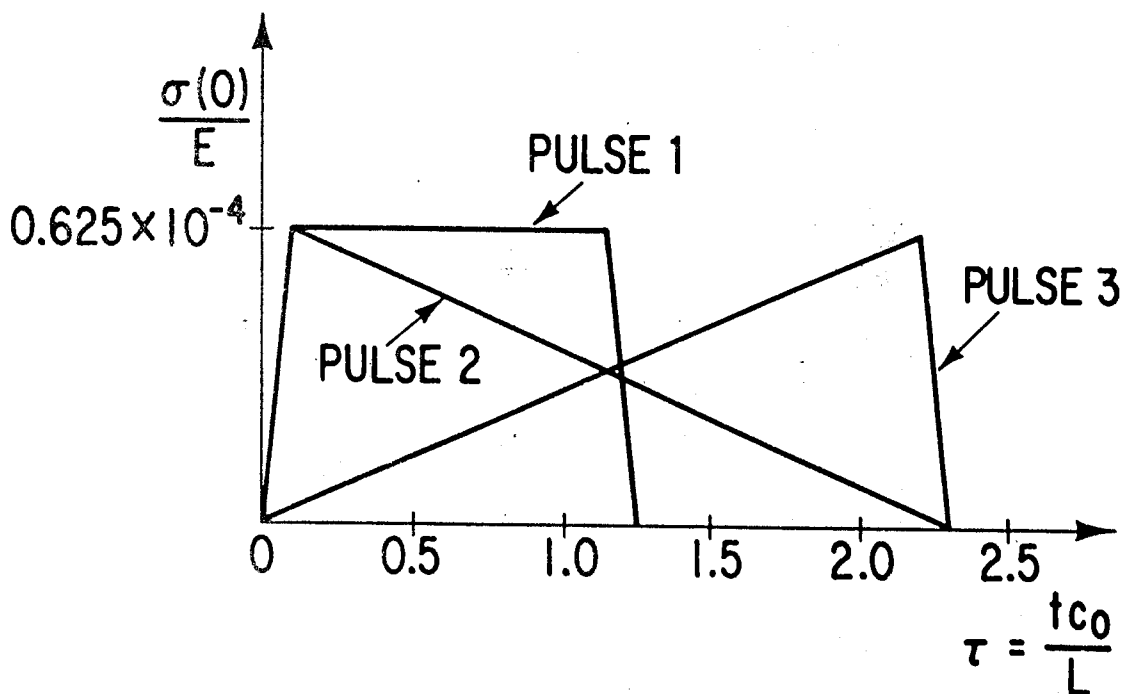


Fig. 2. Stress Pulses Applied at Free End $x = 0$

As a numerical example consider a rod of length L with both ends free subjected to a compressive stress-pulse at its left free end. The damage modulus S is taken to be $0.5 \times 10^{-3} E$ (corresponding roughly to concrete [21]) and the peak value of the pulse is equal to $S/8$ which corresponds, according to (6), to half the rupture stress. Non-dimensionalizing the length with respect to L , all stresses with respect to E , the velocities with respect to c_0 and time with respect to L/c_0 , the non-dimensional steps Δx and Δt are taken to be 0.05.

The energy supplied to the rod is equal to the work of the applied pulse and is given by

$$E_{\text{input}} = A \int_0^{t_{\text{max}}} \sigma(0,t)v(0,t)dt \quad (28)$$

where A is the cross-sectional area and t_{max} the duration of the pulse. The total dissipated energy is given (see [26]) as

$$E_{\text{dissipated}} = \frac{ABL}{2} \int_0^t \epsilon^2 \omega dt \quad (29)$$

The energies are non-dimensionalized with respect to the factor ABL . They are computed by numerical integration using Simpson's rule.

Results for three different pulse shapes were computed for the illustration of the proposed model. All three pulses (Fig. 2) had the same peak value of $S/8$ and the same total impulse. While pulse 1 is symmetric and has a shorter duration, pulses 2 and 3 are unsymmetric and of a longer duration. Pulse 2 loads at a rapid rate and unloads at a much slower rate while pulse 3 loads at the slower rate and unloads at the faster rate.

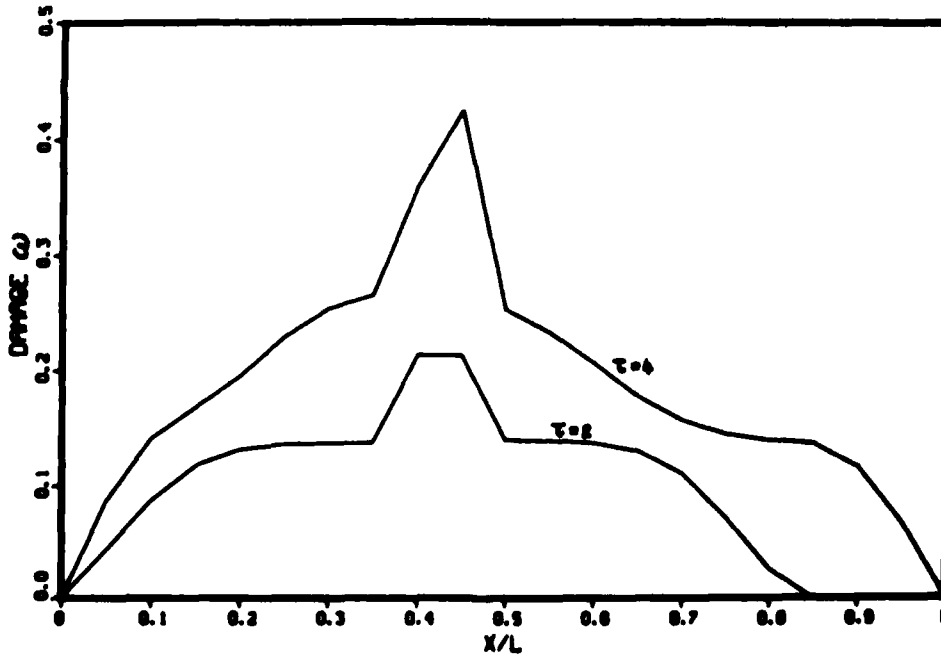


Fig. 3. Damage along Length of Rod due to Pulse #1

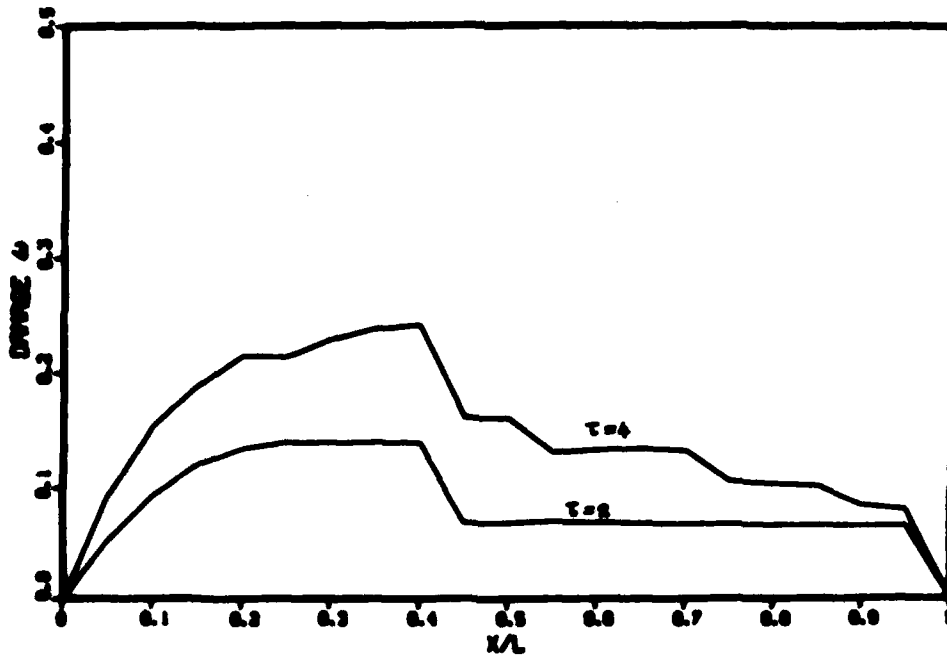


Fig. 4. Damage along Length of Rod due to Pulse #2

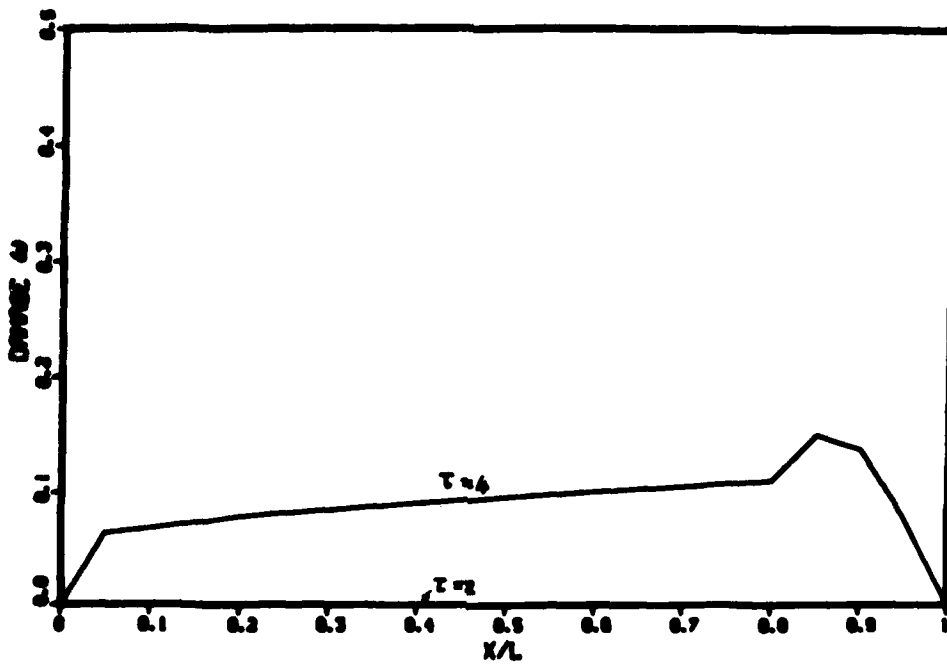


Fig. 5. Damage along Length of Rod due to Pulse #3

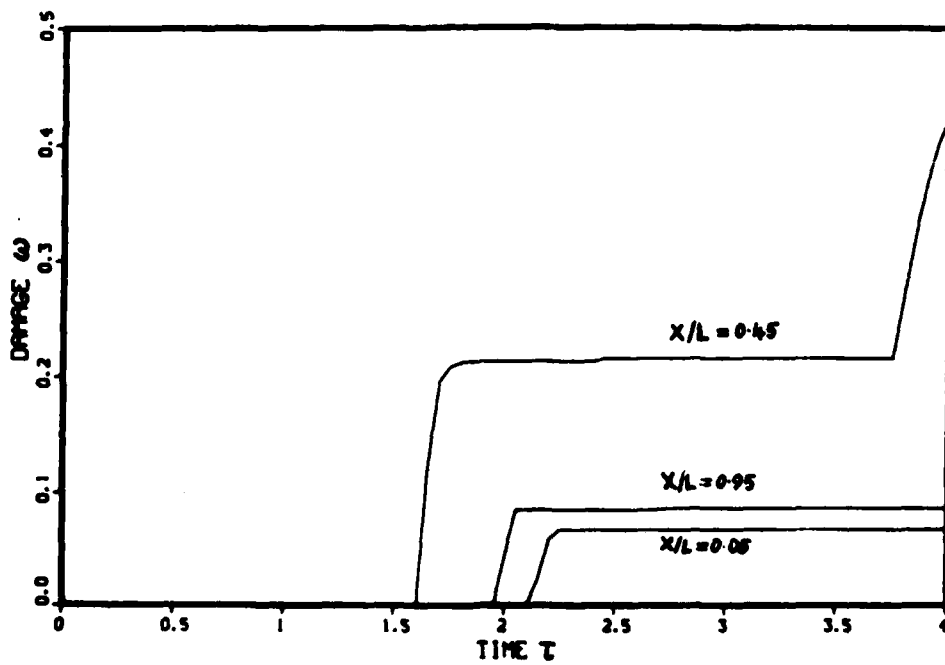


Fig. 6. Evolution of Damage at Sections of Rod due to Pulse #1

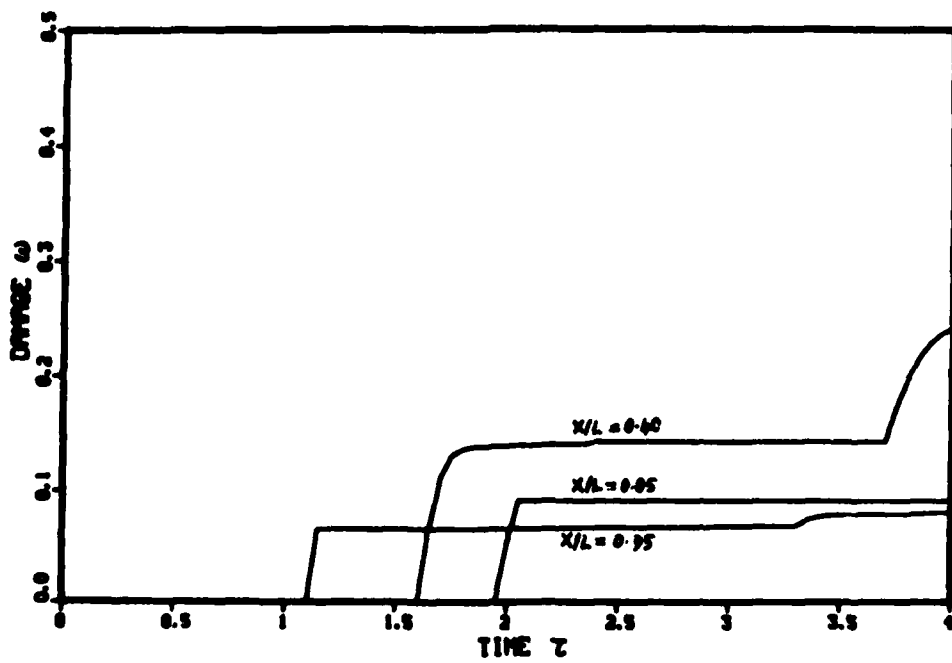


Fig. 7. Evolution of Damage at Sections of Rod due to Pulse #2

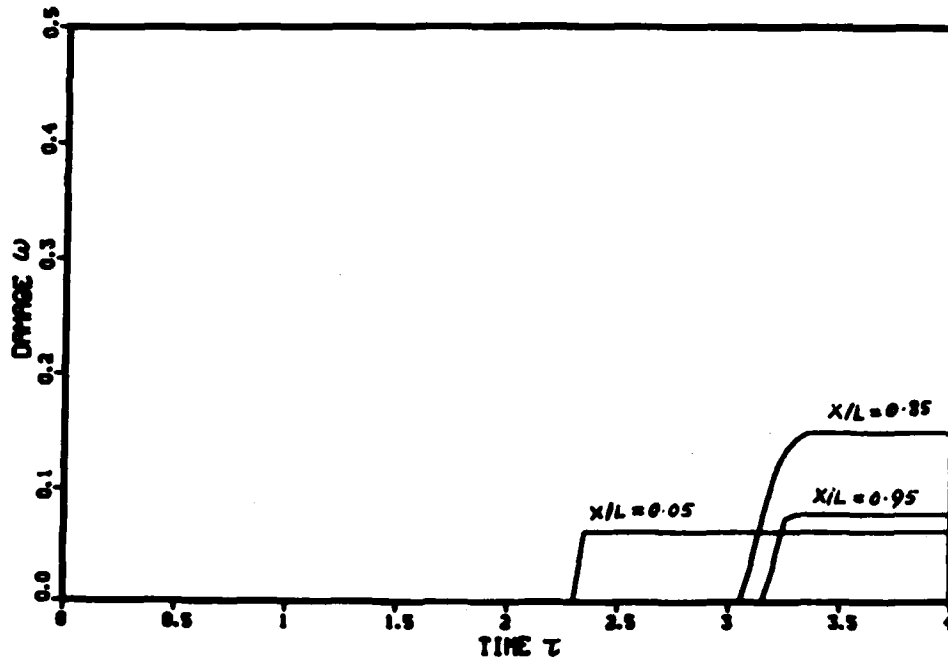


Fig. 8. Evolution of Damage at Sections of Rod due to Pulse #3

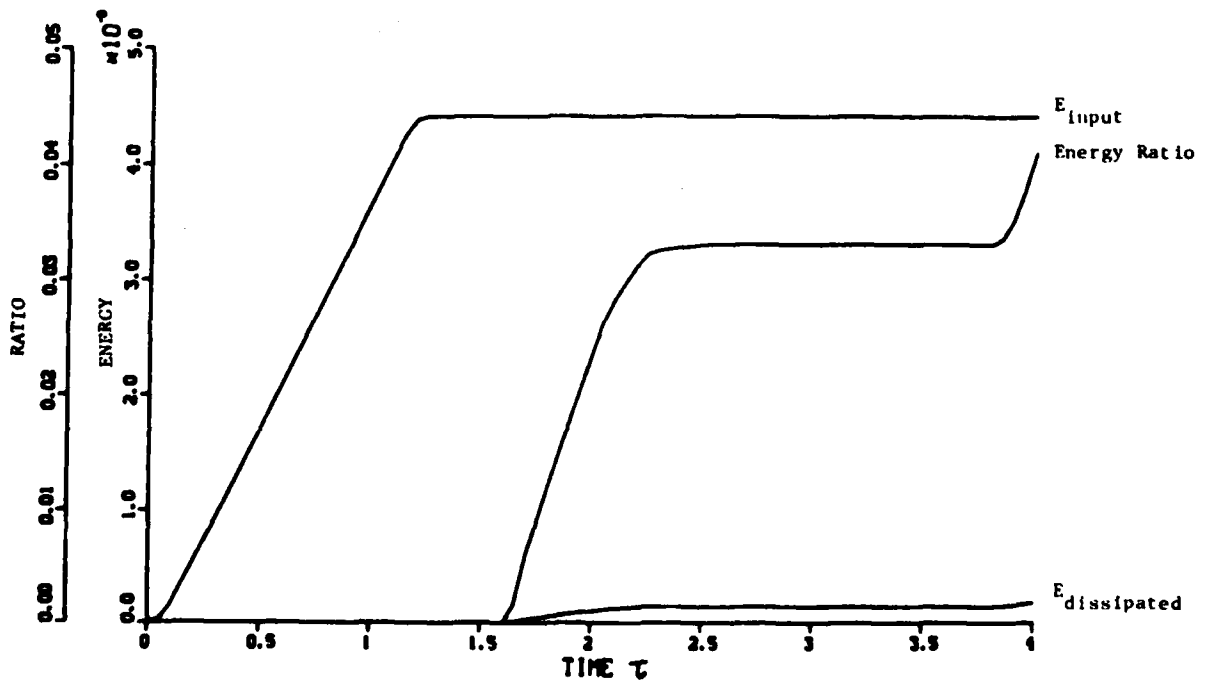


Fig. 9. Energy Input and Energy Dissipation due to Pulse #1

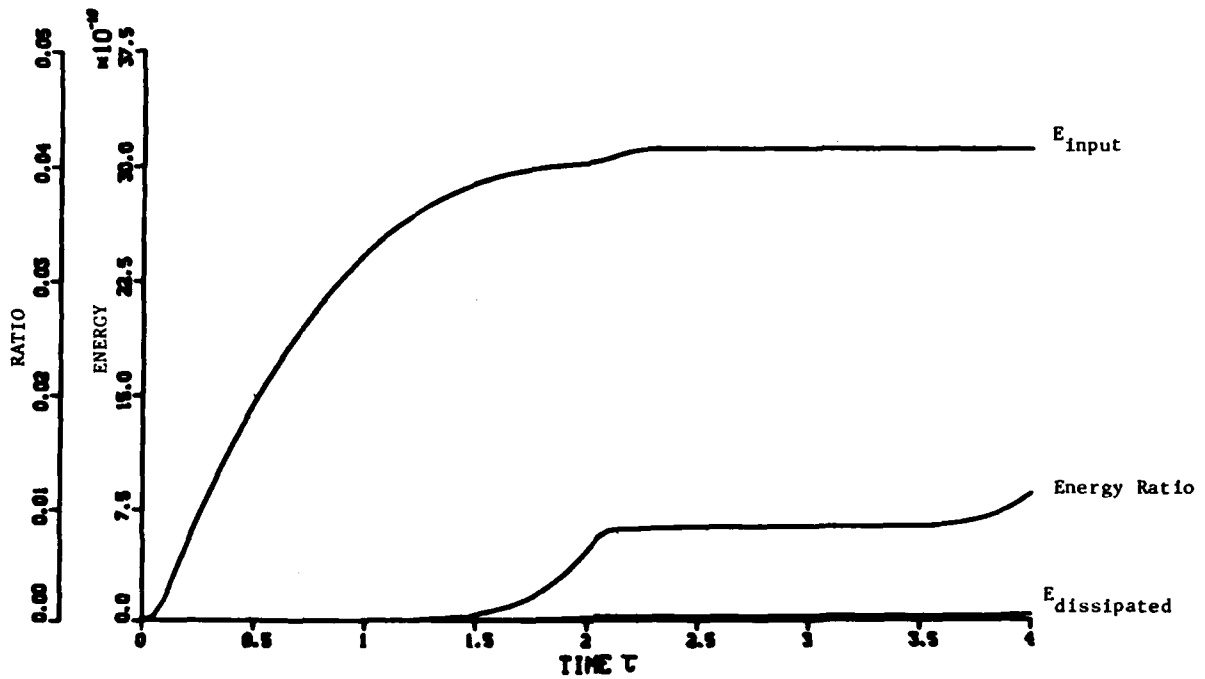


Fig. 10. Energy Input and Energy Dissipation due to Pulse #2

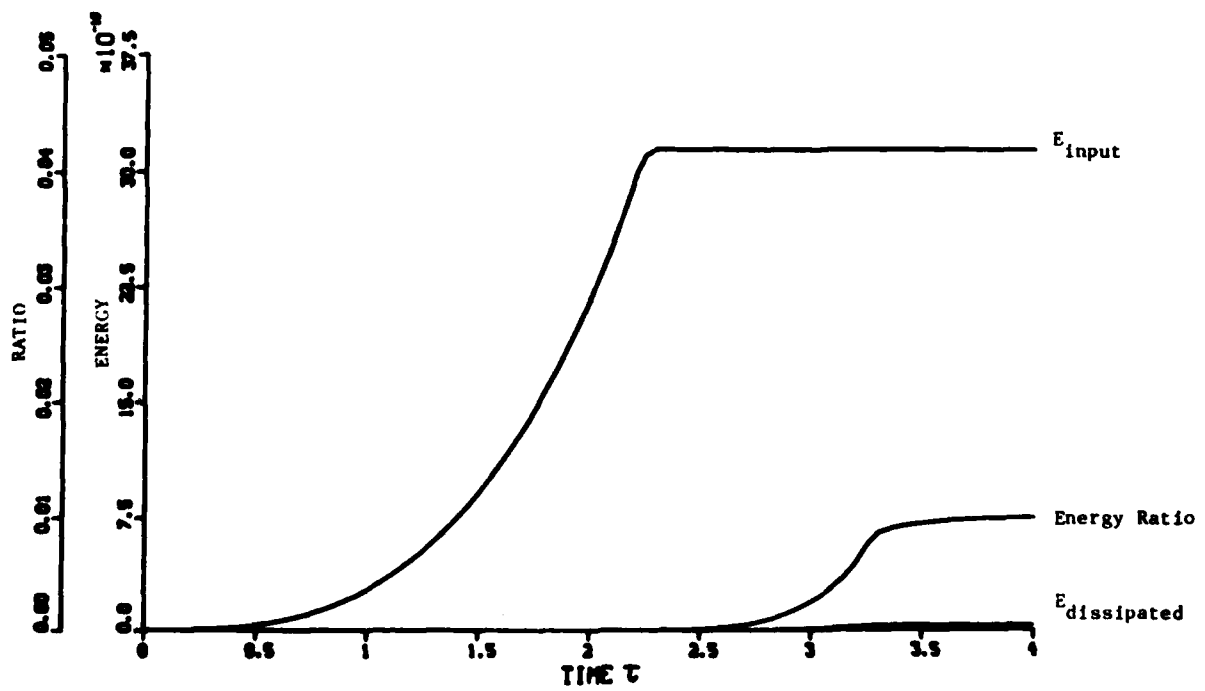


Fig. 11. Energy Input and Energy Dissipation due to Pulse #3

The distribution of damage along the length of the rod at two different time instants (corresponding to two and four passages of phase through the rod) is shown in Figures 3, 4 and 5 for the three pulses. It is evident from these figures that the maximum damage and its location are dependent upon the pulse shape even if the peak values of all the pulses are identical. This is explained by the fact that only monotonically increasing tensile stresses can cause damage and the interaction of the incident and reflected pulses at any section depends upon the pulse shape. For instance, there is no damage at any section for $\tau = 2$, for pulse 3. This is because for times $\tau \leq 2$, the incoming compressive pulse cancels out the reflected tensile pulse at all sections of the rod. It is an important point that the damage is continuous. In other words, even though failure will occur at the section where ω reaches 0.5, every section of the rod is damaged to some extent.

Figures 6, 7 and 8 show the evolution of damage due to the three pulses at three different sections of the bar. All three figures show the damage at $x/L = 0.05$ (near the loaded end) and at $x/L = 0.95$ (near the far end). In addition each figure shows damage growth at a section at which maximum damage occurs, this section being different for different pulses. In each case it is observed that the damage rate is rather large at specific times. These times correspond to the instants during which reflected tensile pulses traverse the cross section. Following the passage of these pulses the damage remains constant until the next tensile pulse arrives. Here again it may be noted that the damage in an arbitrary cross section is a continuous function of time.

The dissipated and input energies as functions of time are shown in Figures 9, 10 and 11 for the three pulses. In all cases the greatest dissipation is seen to occur at the first passage of the reflected wave. The ratio of energy dissipated to energy input is seen to be of the order of only a few hundredths. In the event of an ultimate spall ($\omega = \omega_F = 0.5$) the dissipated energy locally may provide a useful estimate for the fly-off velocity.

CONCLUSIONS

The proposed model, based on the continuum theory with internal variables, is capable of providing estimates of the damage level incurred locally along the rod. The newly introduced internal variable reflects the spatial and temporal

evolution of damage. In other words the accumulation of damage associated with passage of tensile waves is described as a continuous process.

It was not the intent of the paper to fit the experimental data for any particular material. Rather, attention is focused on the fact that a rational description of the spall phenomenon should include an internal variable reflecting the change in material integrity. Hence for a specific material it might be necessary to establish a different damage law based on simple experimental data.

The numerical example illustrates how the theory may be used for predicting damage in a structural member. When generalized to a three-dimensional case and damage laws characteristic of particular real materials this theory opens the way for describing the damage throughout a structure subjected to severe loading.

REFERENCES

1. J.H. Oscarson, K.F. Graff, "Summary Report on Spall Fracture and Dynamic Response of Materials," Report No. BAT-197A-4-3, Battelle Mem. Inst., 1968.
2. W.F. Waldorf, "Final Report, Studies of the Theory of Spallation," Rep. AFSWC-TR-60-20, Kirtland AFB, New Mexico, 1960.
3. J.S. Rinehart, "On Fractures Caused by Explosions and Impacts," Quart. of the Colorado School of Mines, Vol. 55, No. 4, pp. 1-155, 1960.
4. R.F. Rolsten, "A Study of the Shock Loading of Materials," Trans. New York Ac. of Sci., Series II, Vol. 36, No. 5, pp. 416-480, 1974.
5. S. S. Grigoryan, "Some Problems of the Mathematical Theory of Deformation and Fracture of Solid Rock Masses," Prikl. Mat. i Mekh., Vol. 31, pp. 643-669, 1967 (in Russian).
6. L.I. Slepyan, L.V. Troyankina, "The Failure of the Longitudinally Impacted Brittle Bar," Izv. AN SSSR, Mekh. i Tverdogo Tela, No. 4, No. 2, pp. 63-72, 1969 (in Russian).
7. M.S. Kachan, Yu.A. Trishin, "Tensile Stress in Targets Impacted by Rigid Bodies," Zhurnal Prikl. Mekh. i Tekhn. Fiziki, No. 4, pp. 114-124, 1977 (in Russian)

8. S.S. Grigoryan, "Some Recent Studies of Fracture of Dynamically Loaded Bodies," *Izv. AN SSSR, Mekh. Tverdogo Tela*, Vol. 12, No. 1, pp. 173-181, 1977 (in Russian).
9. L.I. Slepyan, "Models in the Theory of Brittle Fracture Waves," *Izv. AN SSSR*, Vol. 12, No. 1, pp. 181-186, 1977 (in Russian).
10. G.P. Cherepanov, *Mechanics of Brittle Fracture*, Nauka, Moscow, 1974 (in Russian).
11. L. Seaman, D.R. Curran, D.A. Shockey, "Computational Models for Ductile and Brittle Fracture," *J. Appl. Phys.*, Vol. 47, No. 11, pp. 4814-4826, 1976.
12. D.R. Curran, L. Seaman, D.A. Shockey, "Dynamic Failure in Solids," *Physics Today*, Vol. 30, pp. 46-55, 1977.
13. D.R. Curran, D.S. Shockey, L. Seaman, "Dynamic Fracture Criteria for a Polycarbonate," *J. Appl. Phys.*, Vol. 44, No. 9, pp. 4025-4038, 1973.
14. L. Davison, L.A. Stevens, "Continuum Measures of Spall Damage," *J. Appl. Phys.*, Vol. 43, No. 3, pp. 988-994, 1972.
15. L. Davison, L.A. Stevens, "Thermomechanical Constitution of Spalling Elastic Bodies," *J. Appl. Phys.*, Vol. 44, No. 2, pp. 668-674, 1973.
16. L. Davison, L.A. Stevens, M.E. Kipp, "Theory of Spall Damage Accumulation in Ductile Metals," *J. Mech. Phys. Solids*, Vol. 25, pp. 11-28, 1977.
17. L.M. Kachanov, "On the Creep Fracture Time," *Izv. AN SSSR, Otd. Tekhn. Nauk* No. 8, pp. 26-31, 1958 (in Russian).
18. I.N. Rabotnov, "On the Equations of State for Creep," *Progress in Applied Mechanics - The Prager Anniversary Volume*, pp. 307-315, 1963.
19. F.K.G. Odquist, *Mathematical Theory of Creep and Creep Rupture*, Clarendon Press, Oxford, 1966.
20. J. Janson, J. Hult, "Fracture Mechanics and Damage Mechanics: A Combined Approach," *J. de Mecanique Appliquee*, Vol. 1, pp. 69-84, 1977.
21. D. Krajcinovic, "Distributed Damage Theory of Beams in Pure Bending," *J. Appl. Mech.*, Vol. 46, pp. 592-596, 1979.
22. M. G. Srinivasan, D. Krajcinovic, G.U. Fonseka, R.A. Valentin, "The Distributed Damage Theory and Its Application in Dynamically Loaded Structures," *Abstracts, 16th Annual Meeting, Society of Engineering Science, Inc.*, September 1979.
23. J. Lemaitre, J.L. Chaboche, "Aspect Phenomenologique de la Rupture par Endommagement," *J. de Mecanique Appliquee*, Vol. 2, pp. 317-365, 1978.
24. P.O. Bostrom, "Damage Induced Instability in Beam Bending," *Int. J. Non-Linear Mech.*, Vol. 11, pp. 303-311, 1976.
25. J.L. Chaboche, "Description Thermodynamique et Phenomenologique de la Viscoplasticite Cyclique avec Endommagement," *ONERA, Publ. No. 1978-3*, 1978.
26. D. Krajcinovic, M.G. Srinivasan, G.U. Fonseka, R.A. Valentin, "Progressive Damage of Dynamically Loaded Brittle Rod," *Preprint, ASCE Annual Convention and Exposition, October 27-31, 1980*.
27. R. Courant, D. Hilbert, *Methods of Mathematical Physics II, Partial Differential Equations*, Interscience Publishers, New York, 1962.

VEHICLE SYSTEMS

LATERAL DYNAMICS OF C4 MISSILE

F. H. Wolff
Westinghouse R&D Center
Pittsburgh, Pennsylvania

A planar model of the C4 missile involving nonlinear force-deflection characteristics for the seals and pads was developed. Rigid body equations of motion based on small angle motion were solved to calculate the lateral motion of the missile during launch. After matching the calculated results to a PS-80 test record, variations in seal characteristics, pad characteristics, missile travel time, and initial conditions were studied to determine the sensitivity of the lateral dynamic calculations.

NOMENCLATURE

v - lateral deflection of missile (in)
 θ - angular deflection of missile (rad)
 y - vertical motion of missile (in)
 Y_G - missile C.G. (in)
 W_G - missile weight (lb)
 I - missile mass moment of inertia (lb sec²/in)
 Y_{P_j} - pad locations (in)
 $K_{P_j^1}, K_{P_j^2}, K_{P_j^3}$ - linearized pad stiffness (lb/in)
 ΔP_j - pad precompression (in)
 e_j - pad offset (in)
 δP_j - relative deflection across pad (in)
 F_{P_j} - pad force (lb)
 Y_{S_j} - seal locations (in)
 K_{S_j} - linear seal stiffness before inverting (lb/in)
 ΔS_j - deflection at which seal inverts (in)
 δS_j - relative deflection across seal (in)

\hat{F}_{S_j} - maximum seal force (lb)
 F_{S_j} - seal force (lb)
 F_T - tether force (lb)
 $F_{\Delta p}$ - destabilizing pressure force (lb)

INTRODUCTION

The Westinghouse Marine Division (MARD) in Sunnyvale, California under contract with the Navy to provide launch seals for the trident missile, test the proposed designs during launch conditions. Peashooter tests (PS) at the Hunters Point Facility in San Francisco involve firing a missile from a tilted launch tube (dock mounted) with a gas generator. During a launch several variables are monitored; e.g., pressure and missile deflections. For some of the Peashooter tests lateral motions were recorded which exceeded acceptable limits. MARD then contracted the Westinghouse Research and Development Center to perform an analysis of the launch dynamics. The analysis involved developing a model of the missile to predict the dynamics of the missile during a launch. Supplementing the calculations with results from a R&D analysis of the destabilizing forces on the missile gave insight into what caused the undesirable motions and what could be done to reduce them.

A planar model which represents motion in the 90-270° plane of the

missile was developed. The seal and pad characteristics were modeled with nonlinear springs acting between the missile and launch tube. Rigid body equations of motion were formulated to describe the missile dynamics during launch: x-horizontal deflection and θ -angular motion. The vertical travel of the missile (y) was obtained from test data. The equations were written in terms of small angle motion where second order terms such as θ^2 were neglected. After calibrating the model, the calculations were validated by closely matching the PS-80 test record. In addition, the extreme sensitivity of the calculated deflections to slight variations in certain parameters was demonstrated.

A Fortran computer program was written to enable numerous calculations to be made. The equations of motion were integrated using a 4th Order Runge-Kutta algorithm with error control. Basically, the error control involved calculating a single and a double step solution. Then an extrapolated solution formed from the above was compared with the double step solution. If the solutions were not within specified error bounds, the entire algorithm was repeated for one half the original step size. This procedure was repeated until either the error criteria was satisfied or nonconvergence occurred.

MODEL

To determine the lateral excursion of a C4 missile during a launch, the planar model of Fig. 1 was considered to represent displacements occurring in the 90-270° plane. The near diametric symmetry of the missile-tube configuration permitted a planar model to be used. Considering the missile to be a rigid body, three degrees of freedom are involved: lateral motion of the missile c.g., x; missile travel along the tube, y; and rotation about the missile c.g., θ . However, the y motion was eliminated as a degree of freedom by using empirical data on the vertical travel.

The shock isolation pads which vary in height from 7 in. to 14 in. concentrically enclose the missile at various elevations. The pads were considered to be nonlinear springs acting at 8 elevations with the force-deflection characteristics shown in Fig. 2. A conduit which extends the length of the missile in the 255° plane causes a slight asymmetric affect on the pad force-deflection characteristic; i.e., there is more stiffness from the pads

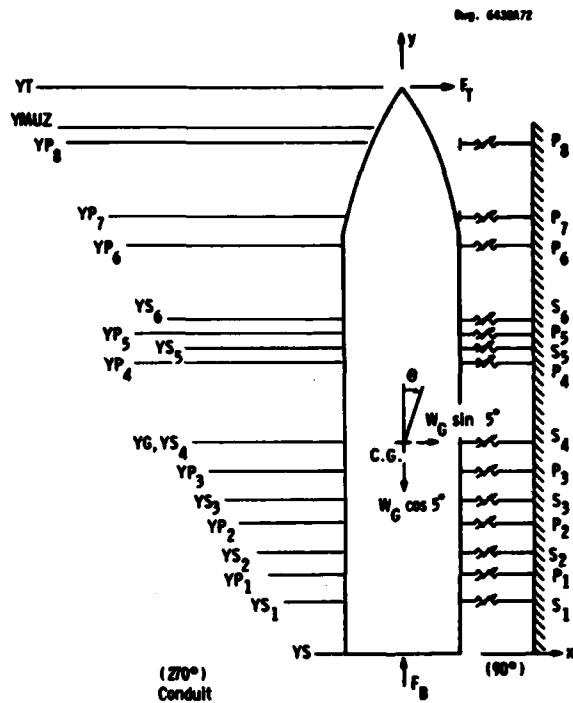


Fig. 1 - Model for calculating lateral excursion of C4 missile during launch (PS-80 Test Model)

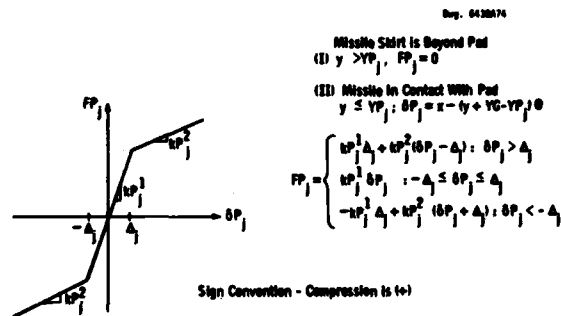


Fig. 2 - Pad force-deflection characteristics (symmetric pad arrangement - no conduit)

in the plane diametrically opposite the conduit so that at the tube centerline* there is a net pad force towards the 270° plane (Fig. 3). The actual parameter values used for the base case (Table 1) were taken from static deflection tests reported in reference 1. The force-deflection characteristics constructed from tests on neoprene and

* Zero displacement

urethane pads are shown in Fig. 4. These characteristics are based on a precompression of 0.15 in. of the pads by the missile. Dashed lines represent test results while solid lines represent resulting composite characteristics which were used in this analysis (Fig's. 2 and 3). Bottoming characteristics of the pads were not included in the simulation.

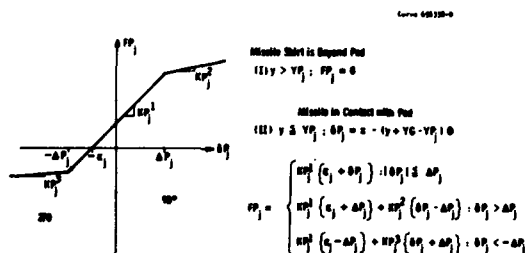


Fig. 3 - Pad force-deflection characteristics (Azimuth effects - conduit in 270° direction)

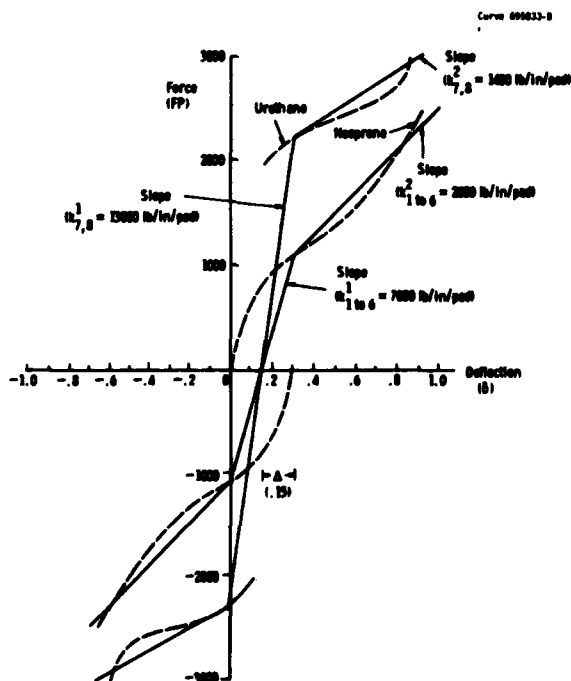


Fig. 4 - Composite spring constants for 22-1/2°, 14 in. high neoprene and urethane pads

TABLE 1
Neoprene and Urethane* Pad Characteristics for Base Case #80-17

Pad No.	'Location' YPj (in.)	KPj ¹ (lb./in.)	KPj ² (lb./in.)	KPj ³ (lb./in.)	ΔPj (in.)	εj (in.)
1	95	4000	1600	1300	.15	.05
2	90	3400	1200	1000	.15	.05
3	125	4000	1600	1300	.15	.05
4	200	2300	900	600	.15	.05
5	230	2300	900	600	.15	.05
6	200	4300	1400	1200	.15	.05
7*	300	8000	11200	9200	.15	.05
8*	300	6400	900	600	.15	.05

(I) $y > YP_j$, then $FP_j = 0$

(II) $y \leq YP_j$; $\delta P_j = x - (y + YG - YP_j)$

$$FP_j = \begin{cases} KP_j^1 (\epsilon_j + \delta P_j) : 0 \leq \delta P_j \leq \Delta P_j \\ KP_j^1 (\epsilon_j + \Delta P_j) + KP_j^2 (\delta P_j - \Delta P_j) : \delta P_j > \Delta P_j \\ KP_j^1 (\epsilon_j - \Delta P_j) + KP_j^2 (\delta P_j + \Delta P_j) : \delta P_j < -\Delta P_j \end{cases}$$

Although the pads have shown to exhibit hysteresis effects by test, this complicated behavior was not included in the model. The damping mechanism of the pads would tend to remove energy from the lateral response so the occasional oscillations present in the calculations could be eliminated by including pad hysteresis.

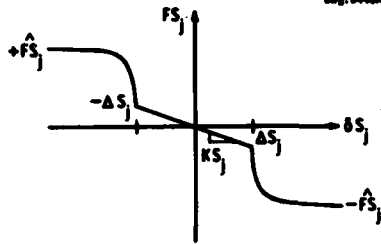
The seals which are located at 6 elevations were also modeled as non-linear springs. Briefly, the seals exert a destabilizing force on the missile; i.e., as the missile moves towards the tube the force on the missile is in a direction to produce even greater motion. The very complicated behavior of the seals was the subject of extensive analytical studies^{2,3}. Figure 5 used in this analysis represents the approximation of these results for the net lateral destabilizing forces from a pressurized launch seal.

EQUATIONS OF MOTION

There are several external forces which act on the missile during launch:

1. A tether force (F_T) which simulates a hydrodynamic load on the missile as the submarine moves through the water is applied to the missile nose via a cable during the pea shooter

* Zero displacement



- (I) Missile Skirt is Beyond Seal
 $y > Y_{Sj}, FS_j = 0$
- (II) Missile in Contact with Seal
 $y \leq Y_{Sj}$ and $FS_1 = FS_2 = \dots = FS_{j-1} = 0$
 $\delta S_j = x - (y + YG - Y_{Sj}) \theta$

$$FS_j = \begin{cases} -KS_j \delta S_j & : -\Delta S_j \leq \delta S_j \leq \Delta S_j \\ -\left\{ \Delta S_j \cdot KS_j \frac{\delta S_j}{|\delta S_j|} + \left(FS_j - \Delta S_j \cdot KS_j \right) \sqrt{\frac{\delta S_j^2 - \Delta S_j^2}{|\delta S_j|}} \right\} & : |\delta S_j| > \Delta S_j \end{cases}$$

Sign Convention - Compression is (-)

Fig. 5 - Negative seal force-deflection characteristics

TABLE 2
 Seal Characteristics for
 Base Case #80-17

Seal No.	'Location' Y_{Sj} (in.)	KS_j (lb./in.)	'Maximum Seal' Force (FS_j) (lb.)	ΔS_j (in.)
1	35	15750	10000	.05
2	70	15750	10000	.05
3	105	15750	10000	.05
4	145	15750	10000	.06
5	215	15750	10000	.10
6	235	15750	10000	.10

- (I) $y > Y_{Sj}$ then $FS_j = 0$
- (II) $y \leq Y_{Sj}$ and $FS_1 = FS_2 = \dots = FS_{j-1} = 0$
 $\delta S_j = x - (y + YG - Y_{Sj}) \theta$

$$FS_j = \begin{cases} -KS_j \delta S_j & : -\Delta S_j \leq \delta S_j \leq \Delta S_j \\ -\left\{ \Delta S_j \cdot KS_j \frac{\delta S_j}{|\delta S_j|} + \left(FS_j - \Delta S_j \cdot KS_j \right) \sqrt{\frac{\delta S_j^2 - \Delta S_j^2}{|\delta S_j|}} \right\} & : |\delta S_j| > \Delta S_j \end{cases}$$

tests. This load was modeled as a linearly varying force starting when the missile first enters the water ($y = 30$ in.) to full valve 4400 lb (PS-80 test) at $y = 120$ in.

$$F_T = 4400 \frac{(y-30)}{90} \quad 30 \leq y < 120$$

and (1)

$$F_T = 4400 \quad y \geq 120$$

2. Since the missile and tube are tilted 5° (PS-80 test) there is a component of weight which acts in the horizontal direction

$$W_G \sin 5^\circ = 70,000 \sin 5^\circ \approx 7000 \text{ lb} \quad (2)$$

The gravity load and the initial pad forces due to the conduit cause the missile to misalign initially. Although there is a retainer force (the exact nature of which is not known) there is some unknown initial condition which for this analysis was considered to be 0.

From the free body diagram (Fig. 1) the 2 differential equations of motion can be written. The horizontal motion equation is

$$\frac{W_G}{386} \ddot{x} = F_T - \sum_{j=1}^6 FS_j - \sum_{j=1}^8 FP_j \quad (3)$$

where the pad (FP) and seal (FS) forces are defined in Fig's. 2, 3, and 5. From a balance of moments about the missile c.g., the angular rotation equation is

$$I \ddot{\theta} = (YT - YG) F_T + \sum_{j=1}^6 (y + YG - Y_{Sj}) FS_j + \sum_{j=1}^8 (y + YG - Y_{Pj}) FP_j \quad (4)$$

where I is the mass moment of inertia.

UNBALANCE PRESSURE FORCE

The additional load needed to account for the lateral dynamics after the 6th seal is passed appears to be due to the unbalance of pressure around the missile. Once the missile passes the 6th seal the missile-eccentricity in the tube causes gas flow past the muzzle seal. This gives an unbalance pressure around the missile which is a destabilizing load. Figure 6 shows 3 pressure readings taken during the PS-80 shot which helps to identify the magnitude of the load. P1 was recorded at an

elevation of 250 in. while P7 and P9 were taken at 340 in. Since P7 and P9 are diametrically opposed and at the same elevation they can be used to estimate the subsequent unbalance force.

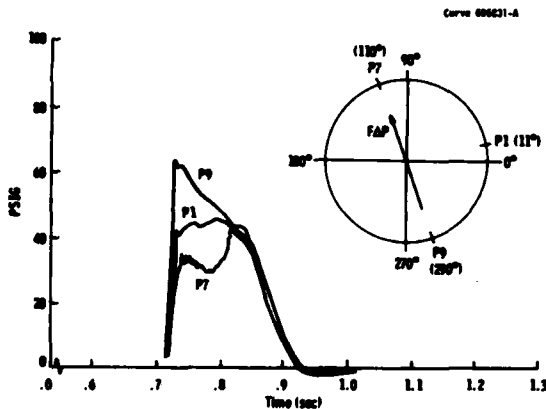


Fig. 6 - Pressure loss in upper tube annulus (PS-80 test)

Assuming a sinusoidal distribution of pressure around the missile periphery of

$$\left\{ \frac{P7 + P9}{2} + \frac{(P9 - P7)}{2} \cos \phi \right\}$$

where ϕ is measured from the 90-270° plane, the differential force $d(FAP)$ at any position ϕ is then

$$d(FAP) = \left\{ \right\} h r d\phi$$

where h is the height over which the unbalance pressure acts. The component of force acting along the 90-270° plane is

$$FAP = \int_0^{2\pi} d(FAP) \cos \phi = hr \frac{\pi}{2} (P9 - P7)$$

Using average pressures of $P7 \approx 35$ psi and $P9 \approx 50$ psi (Fig. 6) acting over the entire height of $h = YM - YS_6 = 125$ in. gives

$$FAP \approx 125 \times 37 \times \frac{\pi}{2} (50 - 35) \approx 100,000 \text{ lbs}$$

The destabilizing pressure force which decreases linearly as h decreases was applied at a location halfway between the c.g. and the skirt

$$FAP = 100,000 \left\{ 1 - \frac{(y - YS_6)}{YM - YS_6} \right\}$$

for $YS_6 \leq y < YM$

The equations of motion (eq's. (3), (4)) then become

$$\frac{W_G}{386} \ddot{x} = F_T - \sum_{j=1}^6 FS_j - \sum_{j=1}^8 FP_j + FAP \quad (5)$$

and

$$I\ddot{\theta} = (YT - YG) F_T + \sum_{j=1}^6 (y + YG - YS_j) FS_j + \sum_{j=1}^8 (y + YG - YP_j) FP_j - (YG - \frac{YM - Y}{2}) FAP \quad (6)$$

COMPARISON OF PS-80 TEST AND CALCULATED RECORDS

After adjusting parameters, the results of the PS-80 trajectory calculation compared favorably with the PS-80 test record (Fig. 7). The initial pad forces due to the azimuth effects yield a transient sufficient to cause the first seal to go onto the pads; e.g., in PS-80 where the pad forces oppose the gravity load, the initial pad offset must be great enough ($\epsilon_j > .04$ in.) to cause initial motion towards the 270° direction. Hence, the 1st seal destabilizing force causes the initial 0.2 in. peak. The 2nd and 3rd seals also go onto the pads; if they did not the response would show oscillations. These destabilizing seal forces oppose the restoring pad forces preventing the skirt from swinging beyond the reference axis.

The missile lateral excursion recovers until the 4th seal inverts at about $y = 120$ in. The 4th, 5th, and 6th seals all go onto the pads causing the skirt and muzzle deflections to reach 0.55 in. and -0.3 in., respectively, before the pads begin to limit them. However, when the skirt passes the 6th seal ($y > 235$ in.) the effects of the large destabilizing pressure forces become evident.

The best match to the PS-80 test record (Fig. 7) is labeled Run #80-17 which is referred to as the base case. The base case pad and seal parameters are shown in Table 1 and 2. All of the computer runs made are listed in Table 3 which describes their deviations from the base case.

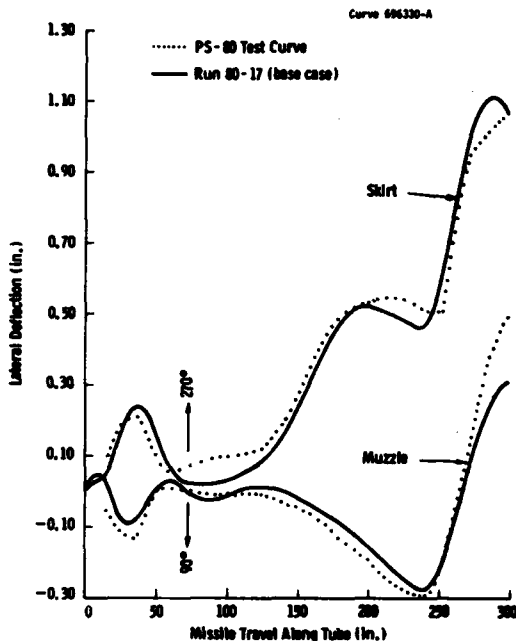


Fig. 7 - Calculated and test deflections of C4 missile skirt and muzzle during simulated launch (PS-80) (Tether Load = 4000 lb)

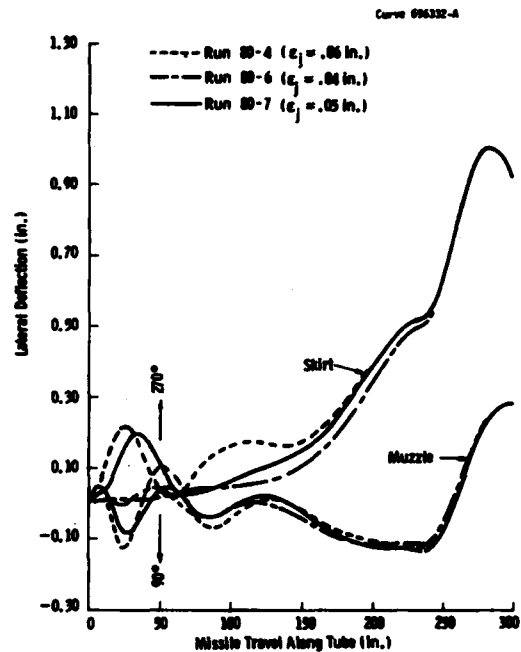


Fig. 8 - Effects of various pad offsets (.04, .05, .06) on PS-80 calculated lateral deflections

SENSITIVITY OF LATERAL DYNAMIC CALCULATIONS TO PARAMETER VARIATIONS

The lateral motion calculations exhibit a significant dependence on choice of pad and seal parameters, initial conditions, and vertical travel curve. Figures 8 through 12, which dramatize these effects, suggests that as a predictive tool for launch dynamics, the calculations without supportive test data are questionable.

The pad asymmetry due to the conduit near the 270° plane appears to be largely responsible for the initial transient by causing the first seal to go onto the pad. Figure 8 shows the PS-80 calculated deflections for 3 different pad force-deflection curve offsets (.04, .05, and .06 in.). For an offset of .04 in. (Run #80-6), the pad forces are not sufficient to overcome the gravity load (7000 lb); accordingly, the initial large deflections are absent. The subsequent response is also smaller. Runs #80-4 (.06 in.) and #80-7 (.05 in.) illustrate the initial transient when the pad offset is great enough to cause the first seal to go onto the pad. Pad offset of .05 in. was chosen as base

case because it gave the best overall match to the test record, particularly, the initial deflection.

Figure 9 shows the influence of slight changes in maximum seal forces \bar{F}_S : refer to Table 3 for exact description of computer runs. Run #80-10 with the 2nd seal at 12,000 lb while all others at 10,000 lb has the largest initial peak, because the 2nd seal is largely responsible for the response between $y = 35$ in. and 70 in. For Run #80-11 the 2nd seal was reduced to 10,000 lb while the 4th seal was increased to 12,000 lb, hence, the smaller initial excursion but larger motion when the 4th seal dominates ($y = 105$ in. to 145 in.). Run #80-12 shows all seals at 10,000 lb (base case). When all seal maximum forces are 9000 lb (Run #80-13) the response is smaller.

Because the exact position of the missile at the initiation of the launch is not known, the base case initial condition was selected to be 0. However, consider what happens if the missile is given an initial displacement of .03 in. (Fig. 10); there is a significant difference in the lateral

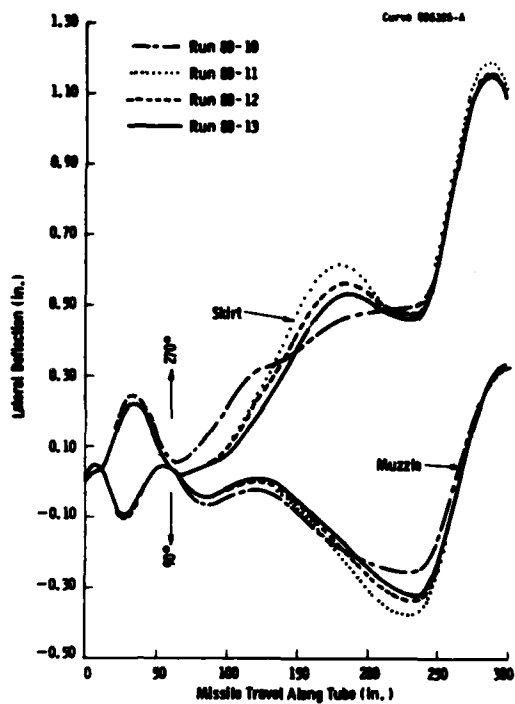


Fig. 9 - Influence of different seal characteristics on PS-80 calculated lateral deflections

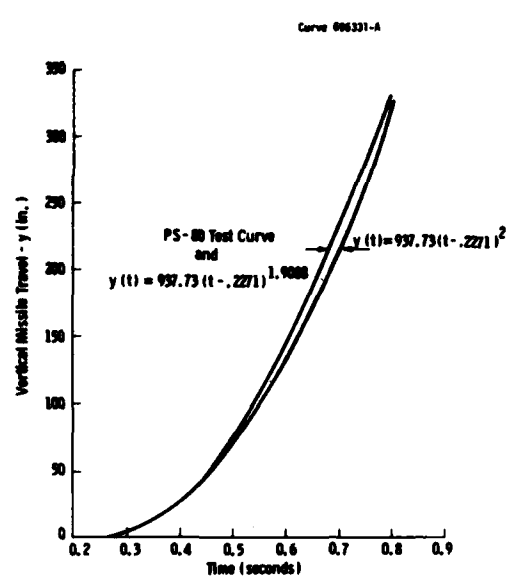


Fig. 11 - C4 missile travel curves for PS-80 test

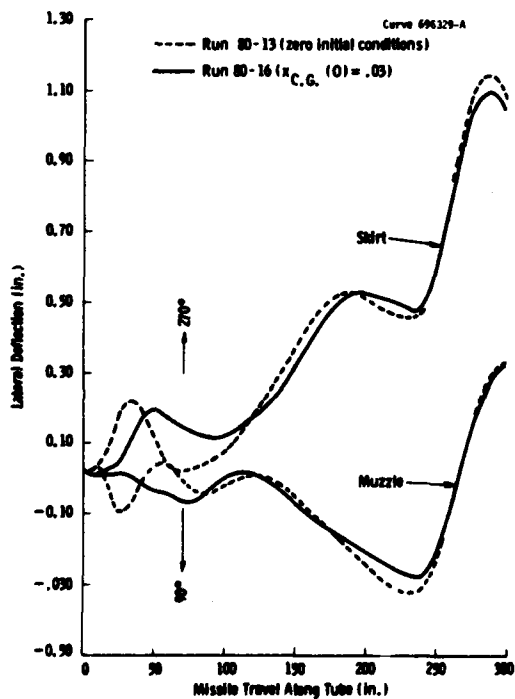


Fig. 10 - Initial condition effects on PS-80 calculated lateral deflections

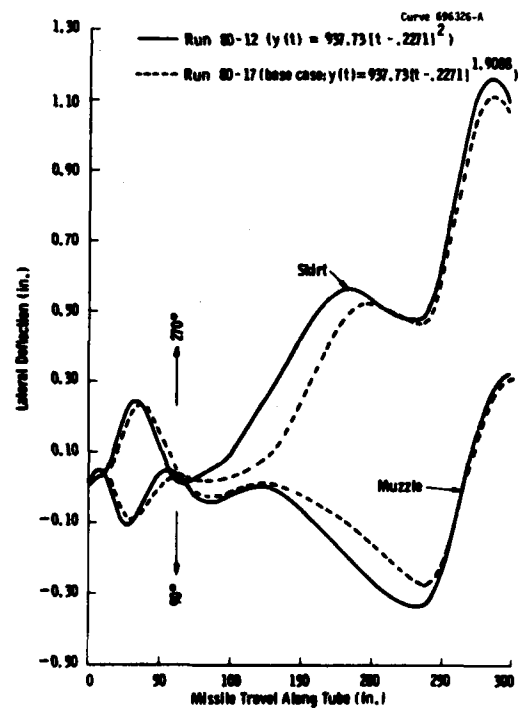


Fig. 12 - Comparison of slight variation of missile vertical travel on PS-80 calculated lateral deflections

deflections, particularly, during the early portion of the record.

Knowing the exact missile vertical travel curve is important. Figure 11 shows two slightly different travel curves both of which would be in the physical range. Figure 12 illustrates a significant difference in the trajectory motions for the two travel curves. Run #80-17 (base case) where the missile moves slightly faster shows significantly smaller deflections because the seal destabilizing forces are acting for slightly shorter time. The faster missile travel gives lower maximum deflections which also occur later in the travel variations in this parameter could explain different trajectories measured during "identical" test shots.

ADDITIONAL TRAJECTORY CALCULATIONS

Figure 13 which shows a poor comparison between test record PS-93 and calculation Run #80-23 illustrates the difficulty in predicting trajectory calculations. However, when the unbalance pressure was arbitrarily halved the calculated motions compared well with the test record.

Regardless of the quantitative merits of the calculations, the effect of variations can be studied. For example, Fig. 14 shows the favorable influence of removing the 4th seal (Run #80-20) and removing the first 4 seals (Run #80-18) when compared to the base case. The lateral deflections are reduced by removing seals.

TABLE 3
Data for PS-80 Computer Simulations (Tether = 4000 lb, Tilt = 5°)

Run No.	Vertical Motion $Y=C(1-t)^a$			L.C.'s On x C.G. (in.)	Psd Characteristic e_j (in.)	Seal Characteristics Seal No.						Pressure Pulse After 6th Seal Force/Time lb./sec.
	C	a	u			$f_{2j}/\Delta S_j$						
						1	2	3	4	5	6	
80-1	937.73	.2271	2.0	0.	.00	8000/.04	8000/.05	8000/.10	8000/.10	8000/.10	8000/.10	30000/.01
80-2												30000/.0
80-3												100000/0
80-4						8000/.05	8000/.06	8000/.15	8000/.15	10000/.10	10000/.10	
80-5					.00							
80-6					.04							
80-7					.05							
80-8						12000/.05	12000/.05	12000/.05	12000/.05	10000/.10	10000/.10	
80-9					.005							
80-10					.05	10000/.05	12000/.05	10000/.05	10000/.05	10000/.10	10000/.10	
80-11							10000/.05		12000/.05			
80-12									10000/.05			
80-13						9000/.05	9000/.05	9000/.05	9000/.05	9000/.10	9000/.10	
80-14												
80-15										9000/.10	9000/.10	
80-16				0.05		9000/.05	9000/.05	9000/.05	9000/.05	9000/.10	9000/.10	
80-17		1.9088		0.0		10000/.05	10000/.05	10000/.05	10000/.05	10000/.10	10000/.10	
80-18					.05 ¹							
80-19					.05 ¹					10000/.20	10000/.20	
80-20					.05	10000/.05	10000/.05	10000/.05		10000/.10	10000/.10	
80-21					.05 ²							
80-22					.05							
80-23					.05 ¹					8000/.10	8000/.10	

.05¹ = Pads 1, 6 Symmetric
.05² = Solid Urethane Pads (Pads 7, 8)

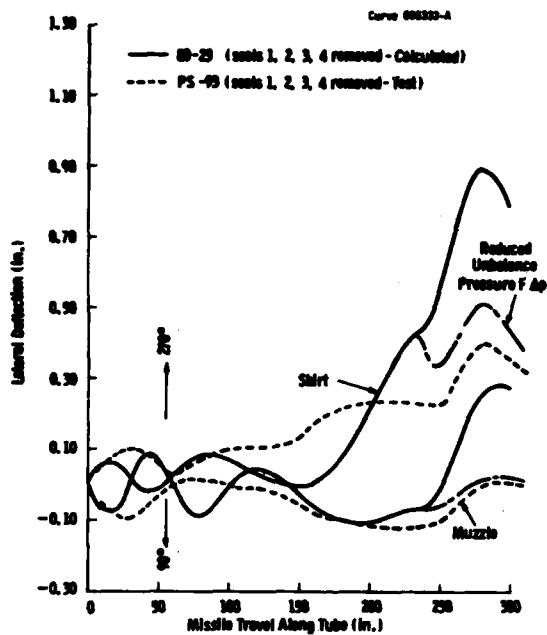


Fig. 13 - Comparison of test and calculated lateral deflections when first 4 seals are removed

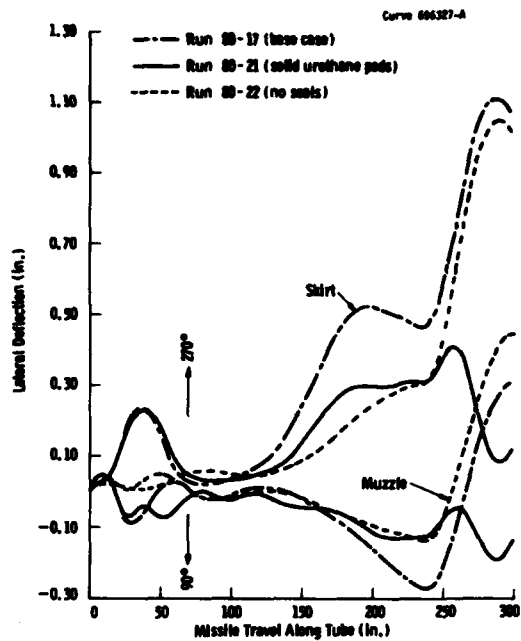


Fig. 15 - Improvement of solid urethane pads near top of missile on PS-80 calculated lateral deflections

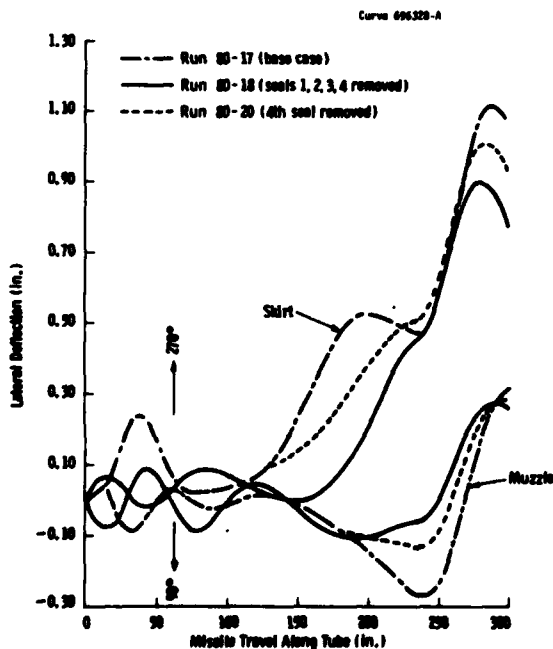


Fig. 14 - Effect of removing seals on PS-80 calculated lateral deflections

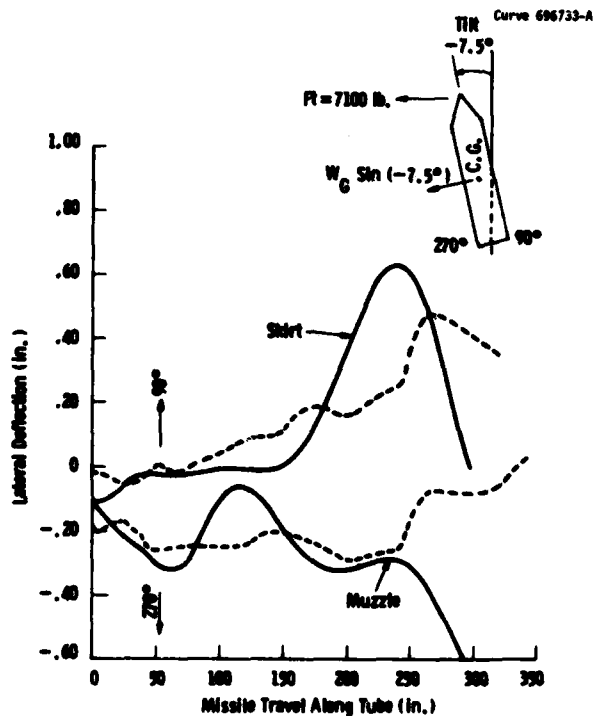


Fig. 16 - Test and calculated lateral deflections of skirt and muzzle during Shot #413

Figure 15 shows how the lateral deflections are reduced to acceptable levels when stiff upper pads (pads 7, 8) are considered. It is likely that a fix such as this would correct the stability problem regardless of the seal designs. The lateral excursions are only slightly greater than the optimum case when all 6 seals are removed (Run #80-22).

Figure 16 contains test and calculated deflections for shot #413 where tilt and tether load are directed towards conduit (270° plane). The comparison is good for most of the trajectory with the calculated response showing some oscillation that most likely would be eliminated if pad hysteresis were included. Also, the calculation is somewhat over-predictive. The tilt and tether load in the direction of the conduit appears to improve the lateral motions.

CONCLUSIONS

The investigation reported herein establishes that C4 missile trajectories can be calculated with sufficient accuracy to match Peashooter tests in spite of the complicated destabilizing seal forces if calibrating the model is permitted. By adjusting certain variables over a narrow range of physical values a close match can usually be obtained. The extreme sensitivity of the calculations to slight variations in key parameters, which are not precisely known, make it virtually impossible to predict exactly the trajectory motions without calibrating. However, qualitative effects can be studied confidently and with available test data trajectory calculations can be a valuable design tool.

Both test and calculated trajectories indicate the factors which adversely affect the lateral stability during a launch:

1. Destabilizing seal forces caused by seals inverting onto the pads (particularly the 4th and 6th seals).
2. Destabilizing non-uniform pressure load which occurs once the missile passes the 6th seal because of missile eccentricity in the tube and flow past the muzzle seal (this force may be small and insignificant in a tactical underwater launch).
3. The azimuth effects of the pads strongly influence the initial transients.

Removing seal forces resulted in significant reduction in lateral deflections: eliminating all 6 seal forces and the destabilizing pressure load gave deflections less than 0.2 in.

Increasing the stiffness of the top 2 pads provides a possible method of limiting the missile deflections even with destabilizing seal and pressure forces present. Preliminary calculations indicate that the forces exerted on the missile by the stiffer pads are less than present design.

REFERENCES

1. G.E. Rudd and J.F. Meier, "Long Term Stiffening of Neoprene Launch Tube Liner Pads for the Poseidon Missile", Westinghouse Research Report 70-8B7-MONIT-R1, May 1970.
2. A.J. Molnar, "Missile Launch Seal Analysis", Westinghouse Research Report 73-1B5-MSEAL-R1, October 1973.
3. A.J. Molnar, "Destabilizing Lateral Forces from Pressurized Launch Seals", Westinghouse Research Report 78-8E7-SEALB-R1, August 1978.

ANALYSIS OF SUBCRITICAL RESPONSE MEASUREMENTS FROM
AIRCRAFT FLUTTER TESTS

J. C. Copley
Royal Aircraft Establishment
Farnborough, Hampshire, England

This paper describes a method for the analysis of subcritical response measurements obtained during aircraft flutter tests. Suitable forms of input signal, and the derivation of transfer functions using Fast Fourier Transforms are discussed. The transfer functions are subsequently analysed to give frequency and damping estimates. Because the effects of atmospheric turbulence degrade the measurements, and hence the estimated parameters, a method for assessing the magnitude of the accuracy of the estimates is developed. Examples of the application of the analysis method to typical response data are given.

INTRODUCTION

An important part of the design of an aircraft is the avoidance of flutter within the intended flight envelope. Initially the designer must rely on theoretical calculations, but these are followed by wind-tunnel model tests and eventually a flight flutter test to confirm that satisfactory flutter margins have been achieved.

In the simplest form of these tests, the aim is to determine the critical conditions at which flutter occurs. One experimental approach is the 'peak hold' technique, in which the power spectrum of the response to turbulence is monitored. This can provide an indication of the critical conditions, and possibly of system frequency and damping trends. An alternative approach is to measure the trend of significant system properties at a set of subcritical conditions. A known excitation is applied, and various responses are measured. The data may then be analysed to provide numerical values for system frequencies and dampings. These allow the approach to flutter to be monitored, and allow an assessment of the validity of theoretical calculations.

The analysis may be performed in many ways (see for example [1]); this report describes a technique of fitting to system transfer functions in

the frequency domain. This is similar to the approach adopted in modal analysis of structures but the nature of aircraft flutter makes the analysis more difficult. The modes may be close in frequency and/or highly damped, and in some cases a lightly damped mode obscures a significant heavily damped mode. A further complication is that atmospheric turbulence introduces errors into the response measurements which affect the accuracy of any estimates of frequency and damping. A method is given here for the estimation of the magnitude of possible errors.

TRANSFER FUNCTION MEASUREMENT

Before considering the problems of transfer function analysis it is appropriate to examine how the transfer functions may be measured. The availability of Fast Fourier Transform techniques applied to digitally sampled inputs and outputs has contributed to the achievement of short test times. Many possible input signals may be used, the commonest being slow or fast frequency sweeps, pseudo random or periodic random noise, or impulses. Use of pseudo random noise requires the introduction of windowing [2] and possibly overlapping of successive records during the data processing in an attempt to minimise the effect of leakage. Slow sweeps may be similarly treated [3]. The effect of these additional operations on the

measured transfer function is not easily calculable, but empirically it has been found to introduce errors. For periodic random noise, fast sine sweeps, and impulses, it is usually possible to ensure that, for practical purposes, conditions for a leakage free measurement are met. Fast sine sweeps and periodic random inputs are normally preferred because it is relatively easy to control their spectral energy distributions.

Calculation of transfer functions from input and responses may be performed using standard techniques [2]. It is desirable to use as many independent records as flight conditions and considerations of test time permit. The coherence function may be used as a method of assessing the accuracy of the transfer function measurement, but in aircraft flutter testing there is usually little that can be done to improve measurements where the coherence is low.

TRANSFER FUNCTION ANALYSIS

The aim of the analysis process is to determine numerical values for the parameters of a suitable theoretical expression so as to provide the best representation of the measured transfer function.

Using the British form of flutter equations, the response of the system to a sinusoidal input $Qe^{i\omega t}$ may be calculated from

$$(-I\omega^2 + i\omega B + C)q = Q \quad (1)$$

where B and C are square matrices, q is a column of generalised displacement coordinates and Q is a column of generalised forces. Eq. (1) is the usual equation of motion for an n degree of freedom system with viscous damping. The transfer function of the system it represents may be written [4,7]

$$H_p(i\omega) = \sum_{j=1}^n \frac{F_{pj} + i\omega G_{pj}}{-\omega^2 + 2i\omega\zeta_j\omega_j + \omega_j^2} \quad (2)$$

for any position p on the structure.

Eq. (2) includes all the modes of the system, but the experimental data may only contain a few of them. The modified form

$$H_p(i\omega) = \sum_{j=1}^m \frac{F_{pj} + i\omega G_{pj}}{-\omega^2 + 2i\omega\zeta_j\omega_j + \omega_j^2} + F_p + i\omega G_p + \frac{X_p + i\omega Y_p}{\omega^2} \quad (3)$$

is therefore used as the model. The second and third terms on the right hand side represent contributions to the response in some frequency range from modes above and below that range. The difference between the measured transfer function H_k at frequency ω_k and the theoretical model is

$$e_k = H_k - H_p(i\omega_k) \quad (4)$$

To obtain estimates of the model parameters the weighted summed square ϵ is minimised

$$\epsilon = \sum_{k=1}^{n_p} e_k W_k e_k^* \quad (5)$$

where n_p is the number of data points, and W_k is the weight attached to point k. If measurements of more than one transfer function have been made, the summation is taken over all available data to ensure consistent frequency and damping estimates. To minimise ϵ requires solution of

$$\frac{\partial \epsilon}{\partial x_i} = 0 \quad 1 \leq i \leq n_v \quad (6)$$

where x represents the n_v distinct parameters of Eq. (3).

Eqs. (6) are nonlinear, and are solved iteratively by the Gauss-Newton method. If the solution is \hat{x} , and the current estimate of \hat{x} is x, write $\hat{x} = x + \delta x$. Then

$$0 = \frac{\partial \epsilon}{\partial x_i}(\hat{x}) = \frac{\partial \epsilon}{\partial x_i}(x + \delta x) \\ = \frac{\partial \epsilon}{\partial x_i}(x) + \delta x_j \frac{\partial^2 \epsilon}{\partial x_i \partial x_j}(x)$$

$$\text{or} \quad \delta x = -R^{-1}P \quad (7)$$

$$\text{where } R_{ij} = \frac{\partial^2 \epsilon}{\partial x_i \partial x_j}(x) \text{ and } P = \frac{\partial \epsilon}{\partial x_i}(x).$$

Hence \hat{x} is updated, and the process repeated until convergence is achieved. The convergence is determined by monitoring the error ϵ , rather than the individual values x_i . This iterative solution is numerically well behaved provided suitable initial estimates for frequency and damping values can be obtained. It may be possible for the engineer to supply satisfactory initial estimates, but in some circumstances (eg close frequencies) this is difficult. In such cases estimates are found using the polynomial ratio method proposed by Sanathanan and Koerner [5]. This linearises the least squares fit equations, and therefore allows estimation of parameters directly without any prior knowledge of the system. Experience has however shown that the equations involved may become ill-conditioned for systems with many modes. To avoid this, each frequency range where the transfer function has a large amplitude is analysed separately, and the estimated frequencies and dampings assembled to provide initial estimates for the subsequent iterative solution.

ACCURACY OF RESULTS

Transfer function measurements obtained during flutter tests are inevitably degraded by the effects of atmospheric turbulence which will affect estimates of frequencies and dampings. The coherence function gives an indication of the accuracy of the basic measurement, but this indication cannot easily be extended to the parameter values. Useful results may however be obtained from an analysis of the statistical properties of the least squares fit.

If the errors e_k at each separate data point are uncorrelated, their covariance matrix may be written

$$V(e) = E(e^*e^T) = \sigma^2 V \quad (8)$$

where V is a diagonal matrix expressing the expected magnitude of the errors at each point. If the matrix W of Eq. (5) is taken to be V^{-1} , then it may be shown [6] that

$$E(\hat{x} - x_t) = 0 \quad (9)$$

where x_t is the true solution and \hat{x} the identified solution (ie the results are unbiased),

$$S^2 = \frac{2\epsilon}{2n_p - n_v} \quad (10)$$

is an estimator of σ^2 , and the covariance matrix of the parameters

$$V(\hat{x}) = E[(\hat{x} - x_t)(\hat{x} - x_t)^T] = S^2 R^{-1} \quad (11)$$

Eqs. (10) and (11) allow the estimation of the variance of the i th parameter

$$\sigma_i = S \sqrt{R_{ii}^{-1}} \quad (12)$$

If then x_i is assumed normally distributed, confidence intervals may be calculated, eg

$$\text{pr}\{\hat{x}_i - 2\sigma_i < x_{i_t} < \hat{x}_i + 2\sigma_i\} > 0.95$$

In practice, V is unknown, and some arbitrary choice must be made. For flutter tests, the effect of turbulence may be represented as an additional unknown input to the system. As a first approximation, the response to this extra excitation will be large at frequencies where the response to the known forcing is large, thus we may take

$$|e_k| \propto |H_k|$$

or

$$W_k = \frac{1}{H_k H_k^*}$$

RESULTS

The analysis method described has been applied to data from several flutter tests. The two examples presented are both wind tunnel model tests in which a control surface was used to provide the forcing. The first results were obtained from a low speed binary model in a low turbulence tunnel, with fast sine sweep excitation. The transfer function measurements are of good quality (Fig 1), and this is reflected in the estimated frequency and damping values (Fig 2).

The second set of results are from tests on a high speed model ($M = 0.8$) where the excitation signal was periodic random. This aeroelastic model has many degrees of freedom, but results are presented only for the two modes concerned in the flutter. The transfer function measurements are obviously badly degraded by the response to turbulence (Fig 3), but the estimated frequency and damping values show good agreement with theoretical calculations (Fig 4).

To assess the validity of the estimated confidence intervals, the transfer function of the low speed model was measured one hundred times at a fixed condition, and each transfer function was analysed. The variance of each parameter was calculated from the separate estimates, and compared with the estimated variance. Each separate analysis also gives a confidence interval; the number of times this failed to include the true value was counted. For a 95% confidence interval, there should be about five such failures in one hundred measurements. The results of these calculations are given in Table 1, and indicate that the estimated variance and confidence intervals are valid.

CONCLUSION

This paper has described a method for the analysis of transfer function measurement obtained during flutter tests. The information available from this analysis gives valuable insight into the behaviour of the system, and provides guidance in the conduct of the test. The analysis gives quantitative data that may be compared directly with earlier theoretical calculations, and provides quantitative estimates of the accuracy of that data.

SYMBOLS

B	modified damping matrix
C	modified stiffness matrix
E()	statistical expectation
F, G	terms describing residual contribution of other modes at position p
F _{pj}	effective forcing of mode j at position p
G _{pj}	
H _p (iω)	theoretical transfer function at position p
H _k	measured transfer function at frequency ω _k
I	unit matrix
P	defined by Eq. (7)
Q	column of generalised forces
R	defined by Eq. (7)
S	defined by Eq. (10)
V	diagonal matrix defined by Eq. (8)
V()	statistical covariance matrix
W	a diagonal matrix whose terms are W _k
X _p , Y _p	terms describing residual contribution of other modes at position p
e _k	error at frequency ω _k
n _p	number of experimental data points
n _v	number of parameters in Eq. (3)

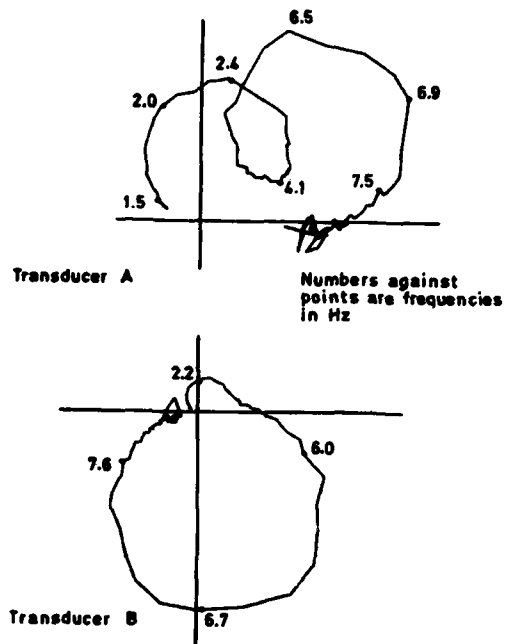


Fig 1 Transfer function plots for low speed model $V = 0.781V_F$

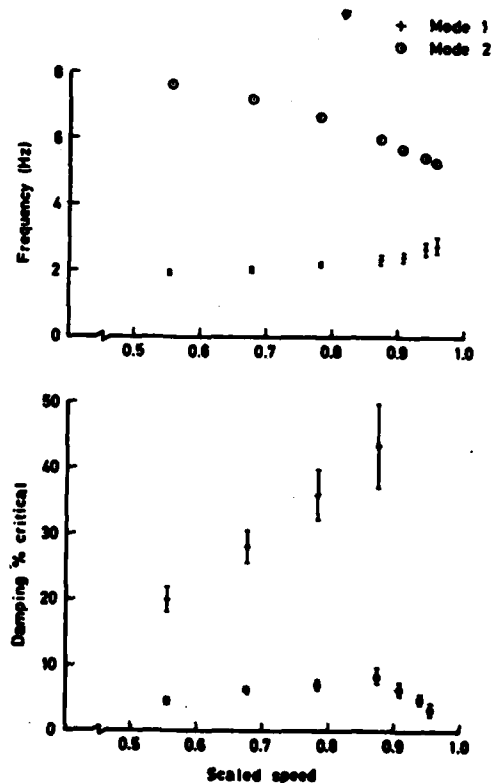


Fig 2 Subcritical frequencies and dampings for low speed model

q column of generalised displacements
 x vector of parameters of Eq. (3)
 x_i element of x
 \hat{x} estimated value of x
 x_t true value of x
 ϵ sum of squares of errors
 ζ_j damping ratio of mode j
 σ measure of experimental variance
 ω angular frequency
 ω_j frequency of mode j

Superscripts

$*$ complex conjugate
 T matrix transpose

REFERENCES

- 1 M. Rades, "Methods for the Analysis of Structural Frequency Response Measurement Data," Shock Vib. Dig. 8 (2), pp 73-88, Feb. 1976
- 2 R.K. Otnes, L. Enochson, Digital Time Series Analysis. Wiley, New York, 1972
- 3 G. Haidl, M. Steiniger, "Excitation and Analysis Technique for Flight Flutter Tests," AGARD 47th SMP Meeting, Athens, September 1978
- 4 R.E.D. Bishop, I. Fawzy, "On the Dynamics of Linear Non-Conservative Systems," Proc. Roy. Soc. Lond. A 352, pp 25-40, 1976
- 5 C.K. Sanathanan, J. Koerner, "Transfer Function Synthesis as a Ratio of Two Complex Polynomials," IEEE Transactions on Automatic Control, 8, pp 56-58, 1963
- 6 M.G. Kendall, The Advanced Theory of Statistics Volume 2. Griffin, London, 1968
- 7 D.R. Gaukroger, C.W. Skingle and K.H. Heron, "Numerical Analysis of Vector Response Loci," JSVR, 29 (3), pp 341-353, 1973

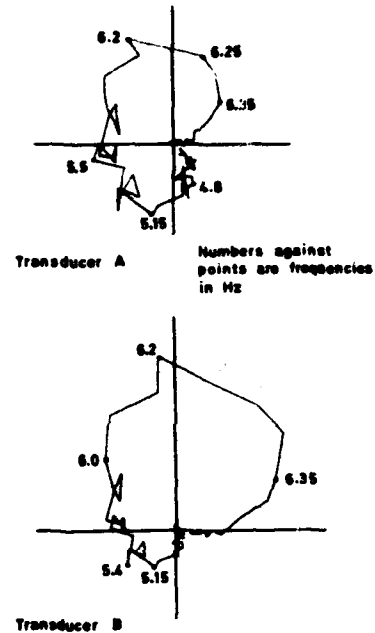


Fig 3 Transfer function measurements for high speed model $Q = 0.800F$

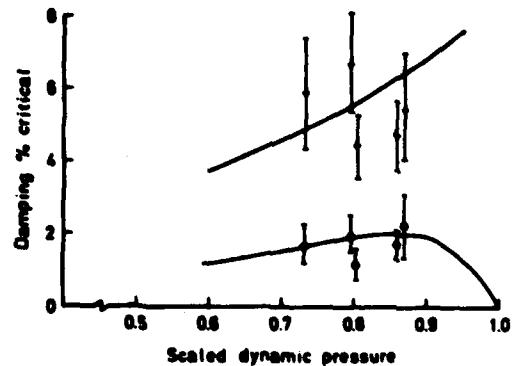
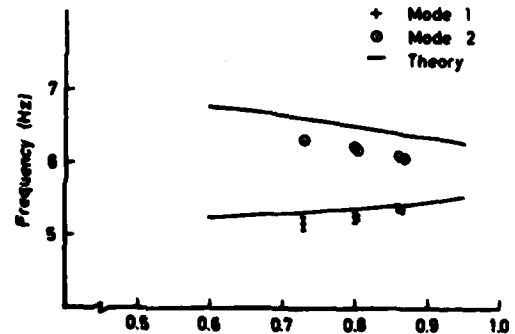


Fig 4 Subcritical frequencies and dampings for high speed model

TABLE 1
Standard Deviation Estimates for Measurements on Low Speed Model

Mode		Mean	Standard Deviation		Failure Count
			Measurement	Prediction	
1	Frequency (Hz)	5.24	0.0730	0.0795	5
	Damping (% critical)	24.8	1.66	1.48	10
2	Frequency	7.20	0.0099	0.0097	11
	Damping	3.41	0.127	0.133	4

AIRCRAFT RESPONSE TO OPERATIONS ON RAPIDLY REPAIRED
BATTLE DAMAGED RUNWAYS AND TAXIWAYS

Tony G Gerardi, Aerospace Engineer for the Structures and Dynamics
Division, Air Force Wright Aeronautical Laboratories
at Wright-Patterson Air Force Base OH

and

Lapsley R Caldwell, Lt Col, HAVE BOUNCE Project Manager, Air Force
Engineering Services Center at Tyndall AFB FL

In a theater of war, airbases will be prime targets of attack. In order to launch and recover our aircraft in retaliation, rapid repair of damaged surfaces is required. Current Air Force Requirements (AFM 93-2) call for the repair of a 15.24m x 1524m (50 x 5000 ft) Minimum Operating Strip (MOS) within four hours after the attack. These rapid repairs will be made using aluminum AM-2 mats and will result in a surface that is rougher than normal and consequently higher than normal loads will be induced into the aircraft. The question of how much surface roughness can a given aircraft configuration tolerate, arises. To answer that question, Air Force project HAVE BOUNCE was born. The goals of project HAVE BOUNCE are to determine the ground loads capabilities of each aircraft. The planned approach for reaching these goals is through computer simulation, flight testing, and subsequent repair criteria development. The objective of this paper is to summarize the Rapid Runway Repair/aircraft response effort.

INTRODUCTION

In a theater of war, airbases will be prime targets of attack. In the European theater, threat analysts suggest very extensive damage to runways, taxiways, command posts, choke points and other important targets. As illustrated in Figure 1, hundreds of craters resulting from general purpose bombs, cannon and rocket fire damage, delayed fuse bombs above and below the surface, live anti-personnel weapons littered on the surface and other special runway denial weapons can be expected during an attack. In order to launch and recover our aircraft in retaliation, rapid runway repair teams must construct a Minimum Operating Strip (MOS).

Before the repairs can begin, however, damage assessments must be made, the unexploded ordnance must be removed, a command post must be set up and a site for the MOS must be selected. This is all part of the Air Force's Rapid Runway Repair (RRR) Program which is a subset of a Base Recovery After Attack (BRAAT) Plan.

Current Air Force requirements (Reference 1) call for the repair of a 15.24m x 1524m (50 x 5000 ft) MOS using aluminum AM-2 mats. The repaired surface will result in a runway that is rougher than normal and consequently

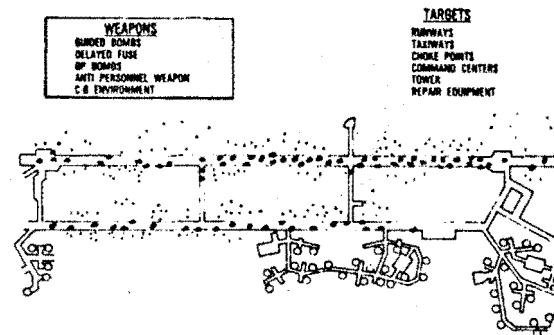


Fig. 1 - Airfield After An Attack

higher than normal loads will be induced into the aircraft. The question arises as to how much surface roughness can a given aircraft configuration tolerate. To answer that question, Air Force project HAVE BOUNCE was born.

HAVE BOUNCE is a subset of the Rapid Runway Repair Program and its objective is to establish runway repair "smoothness" requirements. Figure 2 typifies an AM-2 mat bomb crater

repair. After backfilling with debris, select fill material is compacted in the last .3048m (12 inches) of the repair. Finally, the AM-2 mat, which is assembled off the runway, is towed into place and anchored to the runway with bolts on the leading and trailing edge ramps. A full size AM-2 mat is 23.77m (78 ft) x 16.46m (54 ft) x 3.8cm (1.5 inches) high. The leading and trailing edge ramps are 99. cm (45 inches) long. Notice that some upheaved pavement will remain and that crater settling will occur compounding the roughness problem. Other types of repairs, such as crushed stone with membrane covers are also being considered.

REPAIRED BOMB CRATER

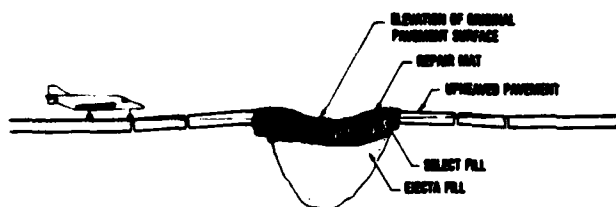


Fig. 2 - Cross Section of Repaired Crater

The objective of this paper is to describe the approach being taken in HAVE BOUNCE, present the status and plans for the future and to solicit fresh ideas relating to the problem from the shock and vibration community.

APPROACH TO HAVE BOUNCE

The goals of project HAVE BOUNCE are to determine the ground roughness capability of most aircraft currently in the USAF inventory and to establish surface "smoothness" repair requirements based on those aircraft capabilities. The planned approach for reaching these goals is through computer simulation, flight testing, and subsequent development of repair criteria.

SIMULATIONS: Unvalidated or partially validated computer programs mathematically describing the dynamic response of an aircraft traversing rough surface profiles are used to identify potentially unsafe test conditions. In addition, these models limit the testing by eliminating unnecessary (low response) tests. Finally, they are used to identify suspected critical aircraft structures.

FLIGHT TESTS: Armed with the knowledge of where and how to instrument the aircraft and an established matrix of test conditions, a fully instrumented aircraft is used to validate the mathematical model. In addition, testing provides for a dynamic demonstration of aircraft

capabilities in the ground environment.

REPAIR CRITERIA: Using the fully validated computer program, surface repair criteria can be established and distributed to the RRR crews in the operational commands. The repair criteria will be designed to provide maximum repair speed and flexibility.

SIMULATIONS

Mathematical modeling of aircraft during ground operations is not new. These models vary in complexity from simple linear single degree of freedom systems to very complex, flexible models incorporating all of the tire and strut non-linearities. Reference 2 from the 47th Shock and Vibration bulletin contains a mathematical model developed at the Air Force Wright Aeronautical Laboratories. Figure 3 is the free body diagram used to develop that mathematical model. This computer program known as TAXI is one of those being used in the HAVE BOUNCE program.

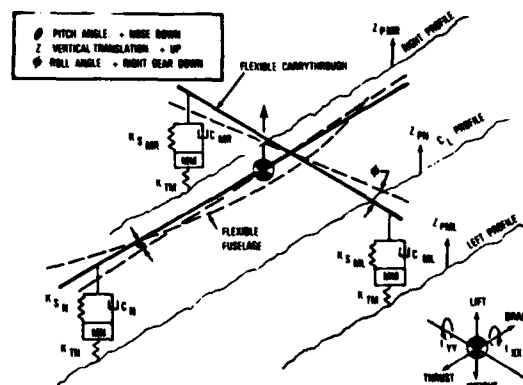


Fig. 3 - Simulation Mathematical Model

F-4E TEST EFFORTS

Most of the work done so far has been on the F-4 aircraft. Beginning in 1977, a simulation study by the Boeing Company (Reference 3), indicated that the F-4 aircraft could exceed certain structural limits when traversing AM-2 mat repairs. Multiple bomb damage repairs in particular could produce excessive loads when traversed at speeds that tune the bump wavelengths to the aircraft's natural frequencies.

The results of this study generated a great deal of interest in the operational commands USAF, TAC, etc. This interest led to more computer simulations and finally to two F-4E test programs. The first test program (Phase I) completed in 1978, (Reference 4) verified that excessive loads could be induced into the aircraft as predicted. In addition, Phase I tests verified that certain changes in strut servicing could dramatically improve the F-4's ability to traverse rough surfaces.

Figure 4 shows a time history of measured vertical load for the left main landing gear for standard and modified strut servicing.

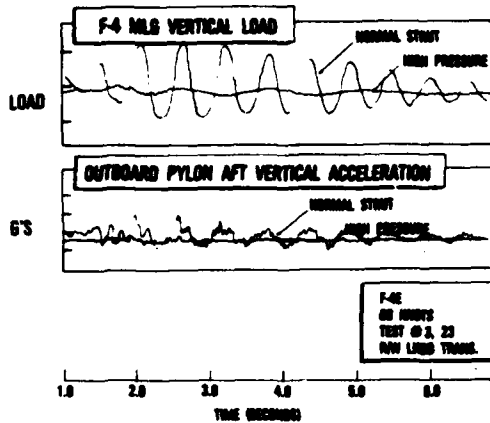


Fig. 4 - Comparison of Measured Response for the Standard and High Pressure Strut Servicing

By increasing the main landing gear upper chamber precharge pressure, the F-4's tolerance to rough runways is dramatically improved. The F-4 main landing gear (MLG) was designed for high sink speed aircraft carrier landings, not for taxiing. These two design conditions work in opposition to each other. When taxiing, the F-4 MLG strut has only 1.27cm (.5 inch) of stroke remaining which results in a very stiff suspension with little energy absorbing capability. By servicing the upper chamber of the strut with higher pressure so that 7.62cm (3 inch) of stroke remains, the aircraft is suspended on a much higher (softer) portion of the load stroke curve as shown in Figure 5. This increase in pressure lowered the F-4's heave (vertical translation) frequency from 1.9 to .9 Hz.

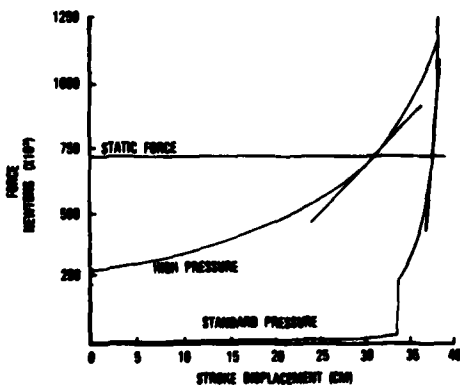


Fig. 5 - F-4 Main Landing Gear Load Stroke Curve

Phase II testing of the F-4E (Reference 5 and 6) was completed in 1980. Using more soph-

isticated instrumentation in Phase II, dynamic response of aircraft components such as external stores was measured. Simulations (Reference 7) predicted that high loads would be measured on the outboard pylon carrying either fuel or bombs. Figure 6 shows that for all speed ranges pylon loads were well under those predicted. There is still uncertainty as to why the external store predictions were incorrect, but improper representation of pylon preload is suspected. Computer predicted vertical loads for the landing gear compared favorably to measured values. Figure 7 is a plot showing peak main landing gear vertical loads, predicted curves and measured data (dots and squares), for the full ground roll speed range of the F-4E.

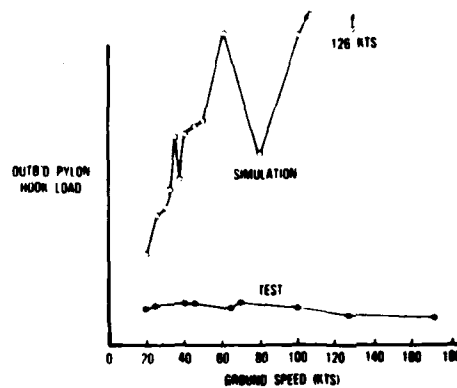


Fig. 6 - Pylon Loads, Predicted and Measured

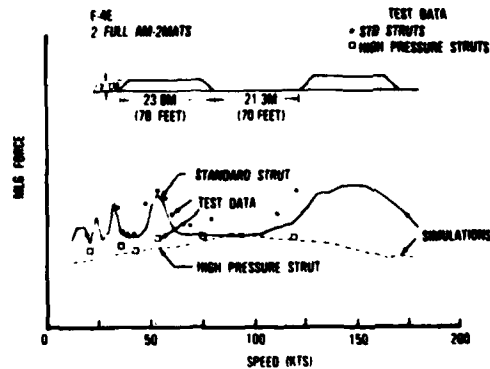


Fig. 7 - Measured vs Predicted Main Landing Gear

A great deal was learned with the extensive F-4E testing and simulation efforts:

1. Rough runway repairs can induce excessive loads in the F-4 aircraft.
2. Simulations can accurately predict F-4 rigid body response.
3. Strut servicing changes can improve the F-4's rough surface operational capability.

4. Current simulations did not predict F-4E pylon response accurately.

OTHER TEST EFFORTS

The C-141B and C-130K aircraft have also undergone HAVE BOUNCE testing. Both aircraft show a greater tolerance to operation on rough surfaces than the F-4. Unlike the F-4, the nose landing gear (NLG) vertical load was the parameter that was most critical for these aircraft. Both the C-141B and the C-130K responded primarily in pitch rather than heave and therefore, NLG loads were of concern under resonant conditions. In addition, the large pitching moment caused by hard braking, as during landing rollout, will result in high NLG loads, which when coupled with a repair mat encounter can cause excessive NLG loads. The braking condition is difficult to simulate because of anti-skid and pilot inputs. The approach taken has been to assume a constant hard brakes application. It is conceivable that the pilot would attempt to control the pitching during landing impact by proper brake applications.

Results indicate that significant engine pylon motion occurred during some of the C-141B testing and some relatively high response was measured on the C-130 wing. This was expected for these more flexible aircraft structures. Plots of predicted and measured values for the rigid body and flexible responses of the C-141B and C-130K aircraft are shown in Figures 8 through 11. Figure 8 is a plot of peak NLG load versus velocity for the C-141B traversing two full length AM-2 mats spaced 21.3m apart. The predicted values were acceptable below 80 knots, but above 80 knots test data shows that NLG peak loads barely exceed static value. Figure 9 shows the engine pylon response for the same test conditions. Here braking tests produced pylon responses well in excess of those predicted particularly at 57 knots. The C-141B simulation program will be modified based on test results so that more accurate predictions can be made.

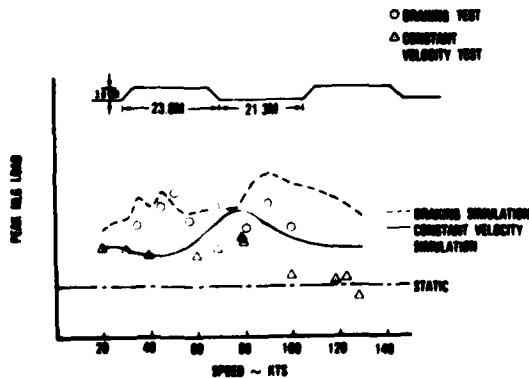


Fig. 8 - C-141B Nose Landing Gear Peak Loads

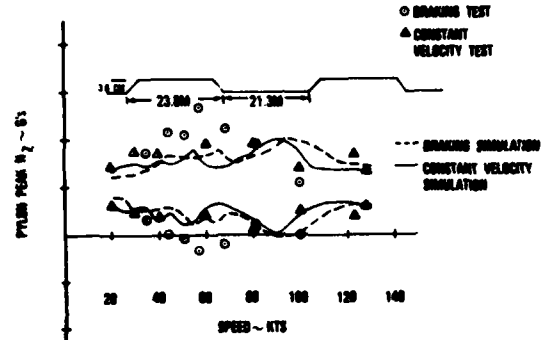


Fig. 9 - C-141B Engine Pylon Peak Vertical Response

The C-130K simulations were more accurate as can be seen in Figure 10 and 11 where simulated (dotted) and test (solid) time histories are compared for the NLG vertical load and wing root vertical acceleration respectively. Peak values are within a few percent.

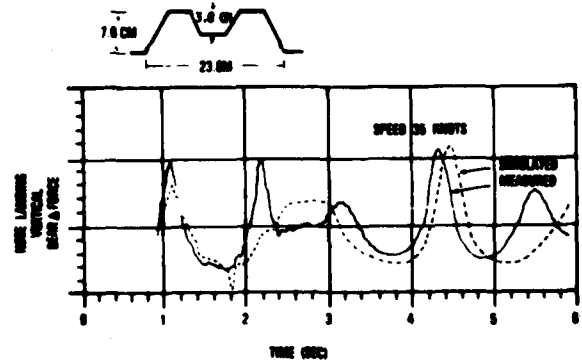


Fig. 10 - Measured and Simulated C-130K Nose Landing Gear Loads

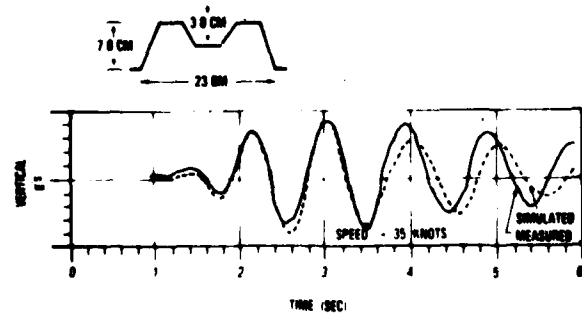


Fig. 11 - Measured and Simulated C-130K Wing Root Response

RAPID RUNWAY REPAIR (RRR) CRITERIA

Based on the test results and thousands of simulations using F-4 computer programs, interim rapid runway repair criteria (Reference 8) was prepared and delivered to the operational commands for the F-4E aircraft. Repair criteria for the C-141B and C-130K have not been generated at this time.

The F-4E repair criteria were designed to give repair crews maximum flexibility in an effort to reduce repair time to a minimum and as a result, these criteria are somewhat complex.

The basis for the repair criteria is de-tuning the F-4E to the bumps. Knowing the aircraft's speed versus distance down the runway for a takeoff roll, certain limitations can be established. Figure 12 is a plot of an F-4's speed versus distance down the MOS. The repair quality and multiple repair spacing requirements depend on where they are located on the MOS.

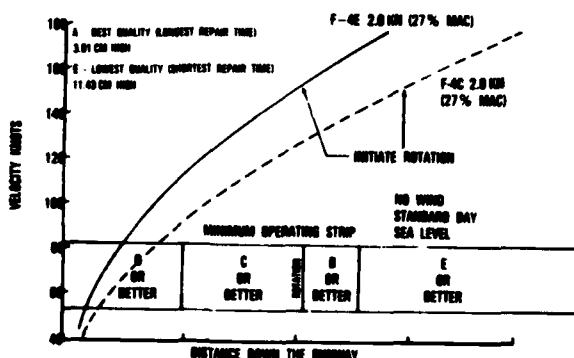


Fig. 12 - F-4/MOS Repair Criteria

Repair quality ranges from an "A" where no upheaval or settling are permitted to "E" where 7.6cm of settling (sag) and upheaval are permitted. The mat height will add another 3.8cm. For the F-4E sample shown in Figure 12, in the first runway section sag in a full length repair would act as a second bump encounter and therefore resonance could cause excessive loads. Beyond the initial section, the aircraft's speed and frequency of response will allow the aircraft to "fly" over the sag, therefore a "C" (3.8cm high with sag permitted) quality repair is sufficient.

During the period where rotation is initiated and until a full 12° angle of attack is achieved, lift is building fast. As the struts are being unloaded, the aircraft becomes more and more tolerant to runway roughness thus permitting rougher ("D" or better in Figure 12) and consequently faster bomb crater repairs.

The spacing between repairs was based on a four second "time to damp" criteria. Test data show that four seconds after an initial bump encounter sufficient damping takes place that a second bump encounter can be treated as a single bump.

Since this repair guidance is based on the speed of the aircraft as it traverses the MOS; density ratio, wind, aircraft gross weight and center of gravity will affect the repair procedures. In fact, as shown in Figure 12, the MOS applies only to the F-4E aircraft.

This interim runway repair criteria, which was delivered to the operational commands is tailored to specific conditions, it is complex and somewhat conservative. It was designed to provide the officer in charge with MOS selection criteria and the repair crews with maximum flexibility so that an acceptable MOS can be constructed in a minimum length of time.

One of the major stumbling blocks associated with the HAVE BOUNCE Project is the transformation of predicted aircraft dynamic response into runway repair criteria. Considering that many different aircraft types and configurations will operate from a variety of runway repair shapes and sizes, establishing repair criteria for a MOS that is acceptable to all of these variations is increasingly difficult. One purpose of this paper is to solicit fresh ideas from the shock and vibration community on how to present MOS selection criteria and repair procedures to the operational commands.

NATO INVOLVEMENT

The RRR problem is in reality a NATO problem. Following an attack, aircraft from many nations will be operating on various types of repaired surfaces. The British use aluminum class-60 repair mats, the Federal Republic of Germany (FRG) uses the U.S. built AM-2 mats, etc. It becomes evident with the large aircraft/repair matrix, that an "international" roughness criteria needs to be established

This subject was addressed at the Advisory Group for Aerospace Research and Development (AGARD) specialists meeting in Williamsburg, Virginia in the Spring of 1979 and in Cologne, Germany in the Fall of 1979. The enthusiastic response from all nations represented has led to two AGARD specialists meetings on the subject. In the Spring of 1981, a half-day "precursor" meeting which highlights the runway/airfield aspects of the problem is planned to be held in Turkey. A full two-day meeting in the Spring of 1982 which will complete the treatment of runway/airfield aspects and add considerations of: landing gear, structural and dynamic analysis and testing, ground and flight operations, and design criteria. The Spring 1982 meeting is planned to be held in Portugal. AGARD's intent is to provide a clearinghouse of information on the subject, bring the experts together and help define

solutions to the runway denial problem within NATO.

ROUGH RUNWAY TEST FACILITY

The Air Force Wright Aeronautical Laboratories is considering the development of a large facility (Figure 13) capable of simulating an aircraft traversing a rough surface. The project called Aircraft Ground Induced Loads Excitation (AGILE), will consist of large computer controlled hydraulic shakers capable of inputting large amplitude, multiple bumps into each landing gear of an instrumented aircraft. AGILE could not completely replace flight testing, but could significantly reduce it as well as add some capabilities that are unattainable from flight testing.

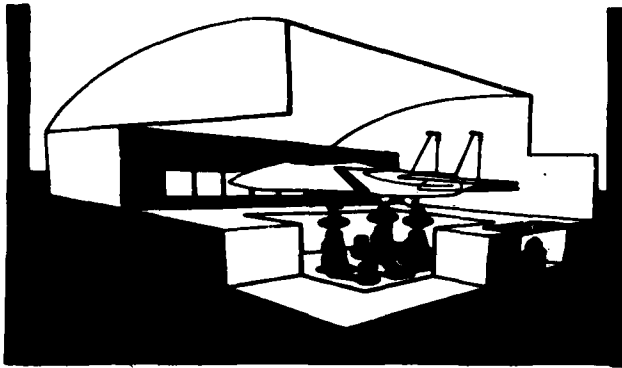


Fig. 13 - Aircraft Ground Induced Loads Excitation (AGILE) Facility

SUMMARY

In summary, the Surface Roughness Portion of the BRAAT problem carries a high U.S. Air Force priority and has stimulated interest within NATO.

The approach of using flight test validated computer programs to generate rapid runway repair criteria has proven to be acceptable, although alternate methods of presenting that criteria to the repair crews are being sought.

Planning is underway to evaluate most aircraft in the U.S. inventory with emphasis on the tactical aircraft (F-15, F-16, A-10, etc). Testing on the F-15 is scheduled to begin in the Summer of 1981.

REFERENCES

1. "Disaster Preparedness and Base Recovery Planning", Department of the Air Force, Washington D.C., AFR 93-2, July 1974
2. Shock and Vibration Paper, "Digital Simulation of Flexible Aircraft Response To Symmetrical and Asymmetrical Runway Roughness", Gerardi, Tony G, Wright-Patterson Air Force Base OH, September 1977
3. "Roughness Criteria for Bomb Damage Repair of Airfield Pavements", Kilner, J R, Boeing Commercial Airplane Company, Seattle WA, Report CEEDO-TR-77-50, February 1980
4. "HAVE BOUNCE Phase I Test Results", Redd, L T, and Borowski, R A, Major, Edwards Air Force Base, California, AFFTC-TR-79-1, 6510 Test Wing, California, April 1979.
5. "HAVE BOUNCE Phase II Test Results", Edwards Air Force Base, AFFTC-TR-80-4, David C Lensi, Captain and Borowski, Richard A, Major, June 1980, Final Report
6. "HAVE BOUNCE Phase II Test Results Spall Tests", Edwards Air Force Base, AFFTC-TR-80-4, Redd, L Tracy, September 1980, Final Report
7. "Digital Computer Program for the Prediction of Taxi Induced Aircraft Dynamic Loads", Boeing Military Airplane Development, FO8635-76-C-0102, July 1979
8. "Interim Guidance For Surface Roughness Criteria", Caldwell, Lapsley R, Lt Col, and Jacobson, Frederick J, 2Lt, ESL-TR-79-37, October 1979

DISCUSSION

Mr. Seville (Structural Dynamics Research Corp.): Is it just the noise gear loads that establish the limits for the aircraft? Or is it perhaps ride quality or the ability of the pilot to see?

Mr. Gerardi: It is going to be dependent on the aircraft. For F-4 it was the main landing gear that was responsible. In the C-130 and the C-141 the noise gear was the problem. We've also other considerations for example in the C-130, we had some fairly high wing root loads. Also, pylons and stores are things that have to be looked at. So it is not just one item.

A METHOD FOR DETERMINING THE EFFECT OF TRANSPORTATION

VIBRATION ON UNITIZED CORRUGATED CONTAINERS

Thomas J. Urbanik, Engineer
Forest Products Laboratory,* Forest Service
U.S. Department of Agriculture

A unitized stack of containers in transit is susceptible to dynamic overloading due to vibrations in the transporting vehicle. The boxes' compressive stiffnesses interact with the content masses to amplify or attenuate the vehicle motions through the height of the column. Modeling a unit load as a multiple-degree-of-freedom vibration system provides a method for evaluating it based on its sensitivity to the frequencies inherent to the transportation environment. This report presents the theoretical analysis of the analog that represents a stack of containers and an example that carries the mathematics through a package design problem. To supplement the manual computations which are too time-consuming for practical packaging design, a computer program--not included herein--is discussed. This program plots the transmissibility in each container over a range in frequencies. An example using the program shows how to interpret the plots and compare the effects of transportation vibration on different unit loads.

ABBREVIATIONS USED

CPS = cycles per second
G = gravities
Hz = hertz
kN = kilonewton
kN/m = kilonewtons per meter
kN·s/m = kilonewtons x seconds per meter
lbf = pounds-force
lbf/in. = pounds-force per inch
LBF SEC/IN. = pounds-force x seconds per inch
LBM = pounds-mass
Mg = megagram
mm = millimeter
 m/s^2 = meters per second squared
N = newton
s = seconds

INTRODUCTION

Shipments of like packages have come increasingly to be unitized for reasons of economy. Mechanically arranging and stacking containers on a single pallet or other platform offers the advantages of mechanized transfer and storage with protection from the hazards of manual handling. Thus, effective methods of packaging can be used which do not require dealing with the levels of shock typical with

manual handling. The unit arrangement, although reducing the potential for shock damage, requires greater consideration of the damage which might be caused by vibration.

Even where dropping or impacting a package does not occur, the product is still exposed to transit vehicle vibrations enroute between the manufacturer and recipient. And this most probable source of damage becomes an environment over which the package designer has little control; his option is to design vibration protection into the package system.

Shocks and impacts acting on single packages in simulated small parcel shipping environments have been well analyzed in numerous reports [5]. Some studies [3,4] have also examined the damage susceptibility of corrugated shipping containers due to vibrations. But all these publications, although accurate documentation of the pertinent vibration theory, were still aimed at the single package environment and are limited to a single-degree-of-freedom analysis.

Where quantities of similar packages are shipped as a unitized lot, a new approach to the vibration analysis is required. The vibration theory developed for the single parcel environment may grossly underestimate the severity of acceleration levels in a unitized load. For example, the dynamics in a stack of containers ten high on a pallet may approach a modeled ten-degree-of-freedom system with ten

*Maintained at Madison, Wis., in cooperation with the University of Wisconsin.

critical frequencies, each being potentially damaging.

Because corrugated boxes compress due to their contained weights, they act like springs and the resulting stack natural frequencies may fall within the range of the transportation environment [3]. The weight of the product supported by the resilient container behaves like an analogous spring-mass system to amplify or attenuate the vibratory motion delivered to its base. It is thus reasonable to evaluate the effectiveness of a unit load based on how well it protects both the product and the container from transportation vibration damage. For instance often a product's component sub-assemblies will necessitate avoiding acceleration levels within certain frequency bands. Or frictional holding forces must be maintained to insure protection from load disarrangement and subsequent stack toppling and product impact damage. Also, the lower containers may require protection from dynamic crushing.

This report was thus written to demonstrate for package engineers how to apply the fundamental theory for analyzing vibration forces in a unitized load. It deals with the most common shipping container, a corrugated fiberboard box, and shows how to evaluate a unit load of boxes for protection against vibration damage. In essence, it presents a theoretical method for predicting the critical frequencies of a unit load, the maximum acceleration level, and the dynamic compression of the bottom boxes.

To do this, this report uses the results obtained by Godshall in the investigation of the effects of vibration on single boxes [3] and extends them to a stack of boxes. It considers the stacking configuration where boxes on a rigid pallet are vertically stacked with their corners alined, and the box, not the product, supports the load. It next uses the theory in a computer program for plotting the containers' responses to vibration. Graphs produced via this program show how the damage susceptibility of a unit load changes when properties of box compression resistance, corrugated damping characteristics, weight per box, and stack height are changed.

I. DESIGN CONSIDERATION

The hazards of transportation frequently reveal themselves with toppled stacks and crushed containers. Sometimes the damage is concealed until the packaged product is put into service. Given enough resources a shipper can make trial and error adjustments to the package system until an effective method of unitizing is determined. But analysis rather than trial and error would improve efficiency. Solving a typical problem shows how the results obtained from an analysis can be used to evaluate the effectiveness of a unit load. The

appendix carries the problem through the detailed mathematics; only the results are presented here.

A manufacturer finds his containers totally disarrayed when unitized and shipped via a particular carrier. The transportation environment is monitored and he learns that a significant input occurs at 0.25 G acceleration at 5 Hz. Before adopting a new design and suggested antiskid treatment, he requests an analysis to learn if the new approach will indeed solve the problem.

The new design calls for vertically alined boxes stacked four high on a pallet with each box containing a rigid, fixed, nonload-supporting content W weighing 246 N (55.3 lbf) and an antiskid treatment applied to the top and bottom flaps of each box. All boxes are identically constructed, and from cyclic top-to-bottom compression tests on similar boxes the box stiffnesses are estimated relative to their equilibrium supporting loads. Also, from vibration test observations it is estimated that the box material contributes about 30 percent of critical damping. To analyze the unit load, first the contents are characterized by lumped masses and the boxes, by spring and damping elements. The pallet in this case is effectively rigid compared to the stiffness of the boxes. Thus, the four high stack (fig. 1) is represented by a 3 degree of freedom model where the weight in the bottom box and the stiffness of the top box do not affect the stack.

Then using the cyclic compression test procedure given by Godshall in (3) the container stiffnesses are linearized from the compression curves at

$$K_1 = 135 \text{ kN/m (771 lbf/in.)}$$

$$K_2 = 106 \text{ kN/m (607 lbf/in.)}$$

$$K_3 = 87.6 \text{ kN/m (500 lbf/in.)}$$

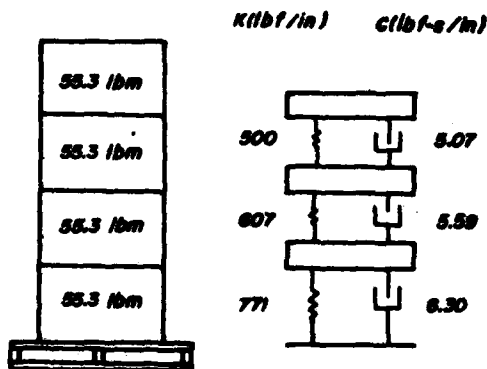
These values and the weights of the contents are used to predict the natural frequencies of the system.

$$f_1 = 4.84 \text{ Hz}$$

$$f_2 = 12.7 \text{ Hz}$$

$$f_3 = 18.5 \text{ Hz}$$

The excitation frequency at 5 Hz is close to the first natural frequency of the box stack.



N 146 029

Figure 1.--Schematic diagram of a four-high stack arrangement, showing the relationship between a column of boxes and the vibration model.

(N 146 029)

The analysis is therefore continued to determine if the damping adequately reduces the stack response to the 5 Hz vibration. A solution to the equations of motion with damping considered gives the acceleration level in each container.

$$\ddot{x}_1 = 4.46e^{j(31.4t-1.168)} \text{ m/s}^2 = 0.46 \text{ G cos } (31.4t-1.168)$$

$$\ddot{x}_2 = 8.37e^{j(31.4t-1.501)} \text{ m/s}^2 = 0.85 \text{ G cos } (31.4t-1.501)$$

$$\ddot{x}_3 = 11.0e^{j(31.4t-1.609)} \text{ m/s}^2 = 1.13 \text{ G cos } (31.4t-1.609)$$

The response in the top box exceeds 1.0 G in acceleration and bouncing would occur, thus making the antiskid treatment ineffective. The design must either be altered, or more effective but costly methods of unitizing be employed.

One can also determine if any box has been loaded beyond its maximum compression strength by examining the compressing load F on a box due to dynamic compression plus the equilibrium

supporting weight. With knowledge of the relative displacements, \bar{D} , between adjacent containers

$$F_1 = K_1 \bar{D}_1 + 3W = 1307 \text{ N (293.9 lbf)}$$

$$F_2 = K_2 \bar{D}_2 + 2W = 966.2 \text{ N (217.2 lbf)}$$

$$F_3 = K_3 \bar{D}_3 + W = 501.3 \text{ N (112.7 lbf)}$$

If no force exceeds the load-carrying capacity for the respective container, the design is not likely to fail from dynamic compression overloading.

II. COMPUTER PROGRAM FOR EVALUATING UNITIZED LOADS

One can examine the response in a container stack by repeatedly solving the equations of motion at different frequencies. However, it can be more useful for design purposes to observe how the response of the unit load changes as one or more of the parameters vary. Computer-plotted graphs can show varying levels of product damage susceptibility across a range of packaging options--for instance, with containers differing in mechanical properties and contained weights. Vibrational analysis computer programs like those commercially available [6] are usually written to deal with general problems beyond the present need so as to have broad spectrums of adaptability. For this reason, we have developed a specialized program for the multiple-degree-of-freedom analysis described in this paper. (Due to limitations of space, our program is not reproduced in this article, but may be requested from the author along with all necessary definitions and subroutines.) The following discussion illustrates the utility of our program and may suggest the benefits to be derived from this and similar computer programs.

To illustrate the computer program in a quantitative comparison, consider again an example where a package designer desires to weigh the advantages between two palletized loads for protection against a 5-Hz input at 0.25 G acceleration. The situation is similar to that in the previous example--that is, four vertically aligned boxes, each containing 246 N (55.3 lbf). Another alternative is to package the product in stronger, larger boxes able to contain 328 N (73.7 lbf), but vertically aligned in a three-high stack. Therefore, the pallet's loaded weight is conserved although the product is packaged and unitized differently.

The designer tests the two box types in top-to-bottom compression to establish their stiffnesses relative to their equilibrium supporting loads, as suggested by Godshall [3];

figure 2 illustrates the results. On the three-tier pallet, the boxes support 328 N (73.7 lbf) at the second layer and 656 N (147.4 lbf) at the bottom layer. Tangents drawn to the solid line curve in figure 2 at these ordinate values suggest relative stiffnesses of 117 (666) and 142 kN/m (810 lbf/in.). For the boxes on the four-tier pallet supporting 246 (55.3), 492 (110.6), and 738 N (165.9 lbf) from top to bottom, their stiffnesses may be similarly assumed from the dashed line curve in figure 2 to be 87.6 (500), 106 (607), and 135 kN/m (771 lbf/in.). Each box is roughly estimated to absorb energy at 0.3 times its critical damping ratio, and the analysis is supplemented with a comparison between 0.1 and 0.7 times the critical damping ratios.

These physical parameters thus define the computer program input and are subsequently organized on cards following two executions.

The plotted output from the two analyses is produced in figures 3 and 4. The damping ratio used in an analysis may be recognized by extending a horizontal line from the last point in a dashed-line curve to intersect the bottom of the characters "DR." Some significant

trends are observed regarding the major amplification and attenuation ranges for the 0.3 critical damping analysis and are summarized in table I.

The potentially damaging frequencies, those amplifying the input by at least two, have broadened from a band of 3.23 to 6.23 Hz for the four-tier pallet to a band of 4.40 to 7.63 Hz for the three-tier pallet. Reducing the stack levels has made the load sensitive to higher frequencies. The attenuation region has also shifted to the higher frequencies for the three-level stack. However, the transmissibilities at the resonant levels are changed. Although the three-high stack is sensitive to a wider frequency range, a greater input magnitude would be necessary to cause damage.

The decision to choose between the two designs would be based on experience with present designs and inferences from this experience regarding anticipated transportation inputs. If the designer feels confident that the 5-Hz vibration is the most prominent, a decision to accept the three-high stack to avoid high-level transmissibilities would be logical.

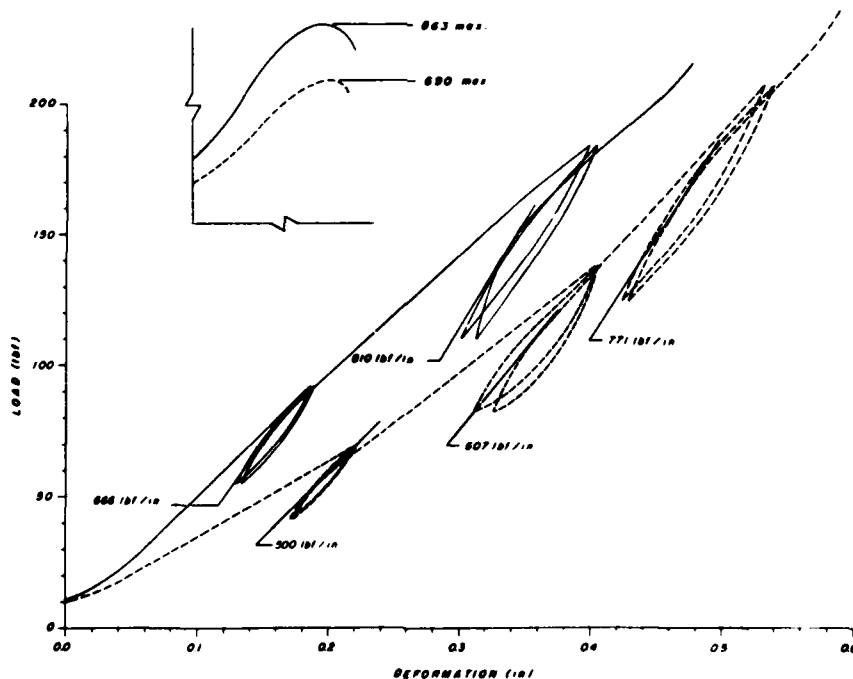


Figure 2.--Top-bottom compression curves for two box types. Solid curve is for a box designed to contain 73.7 pounds in a three-high stack; dashed line is for a box designed to contain 55.3 pounds in a four-high stack.

(M 146 134)

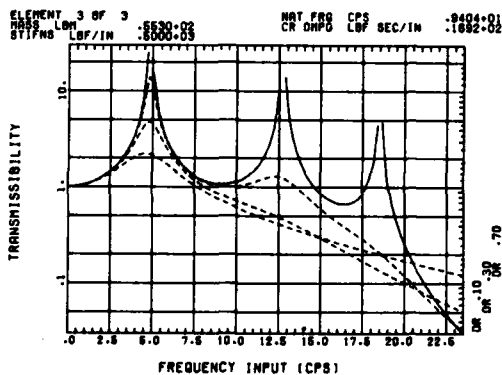
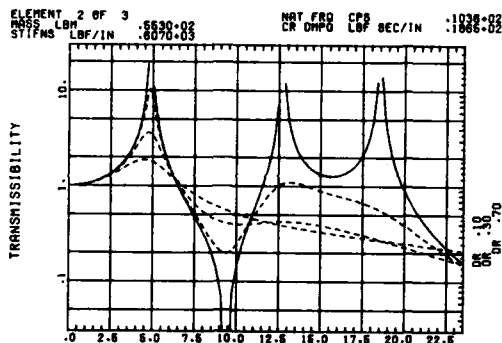
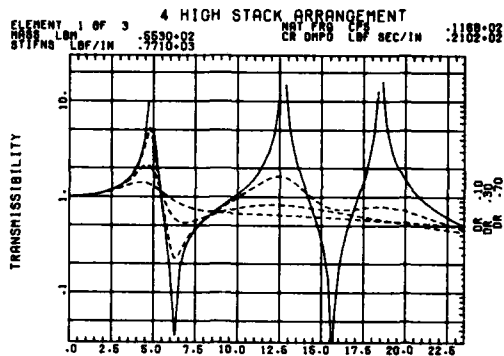


Figure 3.--Vibrational analysis of a four-high stack arrangement using three containers with different stiffness values and equal masses. (Actual computer plots, but with redundant labels deleted.)

(M 145 684)

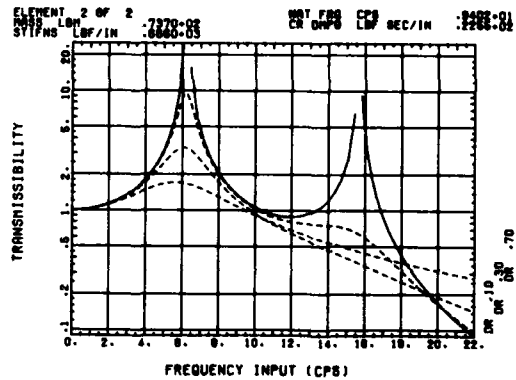
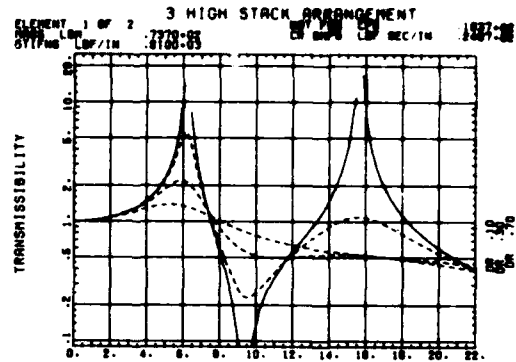


Figure 4.--Vibrational analysis of a three-high stack arrangement using two containers with different stiffness values and equal masses. (Actual computer plots, but with redundant labels deleted.)

(M 145 685)

The significance of damping becomes apparent at the higher frequencies. At these frequencies, damping, which is proportional to the base velocity, dissipates energy at an increasing rate. It can be seen from the plots for all masses that even for a lightly damped system of 0.1 critical, the responses at natural frequencies beyond the first do not even approach the severity of the first resonant response. To the designer this suggests that he may safely abbreviate his analysis by examining only the first natural frequency.

Further analyses can be performed by determining if the bottom containers can withstand the dynamic compression-loading condition. The user may do this by adjusting certain subroutines in the computer program to generate the relative transmissibilities between adjacent masses. The plotted output would then be interpreted as the factors by

Table I.--Summary of 0.3 critical damping analysis (figures 3 and 4)

Stack height	Element No.	Amplification, transmissibility ≥ 2	Attenuation, transmissibility ≤ 1	Maximum transmissibility
		Hz	Hz	
3 boxes	1	5.23-6.46	7.73	2.20
3 boxes	2	4.40-7.63	9.80	3.32
4 boxes	1	4.26-4.90	5.59	2.15
4 boxes	2	3.58-5.64	6.61	3.63
4 boxes	3	3.23-6.23	8.23	4.72

which to multiply a displacement input magnitude to obtain container compressions.

The dynamic compression loading value can be conservatively determined by considering the limiting case of relative displacement between the base and mass one. Adding this to the statically supporting weight gives the maximum force experienced by the bottom box. For an input magnitude \bar{Y} in G's at a frequency f in Hz, and a bottom container stiffness K_1 in kN/m the critical load CL can be determined from the transmissibility in the bottom mass Tr_1 .

$$CL = \frac{9807 K_1 \bar{Y} (Tr_1 + 1)}{(2\pi f)^2} + \Sigma W$$

If this value is greater than the load-carrying capacity of the bottom box, it will obviously cause failure and the design would be rejected.

For the four-high stack example, the transmissibility at 5 Hz and 0.3 critical damping is 1.82. Thus the critical load is

$$CL = \frac{9807 \cdot 135 \cdot 0.25 (1.82 + 1)}{(2 \cdot \pi \cdot 5)^2} + 738 = 946 + 738 = 1684 \text{ N (378.1 lbf)}$$

This compares safely with the exact value of 1307 N (293.9 lbf) determined in the previous example. Because the maximum compressive strength of this box (fig. 2) is at least 3069 N (690 lbf), the critical load of 1684 N (378.1 lbf), is well below the failure level.

III. MULTIPLE-DEGREE-OF-FREEDOM VIBRATION THEORY

A mechanical structure may often be modeled as a multiple-degree-of-freedom system of lumped masses with adjacent linear couplings. The solution to the system becomes an expression for the displacement of each element relative to time t in terms of some known input. For the dynamic system shown in figure 5, the input is a base displacement with a harmonic motion of a constant amplitude Y at the frequency ω .

$$Y = \bar{Y} \cos(\omega t) \quad (1)$$

The analysis will consider only the steady state response that occurs after the input has been applied long enough for the transients to dissipate. If linear stiffness and viscous damping are assumed, the output at each element i will be a similar harmonic displacement at the same frequency ω with an amplitude \bar{X}_i and phase ϕ_i from the input.

$$X_i = \bar{X}_i \cos(\omega t + \phi_i) \quad (2)$$

For design considerations it is usually desirable to express the solution in terms of the transmissibility Tr_i at each element, where

$$Tr_i = \bar{X}_i / \bar{Y} \quad (3)$$

By differentiating equations (1) and (2) with respect to time, it can be shown that the displacement transmissibility is equal to both the velocity (\dot{X}_i / \dot{Y}) and acceleration (\ddot{X}_i / \ddot{Y}) transmissibilities. Therefore, the response ratios developed from a displacement input define also the response ratios when the input is expressed

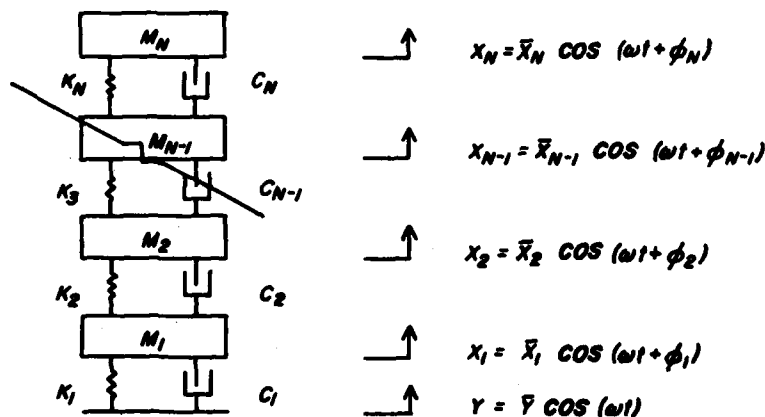


Figure 5.--Schematic diagram of a box stack modeled as a vibration system with N degrees of freedom.

(M 146 030)

in its acceleration mode. The modal shape or pattern may also be of interest. This becomes

$$(\phi_1/\alpha, \phi_2/\alpha, \dots, \phi_N/\alpha)$$

where α is selected to conveniently normalize the series of numbers.

Of primary significance are the natural frequencies of the system. For n degrees of freedom there will be n frequencies where, if damping is neglected, the input would produce an infinite response in each element. Where damping is considered, the system approaches a maximum response near these frequencies and is said to resonate.

The dynamics of the system may be modeled by a series of differential equations expressing the summation of forces existing at each element.

$$M_1 \ddot{X}_1 = K_1(Y - X_1) + C_1(\dot{Y} - \dot{X}_1) - K_2(X_1 - X_2) - C_2(\dot{X}_1 - \dot{X}_2)$$

$$M_i \ddot{X}_i = K_i(X_{i-1} - X_i) + C_i(\dot{X}_{i-1} - \dot{X}_i) - K_{i+1}(X_i - X_{i+1}) - C_{i+1}(\dot{X}_i - \dot{X}_{i+1})$$

$$M_n \ddot{X}_n = K_n(X_{n-1} - X_n) + C_n(\dot{X}_{n-1} - \dot{X}_n)$$

Here, K_i is the resisting force due to a unit compression, C_i is the resisting force due to compressing at a unit velocity, and M_i is the mass lumped at an infinitely small point. Rearranging and collecting terms into a more desirable form produces

$$(K_1 + K_2)X_1 + M_1 \ddot{X}_1 + (C_1 + C_2)\dot{X}_1 - K_2X_2 - C_2\dot{X}_2 = K_1Y + C_1\dot{Y}$$

$$-K_i X_{i-1} - C_i \dot{X}_{i-1} + (K_i + K_{i+1})X_i + M_i \ddot{X}_i + (C_i + C_{i+1})\dot{X}_i$$

$$-K_{i+1}X_{i+1} - C_{i+1}\dot{X}_{i+1} = 0$$

$$-K_n X_{n-1} - C_n \dot{X}_{n-1} + K_n X_n + M_n \ddot{X}_n + C_n \dot{X}_n = 0$$

Expressing the harmonics in the real components of their complex notation equivalents (7) makes the system solution more readily attainable. Accordingly:

$$\begin{aligned}
 Y &= \bar{y} e^{j\omega t} \\
 \dot{Y} &= j\omega \bar{y} e^{j\omega t} \\
 X_i &= \bar{x}_i e^{j(\omega t + \phi_i)} \\
 \dot{X}_i &= j\omega \bar{x}_i e^{j(\omega t + \phi_i)} \\
 \ddot{X}_i &= -\omega^2 \bar{x}_i e^{j(\omega t + \phi_i)}
 \end{aligned}$$

where j denotes the imaginary unit. With these substitutions, the system becomes

$$\begin{aligned}
 & (K_1 + K_2) \bar{x}_1 e^{j(\omega t + \phi_1)} - \omega^2 M_1 \bar{x}_1 e^{j(\omega t + \phi_1)} \\
 & + j\omega(C_1 + C_2) \bar{x}_1 e^{j(\omega t + \phi_1)} - K_2 \bar{x}_2 e^{j(\omega t + \phi_2)} - j\omega C_2 \bar{x}_2 e^{j(\omega t + \phi_2)} \\
 & = K_1 \bar{y} e^{j\omega t} + j\omega C_2 \bar{y} e^{j\omega t} \\
 & - K_1 \bar{x}_{i-1} e^{j(\omega t + \phi_{i-1})} - j\omega C_1 \bar{x}_{i-1} e^{j(\omega t + \phi_{i-1})} \\
 & + (K_i + K_{i+1}) \bar{x}_i e^{j(\omega t + \phi_i)} - \omega^2 M_i \bar{x}_i e^{j(\omega t + \phi_i)} \\
 & + j\omega(C_i + C_{i+1}) \bar{x}_i e^{j(\omega t + \phi_i)} \\
 & - K_{i+1} \bar{x}_{i+1} e^{j(\omega t + \phi_{i+1})} - j\omega C_{i+1} \bar{x}_{i+1} e^{j(\omega t + \phi_{i+1})} = 0 \\
 & - K_n \bar{x}_{n-1} e^{j(\omega t + \phi_{n-1})} - j\omega C_n \bar{x}_{n-1} e^{j(\omega t + \phi_{n-1})} \\
 & + K_n \bar{x}_n e^{j(\omega t + \phi_n)} - \omega^2 M_n \bar{x}_n e^{j(\omega t + \phi_n)} \\
 & + j\omega C_n \bar{x}_n e^{j(\omega t + \phi_n)} = 0
 \end{aligned}$$

Collecting terms again and dividing through each equation by $e^{j\omega t}$ produces the final equation system form.

$$\begin{aligned}
 & [(K_1 + K_2) - \omega^2 M_1 + j\omega(C_1 + C_2)] \bar{x}_1 e^{j\phi_1} - [K_2 + j\omega C_2] \bar{x}_2 e^{j\phi_2} \\
 & = [K_1 + j\omega C_1] Y \\
 & - [K_i + j\omega C_i] \bar{x}_{i-1} e^{j\phi_{i-1}} \\
 & + [(K_i + K_{i+1}) - \omega^2 M_i + j\omega(C_i + C_{i+1})] \bar{x}_i e^{j\phi_i} \\
 & - [K_{i+1} + j\omega C_{i+1}] \bar{x}_{i+1} e^{j\phi_{i+1}} = 0 \\
 & - [K_n + j\omega C_n] \bar{x}_{n-1} e^{j\phi_{n-1}} + [K_n - \omega^2 M_n + j\omega C_n] \bar{x}_n e^{j\phi_n} = 0
 \end{aligned}$$

If this system of equations is expressed in its equivalent matrix notation, matrix algebra may be applied to extract the solution. The component expressions become:

The $(n \times 1)$ output displacement matrix

$$[X] = \begin{bmatrix} \bar{x}_1 e^{j\phi_1} \\ \bar{x}_2 e^{j\phi_2} \\ \vdots \\ \bar{x}_i e^{j\phi_i} \\ \vdots \\ \bar{x}_n e^{j\phi_n} \end{bmatrix}$$

the $(n \times 1)$ input displacement matrix

$$[Y] = \begin{bmatrix} \bar{y} \\ \vdots \\ 0 \end{bmatrix}$$

(4)

the $(n \times n)$ diagonal mass matrix

$$[M] = \begin{bmatrix} M_1 & & & & & \\ & M_2 & & & & \\ & & \ddots & & & \\ & & & M_i & & \\ & & & & \ddots & \\ & & & & & M_n \end{bmatrix} \quad (5)$$

the (n x n) stiffness matrix

$$[K] = \begin{bmatrix} K_1+K_2 & -K_2 & & & & \\ -K_2 & K_2+K_3 & -K_3 & & & \\ & & \ddots & & & \\ & & & -K_{i-1} & K_i+K_{i+1} & -K_{i+1} \\ & & & & \ddots & \\ & & & & & -K_n & K_n \end{bmatrix} \quad (6)$$

and the (n x n) damping matrix

$$[C] = \begin{bmatrix} C_1+C_2 & -C_2 & & & & \\ -C_2 & C_2+C_3 & -C_3 & & & \\ & & \ddots & & & \\ & & & -C_{i-1} & C_i+C_{i+1} & -C_{i+1} \\ & & & & \ddots & \\ & & & & & -C_n & C_n \end{bmatrix} \quad (7)$$

The final mathematical model for the dynamic response of the idealized vibrating system becomes

$$[K] - \omega^2[M] + j\omega[C] [X] = (K_1 + j\omega C_1) [Y] \quad (8)$$

where the system displacement may be expressed as

$$[X] = [K] - \omega^2[M] + j\omega[C]^{-1} (K_1 + j\omega C_1) [Y] \quad (9)$$

Because acceleration transmissibility is equal to displacement transmissibility, an equivalent expression for the acceleration response becomes

$$[\ddot{X}] = [K] - \omega^2[M] + j\omega[C]^{-1} (K_1 + j\omega C_1) [\ddot{Y}] \quad (10)$$

To express the response of each mass in the form of equations (2) and (3), an element from the displacement matrix of equation (9) takes the form

$$\bar{x}_i e^{j\phi_i} = a_i + jb_i$$

where a and b are real numbers. The amplitude is calculated as

$$\bar{x}_i = (a_i^2 + b_i^2)^{1/2}$$

and the phase difference as

$$\phi_i = \tan^{-1} (b_i/a_i)$$

With damping neglected in equation (9), the response becomes infinite when, according to matrix theory (1), the expression

$$[K] - \omega^2[M]$$

is equivalent to the zero-filled matrix. The values of ω that satisfy this condition then become the natural frequencies of the system.

Appendix

The problem presented in the main text can be analyzed once the physical parameters and system input are defined.

The 3 degree of freedom model is subjected to an input of 0.25 G acceleration at 5 Hz. Each element has a weight W of 246 N and it is estimated that the box material contributes about 30 percent of critical damping C_{CR} where

$$C_i CR = 2(M_i K_i)^{1/2}$$

for each model element. The stiffnesses are linearized from the static compression test curves to be

$$K_1 = 135 \text{ kN/m}$$

$$K_2 = 106 \text{ kN/m}$$

$$K_3 = 87.6 \text{ kN/m}$$

The matrices for solution may be set up with appropriate units for compatibility. The mass matrix is

$$M_i = W_i (\text{kN}) / 9.81 (\text{m/s}^2)$$

$$M_1 = M_2 = M_3 = 0.246/9.81$$

$$= 0.0251 \text{ Mg}$$

$$[M] = \begin{bmatrix} 0.0251 & 0 & 0 \\ 0 & 0.0251 & 0 \\ 0 & 0 & 0.0251 \end{bmatrix}$$

The stiffness matrix is

$$[K] = \begin{bmatrix} 241 & -106 & 0 \\ -106 & 194 & -87.6 \\ 0 & -87.6 & 87.6 \end{bmatrix}$$

The damping matrix is

$$C_1 = 0.3 \times 2(0.0251 \text{ Mg} \times 135 \text{ kN/m})^{1/2}$$

$$= 1.10 \text{ kN} \cdot \text{s/m}$$

$$C_2 = 0.3 \times 2(0.0251 \times 106)^{1/2} = 0.979 \text{ kN} \cdot \text{s/m}$$

$$C_3 = 0.3 \times 2(0.0251 \times 87.6)^{1/2} = 0.888 \text{ kN} \cdot \text{s/m}$$

$$[C] = \begin{bmatrix} 2.08 & -0.979 & 0 \\ -0.979 & 1.87 & -0.888 \\ 0 & -0.888 & 0.888 \end{bmatrix}$$

The natural frequencies of the system may be calculated from the matrix formed by

$$[K] - \omega^2[M]$$

Equating the determinant of this matrix to zero, the values for ω^2 may be solved from one of numerous techniques (8). Accordingly,

$$\begin{vmatrix} 241 - 0.0251 \omega^2 & -106 & 0 \\ -106 & 194 - 0.0251 \omega^2 & -87.6 \\ 0 & -87.6 & 87.6 - 0.0251 \omega^2 \end{vmatrix} = 0$$

from which

$$-1.57 \times 10^{-5} \omega^6 + 3.28 \times 10^{-1} \omega^4 - 1.65 \times 10^3 \omega^2$$

$$+ 1.27 \times 10^6 = 0$$

where the roots ω^2 become

$$\omega_1^2 = 930.5 \text{ s}^{-2}$$

$$\omega_2^2 = 6,412. \text{ s}^{-2}$$

$$\omega_3^2 = 1.353 \times 10^4 \text{ s}^{-2}$$

In appropriate units the natural frequencies are

$$f_1 = 4.84 \text{ Hz}$$

$$f_2 = 12.7 \text{ Hz}$$

$$f_3 = 18.5 \text{ Hz}$$

To investigate the effect of damping, equation (10) can be solved when the values with compatible units are substituted. Continuing the analysis,

$$\omega = 5 \text{ Hz} \times 2\pi \text{ radians}$$

$$= 31.42 \text{ s}^{-1}$$

$$\omega^2 = 987.0 \text{ s}^{-2}$$

$$Y = 0.25 \text{ G} \times 9.81 \text{ m/s}^2/\text{G}$$

$$= 2.45 \text{ m/s}^2$$

(11)

The input acceleration matrix becomes

$$[Y] = \begin{bmatrix} 2.45 \\ 0 \\ 0 \end{bmatrix}$$

Real and imaginary components may be collected separately.

$$[K] - \omega^2 [M] = \begin{bmatrix} 217 & -106 & 0 \\ -106 & 169 & -87.6 \\ 0 & -87.6 & 62.9 \end{bmatrix}$$

$$\omega[C] = \begin{bmatrix} 65.4 & -30.8 & 0 \\ -30.8 & 58.6 & -27.9 \\ 0 & -27.9 & 27.9 \end{bmatrix}$$

$$K_1 \ddot{Y} = \begin{bmatrix} 331 \\ 0 \\ 0 \end{bmatrix}$$

$$\omega C_1 \ddot{Y} = \begin{bmatrix} 84.9 \\ 0 \\ 0 \end{bmatrix}$$

The matrix algebraic expression for the acceleration response is now formed:

$$[\ddot{X}] = \begin{bmatrix} 217 + j65.4 & -106 - j30.8 & 0 \\ -106 - j30.8 & 169 + j58.6 & -87.6 - j27.9 \\ 0 & -87.6 - j27.9 & 62.9 + j27.9 \end{bmatrix}^{-1} \times \begin{bmatrix} 331 + j84.9 \\ 0 \\ 0 \end{bmatrix}$$

Without demonstrating the calculations, the indicated matrix is inverted (2,8) and the response becomes

$$[\ddot{X}] = \begin{bmatrix} 19.7 - j129 & -43.4 - j230 & -92.3 - j310 \\ -43.4 - j230 & -83.0 - j488 & -181. - j636 \\ -92.3 - j310 & -181. - j636 & -201. - j877 \end{bmatrix} \times \begin{bmatrix} 0.0331 + j0.00849 \\ 0 \\ 0 \end{bmatrix}$$

Finally

$$[\ddot{X}] = \begin{bmatrix} 1.75 & -j4.10 \\ 0.587 & -j8.24 \\ -0.421 & -j11.0 \end{bmatrix} \quad (12)$$

or

$$\ddot{X}_1 = 4.46e^{j(31.4t-1.168)} \text{ m/s}^2 = 0.46 \text{ G cos } (31.4t-1.168)$$

$$\ddot{X}_2 = 8.37e^{j(31.4t-1.501)} \text{ m/s}^2 = 0.85 \text{ G cos } (31.4t-1.501)$$

$$\ddot{X}_3 = 11.0e^{j(31.4t-1.609)} \text{ m/s}^2 = 1.13 \text{ G cos } (31.4t-1.609)$$

To determine if any box has been loaded beyond its maximum compression strength, combine equations (11) and (12).

$$\ddot{X}_3 - \ddot{X}_2 = 2.88e^{j(31.4t-1.929)} \text{ m/s}^2$$

$$\ddot{X}_2 - \ddot{X}_1 = 4.40e^{j(31.4t-1.838)} \text{ m/s}^2$$

$$\ddot{X}_1 - \ddot{Y} = 4.16e^{j(31.4t-1.741)} \text{ m/s}^2$$

From these the boxes' compressions may be expressed in terms of relative displacements, \underline{D} . Because harmonic displacement is a constant multiple of harmonic acceleration, the constants of integration are equal to zero.

$$D_1 = X_1 - Y = -4.22e^{j(31.4t-1.741)} \text{ mm} = -4.22 \text{ mm cos } (31.4t-1.741)$$

$$D_2 = X_2 - X_1 = -4.46e^{j(31.4t-1.838)} \text{ mm} = -4.46 \text{ mm cos } (31.4t-1.838)$$

$$D_3 = X_3 - X_2 = -2.91e^{j(31.4t-1.929)} \text{ mm} = -2.91 \text{ mm cos } (31.4t-1.929)$$

The compressing load \underline{F} on a box then becomes the force due to dynamic compression plus the equilibrium supporting weight. Accordingly:

$$F_1 = K_1 \underline{D}_1 + 3W = 1307 \text{ N}$$

$$F_2 = K_2 \underline{D}_2 + 2W = 966.2 \text{ N}$$

$$F_3 = K_3 \underline{D}_3 + W = 501.3 \text{ N}$$

Literature Cited

1. R. W. Clough, and J. Penzien, "Analysis of Vibration Frequencies," in Dynamics of Structures, p. 176-178. N.Y., 1975.
2. S. D. Conte, and C. deBoor, "The Triangular Factorization and Calculation of the Inverse," in Elementary Numerical Analysis, p. 127-137. N.Y., 1972.
3. William D. Godshall, "Effects of Vertical Dynamic Loading on Corrugated Fiberboard Containers." USDA Forest Serv. Res. Pap. FPL 94. Forest Prod. Lab., Madison, Wis., 1968.
4. William D. Godshall, "Frequency Response, Damping, and Transmissibility Characteristics of Top-Loaded Corrugated Containers." USDA Forest Serv. Res. Pap. FPL 160. Forest Prod. Lab., Madison, Wis., 1971.
5. Masaji T. Hatae, "Packaging Design," in Shock and Vibration Handbook, ed. C. H. Harris and C. E. Crede, p. 41-1 - 41-30. N.Y., 1976.
6. Naval Research Laboratory, "Shock and Vibration Computer Programs, Reviews, and Summaries," ed. Walter and Barbara Pilkey. Washington, D.C., 1975.
7. Richard M. Phelan, "Complex-Number Representation of Simple Harmonic Motion," in Dynamics of Machinery, p. 81,82. (McGraw-Hill, N.Y.), 1967.
8. N. Willems, and W. M. Lucas, Jr., Matrix Analysis for Structural Engineers. Englewood Cliffs, N.J., 1968.

ACOUSTIC ENVIRONMENT ON THE SURFACE OF A LARGE-SCALE
POWERED MODEL OF A VECTORED-ENGINE-OVER-THE-WING
STOL CONFIGURATION

L. L. SHAW and S. Y. LEE*
Air Force Wright Aeronautical Laboratories
Flight Dynamics Laboratory
Wright Patterson, AFB 45433

This paper presents the results of an acoustic measurement program on a large, powered, highly maneuverable, supersonic STOL fighter model. The model incorporated vectored-engine-over-the-wing (VEO) concept including spanwise blowing to provide lift augmentation. This concept exposes portions of the wing and flap structure to high fluctuating pressure levels. Twelve microphones were installed on the surface of the model to define this environment. Six of these were specially developed high temperature transducers capable of withstanding up to 1093°C. The model was tested at NASA Ames Research Center. Test parameters included engine pressure ratio, wind tunnel dynamic pressure, angle of attack, yaw angle, flap angle and canard angle. The effect of each of these parameters on the fluctuating pressure environment was defined. The results show that levels as high as 167 dB exist on the upper surface of the flap. Levels resulting from a prediction method in the literature agreed with the measured values for only very limited conditions.

INTRODUCTION

Several concepts exist which can augment the life of an aircraft and thus provide STOL capability. One such concept is the vectored-engine-over-the-wing (VEO). Over-the-wing nacelles vector the exhaust over the flap giving lift augmentation. The concept includes spanwise blowing which strengthens the leading edge vortex thus delaying wing flow separations. Both of these concepts were combined in a large powered scale model, representative of a highly maneuverable supersonic STOL fighter configuration which was tested by NASA Ames in the 40X80 foot wind tunnel.⁽¹⁾ The model was powered by two General Electric J-97 turbojet engines. The exhaust was vectored by means of a two-dimensional, half-wedge convergent-divergent nozzle. The nozzle preturns the flow to 25° and exhausts over the flap upper surface, providing exhaust vectoring capability. Sixteen percent of the flow ahead of the nozzle was blown spanwise (SNB) over the wing at an angle nominally parallel to the 40° wing leading edge. Each engine developed 9340N of thrust at a pressure

ratio of 2.0 and exhaust temperature of 593°C. The VEO concept has been jointly developed by General Dynamics, USAF, and NASA. (2,3)

One penalty associated with lift augmentation by directing exhaust over wings and flaps is a significant increase in the fluctuating pressure and temperature on these surfaces and other nearby structure. It is necessary to define these environments so that the structure can be designed to withstand them. Based on this need an acoustic survey was performed to determine the fluctuating pressure levels on the surface of NASA's large scale powered VEO/STOL model. The port side was instrumented with twelve microphones. Six of the microphones were capable of withstanding temperatures up to 1093°C and temperatures as high as 704°C were observed. The main test parameters and respective ranges were engine pressure ratio (EPR) 1.1 to 2.2, tunnel dynamic pressure (q) 527 to 3016 N/m², angle of attack -8° to 36°, yaw angle -10° to 30°, and flap -10° to 30°. Acoustic data were obtained for most locations and test parameters. The data were reduced in the form of one-third octave band spectra. The highest levels were measured on the flap where overall levels of 167 dB were

*Visiting scientist from the Agency for Defense Development of the Republic of Korea under a scientist exchange program.

recorded for the highest EPR. Levels on the center section of the wing near the spanwise blowing nozzle were as high as 150 dB. Total variation of the levels over the range of EPR values was typically 20 dB. The effect in increasing dynamic pressure was to increase levels approximately 4 dB. Angle of attack had only a small effect on the levels. Variations at all locations were less than 2 dB. Yaw angle variations also had a small effect on the levels. Flap angle affected the overall levels approximately 3 dB. Comparison of the measured data with existing prediction methods showed only fair agreement.

MODEL DESCRIPTION

The NASA model tested was a highly maneuverable supersonic STOL fighter. The model incorporated vectored-engine-over-the-wing (VEO) which includes spanwise blowing (SWB), two-dimensional nozzles, canards, and an aft fuselage control surface (beaver tail). Figure 1 and 2 show the model installed in the NASA Ames 40X80



FIGURE 1 Picture of Model in the NASA Ames 40X80 Wind Tunnel

foot wind tunnel where it was tested. Figure 3 illustrates the model and propulsion system geometries. The model was powered by two General Electric J-97 turbojet engines. As shown in Figure 4 16% of the exhaust was diverted into the SWB duct where it blows spanwise over the wing upper surface. The main flow is through a 2-D nozzle which returned the exhaust 25° onto the upper surface of an adjustable trailing edge flap, providing total exhaust vectoring of -10° to +40°. Further details about the model are available in Reference 1.



FIGURE 2 Picture of Model Showing Nozzle and Flap

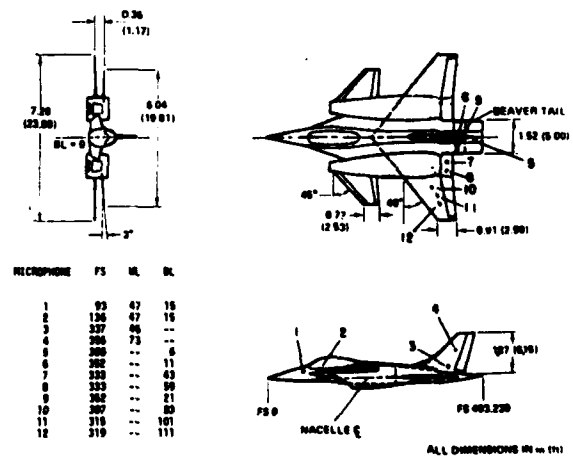


FIGURE 3 Details of Model and Instrumentation Location

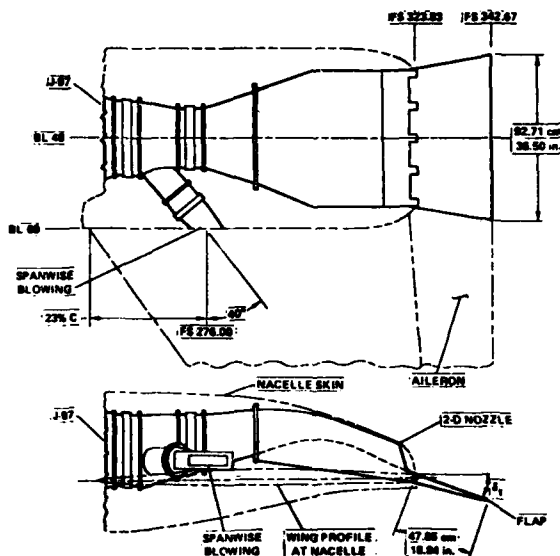


FIGURE 4 Sketch illustrating Spanwise Blowing Nozzle

INSTRUMENTATION

The port side of the model was instrumented with twelve microphones. Six were standard off-the-shelf Gulton microphones Model number 10010028, and six were specially developed high temperature microphones developed by Kaman Sciences Corp. model number KM-2000. The low temperature microphones can operate in temperatures up to approximately 177°C while the high temperature microphones can withstand temperatures up to 1093°C. Approximate locations of the microphones are shown in Figure 3. Two low temperature microphones were installed on the fuselage near the engine inlet, (number 1 and 2) two were on the vertical tail (3 and 4), one was on the strake aft of the wing/flap trailing edge (6), and one on the beaver tail control surface (5). Three high temperature microphones were installed on the wing, (10, 11, 12), two on the flap behind the exhaust nozzle (7 and 8), and one on the aft strake (9). High temperature microphone number 10, mounted nearest to the SWB nozzle was inoperable during the entire test. All of the other microphones were operable most of the time. A complete description of the type of high temperature microphones used is presented in Reference 4.

TEST PROCEDURES

The model was tested in the 40X80 foot NASA Ames wind tunnel facility. The parameters during the test were wind tunnel dynamic pressure, angle of attack, yaw angle, flap angle, canard angle of attack, and engine pressure ratio.

During the test one parameter was varied while all others were fixed, and the data recorded for the range of the parameter. The ranges of each of the test parameters are presented in Table I.

TABLE I
DATA CLASSIFICATION

DYNAMIC PRESSURE Q (PASCAL)	ANGLE OF ATTACK α (DEGREE)	SIDESLIP ANGLE β (DEGREE)	FLAP ANGLE ϕ_f (DEGREE)	CANARD ANGLE ϕ_c (DEGREE)	ENGINE PRESSURE RATIO	
					PORT	STARBOARD
0	0	0	30	0	1.1 to 2.2	1.1 to 2.2
551 ~ 3040	-8 to 36	0	30	0	1.9 to 2.1	1.9 to 2.1
551, 1762	0, 20	-10 to 30	30	0	1.9 to 2.1	1.9 to 2.1
551 ~ 1762	-8 to 36	0	30	0	1.9 to 2.1	OUT
1106	0 to 12	0	30	-10 to 20	2.1	2.1
551 ~ 3040	-8 to 36	0	-10	0	1.9 to 2.1	1.9 to 2.1
551	20	-10 to 30	-10	0	2.1	2.1

LOCATION EFFECT

Microphones were located at twelve positions on the model as shown in Figure 3. The overall acoustic levels from the eleven operable transducer locations showed as much as 40 dB variation. This is shown in Figure 5 where data for two jet Mach numbers of 0.70 and 0.78 are presented. The data spread for one specific Mach number includes data for all other parametric variations. The variation in the overall sound pressure level from most of

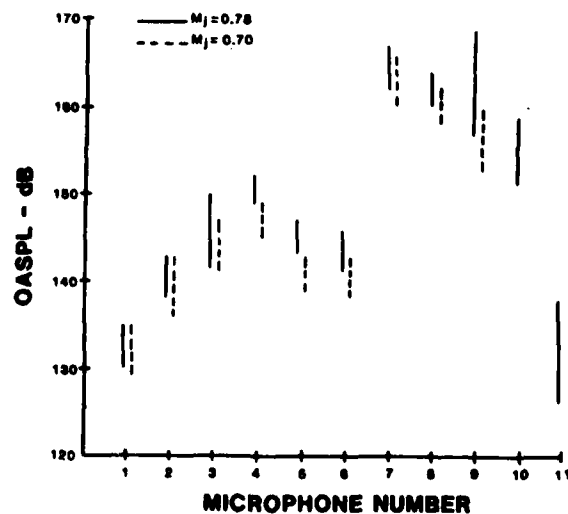


FIGURE 5 Comparisons of Data Spread from all the Microphones

the microphones was less than 9 dB. Microphone locations 11, and 12 exhibited 12 dB data spread. As would be expected the highest average levels occur on the flap, microphones 7 and 8. However, microphone 9, located adjacent to the exhaust flow, shows average levels about the same as on the flap. The lowest levels occur at microphone 1 and 12 located near the cockpit and outer wingtip respectively. A significant change in level between microphone pairs 6-9 and 11-12, can be observed in the figure. An explanation for the large change between locations 11 and 12 is the spanwise blowing. The levels clearly indicate that microphone 11 was in the spanwise flow while microphone 12 was not. The difference in the levels between microphone 6 and 9, both located on the aft strake, is due to microphone 9 being nearer to or in the edge of the jet flow while microphone 6 was inboard of the flow.

Figure 6 shows typical one-third octave band spectra for each of the measurement locations. Variations in the spectrum shapes are readily apparent. The peak frequency is seen to vary with location. The peak frequencies have been normalized with Strouhal based on flap length, and typical spectra shapes are shown in Figure 7. In general, the spectra display, a 20 dB/decade slope below the peak Strouhal value and -8 dB above it.

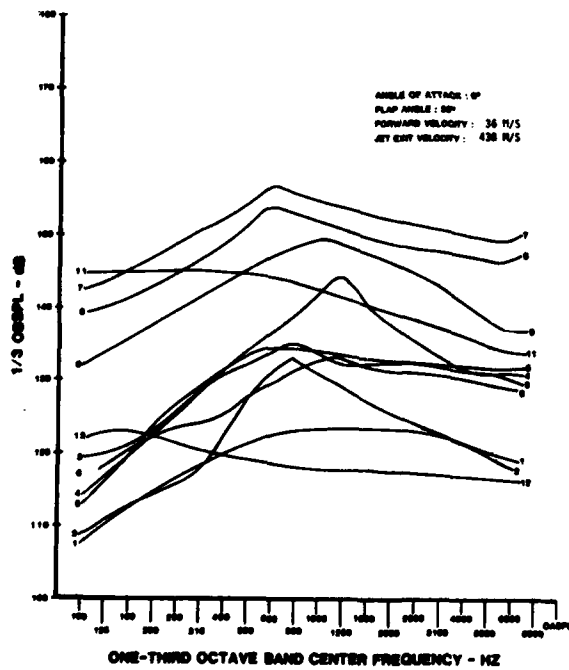


FIGURE 6 Typical Spectra Shapes

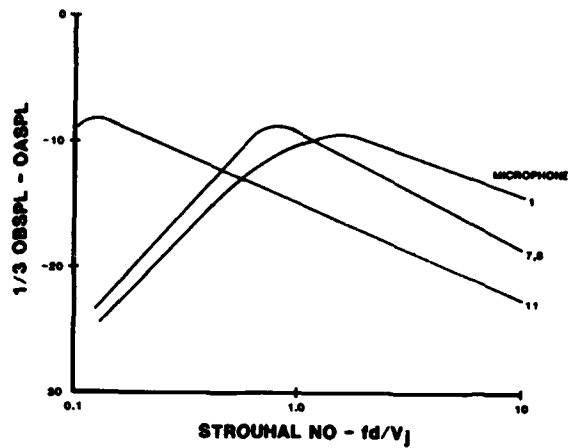


FIGURE 7 Typical Spectra Normalized with Strouhal Number

JET VELOCITY EFFECT

The model was powered by two J-97 turbojet engines. They were operated at jet exit velocities from 116 m/s to 458 m/s corresponding to jet exit Mach numbers from 0.23 to 0.82. The levels on the flap from microphone 7 are shown in Figure 8. The first observation is that the

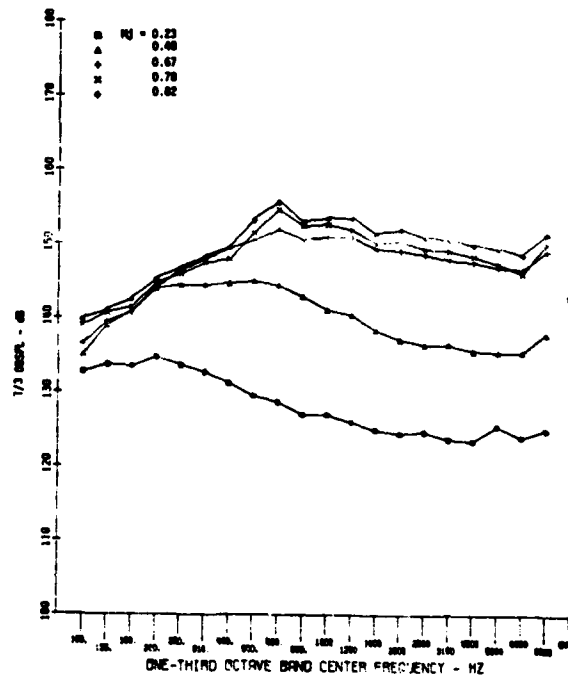


FIGURE 8 One-Third Octave Band Spectral From Microphone 7

overall levels increase 20 dB over this jet Mach number range. The variation of the levels with jet Mach number will be discussed more below. A second observation is that the frequency of the peak broadband level increased with jet Mach number. The frequency for the peak level corresponds to a Strouhal number near 1.0, where the Strouhal number is based on the flap length. The same value, for a similar location, was observed in Reference 5.

In order to evaluate the effect of jet velocity on the OASPL value of n , from the expression

$$p^2 = a V_j^n$$

was determined for all microphone locations. The result was that n varied from 3.0 to 4.0 considering all locations. Reference 5 displayed n values of 3.4 to 4.2 from measurements on the flap directly behind the nozzle and the nearby fuselage. The agreement is very good. As discussed in Reference 5 the deviation of the calculated slope from the generally accepted value of 4 may be due to a nonlinear relationship between the value V_j at the exit, which is used to calculate n , and the local velocity at the transducer location.

The measured levels were compared to the results of a prediction method for USB noise given in Reference 6 where

$$OASPL = 10 \log (\rho^2 V^4 D^2) + 30 - 20 \log(r)$$

$$+ 0.01 \delta_F$$

$$+ 10 \log \left[\frac{1 + \sin \psi}{2} \cos \left(\frac{\theta + \delta_F}{2} \right) \right]$$

where

- ρ = Jet Density
- V = Jet Velocity
- D = Effective jet diameter
- r = Distance between center of flap trailing edge and observation point
- ψ, θ = Angles locating observation point
- δ_F = Flap angle

Measured and predicted levels for microphones 3 and 4 are shown in Figure 9-a. It is evident the prediction method is more accurate at the higher Mach numbers. The predicted levels are more than 10 dB too low at the low Mach number. Predicted levels for the other locations, except 9 and 12, showed similar comparisons. At microphone 9 the predictions were about 15 dB

to low, and at microphone 12 they were 15 dB too high.

The microphones located on the flap, 7 and 8, and microphone 9 were exposed to high speed flow. A second prediction approach is given in Reference 6 for measurement locations in the jet flow. This approach consists of using three different normalized spectra and interpolating these for specific locations. Spectra from microphones 7 and 9 are compared to the second approach in Figure 9-b. At first look it appears that the agreement is very bad but the major variations is a difference in the peak broadband frequency. If the predicted spectra were shifted to a peak broadband frequency of approximately 0.5, the agreement

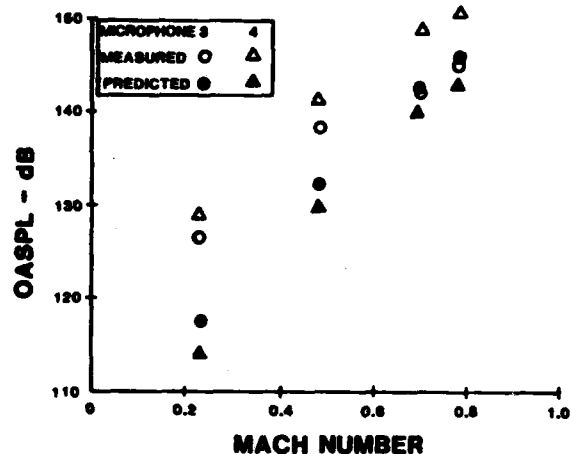


FIGURE 9-a Comparison of Measured and Predicted Levels

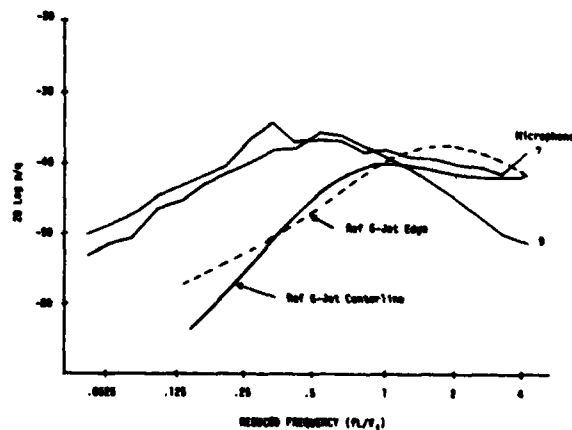


FIGURE 9-b Comparison of Measured and Predicted Spectra

would be much better. The maximum predicted level at the jet edge is only 2 dB lower than the measured level from microphone 9 while the predicted level on the jet centerline is 4 dB below the measured value. No explanation for the difference in the frequency of the peak broadband levels is apparent.

FORWARD VELOCITY EFFECT

Acoustic data were obtained for forward velocities from 0 to 70 m/s. Higher velocities were not obtained because of wind tunnel limitations. In general, the effect of forward velocity was to reduce the sound pressure level. This reduction is illustrated clearly in Figure 10 for the microphone 9 location. The data shown are for the maximum jet velocity and flap angle of 30°. A 10 dB reduction is obtained going from 0 to 7 m/s. Most other locations experienced reductions less than 10 dB. Specifically the levels on the flap were reduced 4-5 dB which agree with the reductions presented in Reference 5.

An equation is given in Reference 6 to predict the forward velocity effect on the sound pressure level. This equation is

$$SPL = 10 K \log \left[1 - V_F/V_J \right]$$

where K is a coefficient depending on relative location, V_F is the forward velocity, and V_J is the jet velocity. For the microphone 9 location this expression predicts less than 1 dB effect for a forward velocity of 71 m/s. For this location, poor correlation is observed between the prediction and the current

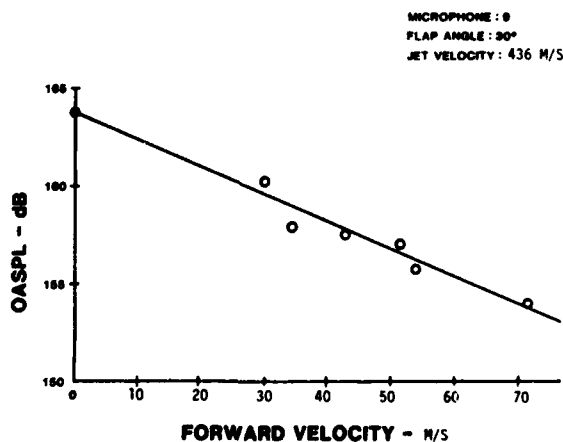


FIGURE 10 Data Illustrating Forward Velocity Effects

test results. An explanation for this is that increasing the forward freestream velocity reduces the spreading of the jet flow and thus reduces the acoustic energy reaching this location.

Somewhat different results were obtained for this location at angles of attack other than 0°. Figure 11 shows that the effect of forward velocity is much less at the angles of attack above 20°. This trend was observed at other locations also.

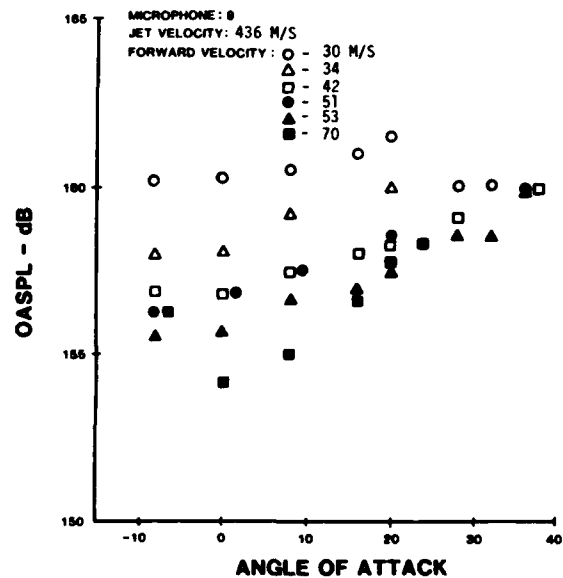


FIGURE 11 Data Illustrating Forward Velocity Effects and Different Angles of Attack

FLAP ANGLE EFFECT

Acoustic data were obtained for two flap angle settings of, 30° and -10°, which represents nominal takeoff/landing and cruise/maneuver configurations respectively. In the -10° position the engine exhaust impinges on the flap at a 25° angle. Figures 12-15 display typical variation of the spectra from the different locations. Flap setting had very little effect on the levels at microphone locations 1 and 2 because they were so far from the engine exhaust. Microphone locations 3 and 4, on the vertical fin, displayed 4 dB increases in the overall level as a result raising the flap to the -10 setting. Figure 12 shows that the increase in energy is above 250 Hz. Microphone locations 5, 6 and 9 located on the aft strake and beavertail, showed variations from 0 to 7 dB. Figure 13 illustrates an increase of 7 dB at microphone 9 with most of the energy being added at the lower frequen-

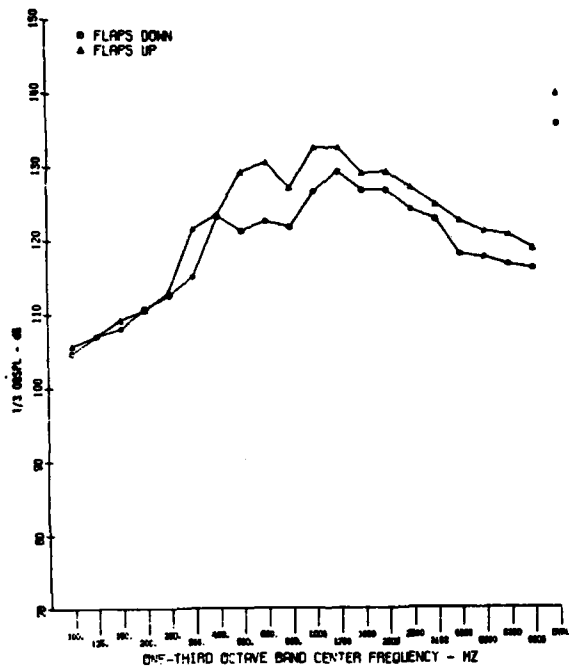


FIGURE 12 One-Third Octave Band Spectra from Microphone 4 showing Flap Angle Effect

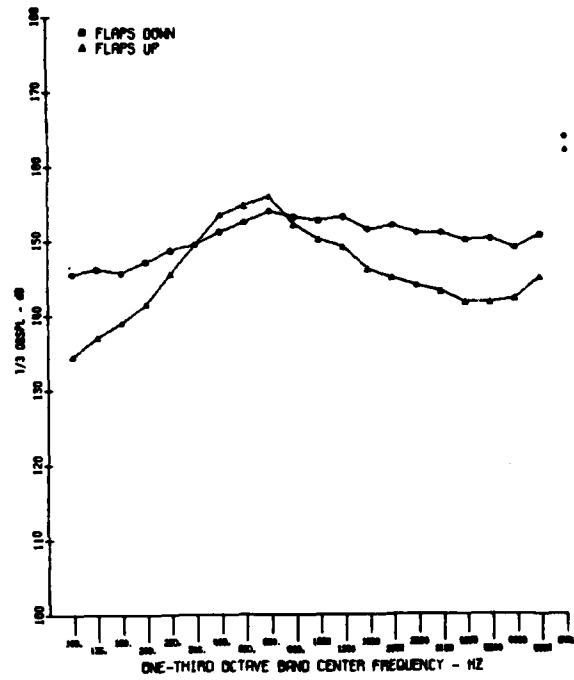


FIGURE 14 One-Third Octave Band Spectra from Microphone 7 Showing Flap Angle Effect

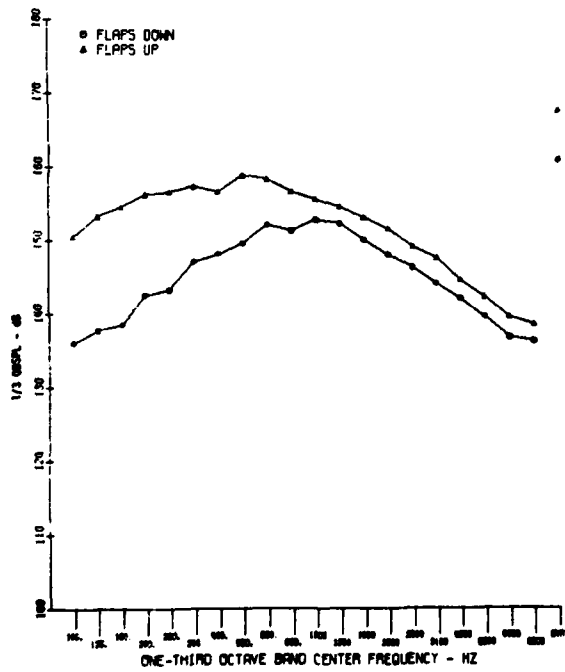


FIGURE 13 One-Third Octave Band Spectra from Microphone 9 showing Flap Angle Effect

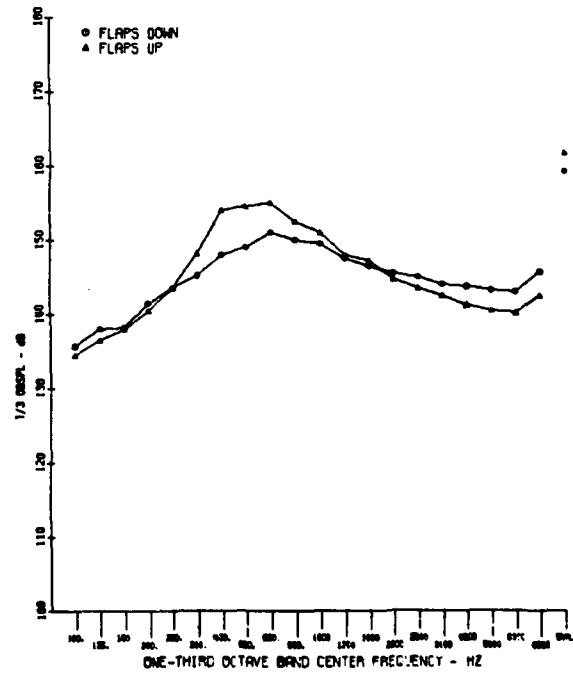


FIGURE 15 One-Third Octave Band Spectra from Microphone 8 Showing Flap Angle Effect

cies. Microphone 7 and 8 were located on the flap directly behind the exhaust nozzle. These were not symmetrically located on the flap. Microphone 8 was twice as far from the nozzle centerline and outboard of microphone 7. Variations in the acoustic levels on the flap were larger than anticipated. Figures 14 and 15 display the results from the surface of the flap. The results reveal that the overall level at the microphone 7 location decreases when the flap is raised to the -10° position while at the microphone 8 location it increases. It is seen in Figure 14 that the spectrum shape changes at microphone 7 but in Figure 15 at microphone 8 the shape is essentially the same. It appears that a frequency band from approximately 200-1000 Hz is amplified due to impingement of the exhaust on the flap. No flaps-up data were obtained from microphones 9, 10 and 11.

SINGLE ENGINE EFFECT

Data were recorded for the port engine only, starboard engine only, and both engines operating. The results in general showed what was expected, that is, both engines operating gives the highest level and the port engine only is higher than starboard engine only. The data in Figure 16 are from Microphone 9. Two of the other measurement locations did not show this trend they were on the beavertail

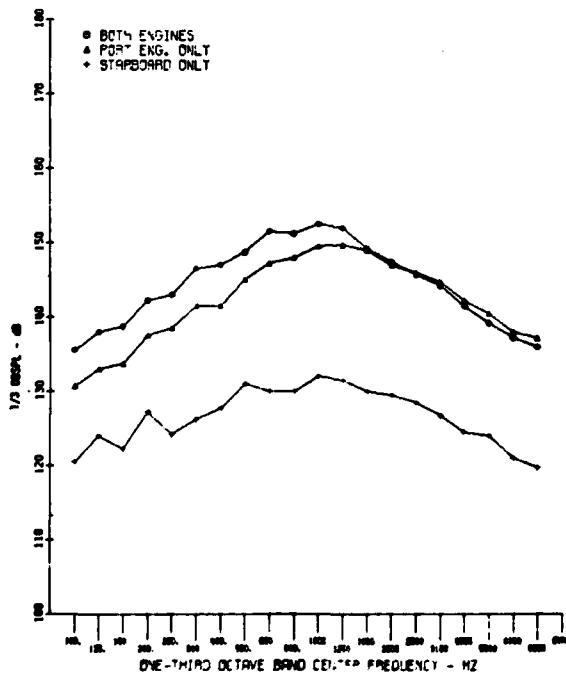


FIGURE 16 One-Third Octave Band Spectra from Microphone 9 Showing Single Engine Effect

and near the cockpit. Figure 17 shows that on the beavertail the levels were about the same as for either engine operating. The reason for this is that microphone 5 was nearly equidistant from both engines. Microphones 1 and 2 showed similar results.

If one tries to sum the acoustic power from each of the engines to obtain the both engines level, it is evident that the measured both engines level does not always agree. Since the engine exhausts are relatively close together, flow interactions could easily cause the both engines level to differ from the sum of the individual engine noise sources.

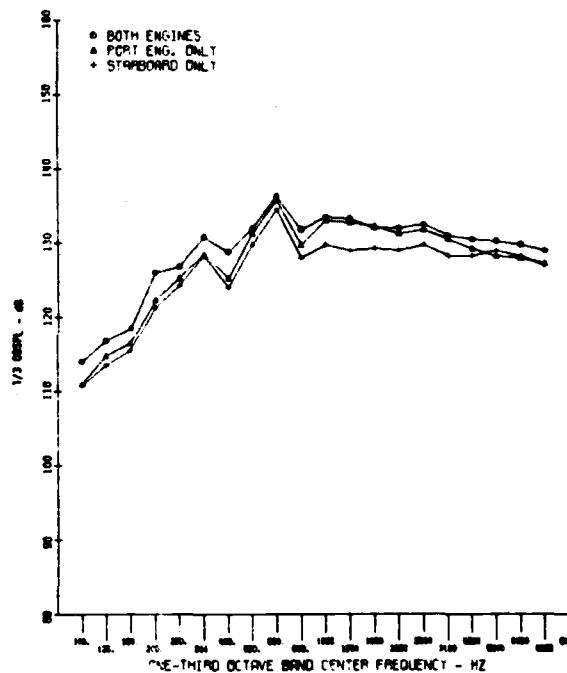


FIGURE 17 One-Third Octave Band Spectra from Microphone 5 Showing Single Engine Effect

ANGLE OF ATTACK EFFECT

The model was tested at angles of attack from -8° to 36° . Data from each microphone for the various angles of attack are shown in Figure 18. Increasing the angle of attack generally increased the sound pressure levels around 2 dB except at the two measurement locations near the cockpit. At these locations the levels increased as much as 9 dB. Most of attack which indicates that separation was occurring. It was noted in Reference 1 that separation on the wing leading edge also occurred at approximately 20° .

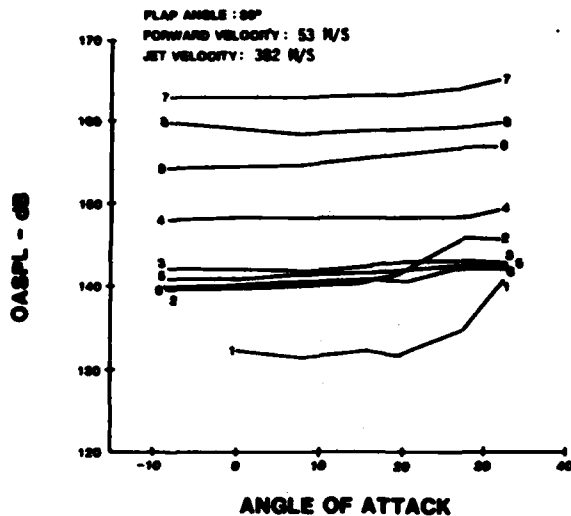


FIGURE 18 One-Third Octave Band Spectra Showing Angle of Attack Effect

CANARD ANGLE EFFECT

Acoustic data were obtained for various canard angles (-10° to $+20^{\circ}$). No significant change in levels were anticipated. The overall levels from all the microphones showed less than 2 dB variation for all of the canard angles.

YAW ANGLE EFFECT

The model was tested at yaw angles from -10° to 30° where positive yaw is nose to the left. Figure 19 presents the overall levels from each of the microphones for the various yaw angles. It is clearly seen that the acoustic levels were not affected significantly with yaw angle. The only microphone location that showed more than 1 dB change was number 1. It is believed that a larger yaw effect would have been experienced if the model was yawed to larger negative values. This is because all of the microphones were located on the port side thus they were partially shielded from the free stream flow when yawed in the position direction.

SUMMARY OF RESULTS AND CONCLUSIONS

The following results and conclusions were observed as a result of this investigation.

1. The high temperature microphones were successful in obtaining acoustic data in a high temperature environment.
2. At some locations the measured level

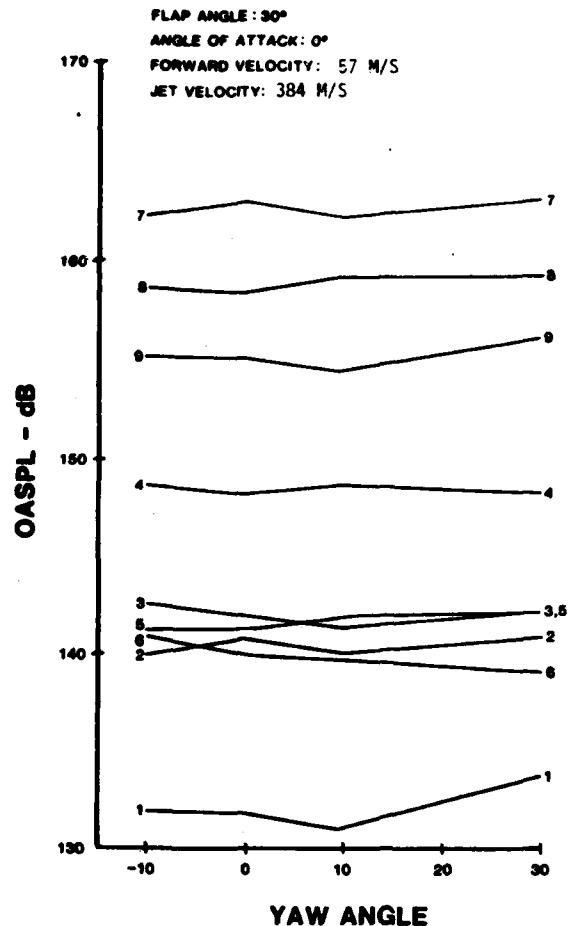


FIGURE 19 One-Third Octave Band Spectra Showing Yaw Angle Effect

from only the port engine was as high as the level from both engines.

3. Higher levels are experienced on the aircraft when the flaps are in the cruise configuration as opposed to take-off configuration.

4. A significant portion of the aircraft structure is exposed to levels high enough to result in acoustic fatigue if not properly designed.

5. Forward velocity reduced the acoustic level at most positions on the aircraft.

6. The angle of attack of the aircraft normally affected the levels around 2 dB except near the cockpit where flow separation may have occurred.

7. Canard angle and yaw angle variations had only a small effect on the acoustic environment.

8. The acoustic levels were shown to vary with jet exit velocity raised to the power of 3.0 to 4.0.

REFERENCES

1. Aerodynamic Characteristics of a Large Scale Model of a Highly Maneuverable Supersonic V/STOL Fighter: STOL Configuration, AIAA-80-0234, Falarski, M.D., et al, January 1980.
2. Lummus, J.R., "Study of Aerodynamic Technology for a V/STOL Fighter/Attack Aircraft", NASA CR-152128, 1978.
3. Whitten, P.D., "An Experimental Investigation of Vectored-Engine-Over-The-Wing Powered Lift Concept " AFFDL-TR-7692 1978.
4. Engineering Manual For the KM-2000 Microphone System, Kaman Sciences Corporation, August 1975.
5. Experimental Study of Acoustic Loads an Upper-Surface-Blown STOL Airplane Configuration, Willis, C.M., and J.A. Schoenster, NASA TP 1577, December 1979.
6. A Guide for Estimation of Aeroacoustic Loads on Flight Vehicle Surfaces, Unger, E.E. et al, AFFDL-TR-76-91, February 1977.

DISCUSSION

Mr. Getline (General Dynamics-Convair):
What microphones were you using?

Mr. Shaw: The high temperature microphones?

Mr. Getline: Yes.

Mr. Shaw: They were developed by Kaman Sciences, Inc. for the Air Force about 5 years ago. They are called Kaman 2000.

Mr. Getline: What was the diameter of the sensitive face of the microphones?

Mr. Shaw: Half inch.

Mr. Getline: Were these microphones flush mounted in the structure?

Mr. Shaw: Yes.

Mr. Getline: Was there any attempt made to separate the acoustic field from the flow field. You have both in there and with a half inch diameter it seems to me that you have lost a lot of your high frequency response from the flow field and I just wondered if any attempt was made to separate these two because you have two different phenomena going on at the same time.

Mr. Shaw: No, that might be an area of improvement.

Mr. Getline: I think you might get a little better correlation with your predictions and your test results because it seems to me that you didn't get within a 10 db even at the closest and if you separate out these two effects you might find you get a little better correlation with your prediction.

Mr. Shaw: A point well taken. Thank you.

Mr. Seville (Structural Dynamics Research Corp.): I have two questions for you that relate to the slides which showed a comparison of the one engine on, two engines on and then both engines on. The plot showed that with one engine on there was a significant difference between one engine on and then the other engine on.

Mr. Shaw: Right.

Mr. Seville: OK, but when you had them both on it was only a minor change from the situation with the single one on. In one plot you showed both of those having the same level when they were both turned on the level didn't change, it was all combined. Can you explain that?

Mr. Shaw: Yes, do you want me to answer your question?

Mr. Seville: OK, the second question is can you go into a little bit of detail on this microphone that you have that goes up to 2000 degrees Fahrenheit?

Mr. Shaw: The special high temperature microphone? Yes there was a need about 5 years ago to develop these microphones because at the Flight Dynamics Lab we felt that we did desire data at the higher temperatures so one of the branches went under contract with Kaman Sciences to develop these. They, in turn investigated and found some special material that could be used to construct these microphones. They did so and we acquired six microphones. I believe these were the only six made at that time. At that time they cost \$5000. We went back and asked to repair these and the possibilities of purchasing more and they said no way because the same material was not available.

Mr. Seville: Are they cold or what is the construction?

Mr. Shaw: No, they are an inductive type transducer. Internally they have two coils and the facing of the coil varies with the fluctuating pressure thus changing the inductance between the two coils. I could give you more information or refer you to a document on the microphones, if you wish.

Mr. Seville: Ok, it sounds like we need to talk.

Mr. Shaw: Kaman Sciences are considering developing these microphones again or trying to develop the material to be used in them to make them available to the public. Since we've done the work there have been a few people expressing interest in obtaining this type of microphone but they are not available at the present.

ACTIVE STABILIZATION OF A SHIP BORNE CRANE

S. Sankar and J. Svoboda
Department of Mechanical Engineering
Concordia University
Montreal, Quebec, Canada

This paper presents the dynamic performance of an active-stabilizer for controlling a ship-borne crane under heavy weather. The governing equations are derived and solved using digital simulation. The mathematical model served as a basis for the dynamic design study of the crane system. The active-stabilizer for the crane uses a heavy compensating boom to decouple the submersible from the motion of the support ship. The motion compensation system uses an active servo-control system operating in parallel with a soft hydro-pneumatic spring. The crane boom maintains its position in respect to the shore by monitoring both the acceleration of the boom tip and the boom angular position. The active compensation system consisting of a linear hydraulic servo actuator coupled in parallel with a hydraulic accumulator allows for adjustment of the gas precharge pressure according to the load. The study indicates that the sizing of the actuator system and its adjustment capability affects significantly the energy requirements of the active damping servo actuator system. The effect of varying system parameters on the dynamic performance of the active-stabilizer is also studied. A multi-variable optimization technique is used to select the optimal gains of the PID controller so as to achieve the minimum movement of the crane boom tip.

INTRODUCTION

Increased offshore activities of the recent years resulted in greater demand for suitable equipment. The safety and performance of offshore operations are severely limited by wave induced vessel motions. As a result, there is a demand for systems or techniques that can make operations possible in higher sea states without sacrificing safety or performance.

Motion compensation systems represent one of the most important equipment design areas. The generalized criterion of performance of a motion compensation system is the amplitude ratio of the dynamic fluctuation of the controlled variable to its steady state value. In other words, the purpose of such systems is to retain a constant position of certain ship-borne equipment component - e.g. a ship-mounted 200-ton derrick [1], a platform [2], or a crane hoist [3]. Thus a safe and efficient operation even in rough sea conditions is possible.

This paper discussed the design and analysis of a motion compensation system for ship-borne crane. The system in question is a 1-axis, active electro-hydraulic system with feedback control,

compensating for heave and for the vertical components of the ship roll and pitch movement. The design is aided by digital computer using the MIMIC language. The system control strategy is presented and the performance of the system in response to wave input is predicted. The effects of various parameters on the compensator is also shown. The feasibility of application of a formal design optimization procedure is briefly discussed.

SYSTEM DESCRIPTION AND MODELLING

The schematic of the system is shown in Fig. 1. The system is based on a similar design described in [3] and operates as follows. The crane boom attached to the crane mast at a pivot point (A) is moved by the hydraulic actuator in such a way that the vertical motion (Y_B) of the crane tip (B) is kept to a minimum. This is achieved by sensing the tip vertical acceleration (\ddot{Y}_B). The acceleration signal is fed into the controller where it is processed and compared with the reference signals. It results in a correction signal (I_R) which drives the actuator via an electro-hydraulic servovalve in order to minimize the discrepancy. The design of the controller is shown in Fig. 2. The measur-

ed boom tip acceleration signal (\ddot{Y}_B) is twice integrated (\dot{Y}_B, Y_B). These three signals are compared with the corresponding acceleration (\ddot{Y}_{BR}), velocity (\dot{Y}_{BR}) and position (Y_{BR}) reference signals. The discrepancies are multiplied by the acceleration, velocity and position gains (K_A, K_V, K_P) and summed into the controller output (I_R). Thus, when the boom velocity (\dot{Y}_B) is considered as the controlled variable, a PID-controller is formed. To keep the boom tip steady, the $\dot{Y}_{BR} = \dot{Y}_{BR} = 0$ and $Y_{BR} = \text{const}$. Obviously other controller configurations, such as P, I, D, PI or PD, can be formed, simply by omitting the irrelevant variables. Also, it is conceivable to expand the system to achieve 2 - or even 3 - axis motion compensation.

The function of the accumulator and the balance valve is to reduce the hydraulic power necessary for the above described active motion compensation. The pressurized oil stored in the accumulator is acting on the actuator piston area (A_3) thus compensating for the load force. The accumulator pressure (P_A) is regulated by charging the accumulator via the balance valve. The valve senses the pressure difference ($P_1 - P_2$) at the servovalve output and charges or bleeds the accumulator (P_A) balancing the servovalve output.

The equations forming the mathematical model of the crane system are as follows (refer to Figs. 1 and 2):

The crane geometry:

$$\phi = \alpha - \arctan(\overline{CD}_0 / \overline{AC}) \quad (1)$$

$$\alpha = \arccos[(\overline{AC}^2 + \overline{AD}^2 - \overline{CD}^2) / (2 \overline{AC} \overline{AD})] \quad (2)$$

$$Y_B = \overline{AD} \cdot \cos \theta + \overline{AB} \cdot \sin \phi \quad (3)$$

$$\overline{CD} = \overline{CD}_0 + Y_H \quad (4)$$

The hydraulic actuator displacement and velocity:

$$Y_H = \int \dot{Y}_H \cdot dt + Y_{H0} \quad (5)$$

$$\dot{Y}_H = (1/M_I) \int (F_H - F_L) dt + \dot{Y}_{H0} \quad (6)$$

where Y_{H0} and \dot{Y}_{H0} are the initial values of

Y_H and \dot{Y}_H respectively.

The actuator and load forces:

$$F_H = P_1 (A_{11} - A_{12}) - P_2 \cdot A_2 + P_A \cdot A_3 - F_f \quad (7)$$

$$F_L = W \cdot \overline{AB} \cdot \cos(\phi - \theta) / (\overline{AC} \cdot \overline{AD} \cdot \sin \alpha / \overline{CD}) \quad (8)$$

The actuator pressures and flowrates:

$$P_1 = (\delta/V_1) \cdot \int [Q_1 - (A_{11} - A_{12}) \dot{Y}_H] dt + P_{10} \quad (9)$$

$$P_2 = (\delta/V_2) \cdot \int (A_2 \cdot \dot{Y}_H - Q_2) dt + P_{20} \quad (10)$$

where P_{10} and P_{20} are the initial pressures of P_1 and P_2 respectively.

$$Q_1 = C_D \cdot A_V \cdot \sqrt{(2/\rho) \cdot (P_S - P_1)} \dots \text{if } X_V > 0 \quad (11)$$

$$Q_2 = C_D \cdot A_V \cdot \sqrt{(2/\rho) \cdot (P_2 - P_0)} \dots \text{if } X_V < 0 \quad (12)$$

The servovalve dynamics:

$$\dot{X}_V = (1/\tau_V) \cdot \int (X_{VR} - X_V) \cdot dt + X_{V0} \quad (13)$$

where X_{V0} is the initial value of X_V .

$$A_V = K_X \cdot X_V \quad (14)$$

The motion compensation controller:

$$I_R = K_A(\ddot{Y}_{BR} - \ddot{Y}_B) + K_V(\dot{Y}_{BR} - \dot{Y}_B) + K_P(Y_{BR} - Y_B) \quad (15)$$

$$X_{VR} = K_I \cdot I_R \quad (16)$$

The accumulator gas pressure and volume:

$$P_A = P_{A0} \cdot V_{A0}/V_A \quad (17)$$

$$V_A = \int (A_3 \cdot Y_H - Q_B) dt + V_{A0} \quad (18)$$

where V_{A0} is the initial value of V_A .

The balance valve operation:

$$X_{VB} = K_B (P_1 - P_2) \quad (19)$$

$$A_{VB} = K_{XB} \cdot X_{VB} \quad (20)$$

$$Q_B = C_D \cdot A_{VB} \cdot \sqrt{(2/\rho) \cdot (P_S - P_A)} \dots \text{if } X_{VB} > 0 \quad (21)$$

$$Q_B = C_D \cdot A_{VB} \cdot \sqrt{(2/\rho) \cdot (P_A - P_0)} \dots \text{if } X_{VB} < 0 \quad (22)$$

The hydraulic power:

$$\dot{W}_H = (Q_1^+ \cdot P_1 + Q_2^- \cdot P_2 + Q_B^+ \cdot P_A) \quad (23)$$

In addition, the model contains several logic controls for the orientation of the friction forces and flowrates and for limiting of the pressure values. Table 1 gives the crane sizing parameters used in the design example.

ACTIVE STABILIZER PERFORMANCE

The active stabilizer model is used for the evaluation of the system feasibility. This is followed by the adjustment of some important parameters and sizes for the performance evaluation. Thus the preliminary system design is accomplished prior to scaled model experiments. It is feasible, as a next step, to consider employment of a formal optimization procedure, to further improve the system performance.

To accomplish the preliminary design task, the system model is subjected to the ship roll movement described as:

$$\theta = C_1 \sin(C_2 \cdot t)$$

where the constants (C_1, C_2) are so chosen, that the amplitude and frequency of the roll

are +15° and 0.25Hz respectively. First a system without an accumulator and with the acceleration control only (recall Fig. 2) was investigated. The acceleration gain (K_A) is adjusted to obtain the best motion compensation of the boom tip (minimum Y_B).

Equations (1-23) governing the dynamics of the crane are solved using MIMIC programming (Continuous System Modelling Language) on a CDC Cyber 172. The Runge Kutta numerical integration method with variable step size is used in the MIMIC language for solving the non-linear system differential equations. It should be noted that the gains K_V and K_P in equation (15) are set to zero for this case. The results indicate that the acceleration of the tip is maintained close to zero; however, the maximum positional error, $(Y_B - Y_{BR})_{max}$ increased with increasing values of K_A . The acceleration gain (K_A) is adjusted to obtain the best motion compensation of the boom tip, i.e. minimum $(Y_B - Y_{BR})$. This procedure was repeated for the velocity control (K_V) only and again for the position control (K_P) only. In both cases, increasing the gain K_V or K_P decreases the maximum positional error. However, it should be pointed out that decreasing K_A or increasing either K_V or K_P beyond certain values introduced instability in the system. Because of the above facts, a feedback scheme that has acceleration, velocity and displacement controls (PID Control) is proposed in this paper. The value of gains K_A , K_V and K_P calculated based on individual controls only, are then used as the gains for a PID control and the simulation of the active crane system was repeated. It was found that the positional error considerably reduced in comparison to the case when only one control was used.

In the following step the accumulator is added and the volume (V_{A0}) and precharge pressure (P_{A0}) are selected. Finally, the balance valve is connected and valve gain (K_B) selected. Here the adjustment is more arbitrary, since both the quality of the motion compensation (Y_B) and minimization of the hydraulic power (W_H) has to be observed.

The effect of feedback gains K_A , K_V and K_P on the performance of the active stabilizer is difficult to be envisaged from the non-linear set of coupled differential and algebraic equations (1-23) describing the dynamic behavior of the system. In order to appreciate the significance of each of the feedback loops, an active isolator of a one-degree of freedom system as shown in Fig. 3 is considered. It is represented by an idealized controllable force generator and a conventional spring. Here the force generator is controlled by an isolated mass acceleration signal and velocity signal generated by integrating the acceleration signal. The acceleration and velocity gains are K_A and K_V respectively. The integration is represented by the $1/s$ term.

Writing the equations of motion and taking

the Laplace transform gives the transfer function of the active system (displacement transmissibility ratio):

$$\frac{X}{X_0} = \frac{K}{(M + K_A)s^2 + K_V s + K}$$

From the above equation it is evident that the undamped natural frequency is given by $[K/(M + K_A)]^{1/2}$. Since K_A can be arbitrarily selected to a positive or negative value, the system natural frequency can be adjusted to any desired value. Positive K_A will produce a low natural frequency and increase the isolation region. Thus K can be selected to produce the desired static deflection.

The damping ratio of the active system is given by $K_V/2[(M+K_A)K]^{1/2}$. Thus, any desired damping ratio can be achieved by selecting an appropriate value of K_V . From the active system transfer function, the high frequency transmissibility is asymptotic to a slope of -40db/decade of frequency as shown in Fig. 4a. Thus the use of the active isolator allows control of the resonant amplitude without compromising the high frequency performance.

From Fig. 3, the relative displacement transmissibility ratio, T_r of the active system can also be expressed as

$$T_r = \left| \frac{X - X_0}{X_0} \right| = \frac{2\xi\omega_n^2 [1 + \tau s]}{s^2 + 2\xi\omega_n s + \omega_n^2}$$

$$\text{where } \omega_n^2 = K/(M+K_A)$$

$$\xi = K_V/2 [(M+K_A)K]^{1/2}$$

$$\tau = 1/2 \xi \omega_n$$

It is evident from the above equation that T_r reaches unity for $\omega \gg \omega_n$ and has a slope of +40db/decade of frequency in the neighbourhood of the natural frequency especially for $\omega \ll \omega_n$ as shown in Fig. 4(b).

The effect of gains in the PID controller on the Crane's performance is presented in Figs. 5, 6 and 7. The results indicate the absolute maximum positional error of the boom tip $|e_{max}|$ at a constant roll amplitude of +15° and a frequency of 0.25Hz. It can be seen from these figures, for a constant value of K_V and K_P , the value of $|e_{max}|$ initially decreases for increasing K_A and then increases with K_A . A similar performance behavior resulted for variation in K_V as shown in Fig. 6. However, in the case of K_P , increasing the gain, monotonically decreases the value of $|e_{max}|$. A typical time response of the crane motion compensation is shown in Fig. 8.

In order to study the influence of K_A , K_V and K_P for various excitation frequencies, the

system simulation was repeated with a constant roll amplitude of $+15^\circ$ and the frequency varied from 0.025 Hz to 25 Hz. The results are presented in Figs. 9, 10 and 11 which indicate a characteristic similar to the relative displacement transmissibility plot of the single degree of freedom active system as shown in Fig. 4(b).

OPTIMAL SELECTION OF K_A , K_V AND K_P IN PID CONTROLLER

The design objective in the active stabilization of a ship borne crane is to minimize the vertical movement of the boom tip, Y_B by adjusting the gains, K_A , K_V and K_P of the PID controller. Although the ships' roll motions induced by wave action are complex, they are typically dominated by sinusoidal motions with $+15^\circ$ amplitude and 0.25 Hz [2]. Then, it is proposed in this paper to identify the optimal gains, for the motion controller, K_A^* , K_V^* and K_P^* using the sinusoidal motion outlined above. Mathematically this problem can be posed as a non-linear programming problem as:

Objective Function:

$$\text{Min} \left[\int_0^t (Y_B - Y_{BR})^2 dt \right]$$

$$K_A^*, K_V^*, K_P^*$$

where $t = 8s$, (two wave cycles)

Subject to Constraints:

$$(K_A^*)_{\text{lower}} \leq K_A^* \leq (K_A^*)_{\text{upper}}$$

$$(K_V^*)_{\text{lower}} \leq K_V^* \leq (K_V^*)_{\text{upper}}$$

$$(K_P^*)_{\text{lower}} \leq K_P^* \leq (K_P^*)_{\text{upper}}$$

The lower and upper bounds in the constraints are selected in such a way that the system stability is not affected.

OPTIMIZATION ALGORITHM

In this work, a modified sequential simplex optimization method is used which has a flexible rather than a rigid geometric simplex of points. This method is also referred to as the 'complex' method and is attractive not only because of its ease of programming, efficiency, and flexibility, but also because of its ability to provide global information [4, 5, 6]. The optimization procedure is outlined below:

1. Minimize $F(\hat{X})$, $\{\hat{X}\} = \{x_1, x_2, x_3, \dots, x_p\}$

where $\{\hat{X}\}$ is a vector of variables

x_1, x_2, \dots, x_p to be optimized subject to

$$a_i \leq x_i \leq b_i \quad ; i = 1, 2, \dots, p$$

$$g_j(\hat{X}) \geq 0 \quad ; j = 1, 2, \dots, q$$

2. The method requires the use of $k > p + 1$ vertices, each of which must satisfy all the imposed constraints. These vertices may be initially found by starting at a point that satisfies all constraints. The remaining $k - 1$ points in the first complex are obtained by the use of pseudorandom number r_i in the relation

$$x_i = a_i + r_i(b_i - a_i) \quad ; i = 2, \dots, k$$

where r_i are uniformly distributed over the interval [0.1]. These points satisfy the lower and upper bound constraints. If some implicit constraints are violated, then the trail point is moved halfway toward the centroid of the already accepted points. The centroid \hat{X} is given by

$$\hat{X} = \frac{1}{s} \sum_{k=1}^s \hat{X}^k$$

where $\hat{X}^1, \hat{X}^2, \dots, \hat{X}^s$ are available feasible vertices. The superscripts represent vertex number. For example, in a two-dimensional optimization,

i.e.,

$$\{\hat{X}\} = \{x_1, x_2\} \quad ; \hat{X}^k \text{ represents } (x_1^k, x_2^k).$$

3. The objective function $F(\hat{X})$ to be minimized is evaluated at each vertex and the vertex \hat{X}^v at which the function $F(\hat{X})$ assumes the largest value is reflected by computing

$$\hat{X}^r = (1 + \alpha)\hat{X}^0 - \hat{X}^v \quad ; \alpha \geq 1$$

where \hat{X}^0 is the centroid of the remaining vertices and calculated from

$$\hat{X}^0 = \frac{1}{k-1} \sum_{i=1}^k \hat{X}^i$$

A recommended value for the over-reflection coefficients α is 1.3 but the choice is not critical [4].

4. If the function value $F(\hat{X}^r) \geq F(\hat{X}^v)$ and \hat{X}^r is feasible, replace the point \hat{X}^r with \hat{X}^v and repeat Step 2. If $F(\hat{X}^r) < F(\hat{X}^v)$, the over-reflection is reduced to $\alpha/2$, and the new \hat{X}^r is computed and tried. This is repeated until $\alpha < \beta$, where $\beta = 10^{-5}$ is a satisfactory value. If the reflection $F(\hat{X}^r) \geq F(\hat{X}^v)$ does not hold even for that small value of α , then the projected point \hat{X}^r is replaced by the original value \hat{X}^v and the second worst vertex is reflected instead. This process keeps the complex moving toward the minimum unless the centroid is very close to it.

5. For a nonconvex function, the centroid of all the feasible points may not itself be feasible. In this case all the points of the complex are discarded except \hat{X}^e , the point at which the objective function was the lowest value. Then a new complex is generated by using

$$x_i^k = x_i^e + r_i(x_i^0 - x_i^e) \quad ; \quad i = 1, 2, \dots, p$$

where $[\hat{x}^0: x_1^0, x_2^0, \dots, x_p^0]$ is the old infeasible centroid.

6. The process is terminated when the complex shrinks to an acceptable small size; such a termination criterion can be expressed as

$$\frac{1}{k} \left\{ \sum_{i=1}^k [F(\hat{x}^0) - F(\hat{x}^k)]^2 \right\}^{1/2} \leq \epsilon$$

where $\epsilon > 0$ is a predetermined small convergence number.

OPTIMIZATION RESULTS AND DISCUSSION

The optimization technique outlined was programmed in Fortran and used as a function retrieval in Mimic main programming. The optimal values obtained are listed in Table 2. The optimal adjustment of the controller resulted in the improvement of the motion-compensation. The integral of the square of the error calculated over a period of 2 wave cycles (8 s) listed in Table 2 indicate that the performance is quite impressive and has improved almost 94% over the initial choice. If it is further desired to reduce the steady-state misalignment of the crane boom, one can introduce an acceleration feed-forward compensation. Such a study will be extended in our future investigation.

CONCLUSION

The computer-aided design study of a simple 1-axis active stabilization of a ship-borne crane is successfully accomplished. The system is simple and uses a single variable sensing of boom tip, i.e., acceleration of boom tip. The study serves as a basis for a scaled hardware model. It is shown that when a PID controller is employed, a satisfactory performance can be expected. The system can be easily expanded to 2- or 3-axis motion compensation. The study also indicates an optimization strategy for minimizing the integral of square of error between the instantaneous vertical position of the boom tip and a reference position. The results show that by selecting optimal gains of the PID controller, the performance index can be improved over 94%.

ACKNOWLEDGMENT

This work was supported by the Natural Sciences and Research Council of Canada grants number A3685 and A4213.

REFERENCES

- [1] T.P. Neal and W.S. Schaefer, "Vertical Stabilization of a Ship-Mounted 200 Ton Derrick," National Conference on Fluid Power, Philadelphia, Pa., Nov. 1978.

- [2] C.R. Burrows and T.P. Adams, "Control of Flexibly Mounted Stabilization Platform," ASME Transactions, J. Dynamic Systems, Measurement and Control, pp. 174-182, Sept. 1977.
- [3] W.D.R. Thomas, "Ship Crane Compensates for Heavy Weather", Design Engineering, Engineering Institute of Canada, pp. 47-48, Oct. 1978.
- [4] Box, M.J., "A New Method of Constrained Optimization and a Comparison with Other Methods", Computer J. No. 8, pp. 42-52, 1965.
- [5] Michaud, D. and Modrey, J., "A Designer-Augmented Optimization Strategy: Concept of Implementation", ASME Paper No. 75-DET-99, 1975.
- [6] Sankar, S. and Hargreaves, D.R., "Hybrid Computer Optimization of a Class of Impact Absorbers", Simulation, Vol. 33, No. 1, 1979.

NOMENCLATURE

- $A_{11,12,2,3}$ = actuator piston areas (m^2)
- A_V = servovalve metering area (m^2)
- A_{VB} = balance valve metering area (m^2)
- \overline{AB} = boom length (m)
- \overline{AC} = boom portion length (m)
- \overline{AD} = mast height (m)
- \overline{CD}_0 = actuator length (initial) (m)
- C_D = valve discharge coefficient
- F_F = actuator friction force (N)
- F_H = actuator net force (N)
- F_L = load force (N)
- I_R = controller output (Amp)
- K_A = acceleration gain ($\text{Amp}\cdot\text{s}^2/\text{m}$)
- K_B = balance valve gain (m/Pa)
- K_I = servovalve gain (m/Amp)
- K_P = position gain (Amp/m)
- K_V = velocity gain ($\text{Amp}\cdot\text{s}/\text{m}$)
- K_X = servovalve spool gain (m^2/m)
- K_{XB} = balance valve spool gain (m^2/m)
- M_I = reflected load inertia mass (kg)
- P_A = accumulator pressure (Pa)

P_0 = return pressure (Pa)	\dot{Y}_{BR} = boom tip vertical displacement reference signal (m)
P_S = supply pressure (Pa)	Y_H = actuator displacement (m)
$P_{1,2}$ = actuator pressures (pa)	\dot{Y}_B = boom tip vertical velocity (m/s)
Q_B = balance valve flowrate (m ³ /s)	\dot{Y}_{BR} = boom tip vertical velocity reference signal (m/s)
$Q_{1,2}$ = actuator flowrates (m ³ /s)	\dot{Y}_H = actuator velocity (m/s)
t = time (s)	\ddot{Y}_B = boom tip vertical acceleration (m/s ²)
V_A = accumulator gas volume (m)	\ddot{Y}_{BR} = boom tip vertical acceleration reference signal (m/s ²)
V = actuator volumes (m)	α = angle between \overline{CD} and \overline{AB} (rad)
W = load weight (N)	β = oil effective bulk modulus (Pa)
\dot{W}_H = hydraulic power (W)	ϕ = boom angle (rad)
X_Y = servovalve spool displacement (m)	ρ = oil density (kg/m ³)
X_{VB} = balance valve spool displacement (m)	θ = ship roll angle (rad)
X_{VR} = servovalve spool displacement reference signal (m)	τ_Y = servovalve time constant (s)
Y_B = boom tip vertical displacement (m)	

TABLE 1: PARAMETERS OF THE MOTION COMPENSATED SHIP-BORNE CRANE

$A_{11}-A_{12} = 1.89 \times 10^{-3} \text{ m}^2$	$C_D = 0.6$	$W = 196 \times 10^3 \text{ N}$
$A_2 = 13.82 \times 10^{-3} \text{ m}^2$	$P_S = 20.7 \times 10^6 \text{ Pa}$	$\beta = 700 \times 10^3 \text{ Pa}$
$A_3 = 15.71 \times 10^{-3} \text{ m}^2$	$V_{Amax} = 50 \times 10^{-3} \text{ m}^3$	$\tau_Y = 0.02 \text{ s}$
$\overline{AB} = 8.0 \text{ m}$	$V_1 = 15 \times 10^{-3} \text{ m}^3$	
$\overline{AO} = 15.0 \text{ m}$	$V_2 = 15 \times 10^{-3} \text{ m}^3$	

TABLE 2: OPTIMAL VALUE OF K_A , K_V and K_P

PARAMETER	QUANTITY	
	PRELIMINARY ADJUSTMENT	OPTIMUM ADJUSTMENT
Acceleration gain K_A	$25.7 \times 10^{-3} \text{ Amp-s}^2/\text{m}$	$20.6 \times 10^{-3} \text{ Amp-s}^2/\text{m}$
Velocity gain K_V	0.1056 Amp-s/m	0.1990 Amp-s/m
Position gain K_P	$7.27 \times 10^{-3} \text{ Amp/m}$	$85.4 \times 10^{-3} \text{ Amp/m}$
Error = $\int_0^t (Y_B - Y_{BR})^2 dt$ (over 2 wave cycles)	$750.0 \times 10^{-3} \text{ m}$	$45.7 \times 10^{-3} \text{ m}$

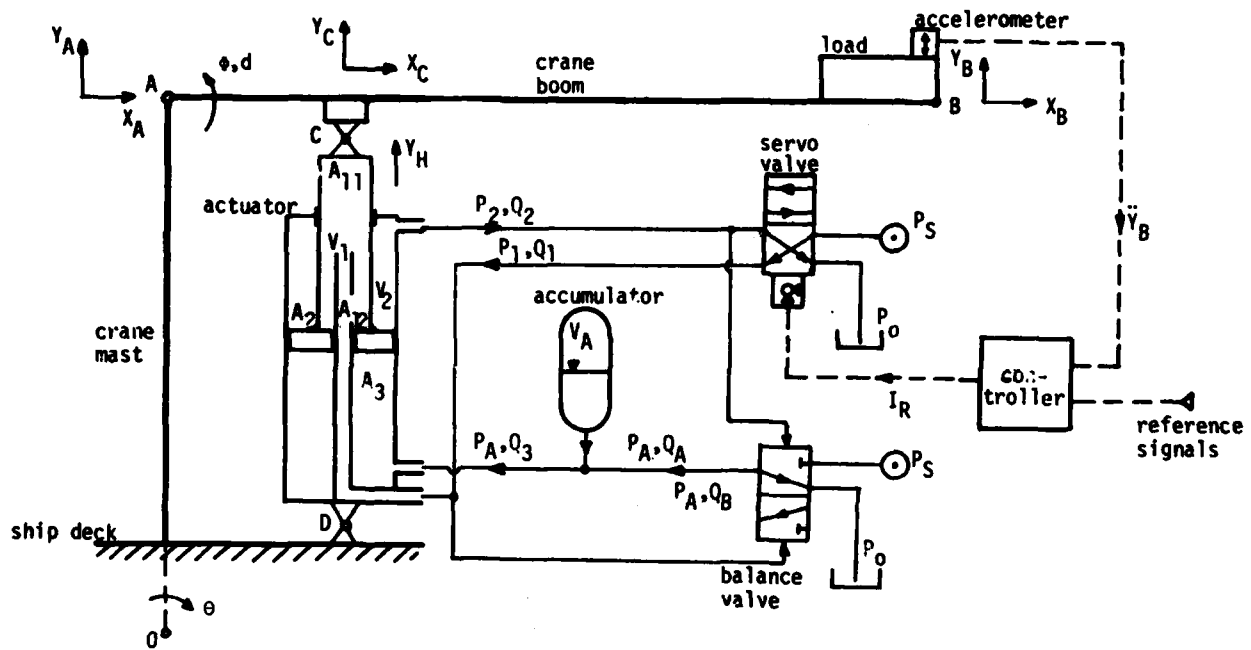


Fig. 1: Schematic Diagram of Motion Compensated Crane

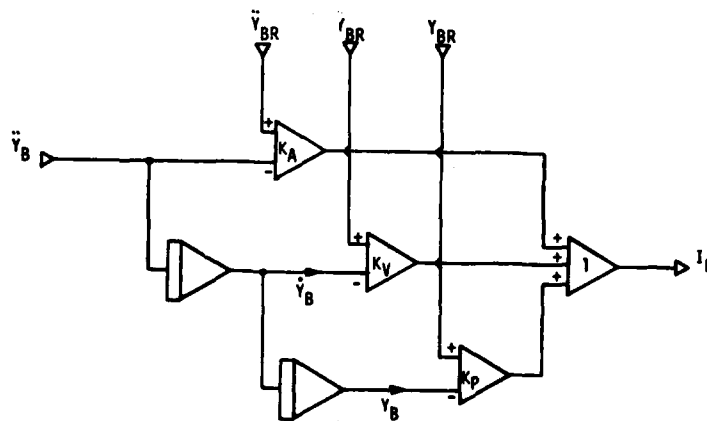


Fig. 2: Crane Controller Design

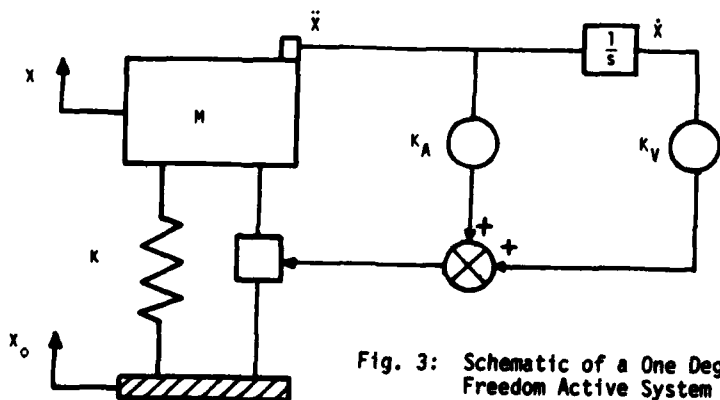


Fig. 3: Schematic of a One Degree of Freedom Active System

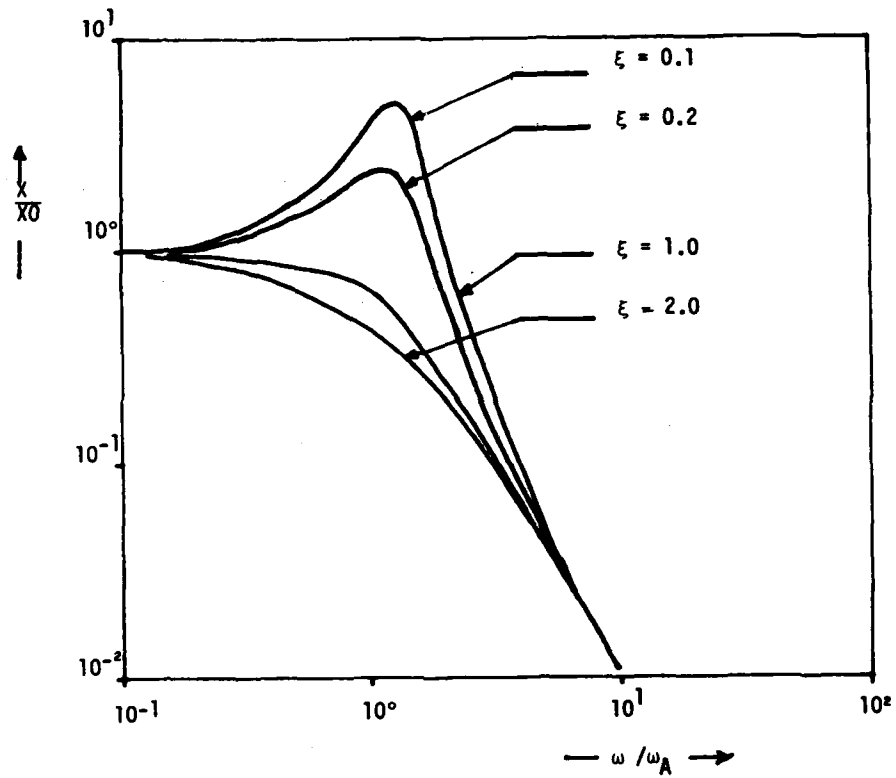


Fig. 4a: Absolute Displacement Transmissibility of a 1 DOF Active System

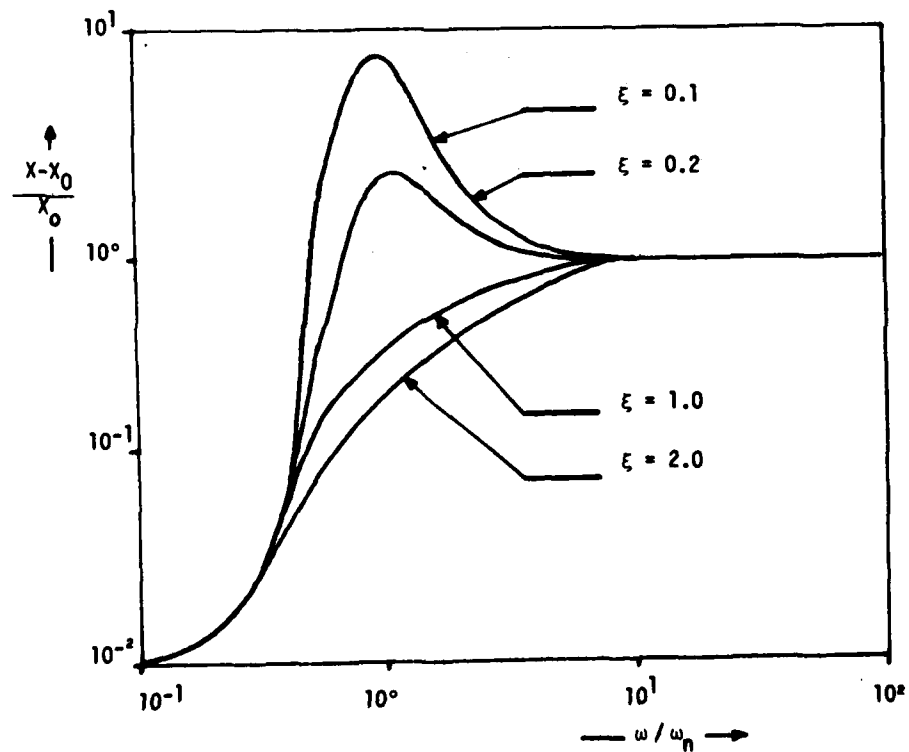


Fig. 4b: Relative Displacement Transmissibility of a 1 DOF Active System

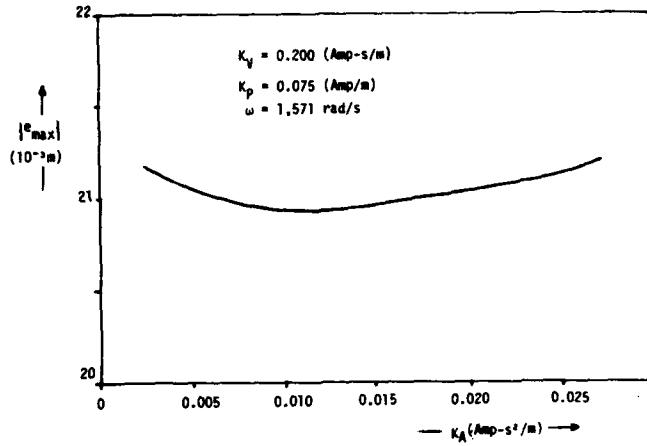


Fig. 5: Effect of Gain K_A for Constant K_V and K_P

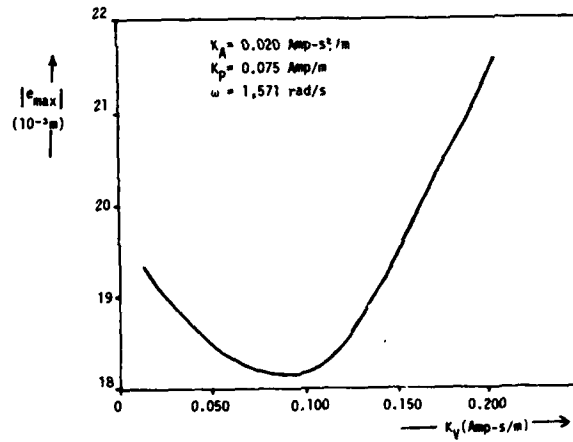


Fig. 6: Effect of Gain K_V for Constant K_A and K_P

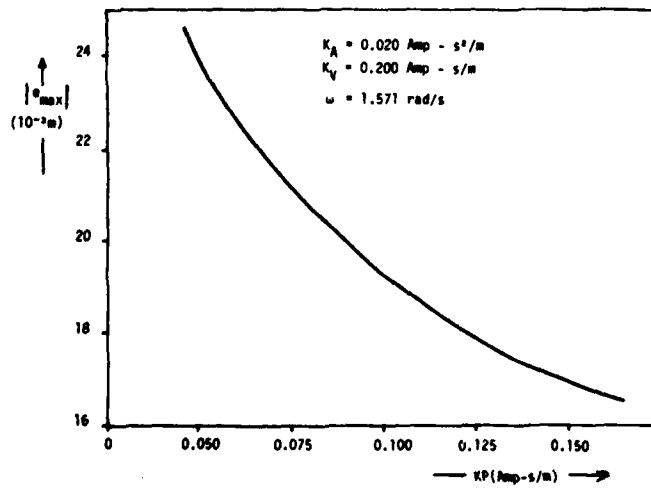


Fig. 7: Effect of Gain K_P for Constant K_A and K_V

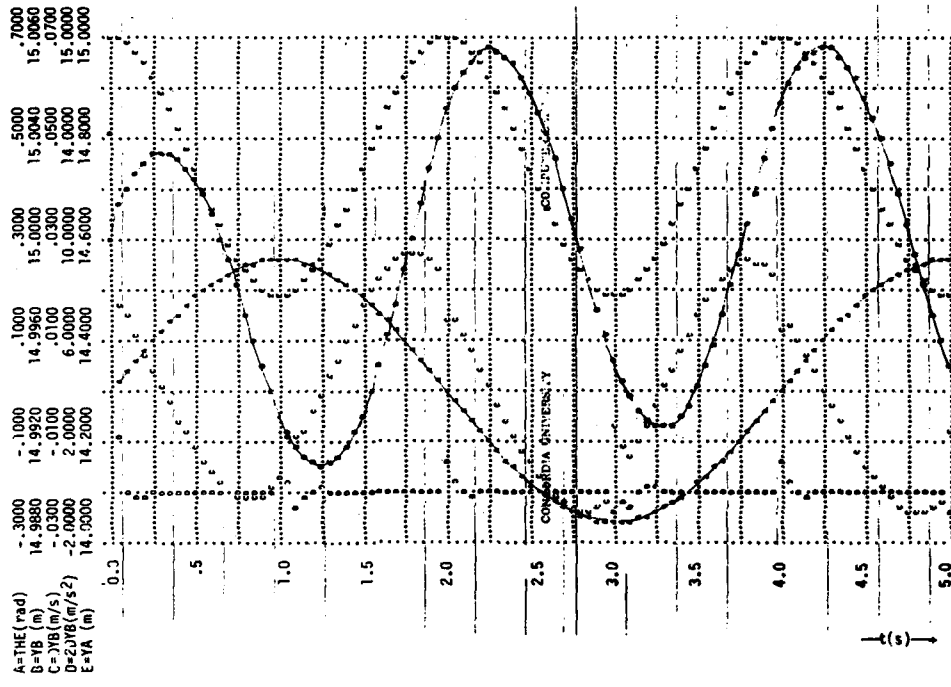


Fig. 8: Response of Crane Boom for Sinusoidal Input

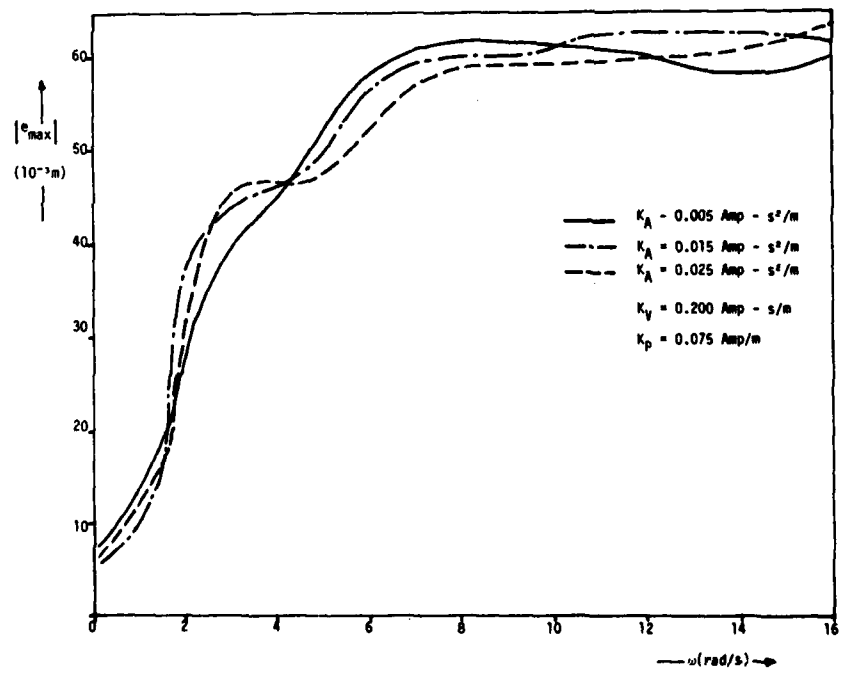


Fig. 9: Plot of $|e_{max}|$ vs ω for K_A Variation

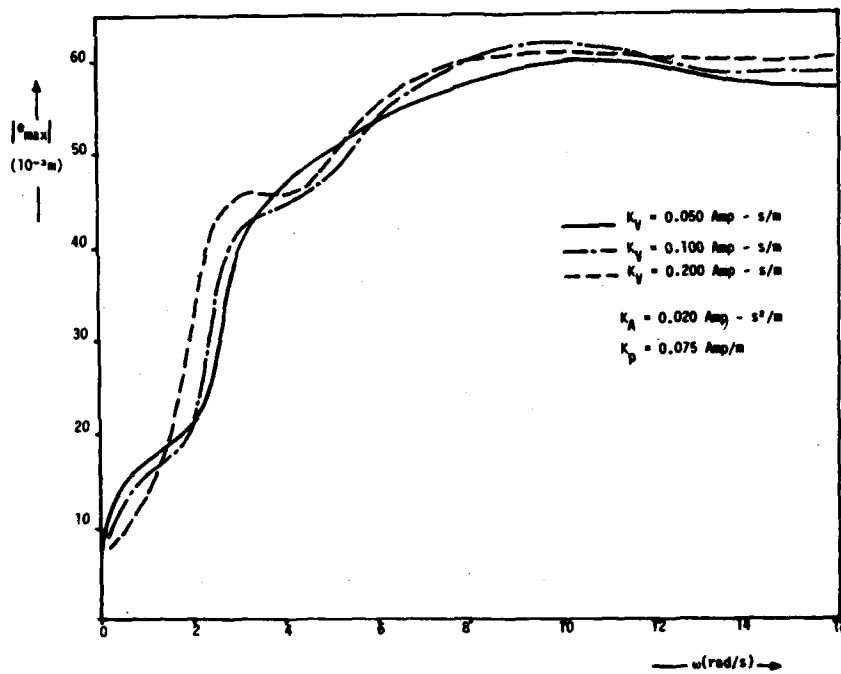


Fig. 10: Plot of $|e_{max}|$ vs ω for K_V Variation

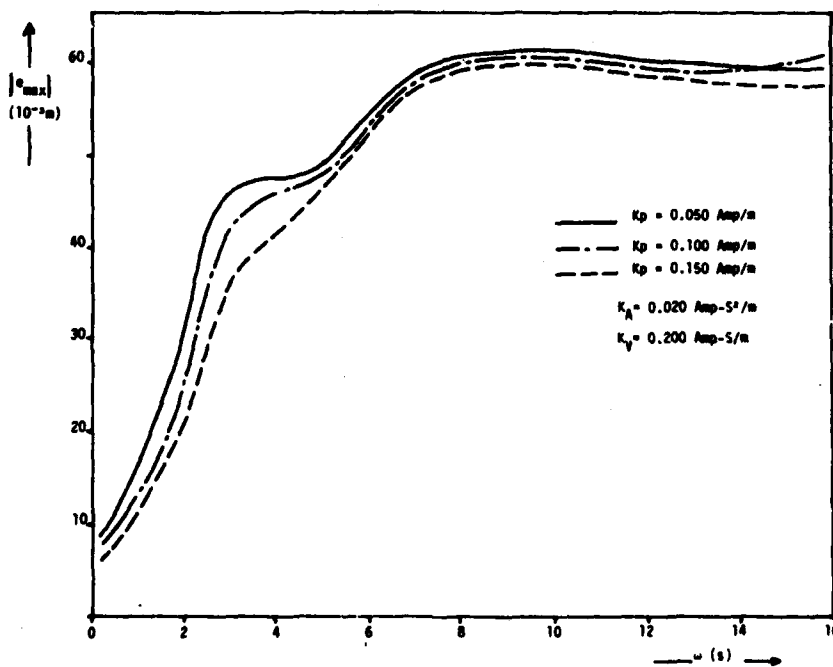


Fig. 11: Plot of $|e_{max}|$ vs ω for K_D Variation